

Les Rencontres de Physique de la Vallée d'Aoste

Results and Perspectives in Particle Physics

edited by M. Greco

La Thuile, Aosta Valley

February 28th - March 6th, 2010



ISTITUTO NAZIONALE DI FISICA NUCLEARE
Laboratori Nazionali di Frascati

Les Rencontres de Physique de la Vallée d'Aoste

Results and Perspectives in Particle Physics



FRASCATI PHYSICS SERIES

Series Editor

Daniilo Babusci

Technical Editor

Marcella Missiroli

Volume LII - Special Issue

Jointly published by:

Istituto Nazionale di Fisica Nucleare - Laboratori Nazionali di Frascati
Divisione Ricerca - SIS - Ufficio Pubblicazioni
P.O. Box 13, I-00044 Frascati (Roma) Italy
Luigina Invidia: sis.publications@lnf.infn.it

Società Italiana di Fisica
Via Saragozza 12, I-40123 Bologna, Italy
<http://www.sif.it>

FRASCATI PHYSICS SERIES

Les Rencontres de Physique de la Vallée d'Aoste

RESULTS AND PERSPECTIVES IN PARTICLE PHYSICS

Copyright © 2011 SIF, Bologna – INFN-Laboratori Nazionali di Frascati
SIS-Ufficio Pubblicazioni

All rights reserved. No part of this publication may be reproduced, stored in a retrieval system or transmitted in any form or by any means, electronic, mechanical, photocopying, recording or otherwise, without the prior permission of the copyright owner.

ISBN: 978-88-7438-060-2

Printed in Italy by Compositori Industrie Grafiche
Via Stalingrado 97/2
40128 Bologna

FRASCATI PHYSICS SERIES

Volume LII

**Les Rencontres de Physique
de la Vallée d'Aoste**

Results and Perspectives in Particle Physics

Editor
Mario Greco

La Thuile, Aosta Valley, February 28th - March 6th, 2010

Conference Organizers

Giorgio Bellettini	Pisa
Giorgio Chiarelli	Pisa
Mario Greco	Roma Tre
Gino Isidori	Laboratori Nazionali di Frascati

Chairpersons

Giorgio Apollinari	Fermilab
Giorgio Bellettini	Pisa
Giorgio Chiarelli	Pisa
Flavio Costantini	Pisa
Maria Curatolo	Laboratori Nazionali di Frascati
Mario Greco	Roma Tre
Gino Isidori	Laboratori Nazionali di Frascati
Tuula Maki	CERN
Mosè Mariotti	Padova
Matey Mateev	Sofia
Victor Novikov	Moscow
Giovanni Punzi	Pisa

Preface

The 2010 Rencontres de Physique de la Vallée d’Aoste were held at the Planibel Hotel of La Thuile, Aosta Valley, on February 28th - March 6th, with the twenty-fourth edition of “Results and Perspectives in Particle Physics”.

The physics programme included various topics in particle physics, also in connection with present and future experimental facilities, as cosmology and astrophysics, neutrino physics, CP violation and rare decays, electroweak and hadron physics with e^+e^- and hadron colliders, heavy flavours, search for new physics and prospects at future facilities.

The Session on “Physics and Society” included special colloquia on “Global Energy Observatory: a One-Stop Site for Information on Global Energy Systems” and “The Energy Problem: a Cost/Financial Approach”. We are very grateful to Rajan Gupta and Alberto De Min for their participation and contribution.

Also a Round Table discussion on the “Role of the Tevatron in the LHC Era” was organized with the participation of Sergio Bertolucci, Dmitri Denisov, Fabiola Gianotti, Andrey Golutvin, Young-Kee Kim, Jacobo Konigsberg and Chris Quigg.

Giorgio Bellettini, Giorgio Chiarelli, Gino Isidori and I would like to warmly thank the session chairpersons and the speakers for their contribution to the success of the meeting.

The regional government of the Aosta Valley, in particular through the Minister of Public Education and Culture, Laurent Vierin, has been very pleased to offer its financial support and hospitality to the Rencontres of La Thuile. Also on behalf of the participants, representatives of some major Laboratories and Institutes in the world, we would like to thank all the Regional Authorities. Special thanks are also due to Bruno Baschiera, local coordinator of the Rencontres.

We are grateful to the President of INFN Roberto Petronzio, the Directors of INFN Laboratori Nazionali di Frascati, Mario Calvetti and INFN Sezione di Pisa, Giovanni

Batignani, for the support in the organization of the Rencontres. We would like to thank also Cristina D'Amato, Lucia Lilli, Claudia Tofani and Paolo Villani for their help in both planning and running the meeting. We are also grateful to Alessandra Miletto for her valuable contribution to the local organization of the meeting. The excellent assistance provided by Mauro Giannini made it possible to set up the computer link to the international network.

Finally we would like to thank the Mayor Gilberto Roulet and the local authorities of La Thuile and the "Azienda di Promozione Turistica del Monte Bianco" for their warm hospitality, and the Planibel Hotel staff for providing us with an enjoyable atmosphere.

November 2010

MARIO GRECO

CONTENTS

M. GRECO – Preface.....	page	VII
SESSION I - COSMOLOGY AND ASTROPHYSICS		
R. SPARVOLI for the PAMELA COLLABORATION – Understanding cosmic rays and searching for dark matter with PAMELA.....	”	1
L. LATRONICO on behalf of the FERMI-LAT COLLABORATION – Studies of cosmic ray electrons with the Fermi-LAT.....	”	11
J. KNÖDLSIEDER on behalf of the FERMI LARGE AREA TELESCOPE COLLABORATION – Studies of gamma-ray sources with the Fermi Large Area Telescope.....	”	19
F. FERRONI – LUCIFER: A new technique for Double Beta Decay.....	”	27
M. CIRELLI – Recent developments in theory and phenomenology of Dark Matter..	”	35
SESSION II - ASTROPARTICLE AND NEUTRINO PHYSICS		
IOANA C. MARIŞ for the PIERRE AUGER COLLABORATION – Results from the Pierre Auger Observatory.....	”	45
E. BEHAR, S. DADO, A. DAR and A. LAOR – The missing cosmic baryons found? .	”	53
N. PICOT CLÉMENTE on behalf of the ANTARES COLLABORATION – The ANTARES deep-sea neutrino telescope—Status and first results.....	”	61
A. IBARRA – Neutrino physics and lepton flavour violation: A theoretical overview .	”	67
E. PENNACCHIO on behalf of the OPERA COLLABORATION – Neutrino oscillations studies with the OPERA experiment at the CNGS beam.....	”	77
Y. SUVOROV on behalf of the BOREXINO COLLABORATION – New results and strategy of Borexino.....	”	85
S. MIHARA – J-PARC kaon and muon programs.....	”	91
D. GREINER for the DOUBLE CHOOZ COLLABORATION – Towards Θ_{13} with Double Chooz.....	”	99
JONATHAN M. PALEY for the MINOS COLLABORATION – Recent results and future prospects for the MINOS experiment.....	”	107
SESSION III - QCD PHYSICS/HADRONIC INTERACTIONS		
M. LAMONT – Turning on the LHC: Commissioning with beam and the outlook for 2010.....	”	115
F. PRINO for the ALICE COLLABORATION – Early physics with ALICE.....	”	123
S. ROLLI – QCD results from the Fermilab Tevatron $p\bar{p}$ Collider.....	”	131
KAI YI for the D0 and CDF COLLABORATIONS – Heavy flavor spectroscopy at the Tevatron.....	”	141

F. AMBROSINO, A. ANTONELLI, M. ANTONELLI, F. ARCHILLI, P. BELTRAME, G. BENCIVENNI, C. BINI, C. BLOISE, S. BOCCHETTA, F. BOSSI, P. BRANCHINI, G. CAPON, T. CAPUSSELA, F. CERADINI, P. CIAMBRONE, E. DE LUCIA, A. DE SANTIS, P. DE SIMONE, G. DE ZORZI, A. DENIG, A. DI DOMENICO, C. DI DONATO, B. DI MICCO, M. DREUCCI, G. FELICI, S. FIORE, P. FRANZINI, C. GATTI, P. GAUZZI, S. GIOVANNELLA, E. GRAZIANI, M. JACEWICZ, G. LANFRANCHI, J. LEE-FRANZINI, M. MARTINI, P. MASSAROTTI, S. MEOLA, S. MISCETTI, M. MOULSON, S. MÜLLER, F. MURTAS, M. NAPOLITANO, F. NGUYEN, M. PALUTAN, A. PASSERI, V. PATERA, P. SANTANGELO, B. SCIASCIA, T. SPADARO, L. TORTORA, P. VALENTE, G. VENANZONI, R. VERSACI and G. XU – Low energy QCD and ChPT studies with KLOE	”	149
JIA XU ZUO for BESIII COLLABORATION – Recent results from BESIII	”	159

SESSION IV - FLAVOUR PHYSICS, CP VIOLATION AND RARE DECAYS

J. BENITEZ on behalf of the BABAR COLLABORATION – Recent results on flavor physics from BaBar	”	171
K. NISHIMURA on behalf of the BELLE and BABAR COLLABORATIONS – Rare decays at the B factories	”	179
D. BERNARD – QCD and hadronic interactions with initial-state radiation at B-factories	”	187
U. NIERSTE – Flavour physics within and beyond the Standard Model	”	195
U. KERZEL – Early data from the LHCb experiment	”	205
E. MARINOVA on behalf of NA48/2 and NA62 COLLABORATIONS – K rare decays with NA62	”	213
B. SCIASCIA for the KLOE COLLABORATION – Kaon physics with KLOE	”	221
C. M. TARBERT for the CLEO COLLABORATION – Recent charmonium results from CLEO-c	”	229

SESSION V - ELECTROWEAK AND TOP PHYSICS

A. WILDAUER on behalf of the ATLAS COLLABORATION – Start-up and first physics results with the ATLAS detector at the LHC	”	239
P. CATASTINI on behalf of the CDF and D0 COLLABORATIONS – Electroweak Physics at the Tevatron	”	247
A. MELNITCHOUK for the CDF and D0 COLLABORATIONS – W mass and width measurements at the Tevatron	”	255
D. WICKE for the CDF and D0 COLLABORATIONS – Single and double top quark production at the Tevatron	”	263
G. COMPOSTELLA on behalf of the CDF and DØ COLLABORATIONS – Top quark properties at the Tevatron	”	271

SESSION VI - HIGGS SEARCHES, HOT TOPICS

SONG-MING WANG for the CDF and DØ COLLABORATIONS – Searches for low mass Higgs boson at the Tevatron	”	283
A. DE RÚJULA – To be or not to be: Higgs impostors at the LHC	”	293

SESSION VII - SEARCHING FOR NEW PHYSICS

C. W. BAUER, Z. LIGETI, M. SCHMALTZ, J. THALER and D. G. E. WALKER – New Physics with earliest LHC data	”	303
G. PIREDDA on behalf of the MEG COLLABORATION – First results from the MEG experiment	”	311
B. GOLOB – Super KEKB/Belle II Project	”	319
C. QUIGG – Looking into particle production at the Large Hadron Collider	”	327
P. SPAGNOLO – Search for neutral Higgs bosons decaying into four taus at LEP2 ...	”	335
M. V. CHIZHOV, V. A. BEDNYAKOV and J. A. BUDAGOV – Anomalously interacting extra neutral bosons	”	343

SESSION VIII - PHYSICS AND SOCIETY

R. GUPTA – The Global Energy Observatory: A one-stop site for information on global energy systems	”	353
--	---	-----

SESSION IX - PERSPECTIVES

M. S. ZISMAN – The muon collider	”	365
M. L. PERL – The possible detection of dark energy on earth using atom interferometry	”	375
Participants	”	383

SESSION I - COSMOLOGY AND ASTROPHYSICS

- Roberta Sparvoli* Understanding cosmic rays and searching for dark matter with PAMELA
- Luca Latronico* Studies of cosmic ray electrons with the Fermi-LAT
- Jürgen Knödlseher* Studies of gamma-ray sources with the Fermi Large Area Telescope
- Fernando Ferroni* LUCIFER: A new technique for Double Beta Decay
- Marco Cirelli* Recent developments in theory and phenomenology of Dark Matter

Understanding cosmic rays and searching for dark matter with PAMELA

R. SPARVOLI for the PAMELA COLLABORATION

INFN and Dipartimento di Fisica dell'Università di Roma "Tor Vergata" - I-00133 Rome, Italy

(ricevuto il 14 Settembre 2010; pubblicato online il 5 Gennaio 2011)

Summary. — The instrument PAMELA, in orbit since June 15th, 2006 on board of the Russian satellite Resurs DK1, is delivering to ground 16 Gigabytes of data every day. The apparatus is designed to study charged particles in the cosmic radiation, with a particular focus on antimatter and signals of dark matter annihilation. A combination of a magnetic spectrometer and different detectors allows antiparticles to be reliably identified from a large background of other charged particles. After 4 years of operation in flight, PAMELA is now delivering coherent results about spectra and chemical composition of the charged cosmic radiation, allowing scenarios of production and propagation of cosmic rays to be fully established and understood.

PACS 95.55.Vj – Neutrino, muon, pion, and other elementary particle detectors; cosmic ray detectors.

PACS 98.80.Cq – Particle-theory and field-theory models of the early Universe (including cosmic pancakes, cosmic strings, chaotic phenomena, inflationary universe, etc.).

PACS 12.60.Jv – Supersymmetric models.

1. – Introduction

One hundred years ago Victor Hess discovered cosmic rays and, from that moment, an impressive experimental study began. Cosmic rays are associated with the most impulsive events in the Universe, and the energies of the observed particles far exceed those reached by the most powerful accelerators at ground. Their chemical composition and energy spectrum give extensive information about their origin, acceleration and propagation mechanisms.

Twenty-one orders of magnitude in energy have been explored up to now, by direct methods—balloon-borne and satellite experiments—up to 10^{14} eV and by indirect methods—ground large-size apparatus—at the highest energies. At medium energy the study is focused on the search of antimatter as a unique tool to investigate several physics and astrophysics phenomena. The search of antimatter is indeed strictly connected with the baryon-antibaryon asymmetry in the Universe, and the detection of antimatter of

primary origin in cosmic rays would be a discovery of fundamental significance. Other possible contributions could come from evaporation of primordial mini black holes by the Hawking process or from exotic particles annihilation, this last having been a very hot physics topic for the last 10 years.

Several observations show that the Universe is prominently composed of dark matter and dark energy. Among the most plausible candidates for dark matter there are weakly interacting massive particles (WIMP), with the supersymmetric neutralino as a favourite candidate. The neutralino arises naturally in supersymmetric extensions of the standard model, and has the attractive feature of giving a relic density adequate to explain cosmological dark matter in a large region of the parameter space. Neutralinos are Majorana fermions and can annihilate in the halo, resulting in a symmetric production of particles and antiparticles, the latter providing an observable signature. Other models of WIMPs privilege lightest Kaluza-Klein particles in the Universal Extra Dimension scenario.

These ideas had a great improvement from the discovery of antiprotons on the top of the atmosphere made from Robert Golden [1] and Edward Bogomolov [2] in 1979 by balloon-borne experiments. They measured a rate of antiprotons much higher than expected from interactions of cosmic rays with the interstellar matter. Many other experiments followed these pioneer ones, performed mainly from the WiZard, HEAT and BESS Collaborations on board balloons, and from AMS-01 on board the Shuttle, using novel techniques developed for accelerator physics. Although the first historical results were not confirmed later, the way for a wide research for primary antimatter and dark matter signals in the cosmic rays was open.

However, possible contributions from dark matter annihilation or other exotic sources are mixed with a huge background produced in the interactions of cosmic rays with the ISM, so that they appear as a distortion of the antiproton and positron energy spectra. Then, a better knowledge of the standard mechanisms of production, acceleration and transport of cosmic rays is required.

New satellite experiments have been devised with the task to measure antiprotons and positrons, but also experimental parameters included in the background calculation. In June 2006 the first of these satellite, PAMELA, was launched in orbit by a Soyuz-U rocket from the Bajkonur cosmodrome in Kazakhstan. The PAMELA experiment is performed by an international collaboration composed by Italy, Russia, Germany and Sweden. Conceived mainly for searching primordial antimatter, signals from dark matter annihilation, exotic matter as strangelets, PAMELA achieves also other important tasks as the study of the mechanisms of acceleration and propagation of cosmic rays in the Galaxy, the cosmic ray solar modulation, the detection of solar flares. Studies of the interaction of particles with the terrestrial magnetosphere complete the PAMELA research program.

2. – The PAMELA instrument

An overview of the PAMELA apparatus is shown in fig. 1. The core of the instrument is a magnetic spectrometer, made of a permanent magnet and a silicon tracking system for a maximum detectable rigidity of 1 TV. A time-of-flight system consisting of three double layers of segmented plastic scintillator provides timing and dE/dx measurements and defines the primary PAMELA trigger. The separation between hadronic and leptonic components is made by an imaging silicon-tungsten detector and a neutron counter. An imaging silicon calorimeter and a neutron detector assures a rejection of protons, compared to positrons, at the order of 10^5 . The calorimeter permits also measurements of

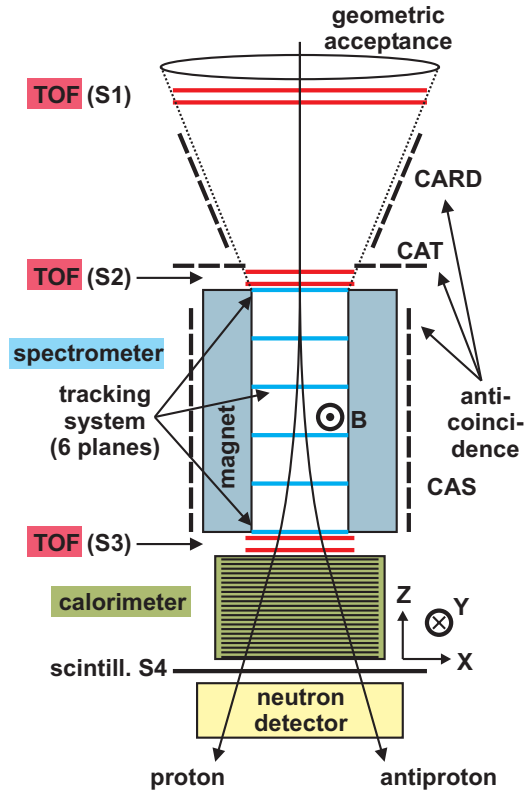


Fig. 1. – Schematic overview of the PAMELA apparatus.

the electron energy up to 300 GeV, with a resolution of few per cent. A thick scintillator placed between the calorimeter and the neutron counters and an anticoincidence system complete the instrument. PAMELA can measure electrons, positrons, antiprotons, protons and light nuclei in an energy range from tens MeV up to hundreds GeV. More details can be found in [3].

PAMELA has been inserted in a pressurized vessel and installed on board of the Russian satellite DK-1 dedicated to Earth observation. It was launched on June 15th 2006 in an elliptical orbit, ranging between 350 and 610 km and with an inclination of 70 degrees. Since July 2006 PAMELA is daily delivering 16 Gigabytes of data to the Ground Segment in Moscow.

3. – Data analysis and results

The results presented here correspond to the data-set collected between July 2006 and December 2008. More than 10^9 triggers were accumulated during a total acquisition time of approximately 500 days.

3.1. Antimatter (antiprotons and positrons). – Particle identification in PAMELA is based on the determination of the rigidity with the spectrometer and the properties of the energy deposit and interaction topology in the calorimeter. One source of background

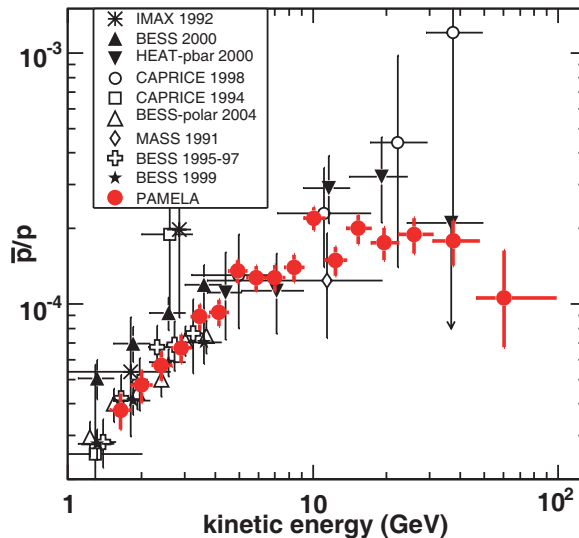


Fig. 2. – PAMELA antiproton-to-proton flux ratio compared with previous measurements [4].

in the antimatter samples comes from spillover (protons in the antiproton sample and electrons in the positron sample). This originates from incorrect determination of the charge sign due to the intrinsic deflection uncertainty in spectrometer measurements at the highest energies and to a possible multiple scattering of the particles in the tracking system. This limits the rigidity interval in which the measurements can be performed. Another source of background comes from the misidentification of like-charged particles (electrons in the antiproton sample and protons in the positron sample).

In order to accurately measure antiprotons, the spillover was eliminated by imposing a set of strict selection criteria on the quality of the fitted tracks. Electrons in the antiproton sample have been rejected by applying conditions on the calorimeter shower topology. The measured antip/p ratio is shown in fig. 2 compared with recent results from other experiments (see [4] and references therein). The ratio increases smoothly from about 4×10^{-5} at a kinetic energy of 1 GeV and levels off at about 1×10^{-4} for energies above 10 GeV. The data do not present the features or structures expected from exotic sources, so they place strong limits to dark matter annihilation models. Moreover, they set tight constraints on parameters relevant for secondary production calculations, *e.g.*, the normalization and the index of the diffusion coefficient, the Alfvén speed, and contribution of a hypothetical “fresh” local cosmic-ray component.

Positrons and electrons data need a very careful analysis, done using the most performing available instrumental and statistical tools, because of the possibility of misidentification of protons as positrons. In fact, the proton-to-positron ratio increases from about 10^3 at 1 GeV to approximately 10^4 at 100 GeV. Particle identification for PAMELA was based on the matching between the momentum measured by the tracker and the total energy measured in the calorimeter, the starting point, the lateral and longitudinal profiles of the reconstructed shower and the neutron detector response. This analysis technique has been tested at the proton and electron beams at CERN for different energies, by Monte Carlo simulations and by using flight data. Figure 3 reports the electron selection efficiency and the proton contamination of the analysis technique, measured on flight

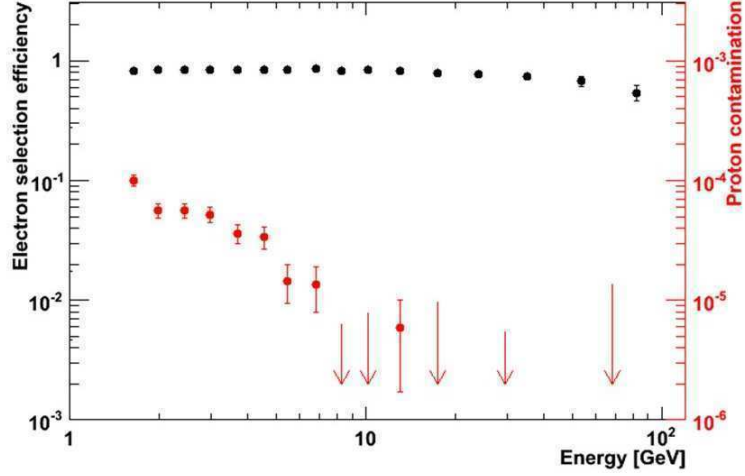


Fig. 3. – The electron selection efficiency and the proton contamination of the analysis technique, measured on flight data.

data; the proton contamination, measured at high energy (> 10 GeV), was better than 10^{-5} on beam test data (upper limit due to statistics).

The positron-to-all-electron ratio measured by the PAMELA experiment is given in fig. 4, compared with other recent experimental results (see [5,6] and references therein). The calculation, shown in the same figure for pure secondary production of positrons during the propagation of cosmic rays in the Galaxy without reacceleration processes, provides evidence that positron fraction is expected to fall as a smooth function of increasing energy if secondary production dominates. The data, covering the energy range 1.5–100 GeV, show two clear features. At low energies, below 5 GeV, the PAMELA

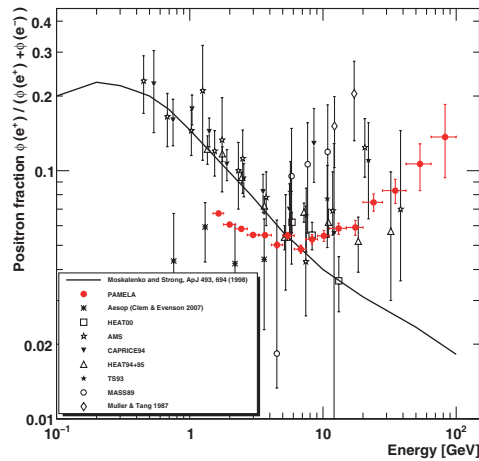


Fig. 4. – The positron fraction measured by the PAMELA experiment, compared with other recent experimental data [5].

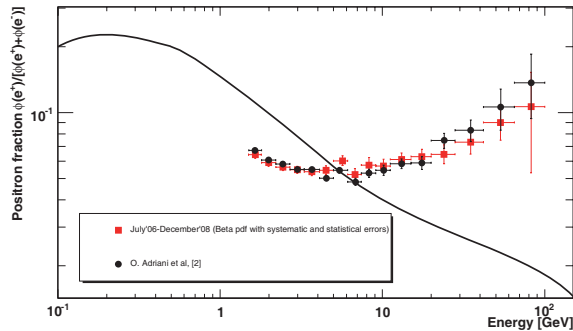


Fig. 5. – (Colour on-line) The positron fraction obtained using a beta-fit with statistical and systematic errors summed in quadrature (red) [7], compared with the positron fraction reported in fig. 4.

results are systematically lower than data collected during the 1990’s; this can be convincingly explained by effects of charge-dependent solar modulation. At high energies, above 10 GeV, they show a positron fraction increasing significantly with energy.

This excess of positrons in the range 10–100 GeV has led to many theoretical models explaining its origin as due to annihilation or decaying of dark matter. The most problematic challenge posed by the PAMELA results is the asymmetry between leptonic (positron fraction) and hadronic (antiproton-proton ratio), difficult to explain in the framework in which the neutralino is the dominant dark matter component. The best explanations are obtained in terms of a direct leptonic annihilation channel for a wide range of the WIMP mass. Another explanation relates to a contribution from nearby and young pulsars, objects well known as particle accelerators. Primary electrons are accelerated in the magnetosphere of pulsars in the polar cup and in the outer gap along the magnetic field lines emitting gamma-rays by synchrotron radiation, gammas that in the presence of pulsar gigantic magnetic field can evolve in positrons and electrons pairs. These, escaping into the interstellar medium, give a further contribution to the electron and positron components.

Results published in [5] refer to data collected by PAMELA between July 2006 and February 2008. We analyzed a larger data set, collected between July 2006 and December 2008, and we applied a different statistical methodology [7]. Figure 5 shows the positron fraction obtained through a beta-fit with statistical and systematic errors summed in quadrature, compared with the PAMELA positron fraction of fig. 4. Compared to what is reported in [5]: a) new experimental data, b) the application of three novel background models and c) an estimate of the systematic uncertainties have been used. The new experimental results are in agreement with what reported in [5] and confirm both solar modulation effects on cosmic rays with low rigidities and an anomalous positron abundance above 10 GeV.

3.2. Cosmic rays. – Reliable calculations of the secondary production contribution in the antiproton and positrons energy spectra are of paramount importance to clearly disentangle a possible signal from not standard sources, but they are affected by uncertainties on the nuclear composition and energy spectra of the cosmic rays. For example, ratios between “secondary” and “primary” nuclei, where the primaries are produced by stellar nucleosynthesis while the secondaries are produced by fragmentation of pri-

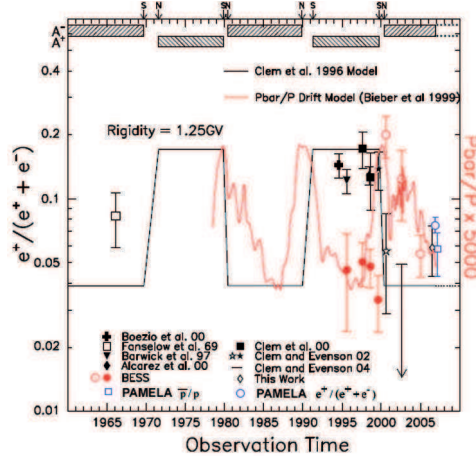


Fig. 6. – Phenomenological calculations for the positron-electron and antiproton-proton ratios along with the PAMELA and other experimental results.

maries interacting with the matter of the interstellar medium, are directly related to the encountered amount of matter and to the nuclei lifetime before escaping from the galaxy. PAMELA is measuring with good precision and high-statistics protons, ^4He , carbon and oxygen (primaries) together to ^3He , Li, Be, B (secondaries). These data constrain existing production and propagation models, providing detailed information on the galactic structure and the various mechanisms involved. Moreover, protons and alphas give the major contribute to the atmospheric neutrino production, therefore an accurate measurement of these components reduces the uncertainties on the expected flux on ground and on the estimation of hadronic cross sections (protons and alphas on O or N) at high energies, not otherwise determinable on ground. Proton and helium fluxes measured by PAMELA will be published very soon, together with the B/C ratio.

3.3. Solar physics. – Continuous monitoring of the solar activity and the detection of solar energetic particle events are other important issues addressed by PAMELA. It is well known that the low energy part of the cosmic ray energy spectra up to about 5–10 GeV is affected by solar modulation in a way depending on the particle electric charge sign. Moreover, this effect is different if the magnetic dipole projection on the solar rotational axis and the same axis is parallel (phase A^+) or anti-parallel (phase A^-). This is due to a systematic deviation from the reflection symmetry of the interplanetary magnetic field. The Parker field has opposite magnetic polarity above and below the equator, but the spiral field lines themselves are mirror images of each other. This anti-symmetry produces drift velocity fields that for positive particles converge on the heliospheric equator in the A^+ state or diverge from it in A^- state. PAMELA positron/electron data have been collected during a A^- phase when the positrons are modulated more than electrons, and this explains the difference at low energy with the results obtained by previous experiments that were performed in A^+ phase. In fig. 6 phenomenological calculations for the positron/electron and antiproton/proton ratios for several solar phases A^+ and A^- and compared with data at 1.25 GV momentum of different experiments are shown [8]. PAMELA data are very important also considering the long duration of its permanence

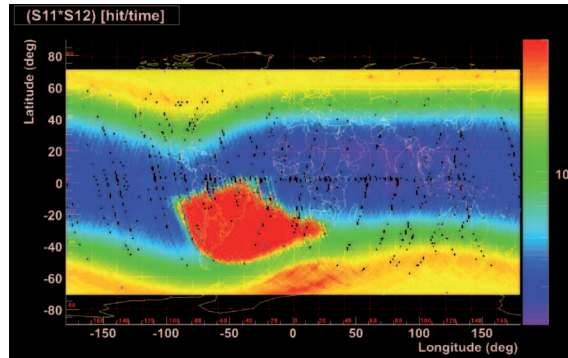


Fig. 7. – A 3-dimensional (latitude, longitude, altitude) mapping of the Van Allen Belts between 350 and 610 km.

in orbit in the recovery phase going towards solar maximum at cycle 24. It is interesting to stress that without a complete modeling of the solar modulation it becomes almost impossible to disentangle exotic signals at low energy.

PAMELA also detected the solar impulsive event of December 13th 2006. The observation of solar energetic particles (SEP) events with a magnetic spectrometer allows for several aspects of solar and heliospheric cosmic ray physics to be addressed for the first time.

3.4. Radiation environment. – One of the first measurements performed by PAMELA was a detailed 3-dimensional (latitude, longitude, altitude) mapping of the Van Allen Belts between 350 and 610 km, showing spectral and latitude electron radiation belt and the proton belt in the South Atlantic Anomaly (fig. 7).

In fig. 8 the particle flux measured in different cutoff regions is shown. It is possible to see the primary (galactic—above cutoff) and the secondary (reentrant albedo—below cutoff) components. At the poles, where field lines are open and cutoff is below the minimum detection threshold of PAMELA, the secondary component is not present. Moving toward lower latitude regions the cutoff increases and it is possible to see the two components, with the position of the gap increasing with the increase of the cutoff.

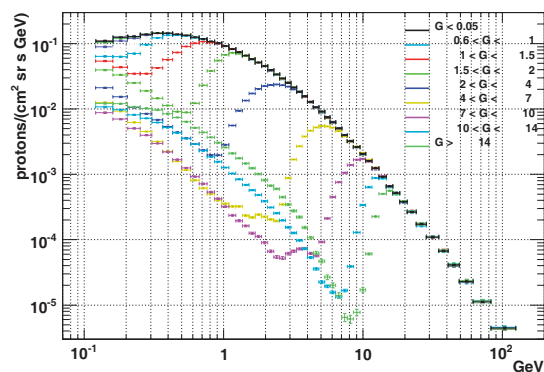


Fig. 8. – PAMELA proton flux in different cutoff regions.

4. – Conclusion

PAMELA is a general-purpose charged particle detector system exploring the antiparticle components of the cosmic radiation over a wide energy range. It has been in orbit since June 2006 and it is daily transmitting to ground 16 GB of data.

The main results obtained by PAMELA in 2009 concern the antiproton-to-proton and the positron-to-electron ratios. In 2010 the PAMELA Collaboration will release results on the energy spectra of charged cosmic particles (protons, alphas, light nuclei, antimatter), allowing scenarios of production and propagation of cosmic rays to be fully established and understood.

REFERENCES

- [1] GOLDEN R. *et al.*, *Phys. Rev. Lett.*, **43** (1979) 1196.
- [2] BOGOMOLOV E. *et al.*, *Proc. 16th ICRC*, **1** (1979) 330.
- [3] PICOZZA P. *et al.*, *Astropart. Phys.*, **27** (2007) 296.
- [4] ADRIANI O. *et al.*, *Phys. Rev. Lett.*, **102** (2009) 051101.
- [5] ADRIANI O. *et al.*, *Nature*, **458** (2009) 607.
- [6] BOEZIO M. *et al.*, *New J. Phys.*, **11** (2009) 105023.
- [7] ADRIANI O. *et al.*, *Astropart. Phys.*, **34** (2010) 1.
- [8] CLEM J. and EVENSON P., *Proc. 30th ICRC, Merida*, **1** (2007) 477.

Studies of cosmic ray electrons with the Fermi-LAT

L. LATRONICO on behalf of the FERMI-LAT COLLABORATION

INFN, Sezione di Pisa - L.go B. Pontecorvo 3, 56127 Pisa, Italy

(ricevuto il 14 Settembre 2010; pubblicato online il 5 Gennaio 2011)

Summary. — The Fermi Large Area Telescope measures the cosmic-ray electron spectrum from 7 GeV up to 1 TeV, covering a broad range of approximately 2.5 decades with unprecedented accuracy. This result is based on an analysis of about 8 million electron candidates detected in the first 12 months of operations of the satellite. It extends our previously published measurement down to 7 GeV, and confirms a spectrum harder than expected and with no prominent spectral features. In this paper we describe key points of the analysis and of its validations, as well as a cross-check measurement of the spectrum via a subset of events selected for the best energy resolution. Possible interpretations of the result and prospects for future Fermi measurements are briefly discussed at the end.

PACS 95.85.Ry – Neutrino, muon, pion, and other elementary particles; cosmic rays.

PACS 96.50.sb – Composition, energy spectra and interactions.

PACS 95.35.+d – Dark Matter (stellar, interstellar, galactic, and cosmological).

1. – Introduction

The Fermi observatory was launched on June 11, 2008 into a circular orbit at 565 km altitude and 25.6° inclination. Since then, observations with the Large Area Telescope (LAT [1]), a pair conversion telescope that is the main instrument onboard, have opened a new and important window on a wide variety of phenomena. These include the discovery of a new population of pulsars pulsing only in gamma-rays, which provides new insight into some of the extreme accelerators in our Galaxy [2]; the detection of photons up to 10s of GeV from gamma-ray bursts, which transforms our understanding of the astrophysics of these extreme explosions [3]; a determination of the diffuse gamma-ray emission with unprecedented accuracy [4] providing new constraints on dark matter models [5]; the discovery of around a thousand new gamma-ray sources [6]. Continuous monitoring of the high-energy gamma-ray sky has uncovered numerous outbursts from active Galaxies and the discovery of as-yet-unidentified transients from the direction of our Galaxy⁽¹⁾. Some

⁽¹⁾ https://www-glast.stanford.edu/cgi-bin/pub_rapid

high-sensitivity gamma-ray observations that are most relevant for cosmic-ray physics are discussed in an accompanying paper (Knödlseider, these proceedings). Beyond these, the LAT Collaboration also provided the first high-precision, systematics-limited measurement of the cosmic-ray electron (CRE) spectrum from 20 GeV to 1 TeV, which indicates an excess in the high energy CRE spectrum with respect to most pre-Fermi experiments and conventional cosmic-ray diffusion and propagation models [7].

2. – The Cosmic-Ray Electron spectrum

CREs with energy greater than ~ 100 GeV lose their energy rapidly ($-dE/dt \propto E^2$) by synchrotron radiation on Galactic magnetic fields and by inverse Compton scattering (IC) on the interstellar radiation field. The typical distance over which a 1 TeV CRE loses half its total energy is estimated to be 300–400 pc (see, *e.g.*, [8]) when it propagates within about one kpc of the Sun. This makes them a unique tool for probing nearby Galactic space.

Recent results from the ATIC [9], PPB-BETS [10], H.E.S.S. [11, 12], PAMELA [13], and Fermi LAT [7] have shed new light on the origin of CREs. The ATIC and PPB-BETS teams reported evidence for an excess of electrons in the range 300–700 GeV compared to the background expected from a conventional homogeneous distribution of cosmic-ray (CR) sources. The H.E.S.S. team reported a spectrum that steepens above ~ 900 GeV, a result which is consistent with an absence of sources of electrons above ~ 1 TeV within 300–400 pc. The PAMELA Collaboration reports that the ratio of the positron flux to the total flux of electrons and positrons increases with energy, a result which has significant implications. The Fermi result either requires a reconsideration of the source spectrum and/or the propagation model or indicates the presence of a nearby source. However, the excess of events reported by ATIC and PPB-BETS was not detected by the LAT.

2.1. Event selection and validations. – The LAT photon analysis is currently optimized for the 100 MeV–300 GeV range, but we demonstrated that a direct measurement of high energy electrons can be performed with great accuracy from a few GeV and up to 1 TeV by using a dedicated event analysis.

The event selection process must balance removal of the overwhelming background events of hadronic origin and retaining signal events, while limiting systematic uncertainties. We first reject those events that are badly reconstructed or are otherwise unusable. The next step is to select electron candidates based on the detailed event patterns in the calorimeter, the tracker and the ACD subsystems.

Generally, the shapes of hadronic showers differ significantly from electromagnetic (EM) showers. EM cascades are tightly confined, while hadronic cascades that leave comparable energy in the calorimeter tend to deposit energy over a much wider lateral region affecting all three detector subsystems. The nuclear fragments tend to leave energy far from the main trajectory of the particle. Thus hadron showers have larger transverse sizes in the calorimeter, larger numbers of stray tracks in the tracker and larger energy deposits in more ACD tiles. Therefore, the most powerful separators are the comparative lateral distributions and the event selection relies on the capabilities of the tracker, calorimeter and anticoincidence subsystems of the LAT, alone and in combination to discriminate between EM and hadronic event topologies.

Since the phenomenology of the EM cascades and hadron interactions varies dramatically over the energy range of interest, we developed two independent event selections,

one tuned for energies between 20 and 1000 GeV and the other for energies between 0.1 and 100 GeV, which we shall refer to as HE and LE. The HE analysis takes advantage of the fact that the on-board filtering (event selections designed to fit the data volume into the available telemetry bandwidth with a minimal impact on the photon yield) is disengaged for events depositing more than 20 GeV in the calorimeter. The source of data for the LE selection is an unbiased sample of all trigger types, prescaled (on-board) by a factor 250, which is continuously down-linked for diagnostic purposes. The region of overlap in energy, between 20 and 80 GeV, allows us to cross-check the two independent analyses. Above about 80 GeV the number of events in the prescaled sample becomes too low to be useful.

Finally, and similarly to what we do for selecting photons [1], a Classification Tree (CT) analysis⁽²⁾ provides the remaining necessary hadron rejection power. Starting from the same quantities (variables) defined in the photon event reconstruction, we identify those that are most sensitive to the differences between EM and hadronic event topologies and build CTs that for each event, based on large simulated training datasets, predict the probability that the event is an electron. Examples of powerful discriminants are the multiplicity of tracks and the extra hits outside of reconstructed tracks in the tracker and several variables mapping the 3-dimensional shower development in the calorimeter. The cut that we have adopted on the resulting CT-predicted electron probability is energy dependent. For HE analysis, a higher probability is required as energy increases. These cuts give us a set of candidate electron events.

As simulations are the starting point for the event selection, we systematically compare them with the flight data. Any variables for which the data-MC agreement was not satisfactory were not used in any part of the selection. Figure 1 shows an example of the data-MC comparison for the CT electron probabilities. The input energy spectra for all the particles are those included in the model of energetic particles in the Fermi orbit [1], with the exception of the electrons that follow instead a power law spectrum that fits our previous publication [7].

2.2. Energy resolution validations. – Since showers above 20 GeV are not fully contained by the LAT calorimeter, the energy reconstruction is a critical step of this analysis. In order to cross check the impact of the energy resolution on the measured spectrum, we performed a dedicated analysis in which we selected events with the longest path lengths (at least $12 X_0$) in the calorimeter. We further selected events that do not cross any of the boundary gaps between calorimeter tower modules and that have sufficient track length (at least $1 X_0$) in the tracker for a good direction reconstruction. For the event sample defined by these three requirements the average amount of material traversed is $\sim 16 X_0$, ensuring that the shower maximum is well contained in the calorimeter up to at least 1 TeV (the average depth of the shower maximum for electrons at this energy is $10.9 X_0$). Correspondingly the instrument acceptance decreases to $\sim 5\%$ of that achieved in the standard analysis described in the previous sections. As illustrated in fig. 2, the energy resolution for events passing this restrictive selection is significantly better than that for the full analysis. The energy dispersion distributions are much narrower and symmetric, with no prominent low energy tails. The energy resolution (half width of the 68% containment window) is around 3% at 100 GeV and increases to approximately 5% at 1 TeV.

⁽²⁾ The reader can refer to [14] for a comprehensive review of the use of data mining and machine learning techniques in astrophysics.

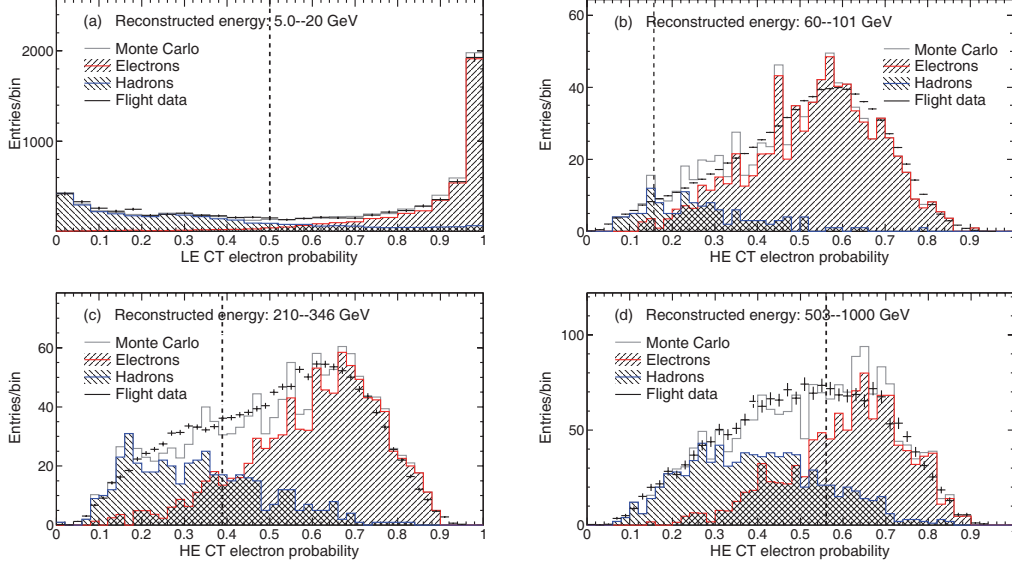


Fig. 1. – Distribution of CT predicted probability (a) for LE analysis and (b), (c) and (d) for HE analysis in different energy intervals. Monte Carlo generated distributions are compared with flight distributions. The cut value is a continuous function of energy and is represented by the vertical dashed line in each panel. The distributions are shown after the cuts on all other variables have been applied.

Figure 3 shows the consistency, within the systematic errors, between the spectrum obtained with the standard analysis and that obtained with the long-path selection. This confirms that the energy resolution quoted for the standard selection is indeed sufficient for the measurement and does not have any significant effect on the spectrum.

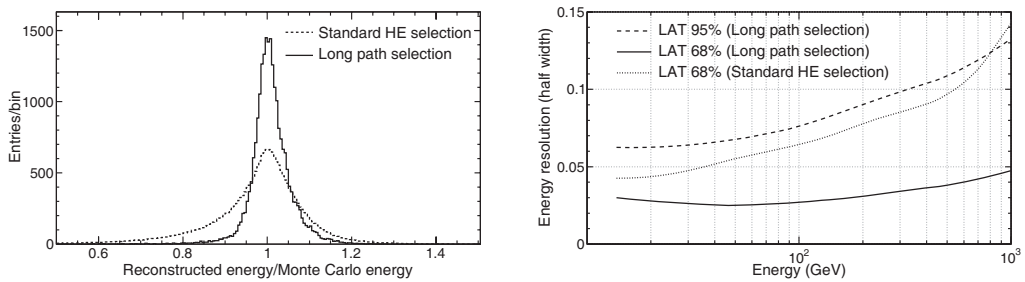


Fig. 2. – Left: energy dispersion distribution in the energy range 242–458 GeV for the long path selection (solid line) and the standard HE analysis (dashed line). Right: energy resolution for the long path selection analysis. The half width of the 68% containment window for the HE analysis, which is comparable with that of the 95% window for the more restrictive analysis, is overlaid for reference.

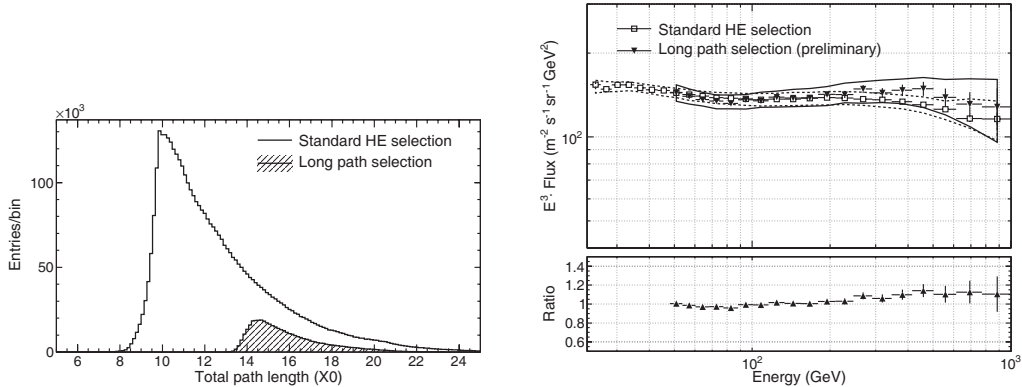


Fig. 3. – Left: distribution of the amount of material traversed by the candidate electrons passing the long path selection, compared with that for the entire data sample used in the standard analysis (the sharp edge at $\sim 10 X_0$ in the latter reflects the total thickness of the instrument on-axis). Note the difference in the number of events. Right: comparison of the spectra obtained with the long path selection and the standard HE selection. The continuous lines represent the systematic uncertainties. The bottom panel shows the ratio of the two spectra.

2.3. Low energy extension of the measurement. – In order to extend the measurement to energies below ~ 20 GeV, we need to consider the shielding effect of the geomagnetic field as characterized by the cutoff rigidity. The lowest allowed primary-electron energy is strongly dependent on geomagnetic position and decreases with increasing geomagnetic latitude. For the orbit of Fermi, the cutoff ranges between about 6 and 15 GeV.

As recognized in [15], the McIlwain L ⁽³⁾ parameter is particularly convenient for characterizing cutoff rigidities and has been used for selecting data in the LE analysis.

Each McIlwain L interval has an associated cutoff energy E_c that we determine by parameterizing the shape of the CRE spectrum as

$$(1) \quad \frac{dN}{dE} = c_s E^{-\Gamma_s} + \frac{c_p E^{-\Gamma_p}}{1 + (E/E_c)^{-6}},$$

where c_s and c_p are the normalization constants for the secondary (albedo) and primary components of the spectrum while Γ_s and Γ_p are their spectral indexes.

Due to the complexity of the particle orbits in the Earth's magnetosphere, the transition to cutoff is smoothed out. Therefore, we increase E_c by 15% to arrive at an effective minimum energy of the primary electron flux not affected by the Earth's magnetic field. We split the LE data sample into 10 intervals of McIlwain L parameter. For each energy bin we use the interval of McIlwain L parameter whose effective minimum energy is lower than the energy in question. This procedure is illustrated in full details in [16] and in fig. 4, where the electron spectrum is shown across the full energy range accessible to this analysis and together with the McIlwain L intervals from which the flux was measured

⁽³⁾ The McIlwain L parameter is a geomagnetic coordinate defined as the distance in Earth radii from the center of the Earth's tilted, off-center, equivalent dipole to the equatorial crossing of a field line.

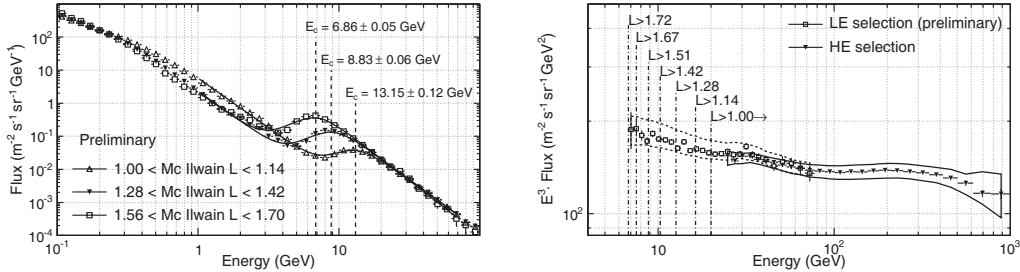


Fig. 4. – Left: the measured electron flux in three McIlwain L bins. For each bin the fit of the flux with eq. (1) and the resulting estimated cutoff rigidity, E_c , is shown. As described in the text, E_c decreases for larger values of McIlwain L. Right: cosmic-ray electron spectra as measured by Fermi LAT for one year of observations for LE events (squares) and HE events (triangles). The continuous lines represent the systematic uncertainties. The two spectra agree within systematic errors in the overlap region between 20 GeV and 80 GeV.

for the LE analysis. The same figure also shows a very nice overlap of the LE and HE independent analysis up to ~ 100 GeV, confirming the robustness of the result.

2.4. Results and discussion. – After electron candidates are selected, we derive event count rates dividing them by the observatory livetime. Similarly, we derive the count rate of residual hadronic events in the sample using a Monte Carlo simulation of the on-orbit background, and finally subtract this from the total count rate to get the CRE only count rate. Ultimately, we compute the CRE flux by scaling count rates in each pre-determined energy bin with the corresponding effective geometric factor, that represents the instrument acceptance as determined from Monte Carlo simulations of pure electrons (see [17] for full details).

The resulting spectrum from all the data collected in nominal sky survey mode from 4 August 2008 to 4 August 2009 is shown in fig. 5.

The CRE spectrum reported here is essentially the same as that published in [7] for the energy above 20 GeV, but with twice the data volume. Within the systematic errors (shown by the grey band in fig. 5) the entire spectrum from 7 GeV to 1 TeV can be fitted by a power law with spectral index in the interval 3.03–3.13 (best fit $\propto E^{-3.08 \pm 0.05}$), similar to that given in [7]. The spectrum is significantly harder (flatter) than that reported by previous experiments. Below ~ 50 GeV the electron spectrum is consistent with previous experiments and does not indicate any flattening at low energies. The cross-check analysis using events with long paths in the instrument confirms the absence of any evident feature in the $e^+ + e^-$ spectrum from 50 GeV to 1 TeV, as originally reported in [7]. To fit the high energy part of the Fermi LAT spectrum and to agree with the H.E.S.S. data, a conventional propagation model requires a power law index $\alpha \simeq 2.5$ above ~ 4 GeV and a cutoff at ~ 2 TeV. However, while providing good agreement with the high energy part of the spectrum, a model with a single power law injection index fails to reproduce the low-energy data.

The spectrum measured with the Fermi LAT suggests some spectral flattening at 70–200 GeV and a noticeable excess above 200 GeV as compared to our power-law spectral fit. These gentle features of the spectrum can be explained within a conventional model by adjusting the injection spectra.

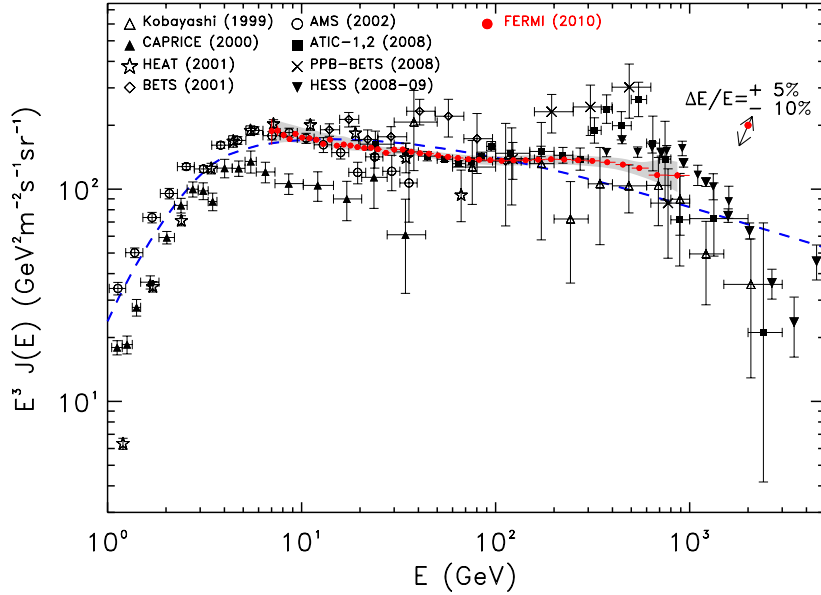


Fig. 5. – Cosmic-ray electron spectrum as measured by Fermi LAT for one year of observations (filled circles, preliminary), with other recent high energy results. Systematic errors are shown by the grey band. The range of the spectrum rigid shift implied by a shift of the absolute energy is shown by the arrow in the upper right corner. Dashed line shows the model based on pre-Fermi results [18]. Data from other experiments are: Kobayashi [19], CAPRICE [20], HEAT [21], BETS [22], AMS [23], ATIC [9], PPB-BETS [10], H.E.S.S. [11, 12]. Note that the AMS data are for e^- only.

Another possibility that provides a good overall agreement with our spectrum is the introduction of an additional leptonic component with a hard spectrum. Such an additional component is motivated by the rise in the positron fraction reported by PAMELA [13]. Recent papers have suggested different models for this component. The data can accommodate a contribution from nearby sources (such as pulsars) or from the annihilation of dark matter particles (see, *e.g.*, [24] for a comprehensive list of references).

The features may also be explained by other astrophysical effects, such as reacceleration of secondary CRs at the source, as in [25] and [26], distribution of the CR acceleration sites, as in [27] and many others.

The different proposed solutions have specific signatures in some CR observables that would help discriminating them. Isolated local sources would give rise to spectral features in the CRE spectrum, secondary CR reacceleration at the source would produce rising fractions of antiprotons over protons and secondary nuclei, *e.g.*, boron over carbon, propagation effects on electrons coming from far-away SNR as in [27] would produce a decrease in the positron fraction at very high energy.

The Fermi Collaboration is actively working on reducing systematic uncertainties on the measurement of the CRE spectrum to be able to identify any possible such feature. Moreover, since an excess of electrons of Dark Matter origin would produce a corresponding excess in the Inverse Compton component of the diffuse gamma-ray emission, our measurement of the extragalactic isotropic diffuse emission [4] already provides powerful constraints on many DM models which are put forward to explain the Fermi and Pamela

lepton excesses [5]. Even more accurate measurements of gamma-ray diffuse emission, that the Fermi Collaboration is actively pursuing, will be crucial to further constrain the manifold DM parameter space. Finally, the Fermi Collaboration has been developing techniques to perform a measurement of small and large scale anisotropies in the arrival direction of electrons [28], in the attempt to detect local sources of electrons, and to perform a measurement of the positron fraction using the Earth magnetic field as a spectrometer to separate leptons of opposite charge.

* * *

The *Fermi* LAT Collaboration acknowledges support from a number of agencies and institutes for both development and the operation of the LAT as well as scientific data analysis. These include NASA and DOE in the United States, CEA/Irfu and IN2P3/CNRS in France, ASI and INFN in Italy, MEXT, KEK, and JAXA in Japan, and the K. A. Wallenberg Foundation, the Swedish Research Council and the National Space Board in Sweden. Additional support from INAF in Italy and CNES in France for science analysis during the operations phase is also gratefully acknowledged.

REFERENCES

- [1] ATWOOD W. B. *et al.*, *Astrophys. J.*, **697** (2009) 1071.
- [2] ABDO A. A. *et al.*, *Science*, **325** (2009) 840.
- [3] GRANOT J., *Proceedings of The Shocking Universe - Gamma-Ray Bursts and High Energy Shock phenomena*, astro-ph/1003.2452 (2010).
- [4] ABDO A. A. *et al.*, *Phys. Rev. Lett.*, **104** (2010) 101101.
- [5] ABDO A. A. *et al.*, *J. Cosmol. Astropart. Phys.*, **04** (2010) 014.
- [6] ABDO A. A. *et al.*, *Astrophys. J. Suppl. Ser.*, **188** (2010) 405.
- [7] ABDO A. A. *et al.*, *Phys. Rev. Lett.*, **102** (2009) 181101.
- [8] AHARONIAN F. A., ATOYAN A. M. and VÖLK H. J., *Astron. Astrophys.*, **294** (1995) L41.
- [9] CHANG J. *et al.*, *Nature*, **456** (2008) 362.
- [10] TORII S. *et al.*, astro-ph/0809.0760 (2008).
- [11] AHARONIAN F. *et al.*, *Phys. Rev. Lett.*, **101** (2008) 261104.
- [12] AHARONIAN F. *et al.*, *Astron. Astrophys.*, **508** (2009) 561.
- [13] ADRIANI O. *et al.*, *Nature*, **458** (2008) 607.
- [14] BALL N. M. and BRUNNER R. J., astro-ph/0906.2173 (2009).
- [15] SMART D. F. and SHEA M. A., *Adv. Space Res.*, **36** (2005) 2012.
- [16] PESCE-ROLLINS M., *Proceedings of 2nd Fermi Symposium*, astro-ph/0912.3611 (2009).
- [17] SGRÓ C., BRIGEON J. and BALDINI L., *Proceedings of 31st ICRC*, astro-ph/0907.0385 (2009).
- [18] STRONG A. W., MOSKALENKO I. V. and REIMER O., *Astrophys. J.*, **613** (2004) 962.
- [19] KOBAYASHI T. *et al.*, *Proceedings of the 26th ICRC* (2009).
- [20] BOEZIO M. *et al.*, *Astrophys. J.*, **532** (2000) 653.
- [21] DUVERNOIS M. A. *et al.*, *Astrophys. J.*, **559** (2001) 296.
- [22] TORII S. *et al.*, *Astrophys. J.*, **559** (2001) 973.
- [23] AGUILAR M. *et al.*, *Phys. Rep.*, **336** (2002) 331.
- [24] GRASSO D. *et al.*, *Astropart. Phys.*, **32** (2009) 140.
- [25] BLASI P., *Phys. Rev. Lett.*, **103** (2009) 051104.
- [26] AHLERS M., MERTSCH P. and SARKAR S., *Phys. Rev. D*, **80** (2009) 123017.
- [27] SHAVIV J. N., NAKAR E. and PIRAN T., *Phys. Rev. Lett.*, **103** (2009) 111302.
- [28] ACKERMANN M. *et al.*, *Phys. Rev. D*, **82** (2010) 092003, astro-ph/1008.5119.

Studies of gamma-ray sources with the Fermi Large Area Telescope

J. KNÖDLSIEDER on behalf of the FERMI LARGE AREA TELESCOPE COLLABORATION

CESR, CNRS/UPS - 9, avenue du Colonel Roche, 31028 Toulouse, France

(ricevuto il 14 Settembre 2010; pubblicato online il 10 Gennaio 2011)

Summary. — With its excellent sensitivity, large field of view, broad energy coverage, and good per-photon angular resolution, the Large Area Telescope aboard the *Fermi Gamma-ray Space Telescope* satellite provides us with an unprecedented view of the high-energy Universe, revealing a large diversity of cosmic particle accelerators that are active at various scales. We present in this paper a selection of science highlights of the *Fermi* mission, with particular emphasis on results that are relevant for cosmic-ray physics. We cover observations of supernova remnants and studies of interstellar gamma-ray emission, reaching from the vicinity of the solar system out to the more distant starburst galaxies.

PACS 95.85.Pw – Gamma ray.

PACS 98.70.Sa – Cosmic rays (including sources, origin, acceleration, and interactions).

1. – Introduction

The *Fermi Gamma-ray Space Telescope* has been successfully launched on 2008 June 11, and since 2008 August it routinely surveys the sky with the Large Area Telescope (LAT). Compared to its predecessor, the EGRET telescope that operated aboard *CGRO* from 1991 to 2000, the LAT brings a sensitivity improvement of more than a factor of 10, provides a wide field of view (2.4 sr at 1 GeV), and covers a wide energy range from 20 MeV to > 300 GeV [1]. In its regular surveying mode, the entire sky is observed every 3 hours, providing information on flux variability for any source in the sky.

We present in this paper a selection of the science highlights of the *Fermi* mission, with particular emphasis on results that are relevant for cosmic-ray physics. While we focus here on observations of gamma-rays, an accompanying paper will present results on direct cosmic-ray measurements *Fermi* (Latronico, these proceedings). We start with an overview of the types of (steady) gamma-ray sources that are observed by *Fermi*/LAT, and summarize results that were obtained on observations of Galactic

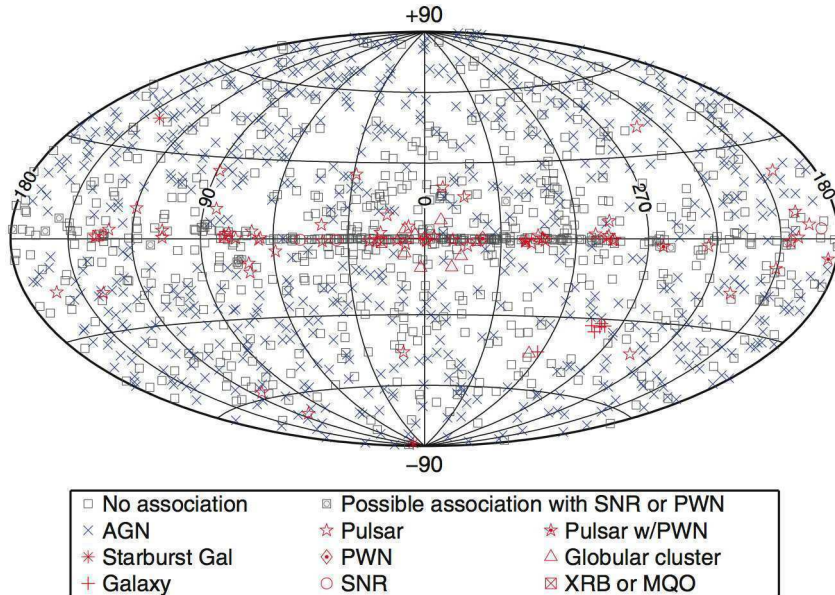


Fig. 1. – (Colour on-line) 1451 1FGL catalogue sources, showing locations on the sky (in Galactic coordinates with Aitoff projection) and associated source class, coded according to the legend. The colour is chosen simply to enhance the visibility of the associated and non-blazar sources (from [2]).

supernova remnants. The remainder of the paper is dedicated to the observation of interstellar gamma-ray emission, and results are presented by gradually moving away from the local interstellar medium to the extragalactic space.

2. – Gamma-ray sources

2.1. Source catalogue. – The combination of deep and fairly uniform exposure, good per-photon angular resolution, and stable response of the LAT has made for the most sensitive, best-resolved survey of the sky to date in the 100 MeV to 100 GeV energy range. During the first 11 months of operations, 1451 gamma-ray sources have been significantly detected in this energy range by the LAT, making up the First *Fermi*-LAT catalogue (1FGL) [2] that provides a significant enhancement over the catalogue of 271 sources that have been by detected the EGRET telescope over its entire mission lifetime [3].

About 56% of the 1FGL sources have been associated to counterparts at other wavelengths based on positional coincidence at the 80% confidence level (cf. fig. 1). The large majority of these associations are with Blazars, *i.e.* active galactic nuclei (AGN) that presumably host supermassive black holes creating relativistic jets that are pointing in the general direction of the Earth and that are the sites of particle acceleration. The second most important source class are pulsars (56 sources) which are firmly identified by the high-confidence detection of periodicity in the arrival times of the gamma-ray photons that is caused by the rotation of the neutron star. While most of the pulsars are young and energetic, an increasingly large number of millisecond pulsars has also been detected by the LAT [4]. Populations of millisecond pulsars are also believed to

account for the gamma-ray emission that is seen towards globular clusters [5] of which 8 are associated with gamma-ray sources in the 1FGL catalogue. Young and energetic pulsars are often associated to pulsar wind nebulae (PWN) and the remnants of their natal supernova explosions (SNR), and consequently there is some ambiguity in associating gamma-ray sources to these 3 source classes. Excluding 1FGL sources that are associated with pulsars, we find 6 1FGL sources associated to PWN and 41 1FGL sources associated to SNRs. Dedicated follow-up studies that investigate the spectral energy distributions and spatial morphologies of the sources may help to clarify the underlying natures of these sources (cf. subsect. 2.2). Finally, 3 1FGL sources are firmly identified as high-mass X-ray binaries based on their orbital variability (LS I + 61°303 [6], LS 5039 [7] and Cyg X-3 [8]), and 2 1FGL sources are associated to the starburst galaxies M 82 and NGC 253 [9]. Furthermore, gamma-ray emission is detected from the LMC [10] and SMC [11] and several 1FGL sources are associated to local emission maxima in these dwarf galaxies.

2.2. *Supernova remnants.* – Supernova remnants have long been considered the primary candidates for the origin of Galactic cosmic rays (CRs). Specifically, diffusive shock acceleration [12, 13] is widely accepted as the mechanism by which charged particles can be accelerated to very high energies at collisionless shocks driven by supernova explosions. However, it has not yet been confirmed whether strong shocks in SNRs are indeed capable of efficiently transferring kinetic energy into the acceleration of CR ions, and the definite proof for cosmic-ray acceleration in SNRs is still missing.

Gamma-ray observations may probe for ion acceleration in SNRs by revealing the characteristic decay signature from π^0 mesons that are produced by collisions between relativistic nuclei with ambient gas. Recent ground-based gamma-ray observations in the TeV domain have revealed several spatially resolved young SNRs (age ~ 1 ky) in our Galaxy, showing a morphology that correlates well with that observed in non-thermal X-rays. The TeV observations, however, cover only the high-energy part of the source spectra, and thus discriminate only poorly between leptonic (inverse Compton and/or Bremsstrahlung) and hadronic (π^0 decay) emission scenarios. Clearly, an improved low-energy coverage of these sources is needed to better constrain the underlying emission mechanism [14].

Fermi has now provided this low-energy coverage for several galactic SNRs (cf. fig. 2). Among those are Cas A [15] and RX J1713.7-3946 that both have been detected also at TeV gamma-rays. Both objects are young SNRs that exhibit broad-band emission spectra ranging from $\lesssim 1$ GeV up to ~ 10 TeV and beyond. The spectra of these sources impose so far only little constraints on the underlying emission mechanism and are satisfactorily modelled by either leptonic or hadronic emission models. Interestingly, regardless of the origin(s) of the observed gamma-rays, the total amount of CRs accelerated in Cas A constitutes only a minor fraction ($\leq 2\%$) of the total kinetic energy of the supernova [15].

A second class of SNRs detected by *Fermi* consists of mid-aged (3–50 ky) remnants that generally are known to be interacting with molecular clouds that might act as target material for π^0 production. These SNRs (W51C [16], W44 [17], IC 433 [18], W28 [19]) are all characterized by spatially extended emission in the GeV domain with spectral breaks near ~ 1 GeV and a spectral steepening towards the TeV domain. Consequently, many of these SNRs are only barely detected at TeV energies with current Cerenkov telescopes. The gamma-ray spectra of these objects can be fitted with either leptonic and hadronic models, yet in general, leptonic models require rather extreme conditions to be met to explain the observations (such as unusually large ratios of injected electrons

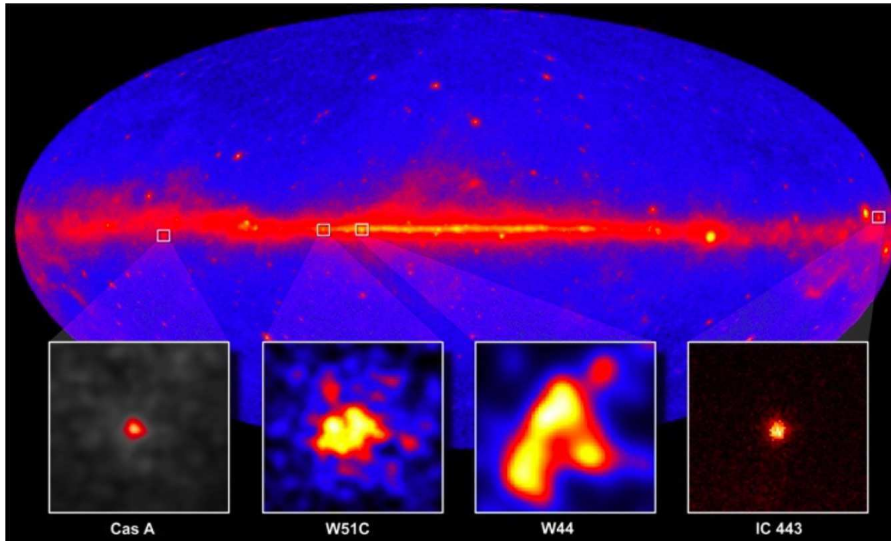


Fig. 2. – *Fermi*/LAT allsky map of the gamma-ray sky with enlarged images of four SNRs superimposed.

to protons, strong magnetic fields, *ad hoc* breaks in the particle spectra, excessively large ambient photon densities or electron energy contents; *e.g.* [16-19]). Consequently, hadronic models provide a more plausible explanation of the observed emissions. The increasing amount of SNRs that are detected by *Fermi* together with a continuously growing database at TeV energies opens up the possibility to study now how particle acceleration responds to environmental effects such as shock propagation in dense clouds and how accelerated particles are released into interstellar space.

3. – Interstellar gamma-ray emission

3.1. Galactic cosmic rays. – Once accelerated, CRs diffuse away from their acceleration sites into the interstellar space of our Galaxy where in encounters with the interstellar gas and radiation fields they produce a diffuse glow of gamma-rays through π^0 decay, inverse Compton scattering and non-thermal Bremsstrahlung processes. This diffuse Galactic glow is in fact the first source of high-energy gamma-rays that was discovered by observations with the OSO-3 satellite in 1968 [20]. Similar to observations of SNRs, the study of the diffuse Galactic gamma-ray emission provides important insights into CR acceleration and propagation within our Galaxy.

Figure 3 shows the differential gamma-ray emissivity of hydrogen in the local interstellar medium (within 1 kpc of the solar system) as determined by *Fermi* from observations of diffuse gamma-ray emission at high Galactic latitudes [21]. The differential emissivity spectrum agrees remarkably well with calculations based on CR spectra that are consistent with those measured directly at Earth, at the 10% level. This indicates that the CR nuclei spectra within 1 kpc from the solar system are comparable to those measured near Earth.

Going further away from the Sun, observations of the gamma-ray emission towards the Cassiopeia and Cepheus constellations allow studying CR density variations in the outer

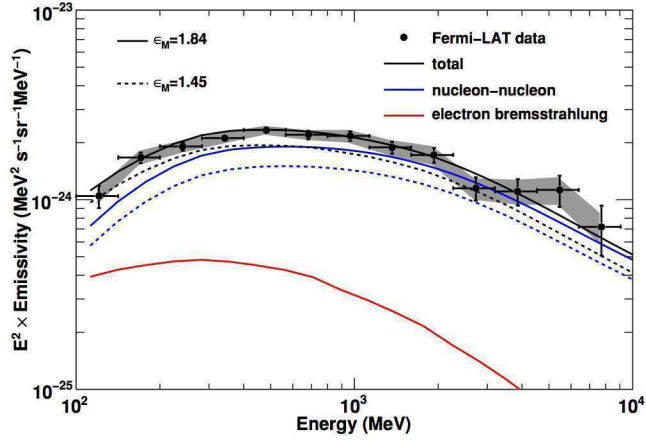


Fig. 3. – Differential gamma-ray emissivity from the local atomic hydrogen gas compared with the calculated gamma-ray production (from [21]).

Galaxy, covering Galactocentric distances from ~ 9 kpc to ~ 20 kpc. A recent *Fermi* study of this region revealed that the gamma-ray emissivity spectrum of the gas in the nearby Gould Belt (within 300 pc from the solar system) is consistent with expectations based on locally measured CR spectra [22]. The gamma-ray emissivity decreases from the Gould Belt to the distant Perseus arm, but the measured gradient is flatter than expectations based on current estimates of the distribution of sources of CRs in the Milky Way and of CR propagation parameters. In addition, the observations present evidence in the Gould Belt for the so-called dark gas, which is gas that is not properly traced by radio and microwave surveys, and of which the mass amounts to $\sim 50\%$ of the CO-traced molecular gas mass.

In the late nineties, measurements with the EGRET telescope indicated a global excess of diffuse emission $\gtrsim 1$ GeV relative to that expected from conventional diffuse galactic emission models [23] which led to speculations about a possible dark matter origin of this so-called “GeV excess” [24]. *Fermi* has measured the diffuse gamma-ray emission with improved sensitivity and resolution with respect to EGRET [25]. Figure 4 compares the LAT data (red) to the earlier EGRET data (blue) which reveals a significant discrepancy between both measurements. In particular, the LAT data do not show the excess reported by EGRET and are in fact well reproduced by a diffuse gamma-ray emission model that is consistent with local CR spectra. The knowledge about the LAT instrument response function comes from detailed simulations that were validated with beam tests of calibration units, and from post-launch refinements based on the actual particle background, and are considered as accurate [25]. It thus is plausible to attribute the “GeV excess” to an instrumental artefact of the earlier EGRET measurements.

3.2. Mapping cosmic-ray acceleration in the LMC. – Nearby galaxies have some advantages as targets for studies of CR physics as they are viewed from outside, and so line-of-sight confusion, which complicates studies of gamma-ray emission from our own Galaxy, is diminished. The Large Magellanic Cloud (LMC) is an excellent target for studying the link between CR acceleration and gamma-ray emission since the galaxy is nearby (~ 50 kpc), can be easily resolved (angular extent $\sim 8^\circ$), and is seen almost

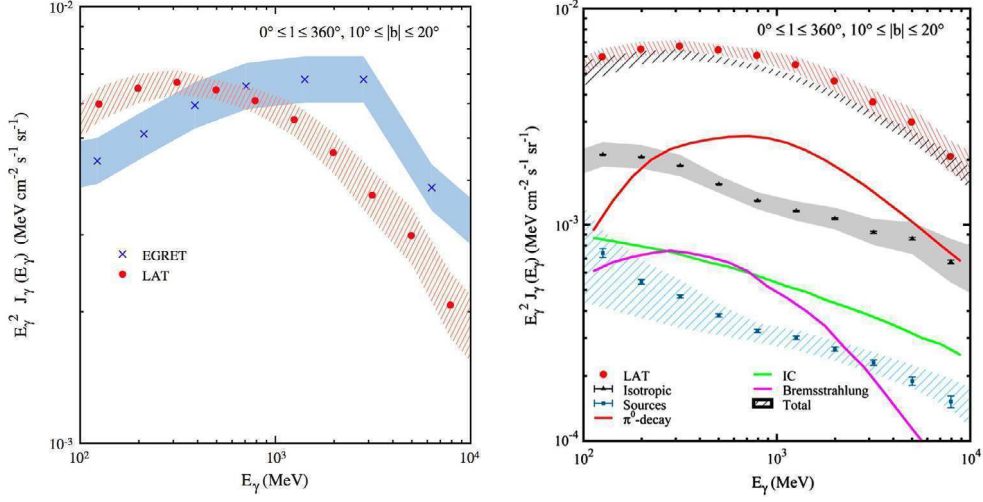


Fig. 4. – (Colour on-line) Diffuse emission intensity averaged over all galactic longitudes for latitude range $10^\circ \leq |b| \leq 20^\circ$. The left plot shows the comparison of LAT data (red) to EGRET data (blue), the right plot shows the comparison of LAT data with a model of Galactic diffuse emission (from [25]).

face-on. The LMC has been initially detected by the EGRET telescope [26], but *Fermi* now provides the instrumental capabilities to perform a detailed study of the galaxy.

The LMC is clearly detected with the LAT ($\gtrsim 33\sigma$) and for the first time the emission is spatially well resolved in gamma-rays [27]. The observations (cf. fig. 5) reveal the

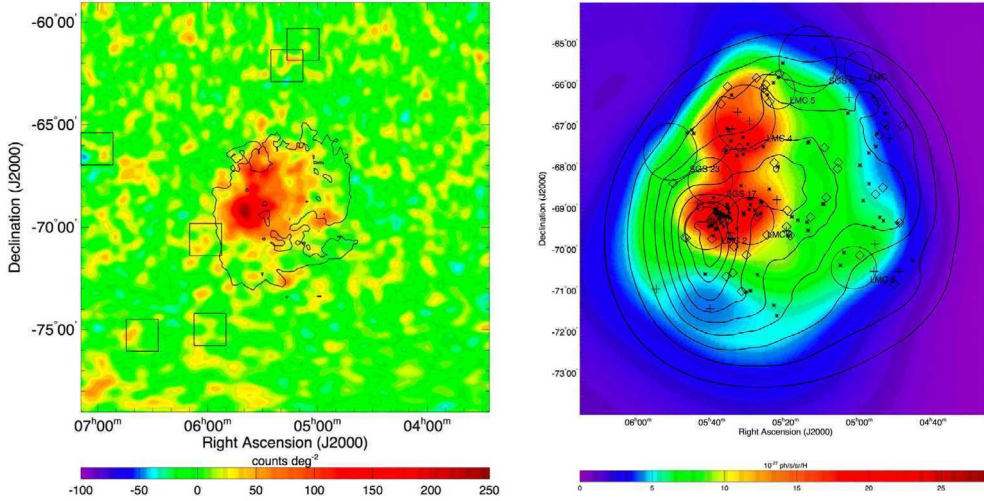


Fig. 5. – Left panel: Gaussian kernel ($\sigma = 0.2^\circ$) smoothed background subtracted counts map of the LMC region for the energy range 200 MeV–20 GeV. Right panel: adaptively smoothed integrated > 100 MeV emissivity map of the LMC revealing the cosmic-ray density distribution within the LMC. The contours indicate the gas density smoothed with the LAT instrumental point spread function (from [27]).

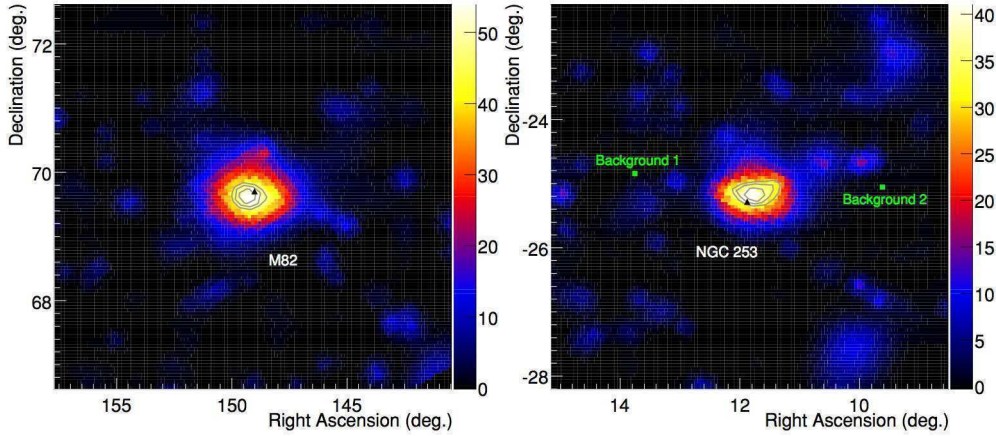


Fig. 6. – (Colour on-line) Test statistic maps obtained from photons above 200 MeV showing the 6° by 6° large regions around M 82 and NGC 253. Aside from the source associated with each galaxy, all other *Fermi*-detected sources (green squares) within a 10° radius of the best-fit position have been included in the background model as well as components describing the diffuse Galactic and isotropic gamma-ray emission. Black triangles denote the centres of M 82 and NGC 253 at optical wavelengths (from [28]).

massive star forming region 30 Doradus as a bright source of gamma-ray emission, in addition to a fainter glow that spreads out over large areas of the galaxy. Surprisingly, the observations reveal little correlation of the gamma-ray emission with gas density, as it would have been expected if CRs propagate throughout the entire galaxy. The gamma-ray emission correlates more with tracers of massive star forming regions, supporting the idea that CRs are accelerated in these regions as a result of the large amounts of kinetic energy that are input by the stellar winds and supernova explosions of massive stars into the interstellar medium.

3.3. Starburst galaxies. – Probing galactic cosmic-ray acceleration even well beyond the local group of galaxies has now become possible thanks to *Fermi*. For the first time, steady GeV gamma-ray emission has been detected significantly by the LAT from sources positionally coincident with locations of the starburst galaxies M 82 and NGC 253 [28]. Test statistic maps obtained with LAT for photons ≥ 200 MeV for regions around both galaxies are shown in fig. 6. Both starburst galaxies have also been detected at TeV energies by VERITAS [29] and H.E.S.S. [30], and the emission is well explained by the interaction of CRs with local interstellar gas and radiation fields. M 82 and NGC 253, though having less gas than the Milky Way, have factors of 2–4 greater gamma-ray luminosity, suggesting a connection between active star formation and enhanced CR energy densities in star-forming galaxies. In particular, the H.E.S.S. observations of NGC 253 localise the gamma-ray emission towards the starbursting core of the galaxy, which is very much like the situation in the LMC where the gamma-ray emission is brightest towards 30 Doradus, a region that is considered as a “mini-starburst” [31]. Star-forming and starburst galaxies are thus a new class of prominent gamma-ray emitters in the Universe, and thanks to their large number, they have the potential to make a significant, $\gtrsim 10\%$ contribution to the extragalactic gamma-ray background at high-energy gamma-rays [28].

* * *

The *Fermi* LAT Collaboration acknowledges generous ongoing support from a number of agencies and institutes that have supported both the development and the operation of the LAT as well as scientific data analysis. These include the National Aeronautics and Space Administration and the Department of Energy in the United States, the Commissariat à l'Énergie Atomique and the Centre National de la Recherche Scientifique/Institut National de Physique Nucléaire et de Physique des Particules in France, the Agenzia Spaziale Italiana and the Istituto Nazionale di Fisica Nucleare in Italy, the Ministry of Education, Culture, Sports, Science and Technology (MEXT), High Energy Accelerator Research Organization (KEK) and Japan Aerospace Exploration Agency (JAXA) in Japan, and the K. A. Wallenberg Foundation, the Swedish Research Council and the Swedish National Space Board in Sweden.

Additional support for science analysis during the operations phase is gratefully acknowledged from the Istituto Nazionale di Astrofisica in Italy and the Centre National d'Études Spatiales in France.

REFERENCES

- [1] ATWOOD W. B. *et al.*, *Astrophys. J.*, **697** (2009) 1071.
- [2] ABDO A. A. *et al.*, *Astrophys. J. Suppl. Ser.*, **188** (2010) 405.
- [3] HARTMAN R. C. *et al.*, *Astrophys. J. Suppl. Ser.*, **123** (1999) 79.
- [4] ABDO A. A. *et al.*, *Science*, **325** (2009) 848.
- [5] ABDO A. A. *et al.*, *Science*, **325** (2009) 845.
- [6] ABDO A. A. *et al.*, *Astrophys. J.*, **701** (2009) 123.
- [7] ABDO A. A. *et al.*, *Astrophys. J.*, **706** (2009) L56.
- [8] ABDO A. A. *et al.*, *Science*, **326** (2009) 1512.
- [9] ABDO A. A. *et al.*, *Astrophys. J.*, **709** (2010) L152.
- [10] ABDO A. A. *et al.*, *Astron. Astrophys.*, **512** (2010) A7.
- [11] ABDO A. A. *et al.*, to be published in *Astron. Astrophys.*
- [12] BELL A. R., *Mon. Not. R. Astron. Soc.*, **182** (1978) 147.
- [13] BLANDFORD R. D. and OSTRIKER J. A., *Astrophys. J.*, **221** (1978) L29.
- [14] FUNK S., *30th ICRC Conference* (2007) astro-ph/0709-3127v1.
- [15] ABDO A. A. *et al.*, *Astrophys. J.*, **710** (2010) L92.
- [16] ABDO A. A. *et al.*, *Astrophys. J.*, **706** (2009) L1.
- [17] ABDO A. A. *et al.*, *Science*, **327** (2010) 1103.
- [18] ABDO A. A. *et al.*, *Astrophys. J.*, **712** (2010) 459.
- [19] ABDO A. A. *et al.*, *Astrophys. J.*, **718** (2010) 348.
- [20] CLARK G. W. *et al.*, *Astrophys. J.*, **153** (1968) 203.
- [21] ABDO A. A. *et al.*, *Astrophys. J.*, **703** (2009) 1249.
- [22] ABDO A. A. *et al.*, *Astrophys. J.*, **710** (2010) 133.
- [23] HUNTER S. D. *et al.*, *Astrophys. J.*, **481** (1997) 205.
- [24] DE BOER W. *et al.*, *Astron. Astrophys.*, **444** (2005) 51.
- [25] ABDO A. A. *et al.*, *Phys. Rev. Lett.*, **103** (2009) 251101.
- [26] SREEKUMAR *et al.*, *Astrophys. J.*, **400** (1992) L67.
- [27] ABDO A. A. *et al.*, *Astron. Astrophys.*, **512** (2010) A7.
- [28] ABDO A. A. *et al.*, *Astrophys. J.*, **709** (2010) L152.
- [29] ACCIARI V. A. *et al.*, *Nature*, **462** (2009) 770.
- [30] ACERO F. *et al.*, *Science*, **326** (2009) 1080.
- [31] REDMAN M. P. *et al.*, *Mon. Not. R. Astron. Soc.*, **344** (2003) 741.

LUCIFER: A new technique for Double Beta Decay

F. FERRONI

Università "La Sapienza" and INFN, Sezione di Roma - P.zza A. Moro 2, Rome, Italy

(ricevuto il 14 Settembre 2010; pubblicato online il 10 Gennaio 2011)

Summary. — LUCIFER (Low-background Underground Cryogenic Installation For Elusive Rates) is a new project aiming to study the neutrinoless Double Beta Decay. It will be based on the technology of the scintillating bolometers. These devices shall have a great power in distinguishing signals from α 's and β/γ 's promising a background-free experiment, provided that the Q value of the candidate isotope is higher than the ^{208}Tl line. The baseline candidate for LUCIFER is ^{82}Se . Here the LUCIFER concept will be introduced and the prospects related to this project will be discussed.

PACS 14.60.Pq – Neutrino mass and mixing.

PACS 23.40.-s – β decay; double β decay; electron and muon capture.

1. – Introduction

In the field of fundamental particle physics the neutrino has become more and more important in the last few years, since the discovery of its mass. In particular, the ultimate nature of the neutrino (if it is a Dirac or a Majorana particle) plays a crucial role not only in neutrino physics, but in the overall framework of fundamental particle interactions and in cosmology. The only way to disentangle its ultimate nature is to search for the so-called Neutrinoless Double Beta Decay ($0\nu 2\beta$) [1]. One of the best technologies for studying this extremely challenging problem is the bolometric one. Bolometers [2] are low-temperature-operated particle detectors which provide better energy resolution, lower energy thresholds and broader material choice than conventional devices. They can be thought of as perfect calorimeters, able to thermalize fully the energy released by a particle. The best features of bolometric detectors are:

- They can contain the candidate nuclei with a favorable mass ratio and be massive.
- They exhibit good energy resolution. This parameter is crucial since the signal is a peak in the energy spectrum of the detector positioned exactly at the Q -value of

the reaction. This peak must be discriminated over the background and therefore has to be narrow.

- They can be built in a way to be characterized by low intrinsic background.

Up to now, the choice for bolometers as $0\nu 2\beta$ detectors has fallen on natural TeO_2 that has very good mechanical and thermal properties together with a very large (27% in mass) content of the candidate ^{130}Te . The success of CUORICINO [3] and the excellent prospects for CUORE [4] are based on this approach. Bolometer-based $0\nu 2\beta$ searches require however extremely low levels of background. Even if you reduce drastically that arising from radioactive contaminants in the bolometers themselves, you still have the problem of the surrounding materials. Surface contamination is of particular concern. In fact, alpha-particles arising from radioactive contaminations located on the surfaces of the detector or of passive elements facing them can lose part of their energy in a few microns and deposit in the detector an energy close to that of the signal, thus mimicking a signal event. A realistic possibility to improve substantially the background rejection capability is to join the bolometric technique proposed for the CUORE experiment with the bolometric light detection technique used in cryogenic dark matter experiments. The bolometric technique allows an extremely good energy resolution while its combination with the scintillation detection offers an ultimate tool for background rejection. Preliminary tests on several double-beta-decay detectors have clearly demonstrated the excellent background rejection capabilities that arise from the simultaneous, independent, double readout (heat + scintillation). Indeed a demonstrator for this technique (LUCIFER) will be constructed in the next couple of here with ERC funding.

2. – The physics case

The oscillation experiments have proven that neutrinos are massive and do mix. They have measured with precision the mass difference squared between the neutrino species and two out of the three parameters of the P-MNS mixing matrix. These values allow to express the composition of the three flavour neutrino states (ν_e, ν_μ, ν_τ) in terms of their mass eigenstates (ν_1, ν_2, ν_3). One shall notice that the ambiguity inherent to the measurement of squared mass differences in the oscillation process leaves two possibilities for the hierarchical mass arrangements of neutrinos. There could also be a common baseline. The measured values of the neutrino mass differences are indeed tiny. Many orders of magnitude smaller than the mass of the lightest of charged leptons, the electron. Long ago E. Majorana formulated an elegant and minimal description of the neutrino field. The question is whether Nature makes use of this simplicity. Seventy years after, Majorana neutrinos are still an exciting possibility, indeed the best description we can find for the physical neutrinos. Majorana neutrino may explain the dominance of matter over antimatter in our Universe, on which asymmetry our very same existence depends. Until the discovery of the massive nature of neutrinos no much attention was paid to the issue of Majorana neutrino: if neutrinos are massless, as everybody believed, it did not matter. The Standard Theory changed the situation and it came (slowly) to be realized that the chiral symmetry is broken, so that there is no reason *a priori* to expect massless neutrinos and that a Dirac neutrino mass requires a right-handed (sterile, *i.e.* not interacting) neutrino, but then why neutrinos are so much lighter than the charged leptons or quarks? Majorana mass and weak isospin selection rules make it possible to find a natural explanation to the smallness of neutrino mass. The pattern of neutrino masses and mixing admit an elegant solution, the so-called see-saw mechanism. Although

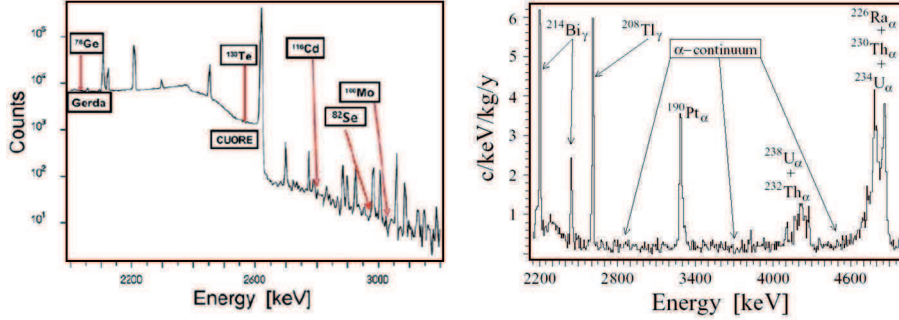


Fig. 1. – Left: Cuoricino background in the DBD region and above. It clearly shows the dominance of degraded α 's. Right: radiative nuclear transitions. It clearly shows that above the ^{208}Tl this contribution to the DBD background becomes negligible.

the possibility for this process was pointed out far in the past, the experimental search looked just impossible. The key element for the process to occur is in fact in the helicity flip needed. As long as the neutrino was thought to be massless this could just not happen. Nowadays we know that this is indeed possible. The DBD are extremely rare processes. In the two neutrino decay mode their half-lives range from $T_{1/2} \simeq 10^{18}\text{y}$ to 10^{25}y . The rate for this process will go as

$$1/\tau = G(Q, Z)|M_{\text{nucl}}|^2 m_{\beta\beta}^2.$$

The first factor (phase space) that goes like Q^5 is easily calculated. The second (nuclear matrix element) is hard to compute. Several calculations made under different approaches exist and the agreement is getting better and better with time.

The experimental investigation of these phenomena requires a large amount of DBD emitter, in low-background detectors with the capability for selecting reliably the signal from the background. The sensitivity of an experiment will go as

$$S^{0\nu} \propto a \left(\frac{MT}{b\Delta E} \right)^{1/2} \epsilon.$$

Isotopic abundance (a) and efficiency (ϵ) will end up in a linear gain, while mass (M) and time (T) only as the square root. Also background level (b) and energy resolution (ΔE) behaves as a square root. In the case of the neutrinoless decay searches, the detectors should have a sharp energy resolution, or good tracking of particles, or other discriminating mechanisms. The choice of the emitters should be made also according to its two-neutrino half-life (which could limit the ultimate sensitivity of the neutrinoless decay), according also to its nuclear factor-of-merit and according to the experimental sensitivity that the detector can achieve.

3. – The experimental challenge

There are three regions of neutrino mass that well separate the possible experiment on $0\nu 2\beta$. The degenerate already attained by experiments like HdM [5] and Cuoricino characterized by a need for sensitivity to masses in excess of 100 meV, the inverted

hierarchy confined between 20 and 100 meV and the direct one with masses in the meV range and below. The sensitivity to neutrino mass requested for probing the entire region of the inverted hierarchy requires a factor 10 with respect to what achieved so far. As the sensitivity goes with the square root of neutrino mass, this unpleasant feature calls for a factor 100 difference in any (or a combination of) parameter regulating the game: mass, live-time, energy resolution and background rate. Today's performance of the most advanced bolometric project, CUORE, already foresees a mass of 1 ton, a running time of 5 years and an energy resolution of 5 keV. As easily seen there is not much to gain from any of these parameters. Conversely the background index so far achieved with this technique is the 0.18 counts/keV/kg/y from Cuoricino (see fig. 1).

CUORE aims to 0.01 and so far has demonstrated a plausible 0.04. The following figure shows the request to experiment performance in terms of background called by the inverted hierarchy region search.

It is clear that a breakthrough is achieved only by going below 10^{-3} counts/keV/kg/y. The experience of Cuoricino shows clearly that energy-degraded α 's, emitted by surface radioactive contamination, populate the spectral region between 2.5 and 4 MeV with a dangerous continuum at the level of 0.1 counts/keV/kg/y. Therefore, the ability to tag α -particles would be a formidable asset. This improvement would be particularly effective if the investigated isotope presented an energy transition higher than the end point of the bulk of the natural radioactivity, *i.e.* the ^{208}Tl 2615 keV line. In this case, the simultaneous suppression of the γ background (thanks to the location of the transition energy) and of the α background (thanks to the identification of these particles), would provide a virtual zero background experiment.

4. – Scintillating bolometers

Bolometers represent the generalization of the Ge diode technique to the majority of the interesting candidates. Bolometers consist of two main parts.

- Energy absorber: It is the main detector part. The energy deposited by a single quantum into this element determines an increase of its temperature. This temperature variation corresponds to the ratio between the energy released by the particle and the heat capacity of the absorber. Therefore, the main requirement is to operate the device at low temperatures (usually less than 0.1 K and sometimes even less than 0.015 K) in order to make its heat capacity low enough. Another requirement is that the absorber material is dielectric and diamagnetic, assuring a very low specific heat at low temperatures.
- Thermometer: It is thermally coupled to the energy absorber and measures its temperature. The thermometer is usually a resistive element with a strong dependence of the resistance on the temperature. For large mass bolometers a reliable and simple thermistor technology consists of the use of neutron transmutation doped (NTD) Ge thermistors.

Scintillating bolometers to the search for $0\nu 2\beta$ bring in an enormous added value, by allowing the use of high Q -value candidates first, and second by providing a substantial α/β discrimination power. When the energy absorber in a bolometer is an efficient scintillator at low temperatures, a small but significant fraction of the deposited energy (up to a few %) is converted into scintillation photons, while the remaining dominant part is detected as usual in the form of heat. The simultaneous detection of the scintillation

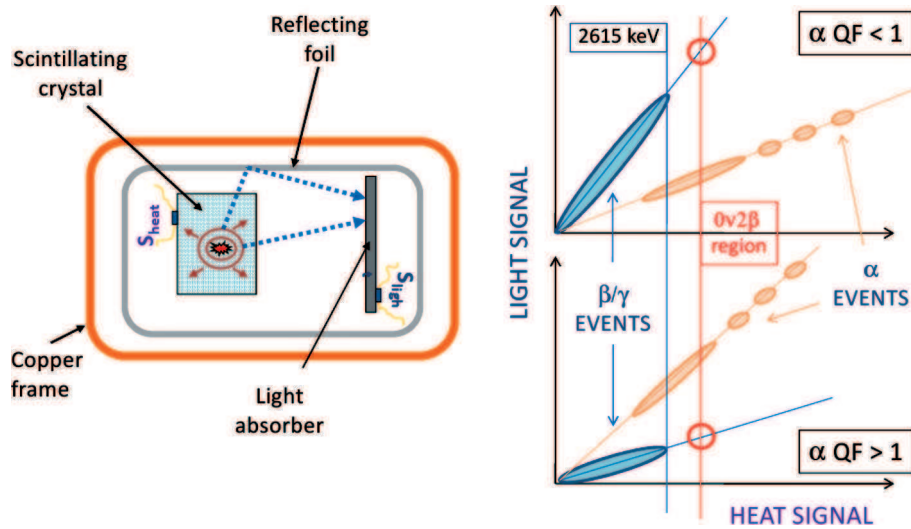


Fig. 2. – Left: schematic structure of a double read-out scintillating bolometer. All the basic elements of the detector are shown. Right: schematic scatter plots of light signals *vs.* heat signals corresponding to events occurring in the scintillating bolometer. Cases with QF larger or smaller than 1 are illustrated. In both circumstances α events can be efficiently rejected and the $0\nu 2\beta$ signal region is background free.

light is a very powerful tool to identify the nature of the interacting particle. In particular, alpha-particles can be discriminated (see fig. 2) with respect to beta and gamma interaction because of the different quenching factor (QF).

A scintillating bolometer for $0\nu 2\beta$ is no new concept in the field and was proposed more than one decade ago for ^{48}Ca with CaF_2 crystals [6]. Nature has kindly provided

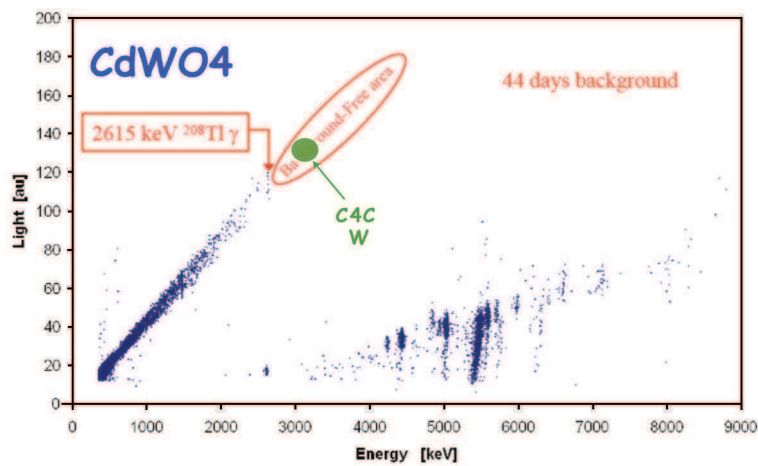


Fig. 3. – Results from a run on a CdWO_4 crystal with double (heat and light) readout exposed to radioactive sources.

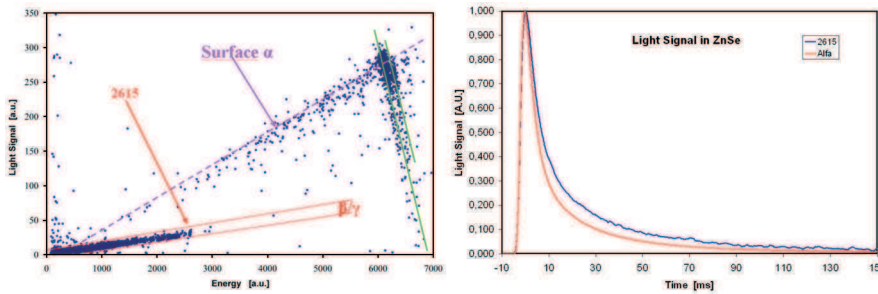


Fig. 4. – Results from a run on a ZnSe crystal with double (heat and light) readout exposed to radioactive sources. Left: scatter plot light *vs.* heat. Right: decay time of the scintillation light for α 's and ^{208}Tl line.

us with a few isotope candidates presenting a transition energy higher than 2615 keV and forming chemical compounds suitable for the growth of large scintillating crystals, which proved to work as highly performing bolometers as well. The most suited are based on Cd, Mo and Se with the drawback of a need for an isotopic enrichment that brings their natural abundances (less than 10%) to a much higher value. This means in practice that although results [7] obtained by using CdWO_4 have basically proven (see fig. 3) the power of this approach the final choice for a practical experiment cannot make use of this crystal. Cd is difficult to enrich, the process is extremely costly and the residual, unavoidable presence of ^{109}Cd and ^{113}Cd too much of a nuisance. Mo does not offer at this point any convincing crystalline compound and it is an element heavily contaminated by the presence of U, Th. When applying different materials to this scheme and considering all the relevant elements (scientific, technical, economical), the final balance is in favour of ^{82}Se (ZnSe crystals).

5. – LUCIFER demonstrator

One of the most striking features of ZnSe is the abnormal QF, higher than 1 unlike all the other studied compounds. Although not really welcome, this unexpected property does not degrade substantially the discrimination power of this material compared to the others and makes it compatible with the requirement of a high-sensitivity experiment. An additional very useful feature is the possibility to perform α/β discrimination on the basis of the temporal structure of the signals, both in the heat and light channel (see fig. 4).

The detector configuration proposed for LUCIFER resembles closely the one selected and extensively tested for CUORE, with an additional light detector, designed according to the recipes developed during the scintillating-bolometer R&D and consisting of an auxiliary bolometer, opaque to the light emitted by the ZnSe crystals (see fig. 5). A preliminary version of the LUCIFER structure consists of an array of 48 crystals, divided in 12 elementary modules with 4 crystals each arranged in a tower, which would fit exactly the experimental volume of the Cuoricino cryostat. This structure assumes that a single light detector, quite large in order to monitor four scintillating crystals simultaneously, is sensitive enough to perform efficiently the α/β discrimination. The total detector mass would be 25 kg, with about 14 kg of enriched material assuming an enrichment level of 97%. A preliminary evaluation of the LUCIFER sensitivity can be made on the basis of the structure discussed above and on the background expectations

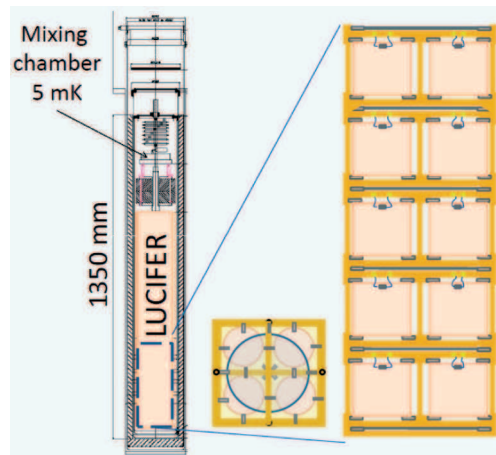


Fig. 5. – Schematics of Lucifer detector. Left: Cuoricino cryostat with Lucifer inserted. Center: top view of 2×2 crystal plane with Ge light detector on top. Right: side view of the detector array.

after α/β rejection. Assuming 5 year live time, an energy window of 20 keV and a specific background coefficient of 10^{-3} counts/keV/kg/y, less than a few background counts are expected in the region of interest (the transition energy for ^{82}Se is 2995 keV). This corresponds to a sensitivity to the Majorana neutrino mass of the order of 100 meV. The most important goal for LUCIFER is to be a demonstrator of the scintillating bolometer technology, with a significant mass and a full test of all the critical elements of this approach:

- large-scale enrichment,
- efficient chemical purification meeting radioactive requirements,
- large-size crystals grown with high efficiency in using the precious (100\$/g) material,
- background rejection investigated in many modules simultaneously operated.

It has the ambition to indicate the way to the experiment for the search of $0\nu 2\beta$ able to span over the whole inverted hierarchy region.

* * *

The project LUCIFER has received funding from the European Research Council under the European Unions Seventh Framework Programme (FP7/2007-2013)/ERC grant agreement n. 247115.

REFERENCES

- [1] AVIGNONE F. T., ELLIOT R. S. and ENGEL J., *Rev. Mod. Phys.*, **80** (2008) 481.
- [2] FIORINI E. and NIINIKOSKI T. O., *Nucl. Instrum. Methods Phys. Res. A*, **224** (1984) 83.
- [3] ARNABOLDI C. *et al.*, *Phys. Rev. C*, **78** (2008) 035502.

- [4] ARDITO R. *et al.*, hep-ex/0501010 (2005).
- [5] KLAPDOR-KLEINGROTHAUS H. V., Proposal MPI-1987-V17 (1987).
- [6] ALESSANDRELLO A. *et al.*, *Phys. Lett. B*, **420** (1998) 109.
- [7] ARNABOLDI C. *et al.*, nucl-ex/1005.1239 (2010).

Recent developments in theory and phenomenology of Dark Matter

M. CIRELLI

*CERN Theory Division - CH-1211 Genève, Switzerland
Institut de Physique Théorique, CNRS & CEA/Saclay - 91191 Gif-sur-Yvette, France*

(ricevuto il 14 Settembre 2010; pubblicato online il 10 Gennaio 2011)

Summary. — Dark Matter constitutes more than 80% of the total amount of matter in the Universe, yet almost nothing is known about its nature. A powerful investigation technique is that of searching for the products of annihilations of Dark Matter particles in the galactic halo, on top of the ordinary cosmic rays. Recent data from the PAMELA and FERMI satellites and a number of balloon experiment have reported unexpected excesses in the measured fluxes of cosmic rays. Are these the first direct evidences for Dark Matter? If yes, which DM models and candidates can explain these anomalies (in terms of annihilations) and what do they imply for future searches and model building? What are the constraints from gamma-rays measurements and cosmology?

PACS 95.35.+d – Dark matter (stellar, interstellar, galactic, and cosmological).

1. – Introduction

While compelling evidence for the existence of Dark Matter (DM) now comes from a number of astrophysical and cosmological probes, no explicit detection has been confirmed yet. The indirect detection strategy relies on the possibility of seeing signals of the presence of DM in terms of the final products (e^\pm , p , d , γ , $\nu \dots$) of DM annihilations in the galactic halo, on top of the ordinary cosmic rays. The recent positive results from a number of indirect detection experiments have suggested the possibility that indeed such a signal has been seen. In particular, the signals point to an excess of electrons and positrons.

- Data from the PAMELA satellite show a steep increase in the energy spectrum of the positron fraction $e^+/(e^+ + e^-)$ above 10 GeV up to 100 GeV, compatibly with previous less certain hints from HEAT and AMS-01.
- Data from PAMELA also show no excess in the \bar{p}/p energy spectrum compared with the predicted background.

- The balloon experiments ATIC-2 and PPB-BETS report the presence of a peak in the $e^+ + e^-$ energy spectrum at around 500–800 GeV.
- This sharp feature is however questioned by the results of the FERMI satellite: while an excess with respect to the expected background is confirmed, the $e^+ + e^-$ spectrum is found to be instead reproduced by a simple power law.
- The HESS telescope also reports the measurement of the $e^+ + e^-$ energy spectrum above energies of 600 GeV, showing a power law spectrum in agreement with the one from FERMI and eventually a steepening at energies of a few TeV.

In this presentation I will address the following issues (the discussion is based on [1-5], where all references are given):

- i) Which characteristics must a DM candidate have in order to fit the above data?
- ii) What are the constraints from other observations (*e.g.* diffuse galactic γ -rays)?
- iii) Are there constraints from cosmological observations?
- iv) Which conclusions can then be drawn on the DM interpretation of the data?

2. – Positrons, electrons and antiprotons: which DM can fit the data?

As a first example, the upper row of fig. 1 shows the spectra of the positron fraction (first column), of the sum of electrons and positrons (second column) and of the antiprotons (third column) from a DM particle with 150 GeV mass and annihilating into W^+W^- . As apparent, the candidate can fit well the positron data, but produces too large a flux of antiprotons: such a DM is excluded by data with pretty high confidence, unless a serious misunderstanding of the \bar{p} background is invoked. Let us instead consider (second row of fig. 1) a candidate with a (very large) 10 TeV mass, again annihilating into W^+W^- . The positron data points are well fitted (by the low energy tail of the spectrum, in this case) and the antiproton bounds are not exceeded, thanks to the fact that an excess would show only at larger energies. However the features reported in the $e^+ + e^-$ spectrum are not reproduced. In the third row we consider a 1 TeV candidate with annihilations into $\mu^+\mu^-$: it fits the PAMELA data in e^+ , \bar{p} (which are not produced by the purely leptonic channel) and it reproduces the peak in the $e^+ + e^-$ spectrum hinted to by ATIC. As a final example, we consider a slightly heavier (3 TeV) candidate with annihilations into $\tau^+\tau^-$ (fourth row of fig. 1): it fits the PAMELA, FERMI and HESS datasets.

We now proceed to presenting the results of the fits in a more systematic way. In performing such fits, we smoothly scan over the charged cosmic ray propagation configurations and DM halo models, within the boundaries described in [1]. Moreover, we assume that the e^+ , e^- , \bar{p} background spectra can be freely renormalized, and have independent ± 0.05 errors in their energy slope. This mimics the main uncertainties in astrophysical backgrounds. We will show plots of the χ^2 as a function of the DM mass: an interval at n standard deviations corresponds (in Gaussian approximation) to $\chi^2 < \chi^2_{\min} + n^2$, irrespectively of the number of data points.

First, let us consider the fit to PAMELA positron data only (16 data points). We see in the upper left panel of fig. 2 that DM annihilations into e, μ, τ, W can reasonably well reproduce the data for any DM mass, while annihilations into Z, t, q, b, h give a good

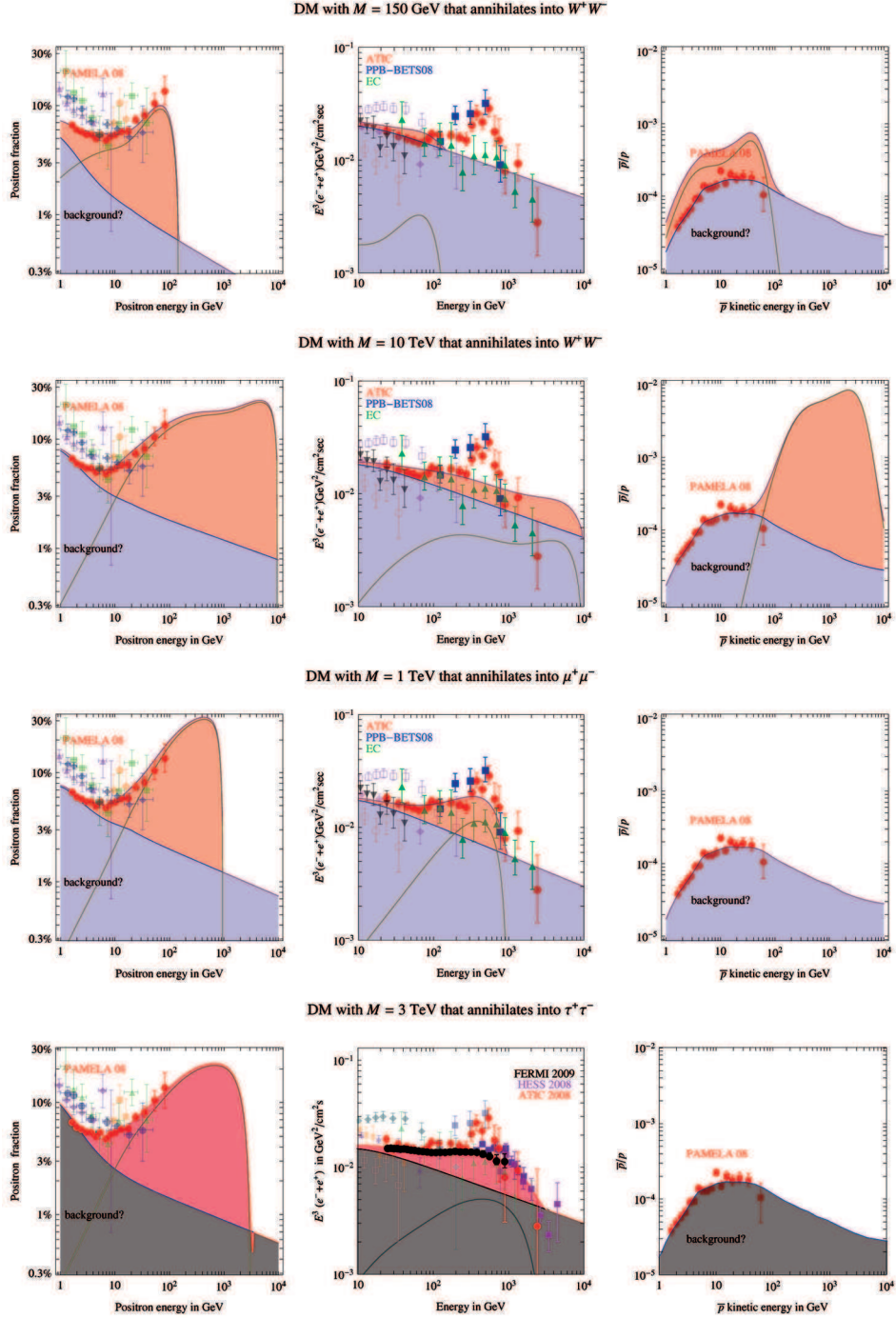


Fig. 1. – Four examples of fits of e^+ (left), $e^+ + e^-$ (center), \bar{p} (right) data, for a DM particle with mass $M = 150$ GeV annihilating into W^+W^- (upper row, excluded by \bar{p}), $M = 10$ TeV into W^+W^- (second row, disfavored by the $e^+ + e^-$ data), $M = 1$ TeV into $\mu^+\mu^-$ (third row, in agreement with ATIC data) and $M = 3$ TeV into $\tau^+\tau^-$ (lower row, favored by FERMI and HESS). Galactic DM profiles and propagation models are varied to provide the best fit.

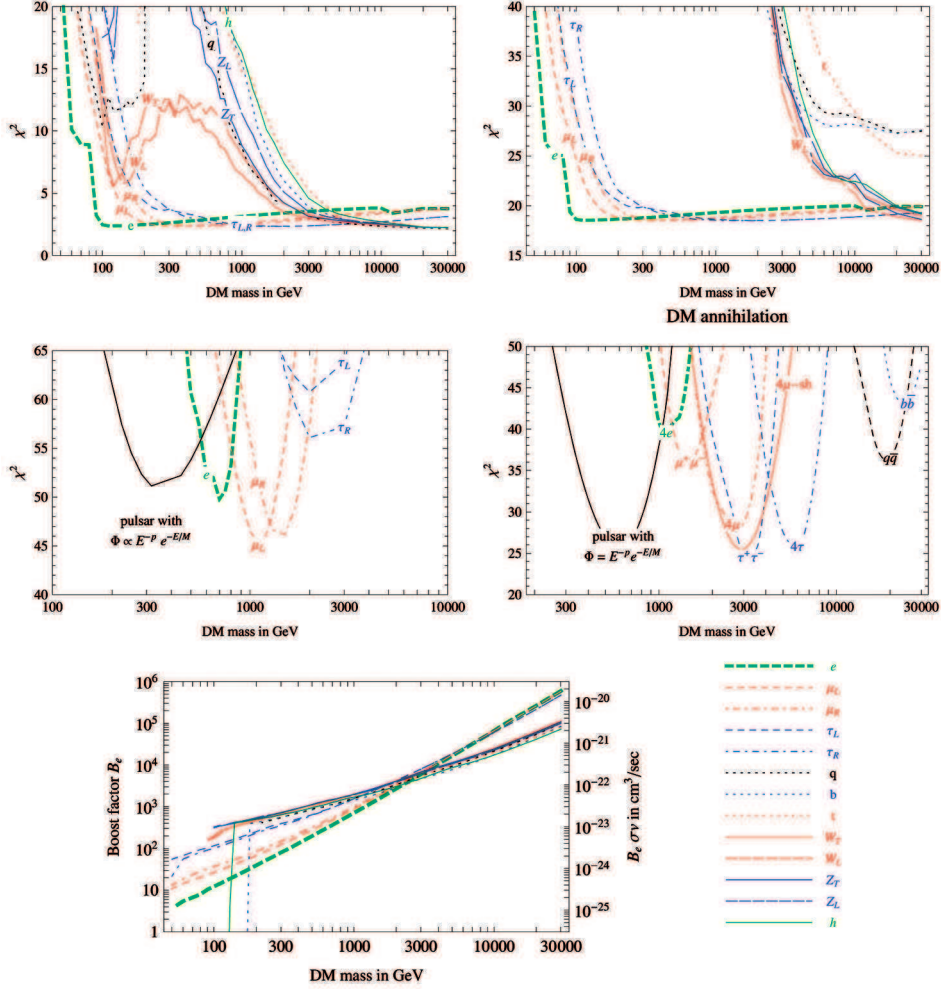


Fig. 2. – Global fits of different DM annihilation channels to the data. The labels on each curve indicate the primary annihilation channel. Upper left: fit to PAMELA e^+ fraction data only. Upper right: with the inclusion of PAMELA antiproton data. Lower left: with the inclusion of balloon $e^+ + e^-$ data. Lower right: replacing balloon data with FERMI and HESS data (figure from P. Meade, M. Papucci, A. Strumia, T. Volansky, arXiv: 0905.0480; the four-lepton lines refer to exotic channels which are not discussed here). Bottom: values of $B_e \cdot \sigma v$ (right axis) and of the boost factor B_e (left axis, for $\sigma v = 3 \cdot 10^{-26}$ cm³/s) needed to fit the data.

fit for DM heavier than about 1 TeV. It is perhaps interesting to note that, contrary to what commonly thought, the spectrum from W^+W^- annihilations is not too flat to give a good fit of the quite steep PAMELA rise.

Next, let us add the PAMELA \bar{p}/p data (17 data points). Since no excess seems present in the \bar{p}/p ratio, annihilations into leptons are not constrained as they do not produce antiprotons. On the contrary, all other annihilations into quarks, vector and Higgs bosons are significantly constrained, and allowed only if the DM particle is heavier than almost 10 TeV (see the upper left panel of fig. 2). Only in such a case the proton

excess lays at energies above those explored currently by PAMELA, while the low energy proton spectrum is consistent with the background (see fig. 1 for illustration). The bound dominantly comes from high energy data points where the solar modulation is negligible. The implications of the complementarity of PAMELA $e^+/(e^+ + e^-)$ and \bar{p}/p data on constraining new physics are therefore evident.

We add now to the fit the balloon (ATIC-2, PPB-BETS and EC) data (37 points in total). Because the balloon data shows a sharp cut-off in the excess just below 1 TeV, the DM mass should be close to 1 TeV, and all other but leptonic DM annihilation channels are strongly disfavored or excluded. This is shown in the lower left panel of fig. 2. More precisely, DM annihilations into μ seem to give the optimal energy spectrum and the best fit (see, *e.g.*, the example discussed above in fig. 1).

Finally, replacing the balloon data by the FERMI and HESS data (lower right panel of fig. 2) modify slightly the best fit in favor of a candidate with a somewhat higher mass (~ 3 TeV) and a channel producing smoother leptonic spectra such as $\tau\tau$.

The lowermost panel of fig. 2 illustrates the last important point: the values of the annihilation cross section which are required in order to fit the data (for a given mass and given primary annihilation channel). Values of the order of 10^{-23} cm³/s or more (for the masses under consideration) are needed. These are much larger than the typical cross section required by DM thermal production in cosmology ($\sim 3 \cdot 10^{-26}$ cm³/s). They can be justified in specific models in terms of some enhancement mechanism which is effective today but not in the early universe (such as a resonance or Sommerfeld enhancement, the presence of an astrophysical boost factor due to DM substructures —unlikely—, or a combination of these).

3. – Constraints from prompt γ -rays, ICS γ -rays and radio observations

Given these tantalizing but surprising hints of Dark Matter annihilations in the charged particle signals, it is now crucial to consider the constraints on this interpretation that come from the photon fluxes that necessarily accompany them. These photon fluxes are produced:

- i) Directly as a product of the DM annihilations themselves (mainly from the bremsstrahlung of charged particles and the fragmentation of hadrons, *e.g.*, π^0 , produced in the annihilations), at energies comparable to the DM mass M , *i.e.* in the γ -ray energy range of tens of GeV to multi-TeV.
- ii) By the Inverse Compton Scattering (ICS) of the energetic electrons and positrons, produced in the DM annihilation, onto the low energy photons of the CMB, the galactic star-light and infrared-light, which are thus upscattered up to energies again comparable to the DM mass.
- iii) At much lower energies, *e.g.*, radio frequency, by the synchrotron radiation emitted in the galactic magnetic field by the e^\pm produced by DM annihilations.

The best targets to search for these annihilation signals are regions with high DM densities, such as the Milky Way Galactic Center (GC), the Milky Way Galactic Ridge (GR) and the Sagittarius Dwarf spheroidal satellite galaxy (Sgr dSph). In the case of the ICS signal, however, an intense flux is expected also from the regions of the galactic halo outside of the messy GC region, a feature which makes this a very interesting and more robust signature. The predicted photon fluxes can then be compared with observational

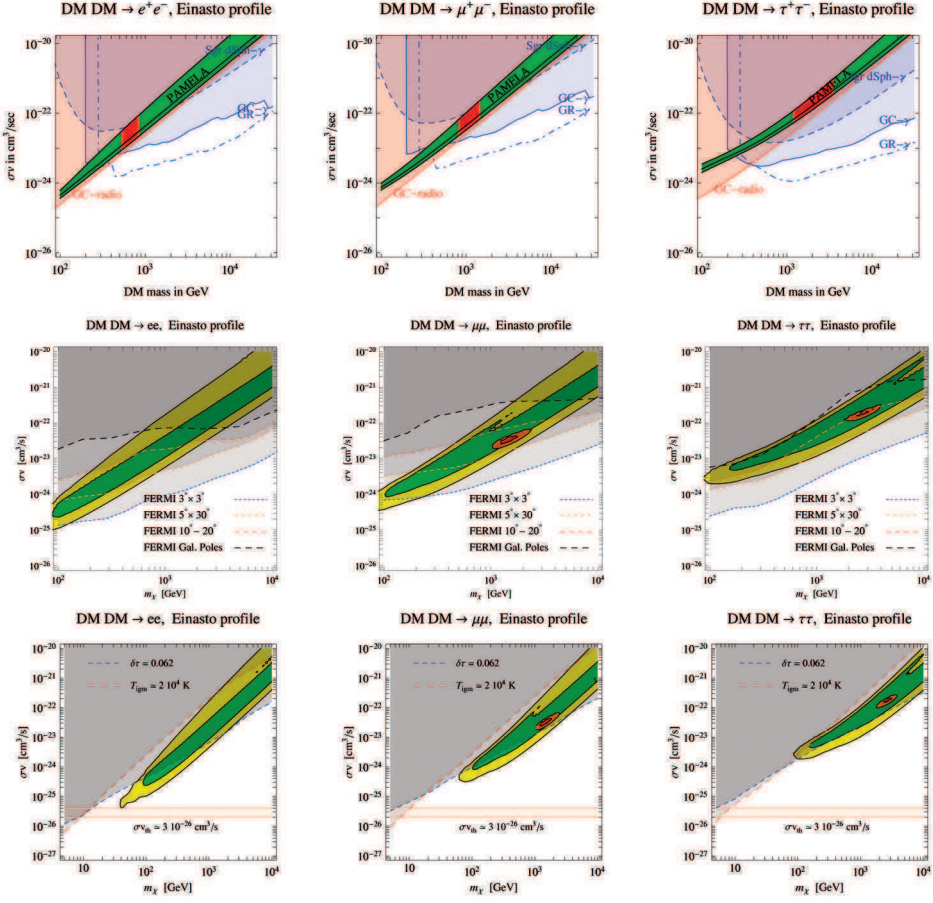


Fig. 3. – (Colour on-line) Comparison of the regions favored by PAMELA (green bands) + ATIC (red or yellow vertical regions within the bands) or + FERMI+HESS (orange blobs) with the bounds from gamma-rays and cosmology. First row: constraints from HESS observations of the Galactic Center (blue continuous line), Galactic Ridge (blue dot-dashed), and SgrDwarf (blue dashed) and of observations of the GC at radio-frequencies by Davies *et al.* (red lines). Second row: constraints from FERMI data of large windows in the galactic halo. Third row: constraints from the optical depth of the Universe and the temperature of the Intergalactic Medium. We considered DM annihilations into e^+e^- (left), $\mu^+\mu^-$ (middle), $\tau^+\tau^-$ (right) and an Einasto DM density profile for the Milky Way and a density profile for Sgr dSph characterized by a large core. We assume unit boost and Sommerfeld factors.

data, in order to rule out combinations of astrophysical and particle physics parameters that violate observational constraints. The results of this are shown in fig. 3, for the case of leptonic annihilations and choosing a benchmark Einasto profile. The first row shows the bounds imposed by prompt gamma-rays and radio waves (shaded areas are excluded). The second row shows the constraints from ICS gamma-rays using different observations from FERMI. It is apparent that the regions identified by PAMELA (and ATIC/FERMI) are excluded by these constraints. It is possible to relax them by assuming a less steep DM profile, such as isothermal (less DM concentration in the GC region leads to less

gamma-ray production), which is however disfavored by numerical simulations. For a full discussion, see refs. [2, 3, 5].

4. – Constraints from the reionization history

The flux of energy injected by DM annihilation (all the way from the recombination epoch down to today through the formation history of DM halos) results in ionization and heating of the intergalactic medium. One way to constrain DM annihilation properties is therefore to look at the total optical depth of the Universe τ , which results from the free electrons produced by the ionization. τ is measured by WMAP to be $\tau = 0.084 \pm 0.016$, of which about 0.038 due to the low-redshift reionization ($z < 6$) produced by stars. A DM-induced optical depth larger than 0.062 (the 1σ upper bound of the above) is therefore excluded by these arguments. Another way of assessing the impact of DM annihilations is to follow the evolution of the temperature of the intergalactic medium: temperatures higher than about $2 \cdot 10^4$ K at low redshift contradict observations.

The third line of fig. 3 shows such excluded regions on the usual plane “DM mass” *vs.* “Annihilation cross section”, for the same benchmark cases of leptonic channels and an Einasto profile. Again one finds that large portions of the regions that allow to fit the PAMELA and FERMI+HESS CR excesses in terms of DM annihilations are ruled out by the optical depth bound. For instance, the entire PAMELA and FERMI+HESS region for the $\tau^+\tau^-$ or $\mu^+\mu^-$ case around $m_\chi = 2$ or 3 TeV is excluded. For a full discussion, see ref. [4].

5. – Conclusions

En lieu of conclusions, let us try to answer the questions raised in the Introduction.

- *Which characteristics must a Dark Matter candidate have in order to fit the above data?*
 - a) on the basis of the e^+ and \bar{p} data from PAMELA, the Dark Matter can be:
 - a1) a particle that dominantly annihilates into leptons, with no strong preference for the mass, if above a few hundred GeV;
 - a2) a particle that annihilates into W, Z or h and that has a mass $\gtrsim 10$ TeV.
 - b) adding the peak from ATIC, a clear indication for the mass emerges: DM has to be a particle with mass ~ 1 TeV that dominantly annihilates into leptons.
 - c) replacing the ATIC peak with the FERMI smoother spectrum and the indication for a cutoff at a few TeV from HESS shifts somewhat the best fit, but not the main features: DM has to be a particle with mass ~ 3 TeV that dominantly annihilates into leptons (τ is best).

Models with $M \ll 1$ TeV appear anyway to be already disfavored. For what concerns the magnitude of the annihilation cross section, the large flux above the background in the PAMELA data indicates a very large σv , of the order of 10^{-23} cm³/s or more (see lower right panel of fig. 2).

- *What are the constraints from other observations (diffuse galactic γ -rays)?*

Constraints are imposed by high energy gamma-rays (generated directly from the DM annihilation process or by the ICS upscattering of the CMB and starlight

photons) from the galactic center region and from satellite galaxies and by synchrotron radiation (generated by e^\pm in the galactic center's magnetic field). The results show that the regions of the parameter space that allow to fit the PAMELA (and ATIC or FERMI+HESS) data are disfavored by about one order of magnitude if a benchmark Einasto (or NFW) profile is assumed. Choosing a smoother profile and/or assuming that a part of the cross section is due to an astrophysical boost factor that would not be present in dwarf galaxies and the Galactic Center due to tidal disruption re-allows part of the space. ICS constraints are however more robust and more difficult to circumvent with these arguments. It is fair to say that a tension is present between the charged CR signals and the gamma-ray constraints.

– *Are there constraints from cosmological observations?*

Yes, robust constraints are imposed by the reionization history of the Universe: DM annihilations that allow to explain PAMELA+FERMI+HESS tend to produce too many free electrons that make the Universe more opaque than what is observed.

– *Which conclusions can be drawn on the Dark Matter interpretation of the data?*

As apparent, the data point to a Dark Matter particle that 1) features really “unexpected” properties and 2) has anyway disturbing “internal” tensions (with γ -ray constraints and cosmology). So, either the DM interpretation is not the right one, *i.e.* an astrophysical source will turn out to be responsible for the excesses. Or we are on the verge of a big change of paradigm in the field of DM modelling.

* * *

I thank my collaborators G. BERTONE, C. BRAÜNINGER, M. KADASTIK, F. IOCCO, P. PANCI, M. RAIDAL, P. D. SERPICO and M. TAOSO for the work presented here. I thank A. STRUMIA for providing the occasion for me to participate to this conference. I thank the EU Marie Curie Research & Training network “UniverseNet” (MRTN-CT-2006-035863) for support.

REFERENCES

- [1] CIRELLI M., KADASTIK M., RAIDAL M. and STRUMIA A., *Nucl. Phys. B*, **813** (2009) 1 [arXiv:0809.2409].
- [2] BERTONE G., CIRELLI M., STRUMIA A. and TAOSO M., *JCAP*, **0903** (2009) 009 [arXiv:0811.3744].
- [3] CIRELLI M. and PANCI P., *Nucl. Phys. B*, **821** (2009) 399 [arXiv:0904.3830 [astro-ph.CO]].
- [4] CIRELLI M., IOCCO F. and PANCI P., *JCAP*, **0910** (2009) 009 [arXiv:0907.0719 [astro-ph.CO]].
- [5] CIRELLI M., PANCI P. and SERPICO P. D., arXiv:0912.0663 [astro-ph.CO].

SESSION II - ASTROPARTICLE AND NEUTRINO PHYSICS

<i>Ioana C. Mariş</i>	Results from the Pierre Auger Observatory
<i>Arnon Dar</i>	The missing cosmic baryons found?
<i>Nicolas Picot Clémente</i>	The ANTARES deep-sea neutrino telescope—Status and first results
<i>Alejandro Ibarra</i>	Neutrino physics and lepton flavour violation: A theoretical overview
<i>Elisabetta Pennacchio</i>	Neutrino oscillations studies with the OPERA experiment at the CNGS beam
<i>Yuri Suworov</i>	New results and strategy of Borexino
<i>Satoshi Mihara</i>	J-PARC kaon and muon programs
<i>Daniel Greiner</i>	Towards Θ_{13} with Double Chooz
<i>Jonathan M. Paley</i>	Recent results and future prospects for the MINOS experiment

Results from the Pierre Auger Observatory

IOANA C. MARIȘ for the PIERRE AUGER COLLABORATION

Laboratoire de physique nucléaire et des hautes énergies - Paris, France

(ricevuto il 14 Settembre 2010; pubblicato online l'11 Gennaio 2011)

Summary. — Ultra high energy cosmic rays are observed at the Pierre Auger Observatory, the largest cosmic rays experiment in operation, through a hybrid technique employing fluorescence and surface detectors. We present the measurements on the evolution of the mass with energy, the energy spectrum features, photon and neutrino limits and anisotropies based on the data collected between 2004 and 2009.

PACS 98.70.Sa – Cosmic rays (including sources, origin, acceleration, and interactions).

PACS 95.55.Vj – Neutrino, muon, pion, and other elementary particle detectors; cosmic ray detectors.

1. – Introduction

The identification of the origin of the highest energy particles relies on the knowledge of the propagation in the magnetic fields, of the space distributions of sources and on their predicted fluxes. The determination of the energy, the mass and the arrival directions of the ultra high energy cosmic rays is an essential element to solve this inquiry. The Pierre Auger Observatory has delivered, even during its construction stage, accurate measurements of the spectral features, evidence for anisotropies at the highest energies, the most stringent limits on the neutrino and photon fluxes and a precise measurement of the evolution of the mass composition with energy.

At the highest energies a flux suppression is present and can be attributed to the interaction of the cosmic rays with the cosmic microwave background (CMB), the Greisen-Zatsepin-Kuz'min (GZK) effect [1, 2], or to the maximum acceleration power of the sources. The ankle, a hardening of the energy spectrum measured at around 3 EeV, can originate from either the transition from the galactic to the extragalactic components or from the e^\pm production of protons interacting with the CMB [3]. These models cannot be distinguished from the spectral shape, but both differ by the mass composition of the cosmic rays that reach the Earth and their anisotropy properties.

The hadronic cosmic rays are accompanied by photons and neutrinos produced at the acceleration sites and during the propagation of protons. The current limits on high energy neutrinos and photons fluxes are excluding the top-down production scenarios, but are still far from predicted GZK flux.

2. – Pierre Auger Observatory

Cosmic rays, entering the atmosphere interact with the air and produce extensive air showers. The Pierre Auger Observatory [4], located in the province of Mendoza (Argentina), is used to measure the properties of extensive air showers by observing their longitudinal development in the atmosphere as well as their lateral spread at ground level. The charged particles that reach the ground are detected with the surface detector (SD), their lateral extension at cosmic rays energies above 10^{18} eV is of the order of a few kilometers. The Observatory contains more than 1600 independent water-Cerenkov detectors, filled with 12 tons of water each and equipped with three photomultipliers to detect secondary photons and charged particles. The tanks are spread over about 3000 km^2 on a triangular grid of 1.5 km spacing.

On the way through the atmosphere charged particles excite nitrogen molecules, which afterwards emit fluorescence light in the ultra-violet band. The amount of light is proportional to the energy deposited by the air shower. The atmosphere above the surface detector is viewed by four fluorescence detectors (FD), each housing six telescopes, located on the border of the area. The field of view of each telescope is 30° in azimuth, and $1.5\text{--}30^\circ$ in elevation. Light is focused with a spherical mirror of 11 m^2 effective area on a camera of 440 hexagonal pixels.

More details on detector setup and calibration can be found in [4, 5]. An extension of the Observatory [6] has been started with AMIGA [7], a denser array of tanks equipped with muon counters which will lower the trigger threshold energy for the SD, HEAT, three telescopes that will increase the field of view of FD up to 60° and AERA a 20 km^2 antenna array to detect the radio signal produced in air showers by e^\pm interactions with the geomagnetic field. The counterpart of the Southern side is in the planning phase in the Northern hemisphere, in Lamar, Colorado and will be built to provide large statistics above 50 EeV.

An example of a reconstruction of the same air shower with the SD and FD is shown in fig. 1. The signals recorded in the tanks are expressed in terms of vertical equivalent muons (VEM), the average of the signals produced in the 3 PMTs by a vertical muon that passes centrally through the detector. The air shower axis, in case of the SD reconstruction, is obtained from the arrival time of the first particles in each surface detector. The angular resolution is better than 1 degree for events that triggered more than 6 stations. The impact point on the ground and the lateral distribution of signals are obtained in a global likelihood maximization which accounts for the station trigger threshold and the overflow of the FADCs counts in the stations very close to the shower axis. The fluctuations of the lateral distribution function, influenced by the array spacing, are minimized at 1000 m. The signal at this specific distance, $S(1000)$, is corrected through a constant intensity method for the attenuation in the atmosphere and then is used as the energy estimator.

About one in ten air showers that reach the surface detector are also observed with the fluorescence detector which operates only on moonless clear nights. The longitudinal profile of the air shower, *i.e.* the energy deposit as a function of traversed matter in the atmosphere, is obtained from fluorescence and Cerenkov light taking into account the

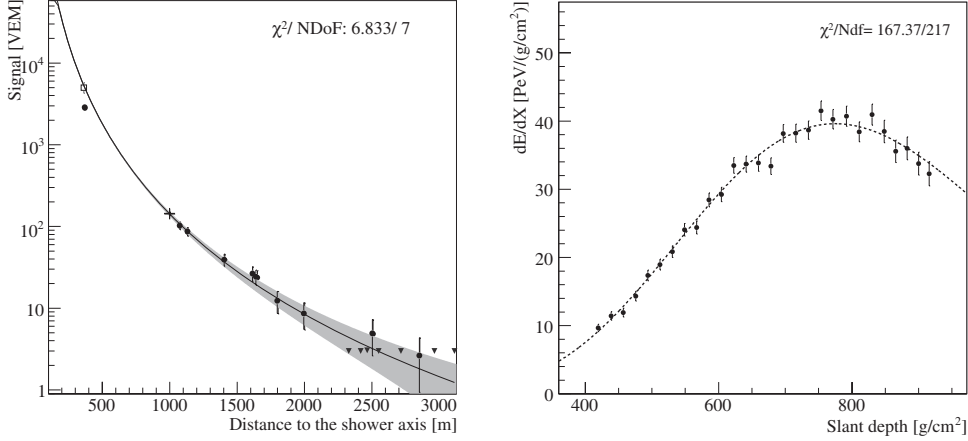


Fig. 1. – A typical golden hybrid event reconstruction, with an energy of 30 EeV and an incoming direction of 27° . Left-hand side: lateral distribution. Filled circles represent acquired signals, triangles are functioning stations without signal used with Poisson probabilities in the maximum likelihood fit. S(1000) is marked with a cross. Right-hand side: longitudinal profile: energy deposit in the atmosphere as a function of the slant depth.

light scattering and attenuation [8]. The energy of the cosmic ray is the integral over the entire longitudinal profile with a correction for the energy carried away by the neutrinos and muons which cannot be seen by FD.

The hybrid reconstruction of events employs, besides the information from the cameras, the timing information of one surface detector, resulting in a good angular and energy resolutions. The energy resolution for the hybrid events is 6% above 1 EeV, while the angular resolution is 0.6 degree.

The energy calibration of the surface detector data is obtained from the events that have been recorded and reconstructed with both SD and FD. The S(1000) shows a power law dependence on the primary energy. The resolution of the energy obtained from S(1000) is energy dependent and varies from 17% at 3 EeV to about 7% at the highest energies.

3. – The flux and the arrival directions

The only quality criteria applied on the surface detector data used for the energy spectrum is that the station with the highest signal is surrounded by 6 active stations. This leads to a simple calculation of the exposure for the surface detector [9], independent of energy above 3 EeV. At this energy, which is the lower bound for the derived surface detector spectrum, all the air-showers trigger at least 3 stations and can be reconstructed. This simple selection criteria makes the acceptance free of MC assumptions, as it does not depend on the reconstruction. The energy resolution and the bias due to signals upward fluctuations (about 20% at the lowest energies with a positive bias of 5% and about 7% with no bias at the highest energies) modify, through bin-to-bin migrations in a steep falling distribution, the flux and the spectral shape. To correct for these effects a forward folding procedure is applied, using an energy migration matrix obtained from MC simulations of the air-showers and of the detector response. The correction factor

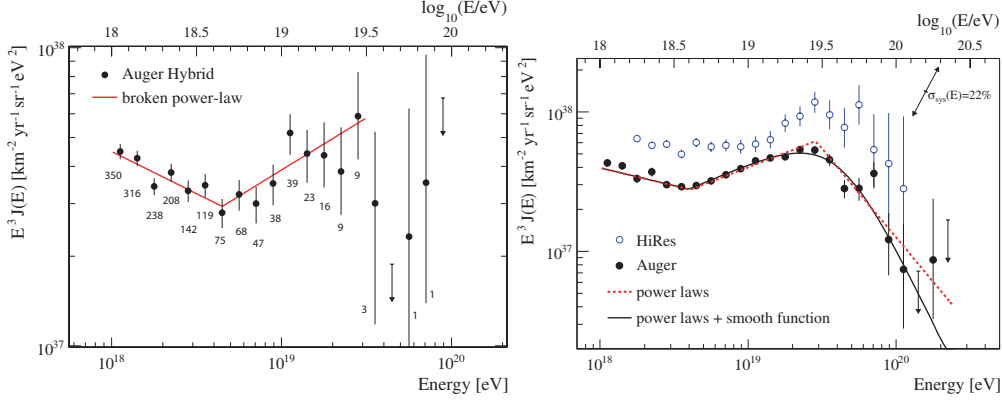


Fig. 2. – (Left) The energy spectrum of the highest energy cosmic rays obtained from hybrid measurements. Only statistical uncertainties are shown. The numbers correspond to the amount of events in each energy bin. (Right) The Auger energy spectrum, fitted with a broken power law function in the ankle region and a soft Fermi-like transition at the highest energies. The HiRes spectrum, illustrated with open symbols, is compatible with the Auger spectrum within the energy systematic uncertainties.

that is applied to the flux, less than 20%, is obtained from a simple flux parametrisation which, folded with the migration, describes best the raw data.

The systematic uncertainties that are inherited from the mass composition and the energy conversion assumed in the MC samples are about 5% over the whole energy range. This, together with the systematic uncertainties on the acceptance (3%) lead to a 6% uncertainty of the flux.

The hybrid events allow to extend the energy spectrum up to 1 EeV in the region of the ankle. The hybrid exposure calculation relies on an accurate simulation of the fluorescence detector and of the atmosphere. A large sample of Monte Carlo simulations is performed to reproduce the exact conditions of the experiment and the entire sequence of given configurations, from camera pixels to the combined SD-FD data taking of the observatory. The rapidly growing array, as well as the seasonal and instrumental effects, are reproduced in the simulations within 10 min time intervals. The systematic uncertainty in the hybrid spectrum is currently dominated by the calculation of the exposure and reaches 10% at 1 EeV and 6% at 10 EeV. The energy spectrum obtained from the hybrid events is illustrated in the left panel of fig. 2 together with the number of events in each energy bin.

The energy calibration of the surface detector data is done with the fluorescence detector events, therefore the systematic uncertainty on energy is common for both data sets and is at a level of 22%. The largest contribution is given by the fluorescence yield measurements (14%) and from the detector calibrations (9.5%). The energy spectra obtained with the surface detector and with the hybrid detector are combined using a maximum likelihood method. The Auger energy spectrum, scaled with E^3 is shown in fig. 2 in the right panel. The presence of a change in the energy spectrum at $\log_{10}(E/\text{eV}) = 18.61 \pm 0.01$, the ankle, is observed, a continuation of the same power law as above the ankle can be rejected with more than 20σ .

The events in the flux suppression energy region have shown a strong correlation with the Veron-Cetty and Cetty catalogue in 3.1° angular distance and within 75 Mpc [10].

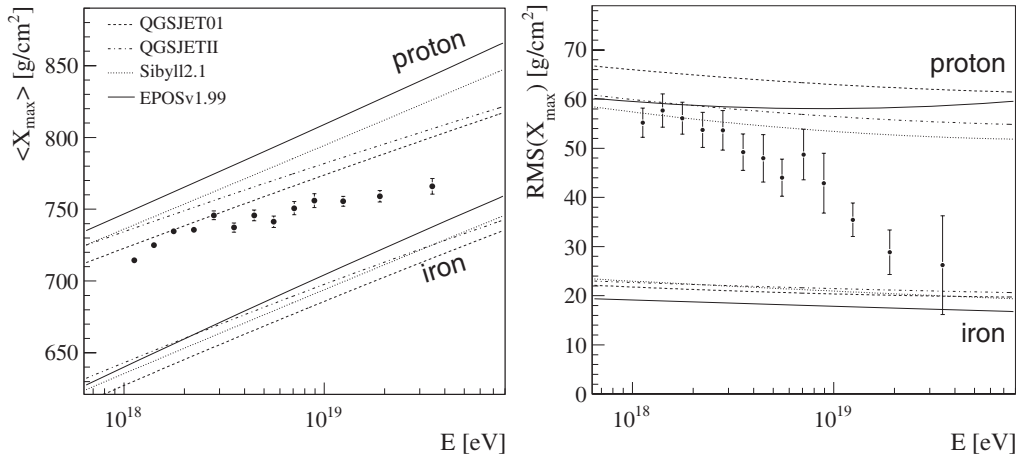


Fig. 3. – The mean (left) and the RMS (right) of the shower maximum as a function of energy. The predictions for proton and iron compositions of different high energy hadronic interaction models are illustrated [11].

The updated data taken after the anisotropy establishment still show a correlation, but weaker than the initial data set [12]. Based on *a posteriori* analysis, an excess of events is also observed from a region of the sky close to Cen A. Larger statistics is still needed to identify the sources of ultra high energy cosmic rays.

4. – Mass composition

4.1. Energy dependence. – The maximum of the shower development (X_{\max}) and its fluctuations are parameters that are sensitive to the mass of the primary particles. The average of X_{\max} , $\langle X_{\max} \rangle$, in a simple Heitler model depends linearly on the logarithm of energy for the same primary and is also a linear function of the mean logarithm of the primary mass. Therefore a change in the elongation rate, *i.e.* the rate of change of $\langle X_{\max} \rangle$ per logarithm of energy can be used to study relative changes in the composition. The shower-to-shower fluctuations of X_{\max} are related to the primary cross section with air and decrease with the number of nucleons.

The measured $\langle X_{\max} \rangle$ and the $\text{RMS}(X_{\max})$ as a function of energy [11] are illustrated in fig. 3. The predictions from air-shower simulations are represented by lines. The achieved resolution on X_{\max} is 20 g/cm² above a few EeV. This has been determined both from simulations and from independent measurements of the same shower with two FD stations. The systematic uncertainties from the calibration, atmospheric conditions, reconstruction and event selection on the average X_{\max} are less than 13 g/cm² and less than 6 g/cm² for the $\text{RMS}(X_{\max})$.

As can be seen from fig. 3, a decrease of the fluctuations from 55 to 26 g/cm² with increasing energy is observed as well as a change in the elongation rate at $\log_{10}(E/\text{eV}) = 18.24 \pm 0.05$ from (106^{+35}_{-21}) g/cm²/decade to (24 ± 3) g/cm²/decade. This energy coincides approximately with the energy of the ankle determined in the energy spectrum.

On the assumption that the hadronic interactions properties do not change drastically in the energy range of interest, the evolution with energy can be interpreted as an increase of the average mass of cosmic rays. The differences between different high energy

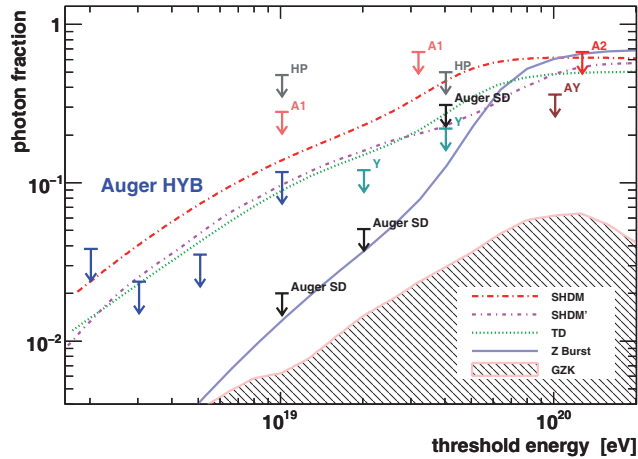


Fig. 4. – Upper limits on the photon fraction in the integral cosmic-ray flux (95% CL) as derived from the data of the surface detector (Auger SD) at highest energies and the limits above 2, 3, 5, and 10 EeV as obtained with the fluorescence detector (Auger Hyb). The shaded region represents the expected GZK photon fraction, while by lines are indicated predictions from top-down models [13].

hadronic interaction models is large and the current models do not cover the whole possible extrapolations of lower energy accelerator data. Within the current model predictions a transition from light to heavy composition is supported.

4.2. Photons and neutrino limits. – The detection of neutrino of ultra high energy would open a new window in the cosmic rays physics, mostly because they would point directly to their sources, being undeflected by the magnetic fields and not interacting with the traversed extraterrestrial mater. At the production sites of hadronic cosmic rays neutrino and photon fluxes are produced and also through the GZK effect photons and neutrinos would result from the secondary pions from the interaction of the cosmic rays with the infrared light or with the CMB.

For the production of UHECRs there exist numerous *top-down* scenarios. In these cases the cosmic rays are originating from decays of meta-stable heavy particles like super-heavy dark matter, topological defects collapses, or from interactions of neutrino with the relic neutrino background. One of the common features for these models is that they predict high fluxes for photons and neutrinos.

A clear signature for photons is the deep X_{\max} . Photon cross section is suppressed by the LPM effect, therefore the first interaction is much deeper in the atmosphere than for protons and also the multiplicity of the secondaries is lower. The shower cascades are mainly produced through electromagnetic processes therefore the particle content on the ground is muon poor. The maximum of the shower development is used in case of the hybrid data and the electromagnetic-like footprint on the ground in the case of the surface detector [13]. The resultant 95% CL upper limits on the photon fractions in the EeV region measured with the hybrid data, are 3.8%, 2.4%, 3.5% and 11.7% for the primary energies above 2, 3, 5 and 10 EeV, respectively, and are illustrated fig. 4. These limits together with the ones derived from the surface detector dismiss or disfavour the *top-down* scenarios.

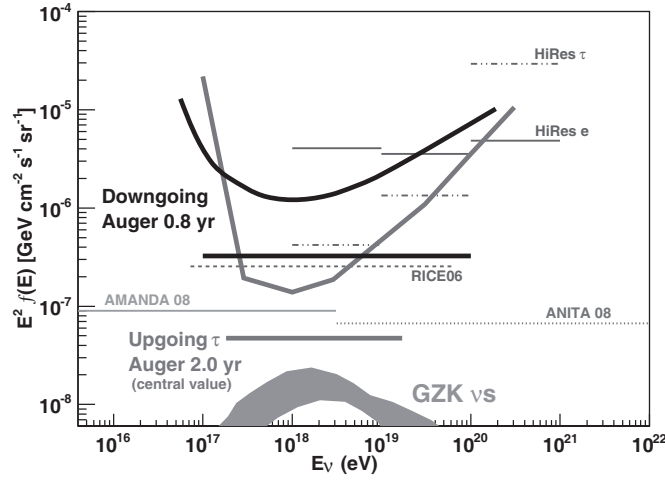


Fig. 5. – Integrated and differential upper limits for single flavour of diffuse neutrino fluxes (90% CL) for up-going ν_τ and down-going ν . The shaded region represents the expected GZK neutrino flux [12].

The neutrinos can be observed at the Auger site [14,12] by their specific signatures as almost horizontal (down-going) or up-going air-showers in an early stage of development. For up-going ν the search is performed in the hypothesis that the tau neutrinos interact in the Earth and produce tau leptons which generate air-showers in the lower part of the atmosphere. An end-to-end chain is simulated, from the earth skimming neutrinos, the extensive air showers in the atmosphere to the detector response to calculate exposure and their discrimination power. The systematic uncertainties at low energies are dominated by the contributions from the τ polarisation ($^{+17\%}_{-10\%}$), the ν cross-section ($^{+5\%}_{-9\%}$) and the τ energy losses ($^{+25\%}_{-10\%}$), while at high energies the contributions from the topography at the site, and from the MC simulations of air-showers and of the detector ($^{+20\%}_{-5\%}$) are prominent. In the period 1 Nov 2007-28 Feb 2009 no down-going ν were observed and in the period 01 Jan 2004-28 Feb 2009 no up-going ν_τ were identified. The differential and integrated limits are shown in fig. 5.

Conclusions

The measurements at the Pierre Auger Observatory, containing data equivalent to 2 years of fully operational experiment, indicate a change in the nature of cosmic rays at around 3 EeV and show a change in the shape of the energy spectrum and the elongation rate. These measurements add support to the hypothesis that an extragalactic component of mixed composition starts to dominate in this energy range. The near-future particle accelerator results will constrain the hadronic interaction models and the interpretation of the evolution of the shower maximum with energy will be more conclusive.

The photon limits exclude most of the top-down scenarios above 2 EeV. In the next 20 years of operation the photon fraction measurement will be sensitive to a level of less than 0.1% and the neutrino limits, if no neutrino is observed, will improve by more than an order of magnitude. These determinations, together with the arrival directions and mass composition analysis will help solving the origin of the highest energy cosmic rays.

REFERENCES

- [1] GREISEN K., *Phys. Rev. Lett.*, **16** (1966) 748.
- [2] ZATSEPIN G. T. and KUZ'MIN V. A., *JETP Lett.*, **4** (1966) 78.
- [3] HILLAS A. M., to be published in *Phys. Rev. Lett.*; BEREZINSKY V. S. and GRIGOREVA I. S., *Astron. Astropart.*, **199** (1988) 1; ALLARD D., PARIZOT E. and OLINTO A. V., *Astropart. Phys.*, **27** (2007) 61.
- [4] PIERRE AUGER COLLABORATION, *Nucl. Instrum. Methods A*, **523** (2004) 50.
- [5] PIERRE AUGER COLLABORATION, *Nucl. Instrum. Methods A*, **568** (2006) 839.
- [6] PIERRE AUGER COLLABORATION, *Proc. 31st ICRC, Lodz, 2009*; arXiv:0908.4422.
- [7] PIERRE AUGER COLLABORATION, arXiv:0710.1646.
- [8] UNGER M. *et al.*, *Nucl. Instrum. Methods A*, **588** (2008) 433.
- [9] PIERRE AUGER COLLABORATION, *Nucl. Instrum. Methods A*, **613** (2010) 29.
- [10] PIERRE AUGER COLLABORATION, *Astropart. Phys.*, **29** (2008) 188; *Science*, **318** (2007) 939.
- [11] PIERRE AUGER COLLABORATION, *Phys. Rev. Lett.*, **104** (2010) 091101.
- [12] PIERRE AUGER COLLABORATION, *Proc. 31st ICRC, Lodz, 2009*; arXiv:0906.2347.
- [13] PIERRE AUGER COLLABORATION, *Astropart. Phys.*, **31** (2009) 399; **29** (2008) 188.
- [14] PIERRE AUGER COLLABORATION, *Phys. Rev. D*, **79** (2009) 102001.

The missing cosmic baryons found?

E. BEHAR, S. DADO, A. DAR and A. LAOR

Department of Physics, Technion Israel Institute of Technology - Haifa 32000, Israel

(ricevuto il 14 Settembre 2010; pubblicato online il 10 Gennaio 2011)

Summary. — The angular power spectrum of the cosmic microwave background radiation (CMB), the relative abundances of primordial hydrogen, deuterium and helium isotopes, and the large-scale structure of the universe all indicate that 4.5% of the current mass density of the universe consists of baryons. However, only a small fraction of these baryons can be accounted for in stars and gas inside galaxies, galaxy groups and galaxy clusters, and in spectral-line absorbing gas in the intergalactic medium (IGM). Too hot to show up in Lyman-absorption, too cool to cause detectable spectral distortions of the cosmic microwave background radiation, and too diffused to emit detectable X-rays, about 90% of the cosmic baryons remain missing in the local universe (redshift $z \sim 0$). Here, we report on prevalent, isotropic, source independent, and fairly uniform soft X-ray absorption along the lines of sight to high- z gamma-ray bursts (GRBs) and quasars. It has the magnitude, redshift and energy dependence that are expected from a hot diffused IGM that contains the missing cosmological baryons and has a mean metallicity similar to that in the intracluster medium (ICM) of galaxy clusters.

PACS 98.80.-k – Cosmology.

PACS 98.70.Rz – γ -ray sources; γ -ray bursts.

PACS 98.54.Aj – Quasars.

1. – Introduction

The intergalactic medium (IGM) is extremely difficult to observe. Its tremendously low density and high temperature are believed to elude most absorption and emission detection. Thus, the observed extragalactic absorption of light from gamma-ray bursts (GRBs) and quasars, the most luminous transient and persistent sources in the universe and the farthest observable objects in it may be the only way to probe the IGM. This absorption is usually assumed to take place mainly in the neutral interstellar medium within their host galaxies (HGs). But, in many cases the equivalent hydrogen column densities that were inferred from their measured UVO and soft X-ray spectra are very different and uncorrelated. Such discrepancies were found both for distant GRBs [1-5] and distant quasars (see, *e.g.*, [6-9] and references therein). In contrast, the metal abundances and column densities of intervening absorbers on the sightlines to galactic and nearby

extragalactic sources inferred from soft X-ray and Lyman- α absorption, in general do not yield such discrepant column densities (see, *e.g.*, [3] and references therein).

The extragalactic absorption of soft X-rays from GRBs and quasars at small redshifts is usually dominated by absorption in their host galaxy. However, at large z , the soft X-ray opacity of absorbers is expected to decrease rapidly with z because both the mean metallicity and the photoabsorption cross section at an observed energy decrease rapidly with z . In contrast, the mean opacity of the IGM to soft X-rays is dominated by absorption at small redshifts. It increases rapidly with increasing z to its asymptotic value $\tau(E)$ independent of z beyond $z \sim 2$. Hence, it is not correlated to the UV absorption in the host galaxy and yields a discrepant column density if assumed to take place in/near the host⁽¹⁾. It was suggested that the discrepant column densities resulted either from misinterpreting flattening of the intrinsic spectral distribution of the soft X-rays at low energy as X-ray absorption, or from the high level of ionization of hydrogen in the absorber in the HG (see, *e.g.*, [6-9] and references therein). Both interpretations, however, required fine tuning in order to reproduce both the E and z dependence of the observed low-energy opacity.

In this paper we propose a different origin for the discrepant column densities inferred from UVO and X-ray observations of high- z GRBs and quasars. While the UVO absorption takes place mainly in the neutral gas in the host galaxies, we suggest that the absorption of their X-rays takes place mainly in the hot intergalactic medium (IGM) that contains all of the missing baryons implied by big bang nucleosynthesis and the observed angular power spectrum of the cosmic microwave background radiation and has the same metallicity as that in the intracluster medium (ICM) of galaxy clusters. We show that the opacity of such an IGM can explain on average the measured soft X-ray absorption of high- z GRBs and quasars. It is isotropic, practically independent of source and saturates at high z , uncorrelated to the UVO absorption in the host and, within observational errors, has the magnitude and energy dependence expected for the hot IGM of standard cosmology.

2. – Intrinsic host column densities from soft X-ray absorption

The extragalactic opacities to soft X-rays emitted by GRBs and quasars that were measured with the X-ray telescope aboard the Swift satellite and with the ROSAT, ASCA, BeppoSAX, Chandra and XMM-Newton satellite, respectively, were assumed to be entirely due to the absorption within the host galaxies at redshift z although the current X-ray spectra contain no redshift information. These opacities were converted to equivalent hydrogen column densities $N_{h,\text{HG}}(z)$ of the GRBs' host galaxies along the GRBs sightline, using

$$(1) \quad \tau(E, z) = \sigma([1 + z]E) N_{h,\text{HG}}(z) (Z/Z_{\odot}),$$

⁽¹⁾ At small redshifts the column densities in the host galaxy of GRBs or quasars that are inferred from UVO and soft X-ray absorption can also differ significantly for a different reason: The ionization of electrons in the external atomic shells by the UVO emission of GRBs, and of blazars in particular, extends to much larger galactic distances than the ionization of the inner shells in the metals responsible for the soft X-ray absorption (see, *e.g.*, [6, 2, 3] and references therein).

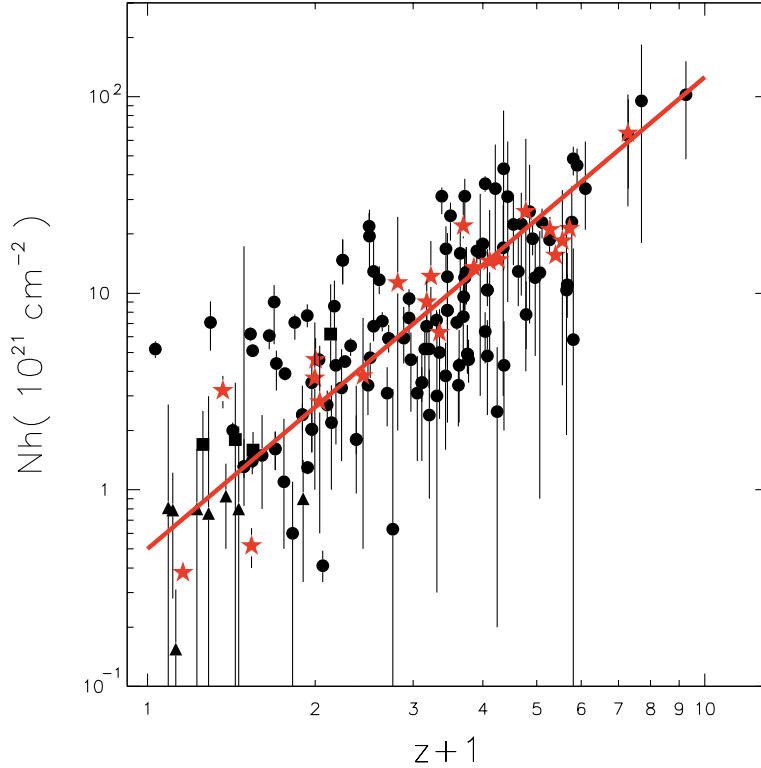


Fig. 1. – Equivalent hydrogen column densities of the HG of GRBs and radio loud quasars as a function of redshift that were inferred from their absorbed soft X-ray spectrum, assuming that the extragalactic absorption took place in the neutral, solar composition [11] ISM of their HG at redshift z . The GRB data points are from observations with the Swift XRT [4,10] of long GRBs (circles), off-center SHBs (triangles) and near-center SHBs (squares). The quasar data points (stars) are from observations with ASCA [12], Chandra [13] and XMM-Newton [7, 8, 14, 9, 15].

where $\sigma([1+z]E)$ is the absorption cross section of soft X-rays with energy $[1+z]E$ per hydrogen atom in the host galaxy, assuming a neutral absorber with standard solar elemental abundances. Figure 1 shows the effective HI column densities of the host galaxies of GRBs with known redshift as measured with the Swift X-ray telescope [10, 4], assuming the standard photospheric solar abundances compiled in [11] and those of radio loud quasars as measured with the X-ray telescopes aboard ASCA [12], Chandra [13] and XMM-Newton [14, 9, 15] satellites. The observed increase of the mean $N_{h,\text{HG}}$ with z like $(1+z)^{2.4}$ is in stark contrast with its expected decrease with redshift due to the general decline of the mean metallicity with redshift in standard galaxy formation and stellar evolution theories and observed in Lyman- α and damped Lyman- α absorbers (see, *e.g.*, [16, 17] and references therein). Moreover, the photoabsorption cross section above the oxygen K edge at $E = 0.54$ keV for a neutral absorber with a solar metallicity is well described by $\sigma([1+z]E) \approx \sigma(E)(1+z)^{-2.4}$. Hence, the universal increase of $N_{h,\text{HG}}$ with z like $(1+z)^{2.4}$ at large z in both GRB and quasar hosts simply reflects the fact that the observed extragalactic opacity for $z > 2$ tends to an asymptotic value independent of z for GRBs and quasars as shown in figs. 2 and 3. In order to produce the observed

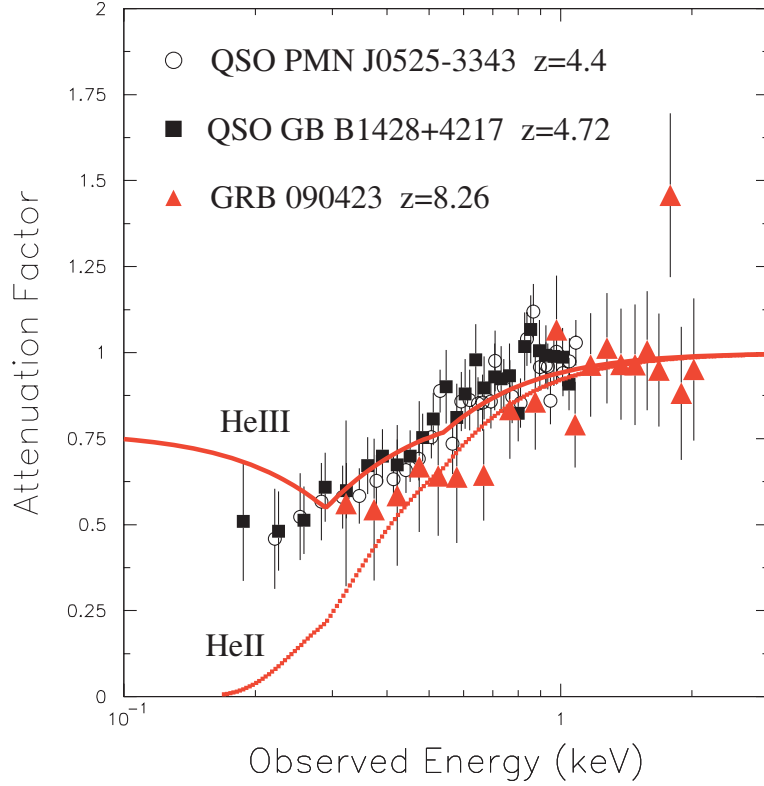


Fig. 2. – Comparison between the extragalactic attenuation of soft X-rays, $\exp[-\tau_{\text{IGM}}]$, from the high-redshift blazars PMN J0525-3343 at $z = 4.4$ (circles) and GB B1428+4217 (squares) at $z = 4.72$ [7, 8] that was measured with XMM-Newton as a function of X-ray energy, and that measured with Swift XRT in GRB 090423 (triangles) at $z = 8.26$, the largest measured redshift of a GRB [26, 10], and the attenuation in the hot IGM of standard cosmology with the opacity given by eq. (2). At energy below 0.5 keV the IGM opacity depends strongly on the ionization state of helium. The upper line (HeIII) corresponds to a hot IGM where helium is fully ionized, while the lower line (HeII) represents a hot IGM where helium is singly ionized. The data show that the absorber is likely in between these two cases.

z -independent opacity at large z , either the metal column density of HGs of GRBs and quasars by some coincidence satisfies $N_{h,\text{HG}}(z) (Z/Z_{\odot}) \propto 1/\sigma([1+z]E) \propto (1+z)^{2.4}$, or there is a simpler reason why the extragalactic opacity to soft X-rays along the line of sight to GRBs and quasars becomes independent of z at $z > 2$ and of the X-ray source⁽²⁾.

3. – The soft X-ray opacity of the IGM

A natural origin of a universal, isotropic, and z -independent X-ray opacity that is observed in high- z GRBs and quasars is the intergalactic medium (IGM) of the

⁽²⁾ We have not included radio quiet quasars in our analysis because their soft X-ray excess masks their soft X-ray absorption.

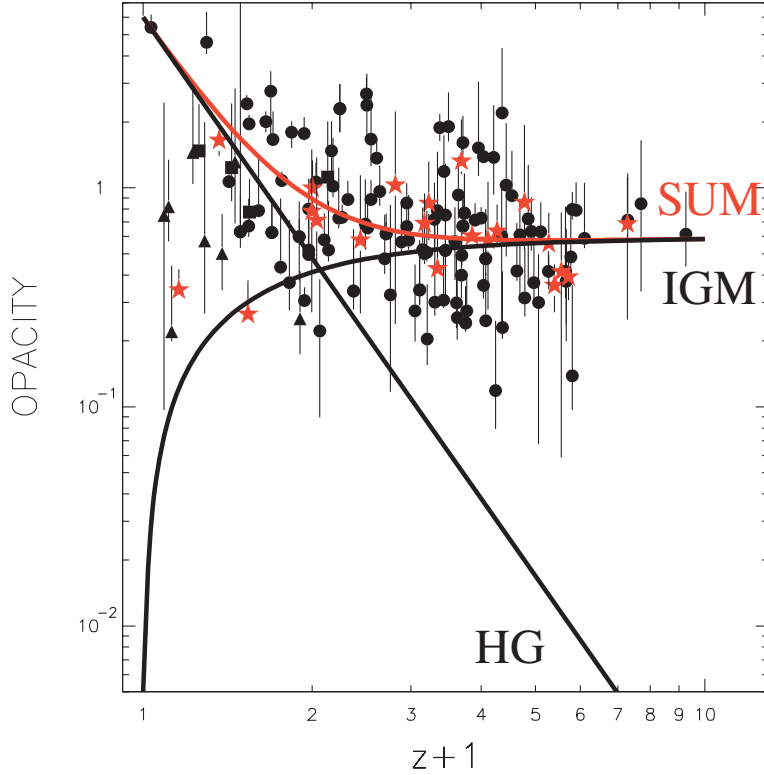


Fig. 3. – Comparison between the extragalactic opacity to soft X-rays at $E \sim 0.5$ keV as a function of redshift measured from GRB and quasar observations and the estimated opacity due to absorption in a hot IGM that contains 90% of the cosmic baryons with completely ionized hydrogen and helium and partially ionized metals. Circles represent long GRBs, squares represent near-center SHBs and triangles represent far-off center SHBs. The GRB data points are from afterglow observations with the Swift XRT [10] and the quasar data points are from observations with ASCA [12], Chandra [13] and XMM-Newton [7, 8, 14, 9, 15]. The contribution to the extragalactic opacity from a host galaxy (HG) with $Nh = 10^{22} \text{ cm}^{-2}$ at redshift z is also shown.

standard cosmology that contains the bulk of the missing baryons⁽³⁾. Using standard cosmology with a Hubble constant $H_0 = 71 \text{ km s}^{-1} \text{ Mpc}^{-1}$ and a baryon mass fraction $\Omega_b = 0.045$ [19] of which $\sim 74\%$ are hydrogen nuclei and only a very small fraction of it ($\sim 10\%$) resides in galaxies and galaxy groups and clusters [20], the mean density of hydrogen nuclei in the IGM is $n_h \approx 0.67 \Omega_b (3 H_0^2 / 8 \pi G m_p) (1+z)^3$, and the opacity of such an IGM to soft X-rays emitted at redshift z with locally observed energy E is given by

$$(2) \quad \tau_{\text{IGM}}(E, z) \approx 2.21 \times 10^{21} \text{ cm}^{-2} \int_0^z \frac{\sigma(E, z') (Z/Z_\odot) (1+z')^3 dz'}{(1+z') \sqrt{(1+z')^3 \Omega_M + \Omega_\Lambda}},$$

⁽³⁾ The baryon mass fraction in the universe that was inferred from Big Bang Nucleosynthesis [18] and from the angular spectrum of cosmic microwave background radiation [19] is $\Omega_b \approx 0.045$. Only 10% of these baryons reside in galaxies and galaxy clusters [20], while the remaining 90% presumably are still in the IGM in the form of a hot gas whose hydrogen and helium are fully ionized.

where $\Omega_M = 0.27$ and $\Omega_\Lambda = 0.73$ [19]. Equation (2) predicts a saturation of τ for $z > 2$ since for $E < 10$ keV the photo-absorption cross section $\sigma(E)$ scales roughly as $E^{-2.4}$, yielding for a redshifted absorber $\sigma(E, z) \sim \sigma(E)(1+z)^{-2.4}$, and $d\tau/dz$, which decreases with z more rapidly than $(1+z)^{-1.9}$. This saturation of $\tau(E, z)$ at $z > 2$ is very different from the increase of τ with z , expected and observed in the universe for Compton scattering and line absorption. It is, however, in good agreement with the observed saturation of the soft X-ray opacity inferred from spectral observations of large z GRBs and quasars, as shown in figs. 2 and 3.

Moreover, the mean high- z opacity $\tau(E)$ calculated for the IGM of the standard cosmological model using the best available priors agrees well with that inferred from the measured spectra of high- z GRBs and quasars: The observed metallicity in the intracluster medium (ICM) at low z is roughly $Z/Z_\odot \approx (0.54 \pm 0.10)(1+z)^{-1.25 \pm 0.25}$, *e.g.*, [24] and references therein. This mean metallicity of the ICM seems to describe well also the mean metallicity in damped Lyman- α (DLA) absorbers at $z < 4$ [16, 17], and is consistent [21] with that expected from the mean star formation rate in the universe as a function of z [22], although the spread in metallicity in DLAs [23, 16, 17], galaxies and galaxy clusters [24] at any given z is quite large, probably reflecting different star formation histories in different galaxies and protogalaxies. Assuming a mean IGM metallicity identical to that of the ICM [24] and adopting the photoabsorption cross sections per ISM hydrogen of [25], after removing the contribution from neutral hydrogen and helium, which presumably are fully ionized in the hot IGM, the IGM opacity to X-rays from large z GRBs and quasars at energy above the carbon edge ($E > 0.29$ keV) tends to

$$(3) \quad \tau_{\text{IGM}}(E) \approx 0.49 (0.54 \text{ keV}/E)^{2.4} - 0. ((0.26 \text{ keV}/E)^{2.4} - 1)\Theta[(0.54 \text{ keV}/E) - 1],$$

where $\Theta(x) = 0$ if $x < 0$ and $\Theta(x) = 1$ if $x > 0$ and $E = 0.54$ keV is the oxygen edge. The approach to this asymptotic behaviour of the opacity at large z is well approximated by $\tau(E, z) = \tau(E)(1 - (1+z)^{-2.15})$. Below 0.5 keV the IGM opacity becomes strongly dependent on the ionization state of helium. The above estimates are valid for a uniform IGM. However, for a clumpy IGM, the observed opacity can deviate significantly from its mean asymptotic value.

4. – Comparison between theory and observations

The intrinsic opacity of the hosts of GRBs and quasars as given by eq. (1) with $N_{\text{Z,HG}}(z) = (Z_{\text{HG}}/Z_\odot) N h_{\text{HG}}(0)$ and $\langle Z_{\text{HG}}/Z_\odot \rangle \sim (1+z)^{-1.25}$, decreases with increasing z like $\tau_{\text{HG}}(E, z) = (1+z)^{-3.65} \tau_{\text{HG}}(E, 0)$. Hence, its mean contribution to the extragalactic opacity becomes negligible at large z . Consequently, the opacity towards high- z GRBs and quasars is dominated by the IGM opacity, which is isotropic, independent of source and redshift and uncorrelated to the UVO absorption in the host. This is demonstrated in fig. 2 where we compare the soft X-ray attenuation of the hot IGM which follows from eq. (2) and the attenuation inferred from observations of the high-redshift blazars PMN J0525-3343 at $z = 4.4$ and GB B1428+4217 at $z = 4.72$ [7, 8] with XMM-Newton and of GRB 090423 [26, 10] at a record redshift $z = 8.26$ with the Swift XRT. These extragalactic opacities were obtained after subtraction of the Galactic absorption using the Galactic HI column densities of [27] and the ISM cross section per HI atom

of [25]⁽⁴⁾. The complex low-energy behaviour of the attenuation in the IGM is caused by the dependence of the photoabsorption cross sections on the ionization state of the most abundant elements in the hot IGM. It has a behaviour much different than that of the attenuation in the neutral ISM in our galaxy and the host galaxy. This is demonstrated in fig. 2 where we show the expected opacity of a hot IGM where He is stripped of its two electrons (HeIII) and a warm IGM where He retains one of its two atomic electrons (HeII).

In fig. 3 we compare our estimate of the mean extragalactic opacity to soft X-rays, $\tau(E, z) = \tau_{\text{HG}}(E, z) + \tau_{\text{IGM}}(E, z)$, as a function of z at $E = 0.5 \text{ keV}$ as given by eqs. (2) and (1) and the opacity inferred from observations of GRBs and radio loud quasars (RLQs) with a good S/N ratio. The contribution from a host galaxy with an arbitrarily chosen large column density $N_{h, \text{HG}} = 10^{22} \text{ cm}^{-2}$ as a function of redshift z is also shown in fig. 3. The observations include all Swift/XRT PC observations of GRBs with known redshift when spectral variability is minimal [10,4], observations with ASCA [12] of relatively low- z RLQs (due to relatively low sensitivity and limited soft X-rays bandpass data) and observations of high- z RLQs with Chandra [13] and with XMM-Newton [7,8,14,9,15] of half a dozen high- z quasars with a relatively good S/N ratio. Only high latitude observations ($N_{h, \text{Gal}} < 10^{21} \text{ cm}^{-2}$ where the absorption is not dominated by the Galactic absorption) were included. Figures 2 and 3 clearly show the general trend towards an asymptotic opacity (isotropic, independent of z and the X-ray source) at large z , consistent with that expected for a diffused IGM of standard cosmology.

Figure 3 also shows a large spread in the extragalactic opacity measured in low-redshift GRBs. Such a spread is expected from the variety of host galaxies and of source locations, source environments and sightlines within them. This spread in short hard bursts (SHBs) is also shown in fig. 3. Most of these SHBs have a very small z where the IGM opacity is quite small compared to the intrinsic opacity in the host galaxy. Consequently, one expects the opacities of far-off-center SHBs to be quite small while those of near-center SHBs to be much larger and similar to those of long GRBs whose massive star progenitors are also found mainly near the center of the host galaxy. These trends are clearly seen in fig. 3.

Part of the observed spread at all redshifts results from the approximate nature of the modelling of the intrinsic spectra of GRBs, and from the approximate knowledge of the Galactic HI column density and metallicity along their sightlines. As expected, at large z , where the contribution of the HG becomes negligible, the spread seems to become smaller and the theory seems to describe well the mean value of the observed opacities. A clumpy IGM at low redshifts, whence most of the IGM opacity comes, may also contribute significantly to the spread.

Figure 3 also indicates that the extragalactic opacities to soft X-rays inferred from RLQs have a spread smaller than that of GRBs. It may be due to a much higher photon statistics and lesser temporal variability during their measurements, or to the much smaller not necessarily complete sample.

5. – Conclusion

The extragalactic opacity to soft X-rays from GRBs and quasars at small redshifts is dominated by absorption in their host galaxy. However, the extragalactic opacity to

⁽⁴⁾ The ISM metallicity adopted by [25] agrees well with the updated solar metallicity compiled in [28], which is smaller by a factor ~ 1.62 than that compiled in [11].

soft X-rays from high- z GRBs and quasars probably is dominated by absorption in the IGM at $z \leq 2$. Such an opacity is isotropic, independent of redshift beyond $z \approx 2$ and of source and not related or correlated to the UV absorption in the host galaxy. It yields a discrepant column density of the host, if it is erroneously assumed to be associated with it. The low-energy X-ray attenuation in the hot ionized IGM is different from that of the mostly neutral ISM in our Galaxy and in the host galaxy of the source. In particular, it seems to confirm [29] that the IGM of the local universe contains practically all the currently missing baryons implied by big bang nucleosynthesis [18], the observed angular power spectrum of the cosmic microwave background (CMB) radiation [19] and the Thomson opacity inferred from its polarization [19], but only $\sim 10\%$ are present in the galaxies, galaxy clusters and UVO absorbers in the local universe [20]. Soft X-ray spectra of very luminous high- z blazars with a large S/N ratio can provide more stringent tests of the IGM origin of the extragalactic opacity to soft X-rays from high- z quasars and GRBs. They may also help determine the mean metallicity and the clumpiness of the ionized IGM.

* * *

The authors thank S. KASPI and A. NUSSER for useful comments and suggestions.

REFERENCES

- [1] JAKOBSSON P. *et al.*, *Astron. Astrophys.*, **460** (2006) L13.
- [2] CAMPANA S. *et al.*, *Astrophys. J.*, **654** (2006) L17.
- [3] WATSON D. *et al.*, *Astrophys. J.*, **660** (2007) L101.
- [4] CAMPANA S. *et al.*, *Mon. Not. R. Astron. Soc.*, **402** (2010) 2429.
- [5] RAU A. *et al.*, preprint arXiv:1004.3261.
- [6] FABIAN A. C. *et al.*, *Mon. Not. R. Astron. Soc.*, **323** (2001) 373.
- [7] WORSLEY M. A. *et al.*, *Mon. Not. R. Astron. Soc.*, **350** (2004a) 207.
- [8] WORSLEY M. A. *et al.*, *Mon. Not. R. Astron. Soc.*, **350** (2004b) L67.
- [9] YUAN W. *et al.*, *Mon. Not. R. Astron. Soc.*, **358** (2005) 432.
- [10] EVANS P. A. *et al.*, *Mon. Not. R. Astron. Soc.*, **397** (2009) 1177.
- [11] ANDERS E. and GREVESSE N., *GeCoA*, **53** (1989) 197.
- [12] REEVES J. N. and TURNER M. J. L., *Mon. Not. R. Astron. Soc.*, **316** (2000) 234.
- [13] BASSETT L. C. *et al.*, *Astrophys. J.*, **128** (2004) 523.
- [14] PAGE K. L. *et al.*, *Mon. Not. R. Astron. Soc.*, **364** (2005) 195.
- [15] GRUPE D. *et al.*, *Astrophys. J.*, **131** (2006) 55.
- [16] SAVAGLIO S., *Proceedings of IAU Symposium 265, Rio de Janeiro 2009*, arXiv:0911.2328.
- [17] KAPLAN K. F. *et al.*, preprint arXiv:1004.3319.
- [18] STEIGMAN G., *Annu. Rev. Nucl. Part. Syst.*, **57** (2007) 463.
- [19] KOMATSU E. *et al.*, submitted to *Astrophys. J. Suppl. Ser.*, preprint arXiv:1001.4538.
- [20] FUKUGITA M. and PEEBLES P. J. E., *Astrophys. J.*, **616** (2004) 643.
- [21] DADO S., DAR A. and DE RÚJULA A., *Chin. J. Astron. Astrophys.*, **8** (2008) 366.
- [22] KISTLER M. D. *et al.*, *Astrophys. J.*, **705** (2009) L104.
- [23] PROCHASKA J. X. *et al.*, *Astrophys. J.*, **595** (2003) L9.
- [24] BALESTRA I. *et al.*, *Astron. Astrophys.*, **462** (2007) 429.
- [25] WILMS J., ALLEN A. and MCCRAY R., *Astrophys. J.*, **542** (2000) 914.
- [26] SALVATERRA R. *et al.*, *Nature*, **461** (2009) 1258.
- [27] KALBERLA P. M. W. *et al.*, *Astron. Astrophys.*, **440** (2005) 775.
- [28] ASPLUND M. *et al.*, *Annu. Rev. Astron. Astrophys.*, **47** (2009) 481.
- [29] BEHAR E. *et al.*, in preparation.

The ANTARES deep-sea neutrino telescope—Status and first results

N. PICOT CLÉMENTE on behalf of the ANTARES COLLABORATION

Centre de Physique des Particules de Marseille - Marseille, France

(ricevuto il 14 Settembre 2010; pubblicato online il 10 Gennaio 2011)

Summary. — The ANTARES neutrino telescope has been accomplished in May 2008. Located at a depth between 2100 and 2500 m in the Mediterranean Sea, 40 km off the Provençal coast, it comprises a large three-dimensional array of 885 Optical Modules deployed on 12 vertical lines. The telescope is aimed to observe high energy cosmic neutrinos through the detection of the Cherenkov light produced by up-going induced muons. The status of the experiment is briefly reviewed, and first results of atmospheric muons and neutrinos analysis will be discussed.

PACS 95.55.Vj – Neutrino, muon, pion, and other elementary particle detectors; cosmic ray detectors.

PACS 96.50.Vg – Energetic particles.

PACS 29.40.Ka – Cherenkov detectors.

1. – Introduction

The study of cosmic rays is one of the most important topics of astrophysics today. It represents an important step toward the understanding of the Universe. Several gamma-ray sources have been detected in the last few years, however their detection cannot give, up to now, a complete understanding of gamma-ray production mechanisms. If they are produced by hadronic mechanisms, and thus if nuclei are accelerated, then a high energy neutrino counterpart should be observed. Contrary to cosmic rays which are sensitive to magnetic fields, and to photons which are easily absorbed, neutrinos can escape from compact objects, and travel over very large distances without being deflected by magnetic fields, or absorbed by interstellar clouds. Nevertheless, because of the weak interaction between neutrino and matter, very large detectors are needed, and are often installed in hostile environments, where the construction represents a challenge.

ANTARES is a neutrino deep-sea telescope, completed in May 2008, and designed for the detection of high energy neutrinos emitted by Galactic (supernova remnants, microquasars, . . .) and extragalactic (active galactic nuclei, gamma ray bursters, pulsars, . . .) sources. It is also aimed to search for neutrinos induced by dark matter annihilation within massive bodies. Moreover the large area of the detector offers the possibility for

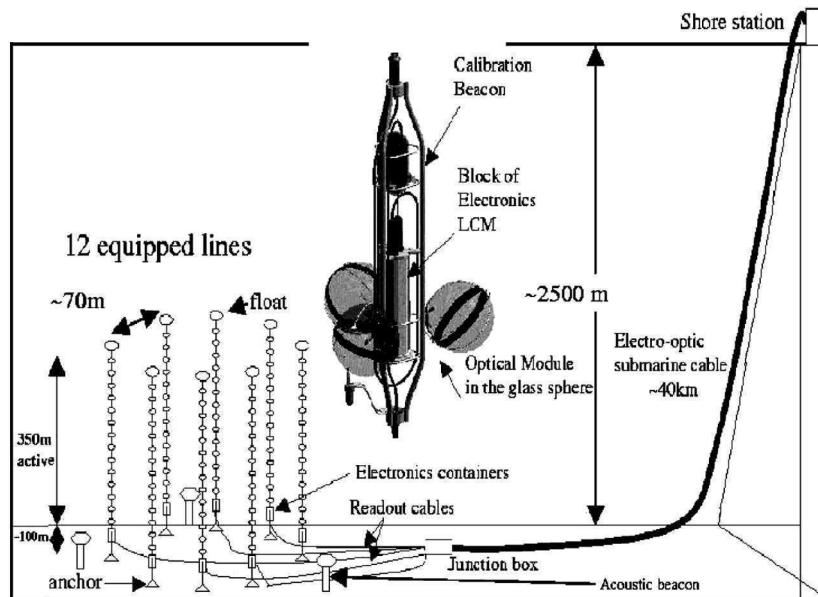


Fig. 1. – Schematic description of the ANTARES detector and of a typical storey containing a LED beacon.

the search for exotic particles such as magnetic monopoles, or nuclearites. ANTARES is the largest neutrino telescope operating in the northern hemisphere, and, by its location, contains the Galactic Centre in its field of view. It provides also a unique platform for multidisciplinary sciences as oceanography, sea biology, seismology, or environment monitoring.

2. – The ANTARES detector

The ANTARES neutrino telescope is located at 2475 m depth in the Mediterranean Sea, offshore from Toulon (France) covering an area of about 0.1 km^2 [1]. The detector is composed by 12 flexible lines of 450 m length, which are fixed on the sea bed thanks to an anchor, and are kept taut by a buoy (see fig. 1). They are connected to a junction box which is relied to the shore station with an electro-optical cable of about 40 km. Every line comprises 25 storeys separated by 14.5 m, whose each contains 3 optical modules. Parallel to an optical module, two Analog Ring Samplers [2] are used to digitize signals with amplitude higher than 0.3 photoelectrons. In addition to photodetectors, some storeys contain devices for *in situ* calibrations such as LED Beacons [3], and for acoustic positioning with hydrophones.

The strategy of the ANTARES data acquisition is based on the “all-data-to-shore” concept [2]. This implementation leads to the transmission of all raw data above a given threshold to shore, where different triggers are applied for storage.

3. – Status of the detector and *in situ* calibration

The ANTARES observatory was built gradually until May 2008, giving rise to various detector layouts used for physics analysis: the first two lines were installed, and connected in 2006, then 3 additional lines were plugged at the beginning of 2007, and in December 2007 the detector reached a 10-line configuration. Finally, ANTARES was completed in May 2008, with its final 12-line configuration.

The telescope has an angular resolution of about 0.2° for high energy neutrinos (> 10 TeV), it is determined by the intrinsic detector resolution, *i.e.* the timing resolution and accuracy of the location of the optical modules. The time calibration is performed for each line in dark room before their deployment, and is then done regularly *in situ* after the immersion. The relative time calibration relies on several independent systems [4]. The master clock system, by sending redundant signals to each storey, gives the time signal propagation through cables to the shore station. Then to obtain time offsets between optical modules, which depend on the front-ends electronics and on the time propagation inside phototubes, LED optical beacons have been installed every 5 storeys on each line. The flashing light emitted by LED beacons allows to compute time differences between signals received by pairs of optical modules in order to extract their time offsets. Moreover, optical beacons provide the possibility to study optical properties of the sea water, as the light absorption length.

Potassium-40 is a radioactive isotope naturally present in the sea water. Its β -decay gives rise to Cherenkov light produced by electrons, producing a detectable signal in ANTARES. This light is then employed to perform crosscheck of time calibration, by studying coincidences between optical modules of a same storey, and to monitor the evolution of the optical module gains, which are tuned if a significant drift is noticed.

Finally, thanks to these two time calibration methods, a *rms* of 0.6 ns on the timing precision is reached, in good agreement with the precision of the ANTARES design goal.

4. – Atmospheric muons

Important backgrounds come from biological activities of micro and macro organisms, called bioluminescence, from the dark noise of photomultipliers, and from the ^{40}K decay. The bioluminescence and the dark noise produce irregular hits in the detector, and can be easily removed by searching for correlated hits, corresponding to the crossing of a muon. The light coming from the ^{40}K decay can only illuminate optical modules of a same storey, and are not selected in the reconstruction algorithm when local coincidences between neighbouring floors are chosen.

However, the most of the background is the one produced by atmospheric downgoing muon events. They are produced by high energy cosmic rays interacting with atomic nuclei of the upper atmosphere, with the production of kaons and pions, which decay into muons. At the ANTARES depth, the muon flux exceeds by several orders of magnitudes the atmospheric neutrino-induced muon flux, but can be extracted by regarding only upgoing reconstructed events. Despite they are an important background for neutrino detection, atmospheric muons can be used to verify the detector response. Moreover a deficit of muons in the moon direction will give some important information about the pointing accuracy of the detector.

A first study, recently published in [5], is based on the observation of coincidence signals in adjacent storeys of the detector, yielding to a low energy threshold of 4 GeV, in

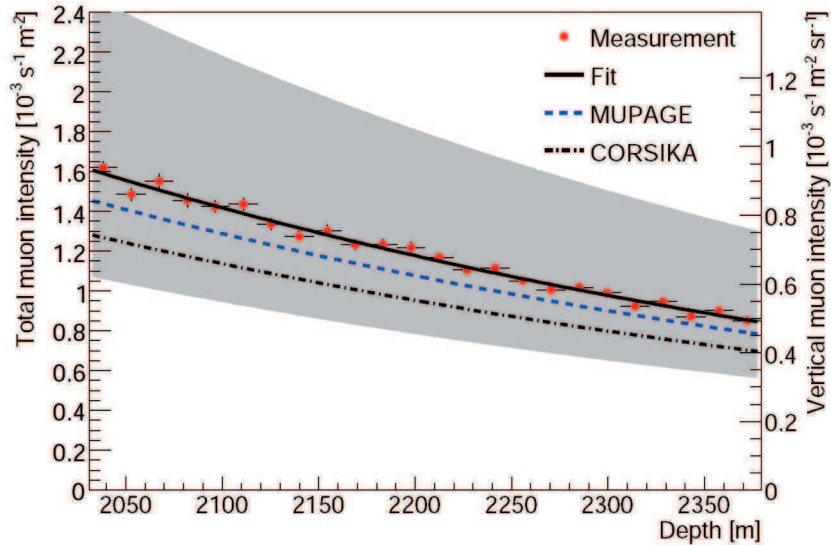


Fig. 2. – (Colour on-line) Depth dependence of the total atmospheric muon flux as measured from coincidence signals on adjacent floors (red points). The measured flux dependence is compared to results from Monte Carlo simulations performed with CORSIKA [7] (dash-dotted black line), using the NSU model [8], and MUPAGE [6] (dashed blue line). The grey band shows the normalisation uncertainty of data.

order to measure the attenuation length of the muon flux. Figure 2 shows the coincidence rates measured in different storeys as a function of depth for atmospheric downgoing muons. The measured depth dependence of the rates can be very well fitted with the expected exponential fall-off of the muon intensity, and is compatible with Monte Carlo simulations performed with MUPAGE [6], and CORSIKA [7] with the NSU model of the primary cosmic ray spectrum [8]. The results are also consistent with previous analysis performed using a full track reconstruction and by converting the reconstructed zenith angle into an equivalent slant depth through the sea water [9].

5. – ANTARES first neutrino events

The online reconstruction method isolates in real time upward going neutrino-induced muon candidates by applying a simple cut on the track fit quality. For 2007 and 2008 (~ 341 days of effective livetime), about 750 upgoing muons have been reconstructed in ANTARES. These events, reconstructed on at least two strings, are shown fig. 3 as a function of their elevation. From atmospheric neutrino simulations, based on the Bartol flux [10], and downgoing atmospheric muons simulations, which uses Corsika [8] with the NSU primary composition [8], one obtains very good agreements with the reconstructed data, with an expected contamination of the neutrino sample less than 4% from misreconstructed atmospheric muons. The agreement with Monte Carlo expectations gives the confidence in the simulation of the detector and of the event reconstruction for downgoing reconstructed muons, confirming a correct understanding of the detector. For the systematic errors the optical modules properties, and the uncertainties in the sea water description are considered. They are larger for downgoing events because of the optical modules orientations (45° downward looking).

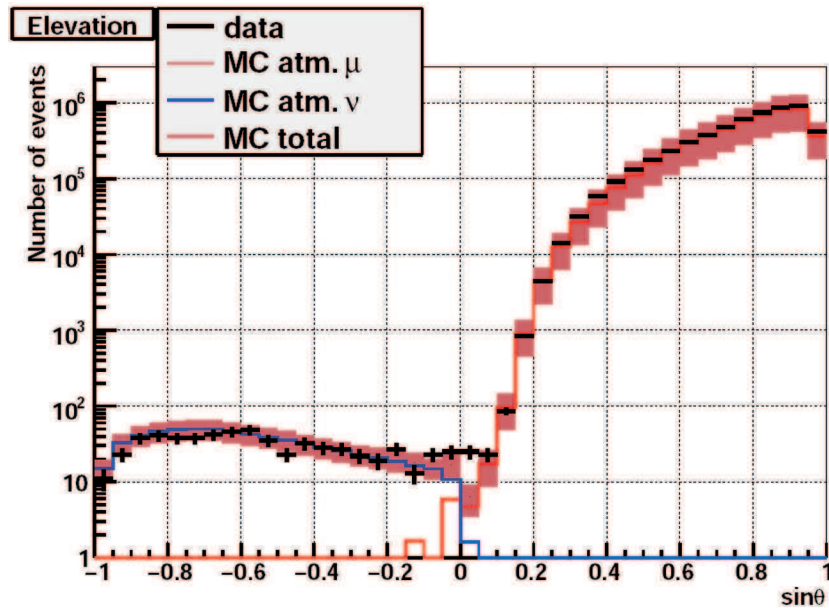


Fig. 3. – (Colour on-line) Elevation of reconstructed data (black crosses) from 2007 and 2008 on at least two strings. The distribution is compared to muon (red line) and neutrino (blue line) simulations, respectively performed according to the NSU primary composition [8], and the Bartol flux model [10].

The 750 upgoing reconstructed events are then selected, and are presently used for the search of cosmic point-like sources. A scrambled sky map of these events is shown in fig. 4 in Galactic coordinates. The grey scale represents the exposure time of ANTARES, which can see the interesting center of the Galaxy. The scrambling, consisting in changing randomly the time of the events, has been employed to avoid any human bias in the analysis.

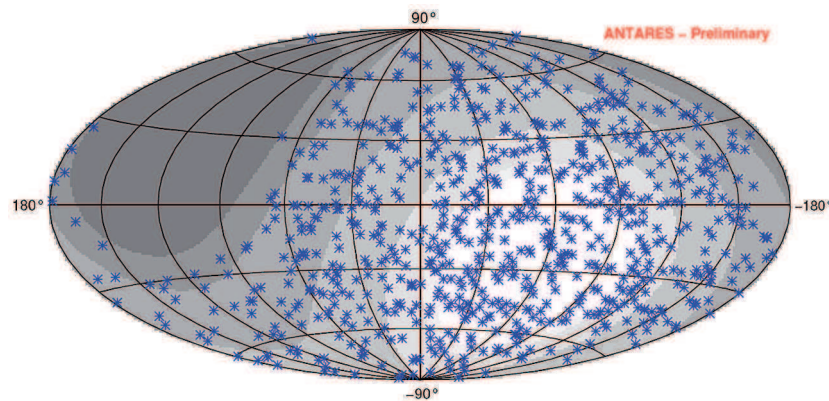


Fig. 4. – (Colour on-line) Scrambled sky map of 750 neutrino candidates (blue crosses) taken from 2007 and 2008 data (~ 341 days of effective livetime). The grey scale represents the exposure time of ANTARES, from permanent (in white) to null exposure (in dark grey).

6. – Conclusion

ANTARES has been completed in May 2008. It is the largest operational neutrino telescope of the northern hemisphere, taking data with a high duty cycle. The flux of atmospheric muons has been measured and is found to be in agreement with Monte Carlo expectations. The detector is now well understood, and very good agreements are obtained with Monte Carlo simulations, performed for atmospheric muons and neutrinos. The first physics analysis for the 2007 and 2008 data are in their finalisation steps, and will be presented in the next few months.

REFERENCES

- [1] CARR J. for the ANTARES COLLABORATION, *J. Phys. Conf. Ser.*, **136** (2008) 022047.
- [2] AGUILAR J. A. *et al.*, *Nucl. Instrum. Methods A*, **570** (2007) 107.
- [3] AGERON M. *et al.*, *Nucl. Instrum. Methods A*, **578** (2007) 498.
- [4] GOMEZ P., *Timing Calibration of the ANTARES Neutrino Telescope*, ICRC2009, arXiv:0911.3052.
- [5] AGUILAR J. A. *et al.*, *Astropart. Phys.*, **33** (2010) 86.
- [6] CARMINATI G., MARGIOTTA A. and SPURIO M., *Comput. Phys. Commun.*, **179** (2008) 915.
- [7] HECK D., SCHATZ G., THOUW T., KNAPP J. and CAPDEVIELLE J. N., Forschungszentrum Karlsruhe Report, FZKA-6019 (1998).
- [8] NIKOLSKY S. I., STAMENOV I. N. and USHEV S. Z., *Sov. Phys. JETP*, **60** (1984) 10; *Zh. Eksp. Teor. Fiz.*, **87** (1984) 18.
- [9] AGERON M. *et al.*, *Astropart. Phys.*, **31** (2009) 277.
- [10] BARR G. *et al.*, *Phys. Rev. D*, **39** (1989) 3532; AGRAWAL V. *et al.*, *Phys. Rev. D*, **53** (1996) 1314.

Neutrino physics and lepton flavour violation: A theoretical overview

A. IBARRA

*Physik-Department T30d, Technische Universität München
James-Frank-Straße, 85748 Garching, Germany*

(ricevuto il 14 Settembre 2010; pubblicato online il 10 Gennaio 2011)

Summary. — We review the theoretical status of neutrino physics and its implications for physics beyond the Standard Model. We also discuss the prospects to observe flavour violation in the charged lepton sector, with special emphasis on the connection to neutrino parameters.

PACS 14.60.Pq – Neutrino mass and mixing.

PACS 13.35.-r – Decays of leptons.

PACS 12.60.Jv – Supersymmetric models.

1. – Introduction

A series of experiments have firmly established the violation of lepton flavour in the neutrino sector [1], with dramatic implications for particle physics. In the Standard Model of particle physics the gauge interactions and the kinetic terms of the leptonic Lagrangian are invariant under the global symmetry $U(3)_{e_R} \times U(3)_L$. This symmetry is broken, however, by the Yukawa coupling of the charged leptons, which eventually lead to charged lepton masses. As a result, the full Standard Model Lagrangian has a smaller symmetry $U(1)_e \times U(1)_\mu \times U(1)_\tau$, which amounts to the conservation of all family lepton numbers. On the other hand, the disappearance of electron and muon neutrinos and antineutrinos observed in experiments constitute *evidences* that lepton flavour is not conserved in Nature, thus revealing the existence of new physics beyond the Standard Model.

The simplest, most elegant and probably correct explanation for the lepton flavour violation observed in experiments is three family neutrino oscillations⁽¹⁾. This statement, which seems obvious almost fifteen years after the discovery of neutrino oscillations, is nevertheless very non-trivial. It is important to remember that several mechanisms were

⁽¹⁾ With the exception of the LSND experiment, which observed electron antineutrino appearance in a muon antineutrino beam from pion decay at short baselines, and which cannot be accommodated in this framework. This result, however, has not been confirmed by MiniBooNE.

TABLE I. – *Status of neutrino parameters (from [2]).*

$\Delta m_{21}^2 = 7.59 \pm 0.20 \begin{pmatrix} +0.61 \\ -0.69 \end{pmatrix} \times 10^{-5} \text{ eV}^2$
$\Delta m_{31}^2 = \begin{matrix} -2.40 \pm 0.11 \begin{pmatrix} +0.37 \\ -0.39 \end{pmatrix} \times 10^{-3} \text{ eV}^2 \text{ (inverted)} \\ +2.51 \pm 0.12 \begin{pmatrix} +0.39 \\ -0.36 \end{pmatrix} \times 10^{-3} \text{ eV}^2 \text{ (normal)} \end{matrix}$
$\theta_{12} = 34.4 \pm 1.0 \begin{pmatrix} +3.2 \\ -2.9 \end{pmatrix}$
$\theta_{23} = 42.3 \begin{matrix} +5.3 \\ -2.8 \end{matrix} \begin{pmatrix} +11.4 \\ -7.1 \end{pmatrix}$
$\theta_{13} = 6.8 \begin{matrix} +2.6 \\ -3.6 \end{matrix} (\leq 13.2)$
$[\sin^2 \theta_{13} = 0.014 \begin{matrix} +0.013 \\ -0.011 \end{matrix} (\leq 0.052)]$
$\delta_{CP} \in [0, 360]$

proposed in the past to explain, without invoking neutrino masses, the lepton flavour violation observed in experiments. All of them are nowadays excluded by experiments, whereas neutrino oscillations is still a viable possibility which moreover can explain *simultaneously* all the experiments. For example, the atmospheric neutrino deficit could be explained by neutrino decay or by quantum decoherence effects. However, these mechanisms could not explain the dip in the L/E dependence of the deficit which was observed by SuperKamiokande. On the other hand, the solar neutrino deficit could be explained by the resonant spin-flip flavour conversion of neutrinos in a postulated strong magnetic field in the interior of the Sun, which is again excluded now by the observation of electron antineutrino disappearance by KamLAND.

2. – Status of neutrino oscillations

If neutrinos are massive particles, the flavour eigenstates $|\nu_\alpha\rangle$ ($\alpha = e, \mu, \tau$) do not necessarily coincide with the mass eigenstates $|\nu_i\rangle$ ($i = 1, 2, 3$). Instead, they are related by the unitary transformation $|\nu_\alpha\rangle = (U_{\text{lep}})_{\alpha i} |\nu_i\rangle$, where the leptonic mixing matrix U_{lep} is usually parametrized in terms of three angles θ_{12} , θ_{23} and θ_{13} and one phase δ for Dirac neutrinos or three phases δ, ϕ, ϕ' for Majorana neutrinos.

$$(1) \quad U_{\text{lep}} = \begin{pmatrix} c_{13}c_{12} & c_{13}s_{12} & s_{13}e^{-i\delta} \\ -c_{23}s_{12} - s_{23}s_{13}c_{12}e^{i\delta} & c_{23}c_{12} - s_{23}s_{13}s_{12}e^{i\delta} & s_{23}c_{13} \\ s_{23}s_{12} - c_{23}s_{13}c_{12}e^{i\delta} & -s_{23}c_{12} - c_{23}s_{13}s_{12}e^{i\delta} & c_{23}c_{13} \end{pmatrix} \cdot (e^{-i\phi/2}, e^{-i\phi'/2}, 1),$$

where $c_{ij} = \cos \theta_{ij}$ and $s_{ij} = \sin \theta_{ij}$.

The neutrino mass eigenstates are labeled such that ν_3 is the eigenvalue which is most split in mass with respect to the other two, while ν_1 and ν_2 are ordered such that ν_1 is the lightest between them. Neutrino oscillation experiments are only sensitive to the mass splittings and not to the masses themselves. Therefore, present experiments allow two possible mass orderings: the “normal” hierarchy, $m_3 > m_2 > m_1$, and the “inverted” hierarchy, $m_2 > m_1 > m_3$. The present status of the determination of neutrino parameters from experiments is summarized in table I.

Even though the information about neutrino parameters is still rather limited one can already notice some features: i) neutrino masses are tiny, at most of the order of 1 eV, ii) there are two large mixing angles, one of them possibly maximal, while the third one is small, iii) the two heaviest neutrinos present a mild mass hierarchy, the ratio between their masses being smaller than six. In order to understand the origin of flavour, it is important to compare these parameters with the same ones in the quark sector or the charged lepton sector. In doing so, one notices very striking differences: i) quark masses and charged lepton masses are in the MeV or GeV range, while neutrino masses lie in the eV or sub-eV range, ii) in the quark sector the three mixing angles are small, while in the neutrino sector there are two large mixing angles, iii) the mass hierarchies between the quark masses are $m_t/m_c \simeq 140$, $m_c/m_u \simeq 550$, $m_b/m_s \simeq 44$, $m_s/m_d \simeq 19$, $m_\tau/m_\mu \simeq 17$, $m_\mu/m_e \simeq 208$, while the mass hierarchy between the two heaviest neutrino states is much smaller, at most a factor of six. Any model of flavour should therefore address the three following questions: why are the neutrino masses tiny?, why are there large mixing angles?, why is there at least one mild mass hierarchy?

3. – Neutrino parameters as a window to new physics

Many neutrino mass models have been proposed to answer these questions, which fall into two main categories depending on how the global symmetry $U(3)_{e_R} \times U(3)_L$ is broken. A few models incorporate Dirac neutrinos, where neutrino masses violate all the family lepton numbers while preserving the total lepton number ($U(3)_{e_R} \times U(3)_L \rightarrow U(1)_{\text{lep}}$). On the other hand, most neutrino mass models proposed incorporate Majorana neutrinos, where all global quantum numbers in the leptonic sector are broken ($U(3)_{e_R} \times U(3)_L \rightarrow$ nothing). Whether neutrinos are Dirac or Majorana particles is still an open question which can only be resolved experimentally. Namely, the observation of neutrinoless double beta decay would constitute an evidence for the violation of total lepton number and thus an evidence for Majorana neutrinos. On the other hand, from the theoretical point of view these two possibilities provide different explanations to the puzzling differences between neutrino and quark parameters.

So far no Majorana fermion has been discovered, whereas we know of the existence of many fundamental Dirac fermions, therefore a very conservative assumption that one can make on the nature of neutrinos is that they are Dirac particles. If this is the case the Yukawa part of the leptonic Lagrangian reads

$$(2) \quad -\mathcal{L}_{\text{lep}} = (h_e)_{ij} \bar{e}_{Ri} L_j \phi + (h_\nu)_{ij} \bar{\nu}_{Ri} L_j \tilde{\phi} + \text{h.c.}$$

Note that in this Lagrangian the conservation of lepton number has been imposed *by hand*: being the right-handed neutrinos singlets under the Standard Model gauge group, the gauge symmetry also allows the Majorana mass term $M_{ij} \bar{\nu}_{Ri} \nu_{Rj}^c$ which has been forbidden by invoking the total lepton number conservation. In this scenario, the tininess of neutrino masses can be explained by a Yukawa coupling $h_\nu \sim 10^{-12}$ for the heaviest generation. The mechanism that generates Yukawa couplings is currently unknown and such a small value cannot be precluded, however, in view of the values of the other Yukawa couplings for the third generation (one billion times larger than that), this explanation looks conspicuous. We can also get some insight on the possibility of Dirac neutrinos by comparing the mass ratio between the two heaviest neutrinos with the mass ratios in other sectors. Again, even though we ignore the concrete mechanism that generates Dirac couplings, measurements of the quark and charged lepton masses suggest that this

mechanism tends to generate large mass hierarchies. Therefore, the existence of a mild mass hierarchy in the neutrino sector is another indication that neutrino masses have a different origin than the quark and charged lepton masses.

On the other hand, the possibility of Majorana masses is without any doubt the option preferred by most theorists, even though no fundamental Majorana fermion has been discovered so far. In this case the Yukawa part of the leptonic Lagrangian reads

$$(3) \quad -\mathcal{L}_{\text{lep}} = (h_e)_{ij} \bar{e}_{Ri} L_j \phi + \frac{(\alpha_\nu)_{ij}}{\Lambda} L_i \tilde{\phi} L_j \tilde{\phi} + \text{h.c.} ,$$

which exhibits two remarkable facts. First, there are no new particles at low energies and secondly, this is the most general Lagrangian up to dimension five consistent with the Standard Model particle content and gauge symmetry (note that no global symmetry has been imposed). For Majorana neutrinos the tininess of the masses can be explained by invoking a small coupling α_ν and/or by invoking a large suppression of the dimension-five operator by a large Λ . Moreover, the coupling α_ν is not a ‘‘Dirac-like’’ Yukawa coupling, therefore the flavour structure can be completely different to the flavour structure of the known Yukawa couplings h_u, h_d, h_e , namely the hierarchy of the eigenvalues of α_ν does not have to be necessarily very large, as in the case of the known ‘‘Dirac-like’’ Yukawa couplings. The facts that the smallness of neutrino masses can be explained by a large Λ and that the coupling α_ν can have a flavour structure different to the quark and lepton Yukawa couplings opens new opportunities to understand the striking differences between neutrino parameters and quark parameters, making the possibility of Majorana masses very appealing from the theoretical point of view.

There are many proposals to explain the origin of Majorana neutrino masses. The most popular one (and perhaps the simplest and most elegant) consists on introducing new heavy degrees of freedom, possibility commonly known as see-saw mechanism. There are three types of see-saw mechanisms: the type I see-saw mechanism assumes the existence of new fermion singlets, type II, new scalar triples, and type III, new fermion triplets. Here we will just discuss the type I see-saw mechanism.

The type I see-saw mechanism consists on adding to the Standard Model particle content at least two right-handed neutrinos. With this particle content, the most general leptonic Lagrangian compatible with the Standard Model gauge symmetry reads

$$(4) \quad -\mathcal{L}_{\text{lep}} = (h_e)_{ij} \bar{e}_{Ri} L_j \phi + (h_\nu)_{ij} \bar{\nu}_{Ri} L_j \tilde{\phi} - \frac{1}{2} M_{ij} \bar{\nu}_{Ri} \nu_{Rj}^c + \text{h.c.} ,$$

where in addition to the neutrino Yukawa coupling we have introduced a Majorana mass term for the right-handed neutrinos. Being the right-handed neutrinos singlets under the Standard Model gauge group, their mass scale is not related to the electroweak symmetry breaking scale: it can be of the same order, much larger or much smaller. The most interesting case arises when this mass scale is much larger than the electroweak scale. If this is the case, the right-handed neutrinos decouple at low energies and the effective theory can be described by the following Lagrangian:

$$(5) \quad -\mathcal{L}_{\text{lep}} = \frac{1}{2} (L_i \tilde{\phi}) [h_\nu^T M^{-1} h_\nu]_{ij} (L_j \tilde{\phi}) + \text{h.c.} ,$$

which gives, after the electroweak symmetry breaking, a neutrino mass matrix which reads $\mathcal{M}_\nu = h_\nu^T M^{-1} h_\nu \langle \phi^0 \rangle^2$. Note that in the type I see-saw mechanism the neutrino

masses are naturally small due to the large suppression by the large right-handed neutrino masses. Moreover, the neutrino Dirac Yukawa coupling enters in a complicated way in this formula. Therefore, it is plausible that even though the neutrino Dirac Yukawa coupling has very hierarchical eigenvalues (in accordance to our general expectation for “Dirac-like” couplings), the neutrino masses can have a mild mass hierarchy due to the complicated way it enters into this formula [3].

The type I see-saw mechanism has many attractive features: it is natural, simple and elegant, the particle content displays a suggestive left-right symmetry, it is nicely compatible with grand-unified theories, and could account for the observed baryon asymmetry of the Universe through the mechanism of leptogenesis [4]. For these reasons it is regarded as the “most standard extension of the Standard model”. However, it has the disadvantage that since the new physics enters at very high energies it cannot be directly tested. Moreover, the best motivated see-saw scenario, where the right-handed neutrinos are much heavier than the electroweak symmetry breaking scale, suffers a serious fine-tuning problem. Namely, the Higgs mass acquires a quadratically divergent correction such that $\delta m_\phi^2 \sim 1/(16\pi^2)h_\nu^2 M^2$. There is a very appealing solution to this problem where the right-handed neutrinos can be arbitrarily heavy while the corrections to the Higgs mass being comparable to the Higgs mass itself. This is the supersymmetric see-saw model, where the large quadratic corrections to the Higgs mass from the right-handed neutrinos are compensated by large quadratic corrections to the Higgs mass from the right-handed *sneutrinos*, which are of the same size but of opposite sign. Therefore, supersymmetry is the natural arena to implement the high-scale see-saw mechanism and, as we will discuss later, offers new opportunities to (indirectly) test the see-saw mechanism.

4. – Flavour violation in the charged lepton sector

As discussed above, the lepton flavour violation observed in neutrino experiments have lead to a leptonic Lagrangian given either by eq. (2) for Dirac neutrinos or eq. (3) for Majorana neutrinos. Both can be regarded as effective Lagrangians containing terms up to dimension five. Clearly, in order to obtain additional information about which physics lies beyond the Standard Model it is desirable to find evidences for the higher-order terms in the effective Lagrangian, which can be inferred from the observation of flavour violating processes in the charged lepton sector. For instance, the dimension-six operators $\bar{e}_{Ri}\sigma_{\mu\nu}L_j\phi B_{\mu\nu}$ and $\bar{e}_{Ri}\sigma_{\mu\nu}\tau_I L_j\phi W_{\mu\nu}^I$, induce processes such as $\mu \rightarrow e\gamma$ or $\tau \rightarrow e\gamma$, whereas $(\bar{L}_i\gamma^\mu L_j)(\bar{L}_k\gamma_\mu L_l)$, $(\bar{e}_i\gamma^\mu e_j)(\bar{e}_k\gamma_\mu e_l)$ and $(\bar{L}_i\gamma^\mu e_j)(\bar{e}_k\gamma_\mu L_l)$ induce processes such as $\mu^+ \rightarrow e^+e^-e^+$ or $\tau^+ \rightarrow \mu^+\mu^-\mu^+$ [5]. There are presently very stringent constraints on these operators. For example, the lowest-dimension operator which induces the process $\mu \rightarrow e\gamma$ is $\mathcal{L} = -m_\mu\bar{\mu}(f_{M1}^{\mu e} + \gamma_5 f_{E1}^{\mu e})\sigma^{\mu\nu}eF_{\mu\nu} + \text{h.c.}$, where $f^{\mu e}$ are form factors. A reasonable parametrization of the form factors is $f^{\mu e} \sim \theta_{\mu e}^2\alpha/\Lambda^2$, which takes into account that these operators usually appear at the one-loop level. Then, the present experimental constraint on $\text{BR}(\mu \rightarrow e\gamma)$ implies $\Lambda \gtrsim 20 \text{ TeV}$ for generic mixing angles, $\theta_{\mu e} \sim 1/\sqrt{2}$. Conversely, if the new particles appear at the electroweak scale, $\Lambda \sim 300 \text{ GeV}$, the mixing angle has to be rather small, $\theta_{\mu e} \lesssim 0.01$. This fact has dramatic implications for new physics: many extensions of the Standard Model postulate new particles at the electroweak scale which couple to the leptons, therefore the non-observation of the process $\mu \rightarrow e\gamma$ imposes very severe constraints on these models. Conversely, from the optimistic point of view, the discovery of $\mu \rightarrow e\gamma$ might be around the corner.

This is in particular the case for the supersymmetric type I see-saw model. In this model, the neutrino Yukawa coupling introduces at tree level sources of lepton flavour violation in the interactions between the right-handed neutrino, the left-handed lepton and the up-type Higgs chiral superfields. Being the right-handed neutrinos and sneutrinos so heavy, this flavour violation decouples completely at low energies, since the dimension-six operator is suppressed by a large mass scale. Interestingly, this lepton flavour violation is transmitted to the soft supersymmetry breaking parameters via the quantum corrections, necessarily inducing at low energies flavour violating terms in the left-handed slepton mass matrices and in the leptonic trilinear term, with just a logarithmic dependence on the right-handed neutrino masses [6]:

$$(6) \quad (\mathbf{m}_L^2)_{ij} \simeq -\frac{1}{8\pi^2}(3m_0^2 + |A_0|^2)(h_\nu^\dagger h_\nu)_{ij} \log\left(\frac{M_X}{M}\right),$$

where m_0 and A_0 are the universal soft scalar mass and trilinear term and M_X is a cut-off, usually identified with the GUT scale. The lepton flavour violation in the scalar sector is suppressed by the loop factor, but can have a rather large impact in low energy phenomena, since the dimension-six operator generated is suppressed only by the scale of the scalar masses, which presumably lies between 100 GeV and 1 TeV.

The lepton flavour violating effects in the type I see-saw scenario are connected to the neutrino Yukawa couplings and the right-handed neutrino Majorana masses. These are the same parameters which generate the neutrino masses, therefore it is very important to analyze whether there is any connection between the rates for the lepton flavour violating processes and the measured neutrino parameters. Unfortunately, this is not the case. The complete see-saw Lagrangian contains twelve real parameters and six phases, whereas neutrino observations can fix at most six real parameters and three phases. Therefore, there are six real parameters and three phases which are completely unconstrained from neutrino observations and that prevent any model-independent prediction for the lepton flavour violating processes. Indeed, there are, compatible with the observed neutrino parameters, an infinite set of Yukawa couplings [7]: $h_\nu = \sqrt{D_M} R \sqrt{D_m} U_{\text{lep}}^\dagger / \langle \phi^0 \rangle$. Here, D_m is a diagonal matrix with the neutrino masses and U_{lep} is the leptonic mixing matrix, which can be in principle measured with experiments. On the other hand, D_M is a diagonal matrix with the right-handed neutrino masses and R is a complex orthogonal matrix, which cannot be determined with low energy experiments and are thus free parameters. Therefore, by changing R and the right-handed neutrino masses, any matrix $h_\nu^\dagger h_\nu$ can be obtained, and thus any value for the lepton flavour violating effects. Furthermore, it can be shown that there is a one-to-one correspondence between the high energy see-saw parameters $\{h_\nu, M\}$ and the low energy parameters that determine any possible low energy observable consequence of the see-saw mechanism in the fermionic sector and in the scalar sector, $\{\mathcal{M}_\nu, h_\nu^\dagger h_\nu\}$ [8]. As a consequence, from the mathematical point of view *any* low energy observation can be accommodated by a set of high energy see-saw parameters (at the price, perhaps, of tuning parameters).

Remarkably, under some well-motivated assumptions about the high energy parameters, it is possible to derive predictions for the lepton flavour violating processes. Namely, one can impose the absence of tunings among parameters and that the eigenvalues of the neutrino Yukawa coupling are hierarchical (as occurs in all Yukawa matrices known).

By assuming the absence of tunings it is possible to derive a lower bound on the rate for the process $\mu \rightarrow e\gamma$ as a function of the rates for the processes $\tau \rightarrow \mu\gamma$ and $\tau \rightarrow e\gamma$. Let us assume that the processes $\tau \rightarrow \mu\gamma$ and $\tau \rightarrow e\gamma$ are both observed. The

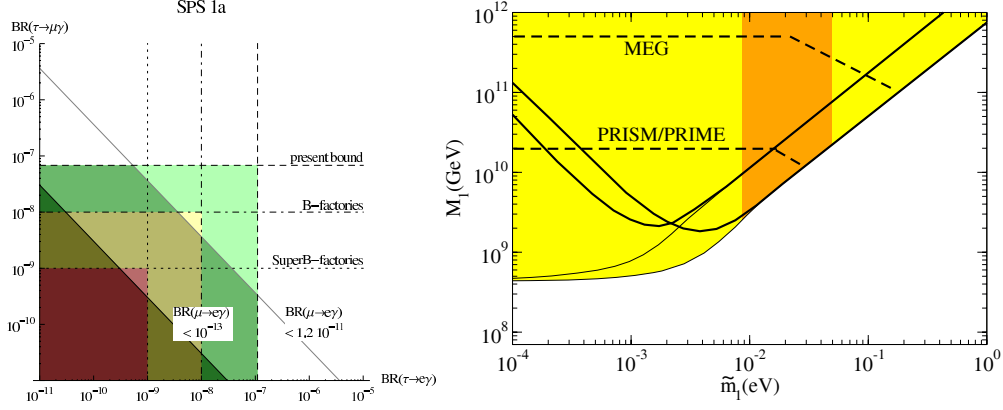


Fig. 1. – Left panel: constraints on the rare tau decays from present B -factories and from the non-observation of $\mu \rightarrow e\gamma$ in the type I see-saw mechanism for generic SUSY parameters. Right panel: constraints on the SUSY leptogenesis parameter space from the non-observation of $\mu \rightarrow e\gamma$. The “natural” region of this parameter space is shown in darker colour.

observation of the former implies new sources of tau and muon flavour violation, while the observation of the latter, new sources of tau and electron flavour violation. Therefore, the new physics that induces these two processes violate all flavour quantum numbers and hence this same physics necessarily generates at some level the process $\mu \rightarrow e\gamma$ [9,10]. Consequently, the following bound holds:

$$(7) \quad BR(\mu \rightarrow e\gamma) \gtrsim C \times BR(\tau \rightarrow \mu\gamma)BR(\tau \rightarrow e\gamma),$$

where C is a model-dependent constant. This bound is saturated when the lepton flavour violation in the $\mu - e$ sector only appears at higher order, via the combination of $\mu - \tau$ and $\tau - e$ flavour violation, whereas much larger rates can arise if there is “direct” $\mu - e$ flavour violation. The impact of this constraint for the SUSY see-saw model is illustrated in fig. 1, left panel, for a typical choice of the SUSY parameters (the SPS1a benchmark point). It follows from eq. (7) that the present constraint on the rate of the process $\mu \rightarrow e\gamma$ rules out the possibility of observing *both* processes $\tau \rightarrow \mu\gamma$ and $\tau \rightarrow e\gamma$ in present B -factories. Moreover, if the MEG experiment reaches the sensitivity $BR(\mu \rightarrow e\gamma) \sim 10^{-13}$ without finding a positive signal, the possibility of observing both rare tau decays at future super B -factories will also be ruled out. Conversely, if present B -factories observe both rare tau decays, the supersymmetric see-saw model will be disfavoured [10].

Moreover, assuming the absence of cancellations and that the neutrino Yukawa eigenvalues are hierarchical, it is possible to derive a lower bound on the process $\mu \rightarrow e\gamma$ as a function of the lightest right-handed neutrino mass [11]:

$$(8) \quad BR(\mu \rightarrow e\gamma) \gtrsim 1.2 \times 10^{-11} \left(\frac{M_1}{5 \times 10^{12} \text{ GeV}} \right)^2 \left(\frac{m_S}{200 \text{ GeV}} \right)^{-4} \left(\frac{\tan \beta}{10} \right)^2,$$

which allows to set an upper bound on the lightest right-handed neutrino mass from the constraint $BR(\mu \rightarrow e\gamma) \leq 1.2 \times 10^{-11}$ [12], namely $M_1 \lesssim 5 \times 10^{12} \text{ GeV}$ for typical SUSY

parameters. This expression also allows to establish an interesting connection between baryogenesis through leptogenesis and the rate for $\mu \rightarrow e\gamma$. The leptogenesis mechanism to generate the observed matter-antimatter asymmetry in our Universe requires a rather large mass scale for the right-handed neutrinos, $M_1 \gtrsim 10^9 \text{ GeV}$ [13]. Therefore, if leptogenesis is the correct mechanism to explain the matter-antimatter asymmetry in our Universe, it follows from eq. (8) that $\text{BR}(\mu \rightarrow e\gamma) \gtrsim 5 \times 10^{-19}$ for typical SUSY parameters. Conversely, the non-observation of $\mu - e$ flavour violation in the charged lepton sector constrains the parameter space of leptogenesis, spanned by the lightest right-handed neutrino mass and by the washout parameter $\tilde{m}_1 = (h_\nu h_\nu^\dagger)_{11}/M_1$. This is illustrated in fig. 1, right panel, where we show the region of the SUSY leptogenesis parameter space (adapted from [14]) that can be probed in present and future experiments searching for $\mu - e$ flavour violation. Furthermore, it can be shown that if there are no cancellations in the parameters that determine the washout of the baryon asymmetry, then $\sqrt{\Delta m_{\text{sol}}^2} \lesssim \tilde{m}_1 \lesssim \sqrt{\Delta m_{\text{atm}}^2}$ (displayed as a darker region in the figure), which gives a more stringent lower bound on M_1 . Therefore, in the absence of tunings, $\text{BR}(\mu \rightarrow e\gamma) \gtrsim 5 \times 10^{-18}$. This sensitivity to $\mu - e$ lepton flavour violation is difficult to reach in experiments searching for $\mu \rightarrow e\gamma$, although it is not far from the projected sensitivity of future experiments searching for $\mu - e$ conversion in nuclei. Namely, the PRISM/PRIME experiment at J-PARC aims to achieve a single event sensitivity to the process $\mu \text{ Ti} \rightarrow e \text{ Ti}$ at the level of 10^{-18} [15], which is equivalent to a sensitivity to the process $\mu \rightarrow e\gamma$ at the level of $\sim 2 \times 10^{-16}$. One should also bear in mind that the lower bound $\text{BR}(\mu \rightarrow e\gamma) \gtrsim 5 \times 10^{-18}$ relies on extremely conservative assumptions, therefore if the SUSY leptogenesis mechanism is the actual origin of the observed matter-antimatter asymmetry in our Universe, there are good chances to observe $\mu - e$ flavour violation in future experiments; probing the whole parameter space of leptogenesis is unfortunately out of the reach of projected experiments.

5. – Conclusions

Many experiments have reported the observation of flavour violation in the neutrino sector, which can be described by adding to the Standard Model Lagrangian a new term of dimension four (Dirac neutrinos) or five (Majorana neutrinos). We have analyzed these two possibilities from the theoretical point of view and we have argued that the striking differences between neutrino and quark parameters are most naturally explained if neutrinos are Majorana particles. We have also discussed the dimension-six operators which presumably appear in the effective Lagrangian and which induce lepton flavour violation in the charged lepton sector. In supersymmetric scenarios these operators are only mildly suppressed, opening the possibility of observing charged lepton flavour violation in the next round of experiments. Lastly, we have analyzed in some detail some predictions for the lepton flavour violating processes in the supersymmetric type I see-saw mechanism and the connection to the observed neutrino parameters.

REFERENCES

- [1] For a review, see GONZALEZ-GARCIA M. C. and MALTONI M., *Phys. Rep.*, **460** (2008) 1.
- [2] GONZALEZ-GARCIA M. C., MALTONI M. and SALVADO J., *JHEP*, **1004** (2010) 056.
- [3] CASAS J. A., IBARRA A. and JIMENEZ-ALBURQUERQUE F., *JHEP*, **0704** (2007) 064.
- [4] FUKUGITA M. and YANAGIDA T., *Phys. Lett. B*, **174** (1986) 45.

- [5] For a review, see RAIDAL M. *et al.*, *Eur. Phys. J. C*, **57** (2008) 13.
- [6] BORZUMATI F. and MASIERO A., *Phys. Rev. Lett.*, **57** (1986) 961.
- [7] CASAS J. A. and IBARRA A., *Nucl. Phys. B*, **618** (2001) 171.
- [8] DAVIDSON S. and IBARRA A., *JHEP*, **0109** (2001) 013.
- [9] IBARRA A., SHINDOU T. and SIMONETTO C., *JHEP*, **0810** (2008) 021.
- [10] IBARRA A. and SIMONETTO C., *JHEP*, **0804** (2008) 102.
- [11] IBARRA A. and SIMONETTO C., *JHEP*, **0908** (2009) 113.
- [12] BROOKS M. L. *et al.* (MEGA COLLABORATION), *Phys. Rev. Lett.*, **83** (1999) 1521.
- [13] DAVIDSON S. and IBARRA A., *Phys. Lett. B*, **535** (2002) 25.
- [14] BLANCHET S. and DI BARI P., *JCAP*, **0703** (2007) 018.
- [15] Letter of Intent to J-PARC, L25, *An Experimental Search for the $\mu - e$ Conversion Process at an Ultimate Sensitivity of the Order of 10^{-18} with PRISM.*

Neutrino oscillations studies with the OPERA experiment at the CNGS beam

E. PENNACCHIO(*) on behalf of the OPERA COLLABORATION

*Institut de Physique Nuclaire de Lyon, UCBL-CNRS/IN2P3
4 rue E. Fermi, F-69622 Villeurbanne, France*

(ricevuto il 14 Settembre 2010; pubblicato online il 10 Gennaio 2011)

Summary. — The OPERA experiment, located in hall C of the Gran Sasso underground laboratory, has been designed to detect the direct appearance of ν_τ in a pure ν_μ beam (CNGS) produced at CERN, travelling over a distance of 730 km. Taus produced in ν_τ charged current interactions are identified by reconstructing their decay path, using the nuclear emulsion technique. After a short introduction on physical motivations, the OPERA detector will be described. The event analysis chain will be explained, and first physics results presented.

PACS 13.15.+g – Neutrino interactions.

PACS 14.60.Lm – Ordinary neutrinos.

PACS 14.60.Pq – Neutrino mass and mixing.

PACS 29.40.Rg – Nuclear emulsions.

1. – Introduction

The measurements of neutrinos fluxes from all usable sources, the Sun, the Earth atmosphere, accelerator beams and nuclear reactors, form a coherent set of compelling experimental evidences of oscillations between neutrino flavours [1]. Till now the observation of the unambiguously appearance of a new flavour in a neutrino flux by identifying the charged lepton produced in its charged current interaction (CC) with matter is still missing. The OPERA experiment [2] precisely aims at identifying the τ produced in the CC interactions of ν_τ appearing in a pure ν_μ beam produced at CERN SPS and thus confirming the preferred interpretation of muonic neutrinos disappearance in the atmospheric sector by probing a similar domain of L/E. Having the capability to observe prompt electrons, OPERA will also allow the search for the sub-leading oscillation channel $\nu_\mu \rightarrow \nu_e$.

(*) E-mail: pennacc@ipnl.in2p3.fr

TABLE I. – *Expected number of τ and background events for nominal 5 years of data taking, corresponding to 22.5×10^{19} p.o.t.*

τ decay channel	Signal ($\Delta m^2 = 2.5 \times 10^{-3} \text{ eV}^2$)	Background
$\tau \rightarrow \mu$	2.9	0.17
$\tau \rightarrow e$	3.5	0.17
$\tau \rightarrow h$	3.1	0.24
$\tau \rightarrow 3h$	0.9	0.17
ALL	10.4	0.75

2. – The OPERA experiment

2.1. The CNGS beam. – The CNGS beam [3] is a wide-band neutrino beam ($\langle E_{\nu_\mu} \rangle = 17 \text{ GeV}$), optimized for ν_τ production and detection. It is produced by a 400 GeV/c proton beam extracted from the SPS accelerator and transported along a 840 m long beam line onto a carbon target producing kaons and pions. The positively charged π s and K s are energy selected, guided with the horn and the reflector in the Gran Sasso direction. They decay into ν_μ and μ . The muon and all the hadrons which do not interact into the target or not decay are stopped. During a CNGS cycle, which lasts 6 s, there are two SPS extractions, 10.5 μ s each, separated by 50 ms. The nominal beam intensity is 4.5×10^{19} proton on target (p.o.t.), with 200 days of beam operation per year.

2.2. The detection principle. – The ν_τ is detected through its charged current interaction, followed by τ decay in one ($\tau \rightarrow e, \tau \rightarrow \mu, \tau \rightarrow h$) or three ($\tau \rightarrow 3h$) prongs. The decay length is $\approx 600 \mu\text{m}$ ($c\tau = 87 \mu\text{m}$). In order to identify the decay topologies occurring over so small distances and produce enough τ neutrino interactions, it is mandatory to have a high granularity target with a big mass. These two conflicting requirements are fulfilled in OPERA using the concept of Emulsion Cloud Chamber (ECC), already employed by the DONUT [4] Collaboration to observe the first ν_τ interactions. The OPERA detector basic unit, the brick, is based on the ECC concept. It is a sandwich of 56 lead plates 1 mm thick, interleaved with emulsion plates (2 emulsion layers, 44 μm thick, poured on a 205 μm plastic base). On the downstream face (with respect to beam direction) a box with a removable pair of nuclear emulsion plates, named Changeable Sheets (CS), is glued. The bricks are completely stand-alone detectors, allowing for neutrino interaction vertex and event topology reconstruction, momentum measurement of charged particles by the detection of multiple Coulomb scattering (MCS) in lead plates, identification and measurement of electromagnetic showers and muon-pion separation (using dE/dx). With a target mass of 1.25 ktons, assuming nominal 5 years of data taking, the expected number of ν_μ charged and neutral current interactions is ≈ 24000 , with $\approx 170 \nu_e$ and $\bar{\nu}_e$ CC interactions. The number of ν_τ charged current interactions is $\approx 115 \nu_\tau$ (for $\Delta m^2 = 2.5 \times 10^{-3} \text{ eV}^2$ and full mixing), leading to the observation of about 10 ν_τ CC events, with less than one background event. The main background sources are the production of charmed particles in charged current events where the primary lepton is unidentified, the events in which the muon undergoes a Coulombian scattering at large angle and hadronic interactions mimicking tau decay topologies. The expected number of τ and background events for each channel are summarized in table I.

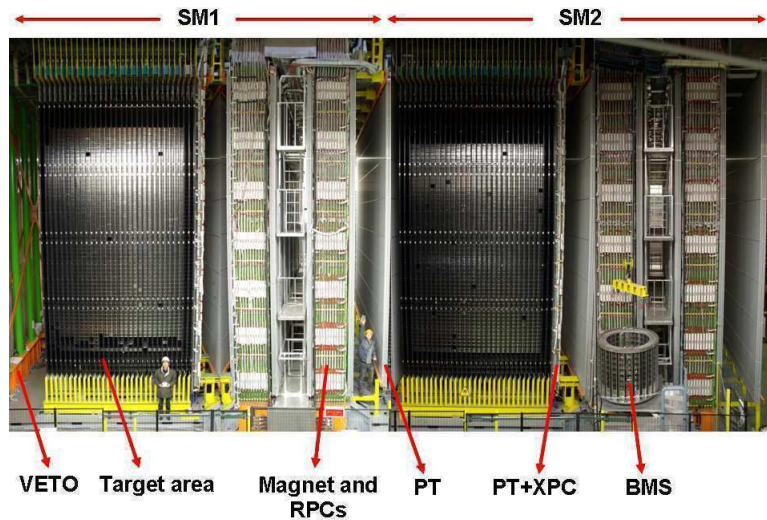


Fig. 1. – View of the OPERA detector. The upper horizontal lines indicate the position of the two identical supermodule (SM1 and SM2). The target area is made of walls filled with the bricks interleaved with planes of plastic scintillators (TT). Arrows show the position of the VETO planes, the drift tubes (PT) pulled alongside the XPC, the magnets and the RPC installed between the magnet iron slabs. The Brick Manipulator System (BMS) is also visible. More details can be found in [5].

2.3. The OPERA detector. – The OPERA hybrid detector, shown in fig. 1, is divided into two identical supermodules. Each supermodule (SM) has a target part, composed by 31 vertical walls transverse to the beam direction, interleaved with planes of plastic scintillator (TT), for a total of ≈ 150000 bricks, and a mass of 1.25 ktons (each brick weights 8.3 kg). The instrumented target is followed by a magnetic spectrometer consisting of a large iron magnet equipped with plastic Resistive Plate Chambers (RPC). The deflection of charged particles inside the magnetized iron is measured by six stations of drift tubes (Precision Trackers, PT). Left-right ambiguities in the reconstruction of particle trajectories inside the PT are removed by means of additional RPC (XPC) with readout strips rotated by 45° with respect to the horizontal and positioned near the first two PT stations. Finally, two glass RPC planes mounted in front of the first target (VETO) allow to reject charged particles originating from outside the target fiducial region, coming from neutrino interactions in the surrounding rock material. The electronic detector has the task to provide a neutrino interaction trigger, the event timing, to identify and measure the trajectory of charged particles, to locate the bricks where interactions occur, to perform the muon identification, charge and momentum measurements. The detector is equipped with an automatic machine (the Brick Manipulator System, BMS) that allows the removal of bricks from the detector. A detailed description of the detector and of the data acquisition system can be found in ref. [5]. Events induced by neutrinos in CNGS are selected on a delayed time coincidence between proton extraction from SPS and the events in OPERA. The synchronization is based on a GPS system, with a precision of ≈ 100 ns. In fig. 2 the time distribution of events in the neutrino run is shown.

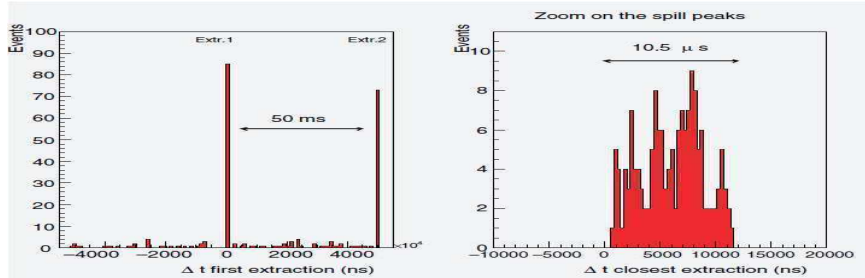


Fig. 2. – Time distribution of the events recorded during the CNGS beam run. Since two extractions are made from the SPS, on the left plot timing is shown with respect to the first one, while on the right plot the more fine distribution on the single extraction is shown.

2'4. Event analysis chain. – When a CNGS neutrino interacts in OPERA, the event is recorded and reconstructed by the electronic detectors. If there is a muon in the produced event its trajectory is traced back through the scintillator planes up to the brick where the track originates. When no muons are observed the scintillator signals produced by electrons or hadronic showers are used to predict the location of the brick that contains the primary neutrino interaction vertex. The selected brick is then extracted from the target by the BMS. The overall procedure minimizes the mass loss, allowing a semi-online target analysis. The two CS (cf. subsect. 2'2) glued on the downstream face of the brick are removed and the films analysed in order to validate the prediction and measure with micrometric precision the direction of the tracks belonging to the event. The global layout of bricks, CS and TT is schematically shown in fig. 3. If the presence of the event in the predicted brick is confirmed the brick is exposed to X-rays beams and to cosmic rays for sheets alignment. The brick is then disassembled, the films developed and sent to the different scanning laboratories to perform the complete analysis: there are 10 scanning laboratories in Europe and 2 in Japan. LNGS and Nagoya are also CS scanning centers. Emulsion scanning is performed with two different types of automatic microscopes: the

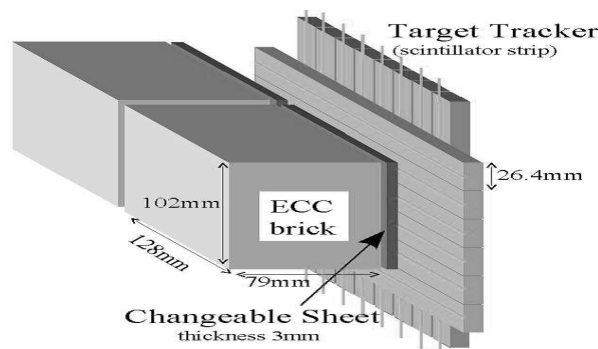


Fig. 3. – Schematic view of two bricks with their Changeable Sheets and target tracker planes.

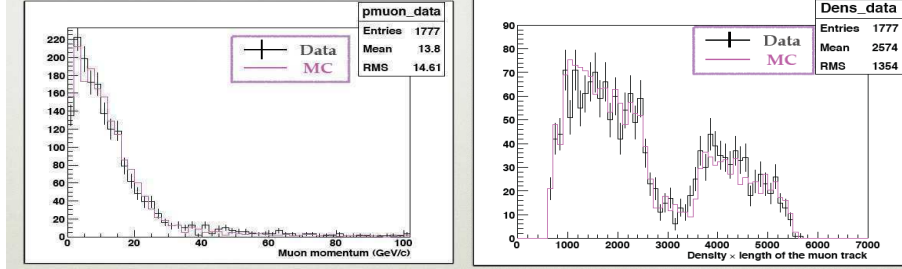


Fig. 4. – Muon momentum distribution (left), product of the muon track length times the density of crossed materials (right).

European Scanning System (ESS) [6] and the Japanese S-UTS [7]. The confirmed tracks are followed back in the brick until their stopping point (a track is considered as stopping if not found in 5 consecutive planes). This operation is called “scanback”. A volume of $\approx 1 \text{ cm}^2$ is then defined around the stopping point, on 5 plates up-stream and 10 down-stream. Track segments are measured within an angular acceptance of 0.6 rad. This region is fully scanned to confirm the presence of the interaction (“volume scan”). Then tracks attached to the vertex can be followed in the forth direction (scan-forth) for kinematical measurement. All the data are then centralized and stored in a Central Database (based on Oracle) existing in two identical master copies at LNGS (Italy) and in the IN2P3 Computing Center in Lyon. The OPERA principle has been fully proved and validated as reported in [8].

3. – Physics results

In this section some distributions for ν_μ charged current events obtained with electronic detector, are compared to Monte Carlo simulation. The results show a reasonable agreement. In the left part of fig. 4 the muon momentum distribution is shown, in the right part the product of the muon track length times the density of crossed materials, *i.e.* the measured range of the particle, the main variable used for muon identification. Continuous line is used for Monte Carlo distribution. The visible ratio between neutral current and charged current has also been measured after the removal of the background from beam neutrino interactions occurring outside the target region and projecting neutral particles which reinteract with the OPERA target. The values NC/CC obtained for 2008 and 2009 data, respectively equal to $0.23 \pm 0.014(\text{stat.})$ and $0.23 \pm 0.009(\text{stat.})$, are in good agreement with the predicted Monte Carlo value $NC/CC = 0.23 \pm 0.014(\text{stat.})$. The event track multiplicity distribution and the muon slopes measured at primary vertex (in the bricks), compared to Monte Carlo predictions, are shown in fig. 5. Soft muon momenta ($p < 6 \text{ GeV}$) are measured in the bricks using the Coulombian multiple scattering (MCS). In order to crosscheck the method of momenta measurements in the bricks the momenta for this sample of muons are also measured using the electronic detector, and the comparison between the results obtained with two methods is shown in fig. 6. The correlation is good.

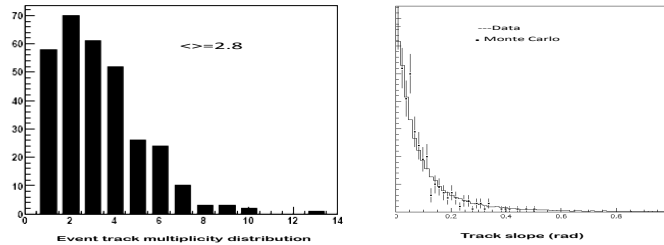


Fig. 5. – Event track multiplicity distribution (left), muon slopes measured at primary vertex (right).

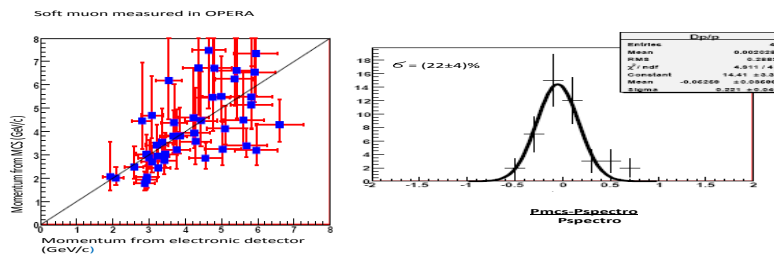


Fig. 6. – Correlation between muon momentum measure in the brick (using MCS) and the electronic detector.

3.1. Decay search. – All the scanning activities till fall 2009 have been focused on vertex location. A systematic decay search (DS) was started on 2008 and 2009 data in order to find all possible decay topologies. This new procedure has the aim to improve the vertex definition and the impact parameter (IP) distribution, to detect all possible kink topologies on tracks attached to the primary vertex and to search for extra tracks from decays not attached to primary vertex. This procedure has already been applied on a large part of 2008 data, and allowed to identify 20 charm candidates, in part already found with the scanback and vertex location procedure. The IP distribution obtained from real data with the application of the DS is shown in fig. 7. For comparison also the IP distribution for τ obtained with Monte Carlo data is shown. To complete

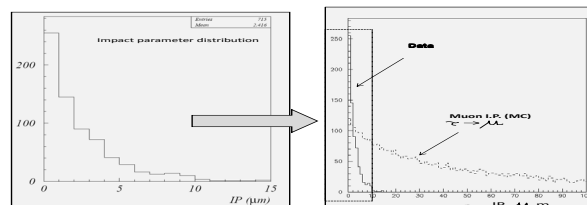


Fig. 7. – IP distribution.

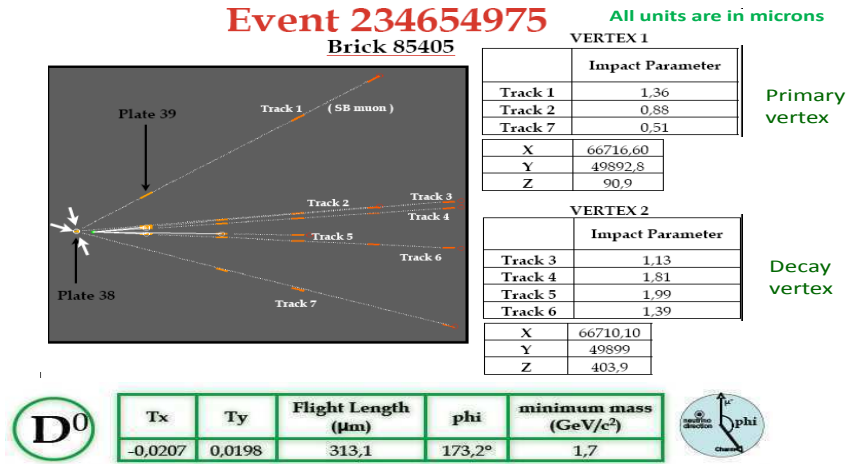


Fig. 8. – Charm candidate: the primary and secondary vertex are clearly visible. Impact parameters are shown in the tables, and kinematical reconstruction results are also shown.

charm candidates search the decay search procedure will be applied to the full 2008 and 2009 statistic. An example of charm candidate is shown in fig. 8: 3 tracks have been reconstructed at the primary vertex, and 4 to the decay one. All the impact parameters (of the order of the micron) have been measured. The minimum invariant mass was estimated to be 1.74 GeV strengthening the charm hypothesis. Topological details of the event are summarized in the table in fig. 8: the ϕ angle is found to be close to 180° which corresponds to a back-to-back emission of the charm with respect to the muon.

4. – Performances

OPERA has already taken data during two physics runs in 2008 and 2009. The CNGS beam performances are summarized in table II.

Till now (March 2010) almost 1500 events have been located, 943 for 2008 data and 438 for 2009. The analysis for 2008 data is completed. A detailed summary of events locations can be found in table III and table IV for 2008 and 2009 run, respectively.

5. – Conclusions

OPERA has taken data in 2008 and 2009 corresponding to a total luminosity of 5.3×10^{19} p.o.t., proving the full chain of the handling and analysis of the events. The performances of the electronic detector are reliable and well understood. A systematic

TABLE II. – *Run statistics.*

CNGS performances	1.782×10^{19} p.o.t.	3.522×10^{19} p.o.t.
On-time events	10122	21428
Candidates in the target	1698	3693

TABLE III. – *Events location summary for 2008 run (March 2010).*

	0μ	1μ	All
Events predicted by the electronic detector	406	1292	1698
Found in CS	271	1045	1316
Vertices located in bricks	151	792	943
Vertice located in dead materials	6	38	44
Interactions in the upstream brick	6	33	39

TABLE IV. – *Events location summary for 2009 run (March 2010).*

	0μ	1μ	All
Events predicted by the electronic detector	865	2297	3162
Extracted CS	829	2211	3040
CS Scanned	666	1802	2468
Found in CS	376	1139	1515
Vertices located in bricks	67	371	438
Vertice located in dead materials	2	11	13
Interactions in the upstream brick	3	36	39

decay search has been started on 2008 and 2009 events in order to find all possible decay topologies. Several charm events have been found as expected. A new run will start by the end of April 2010 allowing to increase the event statistics.

* * *

It is a pleasure to thank the organizer of this conference for the interest to OPERA physics, all the colleagues from the OPERA Collaboration, the founding agencies of the different countries participating to the experiment and the Computing Centre in Lyon (CCIN2P3) supporting the OPERA data analysis infrastructures.

REFERENCES

- [1] STRUMIA A. and VISSANI F., arXiv:hep-ph/0606054v3.
- [2] GULER M. *et al.* (OPERA COLLABORATION), *An appearance experiment to search for ν_τ oscillations in the CNGS beam in experimental proposal, CERN-SPSC-2000-028.*
- [3] CNGS project: online at <http://proj-cngs.web.cern.ch/proj-cngs/>
- [4] KODAMA K. *et al.* (DONUT COLLABORATION), *Phys. Rev. Lett.*, **93** (2004) 101801.
- [5] ACQUAFREDDA R. *et al.* (OPERA COLLABORATION), *JINST*, **4** (2009) P04018.
- [6] ARRABITO L. *et al.*, *JINST*, **2** (2007) P05004.
- [7] AOKI S. *et al.*, *Nucl. Instrum. Methods B*, **51** (1990) 466.
- [8] AGAFONOVA A. *et al.* (OPERA COLLABORATION), *JINST*, **4** (2009) P06020, arXiv:0903.2973.

New results and strategy of Borexino

Y. SUVOROV on behalf of the BOREXINO COLLABORATION

Laboratori Nazionali del Gran Sasso - 67100 Assergi (AQ), Italy

(ricevuto il 14 Settembre 2010; pubblicato online il 10 Gennaio 2011)

Summary. — The Borexino detector was designed to perform the first real-time measurement of the monoenergetic neutrinos from the electron capture on the ${}^7\text{Be}$ in the core of the Sun. The measurement with a precision of 10% has already been reported. The goal of 5% can be obtained in the future thanks to the intense calibration campaign performed in order to tune the Borexino reconstruction code. The ${}^8\text{B}$ solar neutrino analysis with the lowest threshold achieved so far of 3 MeV has also been reported. The unprecedentedly low intrinsic radioactivity achieved in Borexino offers a unique tool for the sensitive anti-neutrino study in the MeV energy range and made possible the first observation at more than 3σ CL of the geo-neutrino ($\text{geo-}\bar{\nu}_e$) signal.

PACS 95.55.Vj – Neutrino, muon, pion, and other elementary particle detectors; cosmic ray detectors.

PACS 29.40.Mc – Scintillation detectors.

1. – Introduction

The first real-time measurement of the solar neutrino fluxes in the sub-MeV energy range became possible with the Borexino multiton liquid scintillator (LS) detector [1] which has been constantly taking data since May 15th of 2007. The main goal of the Borexino experiment is the 5% precision measurement of the monochromatic solar neutrinos of the energy $E_\nu = 0.862\text{ MeV}$ that are emitted in the electron capture decay of ${}^7\text{Be}$ in the core of the Sun. The solar neutrinos in Borexino are detected via the neutrino elastic scattering on the electrons of the LS target.

The expected in Borexino rate of the ${}^7\text{Be}$ solar neutrinos of about 50 counts per day (cpd) in 100 tons of LS imposes to achieve an extremely high level of purity of the target scintillator. The core of the Borexino detector should be 9-10 orders of magnitude less radioactive than anything on Earth. Years of dedicated studies brought to the development of the successful purification strategy which allowed to obtain the desirable purity level of the scintillator [2].

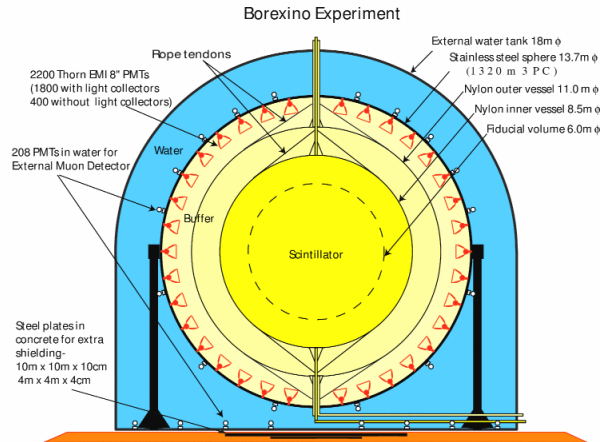


Fig. 1. – Schematic view of the Borexino detector.

2. – Detector design and experiment location

The Borexino detector is an unsegmented multiton liquid-scintillator detector, which can be subdivided into three concentric parts (see fig. 1).

The first, external, part is a Water Tank (WT) with a cylindrical base (18 m in the diameter) and a hemispherical top with a maximum height of 16.9 m. The Water Tank is filled with 2400 m³ of high-purity water which provides a 2m shielding against the external background (γ -rays and neutrons from the rock). Equipped by 208 PMTs that collect the Cerenkov light emitted by the muons in water, the WT also serves as a muon veto.

Inside the WT the Stainless Steel Sphere (SSS), the scintillator container and the holding structure for the 2212 8'' PMTs mounted on its inner surface, is placed. The SSS is divided into two parts: the most inner part, the core of the detector, is filled by the LS target, the mixture of the solvent pseudocumene and the fluor PPO at a concentration of 1.5 g/l, enclosed in a thin 125 μ m nylon Inner Vessel (IV). Outside the IV the SSS is filled with a not scintillating mixture of pseudocumene and DMP (buffer liquid) at a concentration of 5.0 g/l. This buffer liquid represents a second layer (1.5 m) of shielding mainly against the internal radiation from the PMTs and the construction materials. In order to prevent a Rn diffusion toward the central part of the detector a second nylon vessel (shroud) is placed in the SSS, close to the PMTs.

The Borexino experiment is located in the Hall C of the Gran Sasso National underground Laboratory (LNGS, Italy). The surrounding mountain provides 3800 m.w.e. of shielding against the cosmic radiation, the residual muon flux is $1.16 \pm 0.03 \text{ m}^{-2} \text{ h}^{-1}$ with an average energy of $320 \pm 4(\text{stat}) \pm 11(\text{syst}) \text{ GeV}$ [3].

3. – Solar neutrinos

Since the first observation of the solar neutrinos in 1968 [4] a clear discrepancy between the experimental results and the theoretical predictions was noticed, named later as the solar neutrino problem. Among various explanations the most favourite appeared to be the solar neutrino flavour oscillations due to the MSW effect [5] that

was experimentally confirmed by the SNO experiment in 2001 [6]. Further experimental investigation performed by SNO and KamLAND experiments allowed to constrain the MSW parameters to the so-called Large Mixing Angle (LMA) region in the $\theta_{12} : \Delta m^2$ plane [7].

The MSW-LMA scenario predicts the correlation of the neutrino oscillations (and therefore the survival probability) with the neutrino energy [8]. In the energy range above ~ 3 MeV the oscillations are dominated by matter effects, while below ~ 0.5 MeV a more important role is played by the vacuum effects. Before Borexino started to take data, in real time only the matter-dominated region was studied by observation of ^8B neutrinos starting from 5 MeV. The direct measurement of the survival probability (P_{ee}) in the region between ~ 0.5 MeV and ~ 3 MeV, the so-called transition zone, and below represents an important test of the MSW-LMA solution.

3.1. ^7Be solar neutrinos. – The detection of the ^7Be solar monoenergetic electron neutrinos with energy of 0.862 MeV produced in the process $^7\text{Be}(e^-, \nu_e)^7\text{Li}$ allowed for the first time to test the MSW-LMA prediction in the transition zone.

The present Borexino result based on 192 days of statistics is $49 \pm 3(\text{stat}) \pm 4(\text{syst})$ cpd/100 tons of LS [9]. Considering the high-metallicity Standard Solar Model (BS07(GS98) SSM), found rate corresponds to a flux $\Phi(^7\text{Be}) = 5.08 \pm 0.25 \times 10^9 \text{ cm}^{-2} \text{ s}^{-1}$. The expected signal in case of non-oscillating neutrinos is 74 ± 4 cpd/100 tons. The MSW-LMA scenario predicts the rate of 48 ± 4 cpd/100 tons that is in a good agreement with observation. The non-oscillation hypothesis ($P_{ee} = 1$) is rejected at 4σ CL.

Currently reached accuracy of 10% on the ^7Be flux does not allow to resolve the recently arisen problem of the chemical composition of the Sun, the so-called Solar metallicity problem [10].

The originally expected precision of 5% is feasible thanks to the recent improvements performed in the Borexino reconstruction code basing on the new calibration data from the 2008-2009 calibration campaign.

3.2. ^8B solar neutrinos. – The electron neutrinos produced in the decay of ^8B in the core of the Sun were the most accessible for the experimentalists due to the high visible end point energy of 16.3 MeV. Boron solar neutrino spectroscopy, however, has been performed so far only by the water Cerenkov detectors KamiokaNDE, SuperKamiokaNDE and SNO.

The main detection process is the elastic ν -e scattering, SNO experiment used also the nuclear reaction channels on deuterium contained in the heavy water target. The high level of intrinsic contamination and low photon yield impose a high threshold in the water Cerenkov experiments of 5 MeV. The lowest threshold achieved so far is 3.5 MeV after the application of the new analysis technique performed by the SNO Collaboration [11].

The Borexino liquid-scintillator detector has better energy resolution and higher level of radiopurity with respect to the water Cerenkov detectors. This provides an advantage in search of the ^8B neutrinos. At present the Borexino experiment performed the measurement of boron electron neutrinos based on 488 live days of statistics with a threshold of 3 MeV. The current threshold is limited by the 2.6 MeV gamma of the ^{208}Tl decay from the ^{232}Th chain. The observed rate is $0.217 \pm 0.038(\text{stat}) \pm 0.01(\text{syst})$ cpd/100 tons of LS which corresponds to a flux of $\Phi(^8\text{B}) = 2.4 \pm 0.04 \pm 0.01 \times 10^6 \text{ cm}^{-2} \text{ s}^{-1}$ (considering high metallicity SSM) [12]. The obtained result is in a good agreement with previous measurements.

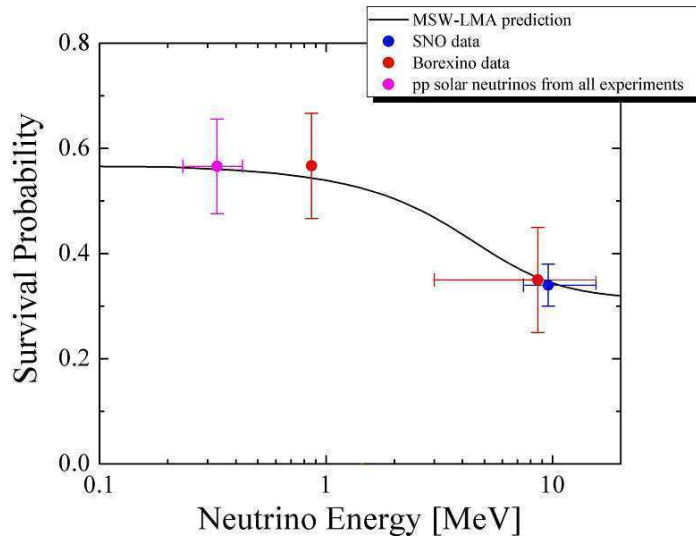


Fig. 2. – (Colour on-line) The mean electron neutrino survival probability (P_{ee}) as a function of neutrino energy. In red dots the $P_{ee}({}^7\text{Be})$ and $P_{ee}({}^8\text{B})$ measured by Borexino are shown.

The mean electron neutrino survival probability for the ${}^8\text{B}$ neutrinos at the effective energy of 8.6 MeV assuming BS07(GS98) SSM is found to be 0.35 ± 0.10 . For the ${}^7\text{Be}$ this value is 0.56 ± 0.01 (see fig. 2). Removing the common sources of uncertainty, the ratio between ${}^7\text{Be}$ and ${}^8\text{B}$ neutrinos survival probabilities becomes 1.60 ± 0.33 which is 1.8σ away from unity. This is the first measurement of the survival probability in both the transition zone and in the matter-dominated oscillation region obtained by the same detector.

4. – Calibrations

During a period of 2008-2009 three intense calibration campaigns were performed in Borexino in order to study in detail the detector response function. Three types of the radioactive sources (α , β and γ) were used for the precise definition of the energy scale in the wide range starting from 0.12 MeV up to 10 MeV.

The main source of uncertainty, as was reported in [9], is caused by the uncertainty on the fiducial volume definition (6%). Performed calibration allowed us to reduce this number down to 3.8%.

5. – First observation of the geo-neutrino signal

The geo-neutrinos, the electron anti-neutrinos ($\bar{\nu}_e$) generated in β decays of the long-lived radioactive isotopes mainly ${}^{40}\text{K}$, ${}^{238}\text{U}$ and ${}^{232}\text{Th}$ which are naturally present in the Earth interior, were introduced in 1960s by Marx [13], Markov [14] and Eders [15] and the subject was reviewed in 2004 by Mantovani *et al.* [16].

The first experimental investigation of geologically produced $\bar{\nu}_e$'s was done by the KamLAND experiment in 2005 [17].

Extreme cleanliness of the scintillator achieved in Borexino together with high photon yield and the large number of free target protons ($\sim 1.7 \times 10^{31}$) offer a unique tool for the anti-neutrino ($\bar{\nu}_e$) study in the MeV energy range.

Borexino detects $\bar{\nu}_e$ by means of the well-established reaction of the inverse β decay $\bar{\nu}_e + p \rightarrow e^+ + n$ with a threshold of 1.806 MeV. This process offers a strong signature given by two signals correlated in space and time. The positron in the LS comes promptly to rest and annihilates emitting two 0.511 MeV γ -rays, giving a prompt signal, with a visible energy of $E_{\text{prompt}} = E_{\bar{\nu}_e} - 0.782$ MeV. The emitted neutron, after the thermalization ($\tau \sim 256 \mu\text{s}$), is typically captured on proton with a resulting emission of a 2.22 MeV γ which provide a coincident delayed signal. Only $\bar{\nu}_e$ from the ^{238}U and ^{232}Th series satisfy the threshold ($E_{\bar{\nu}_e}^{\text{max}}(^{238}\text{U}) = 3.26$ MeV, $E_{\bar{\nu}_e}^{\text{max}}(^{232}\text{Th}) = 2.25$ MeV), while the ^{40}K $\bar{\nu}_e$ are below the threshold ($E_{\bar{\nu}_e}^{\text{max}}(^{40}\text{K}) = 1.3$ MeV) and therefore remain undetected.

The present $\bar{\nu}_e$ analysis is based on the 537.2 days of live-time collected between December 2007 and December 2009 that correspond, after all cuts, to an exposure of 252.6 ton y [18].

Two main sources of $\bar{\nu}_e$'s were considered in the analysis: the reactor $\bar{\nu}_e$'s whose energy spectrum extends up to ~ 8 MeV, and $\bar{\nu}_e$'s from the Earth ($1.8 \text{ MeV} < E_{\bar{\nu}_e} < 3.26$ MeV). The predicted geo-neutrino signal in Borexino with the visible energy up to ~ 2.6 MeV considering the Bulk Silicate Earth (BSE) model [16] is $2.5^{+0.3}_{-0.5}$ events in 100 ton y.

The advantageous location of Borexino detector, far from nuclear plants, guarantees the low contribution from the reactor- $\bar{\nu}_e$'s in the geo-neutrino energy window (~ 1 –2.6 MeV). Among all nuclear plants considered in the analysis 97.5% of the overall signal is given by the 194 reactors in Europe while other 245 reactors around the world contribute to only 2.5%. Based on data about all European nuclear plants (nominal thermal power and monthly load factor) from IAEA and EDF the calculated expected reactor- $\bar{\nu}_e$ signal in whole energy range (up to 8 MeV) in case of 100% detection efficiency is 5.7 ± 0.3 events in 100 ton y (with neutrino oscillations) and 9.9 ± 0.5 events in 100 ton y (without neutrino oscillations). Moreover, only $\sim 35\%$ of the total reactor- $\bar{\nu}_e$ signal will contaminate the geo-neutrinos energy window, while remaining 65% will be in the reactor- $\bar{\nu}_e$ window (2.6–8 MeV).

The intense and detailed study of all possible sources of background, mainly the sources of events capable to mimic the $\bar{\nu}_e$ signature, such as radioactive spallation isotopes (^8He , ^9Li), fast neutrons and fake $\bar{\nu}_e$ from the (α -n) reaction including the study of accidentals, bring to the overall background rate of 0.14 ± 0.02 events in 100 ton y. See [18] for more details.

A total of twenty-one (21) $\bar{\nu}_e$ candidates were selected after application of all cuts (see fig. 3). The expected background in the whole data set is 0.40 ± 0.05 events. Therefore, the resulting signal-to-background ratio is an unprecedented $\sim 50 : 1$. The best estimates of the geo- $\bar{\nu}_e$ and the reactor- $\bar{\nu}_e$ rates obtained from the unbinned maximum likelihood analysis are: $N_{\text{geo}} = 9.9^{+4.1}_{-3.4}$ ($^{+14.6}_{-8.2}$) and $N_{\text{react}} = 10.7^{+4.3}_{-3.4}$ ($^{+15.8}_{-8.0}$) at 68.3% CL (99.73% CL).

6. – Future plans

The recent efforts of the Borexino Collaboration are focused on the achievement of the 5% precision measurement of the ^7Be solar neutrino flux and on the study of the pep, CNO and possibly pp solar neutrinos. In order to extend the Borexino solar neutrino program, further purification of the detector will be done in the near future in order to reduce the contamination which prevents this analysis, mainly ^{85}Kr and ^{210}Bi .

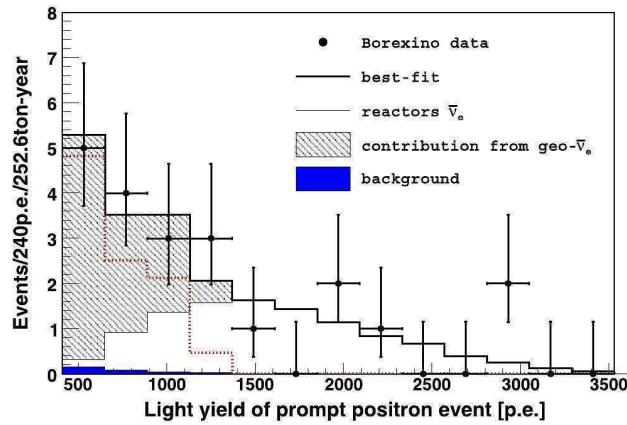


Fig. 3. – The light yield spectrum for the positron signals of 21 selected $\bar{\nu}_e$ candidates and the best fit. See [18] for details.

For what concerns the geo- $\bar{\nu}_e$ study a greater statistics is needed (accumulation of 1000 ton-y exposure is planned) in order to try to perform the spectral measurement of ^{238}U and ^{232}Th components of the geo- $\bar{\nu}_e$ signal.

REFERENCES

- [1] ALIMONTI G. *et al.* (BOREXINO COLLABORATION), *Nucl. Instrum. Methods A*, **600** (2009) 568.
- [2] ALIMONTI G. *et al.* (BOREXINO COLLABORATION), *Nucl. Instrum. Methods A*, **609** (2009) 58.
- [3] AMBROSIO M. *et al.* (MACRO COLLABORATION), *Astropart. Phys.*, **10** (1999) 11.
- [4] DAVIS R., HARMER D. and HOFFMAN K., *Phys. Rev. Lett.*, **20** (1968) 1205.
- [5] MIKHEEV S. and SMIRNOV Y., *Sov. J. Nucl. Phys.*, **42** (1985) 913.
- [6] AHMAD Q. *et al.* (SNO COLLABORATION), *Phys. Rev. Lett.*, **87** (2001) 071301.
- [7] ABE S. *et al.* (KAMLAND COLLABORATION), *Phys. Rev. Lett.*, **100** (2008) 221803.
- [8] BARGER *et al.*, *Phys. Rev. Lett.*, **95** (2005) 211802; FRIEDLAND A. *et al.*, *Phys. Lett. B*, **594** (2004) 347.
- [9] ALIMONTI G. *et al.* (BOREXINO COLLABORATION), *Phys. Rev. Lett.*, **101** (2008) 091302.
- [10] BAHCALL J., SERENELLI A. and BASU S., *Astrophys. J. Suppl.*, **165** (2006) 400; PENAGARAY C. and SERENELLI A., arXiv:0811.2424v1 (2008); SERENELLI A., arXiv:0910.3690 (2009).
- [11] AHMAD Q. *et al.* (SNO COLLABORATION), arXiv:0910.2984v1 (2009).
- [12] BELLINI G. *et al.* (BOREXINO COLLABORATION), arXiv:0808.2868v3 (2010).
- [13] MARX G. and MENYHARD N., *Mitt. Sternwarte, Budapest*, No. 48 (1960).
- [14] MARKOV M. A., *Neutrino* (Nauka, Moscow) 1964.
- [15] EDERS G., *Nucl. Phys.*, **78** (1966) 657.
- [16] MANTOVANI F. *et al.*, *Phys. Rev. D*, **69** (2004) 013001.
- [17] ARAKI T. *et al.* (KAMLAND COLLABORATION), *Nature*, **436** (2005) 499.
- [18] BELLINI G. *et al.* (BOREXINO COLLABORATION), *Phys. Lett. B*, **687** (2010) 299.

J-PARC kaon and muon programs

S. MIHARA

KEK, High Energy Accelerator Research Organization - 1-1 Oho, Tsukuba, Japan

(ricevuto il 14 Settembre 2010; pubblicato online il 10 Gennaio 2011)

Summary. — J-PARC has recently commenced operations. A variety of programs in particle and nuclear physics are planned to be conducted here. Among these, the kaon and muon programs are introduced in this presentation.

PACS 11.30.Hv – Flavor symmetries.

PACS 14.40.Df – Strange mesons.

PACS 14.60.Ef – Muons.

1. – Introduction

The J-PARC, Japan Proton Acceleration Research Complex (J-PARC), is a joint project between the Japan Atomic Energy Agency (JAEA) and the High Energy Accelerator Research Organization (KEK) and is a new and exciting accelerator research facility. The ultimate goal of the project is to generate a megawatt-class high-power proton beam at both 3 GeV and 30 GeV. In this facility, various types of secondary particles such as neutrons, muons, kaons, and neutrinos are produced in proton-nucleus reactions for use in materials and life science experiments as well as particle and nuclear physics experiments.

J-PARC is composed of three accelerators, as illustrated in fig. 1. The linac accelerates the beam (H^-) up to 181 MeV. Then, the beam is transferred to the Rapid Cycle Synchrotron (RCS), a booster after passing through a foil to strip the H^- beam of electrons. In the RCS, the proton beam is accelerated to 3 GeV and extracted by fast kickers to the Material Life Science Facility (MLF), an experiment facility where muons and neutrons are produced on graphite and mercury targets.

Part of the proton beam accelerated in the RCS is transferred to the Main Ring (MR), another synchrotron. The MR accelerates the beam to 30 GeV and supplies it to a neutrino facility by fast extraction using a series of kickers and to a particle and nuclear physics facility by slow extraction using electrostatic septa and septum magnets.

From 2008, J-PARC began producing four different types of secondary beams on schedule. The first was the neutron beam in May 2008 and the second was the muon beam in September 2008 at the MLF. Kaon beam production was successfully carried out



Fig. 1. – J-PARC accelerators.

in May 2009 by using a proton beam extracted from the MR. Neutrino production was then confirmed in April 2009 by using the MR proton beam. Currently, the accelerator group is attempting to improve the beam power while minimizing the beam loss; this should lead to less difficulty in machine maintenance in the future.

The achieved beam powers are listed in table I. Figure 2 shows the expected beam power improvement. It is planned to upgrade the linac to accelerate H^- up to 400 MeV in 2013, thus enabling a further improvement in the beam power in both the RCS and the MR.

As already mentioned above, two extraction methods are used at the MR. One is the fast extraction method that supplies the proton beam all at once to the neutrino experiment (T2K) without destroying the bunch structure necessary for beam acceleration. The other is the slow extraction method that supplies the proton beam to produce sec-

TABLE I. – *J-PARC beam power as of February 2010.*

Accelerator	Energy	Power	Proposed experiments
Linac	181 MeV	113 kW	neutron EDM
RCS	3 GeV	120–300 kW	muon/neutron physics experiments
MR Fast Extraction	30 GeV	50–100 kW	neutrino program
MR Slow Extraction	30 GeV	1.6 kW	secondary beam experiments

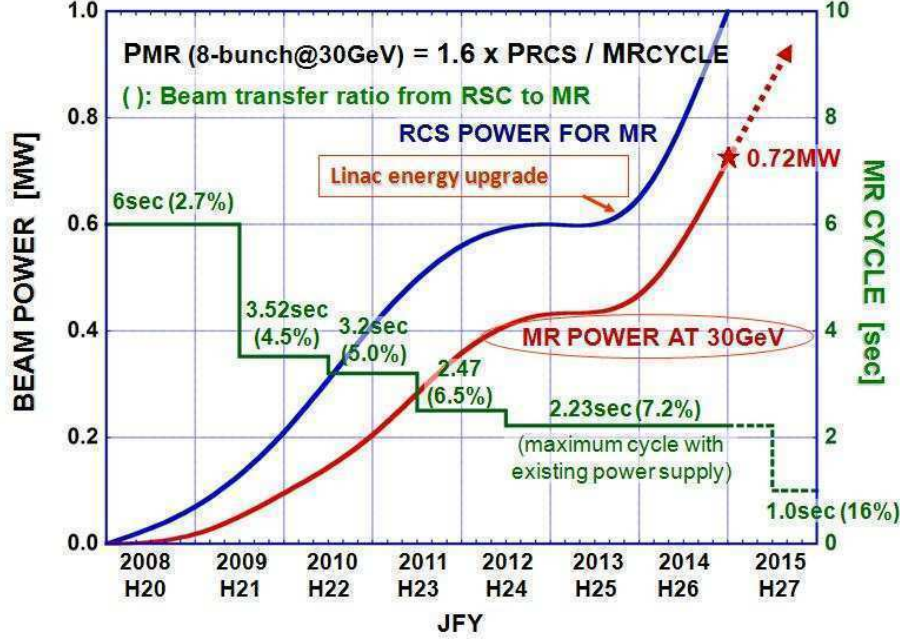


Fig. 2. – Expected beam power improvement of J-PARC.

ondary particles other than neutrinos. In this extraction mode, a part of the beam in the MR is extracted turn-by-turn in order to suppress event overlap in the experiments. Most of the experiments carried out using this extraction mode require a beam with a flattened time structure. Due to this, the acceleration RF is switched off during beam extraction. An exception is the μ -e conversion search experiment that is described later. This experiment requires a slowly extracted proton beam without destroying the bunch structure in the MR. This method is called bunched-slow extraction. The fast and normal slow extractions have already been tested and their performance is being improved, whereas the bunched-slow extraction for the μ -e conversion experiment needs to be proved operationally.

2. – Kaon programs

Two particle physics experiments using the kaon beam have currently been proposed at J-PARC. One is the TREK experiment to measure the T -violating muon P_T in $K^+ \rightarrow \pi^0 \mu^+ \nu_\mu$ decays, and the other is the KOTO experiment to study $K_L \rightarrow \pi^0 \nu \bar{\nu}$ decays.

2.1. TREK. – Time-Reversal violation Experiment with Kaons (TREK) aims to measure a T -odd K^+ decay parameter, the transverse muon polarization P_T in $K^+ \rightarrow \pi^0 \mu^+ \nu_\mu (K_{\mu 3})$ decays, with a sensitivity of 10^{-4} [1], where P_T is defined as

$$P_T = \frac{\sigma_\mu \cdot (p_{\pi^0, \gamma} \times p_{\mu^+})}{|(p_{\pi^0, \gamma} \times p_{\mu^+})|}.$$

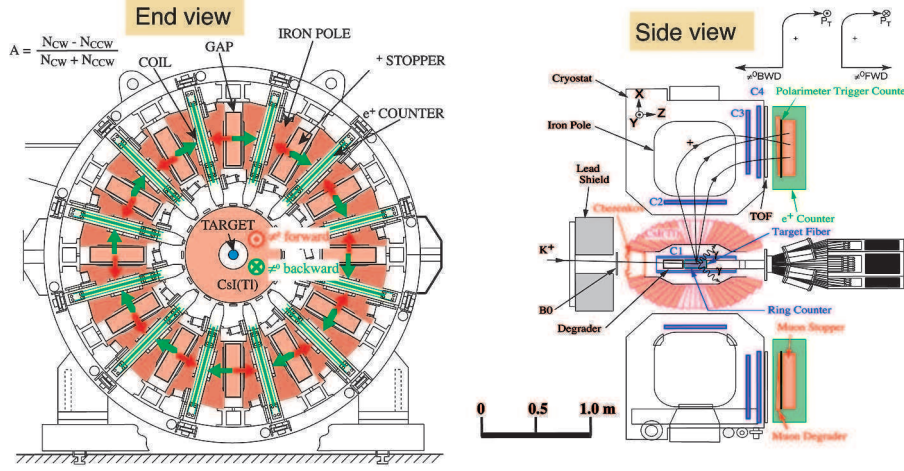


Fig. 3. – TREK spectrometer.

Here, $p_{\pi^0, \gamma}$ and p_{μ^+} denote the π^0 (or γ) and μ^+ momenta, respectively, and σ_{μ} denotes the spin of the μ to be measured using the active polarimeter equipped in the setup. The effects of final-state interactions on P_T are expected to be as small as 10^{-5} . In addition, the Standard Model (SM) contribution to P_T is calculated to be smaller than 10^{-7} . Thus, P_T measurement in the region of $10^{-3} \sim 10^{-4}$ can serve as a sensitive probe of CP violation in the SM because T violation is equivalent to CP violation according to the CPT theorem.

Figure 3 shows a schematic of the TREK spectrometer. The spectrometer is composed of an active polarimeter to measure muon polarization, a tracking system to track μ^+ and to measure its momentum, a CsI(Tl) calorimeter surrounding the target region to identify π^0 (or γ) and to measure its energy. In this experiment, the magnetic field to measure muon momentum is applied in the azimuthal direction parallel to the P_T component and $cw - ccw$ positron asymmetry in the azimuthal direction is measured depending on whether π^0 (or γ) is emitted forward or backward. The most recent measurement of P_T was carried out at the KEK proton synchrotron, as the E246 experiment. This experiment provided the best limit of $P_T = 0.0017 \pm 0.0023$ (stat) ± 0.0011 (syst) known thus far [2].

Currently, the construction of the beam line and the detector system is in progress with the goal of commencing data acquisition in 2012. It is necessary to realize a beam power of more than 100 kW to achieve the target sensitivity of 10^{-4} for two years running.

2.2. KOTO. – K0 at TOkai (KOTO) is an experiment to measure the branching ratio of $K_L \rightarrow \pi^0 \nu \bar{\nu}$ that is predicted by the SM with a small theoretical uncertainty at $(2.8 \pm 0.4) \times 10^{-11}$ [3]. This process is a CP -violating process and the branching ratio is proportional to the square of η , which is one of the Wolfenstein parameters determining the imaginary component of the CKM matrix. Thus, the η parameter can be determined through this measurement with a small ambiguity thanks to the small theoretical uncertainty of the order of 1–2% [4]. It is also important to note that, because the SM contribution to this decay mode is small, the measurement is sensitive to a new physics beyond the SM as predicted by many theoretical models [5, 6].

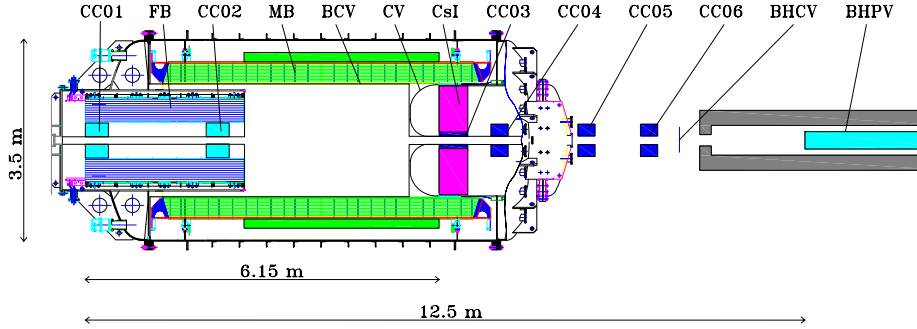


Fig. 4. – KOTO detector.

The current best limit is set by the KEK-PS E391a experiment at 6.7×10^{-8} at 90% CL [7] without any event candidate. The branching ratio of this decay mode is theoretically limited to be smaller than 1.46×10^{-9} at 90% CL; this is called the Grossman-Nir bound [8]. This indirect limit is imposed from a measured branching ratio of $K^+ \rightarrow \pi^+ \nu \bar{\nu}$ (1.73×10^{-10} , obtained by BNL E797/E949 experiments [9]) assuming the isospin symmetry.

The primary goal of the experiment is to reach the limit predicted by the SM below the Grossman-Nir bound using a detector system, shown in fig. 4, integrated by upgrading the previous E391a detector. A new CsI calorimeter will be constructed by assembling crystals obtained from the KTeV experiment. All detector signals are recorded using waveform digitizers in order to improve the event reconstruction reliability and background rejection capability.

A neutral kaon beam line has been newly constructed in the particle and nuclear physics experimental hall. At the beginning of 2010, a beam survey was conducted utilizing a neutral kaon decay mode, $K_L \rightarrow \pi^+ \pi^- \pi^0$ (13%), produced by a 1 kW slow-extraction beam. A clear peak corresponding to K_L was successfully recognized in a mass spectrum with two sets of hodoscopes and two arrays of pure-CsI crystal calorimeters.

In 2010, KOTO plans to complete the construction of the CsI calorimeter. An engineering run is scheduled to study K_L beam properties using the calorimeter. In 2011, it is expected that the detector will be installed, following which a full engineering run will be carried out. Data acquisition (physics run) is expected to start after this with 10% of the proposed beam intensity for one month. It is expected that KOTO will reach the Grossman-Nir limit with these statistics.

3. – Muon programs

The search for lepton-flavor violation (LFV) processes using muons is considered to play an important role in revealing a new physics beyond the SM thanks to the unique features of muons. Extremely precise measurements of well-known muon properties can also address possible new physics effects in comparison with those expected from the SM. At J-PARC, two μ -e conversion search experiments and one precision measurement of muon $g-2$ and EDM are planned to be conducted by utilizing the superior characteristics of the primary proton beam.

3.1. COMET. – The COherent Muon-to-Electron Transition (COMET) experiment is planned to be launched in the particle and nuclear experimental hall [10]. COMET

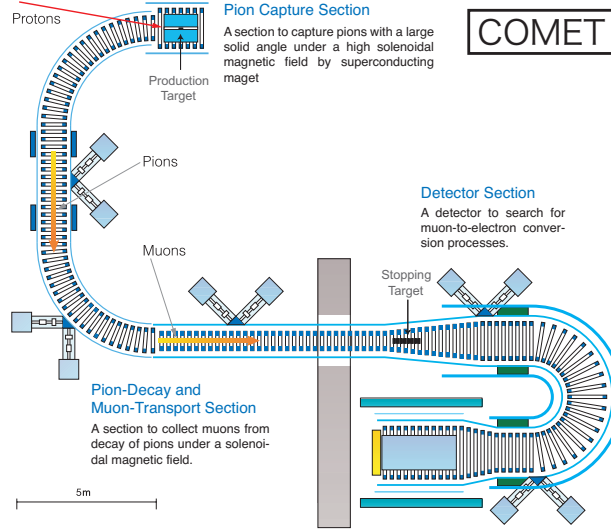


Fig. 5. – Setup of the COMET experiment.

aims to achieve a sensitivity of 10^{-16} to detect an LFV muon-to-electron transition (μ -e conversion) using an aluminum target. Because LFV processes are strictly forbidden in the framework of the SM, the discovery of the μ -e conversion will serve as remarkable evidence of a new physics beyond the SM. Many theoretical models incorporating the insufficiency of the SM predict the existence of the μ -e conversion immediately below the current experimental bound of 7×10^{-13} set by the SINDRUM II experiment [11].

The proton beam used for the COMET experiment is extracted from the MR at 8 GeV in order to suppress anti-proton production that may possibly cause an unwanted background in the experiment. Extraction is carried out by employing the bunched-slow extraction method, as already explained. The extracted beam is transported to a pion production target surrounded by a super-conducting solenoid magnet to collect and transport pions toward the transport solenoid magnet. Most pions decay to muons (and neutrinos) during these capture and transport processes, and these muons are transported through a curved transport solenoid to be stopped at the muon stopping target. The COMET detector located in a larger solenoid magnet is connected to the stopping target with another curved solenoid. A schematic view of the experimental setup is shown in fig. 5.

The signal of the μ -e conversion will be an electron emission with a characteristic energy (105 MeV) as large as the muon mass from muonic atoms. Muons in muonic atoms have a lifetime of 880 ns when aluminum is used as a muon-stopping target. In order to maximize the sensitivity of the experiment, two curved solenoids are used for transporting muons and electrons with large momentum and spacial acceptance. Because the centers of the helical trajectories of charged particle drift vertically as particles travel through curved solenoids depending on their momentum (and charge), a compensating vertical field is applied winding superconducting wires with a small tilt. This feature of the curved solenoid enables us to select the momentum of particles by locating collimators at suitable locations. In the muon transport curved solenoid, high-momentum muons above $75 \text{ MeV}/c$ are stopped by a collimator, and in the detector curved solenoid, electrons below $60 \text{ MeV}/c$ are stopped and $60\text{--}100 \text{ MeV}/c$ electrons are reduced before entering the detector.

In this experiment, the pulse structure of the proton beam is very important because the primary proton beam hitting the pion production target produces a large background with prompt timing. To suppress this, the experiment opens the data acquisition window 600 ns after the primary proton pulse hits the production target. Thus, if any proton arrives at the target off-timing, that can easily produce a background that can possibly be misidentified as a μ -e conversion signal.

Currently, the COMET Collaboration is studying the time structure of the J-PARC proton beam and also conducting R&D on the detector components in order to start physics data acquisition some time around 2016–2017 followed by an engineering run.

3.2. *DeeMe.* – COMET is considered to have a real chance of discovery if it can realize its target sensitivity; however, the construction necessary to start the experiment can take as long as 5–6 years because of the technical and financial requirements. Therefore, another μ -e conversion search experiment has been considered to study the physics with less sensitivity but with the earlier realization. DeeMe plans to attain a μ -e conversion search sensitivity of 10^{-13} – 10^{-14} by using carbon or aluminum as a target. The proton beam at the MLF will be used in this experiment. DeeMe does not transport the muon beam as COMET does but tries to measure only the delayed electrons emitted directly from a pion production target (carbon) or from a muon stopping target (aluminum) that will be located very close to the pion production target. A muon beam line in the MLF facility is used as an electron spectrometer. The feasibility of this experiment is being carefully checked by conducting tests at the beam line.

3.3. *Muon g-2/EDM measurement.* – An experimental proposal has been submitted to measure the muon g-2 and electric dipole moment by using the J-PARC MLF muon beam [12]. In this experiment, the muon beam is generated by accelerating muons produced from muoniums. Those muoniums are formed by stopping the surface muon beam in a material and then shooting a powerful pulsed laser at a suitable timing to remove electrons. Thus, a muon source with very small momentum dispersion, which is actually almost at rest, is obtained. Then, the muons are accelerated by a muon linac to 300 MeV/c for the experiment. Thanks to this innovative method to generate a muon beam with very small momentum spread in a transverse direction, the experiment can conduct a g-2 measurement using a completely different configuration from the previous measurement performed at BNL [13]. This also enables the measurement of the muon EDM with the same setup because no electric field is required to focus the beam. The collaboration is carrying out R&D on components required to realize such an unprecedented muon beam with an intensity of 10^6 muons/s and to start the experiment in a few years.

4. – Conclusions

J-PARC has recently commenced operations and its power is currently being upgraded. As described in this presentation, interesting kaon and muon programs are planned to be conducted using the high-performance beam available at J-PARC. Fruitful particle physics results are expected as the machine demonstrates a step-by-step achievement of its primary performance.

* * *

This presentation was prepared with the valuable support of the J-PARC accelerator group, TREK Collaboration, KOTO Collaboration, COMET Collaboration, DeeMe Collaboration, and J-PARC g-2/EDM Collaboration.

REFERENCES

- [1] TREK COLLABORATION, *Measurement of T-violating Muon Polarization in $K^+ \rightarrow \pi^0 \mu^+ \nu_\mu$* , J-PARC proposal (2006), <http://j-parc.jp/NuclPart/Proposal.e.html>.
- [2] ABE M., *Phys. Rev. D*, **73** (2006) 072005.
- [3] KOTO COLLABORATION, *Proposal for $K_L \rightarrow \pi^0 \nu \bar{\nu}$ Experiment at J-PARC*, J-PARC proposal (2006), <http://j-parc.jp/NuclPart/Proposal.e.html>.
- [4] BURAS A. and SCHWAB F., *Rev. Mod. Phys.*, **80** (2008) 965.
- [5] D'AMBROSIO D. *et al.*, *Nucl. Phys. B*, **645** (2002) 155.
- [6] ISIDORI G. *et al.*, *JHEP*, **0608** (2006) 064.
- [7] AHN J. *et al.*, *Phys. Rev. Lett.*, **100** (2008) 201802.
- [8] GROSSMAN Y. and NIR Y., *Phys. Lett. B*, **398** (1997) 163.
- [9] ARTAMONOV A. *et al.*, *Phys. Rev. D*, **79** (2009) 092004.
- [10] COMET COLLABORATION, *Proposal for COMET Experiment at J-PARC*, J-PARC proposal (2008), <http://j-parc.jp/NuclPart/Proposal.e.html>.
- [11] BERTL W. *et al.*, *Eur. Phys. J. C*, **47** (2006) 337.
- [12] G-2/EDM COLLABORATION, *Proposal on a New Measurement of the Muon Anomalous Magnetic Moment $g-2$ and Electric Dipole Moment at J-PARC*, J-PARC proposal (2008), <http://j-parc.jp/NuclPart/Proposal.e.html>.
- [13] BENNETT G. *et al.*, *Phys. Rev. Lett.*, **92** (2004) 161802.

Towards Θ_{13} with Double Chooz

D. GREINER(*) for the DOUBLE CHOOZ COLLABORATION

*Kepler Center for Astro and Particle physics, University of Tübingen
Auf der Morgenstelle 14, Tübingen, Germany*

(ricevuto il 14 Settembre 2010; pubblicato online il 10 Gennaio 2011)

Summary. — The Double Chooz experiment at the Chooz nuclear power station is designed to measure the last undetermined neutrino mixing angle Θ_{13} with a two-detector setup. This allows a significant reduction of the dominating systematic uncertainties compared to the CHOOZ experiment which currently still sets the limiting bound on Θ_{13} .

PACS 14.60.Pq – Neutrino mass and mixing.
PACS 07.05.Fb – Design of experiments.

1. – Neutrino oscillations

There is now overwhelming evidence [1-4] for a non-diagonal mixing matrix in the neutrino sector, which gives rise to flavour changes of neutrinos and requires at least the addition of right-handed neutrinos to the standard model, observable as non-degenerate neutrino masses. For Dirac neutrinos, the relation of mass and flavour eigenstates can be written as a 3×3 matrix containing three mixing angles Θ_{ij} and one as yet undetermined CP violating Dirac phase δ :

$$(1) \quad \begin{pmatrix} \nu_e \\ \nu_\mu \\ \nu_\tau \end{pmatrix} = \begin{pmatrix} 1 & 0 & 0 \\ 0 & c_{23} & s_{23} \\ 0 & -s_{23} & c_{23} \end{pmatrix} \begin{pmatrix} c_{13} & 0 & s_{13}e^{-i\delta} \\ 0 & 1 & 0 \\ -s_{13}e^{i\delta} & 0 & c_{13} \end{pmatrix} \begin{pmatrix} c_{12} & s_{12} & 0 \\ -s_{12} & c_{12} & 0 \\ 0 & 0 & 1 \end{pmatrix} \begin{pmatrix} \nu_1 \\ \nu_2 \\ \nu_3 \end{pmatrix}$$

with $s_{ij} = \sin \Theta_{ij}$ and $c_{ij} = \cos \Theta_{ij}$, or for short

$$\vec{\nu}_{\text{flavour}} = \mathbf{U} \vec{\nu}_{\text{mass}},$$

(*) E-mail: greiner@pit.physik.uni-tuebingen.de

TABLE I. – *Global fits of neutrino properties [6] with 1σ bounds.*

Θ_{23}	$42.3^{+5.3}_{-2.8}$	Δm_{12}^2	$7.59 \pm 0.20 \cdot 10^{-5} \text{ eV}^2$
Θ_{13}	$6.8^{+2.6}_{-3.6}$	Δm_{31}^2 (inverted)	$-2.40 \pm 0.11 \cdot 10^{-3} \text{ eV}^2$
Θ_{12}	34.4 ± 1.0	Δm_{31}^2 (normal)	$2.51 \pm 0.12 \cdot 10^{-3} \text{ eV}^2$

\mathbf{U} is known as the PMNS matrix. If neutrinos are Majorana particles, two additional phases α and β can occur:

$$\vec{\nu}_{\text{flavour}} = \mathbf{U} \begin{pmatrix} e^{i\alpha/2} & 0 & 0 \\ 0 & e^{i\beta/2} & 0 \\ 0 & 0 & 1 \end{pmatrix} \vec{\nu}_{\text{mass}}.$$

However, as Double Chooz is not sensitive to these phases, we will neglect them for the further discussion.

The neutrino masses enter as differences of squared masses into the description of the oscillation, conveniently written as

$$\Delta m_{ij}^2 = m_i^2 - m_j^2.$$

It is still undetermined if the ordering of the mass eigenstates from lightest to heaviest neutrino is

$$\begin{aligned} & m_{\nu_1} < m_{\nu_2} < m_{\nu_3} \quad \text{normal hierarchy,} \\ \text{or} & m_{\nu_3} < m_{\nu_1} < m_{\nu_2} \quad \text{inverted hierarchy.} \end{aligned}$$

Table I summarizes the state of our current knowledge about these basic neutrino properties. It is important to notice that for the 3σ bound, Θ_{13} fits are compatible with zero.

2. – Reactor neutrinos

The Double Chooz experiment uses beta-decay electron antineutrinos produced in the two 4 GW_{th} reactor cores of the EDF Chooz B power plant at Chooz, France, to investigate the disappearance of these neutrinos over a base line of about 1 km due to non-vanishing Θ_{13} . The energy spectrum of these pure $\bar{\nu}_e$ reactor antineutrinos is determined by the beta-decay spectra of the fuel rod constituents and changes over time with the burn up, with average neutrino energies in MeV range below 10 MeV. To calculate the survival probability of an electron antineutrino of given energy, the general oscillation probability formula

$$P(\nu_\alpha \rightarrow \nu_\beta) = |\langle \nu_\beta | \nu_\alpha \rangle|^2 = \sum_{k,j} U_{\alpha k}^* U_{\beta k} U_{\alpha j} U_{\beta j}^* e^{-\frac{i}{\hbar}(E_k - E_j)t}$$

can be written in ultrarelativistic approximation and with $c = \hbar = 1$

$$(2) \quad P(\bar{\nu}_e \rightarrow \bar{\nu}_e) \approx 1 - \sin^2 2\Theta_{13} \sin^2 \left(\frac{\Delta m_{31}^2 L}{4E} \right) - \cos^4 \Theta_{13} \sin^2 2\Theta_{12} \sin^2 \left(\frac{\Delta m_{21}^2 L}{4E} \right).$$

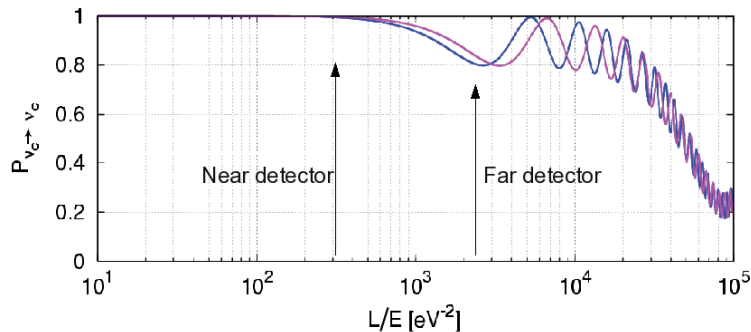


Fig. 1. – Survival probability of electron antineutrinos as a function of L/E for two different Δm_{31}^2 [7].

The resulting oscillation pattern is shown in fig. 1 as a function of L/E . Comparison of measured neutrino rate and spectral shape with calculations for different values of Θ_{13} can give direct evidence of $\bar{\nu}_e \rightarrow \bar{\nu}_x$ oscillations if the effect is large enough compared to systematic and statistic uncertainties. It should be noted that δ does not appear in the formula for the survival probability, eq. (2). Therefore, reactor neutrino experiments provide an unambiguous access to Θ_{13} , whereas beam experiments always suffer from degeneracies between δ and Θ_{13} . If Θ_{13} could be fixed by a reactor experiment, beam experiments could probe for CP violation in the leptonic sector by measuring δ .

3. – From CHOOZ to Double Chooz

The current bound on Θ_{13} is dominated by the results of the CHOOZ experiment [5], the predecessor of Double Chooz, which was located at the same power plant and used a 5 t Gd-doped liquid-scintillator target to identify neutrino-induced inverse beta decay

$$(3) \quad \bar{\nu}_e + p \rightarrow e^+ + n.$$

The signature of such an event is a delayed coincidence of the positron kinetic energy plus annihilation deposition followed by a gamma cascade released after n capture on Gd with $\tau \approx 30 \mu s$. Due to kinematics, the neutrino energy can be directly inferred from the positron kinetic energy, which allows to reconstruct the energy spectrum of the detected neutrinos. The advantage of the Gd doped scintillator lies in the fact that Gd has a very high- n capture cross section and the energy released in gammas after capture is between six and eight MeV, thus clearly above all singles background induced by radioactive sources in the detector materials. CHOOZ had a total runtime of 15 months, with about 7 months of background only data. Its final results were compatible with a no oscillation hypothesis at 90% confidence level.

To improve on the accuracy of CHOOZ, several steps can be taken. Statistics limitations can be tackled by longer runtime (CHOOZ was limited by scintillator degradation in this respect), larger target mass and a more powerful reactor complex. The main systematic uncertainties arise due to incomplete knowledge on reaction cross section, detection efficiency, reactor power, etc., which for CHOOZ resulted in an overall 2.7% relative error. This can be addressed by doing a *relative* measurement with two identical

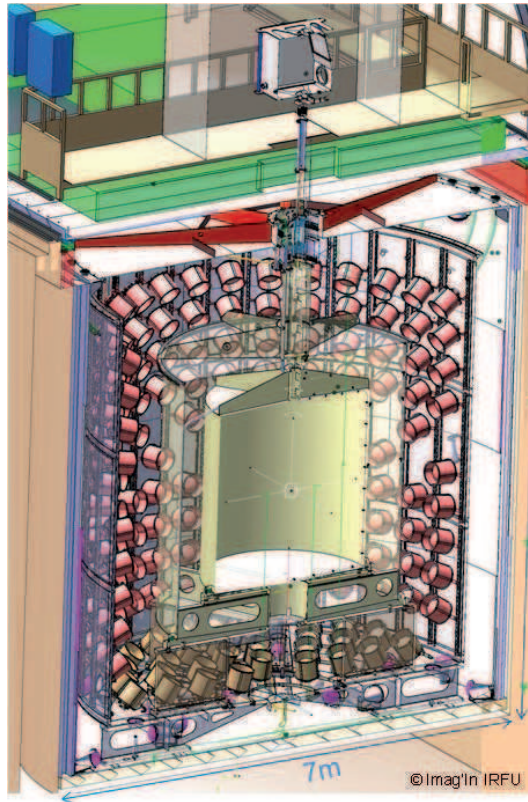


Fig. 2. – The Double Chooz detector design.

detectors—one close to the neutrino source (the near detector), the other one (the far detector) close to the location of maximal oscillation effect (c.f. fig. 1). All reactor-based Θ_{13} experiments follow these well-known and published ideas [8].

For Double Chooz in particular, the chosen detector design (see fig. 2) increases the target mass to 8 t while still using the original CHOOZ lab with its 300 m.w.e. overburden for the far detector, whereas a new tunnel and lab is being constructed at a distance of about 400 m to the reactor cores for the near detector. Table II summarizes near and far detector location properties.

4. – The Double Chooz detectors

The Double Chooz detectors consist of four concentric liquid-filled cylindrical volumes, with a total diameter and height of about 7 m, built into a pit in the rock floor of the laboratories.

The innermost volume is the target, filled with 10 m³ of Gd-doped PXE-based scintillator. The scintillator is contained in an acrylic tank, into which different calibration sources can be introduced by means of a fish line or an articulated arm. In this way, a clearly defined fiducial volume exists, which allows a reduction on the number of analysis cuts.

TABLE II. – *Double Chooz near and far detector location properties.*

	Near	Far
Distance to reactor cores (m)	400	1050
overburden (m.w.e.)	115	300
Neutrino rate (1/d)	500	50
Muon rate in inner veto (Hz)	250	20

Surrounding the target is the gamma catcher, another acrylics vessel containing doped PXE based scintillator with a light yield matched to that of the target scintillator. Its radius is 55 cm larger than the target, and fixed to it are guiding tubes through which calibration sources can be pulled. Its purpose is to make sure all gammas from n capture close to the target wall are fully contained within the scintillating volume.

The third volume is called the buffer volume. It is another 105 cm larger in radius compared to the gamma catcher, consists of stainless steel and is equipped with 390 10 inch Hamamatsu photomultipliers which are all tilted individually to face the detector center. It is filled with non-scintillating mineral oil, reducing the number of background events induced by impurities in the photocathode of the PMTs by separating them from the scintillating liquid itself. It also contains optical fibers and diffusors for LED and laser calibration.

The outermost volume is the inner veto, a 50 cm thick shell filled with LAB based scintillator and instrumented with 78 fully encapsulated 8 inch Hamamatsu PMTs with their own optical fiber plus LED calibration system. It will efficiently tag muons crossing the detector and allow for some monitoring of muon-induced fast neutrons that enter the detector from the surrounding rock.

A 17 cm thick steel shield surrounds the veto volume to suppress gammas from the rock.

Covering the whole top of the detector are four layers of plastic scintillator panels that constitute the outer veto. It will complement the muon detection efficiency of the inner veto, allow for greatly increased tracking capability and extend over the central chimney of the detector, closing this “hole” in the inner veto.

Substantial effort has gone into R&D to improve all aspects of the CHOOZ experiment. One main goal was to ensure target scintillator stability for the run time of the experiment, which is scheduled to be five years. The composition—developed by the Max Planck institute for nuclear physics in Heidelberg—has been shown by now to be stable over a period of 2.5 years, with no discernible degradation on the absorbance length of the liquid.

Other examples of Double Chooz R&D are the FADC modules used to digitize the PMT signals, which were developed in close collaboration of APC Paris and CAEN, or the dedicated muon simulation utilizing topological maps and geological information of the reactor site to faithfully recreate the muon spectrum at the detector locations [9].

5. – Backgrounds

Understanding background is absolutely mandatory for neutrino precision experiments aiming at below the percent level, due to the low event rate. For the delayed

coincidence signature of the neutrino event, one can distinguish two types of background events:

- Accidental background: In this case, two independent processes randomly happen to deposit the right amount of energy with the right delay between them. Contributions to this background come from radioactive impurities in detector components or the surrounding rock, as well as from secondaries induced by muons. Background reduction can be achieved by strict selection of high-purity materials only, good shielding and an efficient muon veto. The Double Chooz Monte Carlo simulations, which have been cross checked against the background data measured by CHOOZ, indicate an expected rate of about 12 accidental background events for the near detector and two for the far detector per day.
- Correlated background: These events occur if one single process induces both a fake positron and neutron signal, effectively mimicking the neutrino signal. One way this can happen is when a fast neutron created in the rock by a muon that just missed the detector reaches the target, where it first loses energy to recoil protons, which can look like a positron signal, and then is captured on Gd. Muons crossing the detector can also create spallation products like ${}^9\text{Li}$, which decay by beta and neutron emission. In principle, these crossing muons are all tagged by the muon veto, however the life time of these isotopes is of the order of 100 ms, which combined with muon rates of order of 100 Hz prohibits a hard vetoing of these events. To deal with this kind of background, one can either choose a deeper detector site, or trust to muon monitoring and detailed Monte Carlo modeling. Again, from the Double Chooz Geant 4 based Monte Carlo software, we expect about eight correlated background events for the near and two for the far detector per day.

6. – Status and time schedule

As of May 2010, the Double Chooz far detector closing and liquid filling is imminent. DAQ and data processing modules and supporting electronics are almost completely installed, and preparations for light tightness tests are ongoing. Fluid delivery and mixing is done in parallel, with the goal of gathering first detector data in late summer of this year.

The construction of the near detector laboratory is starting—the design is approved by EDF, it is fully funded and scheduled to be completed till the end of 2010, which would be followed by the near detector construction until the end of 2011 or the beginning of 2012.

7. – Systematics and sensitivity

Double Chooz will consist of two distinct phases—the first 1.5 years with far detector only data, and another 3.5 years of combined detector data. During the first phase, a systematic error of 2.7% is expected, as we do not profit from the two-detector setup. This will drop to 0.6% total systematic error once the near detector gathers data and many uncertainties cancel in the relative analysis (compare table III). Still, even with far detector only data, Double Chooz will reach a sensitivity limit of

$$\sin^2 2\Theta_{13} < 0.06$$

TABLE III. – *Double Chooz phases one and two systematics.*

Systematic errors	Absolute	Relative
Production cross section	1.9%	–
Reactor power	0.7%	–
Energy per fission	0.6%	–
Detector efficiency	1.5%	0.5%
Number of protons in target	0.8%	0.2%
Total	2.7%	0.6%

after 1.5 years, which will be improved by another factor of two to

$$\sin^2 2\Theta_{13} < 0.03$$

after a total runtime of five years, as is shown in fig. 3. In this way, the current limit on Θ_{13} can be improved by a factor of four.

8. – Conclusions

Double Chooz is one of several reactor antineutrino experiments currently under construction which aims at measuring the last undetermined neutrino mixing angle Θ_{13} . It utilizes improved detector design and a two-detector setup to reduce systematic uncertainties in order to lower the current limit on Θ_{13} by at least a factor of four to $\sin^2 2\Theta_{13} < 0.03$ during its five year run time. Determining Θ_{13} would allow beam experiments to probe CP violation on the leptonic sector in the form of the Dirac phase δ , which appears in the neutrino mixing matrix and is yet completely free. Double Chooz

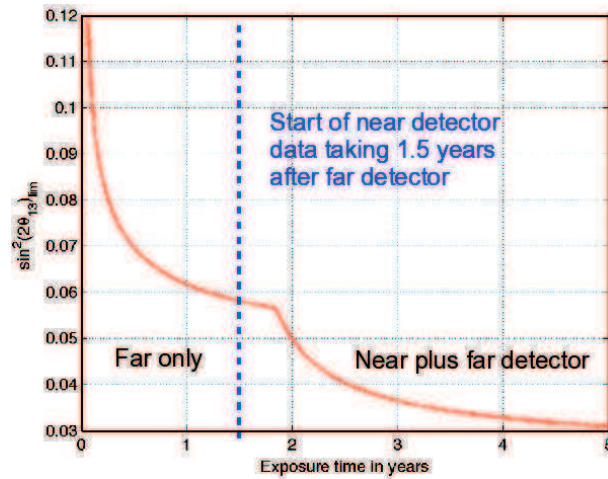


Fig. 3. – Sensitivity limit plot for Double Chooz at 90% CL.

will start data taking with the far detector during spring of 2011, and aims at starting its second, two detector phase at the end of 2011 or the beginning of 2012.

* * *

The author gratefully acknowledges the support of the Organizing Committee of the “XXIV Rencontres de Physique de La Vallée d’Aoste” and the Valle d’Aosta Government for his stay at the La Thuile 2010 conference.

REFERENCES

- [1] ARAKI T. *et al.* (KAMLAND COLLABORATION), *Phys. Rev. Lett.*, **94** (2005) 081801.
- [2] ASHIE Y. *et al.* (SUPER-KAMIOKANDE COLLABORATION), *Phys. Rev. Lett.*, **93** (2004) 101801.
- [3] AHN M. H. *et al.* (K2K COLLABORATION), *Phys. Rev. D*, **74** (2006) 072003.
- [4] MICHAEL D. G. *et al.* (MINOS COLLABORATION), *Phys. Rev. Lett.*, **97** (2006) 191801.
- [5] APOLLONIO M. *et al.* (CHOOZ COLLABORATION), *Phys. Lett. B*, **466** (1999) 415.
- [6] GONZALEZ-GARCIA M. C. *et al.*, *JHEP*, **4** (2010) 1.
- [7] GOODMAN M. *et al.*, *Double Chooz, A Search for the Neutrino Mixing Angle theta-13*, hep-ex/0606025v4 preprint (2006).
- [8] ANDERSON K. *et al.*, *A New Nuclear Reactor Neutrino Experiment to Measure theta 13*, hep-ex/0402041v1 preprint (2004).
- [9] TANG A. *et al.*, *Phys. Rev. D*, **74** (2006) 053007.

Recent results and future prospects for the MINOS experiment

JONATHAN M. PALEY for the MINOS COLLABORATION

Argonne National Laboratory - Argonne, IL, USA

(ricevuto il 14 Settembre 2010; pubblicato online l'11 Gennaio 2011)

Summary. — The MINOS experiment uses the intense NuMI beam created at Fermilab and two magnetized tracking calorimeters, one located at Fermilab and one located 735 km away at the Soudan Mine in Minnesota, to study lepton-flavor violation in the neutrino sector. We present results of the precise measurement of the atmospheric neutrino oscillation parameters, from the search for sterile neutrinos and from the search for the θ_{13} mixing angle by searching for ν_e appearance in the ν_μ beam. Future prospects for measurements by MINOS will also be discussed.

PACS 14.60.Pq – Neutrino mass and mixing.

PACS 14.60.St – Non-standard-model neutrinos, right-handed neutrinos, etc.

1. – The MINOS experiment

The Main Injector Neutrino Oscillation Search (MINOS) experiment was designed to primarily confirm the phenomenon of neutrino oscillations via a precise measurement of the atmospheric neutrino oscillation parameters Δm^2 and $\sin^2(2\theta)$. MINOS data are also used to search for sterile neutrinos and the yet-unobserved θ_{13} mixing angle via $\nu_\mu \rightarrow \nu_e$ oscillations. Furthermore, MINOS is capable of conducting tests of *CPT* and atmospheric neutrino and cosmic ray studies, however these analyses will not be covered in this presentation.

Neutrino oscillation measurements in MINOS primarily utilize the Neutrinos at the Main Injector (NuMI) beam at Fermi National Laboratory. NuMI is a very pure and intense beam of muon neutrinos aimed at an underground laboratory 735 km from the NuMI production target in Soudan, MN. A 5.4 kton magnetized iron tracking calorimeter (the Far Detector, FD) located at the Soudan laboratory is used to detect the neutrinos [1]. A functionally identical 0.98 kton Near Detector (ND) is located approximately 1 km downstream from the NuMI target. The neutrino energy spectrum is measured using both detectors. The shapes of the two energy spectra are compared and used to measure and constrain neutrino oscillation parameters.

In the analyses of MINOS data presented here, neutrino interactions in the MINOS detectors are characterized by an event energy and interaction type. There are three types of neutrino interactions of interest: ν_μ charged-current (CC), neutral-current (NC)

and ν_e CC events. CC events are characterized by having the corresponding lepton in the final state; furthermore, all of the incident neutrino energy is contained in the event. Therefore, ν_μ CC events are characterized by a long muon track with a shower at the vertex, whereas ν_e CC events are shorter and have an electromagnetic shower profile. NC events, on the other hand, are “flavor-blind” and the final state consists of a hadronic shower and a neutrino which carries away at least some of the energy of the incident neutrino; these events are short, but diffuse. Each analysis discussed here uses one of these types of events as the signal and the other events are backgrounds for the same analysis. The energy of the event is the sum of the reconstructed shower energy and the reconstructed energy of the muon (if one is found). Muon energies are determined from a combination of curvature and range; shower energies are determined from Monte Carlo (MC) simulations tuned to external data.

2. – Measurement of Δm^2 and $\sin^2 2\theta$

The determination of the atmospheric neutrino oscillation parameters Δm^2 and $\sin^2(2\theta)$ is accomplished by measuring the probability that a muon neutrino of energy E and traveling a distance L is observed in the muon neutrino weak eigenstate. This neutrino oscillation “survival probability” may be written as

$$(1) \quad P(\nu_\mu \rightarrow \nu_\mu) = 1 - \sin^2(2\theta) \sin^2 \left(1.27 \frac{\Delta m^2 L}{E} \right),$$

where $\theta \simeq \theta_{23}$, $\Delta m^2 \simeq \Delta m_{32}^2$ is in units of eV^2 , L is in km and E in GeV. A comparison of the measured muon neutrino energy spectra in the ND and FD yields the parameters $\sin^2(2\theta)$ and Δm^2 .

The dominant background to ν_μ CC events is NC events that are reconstructed as low-energy ν_μ CC interactions. NC events are separated from ν_μ CC events based on topological characteristics that indicate a muon in the final state: track length, mean pulse height, fluctuation in pulse height and transverse track profile. A CC/NC separation parameter cut is determined that maximizes the CC event selection efficiency and minimizes the NC background [2]. A comparison of the selection parameter distribution in the ND data and MC shows excellent agreement above the final CC/NC parameter cut.

The energy spectrum for ν_μ CC events is measured in the ND and extrapolated to the FD. The extrapolation is non-trivial because the neutrino events seen in the ND appear to be coming from a line source, whereas events in the FD appear to be coming from a point source. MC simulations are therefore used to determine energy smearing and acceptance corrections for the expected FD energy spectrum. The dominant systematic uncertainties in the predicted FD spectrum are a 4% normalization uncertainty, a 10.3% hadronic energy calibration uncertainty and a 50% uncertainty on the NC background that pass the CC cut selection criteria. The normalization and hadronic energy uncertainties primarily effect the measurement of Δm^2 at the level of $\pm 0.081 \times 10^{-3} \text{ eV}^2$ and $\pm 0.052 \times 10^{-3} \text{ eV}^2$, respectively. The NC background is the largest effect on the measurement of $\sin^2(2\theta)$ at the level of ± 0.016 .

Figure 1 shows the measured FD energy spectrum, the expected spectrum with no oscillations, the best oscillation fit to the data, and the NC background (significant only in the lowest energy bin). A total of 848 events are observed in the FD, with 1065 ± 60 events expected under the no-oscillation hypothesis for a data set based on 3.36×10^{20} protons

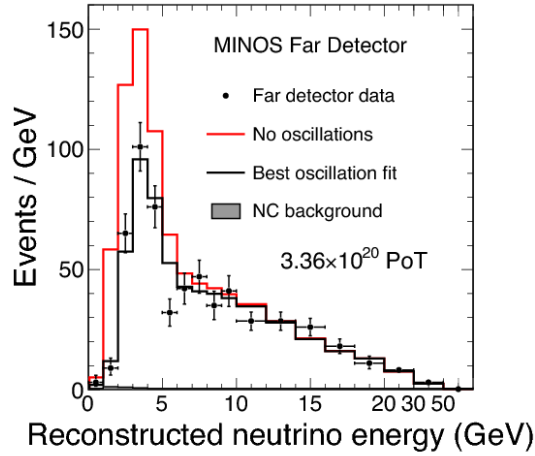


Fig. 1. – (Colour on-line) The Far Detector ν_μ energy spectrum determined from CC events. The data are shown as black points with error bars; the NC background is shown in shaded gray and is only significant in the first bin. The predicted spectrum for the no-oscillation hypothesis is shown in red. The black line represents the best-fit spectrum for the oscillation hypothesis.

on target (POT). Fitting the observed energy spectrum to the survival probability, and constraining the fit parameters to their physically meaningful values, we find $\Delta m^2 = 2.43 \pm 0.13 \times 10^{-3}$ and $\sin^2(2\theta) > 0.90$ (90% CL), with a $\chi^2/ndof = 90/97$. Figure 2 shows the oscillation parameter phase space allowed by the latest MINOS measurement, with comparisons to other experiments. MINOS has the most precise measurement of Δm^2 to-date. Alternative hypotheses of neutrino decay [3] and neutrino decoherence [4] have also been tested with the MINOS data, and these are disfavored with respect to the oscillation hypothesis by 3.7σ and 5.7σ , respectively.

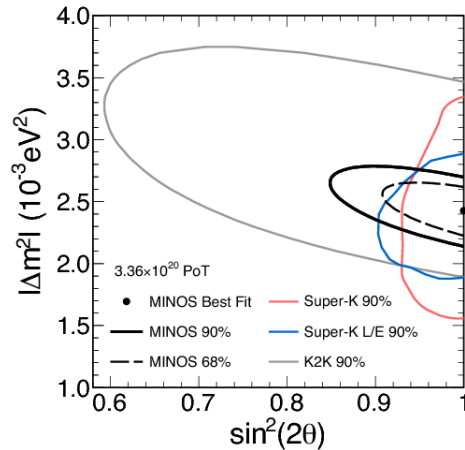


Fig. 2. – 68% and 90% contour lines for the oscillation fit parameters Δm^2 and $\sin^2(2\theta)$ compared to other experimental measurements.

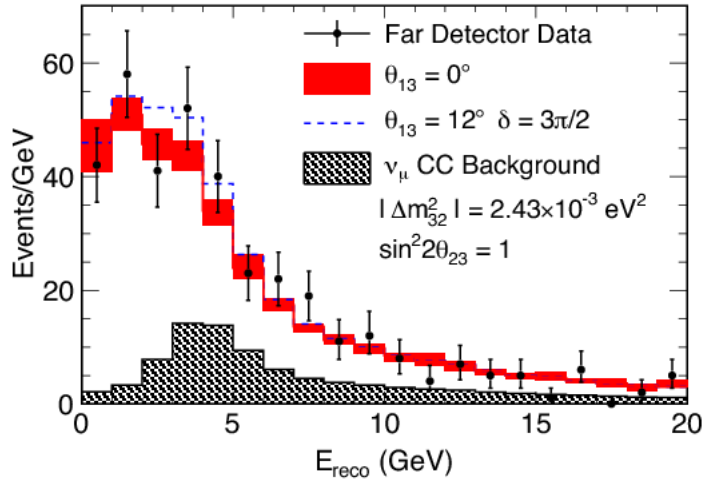


Fig. 3. – (Colour on-line) Visible energy spectrum of NC events in the FD. Data are shown in black points. The predicted spectrum obtained from the ND NC spectrum is shown in red for $\theta_{13} = 0$ (dashed blue for θ_{13} at the CHOOZ limit).

3. – The search for sterile neutrinos

Since the NC event rate is independent of neutrino flavor, and thus unaffected by oscillations between the three active neutrino flavor states, a deficit in the NC rate in the FD would indicate the existence of at least one additional neutrino that does not interact via the weak force (“sterile neutrino”, ν_s). The dominant background in this measurement are low-energy ν_μ CC events that do not have a clear muon track. NC events are selected and their visible energy determined from reconstructed “shower-like” events. The ND NC spectrum is extrapolated to the FD, and several sterile neutrino models are tested against these two spectra.

The quantity $f_s = (P_{\nu_\mu \rightarrow \nu_s}) / (1 - P_{\nu_\mu \rightarrow \nu_\mu})$ describes the fraction of ν_μ that have oscillated to ν_s in a simple four-flavor model where oscillations to sterile neutrinos occur at the same mass splitting as the ν_μ disappearance measured from the CC interactions. The search for sterile neutrinos using MINOS data is sensitive to two sterile neutrino models: the case where $m_4 = m_1$ and the case where $m_4 \gg m_3$.

Figure 3 shows the measured visible energy spectrum in the FD, based on 3.18×10^{20} POT, along with the expected spectra for $\theta_{13}=0$ (solid red) and θ_{13} at the CHOOZ limit [5] (dashed blue) and the predicted ν_μ CC event background (hashed black). In the case where $m_4 = m_1$ and $\theta_{13}=0$, the 90% CL limit on f_s is 0.51 (0.55 for $\theta_{13} = 12^\circ$). In the case where $m_4 \gg m_3$, the limit on f_s is 0.52 (0.55). A detailed description and results of the search for sterile neutrinos in MINOS may be found [6].

4. – The search for θ_{13} via $\nu_\mu \rightarrow \nu_e$

For the search of ν_e appearance in the MINOS detector we again make use of CC events; in this case, we are looking for an excess of events with an electron in the final state in the MINOS FD compared to the expected number from measurements in the MINOS ND. The MINOS detectors were optimized for muon identification in the final

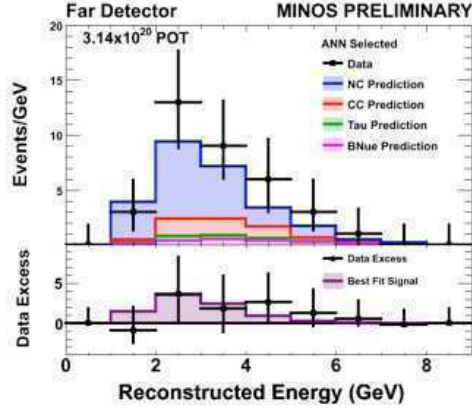


Fig. 4. – (Colour on-line) Top: the Far Detector ν_e energy spectrum determined from CC events. The data are shown as black points with error bars; backgrounds are shown as solid, colored histograms. Bottom: data—predicted background as a function of energy. The data excess is represented by the black points, the best fit to the signal is represented by the solid histogram.

state; therefore the search for electron-neutrino appearance in MINOS is very challenging because of the very large background of NC events (low-energy ν_μ CC events also contribute a non-negligible amount to the background). However as mentioned previously, ν_e CC events do differ topologically from NC events and are tagged by selecting events that have electromagnetic-like shower profiles. Using topological cuts and a neural-network to classify events, the signal-to-background ratio is reduced from 1:55 to 1:4.

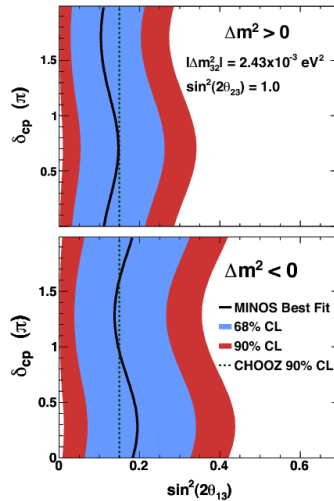


Fig. 5. – (Colour on-line) Best-fit value of $\sin^2(2\theta_{13})$ as a function of the CP -violating phase δ_{CP} . 68% and 90% contour lines for $\sin^2(2\theta_{13})$ are shown as solid red and blue lines. The CHOOZ limit is drawn as a dashed line for comparison.

The top of the left plot of fig. 4 shows the measured ν_e CC spectrum for an exposure of 3.14×10^{20} POT in the MINOS FD (solid black points) with the backgrounds overlaid. The dominant NC background is in blue, the ν_μ CC background in red, and τ and beam ν_e CC events are in green and magenta, respectively. The bottom of the left plot shows the amount of data excess (black points) as a function of energy, with the best fit for the $\nu_\mu \rightarrow \nu_e$ oscillation hypothesis plotted in solid purple. A total of 35 events are observed in the MINOS FD with a predicted background of $27 \pm 5(\text{stat}) \pm 2(\text{syst})$ events, which corresponds to a 1.5σ excess. The observed excess is comparable to the CHOOZ [5] limit for $|\Delta m^2| = 2.43 \times 10^{-3} \text{ eV}^2$ and $\sin^2(2\theta_{23}) = 1.0$. With these results, $\sin^2(2\theta_{13}) = 0$ is included at the 92% confidence level. The contours on the right of fig. 5 show the best-fit values of $\sin^2(2\theta_{13})$ as a function of the CP -violating phase δ_{CP} , with 68% (blue) and 90% (red) CL intervals for the normal (top) and inverted (bottom) hierarchies. Further details of this analysis may be found in [7].

5. – Future outlook

At the time of this conference, the MINOS Collaboration had completed and published analyses based on approximately 3×10^{20} POT exposure but had collected more than twice that amount of data ($\sim 7 \times 10^{20}$ POT). All analyses were being redone to incorporate not only the additional data, but also improvements in reconstruction, particle identification algorithms and background reductions. In some cases, the backgrounds have been reduced by a factor of two. MINOS expects to produce new results for all of these analyses in the summer of 2010 that will incorporate all of these improvements. Furthermore, MINOS has collected $\sim 1.5 \times 10^{20}$ POT of reverse-horn-current data; this configuration results in a $\bar{\nu}_\mu$ -dominated beam. These data will be analyzed and a measurement of the atmospheric oscillation parameters $\Delta \bar{m}^2$ and $\sin^2(2\bar{\theta})$ will be forthcoming from MINOS in the summer of 2010 with obviously limited statistics. MINOS plans to continue collecting data through 2011, but it is not clear yet under which beam configuration.

REFERENCES

- [1] MICHAEL D. G. *et al.*, *Nucl. Instrum. Methods A*, **596** (2008) 190.
- [2] ADAMSON P. *et al.*, *Phys. Rev. Lett.*, **101** (2008) 131802.
- [3] BARGET V. *et al.*, *Phys. Rev. Lett.*, **82** (1999) 2640.
- [4] FOGLI G. L. *et al.*, *Phys. Rev. D*, **67** (2003) 093006.
- [5] APOLLONIO M. *et al.*, *Eur. Phys. J. C*, **27** (2003) 331.
- [6] ADAMSON P. *et al.*, *Phys. Rev. D*, **81** (2010) 052004.
- [7] ADAMSON P. *et al.*, *Phys. Rev. Lett.*, **103** (2009) 261802.

SESSION III - QCD PHYSICS/HADRONIC INTERACTIONS

- Mike Lamont* Turning on the LHC: Commissioning with beam and the outlook for 2010
- Francesco Prino* Early physics with ALICE
- Simona Rolli* QCD results from the Fermilab Tevatron $p\bar{p}$ Collider
- Kai Yi* Heavy flavor spectroscopy at the Tevatron
- Marek Jacewicz* Low energy QCD and ChPT studies with KLOE
- Jiaxu Zuo* Recent results from BESIII

Turning on the LHC: Commissioning with beam and the outlook for 2010

M. LAMONT

CERN - Geneva, Switzerland

(ricevuto il 14 Settembre 2010; pubblicato online l'11 Gennaio 2011)

Summary. — After the September 19th 2008 incident and an intense year of recovery, consolidation and testing, LHC beam commissioning started again on the 23rd November 2009 and continued for three and a half weeks before the annual Christmas stop. A summary of the progress made and the performance of the individual accelerator systems is given. The potential performance of 2010 is discussed.

PACS 29.20.db – Storage rings and colliders.

1. – Introduction

The initial beam commissioning of the LHC saw remarkably rapid progress in the three and half weeks available in November to December 2009. The main commissioning goals were achieved. All key systems went through at least their initial commissioning phases. Collisions with stable beam conditions were established at 450 GeV, and the ramp to the maximum energy at the time of 1.18 TeV was successfully attempted. Most beam-based systems became operational and LHC operations managed to start to master the control of a hugely complex system.

During this period operation was very much in commissioning mode and this initial phase must be seen as part of a necessary learning process with a furious amount of problem resolution and debugging going on. Clearly routine operation will have to be a lot more rigorous and structured.

2. – Preparation

The initial commissioning phase benefited enormously from meticulous preparation. This included a full series of injection tests, extended dry runs of all accelerator systems both separated and combined, and full hardware commissioning of the cold magnet circuits. The curtailed commissioning with beam in 2008 was also very useful in identifying a number of issues that were resolved for the 2009 run.

TABLE I. – *LHC milestones 2009.*

Date	Milestone
20th November	Injection of both beams, rough RF capture
21st November	Circulating beam 1
22nd November	Circulating beam 2
23rd November	First pilot collisions at 450 GeV. First trial ramp
26th November	Pre-cycle established. Energy matching
29th November	Ramp to 1.08 TeV and then 1.18 TeV
14th December	Ramp 2 on 2 to 1.18 TeV—quiet beams—collisions in all four experiments
14th December	16 on 16 at 450 GeV—stable beams
16th December	Ramped 4 on 4 to 1.18 TeV—collisions in all four experiments

3. – Milestones

The main milestones of the 2009 beam commissioning period are outlined in table I. The commissioning process can be briefly summarized: 3 days for first observed collisions at 450 GeV; 9 days for first ramp to 1.18 TeV; 16 days to establish stable beams at 450 GeV; 18 days to take two beams to 1.18 GeV and observe first collisions at this record energy. A more detailed look at the main operational phases follows.

3.1. Injection. – The transfer and injection process from the SPS into the LHC is delicate and complex but operation was well established [1].

- The transfer lines were well optimized after a rigorous measurement campaign.
- Re-phasing of the beam in the SPS, synchronization between the machines and subsequent capture worked well with only some RF controls and procedural issues as negatives.
- Injection sequencing dealt with requirements of multiple injection schemes that covered multi-bunch injection, two beams, and collision scheduling.
- The routine conditioning of the injection kickers (the so-called kicker soft start) is now part of the standard process.
- The injection quality check (IQC) process was deployed, debugged, and became operational.
- The abort gap keeper which prevents injection of beam into the abort gap was commissioned.

A full program of beam-based checks was performed including: positioning of injection protection devices with respect to the beam, positioning of transfer line collimators, aperture checks, and kicker waveform checks [2]. A number of issues were identified, including a general issue with fast losses at injection and the BLM thresholds on shorter timescales. These will be addressed in 2010. Generally the performance at injection was good and clearly benefited from the experience gained during the injection tests. For the moment, however, one would worry about routinely injecting unsafe beam. It is to be

noted that the so-called quenchinos (resistive transitions detected by the quench protection system) were again observed with two accidental quenches caused by intensities as low as $2 \cdot 10^9$ protons.

3'2. 450 GeV. – A full set of instrumentation and associated hardware and software was commissioned and made more-or-less operational. Measurement and control of the key beam parameters (orbit, tune, chromaticity, coupling, dispersion) was routine. Besides this the beam loss monitor (BLM) system performed impeccably. Beam size was measured using the synchrotron light monitors and wire-scanners. Lifetime optimization was performed via adjustment of tune, chromaticity, and orbit.

Energy matching between the SPS and LHC was performed and revealed only small differences between the two beams. A full program of aperture checks was performed covering the arcs and insertions. The experiments solenoids were brought on without fuss and the coupling and orbit perturbations corrected. LHCb and Alices dipoles were brought on at 450 GeV. There are some issues with transfer functions of these dipoles and the associated compensators which are to be resolved.

Two-beam operation was established both with and without separation bumps. Optics checks were performed and the beta beating measured and first attempts at correction made. A full program of polarity checks of correctors and beam position monitors was executed with only a few errors being found [3]. The availability of hardware, instrumentation and software was very impressive reflecting good preparation, very fast problem resolution and the clear benefits of leveraging 21st century technology.

3'3. Collisions at 450 GeV. – Although successful, it is probably worth noting that the LHC was not designed to do collisions at 450 GeV [4]. Nonetheless a full program of machine protection, collimation, aperture and beam dump system checks allowed stable beams to be declared. This permitted the experiments to fully turn on their detectors and start an intense period of commissioning with beam themselves.

Multi-bunch and higher intensities were achieved with a maximum of 16 bunches and a total beam intensity of $1.85 \cdot 10^{11}$ being brought into collision. Luminosity scans were tested gently and successfully [5], and hundreds of thousands of events were collected by the experiments.

3'4. 8 kHz and the hump. – One clear issue at 450 GeV became apparent: the activity in the vertical tune spectrum and associated vertical emittance blow-up. Two main effects were noted: a clear excitation at 8 kHz and a modulated narrow-band excitation that was observed to move slowly around the tune spectrum, particularly in the vertical spectrum of beam two. The latter became known as the hump. The cause of the 8 kHz line was tracked down to the UPS, however the source of the hump is not understood and systematic investigations as to its source will be pursued in 2010 [6].

3'5. Aperture. – A systematic set of aperture measurements was performed in the arcs and insertion regions [7]. The beam clearance in general seems to be OK, and is above or equal to expectations. Some measured bottlenecks agree with model predictions using measured beta functions. However the aperture is out of budget due to beta beating even with the closed orbit reduced to the measured 3.2 mm peak. This implies that correction of beta beating is mandatory at 450 GeV.

3'6. Beta beating. – The availability of measurement and impressive analysis tools should be noted. The uncorrected, measured beating was good although outside the

accepted tolerance of $\approx 20\%$ [7]. Several potential sources of error were identified with possible candidates including the warm magnets in IR3 and IR7 (large corrections required). Potential, somewhat large, corrections also pointed to the triplets in IR2 and IR8. The correction strategy will need to be carefully considered.

The pre-cycling strategy of certain classes of magnets will be revisited for 2010 (*e.g.*, Q6 was not pre-cycled and should be) to avoid any potential errors arising from leaving magnets on the wrong branch of their hysteresis curves. In 2010 it will be important to correct the beating early on to avoid having to re-visit collimation and other optimization after any beating corrections.

3.7. Ramps. – A fully consistent set of machine settings was deployed at injection and for the ramp. These incorporated the output of the LHC magnet model (FIDEL) which consists of all main transfer functions, dipole harmonics, etc. For the RF system the necessary parameter space was in place including frequency and voltage control in the ramp.

Eight ramp attempts were made with notable success [8]. Reproducibility in the ramp looked very good enabling tune feed-forward to be deployed successfully. Tune feedback based on the continuous FFT mode of the BBQ tune system worked pretty much first time and was then used systematically during the ramp [6]. Real time acquisition of the closed orbit in the ramp was immediately available. The orbit clearly moves during the ramp but total deviations were small enough to allow good transmission. A feed-forward strategy is to be established. The bare tunes (*i.e.* those that would have been seen had no corrections been applied) were seen to swing considerably. The effect is bigger in the horizontal plane and for beam 2. The origin of the swing is not yet understood.

3.8. Squeeze. – One successful attempt was made to test the squeeze procedure in IR5 [9]. Although not exactly smooth in terms of procedure, the attempt managed the three planned steps: the shift to collision tunes; squeeze from 11 to 9 m.; squeeze from 9 to 7 m. Clearly there is some tidying up to do but to get this far on the first attempt was encouraging. The settings strategy worked and respected the need for smooth round off of power converter functions at the intermediate optics points. Single quadrant power converter limitations were taken into account. The ramp down of some insertion quadrupole in the squeeze defines the length of the process. Beta beating and dispersion measurements showed better agreement with the machine model at the intermediate points of the squeeze than at 450 GeV and the extrapolated values of β^* were closed to nominal.

4. – System commissioning

4.1. LHC Beam Dump System (LBDS). – There was a rigorous program of measurements and tests to qualify the LBDS with beam [10]. These included: beam based alignment of the protection devices in the vicinity of the beam dump; aperture scans; extraction tests; asynchronous beam dump tests with de-bunched beam. Commissioning of the various sub-systems also took place: *e.g.*, the beam energy tracking System (BETS), external post operation checks (XPOC), internal post operation checks (IPOC); interaction with the timing system, synchronization with RF and the abort gap. Inject and dump, and circulate and dump modes were successfully used operationally.

A number of issues were resolved but the performance of the LBDS was in general very good and experience thus far gives confidence in its ability to perform within its very tight specifications.

4.2. *Collimation system.* – The collimation system saw excellent initial beam based commissioning following careful preparation and tests [11]. The initial phase include a full program of beam based positioning during which the hierarchy was established. Encouragingly this appeared to be respected in planned and unplanned beam loss tests there afterwards, provided the orbit had been corrected to the reference. The collimation setup remained valid over six days, relying on orbit reproducibility and optics stability. TOTEM also saw the first operational tests of their Roman pots with beam.

4.3. *Machine Protection System.* – The machine protection system (MPS) is mission critical and will clearly be vitally important for LHC operation over the safe beam limit. In essence it comprises the beam interlock system (BIS) and the safe machine parameter system (SMP) [12]. The BIS relies on inputs from a large multitude of user. The SMP relies on services from other systems (*e.g.*, the timing system and the bunch current transformers).

Besides this the beam drives a subtle interplay of the LBDS, the collimation system and protection devices, which rely on a well-defined aperture, orbit and optics for guaranteed safe operation. The MPS itself worked as advertised, always pulling a beam abort when called upon to do so. There were some issues with the inputs into the SMP but the system failed safe. The first attempt to establish the LBDS, the orbit, and the collimation as safe for the given aperture and optics was successful at 450 GeV and tests with beam demonstrated that the system setup was effective. Guaranteeing this at all phases of operation has yet to be demonstrated.

4.4. *Beam instrumentation.* – In general performance was excellent. A brief summary of the performance of each system is given in table II.

4.5. *Magnet model.* – A long and thorough magnet measurement and analysis campaign [13] meant that the deployed settings produced a machine remarkable close to the untrimmed model. In terms of tune and momentum, remarkably small discrepancies between the model and the measure machine were observed. For example, the largest momentum offsets by sector seen were: -0.27 per mil in sector 56 for beam 1 and $+0.32$ per mil in sector 78 for beam 2.

The precycle was fully deployed with precycling prescriptions in place for nearly all circuits with only a handful still missing. The result was very good reproducibility. Some optimization of total length is still possible; it was taking over an hour for the full precycle. There were a number of trips of circuits during the process and its clear that the precycle stressed the Quench Protection System (QPS) and power converters.

4.6. *Power converters and radio frequency.* – Superb performance of the power converters was observed with excellent tracking between reference and measured and excellent tracking between the converters around the ring.

In general, there was good performance from the key RF systems: power, beam control, low level and diagnostics [14]. Establishing capture was fast and efficient, the frequency and voltage ramps passed on the first attempts. Cogging worked well with the interaction point being re-positioned to the satisfaction of the experiments. There were, however, a number of controls issues with the de-synchronization/re-synchronization process being particularly problem prone. These issues and others are being addressed.

TABLE II. – *Summary of beam instrumentation performance.*

System	Performance overview.
Beam Position Monitors	In general very good, FIFO mode as used as in the injection tests. Capture mode was commissioned enabling multi-turn acquisition and analysis.
Beam Loss Monitors	Excellent performance following full deployment during injection tests delivering a close to fully operational tool. Some issues with the secondary emission monitors; some thresholds to be adjusted.
Bunch Current Transformers	Along with lifetime measurement, the systems were commissioned and operational. Some calibration and controls issues.
Screens	Fully operational.
Wire scanners	Operational, calibrated and giving reasonable numbers.
Abort Gap Monitor	First tests were encouraging.
Synchrotron Light Monitor	Beam 2: undulator commissioned, operational at 450 GeV and 1.2 TeV. Beam 1: undulator not commissioned, operational at 1.2 TeV.
Tune FFT	BBQ used routinely from day one giving tune, coupling, and chromaticity. Used for tune feedback in the ramp. Tune kickers operational.
Tune PLL	Good progress, feedback to be tested, radial modulation tested.
Chromaticity	Measured using: standard delta RF frequency method; semi-automatic BBQ peak analysis; and radial modulation. Some effort required to ensure fast reliable method is available.

5. – 2010—commissioning continued

The main objectives of LHC operation in 2010 are itemized below.

- Beam commissioning continued with the main, final objective of this phase being colliding, safe, stable, squeezed beams.
- This will be followed by consolidation and routine pilot physics at the safe beam limit for an extended period with machine development periods as required.
- Increased intensity phase one and associated machine protection qualification. The aim is to establish secure and reproducible operation under these conditions. This phase will move the total beam intensity above the safe beam limit.
- Consolidation and routine physics, again for an extended period.
- Increased intensity phase two and associated machine protection qualification, etc.

TABLE III. – *Breakdown of 3.5 TeV beam commissioning plan.*

Phase	Days	Key objectives
Circulating beam	2	Essential checks
450 GeV commissioning	7	Injection, tune, chromaticity, coupling, orbit, collimators, LBDS, beam instrumentation
450 GeV optics checks	3	Beat beating, energy matching tuning
450 GeV two beams	1	Separation bumps as standard
450 GeV collisions	2	Experiments on at 450 GeV, stable beams
Ramp to 3.5 TeV	5	Commission essential machine protection, bring experiments' dipoles on in ramp, commission orbit and tune feedback
Pilot collisions un-squeezed	3	Stable beams
Commission squeeze	4	Orbit and tune, collimation, aperture, bumps, machine protection checks
Collisions squeezed	7	Stable beams up to the safe beam limit

An estimate of the time required for the above phases is shown in table III. Machine protection is clearly hypercritical once the safe beam limit is passed, as is fault-free operations and operational procedures. It could take some time to fully establish the latter.

The pre-requisites and detailed planning for increasing intensity in place will essentially cover: a full verification of aperture, orbit and optics; full verification of beam dump, protection devices, collimation, injection protection; guaranteed beam quality from injectors; a fully tested beam interlock system including transmission of safe machine parameters; fully tested hardware interlock systems; all required feedback systems operational and appropriate interlocks fully tested.

This list is not exhaustive. Resolution of all procedural, operation, controls, MPS, instrumentation, hardware issues must all have been addressed. It is clear that the above will not happen overnight and that a full and careful program of tests and checks is required. An extended operational running period at safe beam limit with all prerequisites in place should be pursued. This will allow confirmation that all operational procedures, controls, and instrumentation are fully and faultlessly functional.

6. – 2010 potential

A proposed staged increase in intensity to a total single beam energy of 2 MJ has recently been approved. The resultant luminosity and estimates for the integrated luminosity are given in [15]. The machine will be moving out of the commissioning phase, treading carefully as experience is gained with potentially dangerous beams. The main aims are to deliver around 100 pb^{-1} in 2010 and finish the year pushing $1 \cdot 10^{32} \text{ cm}^{-2} \text{ s}^{-1}$ in preparation for 2011's target of 1 fb^{-1} . The first 5 months of operations will hopefully deliver a final luminosity of $1 \cdot 10^{31} \text{ cm}^{-2} \text{ s}^{-1}$ —a useful and encouraging first stage deliverable. Given the proposed steps to 2 MJ and a conservative approach to intensity increase it is clear that the final steps to over $1 \cdot 10^{32} \text{ cm}^{-2} \text{ s}^{-1}$ may not be realized in 2010 and represent target for a mature, well-optimized, well-tested machine that one might hope to see in 2011.

7. – Conclusions

A lot of hard work over the years has enabled a truly impressive period of initial commissioning with beam. Given initial indications, the LHC is reproducible; is magnetically well understood; is optically in good shape. It is armed with a powerful set of instrumentation, software, and hardware systems. It is also clear there is still considerable detail to sort out before the machine becomes fully operational with unsafe beams. If things go well at the start of 2010, it will take about 4 weeks to establish stable, safe, squeezed beams at 3.5 TeV. Here the demand is for stable beams, allowing the detectors to turn on fully and continued their commissioning at higher energy. This will be followed by an extended running period at or around the safe beam limit to bed in machine protection and operations. Blocked machine development periods will be taken as required.

Intensity increases will be a judicious and stepwise process with the main aims for 2010 being around 100 pb^{-1} and to be pushing $1 \cdot 10^{32} \text{ cm}^{-2} \text{ s}^{-1}$ at the end of the year in preparation for a 2011 integrated luminosity target of around 1 fb^{-1} .

REFERENCES

- [1] MEDDAHI M., *LHC Injection and Transfer lines, Proceedings of the 2010 Evian workshop on LHC commissioning 19-20th January 2010*, CERN-ATS-2010-028.
- [2] BARTMANN W., *Injection and dump protection, Proceedings of the 2010 Evian workshop on LHC commissioning 19-20th January 2010*, CERN-ATS-2010-028.
- [3] FUCHSBERGER K., *Orbit system including feedback and stability, Proceedings of the 2010 Evian workshop on LHC commissioning 19-20th January 2010*, CERN-ATS-2010-028.
- [4] EVANS L., *Ppbar experience including beam-beam and intrabeam scattering, Proceedings of the 2010 Evian workshop on LHC commissioning 19-20th January 2010*, CERN-ATS-2010-028.
- [5] WHITE S., *Luminosity optimization, Proceedings of the 2010 Evian workshop on LHC commissioning 19-20th January 2010*, CERN-ATS-2010-028.
- [6] STEINHAGEN R. and GASIOR M., *Tune, chromaticity, feed-forward and feedback, Proceedings of the 2010 Evian workshop on LHC commissioning 19-20th January 2010*, CERN-ATS-2010-028.
- [7] THOMAS R., *LHC optical model and necessary corrections, Proceedings of the 2010 Evian workshop on LHC commissioning 19-20th January 2010*, CERN-ATS-2010-028.
- [8] VENTURINI W., *Ramp: experience and issues, Proceedings of the 2010 Evian workshop on LHC commissioning 19-20th January 2010*, CERN-ATS-2010-028.
- [9] REDAELLI S., *Squeeze: strategy and issues, Proceedings of the 2010 Evian workshop on LHC commissioning 19-20th January 2010*, CERN-ATS-2010-028.
- [10] UYTHOVEN J., *Beam Dump Systems and Abort Gap Cleaning, Proceedings of the 2010 Evian workshop on LHC commissioning 19-20th January 2010*, CERN-ATS-2010-028.
- [11] BRACCO C., *Collimators and beam cleaning: first results and future plans, Proceedings of the 2010 Evian workshop on LHC commissioning 19-20th January 2010*, CERN-ATS-2010-028.
- [12] TODD B., *BIS, BIC and SMP, Proceedings of the 2010 Evian workshop on LHC commissioning 19-20th January 2010*, CERN-ATS-2010-028.
- [13] TODESCO E., *Updated magnetic model for ramp and squeeze, Proceedings of the 2010 Evian workshop on LHC commissioning 19-20th January 2010*, CERN-ATS-2010-02.
- [14] BUTTERWORTH A., *RF - performance and operational issues, Proceedings of the 2010 Evian workshop on LHC commissioning 19-20th January 2010*, CERN-ATS-2010-028.
- [15] LAMONT M., *Luminosity estimates, Proceedings of the Chamonix 2010 Workshop on LHC Performance*, CERN-ATS-2010-026.

Early physics with ALICE

F. PRINO for the ALICE COLLABORATION

INFN, Sezione di Torino - Torino, Italy

(ricevuto il 14 Settembre 2010; pubblicato online l'11 Gennaio 2011)

Summary. — The ALICE experiment at the CERN Large Hadron Collider started its p-p data taking at the end of 2009. The availability of the first low luminosity collisions at $\sqrt{s} = 900$ GeV and $\sqrt{s} = 2.36$ TeV allowed to improve and extend the calibration and alignment procedures, started with cosmic rays in 2008. Together with the final commissioning of the detector with real data, the collected data sample of p-p collisions is presently being used to carry out the early physics studies, aimed at assessing the global characteristics of the interaction. In particular, results on the pseudorapidity density of primary charged particle in the central region are discussed here. They were obtained using the two innermost Silicon Pixel layers of the Inner Tracking System, which provided both the primary vertex position and the charged multiplicity, by matching the reconstructed points on the two layers.

PACS 13.85.-t – Hadron-induced high- and super-high-energy interactions.

PACS 29.40.Gx – Tracking and position-sensitive detectors.

1. – The ALICE experiment

ALICE [1] is a general-purpose detector for the study of p-p, p-A and heavy-ion collisions at the LHC [2]. The main physics goal of the experiment is to investigate the properties of strongly-interacting matter in the conditions of high temperature and energy density that are expected to be attained in Pb-Pb collisions at $\sqrt{s_{NN}} = 5.5$ TeV.

The main components of the ALICE detector are a central tracking and particle identification system, a forward muon spectrometer and a set of small detectors in the forward regions used for triggering and global event characterization purposes. The central barrel detectors cover the pseudorapidity range $-0.9 < \eta < 0.9$ and are embedded in the large L3 solenoidal magnet which provides a field of 0.5 T. The main tracking detector in the central rapidity region is a large Time Projection Chamber (TPC) with inner radius of about 85 cm and outer radius of about 250 cm and an overall length along the beam direction of 500 cm. Inside the TPC, a barrel-type silicon tracker called Inner Tracking System is mounted. Outside the TPC, three detectors dedicated to particle identification, namely a Transition Radiation Detector (TRD), a Time-of-Flight detector

(TOF) and a ring-imaging Cherenkov detector (HMPID) are installed together with two electromagnetic calorimeters (PHOS and ECal).

The Inner Tracking System (ITS) is the central barrel detector located closest to the beam axis and is composed of six cylindrical layers of silicon detectors with radii between 3.9 cm and 43.0 cm. The two innermost layers are equipped with Silicon Pixel Detectors (SPD), the two intermediate layers are made of Silicon Drift Detectors (SDD), while Silicon Strip Detectors (SSD) are mounted on the two outermost layers. The main task of the ITS is to provide precise track and vertex reconstruction close to the interaction point, improving the spatial, angular and momentum resolution for tracks reconstructed in the TPC. Moreover, it allows to recover particles that are missed by the TPC (due to either dead regions or low-momentum cut-off), to reconstruct the interaction vertex with a resolution better than $100\ \mu\text{m}$ and to identify the secondary vertices from the decay of hyperons and heavy flavoured hadrons [2]. In addition to that, the track segments (tracklets) built in the two pixel layers provide the initial estimate of the interaction vertex position, prior to full track reconstruction, and a measurement of the charged particle multiplicity in the pseudorapidity range covered by the SPD layers.

Among the forward detectors, the VZERO has an important role in the early physics analyses described here. It consists of two arrays of 32 scintillators each, which are placed around the beam pipe on either side of the interaction region. The two arrays cover the pseudorapidity ranges $2.8 < \eta < 5.1$ and $-3.7 < \eta < -1.7$, respectively. They record the arrival times of particles at the detector in a time window of $\pm 25\ \text{ns}$ around the nominal beam crossing time.

2. – Detector commissioning

All the installed ALICE detectors have been extensively commissioned, calibrated and used for data taking during the two long cosmic ray runs collected in summer 2008 and summer 2009 [3-6]. A large number of sub-detector specific calibration runs have also been collected in these periods to monitor the stability of the detector performance during various months of continuous operation. Data were also taken during various LHC injection tests to perform timing measurements and other calibrations.

2.1. ITS. – The cosmic rays triggered by the SPD allowed to obtain an initial alignment of the parts of the detector that had sufficient exposure to the mostly vertical cosmic ray flux [7]. This has been obtained by applying track-based alignment methods (namely the Millepede II [8] and an iterative local method) starting from the information of the geometrical survey measurements performed (for SDD and SSD) during the construction phase.

In particular, the SPD layers of the ITS, which are the main detectors used for multiplicity measurement, were aligned using cosmic-ray tracks [7]; the residual misalignment was estimated to be below $10\ \mu\text{m}$ for the modules well covered by mostly vertical tracks. This estimate has been extracted from different observables sensitive to the alignment quality. As an example, in fig. 1 (left) the distance in the bending plane between points attached to the same track in the region where there is an acceptance overlap between two modules of the same layer is displayed, before and after the Millepede alignment. The spread of the distribution after re-alignment is $\sigma \approx 18\ \mu\text{m}$, to be compared to $\sigma \approx 15\ \mu\text{m}$ obtained in simulations with ideal geometry.

For SSD, the geometrical survey already provided a very precise alignment, as can be seen in fig. 1 (right) which shows the distribution of the $r\varphi$ residuals between tracks

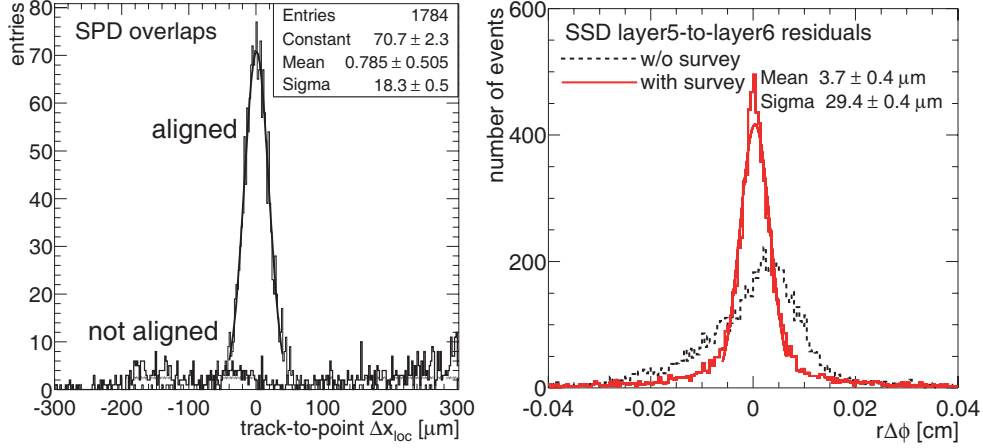


Fig. 1. – Left: track-to-point residuals in the bending plane for SPD double points in acceptance overlaps before and after alignment. Right: distribution of the $r\varphi$ residuals between straight-line tracks defined from two points on SSD layer 6 and the corresponding points on SSD layer 5, with and without applying geometrical information from the survey.

through layer 6 (built from the two points in the top and bottom halves of the barrel) and points on layer 5, before and after applying the geometrical information extracted from the survey. This analysis allowed to estimate the residual misalignment after the survey to be at the level of 5–20 μm (for modules and assemblies of modules, respectively). For this reason, track-based alignment methods were used only to align the whole SPD barrel with respect to the SSD barrel and to optimize the positioning of large sets of SSD modules, namely the upper and lower halves of layers 5 and 6. On top of this, cosmic-ray data was used for SSD gain calibration, allowing in particular to refine the relative calibration of the P and N sides. This charge matching is a strong point of double-sided silicon sensors and helps to remove fake clusters.

The alignment of the SDD is challenged by the interplay with time zero (*i.e.* the measured drift time for particles with zero drift distance) and drift speed calibration. During the cosmic run, it was possible to have a frequent monitoring of the drift speed in many different positions on each of the 260 detector modules, using the MOS charge injectors integrated on the detector surface [5]. This allowed to tune the drift speed calibration procedure and to study the drift speed stability on a long time scale. The cosmic ray tracks allowed to develop the methods to extract the time-zero and the drift speed (for modules with mal-functioning injectors) from track-to-point residuals. However, cosmic tracks are not the ideal sample for this purpose because of the jitter between the time when the muon crosses the detectors and the trigger signal. Hence, the SDD alignment is currently being extracted from p-p data. Cosmic rays were also used to tune the absolute calibration of the dE/dx signal and to test the linear correction for the dependence of the reconstructed charge on the drift time due to the combined effect of charge diffusion and zero suppression [9].

2.2. TPC. – Calibration and commissioning of the ALICE TPC relied, before the availability of any collisions from the LHC, on three different methods: a set of UV

laser beams was used to characterize field distortions and to determine the magnitude of the correction from $E \times B$ effects on the drifting electrons originating from the residual non-parallelism of the electric and magnetic field inside the drift volume. Furthermore, radioactive krypton was inserted through the gas system into the detector to provide efficient and precise amplitude calibration of all 557568 readout channels. Finally, extensive measurements with cosmic rays were performed to determine tracking efficiencies, energy loss, and momentum resolution of the detector. Detailed results can be found in [6].

3. – Early physics analyses

The primary goal of the early physics analyses performed on p-p data collected by the ALICE experiment in the new energy regime attained at the LHC is the measurement of the global characteristics of the collisions, which are dominated by soft (*i.e.* small-momentum-transfer) processes. These observables are useful to study QCD in the non-perturbative regime, to constrain phenomenological models and event generators and to understand the backgrounds for measurements of hard and rare interactions.

3.1. Charged-particle pseudorapidity density. – The pseudorapidity density of charged primary particles has been estimated from the “tracklets” reconstructed by correlating hits in the two silicon-pixel layers. A first analysis has been performed on the very first sample of 284 proton-proton collisions collected on 23rd November 2009, at a centre-of-mass energy $\sqrt{s} = 900$ GeV, during the commissioning of the accelerator [10]. The analysis has then been repeated on larger statistics and with improved trigger selection on a sample of about 150000 interactions at 900 GeV as well as on about 40000 collisions at 2.36 TeV [11].

The event sample was collected with the ALICE Minimum-Bias (MB) trigger based on SPD and VZERO information. At 900 GeV, the MB trigger required a hit in either one of the VZERO counters or in the SPD detector; *i.e.* essentially at least one charged particle anywhere in the 8 units of pseudorapidity covered by these trigger detectors. At the higher energy, the trigger required at least one hit in the SPD detector ($|\eta| < 2$), since the VZERO was not available. The events were collected in coincidence with the signals from two beam pick-up counters (BPTX), one on each side of the interaction region, indicating the presence of passing bunches.

Events which pass some background rejection criteria and which have a reconstructed interaction vertex are selected for the analysis. The pile-up probability is negligible at the typical bunch intensities (5×10^9 protons) of the data-taking period considered here. Beam-gas and beam-halo background events were removed by a cut on the ratio between the number of tracklets and the total number of hits in the ITS. For the 900 GeV data, also VZERO counters were used for background rejection by requiring their timing signals to be compatible with particles produced in collision events. In addition, for 900 GeV data, MB events in coincidence with only one passing bunch, as well as when no bunch was passing through the detector, were also registered. These control triggers were used to measure the beam-induced and accidental backgrounds. The position of the interaction vertex is reconstructed [12] by correlating hits in the two SPD layers. The achieved resolution depends on the track multiplicity and is approximately 100–300 μm in the longitudinal direction and 200–500 μm in the transverse direction. For events with only one charged track, the vertex position is determined by intersecting the SPD tracklet with the mean beam axis determined from the vertex positions of other events in the sample. A vertex was reconstructed in 94% of the selected events. The vertex reconstruction

efficiency decreases for collisions occurring far from the centre of the detector (*i.e.* large $|z|$ values), due to the reduced acceptance of the SPD detector for largely displaced interaction vertices. Therefore, only events with vertices within $|z| < 10$ cm were used. This allows for an accurate charged-particle density measurement in the pseudorapidity range $|\eta| < 1.6$ using both SPD layers.

The number of primary charged particles is estimated by counting the number of tracklets built by matching pairs of hits in the two SPD layers using the reconstructed vertex as the origin. The matching is based on a selection on the sum of the squares of the differences in azimuthal ($\Delta\varphi$, bending plane) and polar ($\Delta\theta$, non-bending direction) angles [13]. When more than one hit in a layer matches a hit in the other layer, only the hit combination with the smallest angular difference is used. This occurs in only 2% of the matched hits. The measured number of tracklets is corrected for geometrical acceptance, detector and reconstruction inefficiencies, combinatorial background caused by an accidental association of hits in the two SPD layers, contamination by decay products of long-lived particles (K_s^0 , Λ , etc.), gamma conversions and secondary interactions.

The total number of collisions used for the normalization was calculated from the number of events selected for the analysis which contains three different classes of inelastic interactions, *i.e.* collisions where new particles are produced: non-diffractive (ND), single-diffractive (SD), and double-diffractive (DD). Experimentally we cannot distinguish among these classes, which, however, are selected by the MB trigger with different efficiencies. In order to compare our data with those of other experiments, the resulting multiplicities are given with two different normalizations: the first one (INEL) corresponds to the sum of all inelastic interactions, and corrects the trigger bias individually for all event classes, by weighting them, each with its own estimated trigger efficiency and abundance. The second normalization (non-single-diffractive or NSD) applies this correction for non-diffractive and double-diffractive processes only, while removing, on average, the single-diffractive contribution. The normalization for INEL and NSD events was obtained by correcting the number of selected events for the trigger and the vertex-reconstruction efficiencies.

For the first analysis on the very first data sample, these efficiencies have been extracted from Monte Carlo simulations separately for ND, SD and DD processes and weighted with their measured cross-sections. In addition, for NSD events, the single-diffractive contribution has been subtracted. The resulting charged-particle density as a function of pseudorapidity is shown in fig. 2 (left) together $p\bar{p}$ data from the UA5 experiment [14].

In the analysis performed successively on larger statistics, two different event samples were used for the measurement of INEL and NSD multiplicities at 900 GeV. For the INEL analysis, events fulfilling a trigger condition requiring logical OR between the signals from the SPD and VZERO detectors were used. For the NSD analysis, a subset of the total sample was selected by requiring a coincidence between the two sides of the VZERO detectors (*i.e.* the detection of at least one charged particle in both the forward and backward hemispheres, separated by 4.5 units of pseudorapidity). In this subset, single-diffraction events are suppressed, therefore, model-dependent corrections and associated systematic errors are reduced. With these selections, the resulting total systematic uncertainty on the pseudorapidity density measurement at 900 GeV is smaller than 2.5% for INEL collisions and is about 3.3% for NSD collisions [11]. The resulting charged-particle density as a function of pseudorapidity obtained for INEL and NSD interactions at a centre-of-mass energy $\sqrt{s} = 900$ GeV compared to $p\bar{p}$ data from the UA5 experiment [14], and to pp NSD data from the CMS experiment [15] is shown in fig. 2 (right).

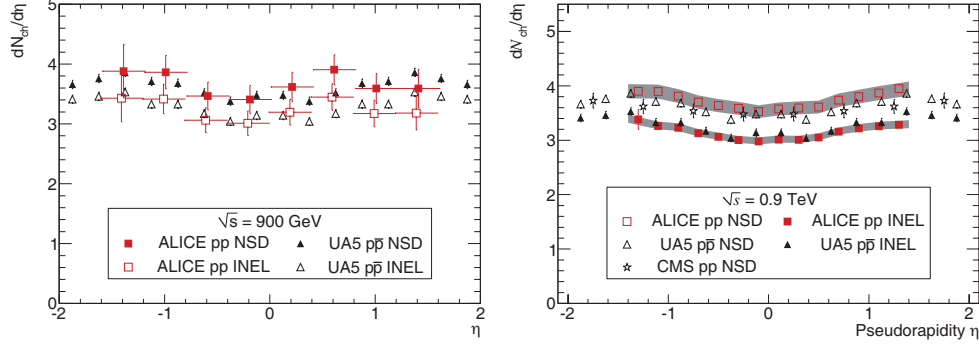


Fig. 2. – Measured $dN_{\text{ch}}/d\eta$ of at $\sqrt{s} = 900$ GeV for INEL and NSD collisions from the very first data samples of 284 p-p collisions (left) and from a larger data sample (right).

The same analysis has been repeated on the sample of collisions collected at $\sqrt{s} = 2.36$ TeV. Figure 3 shows the centre-of-mass energy dependence of the pseudorapidity density in the central region. The measured charged particle density at the higher energy is consistent with the CMS result for NSD collisions. The observed relative increase in multiplicity between the two energies ($22.6 \pm 0.7 \pm 1.0\%$) results to be substantially larger than the one predicted by PYTHIA (tested with three different tunes) and PHOJET models [11].

3.2. Other ongoing analyses. – The statistics collected from the first data sample of proton-proton collisions at the LHC is presently being used in many other analyses aimed at studying the global characteristics of collisions at $\sqrt{s} = 900$ GeV. Multiplicity distributions have been measured [11]. The proton-to-anti-proton ratio has been measured with high precision and found to be very close to unity, as expected in the standard picture of baryon transport at this energy. In addition, p_T spectra of charge hadrons have been reconstructed up to 10 GeV/ c and compared with previous Sp̄S measurements and

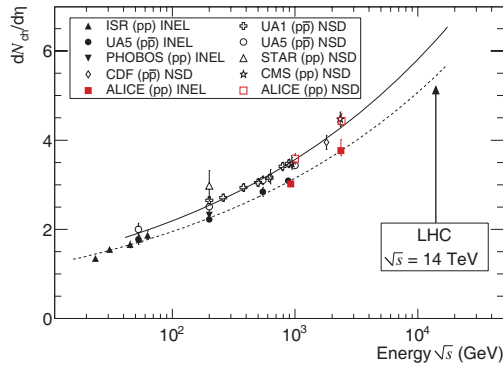


Fig. 3. – Charged-particle pseudorapidity density in the central rapidity region in proton-proton and proton-antiproton interactions as a function of the centre-of-mass energy. The dashed and solid lines (for INEL and NSD interactions, respectively) show a fit with a power-law dependence on energy.

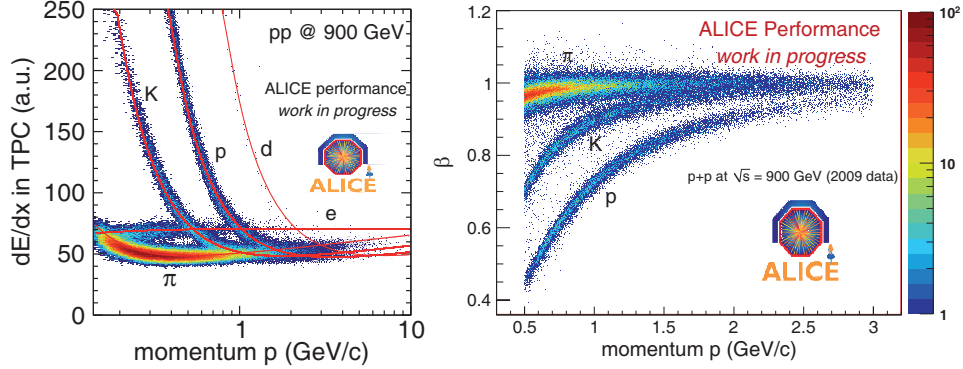


Fig. 4. – Particle identification performance in p-p 2009 data sample. Left: measured energy-deposit of charged particles *vs.* their momentum in the TPC. The lines correspond to the ALEPH parameterization of the Bethe-Bloch curve. Right: dependence of the particle velocity measured by TOF on the particle momentum.

also with CMS results [15]. This allows also to study the increase of average p_T as a function of event multiplicity. Transverse momentum spectra are being reconstructed also for identified hadrons (π , K and p) in an extended p_T range by exploiting the particle identification capabilities provided by the dE/dx measurement in the TPC, the TOF information for high-momentum particles and by the ITS stand-alone tracks in the low- p_T region (*i.e.* below 200 MeV/c). The particle identification performance is illustrated in fig. 4 for the TPC (measured dE/dx as a function of momentum) and TOF (measured particle velocity as a function of momentum) detectors. Strangeness production is also being measured from topological reconstruction of K_s^0 , Λ and Ξ decays.

4. – Conclusions

The first samples of proton-proton collisions at the LHC at $\sqrt{s} = 900$ GeV and 2.36 TeV allowed to perform high-precision measurements of the global characteristics of the collision with the ALICE detector. In particular, the pseudorapidity density of charged primary particles showed a larger-than-expected enhancement of multiplicity when increasing the center-of-mass energy from $\sqrt{s} = 900$ GeV to 2.36 TeV.

REFERENCES

- [1] ALICE COLLABORATION, *JINST*, **3** (2008) S08002.
- [2] ALICE COLLABORATION, *J. Phys. G: Nucl. Part. Phys.*, **32** (2006) 1295.
- [3] KULJER P. G. for the ALICE COLLABORATION, *Nucl. Phys. A*, **830** (2009) 81C.
- [4] SANTORO R. *et al.*, *JINST*, **4** (2009) P03023.
- [5] ALESSANDRO B. *et al.*, *JINST*, **5** (2010) P04004.
- [6] ALME J. *et al.*, arXiv:1001.1950 (2010).
- [7] ALICE COLLABORATION, *JINST*, **5** (2010) P03003.
- [8] BLOBEL V., *Nucl. Instrum. Methods A*, **566** (2006) 5.
- [9] ALESSANDRO B. *et al.*, *JINST*, **5** (2010) P02008.

- [10] AAMODT K. *et al.* (ALICE COLLABORATION), *Eur. Phys. J. C*, **65** (2010) 111.
- [11] AAMODT K. *et al.* (ALICE COLLABORATION), arXiv:1004.3034 (2010).
- [12] BRUNA E. *et al.*, ALICE Internal Note ALICE-INT-2009-018 (2009).
- [13] ELIA D. *et al.*, ALICE Internal Note ALICE-INT-2009-021 (2009).
- [14] ALNER G. J. *et al.* (UA5 COLLABORATION), *Z. Phys. C*, **33** (1986) 1.
- [15] CMS COLLABORATION, *JHEP*, **02** (2010) 041.

QCD results from the Fermilab Tevatron $p\bar{p}$ Collider

S. ROLLI

Tufts University - 4 Colby St, Medford, MA 02155, USA

(ricevuto il 14 Settembre 2010; pubblicato online il 5 Gennaio 2011)

Summary. — Several selected quantum chromodynamics (QCD) measurements performed at the Fermilab Tevatron by the CDF and D0 Collaborations, using proton-antiproton collisions at a centre-of-mass energy of $\sqrt{s} = 1.96$ TeV are reviewed. We will summarize the status of inclusive jet and dijet production cross-section measurements, which can be used to extract a precise value of the strong coupling constant and to search for physics beyond the Standard Model. We will then review results from the inclusive photon production cross-section measurement, as well as the associated production of photon with a light or heavy flavors jet. Finally we will describe various measurements concerning the production of vector bosons and jets.

PACS 14.80.Bn – Standard-model Higgs bosons.

1. – Introduction

Quantum chromodynamics (QCD), the theory of the strong interaction between quarks and gluons, is intrinsic to experimental studies of hadron collisions. This paper reviews several recent QCD results from the CDF and D0 experiments in analyses of $\sqrt{s} = 1.96$ TeV $p\bar{p}$ collisions. The general approach has been to test QCD theory, search for new physics phenomena, and enable electroweak and exotic measurements by informing Monte Carlo (MC) background models, while laying the groundwork for the LHC era of pp collisions.

2. – Inclusive jet production

The measurement of the differential inclusive jet cross section at the Fermilab Tevatron probes the highest momentum transfers in particle collisions currently attainable in any accelerator equipment, and thus is potentially sensitive to new physics such as quark substructure. The measurement also provides a direct test of predictions of perturbative quantum chromodynamics (pQCD). The inclusive jet cross section measurements at Tevatron Run II [1-4] cover up to 600 GeV/ c in jet transverse momentum p_T , and range over more than eight orders of magnitude in cross section. Comparisons of the measured

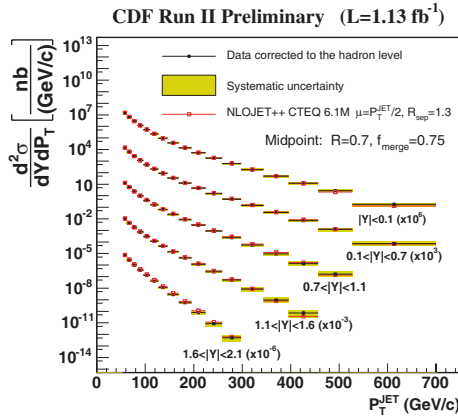


Fig. 1. – Inclusive jet cross section measured by CDF at the hadron level using the Midpoint algorithm in five rapidity regions compared with NLO pQCD predictions based on the CTEQ6.1M PDF. The cross sections for five rapidity regions are scaled by a factor of 10^3 from each other for presentation purposes.

cross section with pQCD predictions provide constraints on the parton distribution function (PDF) of the (anti)proton, in particular at high momentum fraction x ($x > 0.3$) where the gluon distribution is poorly constrained [5]. Further constraints on the gluon distribution at high x will contribute to reduced uncertainties on theoretical predictions of many interesting physics processes both for experiments at the Tevatron and for future experiments at the Large Hadron Collider (LHC). One example is $t\bar{t}$ production at the Tevatron for which the dominant PDF uncertainty arises from the uncertainty in the high- x gluon distribution. In addition, searches for new physics beyond the standard model at high p_T such as quark substructure require precise knowledge of PDFs at high x .

Both CDF [6] and D0 [7] measure the differential jet cross section using, respectively, 1.13fb^{-1} and 0.70fb^{-1} of data. Their measurements are in very good agreement with NLO predictions as can be seen in fig. 1 and fig. 2. The experimental precision now exceeds that of the PDF uncertainty, so that such measurements can be used, for the first time, to inform the PDF global fits.

3. – (α_s) measurement

Asymptotic freedom, the fact that the strong force between quarks and gluons keeps getting weaker when it is probed at increasingly small distances, is a remarkable property of quantum chromodynamics. This property is reflected by the renormalization group equation (RGE) prediction for the dependence of the strong coupling constant α_s on the renormalization scale μ_r and therefore on the momentum transfer. Experimental tests of asymptotic freedom require precise determinations of $\alpha_s(r)$ over a large range of momentum transfer. Frequently, α_s has been determined using production rates of hadronic jets in either e^+e^- annihilation or in deep-inelastic ep scattering (DIS). So far there exists only a single α_s result from inclusive jet production in hadron-hadron collisions. The CDF Collaboration determined α_s from the inclusive jet cross section in $p\bar{p}$ collisions at $\sqrt{s} = 1.8\text{TeV}$ obtaining

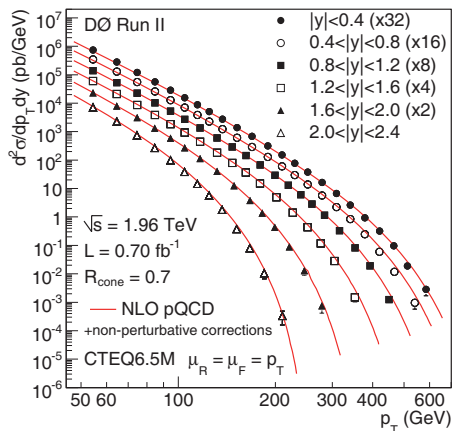


Fig. 2. – The inclusive jet cross section as a function of jet p_T in six $|y|$ bins, as measured by the D0 experiment. The data points are multiplied by 2, 4, 8, 16, and 32 for the bins $1.6 < |y| < 2.0$, $1.2 < |y| < 1.6$, $0.8 < |y| < 1.2$, $0.4 < |y| < 0.8$, and $|y| < 0.4$, respectively.

$\alpha_s(M_Z) = 0.1178 + 0.0081 \pm 0.0095$ (exp.) $+ 0.0071 \pm 0.0047$ (scale) ± 0.0059 (PDF) [8]. The D0 Collaboration has recently determined α_s and its dependence on the momentum transfer using the published measurement of the inclusive jet cross section with the D0 detector at the Fermilab Tevatron Collider in $p\bar{p}$ collisions at $\sqrt{s} = 1.96$ TeV [9]. The measurement used the p_T dependence of the jet cross section and is obtained by minimizing a χ^2 between data and theory (NLO plus two-loop thresholds corrections), where 22 points out of 110 from the jet inclusive cross section are used in the p_T range 50–145, and excluding high- p_T points to minimize PDF uncertainty correlations. A combined fit to all 22 data points yields $\alpha_s(M_Z) = 0.1161 + 0.0041 - 0.0048$ with $\chi^2/\text{ndf} = 17.2/21$. The $\alpha_s(p_T)$ results support the energy dependence predicted by the renormalization group equation. This is the most precise α_s result obtained at a hadron collider.

4. – dijet production

Within the standard model (SM), two-jet (dijet) events are produced in proton-antiproton collisions predominantly from hard quantum chromodynamics (QCD) interactions of two partons. The fragmentation and hadronization of the outgoing partons produce hadronic jets. The dijet mass spectrum predicted by QCD falls smoothly and steeply with increasing dijet mass. Many extensions of the SM predict the existence of new massive particles that decay into two energetic partons (quarks, q , or gluons, g), which can potentially be observed as a narrow resonance in the dijet mass spectrum. Such particles include excited quarks, axigluon, flavor-universal coloron, color-octet techni- ρ , Randall-Sundrum (RS) graviton, W' , Z' and diquark in the string-inspired E6 model. CDF [10] and D0 [11] are both measuring the dijet mass distribution.

In the CDF result, the measured dijet mass spectrum is compared to the next-to-leading-order perturbative QCD (NLO pQCD) predictions from fastNLO [12]. The predictions were obtained using the CTEQ6.1 PDFs with the renormalization and factorization scales both set to μ_0 , the average p_T of the leading two jets. The data and theoretical predictions are found to be in good agreement. CDF then searches for narrow mass res-

onances in the measured dijet mass spectrum by fitting the measured spectrum to a smooth functional form and by looking for data points that show significant excess from the fit. No evidence for the existence of a resonant structure is found and limits on new particle production (W' , Z' , RS graviton, excited quarks) are set (see ref. [10]).

5. – Limits on new physics from dijets measurements

The angular distribution of dijets with respect to the hadron beam direction is directly sensitive to the dynamics of the underlying reaction. While in quantum chromodynamics (QCD) this distribution shows small but noticeable deviations from Rutherford scattering, an excess at large angles from the beam axis would be a sign of new physics processes not included in the SM, such as substructure of quarks (*quark compositeness*), or the existence of additional compactified spatial dimensions (*extra dimensions*). D0 performs a measurement of the variable $\chi_{\text{dijets}} = \exp[|y_1 - y_2|]$ in ten regions of dijet invariant mass M_{jj} , where y_1 and y_2 are the rapidities of the two jets with highest transverse momentum p_T with respect to the beam axis in an event. For massless $2 \rightarrow 2$ scattering, the variable χ_{dijet} is related to the polar scattering angle θ^* in the partonic center-of-mass frame. The choice of this variable is motivated by the fact that Rutherford scattering is independent of χ_{dijet} , while new physics shows an enhancement at low values of the variable. This is the first measurement of angular distributions of a hard partonic scattering process at energies above 1 TeV in collider-based high energy physics. The normalized χ dijet distributions are well described by theory calculations in next-to-leading order in the strong coupling constant and are used to set limits on quark compositeness, ADD large extra dimensions, and TeV^{-1} extra dimensions models. For the TeV^{-1} extra dimensions model this is the first direct search at a collider. For all models considered, this analysis sets the most stringent direct limits to date (see table in ref. [13]).

6. – Inclusive photon production

Photons originating in the hard interaction between two partons are typically produced in hadron collisions via quark-gluon Compton scattering or quark-anti-quark annihilation. Studies of these direct photons with large transverse momenta, p_T , provide precision tests of perturbative QCD (pQCD) as well as information on the distribution of partons within protons, particularly the gluon. These data were used in global fits of parton distributions functions (PDFs) and complement analyses of deep inelastic scattering, Drell-Yan pair production, and jet production. Photons from energetic π^0 and η mesons are the main background to direct photon production especially at small p_T . Since these mesons are produced inside jets, their contribution can be suppressed with respect to direct photons by requiring the photon be isolated from other particles. Isolated electrons from the electroweak production of W and Z bosons also contribute to the background at high p_T . Several measurements of photon production at hadron colliders successfully used these isolation techniques to extract the photon signal.

Both CDF [14] and D0 [15] have measured the cross-section for inclusive production of isolated photons. Results from NLO pQCD calculations agree with the measurement within uncertainties. The ratio between data and pQCD prediction is in good agreement at high p_T but shows an enhancement at low p_T where the effects of theory resummation and background fragmentation are higher.

7. – Production of photon in association with jets

7.1. Photon + jet. – The production of a photon with associated jets in the final state is a powerful probe of the dynamics of hard QCD interactions. Different angular configurations between the photon and the jets can be used to extend inclusive photon production measurements and simultaneously test the underlying dynamics of QCD hard-scattering subprocesses in different regions of parton momentum fraction x and large hard-scattering scales Q^2 .

At D0 [16], the process $p\bar{p} \rightarrow \gamma + \text{jet} + X$ is studied using 1.0 fb^{-1} of data. Photons are reconstructed in the central rapidity region $|y_\gamma| < 1.0$ with transverse momenta in the range $30 < p_T^\gamma < 400 \text{ GeV}$ while jets are reconstructed in either the central $|y_{\text{jet}}| < 0.8$ or forward $1.5 < |y_{\text{jet}}| < 2.5$ rapidity intervals with $p_T^{\text{jet}} > 15 \text{ GeV}$. The differential cross section $d^3\sigma/dp_T^\gamma dy_\gamma dy_{\text{jet}}$ is measured as a function of p_T^γ in four regions, differing by the relative orientations of the photon and the jet in rapidity. Ratios between the differential cross sections in each region are also presented. Next-to-leading order QCD predictions using different parameterizations of parton distribution functions and theoretical scale choices are compared to the data. The predictions do not simultaneously describe the measured normalization and p_T^γ dependence of the cross section in the four measured regions. Similarly, theoretical scale variations are unable to simultaneously describe the data-to-theory ratios in each of the four measured regions. Thus, the data show a need for an improved and consistent theoretical description of the $\gamma + \text{jet}$ production process.

7.2. Photon + heavy flavor jets. – Photons (γ) produced in association with heavy quarks Q (c or b) in the final state of hadron-hadron interactions provide valuable information about the parton distributions of the initial state hadrons. Such events are produced primarily through the QCD Compton-like scattering process $gQ \rightarrow \gamma Q$, which dominates up to photon transverse momenta (p_T^γ) of 90 GeV for $\gamma + c + X$ and up to 120 GeV for $\gamma + b + X$ production, but also through quark-antiquark annihilation. Consequently, $\gamma + Q + X$ production is sensitive to the b , c , and gluon (g) densities within the colliding hadrons, and can provide constraints on parton distribution functions (PDFs) that have substantial uncertainties. The heavy quark and gluon content is an important aspect of QCD dynamics and of the fundamental structure of the proton. In particular, many searches for new physics, *e.g.*, for certain Higgs boson production modes, will benefit from a more precise knowledge of the heavy quark and gluon content of the proton.

First measurements of the differential cross sections $d^3\sigma/(dp_T^\gamma dy_\gamma dy_{\text{jet}})$ for the inclusive production of a photon in association with a heavy quark (b , c) jet are presented by D0 [17], covering photon transverse momenta $30 < p_T^\gamma < 150 \text{ GeV}$, photon rapidities $|y_\gamma| < 1.0$, jet rapidities $|y_{\text{jet}}| < 0.8$, and jet transverse momenta $p_T^{\text{jet}} > 15 \text{ GeV}$. The results are compared with next-to-leading order perturbative QCD predictions. The pQCD prediction agrees with the measured cross sections for $\gamma + b + X$ production over the entire p_T^γ range, and with $\gamma + c + X$ production for $p_T^\gamma < 70 \text{ GeV}$. For $p_T^\gamma > 70 \text{ GeV}$ the measured $\gamma + c + X$ cross section is higher than the prediction by about 1.6 to 2.2 standard deviations (including only the experimental uncertainties) with the difference increasing with growing p_T^γ as shown in fig. 3.

8. – Vector boson + jets production

Collider signatures containing bosons and jets are particularly interesting. Recent theoretical effort has been devoted to determining predictions of $W^\pm/Z + \text{multiple parton}$

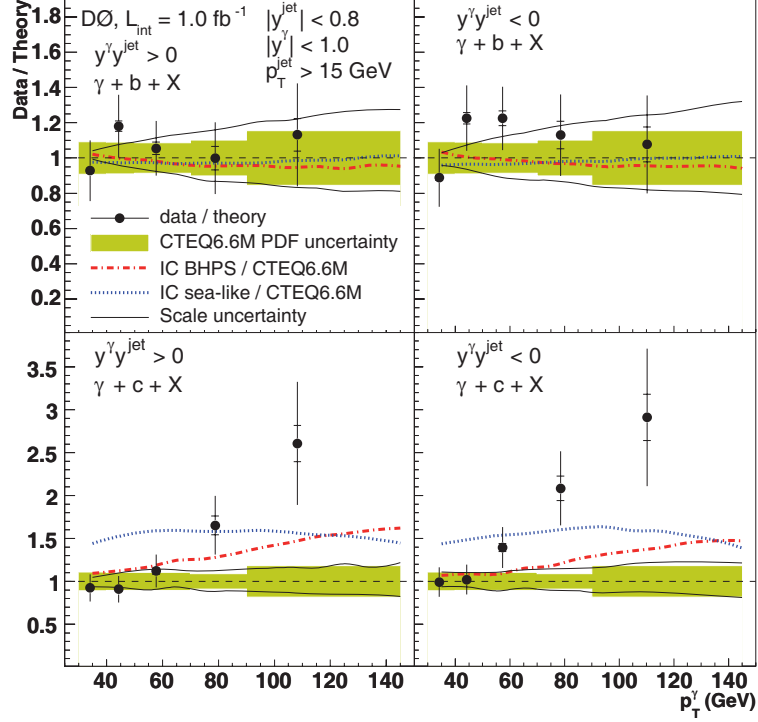


Fig. 3. – The data-to-theory ratio of cross sections as a function of p_T^γ for $\gamma+b+X$ and $\gamma+c+X$ in the regions $y^\gamma y^{\text{jet}} > 0$ and $y^\gamma y^{\text{jet}} < 0$. The uncertainties on the data include both statistical and full uncertainties (entire error bar). Also shown are the uncertainties on the theoretical pQCD scales and the CTEQ6.6M PDFs. The scale uncertainties are shown as dotted lines and the PDF uncertainties by the shaded regions. The ratio of the standard CTEQ6.6M prediction to two models of intrinsic charm is also shown.

production; the high-statistics sample of $W^\pm/Z + \text{jets}$ events collected at the Tevatron is a valuable testbed for probing the validity of these calculations. The final state containing a Z or W boson and one or more b-jets is a promising Higgs search channel at the Tevatron and could be a window to new physics at the LHC. These searches benefit from a deep understanding of the production of $W^\pm/Z + \text{heavy flavor jets}$ which constitutes a significant background to the more exotic sources of this signature. In this section the latest Tevatron results on these production mechanisms are reviewed with an emphasis on comparison of data results to the latest theoretical models.

8.1. $W/Z + \text{jets}$. – The CDF experiment has studied the production of jets in events with W^\pm/Z bosons [18,19]. $W \rightarrow e\nu$ events are selected by identifying a high E_T , central electron along with significant missing transverse energy, MET; $Z \rightarrow e^+e^-$ events are selected by requiring one such electron with another that is either central or in the forward region of the calorimeter, with the invariant mass of the electron pair required to be near the Z mass peak. Events are then assigned to bins of minimum jet multiplicity. Major sources of background in the $W^\pm + \text{jets}$ analysis include events with fake Ws and electroweak sources (tt, single top, dibosons); backgrounds in the $Z + \text{jets}$ analysis are dominated by multijet production and $W^\pm + \text{jets}$ events in which the Z signal is faked.

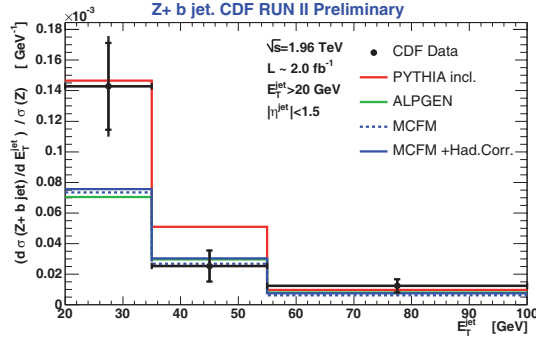


Fig. 4. – $Z + b$ jet differential cross sections as a function of jet p_T from CDF's 2 fb^{-1} result.

Acceptance for these events is studied using simulated signal samples; the differential cross section for the jets in these events is then examined and compared to some available theory predictions. NLO prediction from MCFM is accurately reproducing the jet ET spectrum in $W^\pm + 1$ or 2 jets. For higher multiplicity events, LO calculations are only available. The current preferred method for generating such events at LO relies on generating multiple samples using a matrix element calculation at fixed orders in α_s and then employing a parton shower program to add in additional soft, collinear jets. Matching algorithms have been designed to identify events that could be double counted in this recipe.

8.2. $Z + \text{jets}$ angular distributions. – A recent measurement by D0 of the inclusive cross section for $Z/\gamma^*(\rightarrow e^+e^-) + \text{jets}$ [20] tests NLO pQCD and provides an important control on background to new physics. Events are binned in the p_T of the N -th jet, for $N = 1, 2$, and 3. Data agree well with NLO-MCFM but diverge from predictions by PYTHIA and HERWIG increasingly with jet p_T and N_{jet} . PYTHIA with p_T ordering is found to describe the leading jet well. SHERPA and ALPGEN are seen to improve upon the particle shower-based generators. Some discrepancies persist nonetheless between data and predictions of production rates and jet p_T spectra.

8.3. $W + \text{single-}c$ production. – $W + \text{single-}c$ production is an important process at the Tevatron. $W + \text{single-}c$ events are produced via gluon-strange quark scattering, and thus this process offers insight on the strange content inside the proton. The process also allows an opportunity to measure $|V_{cs}|$ in a Q^2 regime not yet probed. Also, $W + c$ contributes to the background to top production and prominent Higgs search channels at the Tevatron. CDF [21] and D0 [22] have measured the $W + c$ process in Run II using a similar strategy. Leptonic W decays ($W \rightarrow l\nu$ with $l = e$ or μ) are selected via a high- p_T isolated central lepton and large missing E_T . Among the required jets in the selected events, evidence is sought for semileptonic hadron decay through the identification of a soft muon inside the jet cone. It is a feature of $W + c$ production that the electric charge of the W and c are opposite. The sign of the c quark is determined from the charge of the muon used to identify semileptonic hadron decay. An excess of opposite-sign primary lepton and soft muon events is indicative of $W + c$ production. Opposite-sign backgrounds include Drell-Yan production of $\mu^+\mu^-$, Wq production and fake W s. CDF measured in 1.7 fb^{-1} of data the production cross section for $W + c$ times the leptonic branching ratio of the W , $\sigma(Wc)BR(W \rightarrow l\nu) = 9.8 + 3.2$ for events with $p_T^c > 20 \text{ GeV}/c$ and

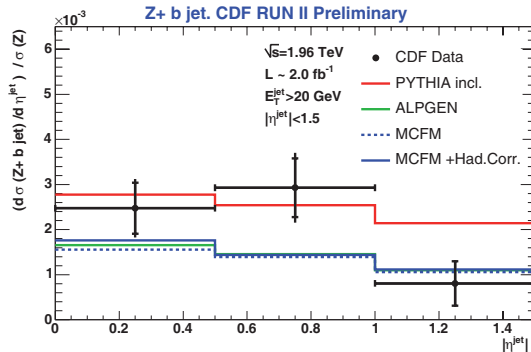


Fig. 5. – Z + b jet differential cross sections as a function of jet η from CDFs 2 fb^{-1} result.

$|\eta| < 1.5$. This can be compared to the NLO prediction from MCFM of $11.0^{+1.4}_{-3.0}$. D0 measured in 1 fb^{-1} of data the ratio $R = \frac{\sigma(Wc)}{\sigma(W+\text{jets})}$; measuring the ratio has the virtue that numerous sources of systematic error cancel out. The result $R = 0.071 \pm 0.017$ is reasonably consistent with a LO prediction from ALPGEN of 0.040 ± 0.003 .

8.4. $W^\pm/Z + b$ jets. – $W^\pm/Z + b$ jet signatures are important backgrounds to top and Higgs channels at the Tevatron. Separate analyses were undertaken to measure the b-jet cross section in W^\pm and Z events with increased precision in the hopes of improving the understanding of these final states. The event selection for the $W^\pm + b$ jets analysis is similar to that employed in the $W + c$ analysis discussed above. Here however b-jets are selected via the identification of a secondary decay vertex well separated from the primary $p\bar{p}$ interaction point.

The b-jet cross section in W^\pm events in 1.9 fb^{-1} of CDF Run II data was measured to be $\sigma + b - \text{jets}(W + b + \text{jets})BR(W \rightarrow l\nu) = 2.74 \pm 0.27(\text{stat}) \pm 0.42(\text{syst}) \text{ pb}$, where the systematic error is dominated by the uncertainty in the vertex mass shape one assumes for b-jets. This jet cross section result can be compared to the prediction from ALPGEN of 0.78 pb , a factor of 3-4 lower than what is observed in the data. Work is ongoing to understand the difference.

The Z+b-jet analysis used a similar technique to extract the b content of its tagged jet sample. This analysis has succeeded in examining differential cross sections for the b-jets in Z events as shown in fig. 4 and fig. 5. One can see that the differential b-jet cross sections *versus* jet p_T and η are not reproduced in all bins by any of the predictions that were constructed. Pythia appears to do a reasonable job at low jet p_T but less so as the jet p_T increases. The ALPGEN and MCFM predictions are consistent with each other but not with the data except for a few bins. It remains to be understood why the predictions are so different.

9. – Conclusions

We have reported on selected recent quantum chromodynamics (QCD) measurements from the Fermilab Run II Tevatron proton-antiproton collisions studied by the CDF and D0 Collaborations at a centre-of-mass energy of $\sqrt{s} = 1.96 \text{ TeV}$. We have reviewed inclusive jet and dijet production cross-section measurements, which are in excellent agreement with the theoretical predictions and are now being used for the first time

to inform parton distribution functions (PDF) determination. Jet and dijets measurements are also used to extract a precise value of the strong coupling constant and to look for new physics. Results from the inclusive photon production cross-section measurement, as well as associated production of photon with a light or heavy flavors jet, reveal still an inability of the next-to-leading-order (NLO) perturbative QCD calculations to describe comprehensively all such measurements. Finally we have summarized various measurements concerning the production of vector bosons and jets. Such measurements are a common prerequisite for many other studies, from top production measurements to search for supersymmetric particles and the Higgs boson. Several pQCD NLO calculations are now becoming available as well as several Monte Carlo tools, which can be validated against such experimental measurements.

REFERENCES

- [1] ABULENCIA A. *et al.*, *Phys. Rev. D*, **74** (2006) 071103.
- [2] ABULENCIA A. *et al.*, *Phys. Rev. Lett.*, **96** (2006) 122001.
- [3] ABULENCIA A. *et al.*, *Phys. Rev. D*, **75** (2007) 092006.
- [4] ABAZOV V. M. *et al.*, *Phys. Rev. Lett.*, **101** (2008) 062001.
- [5] STUMP D. *et al.*, *J. High Energy Phys.*, **10** (2003) 046.
- [6] ALTOONEN T. *et al.*, *Phys. Rev. D*, **78** (2008) 052006.
- [7] ABAZOV V. M. *et al.*, *Phys. Rev. Lett.*, **101** (2008) 062001.
- [8] CDF COLLABORATION, *Phys. Rev. Lett.*, **88** (2002) 042001.
- [9] ABAZOV V. M. *et al.*, *Phys. Rev. D*, **80** (2009) 111107.
- [10] CDF COLLABORATION, *Phys. Rev. D*, **79** (2009) 112002.
- [11] D0 COLLABORATION, arXiv.org:1002.4594.
- [12] KLUGE T., RABBERTZ K. and WOBISCH M., arXiv:hep-ph/0609285 (2006).
- [13] ABAZOV V. M. *et al.*, *Phys. Rev. Lett.*, **103** (2009) 191803.
- [14] <http://www-cdf.fnal.gov/physics/new/qcd/inclpho08/web.html>
- [15] ABAZOV V. M. *et al.*, *Phys. Lett. B*, **639** (2006) 151.
- [16] ABAZOV V. M. *et al.*, *Phys. Lett. B*, **666** (2008) 435.
- [17] ABAZOV V. M. *et al.*, *Phys. Rev. Lett.*, **102** (2009) 192002.
- [18] AALTONEN T. *et al.*, *Phys. Rev. D*, **77** (2008) 011108R.
- [19] AALTONEN T. *et al.*, *Phys. Rev. Lett.*, **100** (2008) 102001.
- [20] ABAZOV V. M. *et al.*, *Phys. Lett. B*, **678** (2009) 45.
- [21] AALTONEN T. *et al.*, *Phys. Rev. Lett.*, **100** (2008) 091803.
- [22] ABAZOV V. M. *et al.*, *Phys. Lett. B*, **666** (2008) 23.

Heavy flavor spectroscopy at the Tevatron

KAI YI for the D0 and CDF COLLABORATIONS

Department of Physics and Astronomy, University of Iowa - Iowa City, IA 52242, USA

(ricevuto il 14 Settembre 2010; pubblicato online l'11 Gennaio 2011)

Summary. — The Tevatron experiments have each accumulated about 6 fb^{-1} of good data since the start of Run II. This large dataset provides excellent opportunities for heavy flavor spectroscopy studies at the Tevatron. This paper will cover the latest $\Upsilon(nS)$ polarization studies as well as exotic meson spectroscopy results.

PACS 14.40.Nd – Bottom mesons ($|B| > 0$).

PACS 14.40.Lb – Charmed mesons ($|C| > 0, B = 0$).

PACS 14.40.Pq – Heavy quarkonia.

1. – Heavy baryon— Ω_b

Here we discuss the most recent observation of $\Omega_b(bss)$ by both the D0 (1.3 fb^{-1} of data) and CDF (4.2 fb^{-1} of data) experiments [1]. Both experiments observe this state through the following decay channel: $\Omega_b^- \rightarrow J/\psi \Omega^-$; $J/\psi \rightarrow \mu^+ \mu^-$, $\Omega^- \rightarrow \Lambda K^-$; $\Lambda \rightarrow p \pi$. Charge conjugate modes are included implicitly in this note. D0 used a boosted decision tree to reconstruct the Ω signal, while CDF used the traditional cut-based selection to reconstruct the Ω signal. The reconstructed Ω_b mass plots from the two experiments are shown in fig. 1. However, the Ω_b mass measured by D0 ($6165 \pm 10(\text{stat}) \pm 13(\text{syst}) \text{ MeV}/c^2$) and CDF ($6054.4 \pm 6.8(\text{stat}) \pm 0.9(\text{syst}) \text{ MeV}/c^2$) experiments disagree at the level of 6σ . The measured relative branching fraction with Ξ_b is also different at a level of 1.3σ between D0 ($0.80 \pm 0.32_{-0.22}^{+0.4}$) and CDF ($0.27 \pm 0.12 \pm 0.01$). D0 is working on an update with much more data to resolve the issue.

2. – $\Upsilon(nS)$ polarization

Vector meson production and polarization in hadronic collisions are usually discussed within the framework of non-relativistic QCD (NRQCD). The theory predicts [2] that the vector meson polarization should become transverse in the perturbative regime; *i.e.* at large transverse momentum p_T of the vector meson. However, the prediction is not supported by experimental observations [3]. We describe new results on this topic from

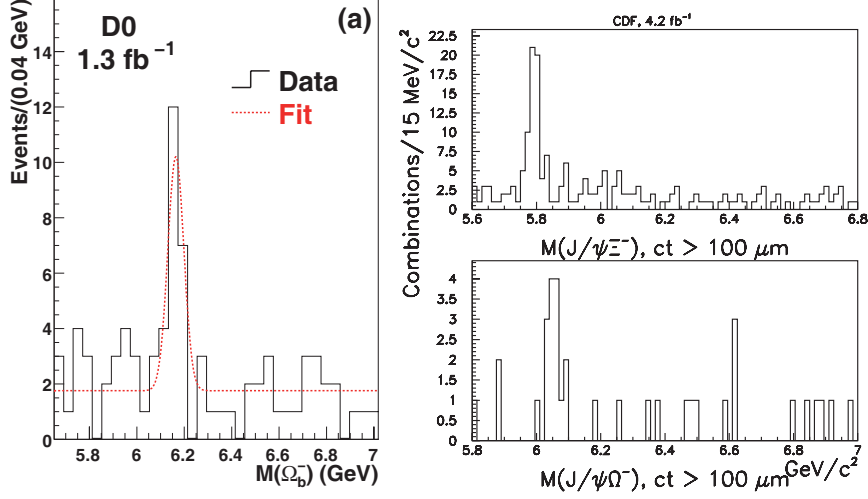


Fig. 1. – The Ω_b mass spectrum from D0 (left), and CDF (right).

the Tevatron. We define a parameter α to measure the polarization:

$$(1) \quad \frac{d\Gamma}{d\cos\theta^*} \propto 1 + \alpha \cos^2\theta^*,$$

where θ^* is the μ^+ angle with respect to the $\Upsilon(nS)$ direction in the lab frame. If the meson is fully polarized in the transverse direction, $\alpha = 1$. If it is fully aligned longitudinally, $\alpha = -1$.

Figure 2 shows the comparison between the theoretical prediction of $\Upsilon(1S)$ (colored band) and the new CDF (left) [4] and D0 (right) [5] experimental results. In the low- p_T region, CDF shows nearly unpolarized events, which is consistent with the CDF Run I result [6]; D0 shows partially longitudinally polarized events. At higher p_T , the CDF results tend toward longitudinal polarization while the D0 result indicates transverse polarization. Both CDF and D0 results at high p_T deviate from theoretical predictions.

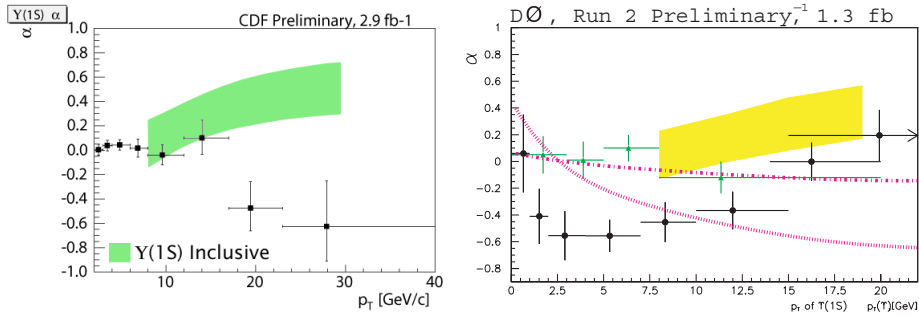


Fig. 2. – (Colour on-line) The polarization parameter α of $\Upsilon(1S)$ measured by CDF (left) and D0 (right, CDF I results are shown as green points).

It will be interesting to investigate with more data and in some detail; *e.g.*, study η dependence since the CDF and D0 analyses have different η acceptance.

3. – Exotic mesons

It has been six years since the discovery of the $X(3872)$ [7]; however, the nature of this state has not yet been clearly understood. Due to the proximity of the $X(3872)$ to the $D^0 D^{*0}$ threshold, the $X(3872)$ has been proposed as a molecule composed of D^0 and D^{*0} mesons. The $X(3872)$ has also been speculated to be two nearby states, as in models such as the *diquark-antidiquark* model. It is critical to make precise measurements of the mass and width of $X(3872)$ to understand its nature. The large $X(3872) \rightarrow J/\psi \pi^+ \pi^-$ sample accumulated at CDF enables a test of the hypothesis that the $X(3872)$ is composed of two states and to make a precise mass measurement of $X(3872)$ if it is consistent with a one-state hypothesis.

There are many more states, similar to $X(3872)$, that have charmonium-like decay modes but are difficult to place in the overall charmonium system [8-10]. These unexpected new states have introduced challenges to the conventional $q\bar{q}$ meson model and revitalized interest in exotic mesons in the charm sector [11], although the existence of exotic mesons has been discussed for many years [12]. Until recently all of these new states involved only c quark and light quark (u, d) decay products. The $J/\psi\phi$ final state enables us to extend the exotic meson searches to c quark and heavy s quark decay products. An investigation of the $J/\psi\phi$ system produced in exclusive $B^+ \rightarrow J/\psi\phi K^+$ decays with $J/\psi \rightarrow \mu^+\mu^-$ and $\phi \rightarrow K^+K^-$ is reported here.

3.1. Measurement of the mass of $X(3872)$. – A CDF analysis tested the hypothesis of whether the observed $X(3872)$ signal is composed of two different states as predicted in some four-quark models using the CDF inclusive $X(3872)$ sample. The $X(3872)$ mass signal is fit with a Breit-Wigner function convoluted with a resolution function [13]. Both functions contain a width scale factor that is a free parameter in the fit and therefore sensitive to the shape of the mass signal. The measured width scale factor is compared to the values seen in simulations which assume two states with the given mass difference and ratio of events. The resolution in the simulated events is corrected for the difference between data and simulation as measured from the $\psi(2S)$. The result of this hypotheses test shows that the data is consistent with a single state. Under the assumption of two states with equal amount of observed events, a limit of $\Delta m < 3.2(3.6) \text{ MeV}/c^2$ is set at 90% (95%) CL.

Since the $X(3872)$ is consistent with one peak in our test, its mass is measured in an unbinned maximum likelihood fit. The systematic uncertainties are determined from the difference between the measured $\psi(2S)$ mass and its world average value, the potential variation of the $\psi(2S)$ mass as a function of kinematic variables, and the difference in Q value between $X(3872)$ and $\psi(2S)$. Systematics due to the fit model are negligible. The measured $X(3872)$ mass is: $m(X(3872)) = 3871.61 \pm 0.16(\text{stat}) \pm 0.19(\text{syst}) \text{ MeV}/c^2$, which is the most precise measurement to date, as shown in fig. 3 [13, 14].

3.2. Evidence for $Y(4140)$. – The procedure for this analysis is to reconstruct the $B^+ \rightarrow J/\psi\phi K^+$ signal and then search for structures in the $J/\psi\phi$ mass spectrum [15]. The $J/\psi \rightarrow \mu^+\mu^-$ events are recorded using a dedicated dimuon trigger. The $B^+ \rightarrow J/\psi\phi K^+$ candidates are reconstructed by combining a $J/\psi \rightarrow \mu^+\mu^-$ candidate, a $\phi \rightarrow K^+K^-$ candidate, and an additional charged track. Each track is required to have

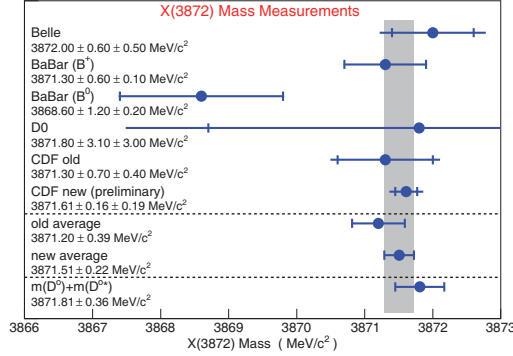


Fig. 3. – An overview of the measured $X(3872)$ masses from the experiments observing the $X(3872)$.

at least 4 axial silicon hits and have a transverse momentum greater than $400 \text{ MeV}/c$. The reconstructed mass of each vector meson candidate must lie within a suitable range from the nominal values ($\pm 50 \text{ MeV}/c^2$ for the J/ψ and $\pm 7 \text{ MeV}/c^2$ for the ϕ). In the final B^+ reconstruction the J/ψ is mass constrained, and the B^+ candidates must have $p_T > 4 \text{ GeV}/c$. The $P(\chi^2)$ of the mass- and vertex-constrained fit to the $B^+ \rightarrow J/\psi\phi K^+$ candidate is required to be greater than 1%.

To suppress combinatorial background, dE/dx and Time-of-Flight (TOF) information is used to identify all three kaons in the final state. The information is summarized in a log-likelihood ratio (LLR), which reflects how well a candidate track can be positively identified as a kaon relative to other hadrons. In addition, a minimum $L_{xy}(B^+)$ is required for the $B^+ \rightarrow J/\psi\phi K^+$ candidate, where $L_{xy}(B^+)$ is the projection onto $\vec{p}_T(B^+)$ of the vector connecting the primary vertex to the B^+ decay vertex. The $L_{xy}(B^+)$ and LLR requirements for $B^+ \rightarrow J/\psi\phi K^+$ are then chosen to maximize $S/\sqrt{S+B}$, where S is the number of $B^+ \rightarrow J/\psi\phi K^+$ signal events and B is the number of background events implied from the B^+ sideband. The requirements obtained by maximizing $S/\sqrt{S+B}$ are $L_{xy}(B^+) > 500 \mu\text{m}$ and $LLR > 0.2$.

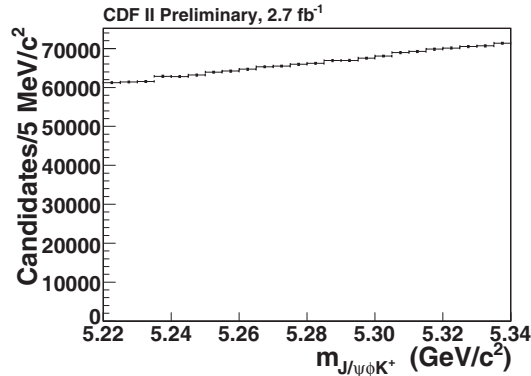


Fig. 4. – The $J/\psi\phi K^+$ mass before minimum $L_{xy}(B^+)$ and kaon LLR requirements.

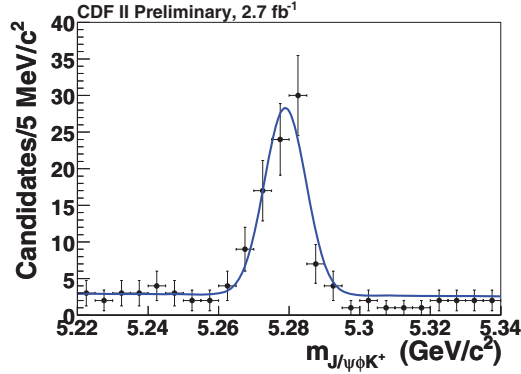


Fig. 5. – The $J/\psi\phi K^+$ mass after minimum $L_{xy}(B^+)$ and LLR requirements; the solid line is a fit to the data with a Gaussian signal function and linear background function.

The invariant mass of $J/\psi\phi K^+$, after J/ψ and ϕ mass window requirements, before and after the minimum $L_{xy}(B^+)$ and kaon LLR requirements, is shown in fig. 4 and fig. 5, respectively. The B^+ signal is not distinguishable before the $L_{xy}(B^+)$ and kaon LLR requirements are applied, but a clear B^+ signal is seen after the requirements. A fit with a Gaussian signal function and a linear background function to the mass spectrum of $J/\psi\phi K^+$ (fig. 5) returns a B^+ signal of $75 \pm 10(\text{stat})$ events. The $L_{xy}(B^+)$ and LLR requirements reduce the background by a factor of approximately 20000 while keeping a signal efficiency of approximately 20%. The B^+ signal candidates are selected with a mass within 3σ of the nominal B^+ mass; the purity of the B^+ signal in that mass window is about 80%.

The combinatorial background under the B^+ peak includes B hadron decays such as $B_s^0 \rightarrow \psi(2S)\phi \rightarrow J/\psi\pi^+\pi^-\phi$, in which the pions are misidentified as kaons. However, background events with misidentified kaons cannot yield a Gaussian peak at the B^+ mass consistent with the $5.9\text{MeV}/c^2$ mass resolution. Figure 6 shows the K^+K^- mass from $\mu^+\mu^-K^+K^-K^+$ candidates within $\pm 3\sigma$ of the nominal B^+ mass with B sidebands

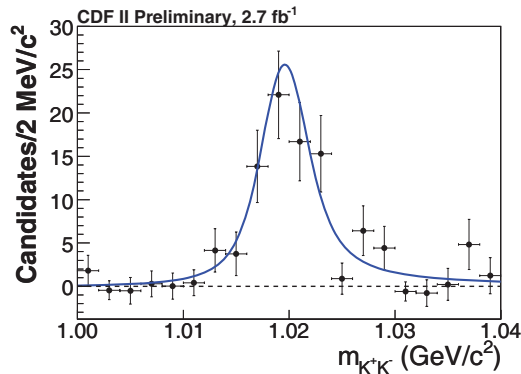


Fig. 6. – The B^+ sideband-subtracted K^+K^- mass without the ϕ mass window requirement. The solid curve is a P -wave relativistic Breit-Wigner fit to the data.

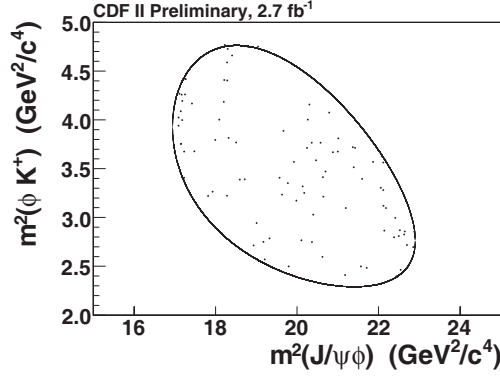


Fig. 7. – The Dalitz plot of $m^2(\phi K^+)$ vs. $m^2(J/\psi\phi)$ in the B^+ mass window. The boundary shows the kinematically allowed region.

subtracted before applying the ϕ mass window requirement. Using a smeared P -wave relativistic Breit-Wigner (BW) [16] lineshape fit to the spectrum returns a χ^2 probability of 28%. This shows that the $B^+ \rightarrow J/\psi K^+ K^- K^+$ final state is well described by $J/\psi\phi K^+$.

The effects of detector acceptance and selection requirements are examined using $B^+ \rightarrow J/\psi\phi K^+$ MC events simulated by a phase-space distribution. The MC events are smoothly distributed in the Dalitz plot and in the $J/\psi\phi$ mass spectrum. No artifacts were observed from MC events. Figure 7 shows the Dalitz plot of $m^2(\phi K^+)$ versus $m^2(J/\psi\phi)$, and fig. 8 shows the mass difference, $\Delta M = m(\mu^+\mu^- K^+ K^-) - m(\mu^+\mu^-)$, for events in the B^+ mass window in our data sample. The enhancement in the ΔM spectrum just above $J/\psi\phi$ threshold is examined. The high-mass part of the spectrum beyond 1.56 GeV/c^2 is excluded to avoid combinatorial backgrounds that would be expected from misidentified $B_s^0 \rightarrow \psi(2S)\phi \rightarrow (J/\psi\pi^+\pi^-)\phi$ decays. The enhancement is modeled by an

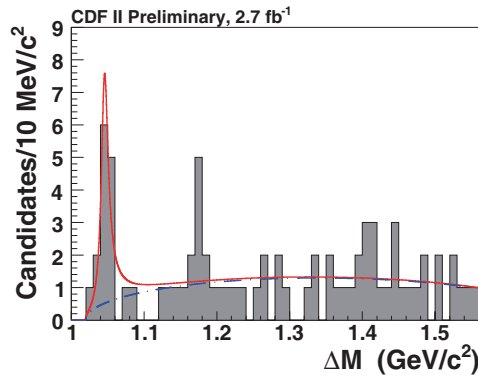


Fig. 8. – (Colour on-line) The mass difference, ΔM , between $\mu^+\mu^- K^+ K^-$ and $\mu^+\mu^-$, in the B^+ mass window. The dash-dotted curve is the background contribution and the red solid curve is the total unbinned fit.

S -wave relativistic BW function⁽¹⁾ convoluted with a Gaussian resolution function with the RMS fixed to $1.7 \text{ MeV}/c^2$ obtained from MC, and three-body phase space [12] is used to describe the background shape. An unbinned likelihood fit to the ΔM distribution, as shown in fig. 8, returns a yield of 14 ± 5 events, a ΔM of $1046.3 \pm 2.9 \text{ MeV}/c^2$, and a width of $11.7_{-5.0}^{+8.3} \text{ MeV}/c^2$. To investigate possible reflections, the Dalitz plot and projections into the ϕK^+ and $J/\psi K^+$ spectra are examined. No evidence for any other structure in the ϕK^+ and $J/\psi K^+$ spectra is found.

The log-likelihood ratio of $-2 \ln(\mathcal{L}_0/\mathcal{L}_{\text{max}})$ is used to determine the significance of the enhancement, where \mathcal{L}_0 and \mathcal{L}_{max} are the likelihood values for the null hypothesis fit and signal hypothesis fit. The $\sqrt{-2 \ln(\mathcal{L}_0/\mathcal{L}_{\text{max}})}$ value is 5.3 for a pure three-body phase space background shape assumption. Using the background distribution alone, ΔM spectra are generated, and searched for the most significant fluctuation with $\sqrt{-2 \ln(\mathcal{L}_0/\mathcal{L}_{\text{max}})} \geq 5.3$ in each spectrum in the mass range of 1.02 to 1.56 GeV/c^2 , with widths in the range of 1.7 (detector resolution) to 120 MeV/c^2 (ten times the observed width).

The resulting p -value from 3.1 million simulations is 9.3×10^{-6} , corresponding to a significance of 4.3σ . This process is repeated with a flat combinatorial non- B background and three-body PS for non-resonance B background, which gives a significance of 3.8σ .

One's eye tends to be drawn to a second cluster of events around 1.18 GeV/c^2 in fig. 8. This cluster is close to one pion mass above the peak at the $J/\psi\phi$ threshold. However, this cluster is statistically insufficient to infer the presence of a second structure.

4. – Conclusions

Both D0 and CDF observed the Ω_b baryon through the same reconstruction channel. However, the measured Ω mass disagrees at a level of 6σ between the two experiments. D0 is working on an update with much more data to resolve this issue.

For $\Upsilon(1S)$ polarization, CDF result shows nearly unpolarized events at low p_T , while D0 shows partially longitudinally polarization. At higher p_T , CDF results tend toward longitudinal polarization while D0 results indicate transverse polarization. Both CDF and D0 results at high p_T deviate from theoretical predictions. CDF is continuing the analysis and will double the dataset. D0 has the opportunity to study the rapidity dependence, since their measurement spans the range $|y| < 1.8$ compared to 0.6 for CDF.

Studies using CDF's $X(3872)$ sample, the largest in the world, indicate that the $X(3872)$ is consistent with the one-state hypothesis and this leads to the most precise mass measurement of $(X3872)$. The value is below, but within the uncertainties of the $D^{*0}D^0$ threshold. The explanation of the $X(3872)$ as a bound D^*D system is therefore still an option.

The $B^+ \rightarrow J/\psi\phi K^+$ sample at CDF enables a search for structure in the $J/\psi\phi$ mass spectrum, and evidence is found for a narrow structure near the $J/\psi\phi$ threshold with a significance estimated to be at least 3.8σ . Assuming an S -wave relativistic BW, the mass (adding J/ψ mass) and width of this structure, including systematic uncertainties, are measured to be $4143.0 \pm 2.9(\text{stat}) \pm 1.2(\text{syst}) \text{ MeV}/c^2$ and $11.7_{-5.0}^{+8.3}(\text{stat}) \pm 3.7(\text{syst}) \text{ MeV}/c^2$, respectively. This structure does not fit conventional expectations for a charmonium state because as a $c\bar{c}$ state it is expected to have a tiny

⁽¹⁾ $\frac{dN}{dm} \propto \frac{m\Gamma(m)}{(m^2 - m_0^2)^2 + m_0^2\Gamma^2(m)}$, where $\Gamma(m) = \Gamma_0 \frac{q}{q_0} \frac{m_0}{m}$, and the 0 subscript indicates the value at the peak mass.

branching ratio to $J/\psi\phi$ with its mass well beyond open charm pairs. The new structure is termed the $Y(4140)$. The branching ratio of $B^+ \rightarrow Y(4140)K^+$, $Y(4140) \rightarrow J/\psi\phi$ is estimated to be $9.0 \pm 3.4(\text{stat}) \pm 2.9(B_{BF}) \times 10^{-6}$.

* * *

We thank the Fermilab staffs and the technical staffs of the participating institutions for their vital contributions.

REFERENCES

- [1] ABAZOV V. *et al.* (D0 COLLABORATION), *Phys. Rev. Lett.*, **101** (2008) 232002; ABULENCIA T. *et al.* (CDF COLLABORATION), *Phys. Rev. D*, **80** (2009) 072003.
- [2] M. KRAMER, arXiv:hep-ph/0106120.
- [3] AFOLDER T. *et al.* (CDF COLLABORATION), *Phys. Rev. Lett.*, **85** (2000) 2886; ABULENCIA T. *et al.* (CDF COLLABORATION), *Phys. Rev. Lett.*, **99** (2007) 132001.
- [4] http://www-cdf.fnal.gov/physics/new/bottom/090903.blessed-Upsilon1S-polarization/blessed_plots.html.
- [5] ABAZOV V. *et al.* (D0 COLLABORATION), *Phys. Rev. Lett.*, **101** (2008) 012001.
- [6] ACOSTA D. *et al.* (CDF COLLABORATION), *Phys. Rev. Lett.*, **88** (2002) 161802.
- [7] CHOI S.-K. *et al.* (BELLE COLLABORATION), *Phys. Rev. Lett.*, **91** (2003) 262001; ACOSTA D. *et al.* (CDF COLLABORATION), *Phys. Rev. Lett.*, **93** (2004) 072001; CHOI S.-K. *et al.* (BELLE COLLABORATION), *Phys. Rev. Lett.*, **94** (2005) 182002; AUBERT B. *et al.* (BABAR COLLABORATION), *Phys. Rev. Lett.*, **95** (2005) 142001; GODFREY S. and OLSEN S. L., *Annu. Rev. Nucl. Part. Sci.*, **58** (2008) 51.
- [8] CHOI S.-K. *et al.* (BELLE COLLABORATION), *Phys. Rev. Lett.*, **94** (2005) 182002; AUBERT B. *et al.* (BABAR COLLABORATION), *Phys. Rev. Lett.*, **101** (2008) 082001.
- [9] AUBERT B. *et al.* (BABAR COLLABORATION), *Phys. Rev. Lett.*, **95** (2005) 142001.
- [10] AUBERT B. *et al.* (BABAR COLLABORATION), *Phys. Rev. Lett.*, **98** (2007) 212001; WANG X. L. *et al.* (BELLE COLLABORATION), *Phys. Rev. Lett.*, **99** (2007) 142002; CHOI S.-K. *et al.* (BELLE COLLABORATION), *Phys. Rev. D*, **78** (2008) 072004; PAKHLOV P. *et al.* (BELLE COLLABORATION), *Phys. Rev. Lett.*, **100** (2008) 202001.
- [11] EICHTEN E., GODFREY S., MAHLKE H. and ROSNER J., *Rev. Mod. Phys.*, **80** (2008) 1161; ZHU S. L., *Phys. Lett. B*, **625** (2005) 212; CLOSE F. and PAGE P., *Phys. Lett. B*, **628** (2005) 215; SWANSON E. S., *Phys. Lett. B*, **588** (2004) 189; MAIANI L., PICCININI F., POLOSA A. D. and RIQUER V., *Phys. Rev. D*, **72** (2005) 031502(R); DRENSKA N. V., FACCINI R. and POLOSA A. D., arXiv:hep-ph/0902.2803v1; CHIU T. W. and HSIEH T. H., *Phys. Lett. B*, **646** (2007) 95.
- [12] AMSLER C. *et al.* (PARTICLE DATA GROUP), *Phys. Lett. B*, **667** (2008) 1.
- [13] AALTONEN T. *et al.* (CDF COLLABORATION), arXiv:0906.5218 [hep-ex].
- [14] ADACHI I. *et al.* (BELLE COLLABORATION), arXiv:0809.1224v1 [hep-ex].
- [15] AALTONEN T. *et al.* (CDF COLLABORATION), *Phys. Rev. Lett.*, **102** (2009) 242002.
- [16] AUBERT B. *et al.* (BABAR COLLABORATION), *Phys. Rev. D*, **78** (2008) 071103.

Low energy QCD and ChPT studies with KLOE

F. AMBROSINO⁽¹⁾⁽²⁾, A. ANTONELLI⁽³⁾, M. ANTONELLI⁽³⁾, F. ARCHILLI⁽⁴⁾⁽⁵⁾,
P. BELTRAME⁽⁶⁾, G. BENCIVENNI⁽³⁾, C. BINI⁽⁷⁾⁽⁸⁾, C. BLOISE⁽³⁾,
S. BOCCHETTA⁽⁹⁾⁽¹⁰⁾, F. BOSSI⁽³⁾, P. BRANCHINI⁽¹⁰⁾, G. CAPON⁽³⁾,
T. CAPUSSELA⁽³⁾, F. CERADINI⁽⁹⁾⁽¹⁰⁾, P. CIAMBRONE⁽³⁾, E. DE LUCIA⁽³⁾,
A. DE SANTIS⁽⁷⁾⁽⁸⁾, P. DE SIMONE⁽³⁾, G. DE ZORZI⁽⁷⁾⁽⁸⁾, A. DENIG⁽⁶⁾,
A. DI DOMENICO⁽⁷⁾⁽⁸⁾, C. DI DONATO⁽²⁾, B. DI MICCO⁽⁹⁾⁽¹⁰⁾, M. DREUCCI⁽³⁾,
G. FELICI⁽³⁾, S. FIORE⁽⁷⁾⁽⁸⁾, P. FRANZINI⁽⁷⁾⁽⁸⁾, C. GATTI⁽³⁾, P. GAUZZI⁽⁷⁾⁽⁸⁾,
S. GIOVANNELLA⁽³⁾, E. GRAZIANI⁽¹⁰⁾, M. JACEWICZ^{(11)(*)}, G. LANFRANCHI⁽³⁾,
J. LEE-FRANZINI⁽³⁾⁽¹²⁾, M. MARTINI⁽³⁾⁽¹³⁾, P. MASSAROTTI⁽¹⁾⁽²⁾,
S. MEOLA⁽¹⁾⁽²⁾, S. MISCETTI⁽³⁾, M. MOULSON⁽³⁾, S. MÜLLER⁽⁶⁾, F. MURTAS⁽³⁾,
M. NAPOLITANO⁽¹⁾⁽²⁾, F. NGUYEN⁽⁹⁾⁽¹⁰⁾, M. PALUTAN⁽³⁾, A. PASSERI⁽¹⁰⁾,
V. PATERA⁽³⁾⁽¹³⁾, P. SANTANGELO⁽³⁾, B. SCIASCIA⁽³⁾, T. SPADARO⁽³⁾,
L. TORTORA⁽¹⁰⁾, P. VALENTE⁽⁸⁾, G. VENANZONI⁽³⁾, R. VERSACI⁽³⁾⁽¹³⁾ and
G. XU⁽³⁾⁽¹⁴⁾

⁽¹⁾ *Dipartimento di Scienze Fisiche dell'Università "Federico II" - Napoli, Italy*

⁽²⁾ *INFN, Sezione di Napoli - Napoli, Italy*

⁽³⁾ *Laboratori Nazionali di Frascati dell'INFN - Frascati, Italy*

⁽⁴⁾ *Dipartimento di Fisica dell'Università "Tor Vergata" - Rome, Italy*

⁽⁵⁾ *INFN, Sezione di "Tor Vergata" - Rome, Italy*

⁽⁶⁾ *Institut für Kernphysik, Johannes Gutenberg, Universität Mainz - Mainz, Germany*

⁽⁷⁾ *Dipartimento di Fisica dell'Università "La Sapienza" - Rome, Italy*

⁽⁸⁾ *INFN, Sezione di Roma - Rome, Italy*

⁽⁹⁾ *Dipartimento di Fisica dell'Università "Roma Tre" - Rome, Italy*

⁽¹⁰⁾ *INFN, Sezione di "Roma Tre" - Rome, Italy*

⁽¹¹⁾ *Department of Physics and Astronomy, Uppsala University - Uppsala, Sweden*

⁽¹²⁾ *Physics Department, State University of New York at Stony Brook
Stony Brook, USA*

⁽¹³⁾ *Dipartimento di Energetica dell'Università "La Sapienza" - Rome, Italy*

⁽¹⁴⁾ *Institute of High Energy Physics of Academica Sinica - Beijing, China*

(ricevuto il 14 Settembre 2010; pubblicato online il 13 Gennaio 2011)

(*) E-mail: marek.jacewicz@lnf.infn.it

Summary. — The KLOE experiment is situated at the ϕ factory DAΦNE in Frascati. ϕ radiative decays have been used to investigate the properties of the light scalar mesons $f_0(980)/a_0(980)$, whose structure is still controversial. Off-peak data allow to investigate $\gamma\gamma$ interaction with a consequent scalar/pseudoscalar meson production. From the large sample of the η and η' produced in $\phi \rightarrow \eta\gamma$ decay we have studied several η and η' decays relevant to η/η' mixing, η' gluonium content, CP violation searches and tests of ChPT. For the hadronic cross section, the pion form factor in the $M_{\pi\pi}$ invariant mass range (0.592–0.975) GeV has been determined and used in the evaluation of the hadronic contribution to the muon anomaly. The result confirms the $3\text{-}\sigma$ discrepancy between SM expectation and the measurement of the muon ($g - 2$) by the E821 experiment at the BNL.

PACS 13.25.Jx – Decays of other mesons.

PACS 13.66.Bc – Hadron production in e^-e^+ interactions.

PACS 14.40.Be – Light mesons ($S = C = B = 0$).

1. – The nature of the scalar mesons

It is still controversial whether the light scalars are $q\bar{q}$ mesons, $qq\bar{q}\bar{q}$ states, or $K\bar{K}$ molecules. Here we describe the measurement of the couplings of the a_0 to $\eta\pi^0$ done at the KLOE detector [1] that together with our previous measurements [2,3] can be used to identify the nature of the scalars. We searched for $a_0(980)$ contribution in $e^+e^- \rightarrow \eta\pi^0\gamma$ with $\eta \rightarrow \gamma\gamma$ and $\eta \rightarrow \pi^+\pi^-\pi^0$ [4]. A kinematic fit has been performed imposing the four-momentum conservation, the photon velocity and the invariant masses of both η and π^0 . A combined fit (for the two η decay modes) to the $\eta\pi^0$ invariant mass distribution has been done with the “no-structure” (NS) [5] and the “kaon loop” (KL) [6] models after background subtraction. The results of the fit are shown in fig. 1 and table I.

It is interesting to note that both models give a large coupling of the $a_0(980)$ with the ϕ meson, indicating a sizable strange quark content in the $a_0(980)$. The branching ratios

$$\begin{aligned} BR(\phi \rightarrow \eta\pi^0\gamma) &= (7.01 \pm 0.10_{\text{stat}} \pm 0.20_{\text{syst}}) \times 10^{-5}, \text{ with } \eta \rightarrow \gamma\gamma, \\ BR(\phi \rightarrow \eta\pi^0\gamma) &= (7.12 \pm 0.13_{\text{stat}} \pm 0.22_{\text{syst}}) \times 10^{-5}, \text{ with } \eta \rightarrow \pi^+\pi^-\pi^0 \end{aligned}$$

are obtained normalizing to $\phi \rightarrow \eta\gamma$ decays. Results from both models give $R_\eta = BR(\eta \rightarrow \gamma\gamma)/BR(\eta \rightarrow \pi^+\pi^-\pi^0)$ compatible with PDG'08 value, confirming the consistency between the two samples.

Predictions on scalar mesons can be tested also from $\phi \rightarrow K^0\bar{K}^0\gamma$ decays. This decay is expected to proceed mainly through $\phi \rightarrow [a_0(980) + f_0(980)]\gamma \rightarrow K^0\bar{K}^0\gamma$. The $K^0\bar{K}^0$ pair is produced with positive charge conjugation and a limited phase space due to the small mass difference between the ϕ and the production threshold of two neutral kaons. The signature of this decay is provided by the presence of either 2 K_S or 2 K_L and a low energy photon. We select only the $K_S K_S$ component, looking for double $K_S \rightarrow \pi^+\pi^-$ decay vertex, because of the clean topology. After the selection cut we found 5 candidate events in data whereas 3 events are expected from Monte Carlo background samples.

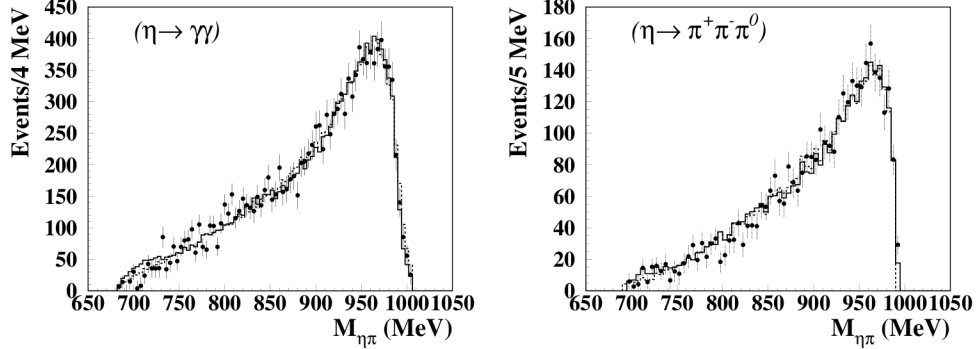


Fig. 1. – Fit results: points are data after background subtraction; histograms represent fit results (KL solid, NS dashed—differences between KL and NS models not appreciable on this scale).

This leads to: $BR(\phi \rightarrow K^0 \bar{K}^0 \gamma) < 1.9 \times 10^{-8}$ at the 90% CL [7]. Theory predictions for the BR spread over several orders of magnitude; several of them are ruled out by our result. Using the $a_0 f_0$ couplings shown in table I, we may also obtain estimates for $BR(\phi \rightarrow K^0 \bar{K}^0 \gamma)$. These lie in the range 4×10^{-9} – 6.8×10^{-8} , consistent with the above quoted upper limit, which excludes only the higher values.

2. – $\gamma\gamma$ physics at KLOE

The $\gamma\gamma$ coupling to scalar and pseudoscalar mesons brings information on meson's quark structure and can be measured directly in e^+e^- colliders via the reaction $e^+e^- \rightarrow e^+e^-\gamma^*\gamma^* \rightarrow e^+e^-X$. In fig. 2 left, the $\gamma\gamma$ flux expected at DAΦNE is shown. The question concerning $\sigma/f_0(600)$ meson has been debated for a long time. Our preliminary result, based on 240 pb^{-1} collected at $\sqrt{s} = 1 \text{ GeV}$, shows a clear enhancement over estimated backgrounds at low $M_{4\gamma}$; see fig. 2, right [8]. We continue the analysis to better understand this effect and perhaps link it to the production of the σ .

TABLE I. – Results from fit for $\phi \rightarrow a_0 \gamma \rightarrow \eta \pi^0 \gamma$ with KL and NS model.

Fit parameter	KL	NS	PDG'08
M_{a_0} (MeV)	$982.5 \pm 1.6 \pm 1.1$	982.5(fixed)	
$g_{a_0 K^+ K^-}$ (GeV)	$2.15 \pm 0.06 \pm 0.06$	$2.01 \pm 0.07 \pm 0.28$	
$g_{a_0 \eta \pi}$ (GeV)	$2.82 \pm 0.03 \pm 0.04$	$2.46 \pm 0.08 \pm 0.11$	
$g_{\phi a_0 \gamma}$ (GeV $^{-1}$)	$1.58 \pm 0.10 \pm 0.16$	$1.83 \pm 0.03 \pm 0.08$	
$BR(VDM) \times 10^6$	$0.92 \pm 0.40 \pm 0.15$	0	
R_η	$1.70 \pm 0.04 \pm 0.03$	$1.70 \pm 0.03 \pm 0.01$	1.729 ± 0.028
$(g_{a_0 K^+ K^-} / g_{a_0 \eta \pi^0})^2$	$0.58 \pm 0.03 \pm 0.03$	$0.67 \pm 0.06 \pm 0.13$	
$P(\chi^2)$	10.4%	30.9%	
Γ_{a_0} (MeV)	105	80	50-100

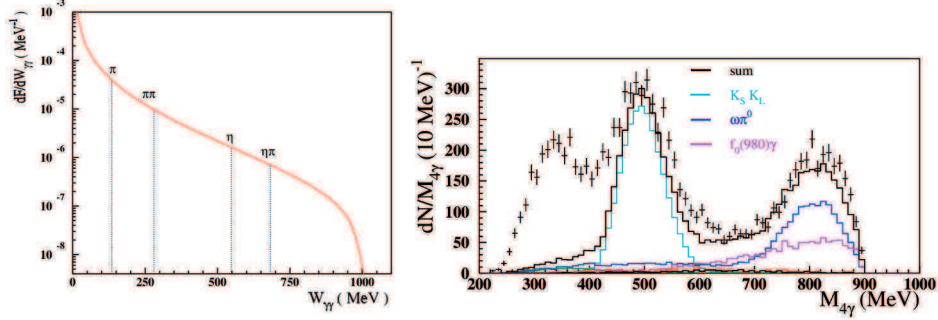


Fig. 2. – Left: $\gamma\gamma$ flux as a function of the $\gamma\gamma$ center-of-mass energy. Right: clear evidence of $e^+e^- \rightarrow e^+e^-\pi^0\pi^0$ events at low $M_{4\gamma}$ invariant mass.

We have investigated $\gamma\gamma$ processes also looking at the $e^+e^-\pi^+\pi^0$ final state. The preliminary analysis shows evidence for a signal of ~ 600 events from process $\gamma\gamma \rightarrow \eta$.

3. – $\eta - \eta'$ mixing and η' gluonium content

The question of a gluonium component in the η' meson has been extensively investigated in the past but it is still without a definitive conclusion. The KLOE paper on $\eta - \eta'$ mixing [9], reporting a 3σ evidence of gluonium content in the η' meson, has triggered a large amount of discussion among theoreticians.

Therefore a new and more detailed study on this topic has been performed [10]. In the constituent quark model one can extract gluonium content together with $\eta - \eta'$ mixing angle as described in [11]:

$$\begin{aligned} |\eta'\rangle &= \cos \Psi_G \sin \Psi_P |q\bar{q}\rangle + \cos \Psi_G \cos \Psi_P |s\bar{s}\rangle + \sin \Psi_G |G\rangle, \\ |\eta\rangle &= \cos \Psi_P |q\bar{q}\rangle - \sin \Psi_P |s\bar{s}\rangle, \end{aligned}$$

where Ψ_P is the $\eta - \eta'$ mixing angle, $Z_G^2 = \sin^2 \Psi_G$ is the gluonium content and $|q\bar{q}\rangle = (|u\bar{u}\rangle + |d\bar{d}\rangle)/\sqrt{2}$ and $|G\rangle = |\text{gluonium}\rangle$.

In comparison to the previous fit five more relations were added to constrain the fit in the new approach, thus allowing an independent determination of more free parameters. In addition the BR values from PDG 2008 [12] and the new KLOE results on the ω meson branching ratios [13] were used. The fit has been performed both imposing the gluonium content to be zero or allowing it free. The results are shown in table II: gluonium content of the η' is confirmed at 3σ level.

4. – η decays into four charged particles

There are several theoretical reasons to study the $\eta \rightarrow \pi^+\pi^-e^+e^-$ decay. First, by using the virtual photon it is possible to probe the structure of the η meson in the time-like region of four-momentum transfer square, which is equal to the invariant mass squared of the lepton pair [14]. One may also compare the predictions of the branching ratio value based on Vector Meson Dominance model and the Chiral Perturbation Theory. Moreover, it would be possible to study CP violation beyond the prediction of the Standard Model [15]. CP violation can be introduced by a flavor-conserving, CP violating,

TABLE II. – Output of the fit fixing or not the gluonium content to be zero.

	Gluonium content forced to be zero	Gluonium content free
Z_G^2	fixed 0	0.115 ± 0.036
ϕ_P	$(41.4 \pm 0.5)^\circ$	$(40.4 \pm 0.6)^\circ$
Z_q	0.93 ± 0.02	0.936 ± 0.025
Z_s	0.82 ± 0.05	0.83 ± 0.05
ϕ_V	$(3.34 \pm 0.09)^\circ$	$(3.32 \pm 0.09)^\circ$
m_s/\bar{m}	1.24 ± 0.07	1.24 ± 0.07
χ^2/dof	14.7/4	4.6/3
$P(\chi^2)$	0.005	0.20

four-quark operators involving two strange quarks together with combinations of other light quarks. It can be experimentally tested by measuring the angular asymmetry, A_ϕ , between pions and electrons decay planes in the η rest frame.

KLOE has studied the $\eta \rightarrow \pi^+\pi^-e^+e^-$ decay using 1.7fb^{-1} of data [16]. After background rejection a fit of the sidebands of the four-track invariant distribution has been performed to obtain the background scale factors. Most of the background is due to ϕ decays, but there is still a non-negligible contribution from continuum events. Signal events have been counted in the η mass region, giving $BR(\eta \rightarrow \pi^+\pi^-e^+e^-) = (26.8 \pm 0.9_{\text{stat}} \pm 0.7_{\text{syst}}) \times 10^{-5}$ and $A_\phi = (-0.6 \pm 2.5_{\text{stat}} \pm 1.8_{\text{syst}}) \times 10^{-2}$, see fig. 3, left.

More recently KLOE has started studying the $\eta \rightarrow e^+e^-e^+e^-$ decay. This decay, together with the $\eta \rightarrow \mu^+\mu^-e^+e^-$, is interesting for the η meson form factor because there are only leptons in the final state. Most of the background comes from continuum events and a small contribution is due to ϕ decays. The latter is subtracted from data

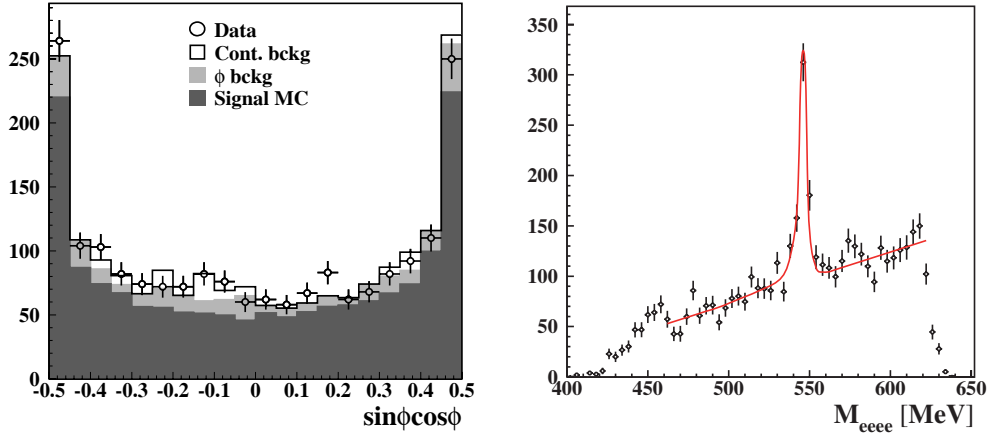


Fig. 3. – Left: $\sin(\phi)\cos(\phi)$ distribution for angle between $\pi^+\pi^-$ and e^+e^- planes. Dots: experimental data, black histogram is the combined MC distribution, *i.e.* signal (dark gray), ϕ background (light gray) and continuum background (white). Right: fit of the four-electron invariant mass, M_{eeee} in $\eta \rightarrow e^+e^-e^+e^-$ analysis.

TABLE III. – Comparison of the existing results for the ratio $\Gamma(\eta \rightarrow \pi^+\pi^-\gamma)/\Gamma(\eta \rightarrow \pi^+\pi^-\pi^0)$.

PDG08 average		0.203 ± 0.008
LOPEZ (CLEO) 2007	859 events	$0.175 \pm 0.007 \pm 0.006$
THALER 1973 [22]	18k events	0.209 ± 0.004
GORMLEY 1970 [21]	7250 events	0.201 ± 0.006
KLOE Preliminary	611k events	$0.201 \pm 0.0006_{\text{stat} \oplus \text{syst}}$

using the MC spectrum. The number of events is obtained fitting the data distribution of the 4 electron invariant mass, M_{eeee} , with signal and background shapes (fig. 3, right). From the fit we obtain 413 ± 31 events. This constitutes the first observation of this decay.

5. – $\eta \rightarrow \pi^+\pi^-\gamma$

In the $\eta \rightarrow \pi^+\pi^-\gamma$ decay, a significant contribution from chiral box anomaly is expected [17]. The box anomaly accounts for the direct (non-resonant) coupling of three pseudoscalar mesons with the photon. The invariant mass of the pions ($m_{\pi\pi}$) is a good observable to disentangle this contribution from other possible resonant ones, *e.g.*, from the ρ -meson. However, the momentum dependence cannot be determined from chiral theory only because the kinematic range of the $\eta \rightarrow \pi^+\pi^-\gamma$ decay extends above the chiral limit, where the Weiss-Zumino-Witten term of the ChPT Lagrangian properly describes the direct coupling. Several theoretical approaches have been developed to treat the contributions of the anomalies to the decay [18-20].

The $\eta \rightarrow \pi^+\pi^-\gamma$ decay has been measured in 1970s [21, 22]. The analysis of the two data sets shows some contradiction. Theoretical papers trying to combine the two measurements have found discrepancies in data treatment and problems with obtaining consistent results [23]. Recently, the CLEO Collaboration published the measurement of the ratio of branching ratios, $\Gamma(\eta \rightarrow \pi^+\pi^-\gamma)/\Gamma(\eta \rightarrow \pi^+\pi^-\pi^0) = 0.175 \pm 0.007 \pm 0.006$, which differs by more than $3\text{-}\sigma$ from old results. We aim at the solution of the inconsistency of experimental data with precision measurements of the branching ratio and $m_{\pi\pi}$ invariant mass distribution.

The preliminary KLOE measurement of the ratio of branching ratios $\Gamma(\eta \rightarrow \pi^+\pi^-\gamma)/\Gamma(\eta \rightarrow \pi^+\pi^-\pi^0) = 0.201 \pm 0.0006_{\text{stat} \oplus \text{syst}}$ is in agreement with the old results from refs. [21, 22] while significantly differs from the recent CLEO results, as compared in table III.

6. – Measurement of the $\eta \rightarrow 3\pi^0$ slope parameter α

Using a clean sample of $\eta \rightarrow \pi^0\pi^0\pi^0$ decays we have measured the Dalitz Plot slope parameter obtaining $\alpha = 0.0301 \pm 0.0035(\text{stat})_{-0.0035}^{+0.0022}(\text{syst})$ [24] in agreement with other recent results of comparable precision. The above value is also consistent with the one obtained from the KLOE study of the $\eta \rightarrow \pi^+\pi^-\pi^0$ decay [25] using the theoretical correlations between the two decay modes. Our α measurement confirms the inadequacy of simple NLO ChPT computations and the need to take into account higher-order corrections.

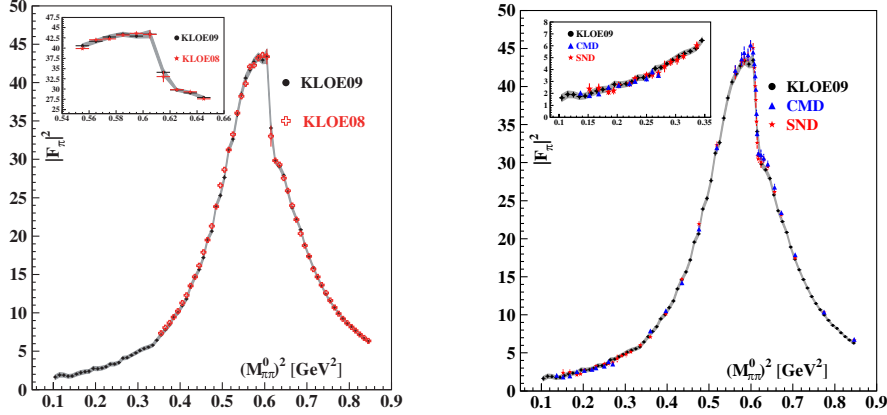


Fig. 4. – Pion form factor $|F_\pi|^2$ obtained in the present analysis (KLOE09) compared with the previous KLOE result (left) and results from the CMD and SND experiments (right). KLOE09 data points have statistical error attached, the superimposed band gives the statistical and systematic uncertainty (added in quadrature). Errors on KLOE08, CMD2 and SND points contain the combined statistical and systematic uncertainty.

7. – The measurement of the hadronic cross section

The published KLOE measurements [26,27] of the hadronic cross section for the process $e^+e^- \rightarrow \pi^+\pi^-$ were based on initial-state-radiation (ISR) events with photon emitted at small angle, resulting in kinematical suppression of events with $M_{\pi\pi}^2 < 0.35 \text{ GeV}^2$. To access the two-pion threshold, a new analysis is performed requiring events with photon at large polar angles ($50^\circ < \theta_\gamma < 130^\circ$), in the same angular region of the pions. The drawback of such acceptance cuts is a reduction in statistics of about a factor of five, as well as an increase of events with final-state-radiation (FSR) and from ϕ radiative decays. The uncertainty on the model dependence of the ϕ radiative decays to the scalars $f_0(980)$ and $f_0(600)$ together with $\phi \rightarrow \rho\pi \rightarrow (\pi\gamma)\pi$ has a strong impact on the measurement [28]. For this reason, the present analysis uses the data taken by the KLOE experiment in 2006 at a value of $\sqrt{s} = 1 \text{ GeV}$, about $5 \times \Gamma(\phi)$ outside the narrow peak of the ϕ resonance. This reduces the effect due to contributions from $f_0\gamma$ and $\rho\pi$ decays of the ϕ -meson to a relative amount of 1%. The radiative differential cross section is obtained subtracting the residual background events and dividing by the selection efficiencies and the integrated luminosity.

The total cross section $\sigma_{\pi\pi}$ is obtained using [29]: $s \cdot \frac{d\sigma_{\pi\pi\gamma\text{ISR}}}{dM_{\pi\pi}^2} = \sigma_{\pi\pi}(M_{\pi\pi}^2) H(M_{\pi\pi}^2, s)$, where H is the radiator function describing the photon emission in the initial state. This formula neglects FSR terms, which are however properly taken into account in the analysis. From $\sigma_{\pi\pi}$, the squared modulus of the pion form factor $|F_\pi|^2$ can be derived. Figure 4 shows $|F_\pi|^2$ as a function of $(M_{\pi\pi})^2$ for the new KLOE measurement (KLOE09) compared with the previous KLOE publication (KLOE08) and with results from CMD-2 [30,31] and SND [32] experiments at the Novosibirsk collider. On the ρ -meson peak and above, the new analysis confirms KLOE08 data being lower than the Novosibirsk results, while below the ρ -peak the three experiments are in agreement.

The cross section, corrected for α_{em} running and inclusive of FSR, is used to determine the dipion contribution to the muon anomalous magnetic moment, $\Delta a_{\mu}^{\pi\pi}$:

$$\Delta a_{\mu}^{\pi\pi}((0.1-0.85) \text{ GeV}^2) = (478.5 \pm 2.0_{\text{stat}} \pm 4.8_{\text{exp}} \pm 2.9_{\text{theo}}) \cdot 10^{-10}.$$

The evaluation of $\Delta a_{\mu}^{\pi\pi}$ in the range between 0.35 and 0.85 GeV^2 allows the comparison of the result obtained in this new analysis:

$\Delta a_{\mu}^{\pi\pi} = 376.6 \pm 0.9_{\text{stat}} \pm 2.4_{\text{exp}} \pm 2.1_{\text{theo}}$ with the previously published result by KLOE [27]: $\Delta a_{\mu}^{\pi\pi} = 379.6 \pm 0.4_{\text{stat}} \pm 2.4_{\text{exp}} \pm 2.2_{\text{theo}}$, showing that these two independent analyses provide fully consistent contributions to the muon anomaly.

8. – KLOE-2

Recently the interaction region of DAΦNE accelerator has been modified allowing for a new beam-crossing scheme operating at larger crossing angle and reduced beam size in the interaction region. These modifications will allow for an increase of the luminosity by a factor 3-4. The KLOE-2 Collaboration is preparing the KLOE detector for the new runs at upgraded DAΦNE machine: e^+e^- taggers for $\gamma\gamma$ physics will be inserted first, then another upgrade with new inner tracker and small angle calorimeters will take place. After the upgrades KLOE-2 can cover the physics program presented in [33] improving on systematics, thanks to the better detector, and on statistics thanks to an integrated luminosity $\geq 20 \text{ fb}^{-1}$.

REFERENCES

- [1] BOSSI F., DE LUCIA E., LEE-FRANZINI J., MISCETTI S., PALUTAN M. and KLOE COLLABORATION, *Riv. Nuovo Cimento*, **31** (2008) 531.
- [2] AMBROSINO F. *et al.*, *Phys. Lett. B*, **634** (2006) 148.
- [3] AMBROSINO F. *et al.*, *Eur. Phys. J. C*, **49** (2007) 473.
- [4] ALOISIO A. *et al.*, *Phys. Lett. B*, **681** (2009) 5.
- [5] ISIDORI G. *et al.*, *JHEP*, **05** (2006) 049.
- [6] ACHASOV N. N. and KISELEV V., *Phys. Rev. D*, **68** (2003) 014006.
- [7] ALOISIO A. *et al.*, *Phys. Lett. B*, **679** (2009) 10.
- [8] CAPRIOTTI D. on Behalf of KLOE COLLABORATION, *Nuovo Cimento C*, **31** (2008) 415.
- [9] AMBROSINO F. *et al.*, *Phys. Lett. B*, **648** (2007) 267.
- [10] AMBROSINO F. *et al.*, *JHEP*, **07** (2009) 105.
- [11] ROSNER J. L., *Phys. Rev. D*, **27** (1983) 1101.
- [12] AMSLER C. *et al.*, *Phys. Lett. B*, **667** (2008) 1.
- [13] AMBROSINO F. *et al.*, *Phys. Lett. B*, **669** (2008) 223.
- [14] LANDSBERG L. G., *Phys. Rep.*, **128** (1985) 301.
- [15] GAO D.-N., *Mod. Phys. Lett. A*, **17** (2002) 1583.
- [16] AMBROSINO F. *et al.*, *Phys. Lett. B*, **675** (2009) 283.
- [17] ADLER S. L., *Phys. Rev.*, **177** (1969) 2426.
- [18] HOLSTEIN B. R., *Phys. Scripta*, **T99** (2002) 55.
- [19] BENAYOUN M. *et al.*, *Eur. Phys. J. C*, **31** (2003) 525.
- [20] BORASOY B. and NISSLER R., *Nucl. Phys. A*, **740** (2004) 362.
- [21] GORMLEY *et al.*, *Phys. Rev. D*, **2** (1970) 501.
- [22] LAYTER *et al.*, *Phys. Rev. D*, **7** (1973) 2565.
- [23] BORASOY B. and NISSLER R., arXiv:0705.0954[hep-ph] (2007).
- [24] AMBROSINO F. *et al.*, arXiv:1004.1319 (2010).
- [25] AMBROSINO F. *et al.*, *JHEP*, **05** (2008) 006.

- [26] ALOISIO A. *et al.*, *Phys. Lett. B*, **606** (2005) 12.
- [27] AMBROSINO F. *et al.*, *Phys. Lett. B*, **670** (2009) 285.
- [28] LEONE D., PhD thesis at Karlsruhe University, KA-IEKP-7-2007.
- [29] BINNER S., KÜHN J. H. and MELNIKOV K., *Phys. Lett. B*, **459** (1999) 279.
- [30] AKHMETSHIN R. R. *et al.*, *Phys. Lett. B*, **648** (2007) 28.
- [31] AKHMETSHIN R. R. *et al.*, *JETP Lett.*, **84** (2006) 413.
- [32] ACHASOV M. N. *et al.*, *J. Exp. Theor. Phys.*, **103** (2006) 380.
- [33] BECK R. *et al.*, <http://www.lnf.infn.it/lnfadmin/direzione/KLOE2-LoI.pdf> (2006).

Recent results from BESIII

JIAXU ZUO(*) for BESIII COLLABORATION

Institute of High Energy Physics, Chinese Academy of Sciences - Beijing 100049, China

(ricevuto il 14 Settembre 2010; pubblicato online l'11 Gennaio 2011)

Summary. — The BESIII experiment, running at 2–4.6 GeV center-of-mass energy, has collected the largest ψ' and J/ψ samples. New results using the data collected by the BESIII detector are presented, which include the measurement of the spin singlet state $h_c(1P)$ from ψ' decays, the χ_{c0} and χ_{c2} decays into $\pi^0\pi^0$ and $\eta\eta$ and the χ_{cJ} decays to vector meson pairs ($\omega\omega$, $\phi\phi$, $\omega\phi$). We also confirmed the $p\bar{p}$ threshold enhancement, which was observed in $J/\psi \rightarrow \gamma p\bar{p}$ at BESII, from the decays of $\psi' \rightarrow \pi^+\pi^- J/\psi$ ($J/\psi \rightarrow \gamma p\bar{p}$) and $J/\psi \rightarrow \gamma p\bar{p}$, respectively. The X(1835) is confirmed too in $J/\psi \rightarrow \gamma\eta'\pi^+\pi^-$.

PACS 13.25.Gv – Decays of J/ψ , Υ , and other quarkonia.

PACS 14.40.Pq – Heavy quarkonia.

1. – Introduction

The upgraded Beijing Electron Positron Collider (BEPCII) is an electron-positron accelerator with separate storage rings for each beam. It is designed to run with 93 bunches for a maximum current of 910 mA per beam. The center-of-mass energy E_{CM} range of the e^+e^- collisions is 2.0–4.6 GeV. The designed luminosity is $1 \times 10^{33} \text{ cm}^{-2} \text{ s}^{-1}$ for $E_{\text{CM}} = M[\psi(3770)]$ and $0.6 \times 10^{33} \text{ cm}^{-2} \text{ s}^{-1}$ near $M[J/\psi]$ and $E_{\text{CM}} > 4 \text{ GeV}$.

The BESIII [1] detector is designed to study the τ -charm physics [2]. The cylindrical BESIII is composed of a helium-gas based drift chamber (MDC), a Time-of-Flight (TOF) system, a CsI(Tl) Electro-Magnetic Calorimeter (EMC) and a RPC-based muon chamber (MUC) with a superconducting magnet providing 1.0 T magnetic field in the central region of BESIII. The nominal detector acceptance is 93% of 4π . The expected charged particle momentum resolution and photon energy resolution are 0.4% and 2.5% at 1 GeV, respectively. The photon energy resolution at BESIII is much better than that at BESII and comparable to those at CLEO [3] and Crystal Ball [4]. Precise measurement of energies of photons enables the BESIII experiment to study physics involving photons, π^0 and η with high accuracy. The read out system of EMC is based on FADC. To reduce incoherent noise such as beam gas and electronic noise and improve the energy resolution, a time information is recorded by counting the timing step number in FADC with a precision of 50 ns besides the read out of energy information [5].

(*) E-mail: zuojx2010@gmail.com

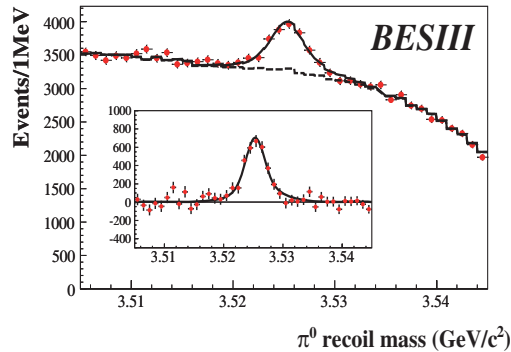


Fig. 1. – The π^0 recoil mass spectrum and fit for the $E1$ -tagged analysis of $\psi' \rightarrow \pi^0 h_c, h_c \rightarrow \gamma \eta_c$. Fits are shown as solid lines, background as dashed lines. The insets show the background-subtracted spectra.

Since July 19, 2008, the first collision happened, the BESIII has collected 106M ψ' events and 226M J/ψ events which are the largest ψ' and J/ψ data samples. A continuum sample of 42.6 pb^{-1} at 3.65 GeV is also accumulated.

The optimization of the event selection and the estimation of physics backgrounds are performed through Monte Carlo simulations. The GEANT4-based simulation software BOOST [6] includes the geometric and material description of the BESIII detectors, the detector response and digitization models, as well as the tracking of the detector running conditions and performance. The production of the ψ' and J/ψ resonances are simulated by the Monte Carlo event generator KKMC [7], while the decays are generated by EvtGen [8] for known decay modes with branching ratios being set to the PDG [9] world average values, and by Lundcharm [10] for the remaining unknown decays. The analysis is performed in the framework of the BESIII Offline Software System (BOSS) [11] which takes care of the detector calibration, event reconstruction and data storage.

With such large data samples, the J/ψ and ψ' decay modes can be measured much more precisely than before. Using J/ψ decays, one can study light hadron spectroscopy and search for new hadronic states. With BESIII, the CKM matrix elements V_{cs} , V_{cd} and V_{us} will be extracted with an expected smaller systematic error. The $D - \bar{D}$ mixing measurement and searching for CP -violation will be possible.

2. – h_c measurement

Although the charmonium family of mesons composed of a charmed quark and its own antiquark ($c\bar{c}$) has been studied for many years, knowledge is sparse on the singlet state $h_c(^1P_1)$. Early predictions for the properties of the h_c are found in refs. [12, 13]. Many theoretical methods are used to study its branching ratios [14-16] and other physics [17]. The CLEO Collaboration first observed the h_c in the cascade process $\psi' \rightarrow \pi^0 h_c, h_c \rightarrow \gamma \eta_c$ in both inclusive and exclusive measurements [18-20]. The E835 experiment [21] scanned antiproton energy and observed $p\bar{p} \rightarrow h_c \rightarrow \gamma \eta_c$. We present the measurements of h_c from $\psi' \rightarrow \pi^0 h_c, h_c \rightarrow \gamma \eta_c$ below.

Figure 1 shows the π^0 recoil mass spectrum and fit for the $E1$ -tagged analysis of $\psi' \rightarrow \pi^0 h_c, h_c \rightarrow \gamma \eta_c$. In $E1$ -tagged selection, we require one photon in the energy range 465–535 MeV. The h_c signals are described by Breit-Wigner functions convoluted

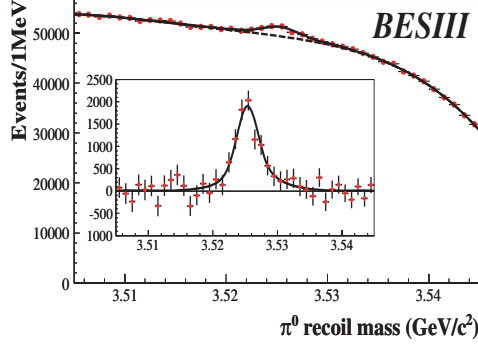


Fig. 2. – The π^0 recoil mass spectrum and fit for the inclusive analysis of $\psi' \rightarrow \pi^0 h_c$. Fits are shown as solid lines, background as dashed lines. The insets show the background-subtracted spectra.

with the instrument resolution function obtained by fitting E1-tagged h_c MC simulation. The fit results are $N^{E1} = 3679 \pm 319$, $M(h_c) = 3525.40 \pm 0.13 \pm 0.18 \text{ MeV}/c^2$, and $\Gamma(h_c) = 0.73 \pm 0.45 \pm 0.28 \text{ MeV}$ with $\chi^2/d.o.f = 33.5/36.0$ (p value 58.8%). The signal significance is 18.6σ for the h_c signal.

In fig. 2's fit, the mass and width of h_c are fixed to the values obtained from the E1-photon tagged analysis. The background is parameterized by a 4th-order Chebychev polynomial. The fit result is $N^{\text{tot}} = 10353 \pm 1097$ with $\chi^2/d.o.f = 24.5/34$. The signal significance is 9.5σ .

Using those fit results, we find $\mathcal{B}(\psi' \rightarrow \pi^0 h_c) = (8.4 \pm 1.3 \pm 1.0) \times 10^{-4}$, $\mathcal{B}(\psi' \rightarrow \pi^0 h_c) \times \mathcal{B}(h_c \rightarrow \gamma \eta_c) = (4.58 \pm 0.40 \pm 0.50) \times 10^{-4}$, and $\mathcal{B}(h_c \rightarrow \gamma \eta_c) = (54.3 \pm 6.7 \pm 5.2)\%$. Our measurements of $\mathcal{B}(\psi' \rightarrow \pi^0 h_c)$ and $\mathcal{B}(h_c \rightarrow \gamma \eta_c)$ and information about the h_c width are the first experimental results for these quantities. The determinations of $M(h_c)$ and $\mathcal{B}(\psi' \rightarrow \pi^0 h_c) \times \mathcal{B}(h_c \rightarrow \gamma \eta_c)$ are consistent with published CLEO results [19] and of comparable precision. The analysis results have been published [22].

3. – Confirmation of $p\bar{p}$ mass threshold enhancement and $X(1835)$

An anomalously strong $p\bar{p}$ mass threshold enhancement was observed by the BESII experiment in the radiative decay process $J/\psi \rightarrow \gamma p\bar{p}$ [23]. An interesting feature of this enhancement is that corresponding structures are not observed in near-threshold $p\bar{p}$ cross section measurements [24-28]. These non-observations disfavor the attribution of the mass-threshold enhancement to the pure effects of $p\bar{p}$ final state interactions (FSI). This observation stimulated a number of theoretical speculations [29-32]. One of these is the intriguing suggestion that it is an example of a $p\bar{p}$ bound state [33], sometimes called baryonium [34]. A resonance, the $X(1835)$, was observed in the $\pi^+\pi^-\eta'$ invariant-mass spectrum with a statistical significance of 7.7σ at BESII [35]. The mass and width of $X(1835)$ are not compatible with any known meson resonance. With BESIII's larger data samples, it is important to confirm those measurements. The improved measurement will be useful to understand the truth of the threshold enhancement and $X(1835)$.

After the selection [36], we get the similar characterize of the $p\bar{p}$ mass threshold enhancement. We fit it with an acceptance weighted Breit-Wigner (BW) function of the form $BW(M) \propto \frac{q^{2L+1} k^3}{(M^2 - M_0^2)^2 + M_0^2 \Gamma^2}$, where Γ is a constant (determined from fit), q is the

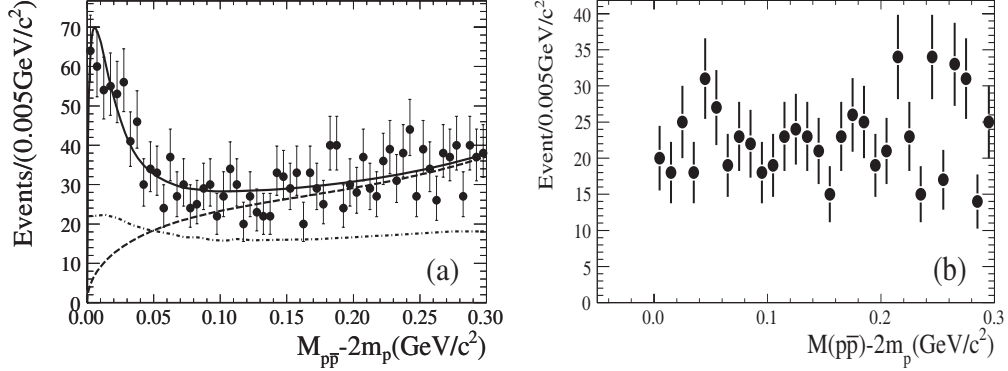


Fig. 3. – (a) The $p\bar{p}$ invariant mass spectrum for the $\psi' \rightarrow \pi^+\pi^- J/\psi (J/\psi \rightarrow \gamma p\bar{p})$ after final event selection. The solid curve is the fit result; the dashed curve shows the fitted background function, and the dash-dotted curve indicates how the acceptance varies with $p\bar{p}$ invariant mass. (b) The $p\bar{p}$ invariant mass spectrum in the threshold region for the selected $\psi' \rightarrow \gamma p\bar{p}$ candidate events with ψ' data.

proton momentum in the $p\bar{p}$ rest-frame, L is the $p\bar{p}$ orbital angular momentum, and k is the photon momentum, together with the background shape. Here, the background shape is described by the function of the form $f_{bkg}(\delta) = N(\delta^{1/2} + a_1\delta^{3/2} + a_2\delta^{5/2})$, where $\delta = M_{p\bar{p}} - 2m_p$ and the shape parameters a_1 and a_2 are determined from a fit to selected $\gamma p\bar{p}$ events for $\psi' \rightarrow \pi^+\pi^- J/\psi (J/\psi \rightarrow \gamma p\bar{p})$ phase-space MC sample. The mass spectrum fitting with S -wave ($L = 0$) in the threshold mass region of $M_{p\bar{p}} - 2m_p < 0.3 \text{ GeV}/c^2$ is shown in fig. 3(a), and it yields a peak mass of $M = 1861^{+6}_{-13} \text{ (stat)}_{-26} \text{ (syst)} \text{ MeV}/c^2$ and a width of $\Gamma < 38 \text{ MeV}/c^2$ at the 90% CL. In the study of $\psi' \rightarrow \gamma p\bar{p}$ with ψ' data, there is no significant narrow threshold enhancement as shown in fig. 3(b). It indicates that the strong $p\bar{p}$ threshold enhancement observed in J/ψ radiative decay is disfavored for the interpretation of pure final state interactions (FSI).

For the $J/\psi \rightarrow \gamma\pi^+\pi^-\eta' (\eta' \rightarrow \gamma\rho)$ channel, the $\pi^+\pi^-\eta'$ invariant-mass spectrum for the selected events is shown in fig. 4(a) and significant peak at $M \sim 1835 \text{ MeV}/c^2$ is observed. If it is fitted with one resonance plus a polynomial background shape, the statistical significance of the resonance is about 9σ as shown in fig. 4(b). In the $J/\psi \rightarrow \gamma\pi^+\pi^-\eta' (\eta' \rightarrow \pi^+\pi^-\eta, \eta \rightarrow \gamma\gamma)$ mode, the $\pi^+\pi^-\eta'$ invariant-mass spectrum for the selected events is shown in fig. 5(a) and significant peak at $M \sim 1835 \text{ MeV}/c^2$ is also observed. If it is fitted with one resonance plus a polynomial background shape, the statistical significance of the resonance is about 18σ as shown in fig. 5(b).

Figure 6 shows the $\pi^+\pi^-\eta'$ invariant-mass spectrum for the combined $J/\psi \rightarrow \gamma\pi^+\pi^-\eta' (\eta' \rightarrow \gamma\rho)$ and $J/\psi \rightarrow \gamma\pi^+\pi^-\eta' (\eta' \rightarrow \pi^+\pi^-\eta)$. It is fitted with a Breit-Wigner function convolved with a Gaussian mass resolution function. The mass and width obtained from the fit are $M = 1842.4 \pm 2.8 \text{ (stat)} \text{ MeV}/c^2$ and $\Gamma = 99.2 \pm 9.2 \text{ (stat)} \text{ MeV}/c^2$ with a statistical significance of 21σ . These values are consistent with the published BESII results [35].

4. – χ_{cJ} to two vector meson decays

In the quark model, the χ_{cJ} ($J = 0, 1, 2$) mesons are $L = 1 c\bar{c}$ states. The measurements of the branching fraction of the hadronic χ_{cJ} decay channels are mandatory to

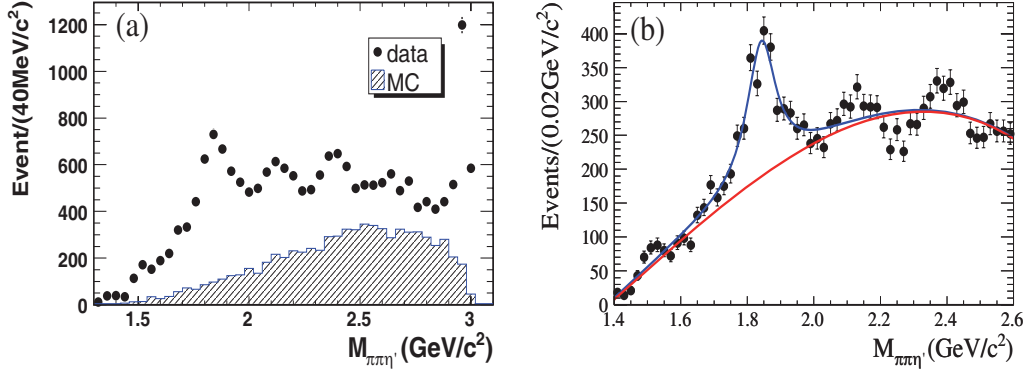


Fig. 4. – Candidate events after final event selection for $J/\psi \rightarrow \gamma\pi^+\pi^-\eta'$ ($\eta' \rightarrow \gamma\rho$). (a) Invariant mass spectrum of $\pi^+\pi^-\eta'$ after final selection, the solid circles are data and the shade histogram is from $J/\psi \rightarrow \gamma\pi^+\pi^-\eta'$ phase space MC events (with arbitrary normalization). (b) Mass spectrum fitting with one resonance and polynomial background shape.

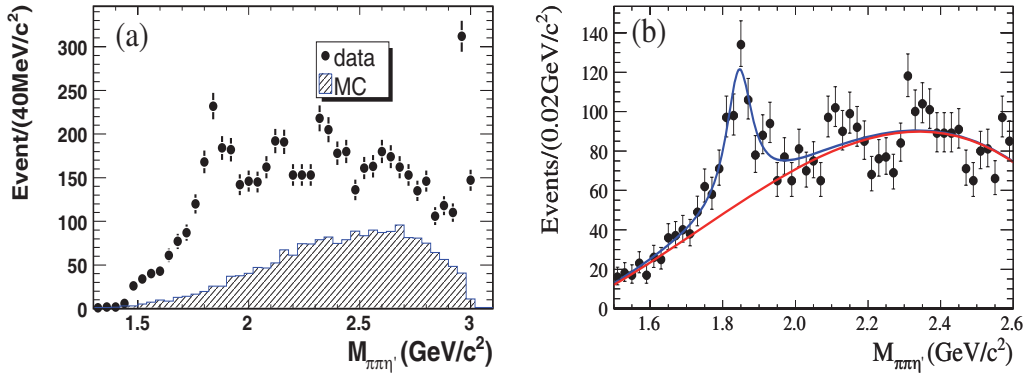


Fig. 5. – Candidate events after final event selection for $J/\psi \rightarrow \gamma\pi^+\pi^-\eta'$ ($\eta' \rightarrow \pi^+\pi^-\eta$, $\eta \rightarrow \gamma\gamma$). (a) Invariant mass spectrum of $\pi^+\pi^-\eta'$ after final selection, the solid circles are data and the shade histogram is from $J/\psi \rightarrow \gamma\pi^+\pi^-\eta'$ phase space MC events (with arbitrary normalization). (b) Mass spectrum fitting with one resonance and polynomial background shape.

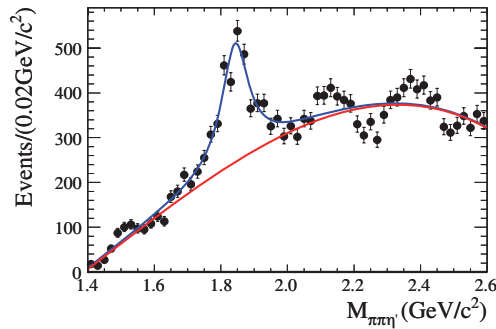


Fig. 6. – The $\pi^+\pi^-\eta'$ invariant-mass spectrum for the combined $J/\psi \rightarrow \gamma\pi^+\pi^-\eta'$ ($\eta' \rightarrow \gamma\rho$) and $J/\psi \rightarrow \gamma\pi^+\pi^-\eta'$ ($\eta' \rightarrow \pi^+\pi^-\eta$). It is fitted with a Breit-Wigner (BW) function convolved with a Gaussian mass resolution function.

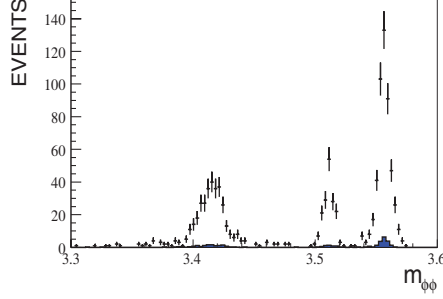


Fig. 7. – Invariant mass of $\phi\phi$ final state.

further test the Color Octet Model (COM) in P -wave charmonium decays. Some studies [37] pointed out that the decay of $\chi_{c0,2}$ into vector meson pairs (VV), pseudoscalars pairs (PP), and scalar pairs (SS) can be investigated in a general factorization scheme.

Branching fractions are only published for $\chi_{cJ} \rightarrow \phi\phi$ and $\chi_{cJ} \rightarrow \omega\omega$ according to the BESII's measurements [38] and [39]. Due to imperfect detection resolution and low statistics, we just report the observation of $\chi_{c0,2}$ at that time, hard to judge that there is any χ_{c1} signal in $\phi\phi$ and $\omega\omega$ final state. For the doubly OZI decay mode, $\chi_{cJ} \rightarrow \omega\phi$, no any measurement is available before. With the large ψ' data sample taken at BESIII, we observed the clear $\chi_{c0,1,2} \rightarrow \omega\omega, \phi\phi$. Particularly, the χ_{c1} signal is observed for the first time. Figures 7 and 8 show the $M_{\phi\phi}$ and $M_{\omega\omega}$ distribution, respectively. Clear χ_{cJ} signal can be seen. For doubly OZI decay, $\chi_{cJ} \rightarrow \omega\phi$. We also observed the clear $\chi_{c0,1}$ signal. It is shown in fig. 9.

5. – χ_{c0} and χ_{c2} decay into $\pi^0\pi^0$ and $\eta\eta$ measurement

We also study the $\chi_{c0,2}$ decay to $\pi^0\pi^0$ and $\eta\eta$ final states. Those measurement provides information on both the χ_{cJ} parents and their pseudo-scalar daughters, as well as a better understanding of the decay mechanisms of χ_{cJ} mesons [40].

The radiative photon energy spectrum of $\chi_{cJ} \rightarrow \pi^0\pi^0$ candidates, shown in fig. 10, is fitted using an unbinned maximum likelihood fit in the range from 0.06 GeV to 0.36 GeV.

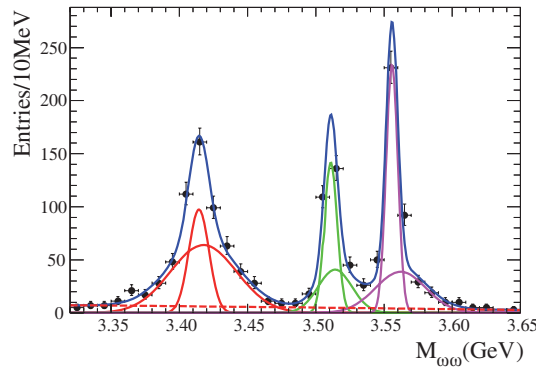


Fig. 8. – Invariant mass of $\omega\omega$ final state.

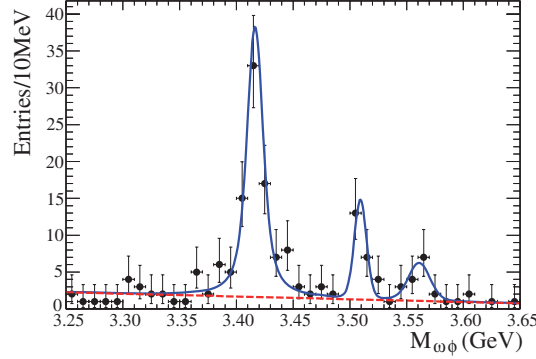


Fig. 9. – Invariant mass of $\omega\phi$ final state.

The shapes of the χ_{c0} and χ_{c2} are obtained from Monte Carlo simulation and the masses and widths of χ_{cJ} are fixed to their PDG values [9]. A 2nd-order Chebychev polynomial is used to describe the backgrounds, including those found in the inclusive MC study and the continuum. The fit gives a χ_{c0} signal yield of 17443 ± 167 events and a χ_{c2} signal yield of 4516 ± 80 events. The selection efficiency from Monte Carlo simulation of $\psi' \rightarrow \gamma\chi_{c0}(\chi_{c0} \rightarrow \pi^0\pi^0, \pi^0 \rightarrow \gamma\gamma)$ is $(55.6 \pm 0.2)\%$ and the efficiency of $\psi' \rightarrow \gamma\chi_{c2}(\chi_{c2} \rightarrow \pi^0\pi^0, \pi^0 \rightarrow \gamma\gamma)$ is $(59.8 \pm 0.2)\%$. The branching fractions are then determined to be $Br(\chi_{c0} \rightarrow \pi^0\pi^0) = (3.23 \pm 0.03 \pm 0.23 \pm 0.14) \times 10^{-3}$, $Br(\chi_{c2} \rightarrow \pi^0\pi^0) = (0.88 \pm 0.02 \pm 0.06 \pm 0.04) \times 10^{-3}$.

The fit to the radiative photon energy spectrum of $\chi_{cJ} \rightarrow \eta\eta$ candidates, shown in fig. 11, gives a χ_{c0} signal yield of 2132 ± 60 events and a χ_{c2} signal yield of 386 ± 25 events. The selection efficiency is $40.3 \pm 0.2\%$ and $43.9 \pm 0.2\%$ for $\chi_{c0} \rightarrow \eta\eta$ and $\chi_{c2} \rightarrow \eta\eta$, respectively. The branching fractions are $Br(\chi_{c0} \rightarrow \eta\eta) = (3.44 \pm 0.10 \pm 0.24 \pm 0.13) \times 10^{-3}$, $Br(\chi_{c2} \rightarrow \eta\eta) = (0.65 \pm 0.04 \pm 0.05 \pm 0.03) \times 10^{-3}$. These analysis results have been published [41].

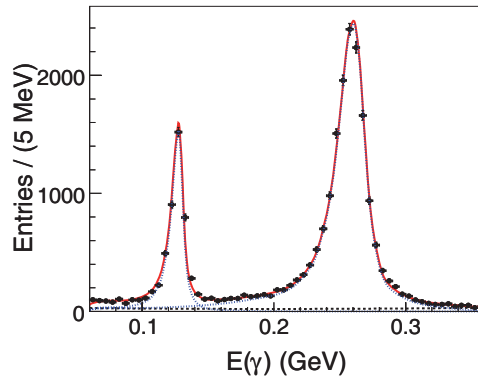


Fig. 10. – The radiative photon energy spectrum of selected $\chi_c \rightarrow \pi^0\pi^0$ events. Dots with error bars are data. The solid curve is the result of a fit described in the text. The dotted curves are the χ_{cJ} signals. The dashed curve is the background polynomial.

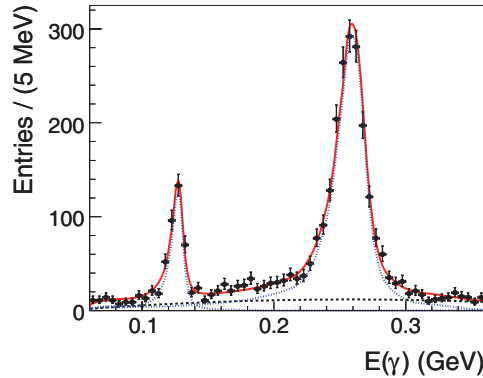


Fig. 11. – The radiative photon energy spectrum of selected $\chi_c \rightarrow \eta\eta$ events. Dots with error bars are data. The solid curve is the result of a fit described in the text. The dotted curves are the χ_{cJ} signals. The dashed curve is the background polynomial.

6. – Conclusions

With the largest sample of ψ' and J/ψ in the BESIII detector, many measurements are reported. We have performed many studies on h_c and χ_c . The $\Gamma(h_c)$, $\mathcal{B}(\psi' \rightarrow \pi^0 h_c)$ and $\mathcal{B}(h_c \rightarrow \gamma\eta_c)$ are measured for the first time. The branching fractions of $\chi_{c0,2} \rightarrow \pi^0\pi^0$ and $\chi_{c0,2} \rightarrow \eta\eta$ are measured with improved precision. We also observed the clear $\chi_{c0,1,2} \rightarrow \omega\omega, \phi\phi$. Particularly, the χ_{c1} signal and the doubly OZI decay mode, $\chi_{cJ} \rightarrow \omega\phi$, are firstly observed. The $p\bar{p}$ threshold enhancement and $X(1835)$ are studied. These results are consistent with the published BESII results.

A new facility for physics in the τ -charm region has become operational. With the running of BEPCII/BESIII, more exciting results are coming.

* * *

I would like to thank my colleagues of BESIII Collaboration. I would also like to thank the organizer for warm hospitality at La Thuile.

REFERENCES

- [1] ABLIKIM M. *et al.* (BESIII COLLABORATION), *Nucl. Instrum. Methods A*, **614** (2010) 3.
- [2] CHAO K. T. and WANG Y. F. (Editors), *Physics at BESIII*, *Int. J. Mod. Phys. A*, **24** (2009) No. 1 supp.
- [3] VIEHHAUSSER G. *et al.*, *Nucl. Instrum. Methods A*, **462** (2001) 146.
- [4] OREGLIA M. *et al.*, *Phys. Rev. D*, **25** (1982) 2559.
- [5] SHAN LI-MIN *et al.*, *HEP & NP*, **30(11)** (2006) 1091 (in Chinese).
- [6] DENG Z. Y. *et al.*, *Chin. Phys. C*, **30** (2006) 371.
- [7] JADACH S., WARD B. F. L. and WAS Z., *Comput. Phys. Commun.*, **130** (2000) 260; *Phys. Rev. D*, **63** (2001) 113009.
- [8] PING R. G. *et al.*, *Chin. Phys. C*, **32** (2008) 599.
- [9] AMSLER C. *et al.* (PARTICLE DATA GROUP), *Phys. Lett. B*, **667** (2008) 1.
- [10] CHEN J. C. *et al.*, *Phys. Rev. D*, **62** (2000) 034003.
- [11] LI W.D and LIU H. M *et al.*, *The Offline Software for the BESIII Experiment, Proceedings of CHEP 2006*.

- [12] KUANG Y. P., TUAN S. F. and YAN T. M., *Phys. Rev. D*, **37** (1988) 1210.
- [13] KO P., *Phys. Rev. D*, **52** (1995) 1710.
- [14] KUANG Y. P., *Phys. Rev. D*, **65** (2002) 094024.
- [15] GODFREY S. and ROSNER J., *Phys. Rev. D*, **66** (2002) 014012.
- [16] DUDEK J. J., EDWARDS R. G. and RICHARDS D. G., *Phys. Rev. D*, **73** (2006) 074507.
- [17] See, for example, SWANSON E. S., *Phys. Rep.*, **429** (2006) 243 and references therein.
- [18] ROSNER J. L. *et al.* (CLEO COLLABORATION), *Phys. Rev. Lett.*, **95** (2005) 102003; RUBIN P. *et al.* (CLEO COLLABORATION), *Phys. Rev. D*, **72** (2005) 092004.
- [19] DOBBS S. *et al.* (CLEO COLLABORATION), *Phys. Rev. Lett.*, **101** (2008) 182003.
- [20] ADAMS G. S. *et al.* (CLEO COLLABORATION), *Phys. Rev. D*, **80** (2009) 051106.
- [21] ANDREOTTI M. *et al.* (E-835 COLLABORATION), *Phys. Rev. D*, **72** (2005) 032001.
- [22] ABLIKIM M. *et al.* (BES COLLABORATION), *Phys. Rev. Lett.*, **104** (2010) 132002.
- [23] BAI J. Z. *et al.* (BES COLLABORATION), *Phys. Rev. Lett.*, **91** (2003) 022001.
- [24] WANG M. Z. *et al.*, *Phys. Rev. Lett.*, **92** (2004) 131801.
- [25] JIN S., *Invited plenary talk at the XXXIIth International Conference on High Energy Physics(ICHEP04), Beijing, 2004.*
- [26] ABLIKIM M. *et al.* (BES COLLABORATION), *Phys. Rev. Lett.*, **99** (2007) 011802.
- [27] ATHAR S. B. *et al.* (CLEO COLLABORATION), *Phys. Rev. D*, **73** (2006) 032001.
- [28] ABLIKIM M. *et al.* (BES COLLABORATION), *Eur. Phys. J. C*, **53** (2008) 15.
- [29] DATTA A. and O'DONNELL P. J., *Phys. Lett. B*, **567** (2003) 273; YAN M. L. *et al.*, *Phys. Rev. D*, **72** (2005) 034027; LOISEAU B. and WYCECH S., *Phys. Rev. C*, **72** (2005) 011001.
- [30] ELLIS J., FRISHMAN Y. and KARLINER M., *Phys. Lett. B*, **566** (2003) 201; ROSNER J. L., *Phys. Rev. D*, **68** (2003) 014004.
- [31] GAO C. S. and ZHU S. L., *Commun. Theor. Phys.*, **42** (2004) 844, hep-ph/0308205.
- [32] DING G. J. and YAN M. L., *Phys. Rev. C*, **72** (2005) 015208.
- [33] KLEMP T. E. *et al.*, *Phys. Rep.*, **368** (2002) 119; RICHARD J.-M., *Nucl. Phys. Proc. Suppl.*, **86** (2001) 361.
- [34] SHAPIRO I. S., *Phys. Rep.*, **35** (1978) 129; DOVER C. B. and GOLDBABER M., *Phys. Rev. D*, **15** (1977) 1997.
- [35] ABLIKIM M. *et al.* (BES COLLABORATION), *Phys. Rev. Lett.*, **95** (2005) 262001.
- [36] ABLIKIM M. *et al.* (BESIII COLLABORATION), *Chin. Phys. C*, **34** (2010) 4, arXiv:1001.5328.
- [37] ZHAO Q., *Phys. Lett. B*, **659** (2008) 221.
- [38] ABLIKIM M. *et al.* (BES COLLABORATION), *Phys. Lett. B*, **642** (2006) 197.
- [39] ABLIKIM M. *et al.* (BES COLLABORATION), *Phys. Lett. B*, **630** (2005) 7.
- [40] ZHAO Q., *Phys. Rev. D*, **72** (2005) 074001.
- [41] ABLIKIM M. *et al.* (BES COLLABORATION), *Phys. Rev. D*, **81** (2010) 052005.

SESSION IV - FLAVOUR PHYSICS, CP VIOLATION AND RARE DECAYS

<i>Jose Benitez</i>	Recent results on flavour physics from BaBar
<i>Kurtis Nishimura</i>	Rare decays at the B factories
<i>Denis Bernard</i>	QCD and hadronic interactions with initial-state radiation at B-factories
<i>Ulrich Nierste</i>	Flavour physics within and beyond the Standard Model
<i>Ulrich Kerzel</i>	Early data from the LHCb experiment
<i>Evelina Marinova</i>	K rare decays with NA62
<i>Barbara Sciascia</i>	Kaon physics with KLOE
<i>Claire M. Tarbert</i>	Recent charmonium results from CLEO-c

Recent results on flavor physics from BaBar

J. BENITEZ on behalf of the BABAR COLLABORATION

SLAC National Accelerator Laboratory - Stanford, CA, USA

(ricevuto il 14 Settembre 2010; pubblicato online l'11 Gennaio 2011)

Summary. — We report an update to our previous measurement of the CKM element $|V_{ub}|$ using exclusive $B \rightarrow \pi \ell \nu$ decays. In the charm sector we have performed a measurement of f_{D_s} using $D_s^+ \rightarrow \tau^+ \nu_\tau$ decays, we have measured the mixing parameter y_{CP} using the lifetime ratio $\frac{\langle \tau_{K\pi} \rangle}{\langle \tau_{hh} \rangle}$ in D^0 decays, and we have also searched for CP violation using T -odd correlations in D^0 decays to $K^+ K^- \pi^+ \pi^-$. Finally, in the tau sector we have performed a search for the lepton flavor violating decays $\tau^\pm \rightarrow e^\pm \gamma$ and $\tau^\pm \rightarrow \mu^\pm \gamma$.

PACS 11.30.Er – Charge conjugation, parity, time reversal, and other discrete symmetries.

PACS 12.15.Hh – Determination of Kobayashi-Maskawa matrix elements.

PACS 11.30.Fs – Global symmetries (*e.g.*, baryon number, lepton number).

1. – Introduction

The physics reach of the *BABAR* experiment encompasses a large part of the *flavor* sector of particle physics. The *BABAR* detector at the SLAC PEP-II asymmetric-energy e^+e^- collider collected approximately 500 fb^{-1} at center-of-mass (CM) energies near 10.58 GeV between 1999 and 2008. At this energy the production cross section for production of fermion-anti-fermion pairs $c\bar{c}$, $b\bar{b}$ and $\tau^+\tau^-$ is roughly the same and yields an event sample of about 600 million produced events of each type. These samples enable precise measurements of Cabibbo-Kobayashi-Maskawa (CKM) parameters, studies of charm meson properties, and searches for rare τ decays among other topics. This paper presents a summary of recent measurements in these areas from *BABAR*.

2. – Determination of $|V_{ub}|$ from $B \rightarrow \pi \ell \nu$ decays

The elements of the CKM quark-mixing matrix are fundamental parameters of the Standard Model (SM) of electroweak interactions. With the increasingly precise measurements of decay-time-dependent CP asymmetries in B -meson decays, in particular $\sin(2\beta)$ [1, 2], improved measurements of $|V_{ub}|$ and $|V_{cb}|$ will allow for more stringent

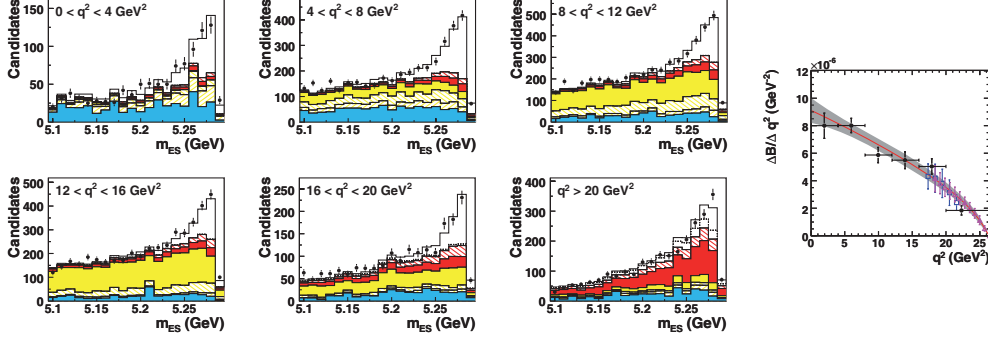


Fig. 1. – (Colour on-line) Left plots show the m_{ES} distributions in each q^2 bin for $B^0 \rightarrow \pi^- \ell^+ \nu$. The points show the data and the histograms show the fit and the different background contributions. The right-most plot shows the simultaneous fit to data (points) and to the FNAL/MILC lattice prediction (magenta, closed triangles). The LQCD results are rescaled according to the $|V_{ub}|$ value obtained from the fit.

experimental tests of the SM mechanism for CP violation [3]. The best method to determine $|V_{ub}|$ is to measure semileptonic decay rates for $B \rightarrow X_u \ell \nu$ (X_u refers to hadronic states without charm), which is proportional to $|V_{ub}|^2$. We have performed a study of four exclusive semileptonic decay modes, $B^0 \rightarrow \pi^- \ell^+ \nu$, $B^+ \rightarrow \pi^0 \ell^+ \nu$, $B^0 \rightarrow \rho^- \ell^+ \nu$, and $B^+ \rightarrow \rho^0 \ell^+ \nu$, and a determination of $|V_{ub}|$. Here ℓ refers to a charged lepton, either e^+ or μ^+ , and ν refers to the associated neutrino. Exclusive decays offer good kinematic constraints, and thus effective background suppression. This analysis represents an update of an earlier measurement [4] that was based on a significantly smaller data set. For the current analysis, the signal yields and background suppression have been improved, and the systematic uncertainties have been reduced through the use of improved reconstruction and signal extraction methods.

In the analysis of $B^0 \rightarrow \pi^- \ell^+ \nu$ we reconstruct the pion and lepton tracks, and determine the neutrino 4-momentum as the missing momentum in the event. A similar reconstruction is performed for the other channels. We then determine the signal yield as a function of q^2 by performing a two-dimensional fit in the variables m_{ES} and ΔE . ΔE is the difference between the reconstructed B energy and half the CM beam energy, and m_{ES} is the mass of the B candidate computed using the reconstructed 3-momentum and half the beam energy. The projections of the fit for $B^0 \rightarrow \pi^- \ell^+ \nu$ are shown in fig. 1. The fit is performed simultaneously to all channels while constraining $B^+ \rightarrow \pi^0 \ell^+ \nu$ using isospin symmetry. The $B^0 \rightarrow \rho^- \ell^+ \nu$ and $B^+ \rightarrow \rho^0 \ell^+ \nu$ modes help constrain the background. From the extracted signal yields the decay rate can be determined using the known total number B events produced and correcting for the reconstruction efficiency.

The decay rate for $B^0 \rightarrow \pi^- \ell^+ \nu$ depends on the momentum, q^2 , carried by the W^+ and takes the following formula in the SM:

$$(1) \quad \frac{d\Gamma(B^0 \rightarrow \pi^- \ell^+ \nu)}{dq^2 d \cos \theta_{W\ell}} = |V_{ub}|^2 \frac{G_F^2 p_\pi^3}{32\pi^3} \sin^2 \theta_{W\ell} |f_+(q^2)|^2,$$

where p_π is the momentum of the pion in the rest frame of the B meson and $\theta_{W\ell}$ is the angle of the charged-lepton momentum in the W rest frame with respect to the

direction of the W boost from the B rest frame. The q^2 -dependent form factor, $f_+(q^2)$, is calculated from Lattice QCD. Using this formula we convert the form factors into decay rates and require that they match the measured values as shown in fig. 1. From the conversion factor $|V_{ub}|$ is determined to be $(2.95 \pm 0.31) \times 10^{-3}$.

3. – Measurement of the branching fraction for $D_s^+ \rightarrow \tau^+ \nu_\tau$ and extraction of the decay constant f_{D_s}

The purely leptonic decays of the D_s^+ meson provide a clean probe of the pseudoscalar meson decay constant f_{D_s} , which describes the amplitude for the c and \bar{s} quarks to have zero spatial separation within the meson. In the SM these decays occur through a virtual W^+ boson which decays to a lepton pair, ignoring radiative processes, the total width is

$$(2) \quad \Gamma(D_s^+ \rightarrow \ell^+ \nu_\ell) = \frac{G_F^2}{8\pi} M_{D_s^+}^3 \left(\frac{m_\ell}{M_{D_s^+}} \right)^2 \left(1 - \frac{m_\ell^2}{M_{D_s^+}^2} \right)^2 |V_{cs}|^2 f_{D_s}^2,$$

where $M_{D_s^+}$ and m_ℓ are the D_s^+ and lepton masses, respectively, G_F is the Fermi coupling constant, $|V_{cs}|$ is the magnitude of the CKM matrix element that characterizes the coupling of the weak charged current to the c and \bar{s} quarks. In the context of the SM, predictions for meson decay constants can be obtained from QCD lattice calculations [5-9]. The most precise theoretical prediction for f_{D_s} is (241 ± 3) MeV [7]. This value is in slight disagreement with the current measurement of f_{D_s} [10]. It is important to validate the lattice QCD predictions through measurements of f_{D_s} as these computational methods are also used in other areas such as B meson decays. In addition, it is possible that physics beyond the SM can induce a difference between the theoretical prediction and the measured value.

The relatively large branching fraction for the τ^+ decay mode motivates the use of the decay sequence $D_s^+ \rightarrow \tau^+ \nu_\tau$, $\tau^+ \rightarrow e^+ \nu_e \bar{\nu}_\tau$ in this analysis. We use the well-known branching fraction $\mathcal{B}(D_s^+ \rightarrow K_s^0 K^+)$ for normalization. This analysis uses an integrated luminosity of 427 fb^{-1} corresponding to the production of approximately 554 million $c\bar{c}$ events.

Signal events are reconstructed in the production processes $e^+ e^- \rightarrow c\bar{c} \rightarrow D_s^{*+} \bar{D}_{\text{TAG}} \bar{K}^{0,-} X$, with the subsequent decay $D_s^{*+} \rightarrow D_s^+ \gamma$. Here, \bar{D}_{TAG} is a fully reconstructed hadronic \bar{D} meson decay, required to suppress the large background from non-charm continuum $q\bar{q}$ pair production; X represents a set of any number of pions (π^0 and π^\pm) produced in the $c\bar{c}$ fragmentation process, and $\bar{K}^{0,-}$ represents a single \bar{K}^0 or K^- from $c\bar{c}$ fragmentation required to balance strangeness in the event. In addition we require a reconstructed e^+ which tags the decay $\tau^+ \rightarrow e^+ \nu_e \bar{\nu}_\tau$. In a similar reconstruction we select $D_s^+ \rightarrow K_s^0 K^+$ events.

We extract the signal yields using the D_s^+ candidate mass determined from the 4-momentum recoiling against the $\bar{D}_{\text{TAG}} \bar{K}^{0,-} X \gamma$ system. The fit results are shown in fig. 2. We compute the branching fraction using the formula

$$(3) \quad \frac{\mathcal{B}(D_s^+ \rightarrow \tau^+ \nu_\tau)}{\mathcal{B}(D_s^+ \rightarrow K_s^0 K^+)} = \frac{\mathcal{B}(K_s^0 \rightarrow \pi^+ \pi^-)}{\mathcal{B}(\tau^+ \rightarrow e^+ \nu_e \bar{\nu}_\tau)} \frac{(N_S)^{\tau \nu_\tau}}{(N_S)^{K_s^0 K^+}} \frac{\epsilon^{K_s^0 K^+}}{\epsilon^{\tau \nu_\tau}},$$

where N_S and ϵ refer to the number of signal events and total efficiency for the $\tau \nu$ and the normalizing decay modes. The values of the $K_s^0 \rightarrow \pi^+ \pi^-$ and $\tau^+ \rightarrow e^+ \nu_e \bar{\nu}_\tau$ branching

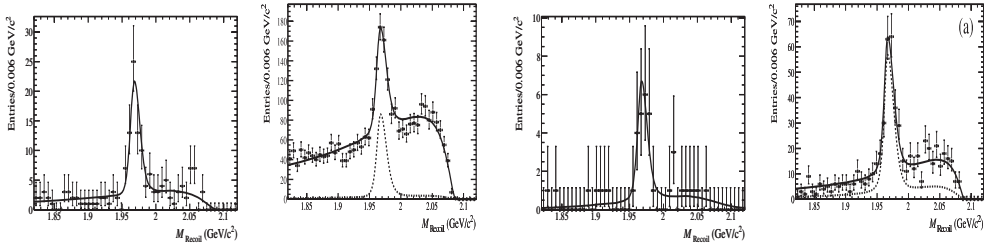


Fig. 2. – Left two plots show the recoil mass for $D_s^+ \rightarrow \tau^+ \nu_\tau$ ($\tau^+ \rightarrow e^+ \nu_e \bar{\nu}_\tau$) with $E_{\text{extra}} = 0$ and $E_{\text{extra}} = 0$. E_{extra} is the remaining energy in the calorimeter after the full event reconstruction. The two right plots show the corresponding distributions for $D_s^+ \rightarrow K_S^0 K^+$ events. The solid curve shows the total fit while the dashed curve shows the signal component.

fractions are obtained from [11]. We find $B(D_s^+ \rightarrow \tau^+ \nu_\tau) = (4.5 \pm 0.5 \pm 0.4 \pm 0.3)\%$ and use eq. (2) to compute $f_{D_s} = (233 \pm 13 \pm 10 \pm 7)$ MeV [12]. Here the errors are statistical, systematic, and due to PDG parameter values.

4. – Measurement of D^0 - \bar{D}^0 mixing using the ratio of lifetimes for the decays $D^0 \rightarrow K^- \pi^+$ and $K^+ K^-$

Mixing in the charm sector has only recently been observed at B-factories. One manifestation of D^0 - \bar{D}^0 mixing is differing D^0 decay time distributions for decays to different CP eigenstates [13]. We present here a measurement of this lifetime difference using a sample of D^0 and \bar{D}^0 decays in which the initial flavor of the decaying meson is unknown.

Assuming CP conservation in mixing, the two neutral D mass eigenstates $|D_1\rangle$ and $|D_2\rangle$ can be represented as

$$(4) \quad \begin{aligned} |D_1\rangle &= p|D^0\rangle + q|\bar{D}^0\rangle, \\ |D_2\rangle &= p|D^0\rangle - q|\bar{D}^0\rangle, \end{aligned}$$

where $|p|^2 + |q|^2 = 1$. The rate of D^0 - \bar{D}^0 mixing can be characterized by the parameters $x \equiv \Delta m/\Gamma$ and $y \equiv \Delta\Gamma/2\Gamma$, where $\Delta m = m_1 - m_2$ and $\Delta\Gamma = \Gamma_1 - \Gamma_2$ are, respectively, the differences between the mass and width eigenvalues of the states in eq. (4), and $\Gamma = (\Gamma_1 + \Gamma_2)/2$ is the average width. If either x or y is non-zero, mixing will occur, altering the decay time distribution of D^0 and \bar{D}^0 mesons decaying into final states of specific CP [11]. In the limit of small mixing, and no CP violation in mixing or in the interference between mixing and decay, the mean lifetimes of decays to a CP eigenstate of samples of D^0 ($\tau_{hh}^{D^0}$) and \bar{D}^0 ($\tau_{hh}^{\bar{D}^0}$) mesons, and the mean lifetime of decays to a state of indefinite CP ($\tau_{K\pi}$), can be combined to form the quantity

$$(5) \quad y_{CP} = \frac{\langle\tau_{K\pi}\rangle}{\langle\tau_{hh}\rangle} - 1,$$

where $\langle\tau_{hh}\rangle = (\tau_{hh}^{D^0} + \tau_{hh}^{\bar{D}^0})/2$. An analogous expression $\langle\tau_{K\pi}\rangle$ holds for the $K^- \pi^+$ final state. If y_{CP} is zero there is no D^0 - \bar{D}^0 mixing attributable to a width difference, although

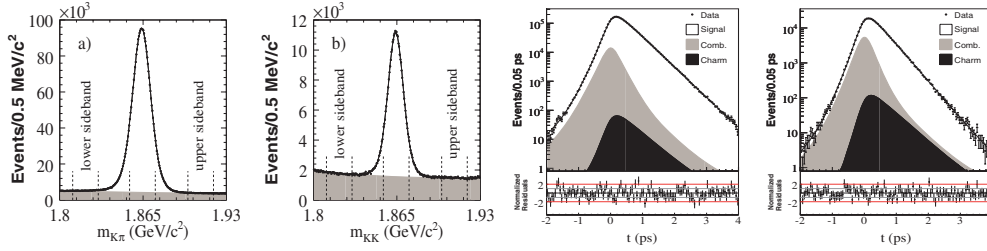


Fig. 3. – The left plots show the D^0 candidate invariant mass distribution for $K^- \pi^+$ and $K^+ K^-$, data are shown by points, total fit as by a curve and background contribution as solid shade. The right plots show the decay time distribution for data (points), total lifetime fit (curve), combinatorial background (gray), and charm background (black) contributions overlaid.

mixing caused by a mass difference may be present. In the limit of no direct CP violation, $y_{CP} = y$.

In this analysis we reconstruct D^0 mesons in reactions of the kind $e^+e^- \rightarrow c\bar{c} \rightarrow D^0 X$, where X is any additional system and D^0 decays to either $K^- K^+$ or $K^- \pi^+$. The decay time of the D^0 candidates is calculated using the measured displacement of the D^0 decay vertex with respect to the e^+e^- interaction region. The D^0 candidate mass distributions and decay time distributions are shown in fig. 3. To determine the D^0 lifetime in each channel we fit the decay time distributions using an exponential distribution convolved with the resolution function determined from simulated signal events. We find a value of $y_{CP}(\text{untagged}) = [1.12 \pm 0.26(\text{stat}) \pm 0.22(\text{syst})]\%$, which excludes the no-mixing hypothesis at 3.3σ [14].

5. – Search for CP violation using T -odd correlations in $D^0 \rightarrow K^+ K^- \pi^+ \pi^-$ decays

Physics beyond the SM, often referred to as New Physics (NP), can manifest itself through the production of new particles, probably at high mass, or through rare processes not consistent with SM origins. SM predictions for CP asymmetries in charm meson decays are generally of $\mathcal{O}(10^{-3})$, *i.e.* at least one order of magnitude lower than current experimental limits [15]. Thus, the observation of CP violation with current sensitivities signal NP. We report the results of a search for CP violation in the decay process $D^0 \rightarrow K^+ K^- \pi^+ \pi^-$ using a kinematic triple product correlation of the form $C_T = \mathbf{p}_1 \cdot (\mathbf{p}_2 \times \mathbf{p}_3)$, where each \mathbf{p}_i is a momentum vector of one of the particles in the decay. The product is odd under time-reversal (T) and, assuming the CPT theorem, T -violation is a signal for CP -violation. Strong interaction dynamics can produce a non-zero value of the A_T asymmetries,

$$(6) \quad A_T \equiv \frac{\Gamma(C_T > 0) - \Gamma(C_T < 0)}{\Gamma(C_T > 0) + \Gamma(C_T < 0)},$$

where Γ is the decay rate for the process, even if the weak phases are zero. After defining a similar formula for the CP -conjugate decay process we can construct $\mathcal{A}_T = \frac{1}{2}(A_T - \overline{A}_T)$; a non-zero value of \mathcal{A}_T would signal CP -violation [16].

Following the suggestion by Bigi [17] to study CP violation using this technique, the FOCUS Collaboration made the first measurements using approximately 800 events and

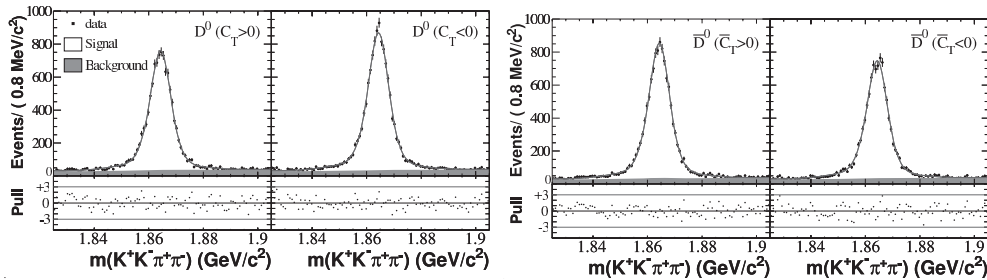


Fig. 4. – Fit projections onto $m(K^+K^-\pi^+\pi^-)$ for the four different C_T subsamples after a Δm signal selection. The shaded areas indicate the total backgrounds. The normalized fit residuals, represented by the pulls, are also shown under each distribution.

reported $\mathcal{A}_T(D^0 \rightarrow K^+K^-\pi^+\pi^-) = 0.010 \pm 0.057 \pm 0.037$ [18]. We perform a similar study using approximately 1.5×10^5 signal events.

Reactions of the kind $e^+e^- \rightarrow X D^{*+}$; $D^{*+} \rightarrow \pi_s^+ D^0$; $D^0 \rightarrow K^+K^-\pi^+\pi^-$, where X indicates any additional (unreconstructed) system, have been selected. We require the D^0 to have a CM momentum greater than $2.5 \text{ GeV}/c$. According to the D^{*+} tag and the C_T variable, we divide the total data sample into four subsamples. The D^0 yields are determined using a binned, extended maximum-likelihood fit to the 2D $(m(K^+K^-\pi^+\pi^-), \Delta m)$ distribution obtained with the two observables $m(K^+K^-\pi^+\pi^-)$ and $\Delta m \equiv m(K^+K^-\pi^+\pi^-\pi_s^+) - m(K^+K^-\pi^+\pi^-)$. The functional forms of the probability density functions (PDFs) for the signal and background components are based on studies of MC samples. We make use of combinations of Gaussian and Johnson SU [19] lineshapes for peaking distributions, and we use polynomials and threshold functions for the non-peaking backgrounds. Figure 4 shows the $K^+K^-\pi^+\pi^-$ mass distributions for the four different C_T subsamples. The asymmetry determined using the signal yields is found to be consistent with zero: $\mathcal{A}_T = (1.0 \pm 5.1_{\text{stat}} \pm 4.4_{\text{syst}}) \times 10^{-3}$ with a sensitivity of $\sim 0.6\%$ [20].

6. – Searches for lepton flavor violation in the decays $\tau^\pm \rightarrow e^\pm\gamma$ and $\tau^\pm \rightarrow \mu^\pm\gamma$

Despite the existence of neutrino oscillations [21], decays of $\tau^\pm \rightarrow \ell^\pm\gamma$ (where $\ell = e, \mu$) are predicted to have unobservably low rates [22] in the SM. Thus, observation of charged lepton flavor violation would be an unambiguous signature of new physics. Presently, the most stringent limits are $\mathcal{B}(\tau^\pm \rightarrow e^\pm\gamma) < 1.1 \times 10^{-7}$ [23] and $\mathcal{B}(\tau^\pm \rightarrow \mu^\pm\gamma) < 4.5 \times 10^{-8}$ [24] at 90% CL, using 232.2 fb^{-1} and 535 fb^{-1} of e^+e^- annihilation data collected near the $\Upsilon(4S)$ resonance by the *BABAR* and Belle experiments, respectively. This analysis utilizes the entire *BABAR* dataset corresponding to a luminosity of 425.5 fb^{-1} , 28.0 fb^{-1} and 13.6 fb^{-1} recorded at the $\Upsilon(4S)$, $\Upsilon(3S)$ and $\Upsilon(2S)$ resonances, and 44.4 fb^{-1} , 2.6 fb^{-1} and 1.4 fb^{-1} recorded at 40 MeV, 30 MeV and 30 MeV below the resonances, respectively.

The signal is characterized by a $\ell^\pm\gamma$ pair with an invariant mass and total energy in the CM frame ($E_{\ell\gamma}^{\text{CM}}$) close to $m_\tau = 1.777 \text{ GeV}/c^2$ [11] and $\sqrt{s}/2$, respectively. Candidate events must also contain another τ decay product (one or three tracks). The signal-side hemisphere must contain one photon with CM energy E_γ^{CM} greater than 1 GeV and one track within the calorimeter acceptance with momentum in the CM frame less than $0.77\sqrt{s}/2$. This track must be identified as an electron or a muon for the $\tau^\pm \rightarrow e^\pm\gamma$ or $\tau^\pm \rightarrow \mu^\pm\gamma$ search.

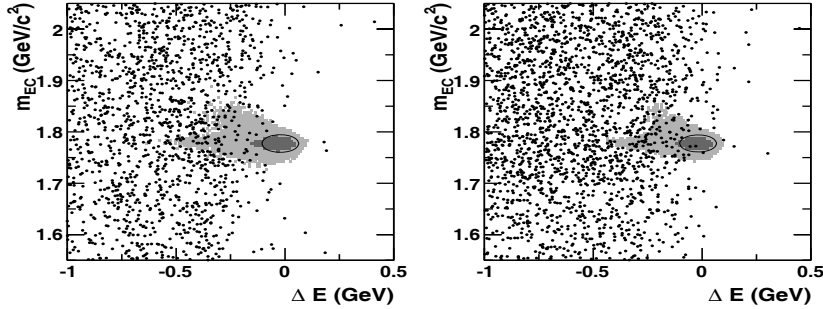


Fig. 5. – Distributions of $\tau^\pm \rightarrow e^\pm\gamma$ (left) and $\tau^\pm \rightarrow \mu^\pm\gamma$ (right) candidate decays in the m_{EC} vs. ΔE plane. Data are shown as dots and contours containing 90% (50%) of signal MC events are shown as light- (dark-) shaded regions. The 2σ ellipse is shown also.

Signal decays are searched for using two kinematic variables: the energy difference $\Delta E = E_{e\gamma}^{\text{CM}} - \sqrt{s}/2$ and the beam-energy constrained τ mass (m_{EC}), obtained from a kinematic fit after requiring the CM τ energy to be $\sqrt{s}/2$. For signal events, the m_{EC} and ΔE distributions are centered at m_τ and small negative values, respectively, where the shifts from zero for the latter are due to radiation and photon energy reconstruction effects. The m_{EC} vs. ΔE distributions are modeled by 2-dimensional probability density functions (PDFs) summed over all background event types. We observe 0 and 2 events for the $\tau^\pm \rightarrow e^\pm\gamma$ and $\tau^\pm \rightarrow \mu^\pm\gamma$ searches inside the 2σ signal ellipse as shown in fig. 5. As there is no evidence for a signal, we set a frequentist upper limit calculated using $\mathcal{B}_{\text{UL}}^{\text{90}} = N_{\text{UL}}^{\text{90}}/(N_\tau \varepsilon)$ to be $\mathcal{B}(\tau^\pm \rightarrow e^\pm\gamma) < 3.3 \times 10^{-8}$ and $\mathcal{B}(\tau^\pm \rightarrow \mu^\pm\gamma) < 4.4 \times 10^{-8}$ at 90% CL [25], where ε is the signal efficiency inside the 2σ signal ellipse and $N_{\text{UL}}^{\text{90}}$ is the 90% CL upper limit on the number of signal events, estimated using the POLE program [26].

7. – Conclusions

In conclusion, the *BABAR* Collaboration continues to exploit its rich data-set to study fundamental aspects of flavor physics. In this paper we report an update to our previous measurement of the CKM element $|V_{ub}|$ using exclusive $B \rightarrow \pi\ell\nu$ decays. In the charm sector we have extracted a value of f_{D_s} from $D_s^+ \rightarrow \tau^+\nu_\tau$ decays, we have measured the mixing parameter y_{CP} using the lifetime ratio $\frac{\langle\tau_{K\pi}\rangle}{\langle\tau_{hh}\rangle}$ in D^0 decays, and we have also searched for CP violation using T -odd correlations in 4-body D^0 decays to $K^+K^-\pi^+\pi^-$. Finally, in the tau sector we have placed upper limits on the rates of lepton flavor violating decays $\tau^\pm \rightarrow e^\pm\gamma$ and $\tau^\pm \rightarrow \mu^\pm\gamma$.

REFERENCES

- [1] AUBERT B. *et al.* (BABAR COLLABORATION), *Phys. Rev. Lett.*, **99** (2007) 171803.
- [2] CHEN K. F. *et al.* (BELLE COLLABORATION), *Phys. Rev. Lett.*, **98** (2007) 031802.
- [3] CABIBBO N., *Phys. Lett.*, **10** (1963) 531 KOBAYASHI M. and MASKAWA T., *Prog. Theor. Phys.*, **49** (1973) 652.
- [4] AUBERT B. *et al.* (BABAR COLLABORATION), *Phys. Rev. D*, **72** (2005) 051102.
- [5] BORDES J., PEÑARROCHA J. and SCHILCHER K., *JHEP*, **0511** (2005) 014.

- [6] KHAN A. ALI *et al.* (QCDSF COLLABORATION), *Phys. Lett. B*, **652** (2007) 150.
- [7] FOLLANA E. *et al.* (HPQCD and UKQCD COLLABORATIONS), *Phys. Rev. Lett.*, **100** (2008) 062002.
- [8] AUBIN C. *et al.* (MILC COLLABORATION), *Phys. Rev. Lett.*, **95** (2005) 122002.
- [9] BERNARD C. *et al.* (FERMILAB LATTICE and MILC COLLABORATIONS), *PoS LATTICE2008*, 278 (2008).
- [10] ONYISI P. U. E. *et al.* (CLEO COLLABORATION), *Phys. Rev.*, **79** (2009) 052002.
- [11] AMSLER C. *et al.* (PARTICLE DATA GROUP), *Phys. Lett. B*, **667** (2008) 1.
- [12] AUBERT *et al.* (BABAR COLLABORATION), arXiv:1003.3063 (2010).
- [13] LIU T. H., *Workshop on the Future of High Sensitivity Charm Experiments: CHARM2000, Batavia, IL, 7-9 Jun 1994* [arXiv:hep-ph/9408330].
- [14] AUBERT *et al.* (BABAR COLLABORATION), *Phys. Rev. D*, **80** (2009) 071103.
- [15] SCHWARTZ A. J. (HFAG CHARM GROUP), arXiv:0911.1464.
- [16] BENSALÉM W., DATTA A. and LONDON D., *Phys. Rev. D*, **66** (2002) 094004 BENSALÉM W. and LONDON D., *Phys. Rev. D*, **64** (2001) 116003 BENSALÉM W., DATTA A. and LONDON D., *Phys. Lett. B*, **538** (2002) 309.
- [17] BIGI I. I., *Proceedings of KAON2001: International Conference on CP Violation, Pisa, Italy, 12-17 Jun 2001*, p. 417 (hep-ph/0107102).
- [18] LINK J. M. *et al.* (FOCUS COLLABORATION), *Phys. Lett. B*, **634** (2006) 165.
- [19] JOHNSON N. L., *Biometrika*, **36** (1949) 149.
- [20] AUBERT B. *et al.* (BABAR COLLABORATION), arXiv:1003.3397 (2010).
- [21] CLEVELAND B. T. *et al.*, *Astrophys. J.*, **496** (1998) 505 FUKUDA Y. *et al.* (SUPER-KAMIOKANDE COLLABORATION), *Phys. Rev. Lett.*, **81** (1562) 1998 AHMAD Q. R. *et al.* (SNO COLLABORATION), *Phys. Rev. Lett.*, **89** (2002) 011301; AHN M. H. *et al.* (K2K COLLABORATION), *Phys. Rev. Lett.*, **90** (2003) 041801.
- [22] LEE B. W. and SHROCK R. E., *Phys. Rev. D*, **16** (1444) 1977.
A value of $\Delta m_{32}^2 \approx 3 \times 10^{-3} (\text{eV}/c^2)^2$ [21] and maximal mixing implies $\mathcal{B}(\tau^\pm \rightarrow \mu^\pm \gamma) \approx \mathcal{O}(10^{-54})$.
- [23] AUBERT B. *et al.* (BABAR COLLABORATION), *Phys. Rev. Lett.*, **96** (2006) 041801.
- [24] HAYASAKA K. *et al.* (BELLE COLLABORATION), *Phys. Lett. B*, **666** (2008) 16.
- [25] AUBERT B. *et al.* (BABAR COLLABORATION), *Phys. Rev. Lett.*, **104** (2010) 021802.
- [26] CONRAD J., BOTNER O., HALLGREN A. and DE LOS HEROS C. PEREZ, *Phys. Rev. D*, **67** (2003) 012002.

Rare decays at the B factories

K. NISHIMURA on behalf of the BELLE and BABAR COLLABORATIONS

*Department of Physics and Astronomy, University of Hawai'i at Mānoa
Honolulu, Hawai'i, USA*

(ricevuto il 14 Settembre 2010; pubblicato online il 5 Gennaio 2011)

Summary. — Over the past ten years, the Belle and BaBar B factories have collected datasets with a combined total of over a billion $B\bar{B}$ pairs. This enormous amount of data has allowed a number of rare B meson decays to be studied in increasing detail. We review some recent results from Belle and BaBar on rare B decays, focusing on those that involve radiative, electroweak, and hadronic penguin processes.

PACS 13.20.He – Leptonic, semileptonic, and radiative decays of bottom mesons.
PACS 13.25.Hw – Hadronic decays of bottom mesons.

1. – Introduction

The two B factories, Belle at the KEKB collider at KEK, Japan, and BaBar at the PEP-II collider at SLAC, USA, have collected data sets with approximately 770 million and 470 million $B\bar{B}$ pairs, respectively. In addition to fulfilling their primary purpose, confirmation of the Kobayashi-Maskawa mechanism of CP violation [1], the large accumulated statistics and the clean experimental environments afforded by a lepton collider have allowed a number of increasingly precise studies into rare decays of the B meson. We focus in these proceedings on selected charmless B meson decays involving three types of penguin transitions: radiative penguins that probe the $b \rightarrow s\gamma$ process, the electroweak penguin processes $b \rightarrow s\ell^+\ell^-$ and $b \rightarrow s\nu\bar{\nu}$, and hadronic penguins with η or η' mesons in the final state. As all of these processes involve loop transitions, they may be influenced by amplitudes that include new particles outside of the Standard Model (SM). As such, measurements of these decays serve as searches for new physics and provide constraints on its origin. For each class of decays, we discuss both inclusive measurements and their exclusive counterparts. The inclusive studies are typically prone to higher experimental uncertainties, but can be compared with more precise theoretical expectations for their rates. The rates for the complimentary exclusive channels can usually be measured more precisely experimentally, but the corresponding theoretical predictions suffer from large hadronic uncertainties, making ratios, asymmetries, and angular observables more powerful discriminators of new physics.

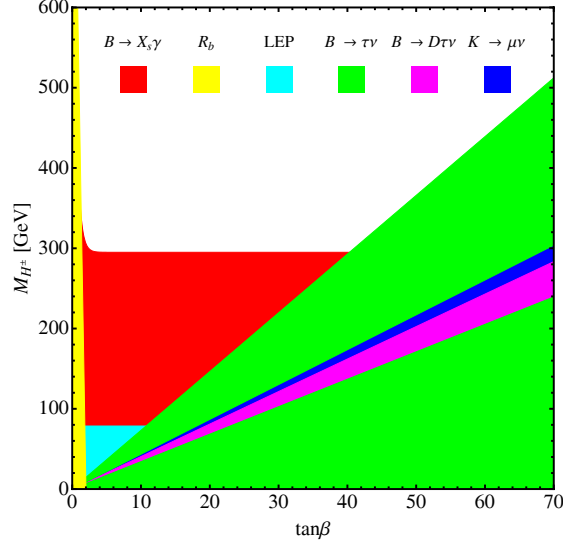


Fig. 1. – Direct and indirect bounds on M_{H^\pm} in the type II two-Higgs doublet model. Plot is from ref. [10].

2. – Radiative penguins

The $b \rightarrow s\gamma$ transition provides a rich environment for both precision tests of the SM and searches for new physics. Experimental measurements of the inclusive branching fraction can be compared to precise theoretical SM predictions, while the exclusive $b \rightarrow s\gamma$ processes can serve as valuable tools to test hadronization models used by Monte Carlo generators, as well as search for anomalous asymmetries for which the SM theoretical expectations are much more constrained.

Measurements of the inclusive $B \rightarrow X_s\gamma$ process have been conducted by CLEO, BaBar, and Belle [2-6]. The most recent is a fully inclusive analysis by Belle [7] in which only the high energy photon is reconstructed and the signal is obtained by subtracting the photon spectrum of scaled off-resonance data (68 fb^{-1}) from that of the on-resonance data (605 fb^{-1}). The spectra from analysis streams with and without a lepton tag from the other B in the event are combined to improve the overall sensitivity. After the statistical correlations between the two streams are properly accounted for, the final branching fraction is measured over the photon energy range from 1.7 to 2.8 GeV as $\mathcal{B}(B \rightarrow X_s\gamma) = (3.45 \pm 0.15 \pm 0.40) \times 10^{-4}$. This analysis has the lowest photon energy thresholds of all $b \rightarrow s\gamma$ analyses performed to date. Since the latest theoretical predictions are valid for $E_\gamma > 1.6 \text{ GeV}$, this reduction in the lower energy threshold helps to minimize theoretical uncertainties in extrapolating to the appropriate energy range. The result is consistent both with previous measurements and SM expectations [8,9]. This measurement places very strong constraints on some new physics models. For example, in the type II two-Higgs doublet model, the measured $B \rightarrow X_s\gamma$ branching fraction imposes a limit on the charged Higgs mass of $M_{H^\pm} > 295 \text{ GeV}/c^2$ at the 95% confidence level [10]. It is especially notable that unlike many other decay modes, this limit is independent of $\tan\beta$, as demonstrated in fig. 1.

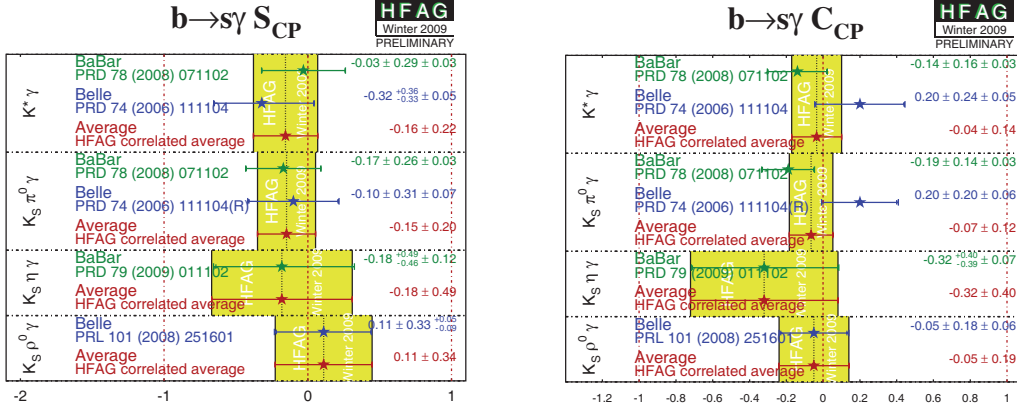


Fig. 2. – Measured time-dependent CP violating parameters S (left) and C (right) for exclusive $b \rightarrow s\gamma$ decays. Plot is from ref. [13].

In the exclusive $b \rightarrow s\gamma$ channels, the BaBar Collaboration has produced the most precise branching fraction measurement to date for $B \rightarrow K^*\gamma$ using a data sample of $383 \times 10^6 B\bar{B}$ pairs [11], improving upon its previous branching fraction measurement as well as those of CLEO and Belle. The measured branching fractions are $\mathcal{B}(B^0 \rightarrow K^{*0}\gamma) = (4.47 \pm 0.10 \pm 0.16) \times 10^{-5}$ and $\mathcal{B}(B^+ \rightarrow K^{*+}\gamma) = (4.22 \pm 0.14 \pm 0.16) \times 10^{-5}$. These and previous measurements are already in agreement with, and more precise than, theoretical estimates of the SM expectation. Predictions for the isospin asymmetry, Δ_{0-} , and the direct CP asymmetry, \mathcal{A} , are considerably more precise, and are between 2–10% for Δ_{0-} and approximately 1% for \mathcal{A} . BaBar has measured these parameters and finds $\Delta_{0-} = 0.066 \pm 0.021 \pm 0.022$ and $\mathcal{A} = -0.003 \pm 0.017 \pm 0.007$, both consistent with theoretical expectations.

In the SM, the $b \rightarrow s\gamma$ process produces a photon with polarizations strongly correlated with the b flavor, *i.e.* b decays produce primarily right-handed photons, and \bar{b} decays produce primarily left-handed photons, with the alternate production mechanisms suppressed by a factor of m_s/m_b . In some new physics models, such as the left-right symmetric model, right-handed currents enhance the rate of these suppressed transitions, leading to the potential for mixing-induced CP violation in $b \rightarrow s\gamma$ processes, which is otherwise negligible for $b \rightarrow s\gamma$ modes in the SM.

A number of searches for such right-handed currents have been conducted. CP violating parameters for these modes are summarized in fig. 2. One of the most recent is a BaBar measurement of CP violating asymmetries in $B \rightarrow K\eta\gamma$ using $465 \times 10^6 B\bar{B}$ pairs [12]. The CP asymmetries of this and all other modes measured to date are consistent with zero. It is obvious from fig. 2 that significantly improved statistics will be required to find any possible CP violation in these modes.

Other exclusive $b \rightarrow s\gamma$ decays are being studied that could ultimately be used for new searches for right-handed currents. Belle has found first evidence for the decay $B^+ \rightarrow K^+\eta'\gamma$ with a branching fraction of $\mathcal{B}(B^+ \rightarrow K^+\eta'\gamma) = (3.6 \pm 1.2 \pm 0.4) \times 10^{-6}$ [14]. However, the analysis was only able to place an upper limit on the neutral mode, with branching fraction $\mathcal{B}(B^+ \rightarrow K_S^0\eta'\gamma) \leq 6.4 \times 10^{-6}$ at the 90% confidence level. This analysis uses $657 \times 10^6 B\bar{B}$ pairs. As this is approximately 85% of the full Belle data sample, no study of time-dependent CP violation parameters is likely to be possible,

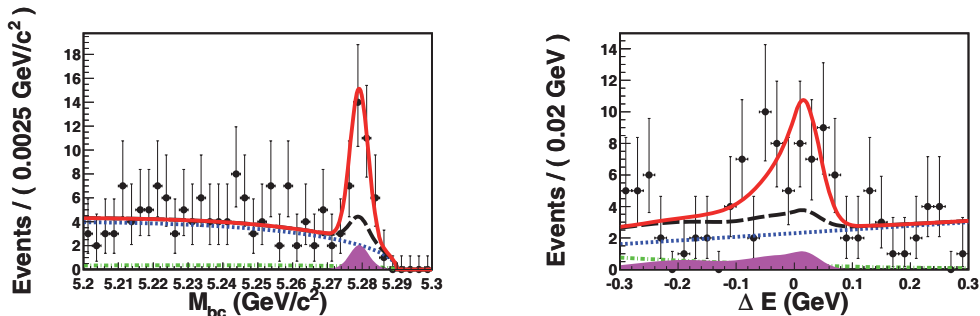


Fig. 3. – (Colour on-line) Fit projections for the Belle $B^0 \rightarrow \phi K_S^0 \gamma$ analysis. (Left) The beam constrained mass, M_{bc} , and (right) the energy difference, ΔE . In both plots, points with errors are data and the curves correspond to the total fit function (solid red), the total background function (long-dashed black), the continuum background (dotted blue), the generic $b \rightarrow c$ backgrounds (dash-dotted green), and non-resonant and other charmless backgrounds (filled magenta).

even with the entirety of Belle data. The mode $B \rightarrow \phi K \gamma$ is also being studied by Belle with $772 \times 10^6 B\bar{B}$ pairs. Belle has reported first observation of $B^0 \rightarrow \phi K_S^0 \gamma$ with 5.4σ significance, with branching fraction $\mathcal{B}(B^0 \rightarrow \phi K_S^0 \gamma) = (2.66 \pm 0.60 \pm 0.32) \times 10^{-6}$ [15]. The fitted projections for the neutral mode are shown in fig. 3. This analysis has enough events to allow for a time-dependent CP study, and this result is expected soon.

3. – Electroweak penguins

Like $b \rightarrow s\gamma$, the electroweak penguin processes $b \rightarrow s\ell^+\ell^-$ and $b \rightarrow s\nu\bar{\nu}$ can be used to probe for contributions from new physics. Predictions for the branching fraction of the exclusive channels $B \rightarrow K^{(*)}\ell^+\ell^-$ suffer from large hadronic uncertainties, making it difficult to compare them precisely with the recent data from Belle and BaBar [16,17], though they are consistent within the experimental and theoretical errors. Predictions for the lepton flavor ratio, $R_{K^{(*)}}$ are better constrained, and no deviation from the SM is seen.

Other tests of the SM can be performed using the angular observables: the forward-backward asymmetry, A_{FB} , and longitudinal polarization fraction, F_L of the K^* mode. Results from Belle [16] and BaBar [18] can be found in fig. 4. Of particular interest are the results for A_{FB} and F_L , where both the Belle and BaBar data hint at a deviation from the SM, such as a model in which the Wilson coefficient C_7 is of opposite sign to the usual SM convention, though this deviation is subject to large experimental errors.

The isospin asymmetry, A_I , has also been a topic of interest, as a measurement by BaBar [19] indicated a deviation from the null value (and SM expectation) at a level of 3.9σ for the combination of the K^* and K modes. However, the recent Belle data shows no significant asymmetry. These results are also shown in fig. 4.

To gain further insight, one can examine the branching fraction of the inclusive mode $B \rightarrow X_s\ell^+\ell^-$, as this decay rate is enhanced if C_7 is of opposite sign [20]. A recent Belle measurement of this decay using the technique of a sum-of-exclusive modes shows no obvious enhancement [21]. Rather, the measured branching fraction in the range $q^2 > (0.2 \text{ GeV}/c)^2$ is $\mathcal{B}(B \rightarrow X_s\ell^+\ell^-) = (3.33 \pm 0.80_{-0.24}^{+0.19}) \times 10^{-6}$, which is consistent within uncertainties with the SM prediction of $\mathcal{B}_{SM}(B \rightarrow X_s\ell^+\ell^-) = (4.2 \pm 0.7) \times 10^{-6}$.

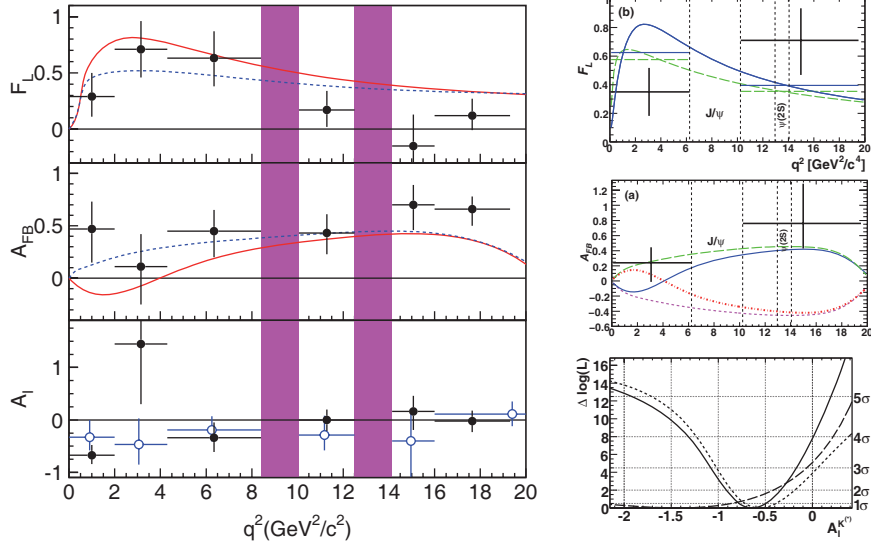


Fig. 4. – Distributions of F_L , A_{FB} , and A_I for Belle (left) and BaBar (right). For the Belle result, the open (filled) points with errors correspond to $B \rightarrow K^{(*)} \ell^+ \ell^-$. The solid curves correspond to the SM expectation, and the dotted lines represent the expectation when $C_7 = -C_7$. The solid bands are veto regions for the J/ψ and $\psi(2S)$. For the BaBar data, the points with errors in F_L and A_{FB} are the data for $B \rightarrow K^* \ell^+ \ell^-$, and the curves correspond to the expectations with the SM (solid), $C_7 = -C_7$ (long dashed), $C_9 C_{10} = -C_9 C_{10}$ (short dashed), and both $C_7 = -C_7$ and $C_9 C_{10} = -C_9 C_{10}$ (dash-dotted). In the BaBar A_I plot, the likelihood profiles correspond to $B \rightarrow K^* \ell^+ \ell^-$ (dashed), $B \rightarrow K \ell^+ \ell^-$ (long dashed), and the two modes combined (solid).

The decay $B \rightarrow K \nu \bar{\nu}$ is theoretically similar to $b \rightarrow s \ell^+ \ell^-$, providing another rare electroweak penguin to test against SM predictions. Previous measurements have been able to set only an upper limit on this process, with Belle setting the lowest limits of $\mathcal{B}(B^+ \rightarrow K^+ \nu \bar{\nu}) < 1.4 \times 10^{-5}$ and $\mathcal{B}(B^0 \rightarrow K^0 \nu \bar{\nu}) < 16 \times 10^{-5}$ [22]. BaBar has recently improved [23] on both of these limits with a multivariate analysis using bagged decision trees [24]. They find, using a data sample of $459 \times 10^6 B\bar{B}$ events, improved upper limits of $\mathcal{B}(B^+ \rightarrow K^+ \nu \bar{\nu}) < 1.3 \times 10^{-5}$ and $\mathcal{B}(B^0 \rightarrow K^0 \nu \bar{\nu}) < 5.6 \times 10^{-5}$. Unfortunately, these limits remain significantly above the SM expectation of $\mathcal{B}(B \rightarrow K \nu \bar{\nu}) = (3.8_{-0.6}^{+1.2}) \times 10^{-6}$.

4. – Hadronic penguins

B decays to modes with the η and η' have long been a subject of significant activity. These modes are characterized by interference patterns in their dominant amplitudes, and have a history of unexpectedly large decay rates.

BaBar has recently reported first observation of $B^+ \rightarrow \eta' \rho^+$ and $B^{(0,+)} \rightarrow \eta' K_2^*(1430)^{(0,+)}$, as well as evidence for $B^{(0,+)} \rightarrow \eta' K^{*(0,+)}$. The fitted distributions for this analysis can be seen in fig. 5. The analysis includes branching fractions and CP asymmetries, and uses the full BaBar data sample of $467 \times 10^6 B\bar{B}$ pairs [25]. No significant CP asymmetry is observed in any mode. However, the branching fractions for $B \rightarrow \eta' K_2^*(1430)$ show an unexpected enhancement over the $B \rightarrow \eta' K^*$ modes. Further, results from the $B^+ \rightarrow \eta' \rho^+$ channel seem to be more consistent with SM predictions us-

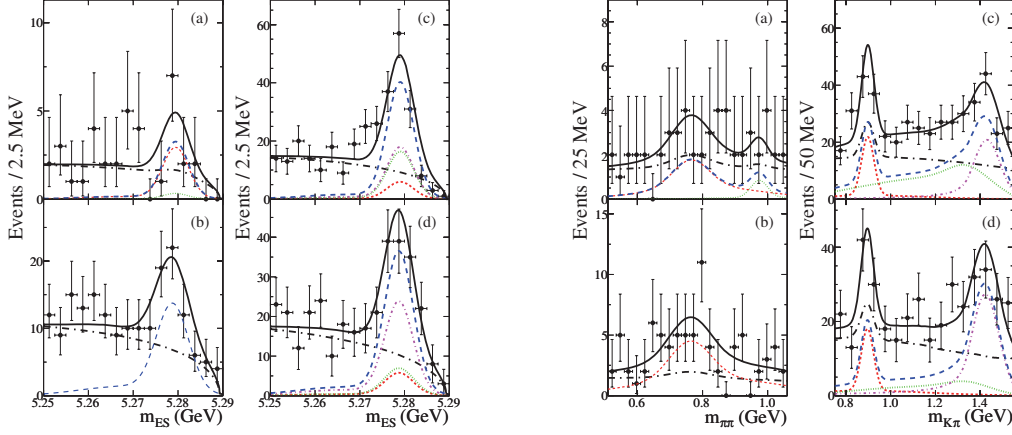


Fig. 5. – (Colour on-line) (Left) BaBar’s projections of B candidate energy substituted mass, m_{ES} for (a) $\eta' \rho^0 / \eta' f_0$, (b) $\eta' \rho^+$, (c) $\eta' K^{*0}$, and (d) $\eta' K^{*+}$. The solid curve is the fit function, black long-dash-dotted curve is the total background, and the blue dashed curve is the total signal contribution. For (a), the red dashed curve is the ρ^0 component and the green dotted curve is the f_0 component. In (c) and (d) the red dashed curve is $K^*(892)$ component, the green dotted is the $(K\pi)_0^*$ component, and the magenta dot-dashed is the $K_2^*(1430)$ component. (Right) The corresponding projections of $m_{\pi\pi}$ in (a) and (b), and $m_{K\pi}$ in (c) and (d). The letter and color codes are the same as for the m_{ES} distributions.

ing perturbative QCD and QCD factorization compared to those made with soft collinear effective theory (SCET), a result which may help to guide future theoretical work in these areas.

In the inclusive sector, Belle recently reported first observation of the inclusive process $B \rightarrow X_s \eta$, using a sum-of-exclusive modes method over $657 \times 10^6 B\bar{B}$ pairs [26]. The X_s mass spectrum, seen in fig. 6 contains known contributions, such as those from $B \rightarrow K\eta$ and $B \rightarrow K^* \eta$. In the higher mass regions, fit projections of which are shown in fig. 6, there are signals around the $K_{(0,2)}^*(1430)$ region, which was previously observed as an exclusive mode by BaBar [27] and for which no theoretical expectation has yet been calculated, as well as significant signal in the region $M_{X_s} > 1.8 \text{ GeV}/c^2$, which was previously unobserved, and for which no predictions are currently available.

The result for the entire measured mass spectrum, $M_{X_s} < 2.6 \text{ GeV}/c^2$, is $\mathcal{B}(B \rightarrow X_s \eta) = (25.5 \pm 2.7 \text{ (stat.)} \pm 1.6 \text{ (syst.)}_{-14.1}^{+3.8} \text{ (model)}) \times 10^{-5}$, where the large model errors are primarily due to uncertainties in the PYTHIA fragmentation models used to generate Monte Carlo for the signal extraction studies.

It has been suggested that the large rate measured in the complementary mode, $B \rightarrow X_s \eta'$, was due to enhancements from the QCD anomaly coupling of the singlet component of the η to two gluons. Naively, this suggests that the rate for the η process should be suppressed by a factor of $\tan^2 \theta \sim 0.1$, where θ is the $\eta - \eta'$ mixing angle. The current world average for the η' branching fraction is $\mathcal{B}(B \rightarrow X_s \eta') = (42.0 \pm 9.0) 10^{-5}$ [28], only a factor of ~ 2 larger than the η mode, thus implying that the QCD anomaly coupling is unlikely to explain the $B \rightarrow X_s \eta'$ decay. Rather, recent theoretical treatments using SCET indicate that non-perturbative charming penguins may play a significant role in these decays [29]. This measurement may help to guide future theoretical work by constraining the level of these non-perturbative contributions.

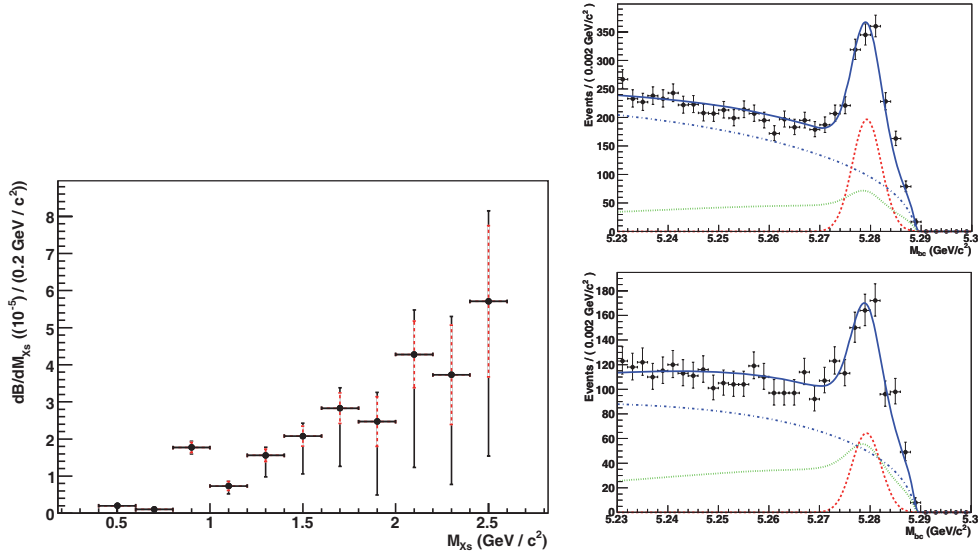


Fig. 6. – (Colour on-line) (Left) Belle’s measured differential branching fraction, $d\mathcal{B}/dM_{X_s}$, for $B \rightarrow X_s \eta$. The error bars are statistical only (dashed red), and the quadratic sum of statistical, systematic, and modeling errors (solid black). (Upper right) Fit to M_{bc} for the X_s mass range above the $K^*(892)$, $1.0 \text{ GeV}/c^2 < M_{X_s} < 2.6 \text{ GeV}/c^2$. (Lower right) Fit to M_{bc} for the X_s mass range above all known kaonic resonances, $1.8 \text{ GeV}/c^2 < M_{X_s} < 2.6 \text{ GeV}/c^2$. The points with errors are data, the curves represent the total fit function (solid blue), the signal component (dashed red), generic $b \rightarrow c$ backgrounds (dotted green), and combinatorial background (dash-dotted blue).

5. – Conclusions

Significant progress has been made at Belle and BaBar in the experimental study of many rare B decay channels, only some of which have been discussed here. Though impressive precision has been attained in both theory and experiment for the inclusive $b \rightarrow s\gamma$ rate, no deviations from the SM predictions have yet been found. Likewise time-dependent searches for right-handed currents in exclusive $b \rightarrow s\gamma$ processes are ongoing, but remain statistically limited. Some hints of new physics may be evident in the electroweak decay $B \rightarrow K^* \ell^+ \ell^-$, but seem to contradict the results in the inclusive channel. In the hadronic decays involving η and η' , a number of new signals have been detected for which no predictions exist.

The B factories are completing data-taking, with BaBar already finished as of 2008 and Belle concluding later this year. We look forward to new and updated analyses of rare B decays utilizing the full data samples of these experiments. However, a common theme of many analyses we have discussed is the large statistical uncertainty. Thus, many analyses require statistical improvements beyond those available from the existing data sets, suggesting a promising future for the planned enhanced luminosity B factories [30, 31].

* * *

The author would like to thank all the members of the Belle and BaBar Collaborations for providing these beautiful results, as well as the conference organizers for the opportunity to share them.

REFERENCES

- [1] KOBAYASHI M. and MASKAWA T., *Prog. Theor. Phys.*, **49** (1973) 652.
- [2] CHEN S. *et al.* (CLEO COLLABORATION), *Phys. Rev. Lett.*, **87** (2001) 251807.
- [3] AUBERT B. *et al.* (BABAR COLLABORATION), *Phys. Rev. D*, **72** (2005) 052004.
- [4] AUBERT B. *et al.* (BABAR COLLABORATION), *Phys. Rev. Lett.*, **97** (2006) 171803.
- [5] AUBERT B. *et al.* (BABAR COLLABORATION), *Phys. Rev. D*, **77** (2008) 051103.
- [6] KOPPENBURG P. *et al.* (BELLE COLLABORATION), *Phys. Rev. Lett.*, **93** (2004) 061803.
- [7] LIMOSANI A. *et al.* (BELLE COLLABORATION), *Phys. Rev. Lett.*, **103** (2009) 241801.
- [8] MISIAK M. *et al.*, *Phys. Rev. Lett.*, **98** (2007) 022002.
- [9] BECHER T. and NEUBERT M., *Phys. Rev. Lett.*, **98** (2007) 022003.
- [10] HAISCH U., [arXiv:0805.2141].
- [11] AUBERT B. *et al.* (BABAR COLLABORATION), *Phys. Rev. Lett.*, **103** (2009) 211802.
- [12] AUBERT B. *et al.* (BABAR COLLABORATION), *Phys. Rev. D*, **79** (2009) 011102.
- [13] HEAVY FLAVOR AVERAGING GROUP, [<http://www.slac.stanford.edu/xorg/hfag>].
- [14] WEDD R. *et al.* (BELLE COLLABORATION), *Phys. Rev. D*, **81** (2010) 111104.
- [15] ADACHI I. *et al.* (BELLE COLLABORATION), [arXiv:0911.1779].
- [16] WEI J. T. *et al.* (BELLE COLLABORATION), *Phys. Rev. Lett.*, **103** (2009) 171801.
- [17] AUBERT B. *et al.* (BABAR COLLABORATION), *Phys. Rev. D*, **73** (2006) 092001.
- [18] AUBERT B. *et al.* (BABAR COLLABORATION), *Phys. Rev. D*, **79** (2009) 031102.
- [19] AUBERT B. *et al.* (BABAR COLLABORATION), *Phys. Rev. Lett.*, **102** (2009) 091803.
- [20] ALI A. *et al.*, *Phys. Rev. D*, **66** (2002) 034002.
- [21] BELLE COLLABORATION, unpublished, reported at *Lepton Photon 2009*.
- [22] CHEN K. F. *et al.* (BELLE COLLABORATION), *Phys. Rev. Lett.*, **99** (2007) 221802.
- [23] BABAR COLLABORATION, unpublished.
- [24] NARSKY I., [arXiv:physics/0507157].
- [25] DEL AMO SANCHEZ P. *et al.* (BABAR COLLABORATION), *Phys. Rev. D*, **82** (2010) 011502.
- [26] NISHIMURA K. *et al.* (BELLE COLLABORATION), *Phys. Rev. Lett.*, **105** (2010) 191803.
- [27] AUBERT B. *et al.* (BABAR COLLABORATION), *Phys. Rev. Lett.*, **97** (2006) 201802.
- [28] AMSLER C. *et al.* (PARTICLE DATA GROUP), *Phys. Lett. B*, **667** (2008) 1.
- [29] CHAY J. *et al.*, *Phys. Rev. D*, **76** (2007) 094031.
- [30] DOLEZAL Z. (for the BELLE II COLLABORATION), [arXiv:0910.0388].
- [31] BONA M. *et al.* (SUPERB COLLABORATION), [arXiv:0709.0451].

QCD and hadronic interactions with initial-state radiation at B-factories

D. BERNARD^(*)

Laboratoire Leprince-Ringuet - Ecole polytechnique, CNRS/IN2P3 - 91128 Palaiseau, France

(ricevuto il 14 Settembre 2010; pubblicato online il 5 Gennaio 2011)

Summary. — The efforts to improve on the precision of the measurement and theoretical prediction of the anomalous magnetic moment of the muon a_μ have turned into a test of our understanding of the hadronic contribution to vacuum polarisation. I describe how recent measurements of hadron production in e^+e^- interactions with initial-state radiation provide precision measurements of the hadron cross section, and have improved on the contribution to the prediction of the value of a_μ that dominates the global uncertainty.

PACS 13.66.Bc – Hadron production in e^-e^+ interactions.

PACS 12.38.Qk – Quantum chromodynamics: Experimental tests.

PACS 13.40.Em – Electric and magnetic moments.

1. – Introduction

Elementary particles have a magnetic moment $\vec{\mu}$ proportional to their spin \vec{s} , with $\vec{\mu} = (ge)/(2m)\vec{s}$. While pointlike Dirac particles would have $g = 2$, *i.e.* an “anomalous” relative deviation of $a \equiv (g - 2)/2 = 0$, Nafe *et al.* observed the first hints of a significant deviation from $a_e = 0$ more than 60 years ago [1]. The following year, Schwinger computed [2] the first-order contribution to a , equal to $\alpha/(2\pi)$, the diagram for which is shown in fig. 1-left.

The development of quantum electro-dynamics (QED) followed, and later of gauge theories in general, making these early works the very basis of our present understanding of the elementary world. Tremendous efforts have been devoted to improving the precision of the theoretical prediction and of the direct measurement of a since then [3].

More than 60 years later the situation is pretty exciting, with the experimental and theoretical precision on the anomalous magnetic moment of the muon a_μ both of the order of 6×10^{-10} , and a discrepancy of $(29 \pm 9) \times 10^{-10}$ between them, *i.e.* amounting to 3.2σ , should Gaussian statistics be assumed (table I).

^(*) From the BaBar Collaboration. E-mail: denis.bernard@in2p3.fr

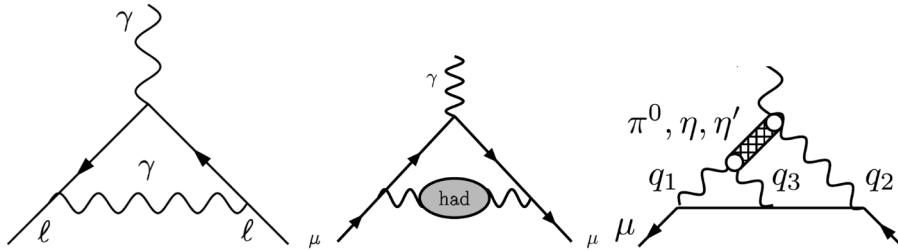


Fig. 1. – Left: 1st order contribution to a . Center: Lowest-order hadronic VP diagram. Right: A light-by-light diagram [3].

The largest contribution to a_μ by far is from QED but its contribution to the uncertainty is negligible. In terms of uncertainty, the main contribution is from the hadronic component of the one-loop vacuum polarisation (VP, fig. 1-center) and, to a lesser extent, from the hadronic component of the light-by-light processes (fig. 1-right).

The photon propagator with VP is obtained from the bare propagator by replacing the electric charge e by the energy-dependent quantity

$$e^2 \rightarrow e^2/[1 + (\Pi'(k^2) - \Pi'(0))],$$

where k is the photon 4-momentum. At low energy, hadronic processes are not computable with the desired precision. Instead the VP amplitude $\Pi'(k^2)$ is obtained from the dispersion relation

$$\Pi'(k^2) - \Pi'(0) = \frac{k^2}{\pi} \int_0^\infty \frac{\text{Im} \Pi'(s)}{s(s - k^2 - i\epsilon)} ds,$$

which in turn is related through the optical theorem

$$\text{Im} \Pi'(s) = \alpha(s) R_{\text{had}}(s)/3$$

TABLE I. – Summary of the contribution to the theory prediction of the value of a_μ , compared with the experimental measurement [3].

QED	11 658 471.81	± 0.02
Leading hadronic VP	690.30	± 5.26
Sub-leading hadronic VP	-10.03	± 0.11
Hadronic light-by-light	11.60	± 3.90
Weak (incl. 2-loops)	15.32	± 0.18
Theory	11 659 179.00	± 6.46
Experiment [4]	11 659 208.00	± 6.30
Exp – theory	29.00	± 9.03

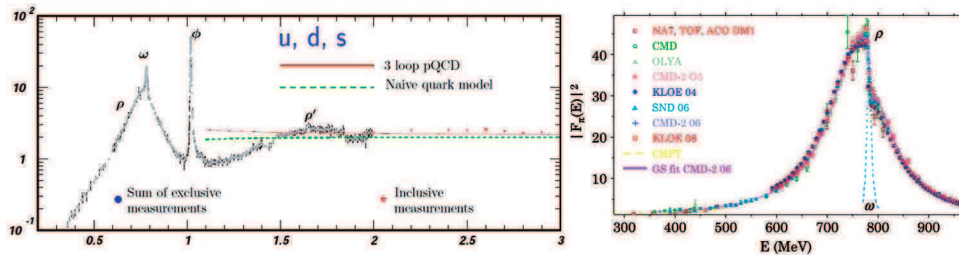


Fig. 2. – Left: R_{had} as a function of \sqrt{s} (GeV) [5]. Right: variation of the pion form factor squared with energy [3] (KLOE 04 is superseded by KLOE 08).

to the ratio

$$R_{\text{had}}(s) = \sigma_{\text{had}} \frac{3s}{4\pi\alpha(s)} = \frac{\sigma_{e^+e^- \rightarrow \text{hadrons}}}{\sigma_{e^+e^- \rightarrow \mu^+\mu^-}}.$$

Finally, the hadronic VP contribution is obtained from the “dispersion integral”

$$a_\mu^{\text{had}} = \left(\frac{\alpha m_\mu}{3\pi}\right)^2 \int \frac{R_{\text{had}}(s) \hat{K}(s)}{s^2} ds,$$

where $\hat{K}(s)$ is an analytical function that takes values close to 1. We note, from the $1/s^2$ variation of the integrand, that the dominant contribution comes from the low energy part of the integral. A good experimental precision of the measurement of $R_{\text{had}}(s)$ at low energy is therefore welcome. Figure 2-right shows a summary of the present measurements of $R_{\text{had}}(s)$ [5], where the presence of $J^{PC} = 1^{--}$ mesons can be seen.

The $\pi^+\pi^-$ channel has both the largest contribution and dominates the uncertainty, with $a_\mu^{\pi^+\pi^-} [2m_\pi, 1.8 \text{ GeV}/c^2] = (504.6 \pm 3.1(\text{exp}) \pm 0.9(\text{rad})) \times 10^{-10}$, compared to the full $a_\mu^{\text{had}} = (690.9 \pm 5.3) \times 10^{-10}$ from table I. A summary of direct measurements in terms of the squared pion form factor is shown in fig. 2-left. The 3.2σ discrepancy mentioned above is computed using this $\pi\pi$ input.

2. – τ decay spectral functions

The $I = 1$ part of the $e^+e^- \rightarrow \pi^+\pi^-$ cross-section can be estimated from the spectral function of τ decays to $\nu\pi^+\pi^0$, under the hypothesis of conservation of the weak vector current (CVC). The method was pioneered by the ALEPH Collaboration [6] and followed by OPAL [7] and CLEO [8]. Recently the Belle Collaboration has performed an analysis using much larger statistics [9], obtaining a value compatible with, and more precise than, the combination of all previous results [10].

The τ method provides a high experimental precision, but extracting the contribution to a_μ depends on making a number of isospin-breaking (IB) corrections. A recent update [11] of [10] lowers the correction by $\approx 7 \times 10^{-10}$, while the uncertainty on the correction is now 1.5×10^{-10} .

The branching fraction of the $\tau \rightarrow \nu\pi^+\pi^0$ decay also takes part in the calculation, with a 0.5% uncertainty.

3. $e^+e^- \rightarrow \pi^+\pi^-$ using ISR method

Initial-state radiation (ISR) makes it possible to measure the cross-section of the production of a final state f in e^+e^- collisions at a squared energy s , over a wide range of energies, lower than \sqrt{s} , through the radiation of a high energy photon by one of the incoming electrons, after which the electrons collide at a squared energy s' .

The BaBar experiment has developed a systematic program of measurements of cross-sections of e^+e^- to hadrons at low energy using the ISR method [12]. The boost undergone by the final state f provides an excellent efficiency down to threshold. In all studies by BaBar, the ISR photon is observed (γ -tag) and its direction is compared to the direction predicted from the direction of f , providing a powerful rejection of background noise. Most of these measurements are more precise than the previously available results by about a factor of three.

3'1. KLOE's result on $e^+e^- \rightarrow \pi^+\pi^-$. – The KLOE experiment, when running on the ϕ resonance, studied the e^+e^- annihilations to $\pi^+\pi^-$ with the ISR method [13]. Here the ISR photon is not reconstructed: the requirement that the photon direction be compatible with its having been emitted in the beam pipe allows mitigation of the background to some extent, but the systematical uncertainty on background subtraction is still a major component of the total uncertainty. The radiator function is provided from simulation, with systematics of 0.5%, and is the other major component.

The value of $a_\mu^{\pi^+\pi^-}$ obtained is compatible with the combination of previous results by CMD-2 & SND over the mass range that they have in common of (630–958 MeV/ c^2).

3'2. BaBar's result on $e^+e^- \rightarrow \pi^+\pi^-$. – BaBar uses a different approach: photon tagging with the ISR luminosity obtained from the muon channel, $e^+e^- \rightarrow \mu^+\mu^-\gamma$ [14]. The systematics related to additional radiation is minimized in this NLO measurement, *i.e.* radiation of one possible additional photon is allowed, so that the final states actually reconstructed are $\pi^+\pi^-\gamma(\gamma)$ and $\mu^+\mu^-\gamma(\gamma)$. The “bare” ratio $R_{\text{had}}(s')$ mentioned above is obtained from the experimentally measured $R_{\text{exp}}(s')$ after correction of final state radiation (FSR) in $e^+e^- \rightarrow \mu^+\mu^-$ and of additional FSR in ISR events $e^+e^- \rightarrow \mu^+\mu^-\gamma$.

A number of important systematics cancel when measuring the π/μ ratio, such as those associated with the collider luminosity, the efficiency of the reconstruction of the ISR photon, and the understanding of additional ISR radiation.

The limiting factor is then the understanding of the possible “double” $\pi-\mu$, MC-data efficiency discrepancies. These are studied in detail, with methods designed to disentangle correlations as much as possible. For example, inefficiency of the track-based trigger is studied using events selected with a calorimetry-based trigger—the small correlation between both triggers being studied separately. Likewise, μ and π particle identification (PID) efficiency is studied in good-quality, two-track ISR events, in which either one, or both, tracks meet the PID selection criteria. Concerning tracking, a sizable degradation of the efficiency for tracks overlapping in the detector was observed and studied in detail.

The systematics finally obtained are of the order of, or smaller than, 1% over the whole mass range studied; *i.e.*, from threshold to 3 GeV/ c^2 .

The $e^+e^- \rightarrow \pi^+\pi^-$ cross section measured by BaBar is shown in fig. 3. The sharp drop due to the interference between the ρ and the ω is clearly visible. The interference between the successive radial excitations of the ρ induces these dips in the cross-section.

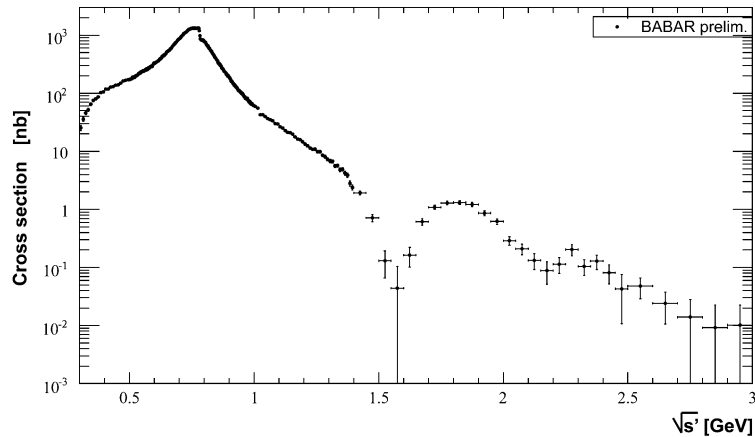


Fig. 3. – Bare, unfolded [15], $e^+e^- \rightarrow \pi^+\pi^-$ cross section measured by BaBar, using the ISR method [14].

The measured value of $a_\mu^{\pi^+\pi^-}[2m_\pi, 1.8 \text{ GeV}/c^2] = (514.1 \pm 2.2 \pm 3.1) \times 10^{-10}$ has a precision similar to the combination of all previous e^+e^- -based results, but is larger by about 2.0σ .

In addition to the measurement of the π/μ ratio, and extraction of the $e^+e^- \rightarrow \pi^+\pi^-$ cross section, BaBar has compared its $\mu^+\mu^-$ spectrum to the Monte Carlo prediction, finding a good agreement within $0.4 \pm 1.1\%$, dominated by the collider luminosity uncertainty of $\pm 0.9\%$.

The distribution of the squared pion form-factor is fitted with a vector-dominance model including the resonances $\rho, \rho', \rho'', \omega$, with the ρ 's being described by the Gounaris-Sakurai model. The fit (figure in ref. [16]) yields a good χ^2/n_{df} of 334/323, and parameters compatible with the world-average values. BaBar can then use the fitted model to compare their result with that of previous measurements (fig. 4). The BaBar result is a bit larger than that obtained by CMD2 [17] and SND [18], nicely compatible with the high-statistics τ -based result by Belle, but shows a clear disagreement with KLOE.

4. – a_μ : the present situation

The present situation in terms of a_μ is summarized in fig. 5:

- The four upper points show that there is a general agreement between the various recent combinations of direct e^+e^- -based $\pi^+\pi^-$ measurement [19, 20, 11].
- The large discrepancy between computations of a_μ based on these and the experimental measurement by BNL-E821 [4] is clear.
- The combination of τ -based results, when corrected for isospin-breaking effects using the most recent calculation [11], is also significantly lower than the experimental measurement [4], by 1.8σ .
- My computation of a_μ using the BaBar $\pi^+\pi^-$ measurement [14] only is larger than the combination of previous e^+e^- -based measurements, and compatible with the τ -based result, but still 2.4σ away from BNL-E821 [4].

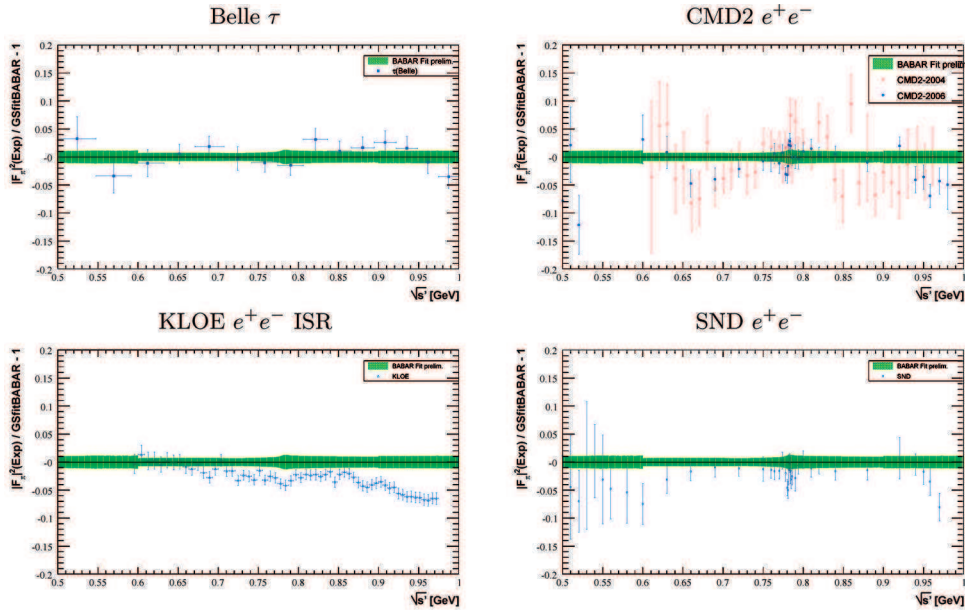


Fig. 4. – Relative difference between the BaBar result with that of previous experiments.

- The combination of all e^+e^- -based measurements, including the recent one by BaBar, shows an uncertainty that has decreased significantly, and a central value that is larger. However, the significance of the difference with respect to BNL-E821 [4] is barely changed, of the order of 3.3σ .

A more sophisticated combination of the available results, published recently [21], yields similar numbers.

5. – What might take place during this decade

5.1. a_μ measurement. – One single high-precision statistics-dominated experimental measurement of a_μ [4] is facing a prediction in which the contribution with largest

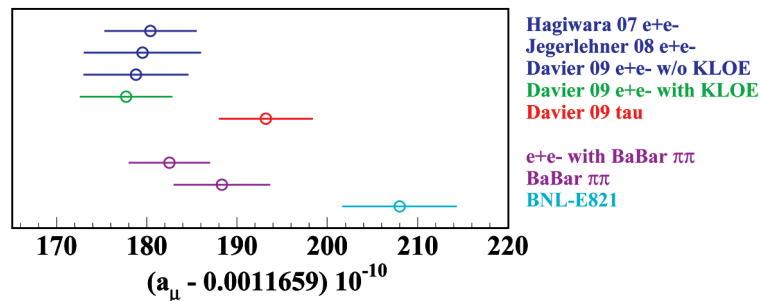


Fig. 5. – a_μ : the present situation.

uncertainty has been confirmed, within reasonable significance, by a number of measurements using various methods, each affected by its own systematics.

The obvious next step, before calling for new physics, is therefore to check the measurement:

- A new collaboration is planning to move the experimental apparatus from BNL to FNAL, and perform a new measurement with statistics increased by a factor of 50, and reduced systematics, bringing the experimental uncertainty down to 0.14 ppm, *i.e.* 1.6×10^{-10} [22].
- It would obviously be intensely desirable to cross-check such a measurement using a completely different set-up. An alternative scheme is explored at J-PARC, with a micro-emittance muon beam inside a high-precision magnetic field, mono-magnet storage “ring” [23].

5.2. Prediction. – On the prediction side, the main effort is understandably devoted to the hadronic VP contribution.

- BaBar will complete its ISR program and provide measurements of all possible hadronic final states in the low energy range relevant to this discussion.
- Belle may check BaBar’s $\pi^+\pi^-$ measurement and BaBar may check Belle’s τ spectral functions. KLOE is working on an analysis with photon tagging too.
- BES-III will measure $R_{\text{had}}(s)$ in the range 2.0–4.6 GeV, something that will improve on a_μ only marginally, but will also measure the $\tau \rightarrow \nu\pi^+\pi^0$ branching fraction with improved precision [24], an important ingredient in the use of the τ -based spectral functions.
- The recent calculation of isospin-breaking corrections [11] will doubtlessly be cross-checked by other authors.
- The collider at Novosibirsk has been upgraded to VEPP-2000 [25], and the CMD [26] and SND experiments too.

Following the vacuum polarisation, the next target in line for improvement is the contribution of light-by-light scattering. Here too work is in progress and there is hope to improve the precision, both theoretically [27], and using results of the $\gamma\gamma$ programme at $D\Phi NE-2$ [28].

In total, there is good hope to bring both the prediction and experimental uncertainties of a_μ at a very few 10^{-10} .

I regret I did not have the time to present the implications of the a_μ discrepancy, if assumed to be due to an underestimated hadronic cross-section, on the estimation of the Higgs mass [29]. Interpretation of the discrepancy as being due to contribution of yet-unknown heavy object(s) in loops is also an interesting possibility [30].

Finally, at higher energy, ISR can be used to understand QCD by exploring the new spectroscopy of $J^{PC} = 1^{--}$ charmonium-like states, opened by the discovery by BaBar of the $Y(4260)$ meson [31].

REFERENCES

- [1] NAFF J. E., NELSON E. B. and RABI I. I., *Phys. Rev.*, **71** (1947) 914.
- [2] SCHWINGER J. S., *Phys. Rev.*, **73** (1948) 416.
- [3] JEGERLEHNER F. and NYFFELER A., *Phys. Rep.*, **477** (2009) 1.
- [4] BENNETT G. W. *et al.* (MUON G-2 COLLABORATION), *Phys. Rev. D*, **73** (2006) 072003.
- [5] AMSLER C. *et al.* (PARTICLE DATA GROUP), *Phys. Lett. B*, **667** (2008) 1.
- [6] BARATE R. *et al.* (ALEPH COLLABORATION), *Z. Phys. C*, **76** (1997) 15.
- [7] ACKERSTAFF K. *et al.* (OPAL COLLABORATION), *Eur. Phys. J. C*, **7** (1999) 571.
- [8] ANDERSON S. *et al.* (CLEO COLLABORATION), *Phys. Rev. D*, **61** (2000) 112002.
- [9] FUJIKAWA M. *et al.* (BELLE COLLABORATION), *Phys. Rev. D*, **78** (2008) 072006.
- [10] DAVIER M., EIDELMAN S., HOECKER A. and ZHANG Z., *Eur. Phys. J. C*, **27** (2003) 497.
- [11] DAVIER M. *et al.*, *Eur. Phys. J. C*, **66** (2010) 127.
- [12] AUBERT B. *et al.* (THE BABAR COLLABORATION), *Phys. Rev. D*, **77** (2008) 092002; **76** (2007) 092005; 012008; **73** (2006) 052003; 012005; **71** (2005) 052001; **70** (2004) 072004.
- [13] AMBROSINO F. *et al.* (KLOE COLLABORATION), *Phys. Lett. B*, **670** (2009) 285.
- [14] AUBERT B. (THE BABAR COLLABORATION), *Phys. Rev. Lett.*, **103** (2009) 231801.
- [15] MALAESCU B., arXiv:0907.3791 [physics.data-an].
- [16] BERNARD D. (BABAR COLLABORATION), arXiv:0910.3294
- [17] AULCHENKO V. M. *et al.* (CMD-2 COLLABORATION), *JETP Lett.*, **82** (2005) 743; AKHMETSHIN R. R. *et al.*, *JETP Lett.*, **84** (2006) 413.
- [18] ACHASOV M. N. *et al.*, *J. Exp. Theor. Phys.*, **101** (2005) 1053.
- [19] HAGIWARA K., MARTIN A. D., NOMURA D. and TEUBNER T., *Phys. Lett. B*, **649** (2007) 173.
- [20] JEGERLEHNER F., *Nucl. Phys. Proc. Suppl.*, **181-182** (2008) 26.
- [21] DAVIER M., HOECKER A., MALAESCU B., YUAN C. Z. and ZHANG Z., *Eur. Phys. J. C*, **66** (2010) 1.
- [22] CAREY R. M. *et al.*, The New (g-2) Experiment, FERMILAB-PROPOSAL-0989.
- [23] AOKI M. *et al.*, *An Experimental Proposal on a New Measurement of the Muon Anomalous Magnetic Moment $g - 2$ and Electric Dipole Moment at J-Parc*, http://j-parc.jp/NuclPart/pac_1001/pdf/KEK_J-PARC-PAC2009-12.pdf.
- [24] ZHEMCHUGOV A., *Nucl. Phys. Proc. Suppl.*, **189** (2009) 353.
- [25] SHATUNOV YU. M., *Phys. Part. Nucl. Lett.*, **5** (2008) 566.
- [26] FEDOTOVICH G. V. (CMD-3 COLLABORATION), *Nucl. Phys. Proc. Suppl.*, **162** (2006) 332.
- [27] PRADES J., *Nucl. Phys. Proc. Suppl.*, **181-182** (2008) 15.
- [28] ARCHILLI F. *et al.*, *Nucl. Phys. Proc. Suppl.*, **181-182** (2008) 248.
- [29] PASSERA M., MARCIANO W. J. and SIRLIN A., *Phys. Rev. D*, **78** (2008) 013009.
- [30] STOCKINGER D., *J. Phys. G*, **34** (2007) R45.
- [31] AUBERT B. *et al.* (BABAR COLLABORATION), *Phys. Rev. Lett.*, **95** (2005) 142001.

Flavour physics within and beyond the Standard Model

U. NIERSTE

Karlsruhe Institute of Technology, Universität Karlsruhe - Karlsruhe, Germany
Institut für Theoretische Teilchenphysik, Universität Karlsruhe - 76128 Karlsruhe, Germany

(ricevuto il 14 Settembre 2010; pubblicato online il 10 Gennaio 2011)

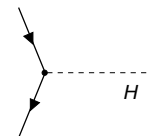
Summary. — I review recent progress in theoretical calculations related to the CKM unitarity triangle. After briefly discussing hints for new physics in B_d - \bar{B}_d and B_s - \bar{B}_s mixing I present three topics of MSSM flavour physics: First I discuss new $\tan\beta$ -enhanced radiative corrections to flavour-changing neutral current (FCNC) amplitudes which go beyond the familiar Higgs-mediated FCNC diagrams and may enhance the mixing-induced CP asymmetry in $B_d \rightarrow \phi K_S$. The second topic is a reappraisal of the idea that flavour violation originates from the soft supersymmetry-breaking terms. Finally I discuss how $\mu \rightarrow e\gamma$ can be used to constrain the flavour structure of the dimension-5 Yukawa interactions which appear in realistic grand-unified theories.

PACS 12.60.Jv – Supersymmetric models.
PACS 13.20.He – Decays of bottom mesons.
PACS 12.10.-g – Unified field theories and models.

1. – Introduction

Flavour physics addresses the transitions between fermions of different generations. Within the Standard Model these transitions originate from the Yukawa couplings of the Higgs field to the fermion fields. In the case of quarks the responsible term of the Lagrangian reads

$$(1) \quad - \sum_{j,k=1}^3 Y_{jk}^u \bar{u}_j^L u_k^R (v + H) - \sum_{j,k=1}^3 Y_{jk}^d \bar{d}_j^L d_k^R (v + H) + \text{h.c.}$$



Here H denotes the field of the yet-to-be-discovered physical Higgs boson and $v = 174 \text{ GeV}$ is the corresponding vacuum expectation value. The indices j and k label

the generations and L and R refer to the chirality of the quark fields. The Yukawa couplings for up-type and down-type quarks are 3×3 matrices in flavour space, denoted by Y^u and Y^d , respectively. Equation (1) entails the mass matrices

$$(2) \quad m^u = Y^u v \quad \text{and} \quad m^d = Y^d v.$$

The diagonalisations of m^u and m^d involve four unitary rotations in flavour space, one each for u^L , u^R , d^L , and d^R . Since the left-handed fields u_k^L and d_k^L , which were originally members of a common $SU(2)$ doublet, undergo different rotations, the electroweak $SU(2)$ symmetry is no more manifest in the physical basis in which mass matrices are diagonal. The mismatch between the rotations of the left-handed fields defines the unitary Cabibbo-Kobayashi-Maskawa (CKM) matrix [1, 2],

$$(3) \quad V = \begin{pmatrix} V_{ud} & V_{us} & V_{ub} \\ V_{cd} & V_{cs} & V_{cb} \\ V_{td} & V_{ts} & V_{tb} \end{pmatrix}.$$

The CKM elements occur in the couplings of the W boson, because the W , *e.g.*, couples the \bar{c}^L field to the linear combination $V_{cd}d^L + V_{cs}s^L + V_{cb}b^L$ as a consequence of the unitary rotations in flavour space. V can be parametrised in terms of three angles and one phase, the CP -violating Kobayashi-Maskawa phase γ [2]. With a history of more than 50 years, research in quark flavour has been essential for the construction of the Standard Model, having guided us to phenomena which were “new physics” at their time: Highlights were the breakdown of the discrete symmetries P [3] and CP [4, 2], the prediction of the charm quark [5] and its mass [6], and a heavy top quark predicted from the size of B_d - \bar{B}_d mixing [7]. In the decade behind us the asymmetric B factories BELLE and BaBar have consolidated the CKM picture of quark flavour physics. With the advent of the LHC era, the focus of flavour physics has shifted from CKM metrology to physics beyond the Standard Model. In the Standard Model flavour-changing neutral current (FCNC) processes (such as meson-antimeson mixing, $B \rightarrow X_s \gamma$ or $K \rightarrow \pi \bar{\nu} \nu$) are forbidden at tree-level and only occur through highly suppressed one-loop diagrams. FCNC processes are therefore excellent probes of new physics. This is a strong rationale to complement the high- p_T physics programs at ATLAS and CMS with precision flavour physics at LHCb, NA62, BELLE-II, Super-B, BES-III, J-PARC and the future intense proton source Project X at Fermilab.

With the discovery of neutrino flavour oscillations, the much younger field of lepton flavour physics has emerged. The Standard Model in its original formulation [8] lacks a right-handed neutrino field and can neither accommodate neutrino masses nor neutrino oscillations. The simplest remedy for this is the introduction of a dimension-5 Yukawa term composed of two lepton doublets $L = (\nu_\ell^L, \ell^L)$ and two Higgs doublets leading to Majorana masses for the neutrinos and generating the desired lepton flavour mixing. Alternatively one can mimic the quark sector by introducing right-handed neutrino fields (and imposing $B - L$, the difference between baryon and lepton numbers, as an exact symmetry). With both variants FCNC transitions among charged leptons (such as $\mu \rightarrow e \gamma$) are unobservably small, so that any observation of such a process will imply the existence of further new particles. Charged-lepton FCNC decays are currently searched for in the dedicated MEG experiment (studying $\mu \rightarrow e \gamma$), in B factory data (on, *e.g.*, $\tau \rightarrow \mu \gamma$) and at three of the four major LHC experiments (searching, *e.g.*, for $\tau \rightarrow \mu \bar{\mu} \mu$).

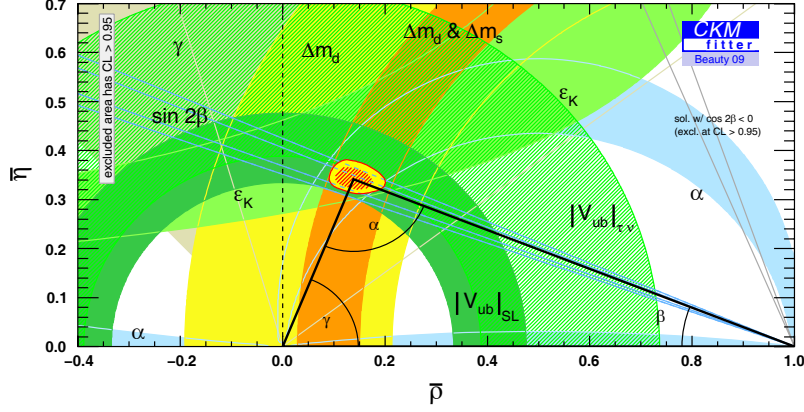


Fig. 1. – (Colour on-line) Experimental constraints on the unitarity triangle, from ref. [11].

In the following section I briefly review recent theoretical progress on the Standard-Model predictions for FCNC processes. Subsequently I discuss new developments in flavour physics beyond the Standard Model. I limit myself to supersymmetric theories, which reflects my personal research interests. For a recent broader overview, which also covers extra dimensions and Little-Higgs models, see ref. [9]. Exhaustive studies of the flavour sector in a four-generation Standard Model can be found in refs. [10].

2. – Standard Model

The standard unitarity triangle (UT) is a triangle with unit baseline and apex $(\bar{\rho}, \bar{\eta})$, which is defined through

$$(4) \quad \bar{\rho} + i\bar{\eta} \equiv -\frac{V_{ub}^* V_{ud}}{V_{cb}^* V_{cd}}.$$

The two non-trivial sides of the triangle are $R_u \equiv \sqrt{\bar{\rho}^2 + \bar{\eta}^2}$ and $R_t \equiv \sqrt{(1 - \bar{\rho})^2 + \bar{\eta}^2}$. The triangle's three angles

$$(5) \quad \alpha = \arg \left[-\frac{V_{td} V_{tb}^*}{V_{ud} V_{ub}^*} \right], \quad \beta = \arg \left[-\frac{V_{cd} V_{cb}^*}{V_{td} V_{tb}^*} \right], \quad \gamma = \arg \left[-\frac{V_{ud} V_{ub}^*}{V_{cd} V_{cb}^*} \right]$$

are associated with CP -violating quantities. Measurements of flavour-changing quantities imply constraints on $(\bar{\rho}, \bar{\eta})$. Last year's global analysis of the UT performed by the CKMfitter Collaboration is shown in fig. 1. For the results of the UTFit Collaboration, which uses a different statistical approach see ref. [12]. The figure shows the consistency of the various measurements, which single out the small yellow area as the allowed region for the apex of the triangle. Clearly, the CKM mechanism is the dominant source of flavour violation in the quark sector.

From the quantities entering the global UT analysis in fig. 1 the meson-antimeson mixing amplitudes are the ones most sensitive to generic new physics. While the extraction of the UT angle β from the CP phase in $B_d - \bar{B}_d$ mixing is theoretically very clean, all other quantities related to meson-antimeson mixing are plagued by theoretical uncertainties. Namely, the uncertainties in the mass differences Δm_q and Δm_s of the two $B - \bar{B}$

mixing complexes and in ϵ_K , which quantifies CP violation in K - \bar{K} mixing, completely dominate over the irrelevantly small experimental errors. Note that Δm_s is practically independent of $\bar{\rho}$ and $\bar{\eta}$ and is only useful for the UT fit because the ratio $\Delta m_d/\Delta m_s$ has a smaller uncertainty than Δm_d . The K - \bar{K} mixing amplitude M_{12} involves the matrix element $\langle K^0 | H^{\Delta S=2} | \bar{K}^0 \rangle$ of the $\Delta S = 2$ Hamiltonian $H^{\Delta S=2}$ [13]. $H^{\Delta S=2}$ is proportional to the four-quark operator $\bar{d}^L \gamma_\nu s^L \bar{d}^L \gamma^\nu s^L$ with the relevant matrix element

$$(6) \quad \langle K^0 | \bar{d}^L \gamma_\nu s^L \bar{d}^L \gamma^\nu s^L(\mu) | \bar{K}^0 \rangle = \frac{2}{3} M_K^2 f_K^2 \frac{\hat{B}_K}{b(\mu)}.$$

This equation merely defines the parameter \hat{B}_K which is commonly used to parametrise the matrix element of interest. In eq. (6) $M_K = 497.6 \text{ MeV}$ and $f_K = 160 \text{ MeV}$ are mass and decay constant of the neutral kaon and $b_K(\mu)$ is introduced to render \hat{B}_K independent of the unphysical renormalisation scale μ and the renormalisation scheme chosen for the definition of the operator $\bar{d}^L \gamma_\nu s^L \bar{d}^L \gamma^\nu s^L(\mu)$. In the commonly used $\overline{\text{MS}}$ scheme one has $b_K(\mu = 1 \text{ GeV}) = 1.24 \pm 0.02$. The matrix element in eq. (6) must be calculated with lattice gauge theory. A new computation by Aubin, Laiho and Van de Water finds [14]

$$(7) \quad \hat{B}_K = 0.724(8)(29).$$

This result is in good agreement with the 2007 result of the RBC and UKQCD Collaborations, $\hat{B}_K = 0.720(13)(37)$ [15]. In view of the superb experimental precision in $|\epsilon_K| = (2.23 \pm 0.01) \times 10^{-3}$ further progress on \hat{B}_K is certainly highly desirable. The increasing precision in \hat{B}_K has also stimulated more precise analyses of other ingredients of M_{12} . Recently a reanalysis of the long-distance contribution to $\text{Im} M_{12}$ has resulted in an upward shift of 2% in ϵ_K [16]. A similar contribution constituting the element Γ_{12} of the decay matrix, affects ϵ_K at the few-percent level [17, 18].

In the case of B - \bar{B} mixing all long-distance contributions are highly GIM-suppressed and only the local contribution from the box diagram with internal top quarks and W bosons matters. The two mass eigenstates of the neutral B_q - \bar{B}_q system differ in their masses and widths. The mass difference Δm_q , $q = d, s$, which equals the B_q - \bar{B}_q oscillation frequency, is given by $\Delta m_q \simeq 2|M_{12}^q| = 2|\langle B_q | H^{\Delta B=2} | \bar{B}_q \rangle|$. Lattice calculations are needed to compute $f_{B_q}^2 \hat{B}_{B_q}$, which is defined in analogy to eq. (6). Here I focus on the ratio $\Delta m_d/\Delta m_s$ yielding the orange (medium gray) annulus centered around $(\bar{\rho}, \bar{\eta}) = (1, 0)$ in fig. 1. This ratio involves the hadronic quantity

$$(8) \quad \xi = \frac{f_{B_s} \sqrt{\hat{B}_{B_s}}}{f_{B_d} \sqrt{\hat{B}_{B_d}}} = 1.23 \pm 0.04.$$

The numerical value in eq. (8) is my bold average of the values summarised by Aubin at the *Lattice'09* conference [19]. With this number and the measured values $\Delta m_{B_d} = (0.507 \pm 0.005) \text{ ps}^{-1}$ [20] and $\Delta m_{B_s} = (17.77 \pm 0.10 \pm 0.07) \text{ ps}^{-1}$ [21] one finds

$$(9) \quad \left| \frac{V_{td}}{V_{ts}} \right| = \sqrt{\frac{\Delta m_{B_d}}{\Delta m_{B_s}}} \sqrt{\frac{M_{B_s}}{M_{B_d}}} \xi = 0.210 \pm 0.007.$$

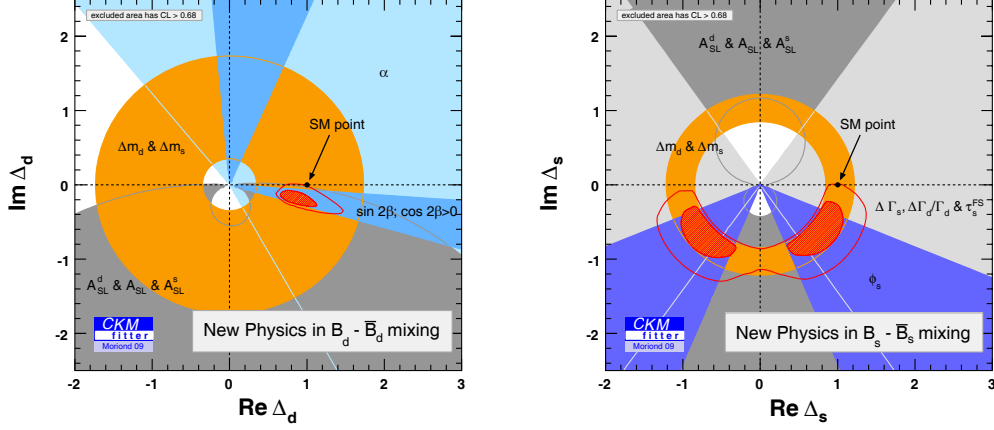


Fig. 2. – Complex Δ_d and Δ_s planes, plots taken from the web site in ref. [11]. (See ref. [23] for details of the analysis.) Similar analyses by the UTfit Collaboration can be found in refs. [12,24].

With $|V_{td}/V_{ts}| = 0.228 R_t$ one finds $R_t = 0.92 \pm 0.03$ for the side of the UT opposite to γ . For a pedagogical introduction into meson-antimeson mixing and CKM phenomenology cf. ref. [22].

3. – Beyond the Standard Model

3.1. Phenomenology of new physics in $B-\bar{B}$ mixing. – The plot of the UT in fig. 1 is not the best way to show possible deviations from the Standard Model, because it conceals certain correlations between different quantities. In the LHC era we will more often see plots of quantities which directly quantify the size of new physics contributions. In the case of meson-antimeson mixing new physics can be parametrised model-independently by a single complex parameter [25]. For $B_q-\bar{B}_q$ mixing, $q = d, s$, one defines

$$(10) \quad \Delta_q = \frac{M_{12}^q}{M_{12}^{\text{SM},s}}.$$

The CKMfitter Collaboration has found that the Standard-Model point $\Delta_d = 1$ is ruled out at 95% CL (left plot in fig. 2), if all other quantities entering the global UT analysis are assumed free of new physics contributions. This discrepancy is largely driven by $B(B^+ \rightarrow \tau^+\nu)$ and, if interpreted in terms of new physics, may well indicate non-standard physics in quantities other than $B_d-\bar{B}_d$ mixing. A tension on the global UT fit was also noted by Lunghi and Soni [26] and by Buras and Guadagnoli [18]. The situation is much simpler in the case of $B_s-\bar{B}_s$ mixing, which shows a deviation from the Standard Model expectation of similar size (right plot in fig. 2). The allowed region for Δ_s is essentially independent of input other than the $B_s-\bar{B}_s$ mixing amplitude M_{12}^s . The quantities entering the analysis are primarily Δm_s , the width difference $\Delta\Gamma_s$ [27,25], the time-dependent angular distribution in $B_s \rightarrow J/\psi\phi$ (with access to the mixing-induced CP asymmetry $A_{CP}^{\text{mix}}(B_s \rightarrow J/\psi\phi)$ if the B_s flavour is tagged), and the CP asymmetry in flavour-specific decays a_{fs}^s [27,25]. The first global analysis of these quantities, which

used improved Standard-Model predictions, was performed in 2006 [25] showing a 2σ deviation from the Standard-Model value $\Delta_s = 1$. At the time of this talk the discrepancy from the combined $D\bar{O}$ and CDF data on $B_s \rightarrow J/\psi\phi$ alone was between 2.0σ and 2.3σ , depending on details of the statistical analysis [28]. After this conference the discrepancy in a_{FB}^e has increased due to a new $D\bar{O}$ measurement of the dimuon asymmetry in a mixed B_d, B_s data sample [29]. On the other hand, new CDF data on $A_{CP}^{\text{mix}}(B_s \rightarrow J/\psi\phi)$ have pulled the result towards the Standard Model [30]. Still all measurements favour $\arg \Delta_s < 0$.

3.2. Supersymmetry with large $\tan\beta$. – Extensions of the Standard Model typically come with new sources of flavour violation, beyond the Yukawa couplings in eq. (1). In the Minimal Supersymmetric Standard Model (MSSM) the soft supersymmetry breaking terms *a priori* possess a flavour structure which is unrelated to Y^u and Y^d . To avoid excessive FCNCs violating experimental bounds the MSSM is often supplemented with the assumption of Minimal Flavour Violation (MFV), which amounts to a flavour-blind supersymmetry-breaking sector. In the MFV-MSSM supersymmetric FCNC transitions are typically smaller than the error bars of today's experiments, unless the parameter $\tan\beta$ is large. Probing values around $\tan\beta = 60$ tests the unification of top and bottom Yukawa couplings. Importantly, loop suppression factors can be offset by a factor of $\tan\beta$ and may yield contributions of order one, with most spectacular effects in $B(B_s \rightarrow \mu^+\mu^-)$ [31]. The $\tan\beta$ -enhanced loop corrections must be summed to all orders in perturbation theory. In the limit that the masses of the SUSY particles in the loop are heavier than the electroweak vev and the masses of the five Higgs bosons, $M_{\text{SUSY}} \gg v, M_{A^0}, M_{H^\pm} \dots$, one can achieve this resummation easily: After integrating out the heavy SUSY particles one obtains an effective two-Higgs doublet model with novel loop-induced couplings [32]. In supersymmetric theories, however, it is natural that M_{SUSY} is not much different from v and further $M_{\text{SUSY}} \gg M_{A^0}$ involves an unnatural fine-tuning in the Higgs sector. Phenomenologically, large- $\tan\beta$ scenarios comply with the experimental bound from $B(B_s \rightarrow \mu^+\mu^-)$ more easily if M_{A^0} is large, which may easily conflict with $M_{\text{SUSY}} \gg M_{A^0}$. To derive resummation formulae valid for arbitrary values of M_{SUSY} one cannot resort to the method of an effective field theory. Instead one should work strictly diagrammatically in the full MSSM to identify $\tan\beta$ -enhanced corrections. This procedure requires full control of the renormalisation scheme: The analytical results for the resummed expressions differ for different schemes and not all renormalisation schemes permit an analytic solution to the resummation problem. The diagrammatic resummation has been obtained for the flavour-diagonal case in ref. [33] and recently for flavour-changing interactions in ref. [34]. This opens the possibility to study $\tan\beta$ -enhanced corrections also to supersymmetric loop processes which decouple for $M_{\text{SUSY}} \gg v$ and to collider processes involving supersymmetric particles. In ref. [34] a novel large effect, which does not involve Higgs bosons, in the Wilson coefficient C_8 has been found, with interesting implications for the mixing-induced CP asymmetry $S_{\phi K_S}$ in $B_d \rightarrow \phi K_S$ (see fig. 3).

3.3. Radiative flavour violation. – A symmetry-based definition of MFV starts from the observation that the MSSM sector is invariant under arbitrary unitary rotations of the (s)quark multiplets in flavour space. This $[U(3)]^3$ flavour symmetry ($[U(3)]^5$ if (s)leptons are included) is broken by the Yukawa couplings, and MFV can be defined through the postulate that the Yukawa couplings are the only spurion fields breaking the $[U(3)]^3$ flavour symmetry [35]. Interestingly, there is a viable alternative to MFV to solve the

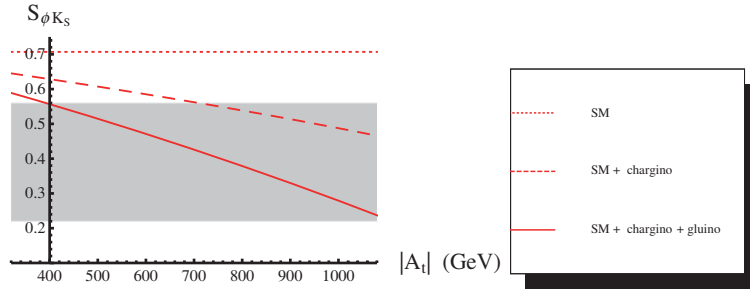


Fig. 3. – $S_{\phi K_S}$ as a function of $|A_t|$ for a parameter point compatible with other experimental constraints (see ref. [34] for details). Solid: full result including the new contribution, dashed: SM plus one-loop chargino diagram, dotted: SM value. Shaded area: experimental 1σ range.

supersymmetric flavour problem: We may start with a Yukawa sector in which all Yukawa couplings of the first and second generation are zero. That is, the MSSM superpotential possesses an *exact* $[U(2)]^3 \times U(1)$ symmetry. Then we postulate that the trilinear SUSY breaking terms A_{ij}^u and A_{ij}^d are the spurion fields breaking this symmetry. The observed off-diagonal CKM elements and the light quark masses are generated radiatively through squark-gluino loops, explaining their smallness in a natural way. In ref. [36] it has been found that this setup of Radiative Flavour Violation (RFV) complies with all FCNC bounds, if the squark masses are larger than roughly 500 GeV. By contrast, the bilinear SUSY breaking terms cannot be the spurion fields breaking $[U(2)]^3 \times U(1)$ without violating the constraints from FCNC processes. The idea that SUSY breaking could be the origin of flavour violation is not new [37, 38], remarkably the absence of tree-level light-fermion Yukawa couplings substantially alleviates the supersymmetric CP problem associated with electric dipole moments [38].

The finding that loop contributions involving A_{ij}^q , $q = u, d$, can be large has also consequences for the generic MSSM: In FCNC analyses aiming at constraints on flavour-violating SUSY-breaking terms one must include chirally enhanced higher-order corrections involving A_{ij}^q and, if $\tan\beta$ is large, also corrections with bilinear SUSY-breaking terms [39]. The trilinear terms further imply important loop corrections to quark and lepton masses [40] and can induce right-handed W couplings [41].

3.4. MSSM with GUT constraints. – In grand-unified theories (GUTs) quarks and leptons are combined into symmetry multiplets. As a consequence, it may be possible to see imprints of lepton mixing in the quark sector and vice versa. In particular, the large atmospheric neutrino mixing angle may influence $b \rightarrow s$ transitions through the mixing of right-handed \tilde{b} and \tilde{s} squarks [42]. Yet the usual small dimension-4 Yukawa interactions of the first two generations are sensitive to corrections from dimension-5 terms which are suppressed by $M_{\text{GUT}}/M_{\text{Planck}}$ [43]. These contributions are welcome to fix the unification of the Yukawa couplings, but may come with an arbitrary flavour structure, spoiling the predictiveness of the quark-lepton flavour connection. $SU(5)$ and $SO(10)$ models with dimension-5 Yukawa couplings have been studied in great detail [44]. Phenomenologically one can constrain the troublesome flavour misalignment using data on FCNC transitions between the first two generations. Here I present a recent $SU(5)$ analysis exploiting the experimental bound on $B(\mu \rightarrow e\gamma)$ [45]. At the GUT scale the

Yukawa matrices for down-type quarks, Y_d and Y_l , read

$$(11) \quad Y_d = Y_{\text{GUT}} + k_d \frac{\sigma}{M_{\text{Planck}}} Y_\sigma, \quad Y_l^\top = Y_{\text{GUT}} + k_e \frac{\sigma}{M_{\text{Planck}}} Y_\sigma.$$

Here Y_{GUT} is the unified dimension-4 Yukawa matrix, $\sigma = \mathcal{O}(M_{\text{GUT}})$ is a linear combination of Higgs vevs and the prefactors k_d and k_e differ from each other due to GUT breaking. If the universality condition $A_l = A_d = a_0 Y_{\text{GUT}}$ is invoked at the GUT scale, any misalignment between Y_{GUT} and Y_σ will lead to a non-MFV low-energy theory, because $A_l \not\propto Y_l$ and $A_d \not\propto Y_d$. We may parametrise this effect as

$$(12) \quad A_l \simeq A_0 \begin{pmatrix} \cos \theta & -\sin \theta & 0 \\ \sin \theta & \cos \theta & 0 \\ 0 & 0 & 1 \end{pmatrix} Y_l.$$

Now the experimental upper bound on $B(\mu \rightarrow e\gamma)$ determines the maximally allowed $|\theta|$ as a function of A_0 . In ref. [45] it is found that $|\theta|$ can hardly exceed 10 degrees once $|A_0|$ exceeds 50 GeV. An analysis in the quark sector (studying $SO(10)$ models [42]) finds similar strong constraints from ϵ_K [46]. As a consequence, the dimension-5 terms can barely spoil the GUT prediction derived from the dimension-4 relation $Y_d = Y_l^\top = Y_{\text{GUT}}$, unless $|A_0|$ is small. This result may indicate that dimension-4 and dimension-5 Yukawa couplings are governed by the same flavour symmetries.

* * *

I thank the organisers for the invitation to this wonderful conference and for financial support. The presented work is supported by the DFG Research Unit SFB-TR 9, by BMBF grant no. 05H09VKF and by the EU Contract No. MRTN-CT-2006-035482, “FLAVIANet”.

REFERENCES

- [1] CABIBBO N., *Phys. Rev. Lett.*, **10** (1963) 531.
- [2] KOBAYASHI M. and MASKAWA T., *Progr. Theor. Phys.*, **49** (1973) 652.
- [3] LEE T. D. and YANG C. N., *Phys. Rev.*, **104** (1956) 254.
- [4] CHRISTENSON J. H., CRONIN J. W., FITCH V. L. and TURLAY R., *Phys. Rev. Lett.*, **13** (1964) 138.
- [5] GLASHOW S. L., ILIOPOULOS J. and MAIANI L., *Phys. Rev. D*, **2** (1970) 1285.
- [6] GAILLARD M. K. and LEE B. W., *Phys. Rev. D*, **10** (1974) 897.
- [7] ALBRECHT H. *et al.* (ARGUS COLLABORATION), *Phys. Lett. B*, **192** (1987) 245.
- [8] GLASHOW S. L., *Nucl. Phys.*, **22** (1961) 579; WEINBERG S., *Phys. Rev. Lett.*, **19** (1967) 1264; SALAM A., in *Elementary Particle Physics (Nobel Symp. 8)*, edited by SVARTHOLM N. (Almqvist and Wilsell, Stockholm) 1968.
- [9] BURAS A. J., to appear in *Proceedings of Europhysics Conference on High Energy Physics, EPS-HEP 2009, July 16–22, 2009, Krakow, Poland*; arXiv:0910.1032 [hep-ph].
- [10] BOBROWSKI M., LENZ A., RIEDL J. and ROHRWILD J., *Phys. Rev. D*, **79** (2009) 113006; BURAS A. J., DULING B., FELDMANN T., HEIDSIECK T., PROMBERGER C. and RECKSIEGEL S., arXiv:1002.2126 [hep-ph]; EBERHARDT O., LENZ A. and ROHRWILD J., arXiv:1005.3505 [hep-ph].
- [11] HÖCKER A., LACKER H., LAPLACE S. and LE DIBERDER F., *Eur. Phys. J. C*, **21** (2001) 225; CHARLES J. *et al.* (CKMFITTER GROUP), *Eur. Phys. J. C*, **41** (2005) 1. Figures taken from the web site: <http://ckmfitter.in2p3.fr>.

- [12] CIUCHINI M. *et al.*, *JHEP*, **0107** (2001) 013; BONA M. *et al.* (UTFIT COLLABORATION), arXiv:hep-ph/0509219. For updated analyses see: <http://utfit.roma1.infn.it>.
- [13] BURAS A. J., JAMIN M. and WEISZ P. H., *Nucl. Phys. B*, **347** (1990) 491; HERRLICH S. and NIERSTE U., *Nucl. Phys. B*, **419** (1994) 292; *Phys. Rev. D*, **52** (1995) 6505; *Nucl. Phys. B*, **476** (1996) 27.
- [14] AUBIN C., LAIHO J. and VAN DE WATER R. S., *Phys. Rev. D*, **81** (2010) 014507.
- [15] COHEN S. D. and ANTONIO D. (RBC and UKQCD COLLABORATIONS), *PoS, LAT2007* (2007) 347.
- [16] BURAS A. J., GUADAGNOLI D. and ISIDORI G., *Phys. Lett. B*, **688** (2010) 309.
- [17] NIERSTE U., in ANIKEEV K. *et al.*, *B physics at the Tevatron: Run II and beyond* [hep-ph/0201071].
- [18] BURAS A. J. and GUADAGNOLI D., *Phys. Rev. D*, **78** (2008) 033005.
- [19] AUBIN C., contribution to *Lattice 2009, Beijing, China, 25-31 Jul 2009*, arXiv:0909.2686 [hep-lat].
- [20] AMSLER C. *et al.* (PARTICLE DATA GROUP), *Phys. Lett. B*, **667** (2008) 1.
- [21] ABAZOV V. M. *et al.* (DØ COLLABORATION), *Phys. Rev. Lett.*, **97** (2006) 021802; DØ Note 5618-CONF; ABULENCIA A. *et al.* (CDF COLLABORATION), *Phys. Rev. Lett.*, **97** (2006) 242003.
- [22] NIERSTE U., *Three Lectures on Meson Mixing and CKM Phenomenology*, in *Heavy Quark Physics*, edited by ALI A. and IVANOV M., ISBN 978-3-935702-40-9, arXiv:0904.1869 [hep-ph].
- [23] DESCHAMPS O., *CKM global fit and constraints on New Physics in the B meson mixing*, arXiv:0810.3139 [hep-ph].
- [24] BONA M. *et al.* (UTFIT COLLABORATION), *JHEP*, **0803** (2008) 049.
- [25] LENZ A. and NIERSTE U., *JHEP*, **0706** (2007) 072.
- [26] LUNGI E. and SONI A., *Phys. Lett. B*, **666** (2008) 162.
- [27] BENEKE M., BUCHALLA G., GREUB C., LENZ A. and NIERSTE U., *Phys. Lett. B*, **459** (1999) 631; BENEKE M., BUCHALLA G., LENZ A. and NIERSTE U., *Phys. Lett. B*, **576** (2003) 173; CIUCHINI M., FRANCO E., LUBICZ V., MESCIA F. and TARANTINO C., *JHEP*, **0308** (2003) 031.
- [28] CDF and DØ COLLABORATIONS, Public Note *CDF/PHYS/BOTTOM/CDFR/9787 (DØ Note 5928-CONF)*.
- [29] ABAZOV V. M. *et al.* (THE DØ COLLABORATION), *Evidence for an anomalous like-sign dimuon charge asymmetry*, arXiv:1005.2757 [hep-ex].
- [30] OAKES LOUISE, talk at *FPCP 2010, May 25-29, 2010, Torino, Italy*, <http://agenda.infn.it/materialDisplay.py?contribId=12&materialId=slides&confId=2635>.
- [31] BABU K. S. and KOLDA C. F., *Phys. Rev. Lett.*, **84** (2000) 228 [arXiv:hep-ph/9909476]; HUANG C. S., LIAO W., YAN Q. S. and ZHU S. H., *Phys. Rev. D*, **63** (2001) 114021; **64** (2001) 059902 (Erratum) [arXiv:hep-ph/0006250]; DEDES A., DREINER H. K. and NIERSTE U., *Phys. Rev. Lett.*, **87** (2001) 251804 [arXiv:hep-ph/0108037].
- [32] HALL L. J., RATAZZI R. and SARID U., *Phys. Rev. D*, **50** (1994) 7048 [arXiv:hep-ph/9306309]; HEMPFLING R., *Phys. Rev. D*, **49** (1994) 6168; CARENA M., OLECHOWSKI M., POKORSKI S. and WAGNER C. E. M., *Nucl. Phys. B*, **426** (1994) 269 [arXiv:hep-ph/9402253]; BLAZEK T., RABY S. and POKORSKI S., *Phys. Rev. D*, **52** (1995) 4151 [arXiv:hep-ph/9504364]; HAMZAoui C., POSPELOV M. and TOHARIA M., *Phys. Rev. D*, **59** (1999) 095005 [arXiv:hep-ph/9807350]; BURAS A. J., CHANKOWSKI P. H., ROSIEK J. and SLAWIANOWSKA L., *Nucl. Phys. B*, **619** (2001) 434; *Phys. Lett. B*, **546** (2002) 96 [arXiv:hep-ph/0207241]; *Nucl. Phys. B*, **659** (2003) 3 [arXiv:hep-ph/0210145]; GORBAHN M., JÄGER S., NIERSTE U. and TRINE S., arXiv:0901.2065 [hep-ph].
- [33] CARENA M., GARCIA D., NIERSTE U. and WAGNER C. E. M., *Nucl. Phys. B*, **577** (2000) 88 [arXiv:hep-ph/9912516]; MARCHETTI S., MERTENS S., NIERSTE U. and STOCKINGER D., *Phys. Rev. D*, **79** (2009) 013010 [arXiv:0808.1530 [hep-ph]].
- [34] HOFER L., NIERSTE U. and SCHERER D., *JHEP*, **0910** (2009) 081 [arXiv:0907.5408 [hep-ph]]; to appear in *Proceedings of the 2009 Europhysics Conference on High Energy Physics (EPS-HEP 2009), Cracow, Poland, 16-22 Jul 2009*, arXiv:0909.4749 [hep-ph].

- [35] D'AMBROSIO G., GIUDICE G. F., ISIDORI G. and STRUMIA A., *Nucl. Phys. B*, **645** (2002) 155.
- [36] CRIVELLIN A. and NIERSTE U., *Phys. Rev. D*, **79** (2009) 035018.
- [37] BUCHMULLER W. and WYLER D., *Phys. Lett. B*, **121** (1983) 321; FERRANDIS J. and HABAN., *Phys. Rev. D*, **70** (055003) 2004.
- [38] BORZUMATI F., FARRAR G. R., POLONSKY N. and THOMAS S. D., arXiv:hep-ph/9805314; *Nucl. Phys. B*, **555** (1999) 53.
- [39] CRIVELLIN A. and NIERSTE U., *Phys. Rev. D*, **81** (2010) 095007.
- [40] GABBIANI F., GABRIELLI E., MASIERO A. and SILVESTRINI L., *Nucl. Phys. B*, **477** (1996) 321; CRIVELLIN A. and GIRRBACH J., *Phys. Rev. D*, **81** (2010) 076001.
- [41] CRIVELLIN A., *Phys. Rev. D*, **81** (2010) 031301.
- [42] MOROI T., *Phys. Lett. B*, **493** (2000) 366; CHANG D., MASIERO A. and MURAYAMA H., *Phys. Rev. D*, **67** (2003) 075013.
- [43] ELLIS J. R. and GAILLARD M. K., *Phys. Lett. B*, **88** (1979) 315.
- [44] BAEK S., GOTO T., OKADA Y. and OKUMURA K. I., *Phys. Rev. D*, **64** (2001) 095001 [arXiv:hep-ph/0104146]; BORZUMATI F. and YAMASHITA T., arXiv:0903.2793 [hep-ph]; BORZUMATI F. and YAMASHITA T., *AIP Conf. Proc.*, **1200** (2010) 916.
- [45] GIRRBACH J., MERTENS S., NIERSTE U. and WIESENFELDT S., *JHEP*, **1005** (2010) 026.
- [46] TRINE S., WESTHOFF S. and WIESENFELDT S., *JHEP*, **08** (2009) 002.

Early data from the LHCb experiment

U. KERZEL(*)

Cavendish Laboratory (HEP) - JJ Thomson Avenue, Cambridge, CB3 0HE, UK

(ricevuto il 14 Settembre 2010; pubblicato online l'11 Gennaio 2011)

Summary. — The LHCb experiment at the Large Hadron Collider (LHC) has been optimised for high-precision measurements of the charm and beauty sector. This talk summarised the first results obtained from the pilot run of the LHC at the end of 2009.

PACS 07.05.-t – Computers in experimental physics.

PACS 13.25.-k – Hadronic decays of mesons.

PACS 13.30.-a – Decays of baryons.

PACS 13.20.-v – Leptonic, semileptonic, and radiative decays of mesons.

1. – Introduction

The LHCb experiment [1] is one of the four major experiments at the Large Hadron Collider (LHC) and focuses on detailed studies of decays of charm and bottom hadrons. Its main objective is to determine precisely and over-constrain the parameters of the CKM matrix, and to search for further sources of CP violation and New Physics beyond the Standard Model in rare B- and charm hadron decays.

Particles containing charm and bottom quarks are produced mainly in the forward (or backward) direction which motivates the design of the LHCb experiment as a single-arm forward spectrometer as illustrated in fig. 1.

Its main features are a high-precision silicon vertex detector, tracking stations, electromagnetic and hadronic calorimeters, muon detectors and two Ring-Imaging Cherenkov (RICH) detectors which provide excellent particle identification capabilities between approximately 2 to 100 GeV/c.

2. – Performance with first data

During the pilot run in 2009, approximately 26000 proton-proton collisions were recorded by the LHCb experiment for which all sub-detectors were operational and in

(*) On behalf of the LHCb Collaboration.

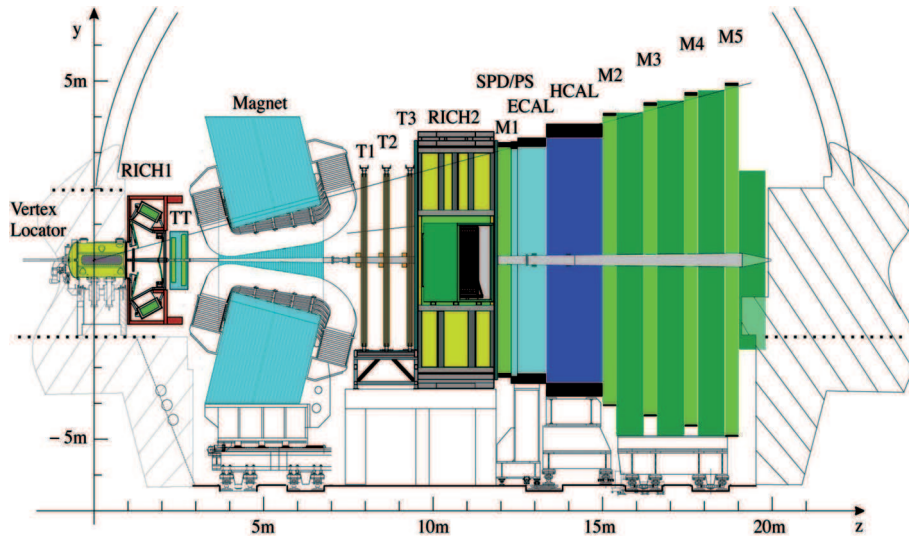


Fig. 1. – Schematic overview of the LHCb experiment.

stable running conditions. More than 99% of all read-out channels in each sub-detector were operational during the pilot run. Special care has to be taken when including the vertex-detector (VELO) in the detector read-out: the VELO consists of 21 stations of silicon wafers with R and Φ readout arranged on two retractable detector halves inside the beam vacuum. During injection and beam setup, both halves are retracted by 30 mm from the nominal beam position in a safe position behind the LHC collimator aperture. During nominal data-taking conditions, both halves are then successively moved closer to the beam until they are 8 mm away from the nominal beam line. The detector modules were closed to 15 mm from this nominal position during the pilot run as the lower energy of the proton beam could potentially reach the nominal detector position in case of a misbehaviour of some beam optic magnets. Figure 2 shows the distribution of the vertex resolution as a function of the track multiplicity in the first data.

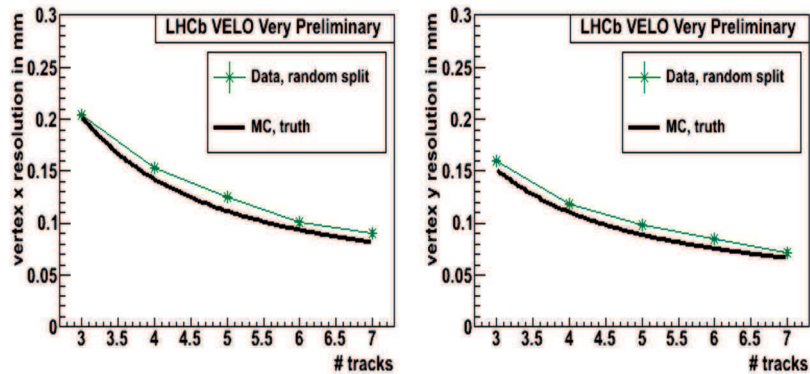


Fig. 2. – Vertex detector resolution as a function of track multiplicity (VELO 15 mm from nominal position). The expectation from simulation is overlaid.

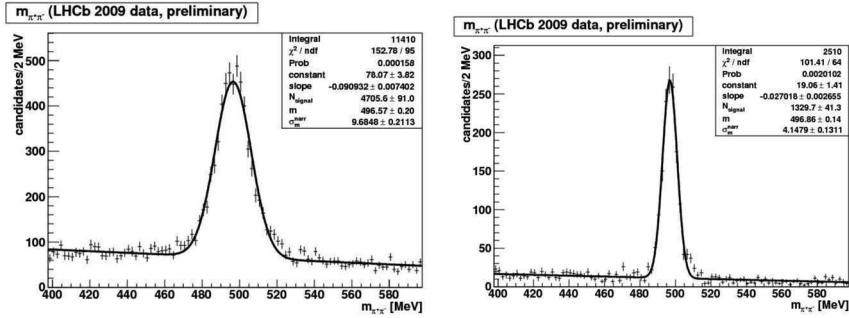


Fig. 3. – The decay $K_s \rightarrow \pi\pi$ without (left) and with (right) VELO information.

The improvement in the mass resolution obtained by including data recorded by the (half-closed) VELO is illustrated by reconstructing the decay $K_s \rightarrow \pi\pi$ (fig. 3) and $\Lambda \rightarrow p\pi$ (fig. 4): The width of a single Gaussian function fitted to the invariant mass distribution reduces from $\sigma = 2.6 \pm 0.1$ (stat.) MeV/ c^2 to $\sigma = 1.4 \pm 0.1$ (stat.) MeV/ c^2 in the case of the K_s and from $\sigma = 9.7 \pm 0.2$ (stat.) MeV/ c^2 to $\sigma = 4.1 \pm 0.1$ (stat.) MeV/ c^2 in the case of the Λ . Although the amount of data collected so far does not yet allow a full alignment of the LHCb detector, the obtained widths of the distributions are already very close to the expectations from simulated events. The central values of the mass peaks agree with the current world average (obtained from the Particle Data Group), indicating that the detector material is correctly described in the reconstruction software and the magnetic field is well calibrated.

Figure 5 illustrates the excellent performance of the calorimeter showing reconstructed decays of $\pi^0 \rightarrow \gamma\gamma$ and $\eta \rightarrow \gamma\gamma$.

The efficiency measured by the muon system exceeds 99% and the measured invariant di-muon mass spectrum is shown in fig. 6. Due to the low yield of di-muon events in the data recorded during the pilot run, a more quantitative evaluation will be done with the data recorded in 2010.

Highly efficient particle identification is of vital importance to most physics analyses being prepared by the LHCb experiment. The LHCb spectrometer features two Rich Imaging Cherenkov (RICH) detectors which offer unique particle identification capabilities over a large momentum range. As particles traverse the radiator material, Cherenkov

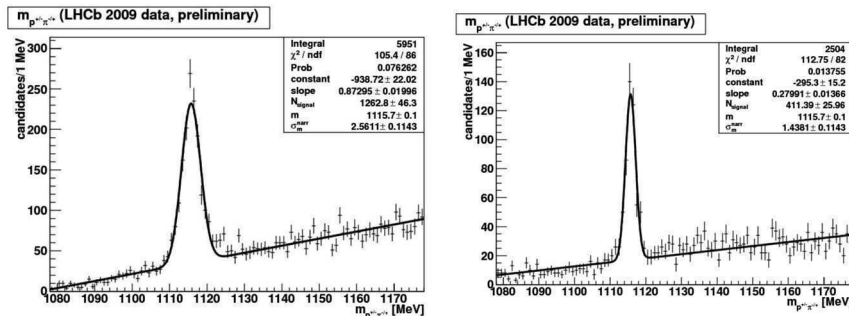


Fig. 4. – The decay $\Lambda \rightarrow p\pi$ without (left) and with (right) VELO information.

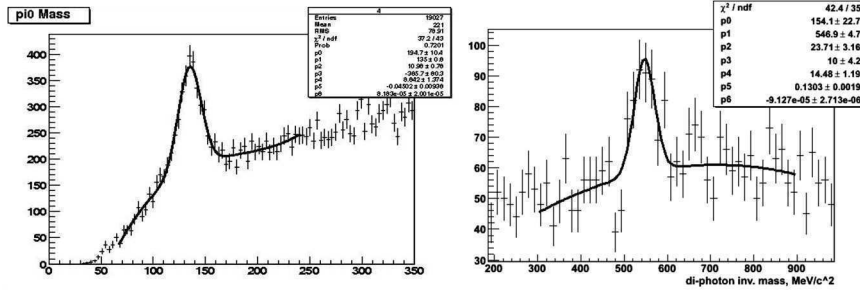


Fig. 5. – The decays $\pi^0 \rightarrow \gamma\gamma$ (left) and $\eta^0 \rightarrow \gamma\gamma$ measured in the calorimeter (LHCb preliminary).

light is being emitted which is then detected by photo-detectors. Together with momentum information obtained from the tracking system, the resulting rings allow to deduce the particle species from the size of the measured Cherenkov ring as illustrated in fig. 7. Figure 8 shows the invariant mass spectrum of $\Phi \rightarrow KK$ candidates: Starting from all candidates (left), a clean mass peak is obtained after selecting tracks compatible with the kaon mass hypothesis (right).

3. – LHCb physics programme

The LHCb physics programme focuses on discovering New Physics beyond the current understanding in the context of the Standard Model by performing precision measurements of charm and bottom quarks. The physics analyses focus on measurements related to:

- CP violation (*e.g.*, quark mixing, CKM angle γ , ...),
- Rare decays (*e.g.*, $B_s \rightarrow \mu^+\mu^-$, $B \rightarrow K^*\mu^+\mu^-$, ...)
- Flavour physics (*e.g.*, spectroscopy, electro-weak physics, soft QCD, ...)

A detailed summary of the key analyses is given in the physics road-map document [2].

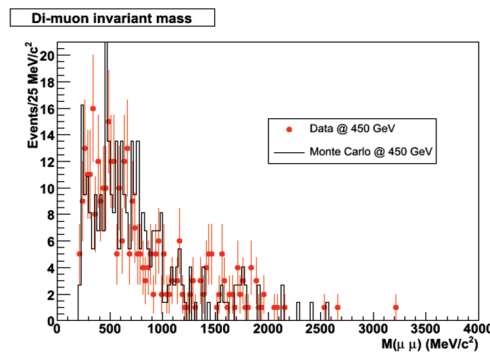


Fig. 6. – Invariant di-muon mass spectrum (LHCb preliminary). The predictions from simulation are overlaid.

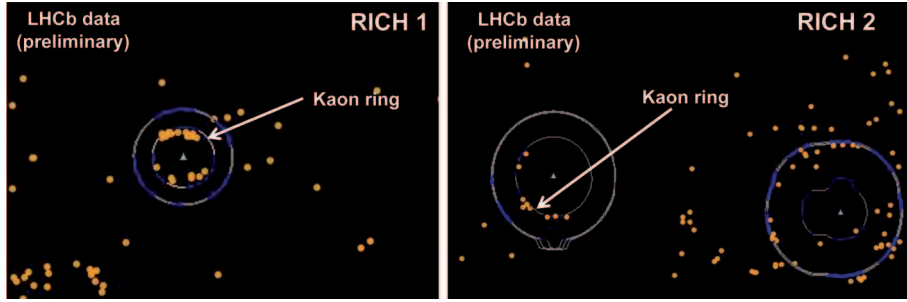


Fig. 7. – Reconstructed Cherenkov photons with expected distribution for a given mass hypothesis.

3.1. 2009 data. – The analysis of the data recorded during the LHC pilot run is not only vital to the commissioning and understanding of the detector but also offers unique opportunities for physics measurements. Due to its unique rapidity range between $2 \leq \eta \leq 5$, data recorded by the LHCb experiment is a key ingredient in improving and tuning event simulations used in physics analyses. Studies investigating the charged track multiplicities, the cross-section of K_s and Λ meson production as a function of p_t and η , as well as the ratio of the Λ *vs.* $\bar{\Lambda}$ production are currently in progress.

3.2. Charm physics. – Analyses focusing on decays involving the charm quark offer unique potential to discover New Physics beyond the Standard Model in the early phase of LHCb operation as the charm quark production cross-section is approximately seven times larger than the one for the bottom quark. $4 \cdot 10^6 D^{*+} \rightarrow D^0(K^+K^-)\pi^+$ decays are expected to be recorded per 100 pb^{-1} integrated luminosity which is competitive to the sample currently available to the BaBar Collaboration [3]. The extensive charm physics programme of the LHCb Collaboration focuses on the discovery of rare decays such as $D^0 \rightarrow \mu^+\mu^-$ and observation of CP violation in decays such as $D^0 \rightarrow K^+K^-$ and $D^0 \rightarrow K^+\pi^-$. One of the first key analyses is a detailed measurement of the relative lifetime $\tau(D^0 \rightarrow K^+\pi^-)$ *vs.* $\tau(D^0 \rightarrow K^+K^-)$ which is related to the quantity y_{CP} in the theory of D^0 meson mixing. Although no single measurement has been able to establish the mixing of D^0 meson mixing to better than 5σ , the combination of all available data shows compelling evidence [4]. The direct observation of charm

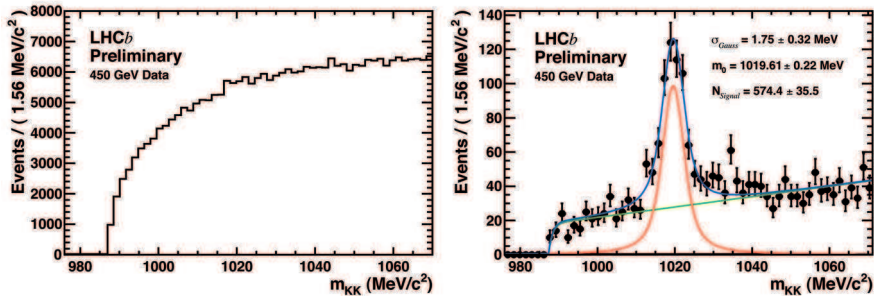


Fig. 8. – Invariant KK mass spectrum without particle ID (left) and with particle ID (right).

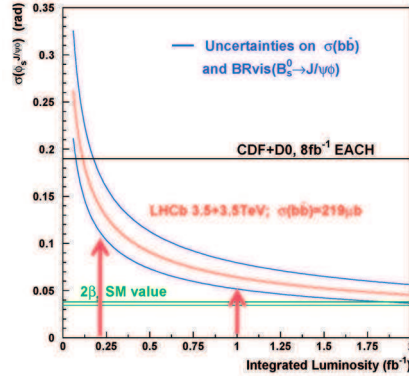


Fig. 9. – Sensitivity of the analysis of the angle Φ_s . The arrows indicate the projected integrated luminosity recorded by the end of 2010 (200 pb^{-1}) and at the end of 2011 (1 fb^{-1}).

meson mixing plays a vital role in understanding and constraining particular New Physics models (see, *e.g.* [5]).

Due to the lower energy and luminosity delivered by the LHC in the early running, the trigger thresholds have been optimised in the low luminosity regime ($\mathcal{L} < 10^{31} \text{ s}^{-2} \text{ cm}^{-1}$) to improve the number of recorded prompt charm events by a factor ≈ 4 without impact on the B physics performance. This is achieved by lowering the thresholds on the transverse momentum and impact parameter of the tracks forming the charm meson candidate. The resulting higher background is manageable since the computing capability of the trigger farm is designed for higher luminosities.

3.3. Beauty physics. – The analysis of decays of beauty hadrons is the main research area of the LHCb experiment. A multitude of analyses are currently being prepared in anticipation of the beginning of data-recording in spring 2010. Two example analyses are highlighted which offer high potential to discover New Physics with data recorded in 2010/11.

3.4. $B_s \rightarrow J/\psi\Phi$. – The decay $B_s \rightarrow J/\psi\Phi$ is sensitive to the mixing phase Φ_S in the heavy quark sector and is the counter-part to the “golden-mode” decay $B^0 \rightarrow J/\psi K_s$. This decay mode is very sensitive to the existence of New Physics as the value of Φ_s calculated within the Standard Model is very small and precisely known: $\Phi_s = -2\beta_s = -\arg(V_{ts}^2) = -0.036 \pm 0.002$ [2]. The current analyses performed by the CDF and D0 Collaborations at the Tevatron [6] show a 2σ tension w.r.t. the value expected within the Standard Model which may indicate that New Physics is “around the corner”. Figure 9 illustrates that—depending on Nature—New Physics may already be discovered using the data recorded in 2010. Experimentally, this analysis is very challenging as two CP -even and one CP -odd state have to be disentangled in an angular analyses. Excellent particle identification and vertex resolution capabilities are crucial ingredients to this analysis and the study of the data recorded during the pilot run confirms that the LHCb experiment is in excellent shape.

3.5. $B_s \rightarrow \mu^+\mu^-$. – The decay $B_s \rightarrow \mu^+\mu^-$ is extremely rare in the Standard Model as its branching fraction is calculated to be $(3.35 \pm 0.32) \cdot 10^{-9}$ [7]. However, many

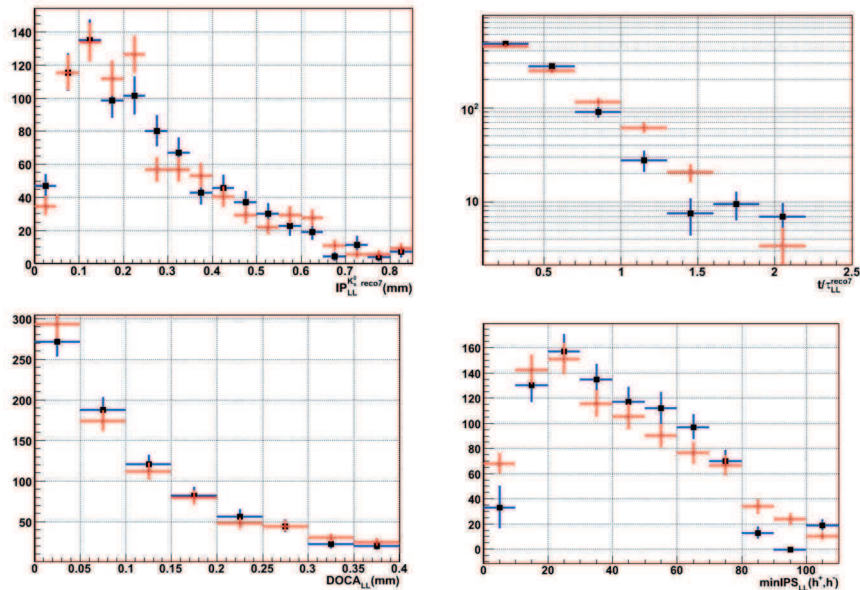


Fig. 10. – (Colour on-line) Agreement between data and simulated events for the key quantities entering the geometrical likelihood using the decay $K_s \rightarrow \pi^+\pi^-$. The figures show the distribution of the K_s impact parameter (top left), the K_s lifetime (top right), the distance of closest approach of the two pion tracks (bottom left) and the minimal impact parameter of the pion tracks (bottom right) forming the K_s candidate. Simulated events are shown in red, data recorded during the LHC pilot run in blue.

New Physics scenarios (*e.g.*, super-symmetry) lead to a greatly enhanced branching ratio and hence any observation of this decay in the early LHCb data would immediately imply the discovery of New Physics. The main experimental challenge of this analysis is the efficient rejection of background which is done by a geometrical likelihood. Key ingredients in this likelihood are the vertex separation, mass resolution and the pointing constraint of the two muon candidates. Since no $B_s \rightarrow \mu^+\mu^-$ candidate is expected in the data recorded during the pilot run, the analysis strategy is exercised using the decay $K_s \rightarrow \pi^+\pi^-$ which allows to test all elements of the analysis chain with real data instead of simulated events. The quantities used in the geometrical likelihood agree well with expectations from simulated events as shown in fig. 10.

Figure 11 illustrates the discovery potential for this analysis as the value predicted by the Standard Model will (almost) be reached with the projected integrated luminosity recorded by the end of the 2010/11 data-taking.

4. – Conclusion

The LHCb experiment started very successfully recording data in the LHC pilot run of 2009. All sub-detectors are ready and in excellent shape. The first “standard candles” such as K_s , Λ and Φ mesons have been reconstructed which demonstrates that both the data-acquisition and event reconstruction software, as well as the detector hardware, are ready for the physics analyses currently being prepared. The ongoing studies of the initial data taken during the pilot run of the LHC confirm that the LHCb experiment

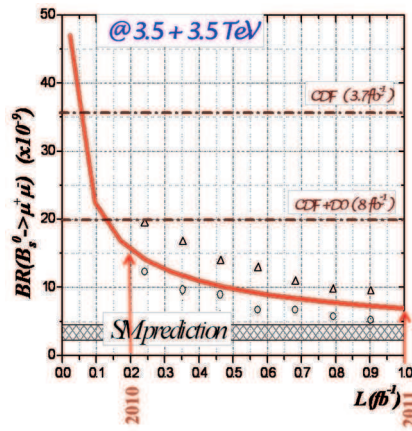


Fig. 11. – Sensitivity of the analysis of decay $B_s \rightarrow \mu^+ \mu^-$. The arrows indicate the projected integrated luminosity recorded by the end of 2010 (200 pb^{-1}) and at the end of 2011 (1 fb^{-1}).

is meeting the stringent design criteria. The integrated luminosity available for physics analysis is projected to be up to 200 pb^{-1} by the end of 2010 and up to 1 fb^{-1} by the end of 2011 which will make the LHCb experiment very soon competitive with both the B-factories BaBar and Belle, as well as the Tevatron experiments CDF and D0. Sensitivity studies based on simulated events illustrate that New Physics may already be discovered early in the data-taking.

REFERENCES

- [1] THE LHCb COLLABORATION, *JINST*, **3** (2008) S08005.
- [2] THE LHCb COLLABORATION, arXiv hep-ex 0912.4179 (2009).
- [3] THE BABAR COLLABORATION, *Phys. Rev. D*, **80** (2009) 071103.
- [4] HEAVY FLAVOUR AVERAGING GROUP, <http://www.slac.stanford.edu/xorg/hfag>.
- [5] PETROV A., *Proceedings of Science*, arXiv:1003.0906 (2010).
- [6] CDF and D0 COLLABORATIONS, Public note, CDF9787, D0 5928-CONF (2009).
- [7] BLANKE M., BURAS A., GUADAGNOLI D. and TARANTINO C., *JHEP*, **610** (2006) 003.

K rare decays with NA62

E. MARINOVA on behalf of NA48/2 and NA62 COLLABORATIONS

INFN, Sezione di Perugia - Perugia, Italy

(ricevuto il 14 Settembre 2010; pubblicato online il 12 Gennaio 2011)

Summary. — The long-term goal of NA62 is to measure the ultra rare $K^\pm \rightarrow \pi^\pm \nu \bar{\nu}$ decay with a sensitivity of 10^{-12} per event. This is done by using the decay-in-flight technique which allows a signal acceptance of $\sim 10\%$. The aim is to collect about 100 signal events in two years of data taking with a background-to-signal ratio smaller than 10%. The principle of the experimental measurement and the layout of the detector are presented. During 2007/2008 a dedicated run devoted to NA62 prototype tests and study of K_{e2} decays was taken. The first phase of the NA62 experiment is aiming at a high-precision test of the lepton universality by measuring the helicity suppressed ratio R_K . The preliminary result based on 40% of the 2007 NA62 data sample, $R_K = K_{e2}/K_{\mu 2} = (2.500 \pm 0.016) \times 10^{-5}$, which is the first result with a precision better than 1%, is consistent with the Standard Model. Aiming at charge asymmetry measurements, the NA48/2 experiment collected an unprecedented amount of charged $K_{3\pi}$ events. The large samples allowed a precision measurement of rare charged kaon decays. New measurements of the $K_{\pi\ell\ell}^\pm$ decays based on the full NA48/2 data sample collected during 2003/2004 are reported in this paper. Samples of about 7200 reconstructed $K^\pm \rightarrow \pi^\pm e^+ e^-$ events, and more than 3000 $K^\pm \rightarrow \pi^\pm \mu^+ \mu^-$ events, with a few percent background contamination, have been collected. A precise measurement of the branching fractions and the form factors of the rare decays $K_{\pi\ell\ell}^\pm$ were performed. Measurements of the CP -violating and the forward-backward asymmetries are reported.

PACS 13.25.Es – Decays of K mesons.

PACS 11.30.Hv – Flavor symmetries.

PACS 12.15.Mn – Neutral currents.

1. – Introduction

The field of rare kaon decays gives opportunities for various interesting studies, like testing low energy structure of QCD by studying the long-distance effects dominated $K^\pm \rightarrow \pi^\pm \ell^+ \ell^-$ decays, testing the lepton universality in $K_{\ell 2}$ decays, and searching for New Physics (NP) effects in the rarest decays $K^\pm \rightarrow \pi^\pm \nu \bar{\nu}$.

The NA48 experiments have a long history in studying direct CP violation effects in the kaon system, but many rare kaon decays were studied as well. The NA62 experiment

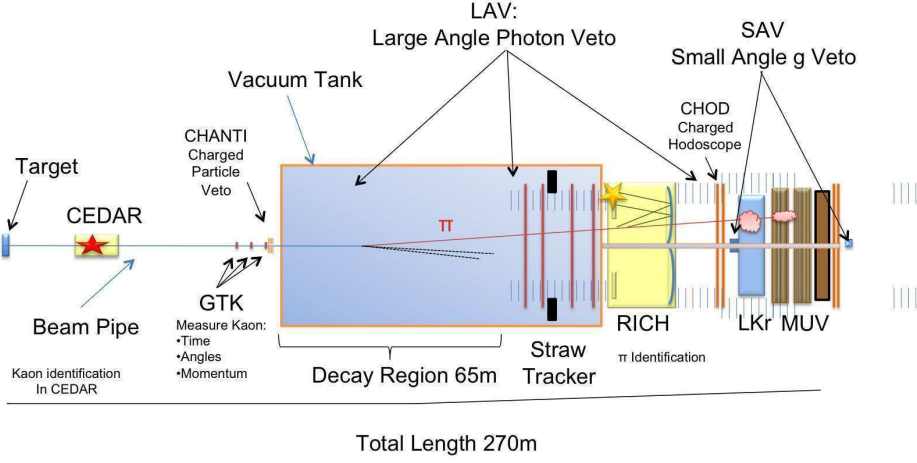


Fig. 1. – The NA62 detector.

is a continuation of the CERN based kaon research program which probes the very rare decays and searches for NP contributions.

2. – The $K^\pm \rightarrow \pi^\pm \nu \bar{\nu}$ decay with NA62

$K^\pm \rightarrow \pi^\pm \nu \bar{\nu}$ is a flavour-changing neutral current (FCNC) process that proceeds via one loop Z-penguin and W-box diagrams. Due to the t-quark contribution in the loops, it is sensitive to the V_{td} parameter of the CKM matrix. Theoretically, it is one of the cleanest kaon decays, which are most sensitive to NP because the hadronic matrix element can be extracted with a very high precision from $K_{\ell 3}$ decays [1]. The calculated values for its branching ratio $\text{BR}(K^\pm \rightarrow \pi^\pm \nu \bar{\nu}) \times 10^{10}$ vary between 0.75 up to 4: the Standard Model (SM) prediction is 0.85 ± 0.07 [1], the Minimal Flavour Violation Model—1.91 [2], the Enhanced Electroweak Penguin model— 0.75 ± 0.21 [3], the Extra Down type Singlet Quark model—up to 1.5 [4], and the Minimal Supersymmetric Standard Model (MSSM) up to 4.0 [5]. The only experimental measurement, based on 7 events, done by the E787/E949 experiment, gives $\text{BR}(K^\pm \rightarrow \pi^\pm \nu \bar{\nu}) \times 10^{10} = 1.73^{+1.15}_{-1.05}$ [6]. The central value is two times larger than the SM calculation but, due to the large experimental errors, the result is perfectly in agreement with the theory.

$K^\pm \rightarrow \pi^\pm \nu \bar{\nu}$ decay has one charged track signature in the initial state, one charged track in the final state, and nothing else. All other kaon decays, as well as accidentals, with a similar signature are backgrounds. The successful background rejection relies on 1) precise timing for associating the secondary π^+ to the decaying K^+ ; 2) kinematic rejection of two- and three-body kaon decays; 3) μ and γ vetoing; 4) particle identification (ID) for K^+/π^+ and π/μ separation.

Currently, the experiment is in the construction phase. It will reuse the existing infrastructure for the NA48 experiments at CERN. In the proposed setup, 400 GeV/c primary protons are delivered by CERN SPS on a Be target. A 75 GeV/c, narrow momentum-band (1.2% RMS) hadron beam, out of which $\sim 6\%$ are the K^+ , is formed. To reduce the accidentals background, a positive identification of the kaons is provided by a differential Cherenkov counter (CEDAR)(see fig. 1). The challenge for this detector

is to identify the K in a ~ 800 MHz beam rate environment. The position of the kaons, their time and momenta are measured by 3 silicon pixel detectors forming the beam spectrometer (Gigatracker) which will operate in vacuum. Each station covers an area of $60 \times 27 \text{ mm}^2$ with pixels size $300 \times 300 \mu\text{m}^2$ wide and $200 \mu\text{m}$ thick. The time resolution for each station should be better than 200 ps in order to provide proper reconstruction of the K tracks.

The decay region is 65 m long and it starts 5 m after the last Gigatracker station. The momenta and the coordinates of the charged secondary decay products will be measured by a spectrometer built of a dipole magnet and four chambers of straw tubes, each chamber of which has 4 layers of straws rotated by 45 degrees with respect to each other. To minimize the multiple scattering of the outgoing pion, the magnetic spectrometer will operate in vacuum upstream the decay region. This means that the decay and spectrometer regions are not separated and share a common vacuum volume. A set of ring anticounters, CHANTI, surrounding the last Gigatracker station form a guard ring and veto charged particles coming from the collimator.

An 18 m long neon-filled Ring Imaging Cherenkov Detector (RICH) at atmospheric pressure is placed between the forth Straw Tracker Chamber and the Charged Hodoscope (CHOD). It is used for a π - μ separation for particles with momenta 15–35 GeV/ c and to measure the time of the passing particles. Its inefficiency for the given momentum range is lower than 10^{-2} and its time resolution is better than 100 ps [7]. The precise timing of the charged π is obtained combining information from the RICH and the CHOD.

The photon veto system of the experiment, consisting of several detectors, ensures the hermetic coverage for photons flying at angles between 0 and $\sim 50 \mu\text{rad}$ originating from K^+ decays in the fiducial region. A high-resolution electromagnetic liquid-krypton calorimeter, LKr, used in the NA48 experiments, detects and measures the energies of the electromagnetic showers. Another veto ring—Intermediate Ring Calorimeter (IRC)—is placed in front of the LKr and covers the inactive LKr region around the beam pipe. The LKr, together with IRC, are used for vetoing photons flying at angles from $1 \mu\text{rad}$ to $8.5 \mu\text{rad}$. 12 Large Angle Photon Veto stations (LAV), surrounding the decay and detector volumes, are built of radial arrays of lead-glass blocks, arranged in overlapping layers. The LAV system covers up to $50 \mu\text{rad}$. The photon veto system is completed by a Small Angle shashlyk Calorimeter (SAC) placed at the end of the beamline. Its purpose is to provide a hermetic coverage for photons flying at small angles below $1 \mu\text{rad}$.

The hadron and muon ID downstream of the LKr is done by the muon veto detector (MUV) which consists of two parts—a hadron calorimeter and x - and y - segmented scintillator planes separated by an 80 cm thick iron wall. The MUV is followed by a dipole magnet that deflects the charged particles out of the acceptance of the SAC.

The sensitivity evaluation, with the configuration described in the proposal [8], is based on the missing square mass studies $m_{\text{miss}}^2 = (P_K - P_\pi)^2$, assuming that the outgoing particle is a π . Using m_{miss}^2 , two types of background can be distinguished: one kinematically constrained corresponding to $\sim 92\%$ of the kaon decays (see fig. 2), and kinematically unconstrained (see fig. 2b). In fig. 2a one could see that the $K^\pm \rightarrow \pi^\pm \pi^0$ ($K_{2\pi}$) decays are particularly dangerous because they are in the middle of the $K^\pm \rightarrow \pi^\pm \nu \bar{\nu}$ signal region. Therefore, two independent $K_{2\pi}$ “free” regions on both sides of the $K_{2\pi}$ missing mass peak, called region I and region II, are chosen for the analysis. The kinematical rejection power is estimated to be at the order of 10^{-5} . The $K_{2\pi}$ background can be additionally suppressed if there is a cut on the charged π momentum to be lower than 35 GeV/ c . Then, a 40 GeV/ c π^0 is difficult to be missed by the photon veto system. The inefficiency of the photon veto system is estimated to be between 2.0 and 3.5×10^{-8} .

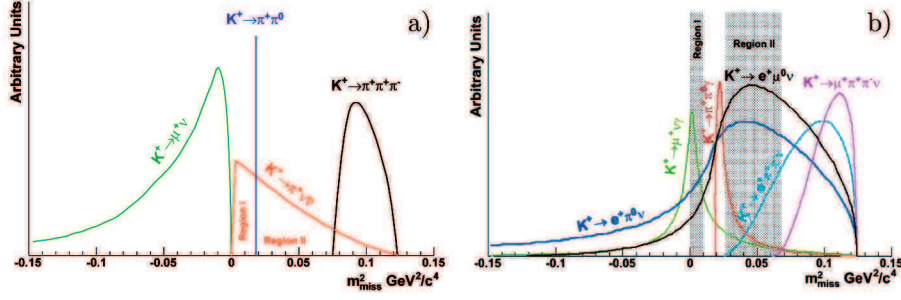


Fig. 2. – a) m_{miss}^2 distribution for $K^\pm \rightarrow \pi^\pm \nu \bar{\nu}$ signal, and kinematically constrained background; b) and kinematically unconstrained background (Monte Carlo simulation based).

The MUV assures additional rejection for $K_{\mu 2}$ background and its muon rejection inefficiency is at the order of 10^{-5} . This information, combined with the kinematical rejection and the particle ID from the RICH (with $< 10^{-2}$ misidentification inefficiency for $p_\pi < 35 \text{ GeV}/c$) gives a total suppression inefficiency of the $K_{\mu 2}$ background as low as 10^{-12} . For all the kinematically unconstrained background, coming from kaon decays with much smaller BR, the background rejection strongly relies on the photon vetoes, muon veto and particle ID.

According to the SM calculation, in one year (~ 100 days/year; $\sim 60\%$ efficiency) it is expected to collect ~ 55 events. Preliminary sensitivities studies show that the targets of 10% of signal acceptance and 10% background appear to be within reach. NA62 is optimized for a $K^\pm \rightarrow \pi^\pm \nu \bar{\nu}$ analysis but given the high demands for the performance of the detectors, the experiment can support a broader physics program⁽¹⁾.

3. – $K^\pm \rightarrow \pi^\pm \ell^+ \ell^-$ decays with NA48/2

The NA48/2 fixed target experiment at CERN-SPS uses simultaneous K^+ and K^- beams with momenta of $60 \pm 3 \text{ GeV}/c$ momenta. The experiment was designed for charge asymmetry measurements of $K_{3\pi}$ decays, and along with the main $K_{3\pi}$ samples, it has collected large amounts of charged K rare decays. The main components of the detector are a magnetic spectrometer for measuring the momenta of the charged particles, a hodoscope providing fast time signals for triggering, LKr measuring the energies of the electromagnetic showers, and a muon detector for μ ID. A more detailed description of the detector system can be found elsewhere [9]. The NA48/2 experiment has recently finalized the measurement of the FCNC transitions decays $K^\pm \rightarrow \pi^\pm \ell^+ \ell^-$ for both the e and the μ mode.

The rare decays $K^\pm \rightarrow \pi^\pm \ell^+ \ell^-$ induced at the one-loop level in the SM constitute a ground for testing the SM and its low-energy extensions. The decay rate for these decays is given in terms of the phase space factor and the form factors which depend on the main kinematical variable $z = M_{\ell\ell}^2/M_K^2$, where $M_{\ell\ell}$ is the dilepton mass, and M_K is the kaon mass. The spectrum in the dilepton invariant mass is then given by

⁽¹⁾ The new possibilities were discussed at The NA62 physics workshop; the web pages can be found at <http://indico.cern.ch/conferenceDisplay.py?confId=65927>

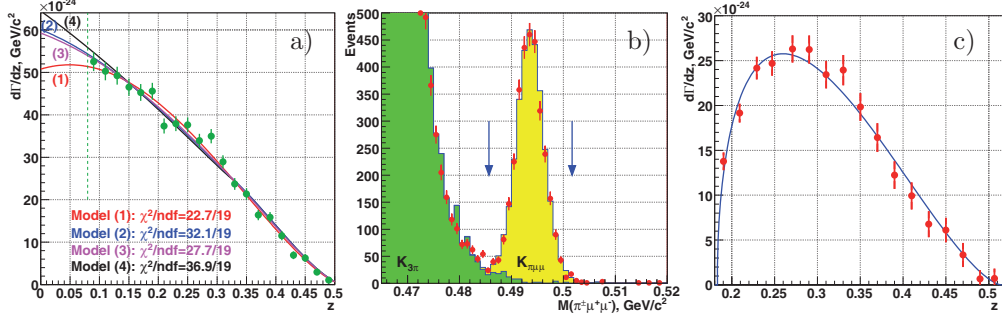


Fig. 3. – (Colour on-line) a) The reconstructed $d\Gamma_{\pi ee}/dz$ spectrum fitted to the four models for the form factors. b) The signal region for $K^\pm \rightarrow \pi^\pm \mu^+ \mu^-$ events (in yellow), and the $K_{3\pi}$ background tail (in green). c) The reconstructed $d\Gamma_{\pi\mu\mu}/dz$ spectrum fitted to a linear form factor.

$$\frac{d\Gamma}{dz} = \frac{\alpha^2 M_K^2}{12\pi(4\pi)^4} \lambda^{3/2}(1, z, r_\pi^2) \sqrt{1 - 4\frac{r_\ell^2}{z} \left(1 + 2\frac{r_\ell^2}{z}\right)} |W(z)|^2, \text{ with } r_\ell = m_\ell/M_K, 4r_\ell^2 \leq z \leq (1 - r_\pi)^2 \text{ [10] and } \lambda(a, b, c) = a^2 + b^2 + c^2 - 2ab - 2ac - 2bc.$$

The form factor $W(z)$ is calculated in next-to-leading order (NLO) [10]. The following parameterizations of the form factors $W(z)$ are considered: 1) Linear: $W(z) = G_F M_K^2 |f_0| (1 + \lambda z)$ with normalization $|f_0|$ and linear slope λ ; 2) ChPT at NLO: $W(z) = G_F M_K^2 W_+^{\text{pol}} + W_+^{\pi\pi}(z)$, [10], with free parameters a_+ and b_+ , entering the polynomial term of the equation; 3) combined framework of ChPT and large- N_c QCD: $W(z) \equiv W(\tilde{w}, \beta, z)$, [11], with free parameters \tilde{w} and β ; 4) the ChPT parametrization involving the resonances a and ρ contribution $W(z) \equiv W(M_a, M_\rho, z)$ [12], with resonance masses (M_a, M_ρ) treated as free parameters. Each pair of parameters can be measured, and then, a model-dependent BR can be calculated for each pair. In addition, a model-independent ratio can be performed in the accessible kinematical range of z .

The interference of the long-distance $K \rightarrow \pi\gamma^*$ amplitude and the short-distance contribution leads to an asymmetry between the widths of $K^+ \rightarrow \pi^+ e^+ e^-$ and $K^- \rightarrow \pi^- e^+ e^-$ which is a clear signal of direct CP violation. This quantity is defined by $\Delta(K_{\pi^\pm \ell^+ \ell^-}^\pm) = \frac{\Gamma(K^+ \rightarrow \pi^+ e^+ e^-) - \Gamma(K^- \rightarrow \pi^- e^+ e^-)}{\Gamma(K^+ \rightarrow \pi^+ e^+ e^-) + \Gamma(K^- \rightarrow \pi^- e^+ e^-)} \sim \Im m \lambda_t$, where $\lambda_t = V_{td} V_{ts}^*$ [10]. However, with $\Im m \lambda_t \sim 10^{-4}$ [13], it is very difficult to detect this effect within the SM.

3.1. The rare decay $K^\pm \rightarrow \pi^\pm e^+ e^-$. – The measurement of the $K^\pm \rightarrow \pi^\pm e^+ e^-$ decay is based on 7253 events, with a background of $(1.0 \pm 0.1)\%$. The very similar decay $K^\pm \rightarrow \pi^\pm \pi_D^0$, where $\pi^0 \rightarrow e^+ e^- \gamma$, was chosen as a normalization channel. The accessible kinematical region in z is above $z < 0.08$ due to the presence of background coming from the normalization channel which cannot be efficiently suppressed⁽²⁾. The reconstructed $d\Gamma_{K_{\pi ee}}/dz$ spectrum was fitted to the four models, and the form factor parameters were extracted. The four models cannot be distinguished in the visible kinematical region for $K^\pm \rightarrow \pi^\pm e^+ e^-$. However, below $z < 0.08$, the theory predicts different behavior of the four models. The form factor fits to the $d\Gamma_{K_{\pi ee}}/dz$ spectrum are presented in fig. 3a,

⁽²⁾ There is the possibility to remeasure it with NA62 whose hermetic veto system will allow suppressing backgrounds with additional photons, and access the region $z < 0.08$.

TABLE I. – Results of fits to the four models and the BR of $K^\pm \rightarrow \pi^\pm \ell^+ \ell^-$ decays.

Model	Parameter	Results $K^\pm \rightarrow \pi^\pm e^+ e^-$	Results $K^\pm \rightarrow \pi^\pm \mu^+ \mu^-$
Model 1	λ	2.32 ± 0.18	3.11 ± 0.56
	$ f_0 $	0.531 ± 0.016	0.470 ± 0.039
Model 2	a_+	-0.578 ± 0.016	-0.575 ± 0.038
	b_+	-0.779 ± 0.066	-0.813 ± 0.142
Model 3	\tilde{w}	0.057 ± 0.007	0.064 ± 0.014
	β	0.531 ± 0.016	0.064 ± 0.014
Model 4	M_a	0.974 ± 0.035	1.014 ± 0.090
	M_ρ	0.716 ± 0.014	0.725 ± 0.028
Combined result	BR	$(3.11 \pm 0.12) \times 10^{-7}$	–
Model independent	BRmi	$z > 0.08$ $(2.28 \pm 0.08) \times 10^{-7}$	full range $(9.25 \pm 0.62) \times 10^{-8}$

and the results are reported in table I, together with the model-independent BR in the visible kinematic region, and the combined result of the four models for the BR over the whole z range. The results of the first three models and the BR are in agreement with the results reported in [14-16], and with the theoretical prediction for $a_+ = -0.6_{-0.6}^{+0.3}$ [17]. Model 4 was never tested before.

The first measurement of the CP violating asymmetry, done by NA48/2, $\Delta(K_{\pi^\pm e^+ e^-}^\pm) = (-2.2 \pm 1.5_{\text{stat}} \pm 0.6_{\text{syst}}) \times 10^{-2}$ is consistent with no CP violation. However, its precision is far from the SM expectation [13].

3.2. The rare decay $K^\pm \rightarrow \pi^\pm \mu^+ \mu^-$. – The analysis is based on 3120 reconstructed events, 4 times more than the total world’s sample, with a background of $(3.3 \pm 0.5)\%$. The main technique of background estimation is based on choosing events with two μ with the same sign from the data sample, and the result is confirmed by a $K_{3\pi}$ MC simulation. Each of the four models for the form factors provides a reasonable fit to the data: the values of χ^2 per degree of freedom are 12.0/15, 14.8/15, 13.7/15 and 15.4/15. The results of the fits are reported in table I. The data sample size is insufficient to distinguish between the models considered. A measurement of the CP -violating asymmetry, $\Delta(K_{\pi^\pm \mu^+ \mu^-}^\pm) = (1.1 \pm 2.3) \times 10^{-2}$, is consistent with CP conservation, but its precision is far from the theoretical predictions [13]. Another interesting observable, the forward-backward asymmetry in terms of the $\Theta_{K\mu}$ angle between three-momenta of the kaon and the muon of opposite sign in the $\mu^+ \mu^-$ rest frame, was measured for the first time: $A_{FB} = \frac{N(\Theta_{K\mu} > 0) - N(\Theta_{K\mu} < 0)}{N(\Theta_{K\mu} > 0) + N(\Theta_{K\mu} < 0)} = (-2.4 \pm 1.8) \times 10^{-2}$, where the error is dominated by the statistical uncertainty. The achieved precision does not reach the upper limits of the SM [18] and the MSSM [19], both at the order of 10^{-3} . The result on the BR agrees with two of the previous measurements [20, 21], and disagrees with [22]. The measurements

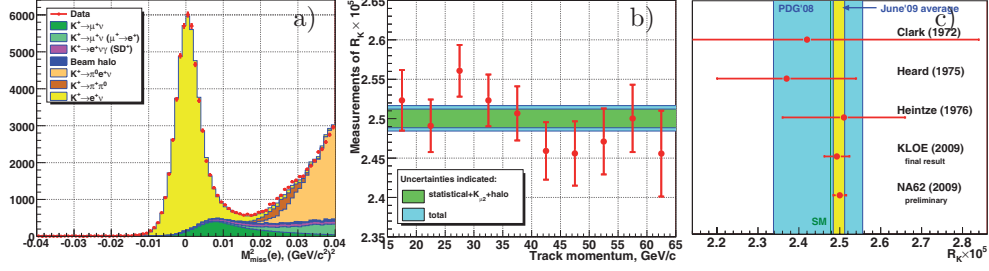


Fig. 4. – a) Reconstructed squared missing mass distribution M_{miss}^2 (e hypothesis) for the K_{e2} events and the different backgrounds contributions. b) Measurements of R_K in independent lepton momentum bins. c) R_K experimental results and SM expectation.

on the form factors agree with the $K^\pm \rightarrow \pi^\pm e^+ e^-$ results of NA48/2 [23], with the λ value measured by [20], and with theoretical expectation of $a_+ = -0.6_{-0.6}^{+0.3}$ [17].

4. – The $R_K = K_{e2(\gamma)}/K_{\mu 2(\gamma)}$ measurement—NA62, phase I

The leptonic ratio $R_K = \left(\frac{m_e}{m_\mu}\right)^2 \left(\frac{m_K^2 - m_e^2}{m_K^2 - m_\mu^2}\right)^2 (1 + \delta R_{\text{QED}}) = (2.477 \pm 0.001) \times 10^{-5}$ (SM) [24], where $\delta R_{\text{QED}} = (-3.78 \pm 0.04)\%$ is a correction due to the IB radiative process, can be predicted with a high accuracy within SM due to the cancellation of the hadronic uncertainties. The factor $\left(\frac{m_e}{m_\mu}\right)^2$ accounts for the helicity suppression of the K_{e2} decay with respect to $K_{\mu 2}$ decay. This helicity suppression enhances the sensitivity to non-SM lepton flavour violating (LFV) effects which are not ruled out experimentally. It was realized recently that LFV effects can shift the R_K value by a few percent [25,26].

The worlds average on R_K in 2008 is $R_K = (2.45 \pm 0.11) \times 10^{-5}$, ($\delta R_K/R_K = 4.5\%$), [27] based on three experiments in the 1970s. KLOE has recently published their improved precision result, $R_K = (2.493 \pm 0.031) \times 10^{-5}$, ($\delta R_K/R_K = 1.3\%$) based on 13800 K_{e2} candidates, with 16% background [28]. NA62 set a goal of collecting 150000 K_{e2} events with a background less than 10% for measuring R_K with a 0.5% precision. For this measurement, NA62 used the old NA48/2 experimental setup, slightly optimized for the K_{e2} measurement. For example, the kaon momentum was increased to $74 \pm 2 \text{ GeV}/c$. The narrow momentum band aimed to minimize the contribution of the momentum resolution in the kinematical variables.

The preliminary results reported here are on 40% of the total statistics which corresponds to 51 089 K_{e2} events with a background of $(8.03 \pm 0.23)\%$ (see fig. 4a). The estimate is to reach 135 thousand events with the full sample. 15.56×10^6 events were collected for the normalization $K_{\mu 2}$ channel, with a very low background of 0.25%. The analysis was done in independent lepton momentum bins (see fig. 4b). The preliminary NA62 result of R_K has a much better precision than the previous measurements: $R_K = (2.5 \pm 0.012_{\text{stat}} \pm 0.011_{\text{syst}}) \times 10^{-5}$, ($\delta R_K/R_K = 0.64\%$) (see fig. 4c), where the statistical uncertainties dominate the systematical ones. The main systematical uncertainties to this measurement are due to the $K_{\mu 2}$ background contribution to K_{e2} with a μ misidentified as an electron, beam halo background estimation, the positron ID, the simulation of the IB radiative process, the trigger dead time and uncertainties due to corrections on the geometric acceptance. The analysis of the full data sample should achieve the desired precision of 0.5%.

5. – Conclusions

Using a sample of 7253 events $K^\pm \rightarrow \pi^\pm e^+ e^-$ collected by NA48/2 during 2003/2004, a high-precision measurement of the form factors within four different models, and the BR have been measured. A first measurement of the CP -violating asymmetry, $\Delta(K_{\pi^\pm e^+ e^-}^\pm) = (-2.2 \pm 1.5_{\text{stat}} \pm 0.6_{\text{syst}}) \times 10^{-2}$, is consistent with no CP violation. Using an unprecedented amount of $K^\pm \rightarrow \pi^\pm \mu^+ \mu^-$ decays, with a very low background of $(3.3 \pm 0.5)\%$, a model-independent BR has been measured $BR = (9.62 \pm 0.62) \times 10^{-8}$, and the form factors described within the four available models were extracted. An improved precision measurement of the CP -violating charge asymmetry and (for the first time) the forward-backward asymmetry of the integrated decay rate were presented.

NA62 phase I data taking in 2007/08 was dedicated to a precision measurement of R_K . The analysis of a partial Ke2 sample ($\sim 40\%$) reached the record accuracy of 0.64% and the preliminary result: $R_K = (2.500 \pm 0.016) \times 10^{-5}$ is compatible with the SM prediction. NA62 phase II is a challenging experiment aiming at measuring $K^\pm \rightarrow \pi^\pm \nu \bar{\nu}$ decay by collecting $O(100)$ events with $B/S < 10\%$. It has been approved by CERN SPSC and Research Board. Data taking is foreseen to start in 2012.

REFERENCES

- [1] BROD J. and GORBAN M., *Phys. Rev. D*, **78** (2008) 034006.
- [2] BURAS A., *Acta Phys. Polon. B*, **34** (2003) 5615.
- [3] BURAS A., FLEISCHER R., RECKSIEGEL S. and SCHWAB F., *Nucl. Phys. B*, **697** (2004) 133.
- [4] DESHPANDE N. G., GHOSH D. and HE XIAO-GANG, *Phys. Rev. D*, **70** (2004) 093003.
- [5] BURAS A., EWERTH T., JAGER S. and ROSIEK J., *Nucl. Phys. B*, **714** (2005) 103.
- [6] E949 COLLABORATION, *Phys. Rev. Lett.*, **101** (2008) 191802.
- [7] ANZIVINO G. *et al.*, *Nucl. Instrum. Methods A*, **593** (2008) 314.
- [8] THE NA62 COLLABORATION, CERN-SPSC-2005-013 SPSC-P-326.
- [9] FANTI V. *et al.*, *Nucl. Instrum. Methods A*, **574** (2007) 433.
- [10] D'AMBROSIO G. *et al.*, *JHEP*, **8** (1998) 4.
- [11] FRIOT S., GREYNAT D. and DE RAFAEL E., *Phys. Lett. B*, **595** (2004) 301.
- [12] DUBNICKOVA A. Z. *et al.*, *Phys. Part. Nucl. Lett.*, **5** (2008) 76.
- [13] ECKER G., PICH A. and DE RAFAEL E., *Nucl. Phys. B*, **303** (1988) 665.
- [14] BLOCH P. *et al.* (GENEVA-SACLAY COLLABORATION), *Phys. Lett. B*, **56** (1975) 201.
- [15] ALLIEGRO C. *et al.*, *Phys. Rev. Lett.*, **68** (1992) 278.
- [16] APPEL R. *et al.* (E865 COLLABORATION), *Phys. Rev. Lett.*, **83** (1999) 4482.
- [17] BRUNO C. and PRADES J., *Z. Phys. C*, **57** (1993) 585.
- [18] GAO D. N., *Phys. Rev. D*, **69** (2004) 094030.
- [19] CHEN C. H., GENG C. Q. and HO I. L., *Phys. Rev. D*, **67** (2003) 074029.
- [20] MA H. *et al.*, *Phys. Rev. Lett.*, **84** (2000) 2580.
- [21] PARK H. K. *et al.*, *Phys. Rev. Lett.*, **88** (2002) 111801.
- [22] ADLER S. *et al.*, *Phys. Rev. Lett.*, **79** (1997) 47.
- [23] BATLEY J. R. *et al.*, *Phys. Lett. B*, **677** (2009) 246.
- [24] CIRIGLIANO V. and ROSELL I., *Phys. Rev. Lett.*, **99** (2007) 231801.
- [25] MASIERO A., PARADISI P. and PETRONZIO R., *Phys. Rev. D*, **74** (2006) 011701.
- [26] MASIERO A., PARADISI P. and PETRONZIO R., [arXiv:0807.4721].
- [27] AMSLER C. *et al.* (PDG), *Phys. Lett. B*, **667** (2008) 1.
- [28] THE KLOE COLLABORATION, *Eur. Phys. J. C*, **64** (2009) 627; **65** (2010) 703 (Erratum); [arXiv:0907.3594v2]

Kaon physics with KLOE

B. SCIASCIA for the KLOE COLLABORATION^(*)

INFN, Laboratori Nazionali di Frascati - Frascati (Rome), Italy

(ricevuto il 14 Settembre 2010; pubblicato online l'11 Gennaio 2011)

Summary. — Kaon physics can test new-physics effects in leptonic or semileptonic decays. A unitarity test of the first row of the CKM mixing matrix is obtained from the precision measurements of Kl3 widths for K^\pm , K_L , and (unique to KLOE) K_S . The KLOE measurement of $R_K = \Gamma(Ke2)/\Gamma(K\mu2)$ with an accuracy at the % level, aims at finding evidence of deviations from the SM prediction induced by lepton-flavor violation new-physics effects.

PACS 13.20.Eb – Decays of K mesons.

PACS 12.15.Hh – Determination of Cabibbo-Kobayashi & Maskawa (CKM) matrix elements.

1. – Introduction

Purely leptonic and semileptonic decays of K mesons ($K \rightarrow \ell\nu$, $K \rightarrow \pi\ell\nu$, $\ell = e, \mu$) are mediated in the Standard Model (SM) by tree-level W -boson exchange. Gauge coupling universality and three-generation quark mixing imply that semileptonic processes such as $d^i \rightarrow u^j\ell\nu$ are governed by the effective Fermi constant $G_{ij} = G_\mu V_{ij}$, where i) G_μ is the muon decay constant and ii) V_{ij} are the elements of the unitary Cabibbo-Kobayashi Maskawa (CKM) matrix. This fact has simple but deep consequences, that go under the name of universality relations. In the SM the effective semileptonic constant G_{ij} does not depend on the lepton flavor. If one extracts V_{ij} from different semileptonic transitions assuming quark-lepton gauge universality (*i.e.* normalizing the decay rates with G_μ), the CKM unitarity condition $\sum_j |V_{ij}|^2 = 1$ should be verified.

^(*) F. Ambrosino, A. Antonelli, M. Antonelli, F. Archilli, P. Beltrame, G. Bencivenni, C. Bini, C. Bloise, S. Bocchetta, F. Bossi, P. Branchini, G. Capon, D. Capriotti, T. Capussela, F. Ceradini, P. Ciambone, E. De Lucia, A. De Santis, P. De Simone, G. De Zorzi, A. Denig, A. Di Domenico, C. Di Donato, B. Di Micco, M. Dreucci, G. Felici, S. Fiore, P. Franzini, C. Gatti, P. Gauzzi, S. Giovannella, E. Graziani, M. Jacewicz, V. Kulikov, J. Lee-Franzini, M. Martini, P. Massarotti, S. Meola, S. Miscetti, M. Moulson, S. Müller, F. Murtas, M. Napolitano, F. Nguyen, M. Palutan, A. Passeri, V. Patera, P. Santangelo, B. Sciascia, A. Sibidanov, T. Spadaro, C. Taccini, L. Tortora, P. Valente, G. Venanzoni and R. Versaci.

Beyond the SM, these universality relations can be violated by new contributions to the low-energy $V-A$ four fermion operators, as well as new non $V-A$ structures. Therefore, precision tests of the universality relations probe physics beyond the SM and are sensitive to several SM extensions [1-4].

This paper is organized as follows. The present and future status of DAΦNE accelerator and KLOE experiment is briefly reviewed in sect. 2. The world average measurement of V_{us} is presented in sect. 3 together with the new preliminary KLOE measurements of K_L and K_S lifetimes. The KLOE result for R_K is described in sect. 4.

2. – DAΦNE and KLOE: present and future

DAΦNE, the Frascati ϕ -factory, is an e^+e^- collider working at $\sqrt{s} \sim m_\phi \sim 1.02$ GeV. ϕ mesons are produced, essentially at rest, with a visible cross section of $\sim 3.1 \mu\text{b}$. During year 2008 the Accelerator Division has tested a new interaction scheme with the goal of reaching a peak luminosity of $5 \times 10^{32} \text{ cm}^{-2} \text{ s}^{-1}$, a factor of three larger than what previously obtained.

KLOE is a multipurpose detector, mainly consisting of a large cylindrical drift chamber (DC) with an internal radius of 25 cm and an external one of 2 m, surrounded by a lead-scintillating fibers electromagnetic calorimeter (EMC). Both are immersed in the 0.52 T field of a superconducting solenoid. From 2000 to 2006, KLOE has acquired 2.5 fb^{-1} of data at the $\phi(1020)$ peak, plus additional 250 pb^{-1} at energies slightly higher or lower than that. A collection of the main physics results of KLOE and details of the detector can be found in ref. [5] and references therein.

For the forthcoming run [6], upgrades have also been proposed for the detector. In a first phase, two different devices will be installed along the beam line to detect the scattered electrons/positrons from $\gamma\gamma$ interactions. In a second phase, a light-material internal tracker will be installed in the region between the beam pipe and the drift chamber to improve charged vertex reconstruction and to increase the acceptance for low- p_T tracks. Crystal calorimeters will cover the low- θ region, aiming at increasing acceptance for very forward electrons/photons down to 8° . A new tile calorimeter will be used to instrument the DAΦNE focusing system for the detection of photons coming from K_L decays in the drift chamber. Implementation of the second phase is planned for late 2011. The integrated luminosity for the two phases should be 5 fb^{-1} and 20 fb^{-1} , respectively.

3. – Measurement of V_{us}

Large amount of data has been collected on the semileptonic modes $K \rightarrow \pi\ell\nu$ by several experiments, BNL-E865, KLOE, KTeV, ISTRA+, and NA48 in the last few years. These data have stimulated a substantial progress on the theoretical inputs, so that most of the theory-dominated errors associated to radiative corrections and hadronic form factors have been reduced below 1%. Presently, the unitarity test

$$(1) \quad |V_{ud}|^2 + |V_{us}|^2 + |V_{ub}|^2 = 1 + \Delta_{\text{CKM}}$$

implies that Δ_{CKM} is consistent with zero at the level of 6×10^{-4} . V_{us} from $K \rightarrow \pi\ell\nu$ decays contributes about half of this uncertainty, mostly coming from the hadronic matrix element. Both experimental and theoretical progress in $K_{\ell 3}$ decays will be needed in order to improve the accuracy on Δ_{CKM} in the future.

TABLE I. – Values of $|V_{us}|f_+(0)$ extracted from K_{l3} decay rates.

$K_L e3$	$K_L \mu3$	$K_S e3$	$K^\pm e3$	$K^\pm \mu3$
0.2163(6)	0.2166(6)	0.2155(13)	0.2160(11)	0.2158(14)

It has been shown [4] that presently semileptonic processes and the related universality tests provide constraints on NP that cannot be obtained from other electroweak precision tests and/or direct measurements at the colliders.

In the last years, many efforts have been dedicated to the correct averaging of the rich harvest of recent results in kaon physics. The FLAVIANet kaon working group has published a comprehensive review [7] in 2008 where a detailed description of the averaging procedure can be found. However, the significant progress on both the experimental and theoretical sides, has motivated the same group to publish an updated analysis [8]. Even if these proceedings will focus on the contribution from KLOE, all the V_{us} -related results presented refer to the FlaviaNet working group outcomes.

After four years of data analysis, KLOE has produced the most comprehensive set of results from a single experiment, measuring the main BRs of K_L , K^\pm , and K_S (unique to KLOE), including semileptonic and two-body decays; lifetime measurements for K_L and K^\pm , form factor slopes from the analysis of $K_L e3$ and $K_L \mu3$. The value of $|V_{us}|f_+(0)$ has been obtained from KLOE results [10] using the K_S lifetime from PDG [11] as the only non-KLOE input. The values of $|V_{us}|f_+(0)$ obtained from the world average of K semileptonic measurements [8] are shown in table I.

The five decay modes agree well within the errors and average to $|V_{us}|f_+(0) = 0.2163(5)$, with $\chi^2/\text{ndf} = 0.77/4$ (Prob = 94%). Significant lepton-universality tests are provided by the comparison of the results from different leptonic channels. Defining the ratio $r_{\mu e} = |V_{us}|f_+(0)_{\mu3}^2/|V_{us}|f_+(0)_{e3}^2$ we have $r_{\mu e} = g_\mu^2/g_e^2$, with g_ℓ the coupling strength at the $W \rightarrow \ell\nu$ vertex. Lepton universality can be then tested comparing the measured value of $r_{\mu e}$ with the SM prediction $r_{\mu e}^{\text{SM}} = 1$. Averaging charged- and neutral-kaon modes, we obtain $r_{\mu e} = 1.002(5)$, to be compared with the results from leptonic pion decays, $(r_{\mu e})_\pi = 1.0042(33)$ [12], and from leptonic τ decays $(r_{\mu e})_\tau = 1.000(4)$ [13].

Using the determination of $|V_{us}|f_+(0)$ from K_{l3} decays and the value $f_+(0) = 0.959(5)$ (see ref. [8] for a detailed discussion on this choice), we get $|V_{us}| = 0.2254(13)$.

Furthermore, a measurement of $|V_{us}|/|V_{ud}|$ can be obtained from the comparison of the radiation-inclusive decay rates of $K^\pm \rightarrow \mu^\pm \nu(\gamma)$ and $\pi^\pm \rightarrow \mu^\pm \nu(\gamma)$, combined with lattice calculation of f_K/f_π [14]. Using the $\text{BR}(K^\pm \rightarrow \mu^\pm \nu)$ average value (dominated by KLOE result [15]) and the lattice result $f_K/f_\pi = 1.193(6)$ (again see ref. [8] for a detailed discussion on this choice), we get $|V_{us}|/|V_{ud}| = 0.2312(13)$. This value can be used in a fit together with the measurements of $|V_{us}|$ from K_{l3} decays and $|V_{ud}| = 0.97425(22)$ [16] from superallowed nuclear β decays. The result of this fit is $|V_{ud}| = 0.97425(22)$ and $|V_{us}| = 0.2253(9)$, with $\chi^2/\text{ndf} = 0.014/1$ (Prob = 91%), from which we get $1 - (|V_{ud}|^2 + |V_{us}|^2 + |V_{ub}|^2) = -0.0001(6)$ which is in striking agreement with the unitarity hypothesis.

Using these results, we evaluate $G_{\text{CKM}} = G_\mu \sqrt{|V_{ud}|^2 + |V_{us}|^2 + |V_{ub}|^2} = 1.16633(35) \times 10^{-5} \text{ GeV}^{-2}$, with $G_\mu = 1.166371(6) \times 10^{-5} \text{ GeV}^{-2}$. At present, the sensitivity of the quark-lepton universality test through the G_{CKM} measurement is competitive and even better than the measurements from τ decays and the electroweak precision tests [17]. Thus unitarity can also be interpreted as a test of the universality of lepton and quark

weak couplings to the W boson, allowing bounds to be set on extensions of the SM leading to some kind of universality breaking. For instance, the existence of additional Z' gauge bosons, giving different loop-contributions to muon and semileptonic decays, can break gauge universality [1]. The measurement of G_{CKM} can set constraints on the Z' mass which are competitive with direct search at the colliders. When considering supersymmetric extensions, differences between muon and semileptonic decays can arise in the loop contributions from SUSY particles [2, 3]. The slepton-squark mass difference could be investigated improving present accuracy on the unitarity relation by a factor of $\sim 2-3$.

3.1. K_L lifetime. – The error on the K_L lifetime (τ_L) determination is the limiting factor on $|V_{us}|f_+(0)$ when calculated from K_L . Using all the available data, KLOE can improve statistical and systematic error over its previous measurements [9, 18]. KLOE decided to perform a new τ_L measurement based on 46 million $K_L \rightarrow 3\pi^0$ events, using the same method used in ref. [9]. K_L mesons are tagged by detecting $K_S \rightarrow \pi^+\pi^-$ decays and the time dependence of the $K_L \rightarrow 3\pi^0$ decays is used to measure the K_L lifetime. The $3\pi^0$ mode is chosen because is the most abundant, has high detection efficiency and the tagging efficiency is almost independent of the K_L path length. The preliminary result is: $\tau_L = 50.56 \pm 0.14_{\text{stat}} \pm 0.21_{\text{syst}}$ ns = 50.56 ± 0.25 ns [19] compatible with previous KLOE measurements. The statistical error can be improved by decreasing the lower limit of the fit region, properly accounting for the K_L beam losses on the regenerating surfaces; the statistical error on the K_L lifetime is expected to decrease to ~ 0.1 ns. The systematic error arising from the tagging efficiency, due only to detector acceptance, is expected to decrease also.

3.2. K_S lifetime. – KLOE measures the K_S lifetime (τ_S) with a pure K_S beam and event-by-event knowledge of the K_S momentum. τ_S can be measured as a function of sidereal time which is interesting for tests of quantum mechanics, CPT and Lorentz invariance [20]. The lifetime is obtained by fitting the proper time, t^* , distribution of $K_S \rightarrow \pi^+\pi^-$ decays. The resolution after event reconstruction is not sufficient for obtaining a lifetime accuracy of 0.1%. The t^* resolution improves by reconstructing the IP event-by-event using a geometrical fit, selecting events with pions decaying at large angle with respect to the K_S path, and rejecting poorly measured tracks by a cut on the track fit χ^2 value. The efficiency of this selection is $\sim 13\%$. Since the resolution depends on the K_S direction, we fit to the proper time distribution from -2 to $7 \tau_S$ for each of 270 bins in $\cos(\theta_K)$ and ϕ_K . The statistical error on τ_S is less than 0.1%. With the full KLOE statistics the preliminary result $\tau_S = (89.56 \pm 0.03 \pm 0.07)$ ps [21] has been obtained, with the aim of reaching ~ 0.03 ps final systematic uncertainty. A relative error of 0.03% on τ_S is expected scaling this result to the KLOE-2 data sample.

4. – Measurement of $R_K = \Gamma(Ke2)/\Gamma(K\mu2)$

The SM prediction of R_K benefits from cancellation of hadronic uncertainties to a large extent and therefore can be calculated with high precision. Including radiative corrections, the total uncertainty is less than 0.5 per mil [1, 22]:

$$(2) \quad R_K = (2.477 \pm 0.001) \times 10^{-5}.$$

Since the electronic channel is helicity-suppressed by the $V-A$ structure of the charged weak current, R_K can receive contributions from physics beyond the SM, for example

from multi-Higgs effects inducing an effective pseudoscalar interaction. It has been shown in ref. [23] that deviations from the SM of up to few percent on R_K are quite possible in minimal supersymmetric extensions of the SM and in particular should be dominated by lepton-flavor violating contributions with tauonic neutrinos emitted in the electron channel:

$$(3) \quad R_K = R_K^{\text{SM}} \times \left[1 + \frac{m_K^4}{m_H^4} \frac{m_\tau^2}{m_e^2} |\Delta_R^{31}|^2 \tan^6 \beta \right],$$

where M_H is the charged-Higgs mass, Δ_R^{31} is the effective $e - \tau$ coupling constant depending on MSSM parameters, and $\tan\beta$ is the ratio of the two vacuum expectation values. Note that the pseudoscalar constant f_K cancels in R_K^{SM} . In order to compare with the SM prediction at this level of accuracy, one has to treat carefully the effect of radiative corrections, which contribute to nearly half the $K_{e2\gamma}$ width. In particular, the SM prediction of eq. (3) is made considering all photons emitted by the process of internal bremsstrahlung (IB) while ignoring any contribution from structure-dependent direct emission (DE). Of course both processes contribute, so in the analysis DE is considered as a background which can be distinguished from the IB width by means of a different photon energy spectrum.

Using the present KLOE dataset collected at the ϕ peak, and corresponding to ~ 3.6 billion K^+K^- pairs, a measurement of R_K with an accuracy of about 1% has been performed. ϕ mesons are produced, essentially at rest and decay into K^+K^- pairs with a BR of $\sim 49\%$. Kaons get a momentum of ~ 100 MeV which translates into a low speed, $\beta_K \sim 0.2$. K^+ and K^- decay with a mean length of $\lambda_\pm \sim 90$ cm and can be distinguished from their decays in flight to one of the two-body final states $\mu\nu$ or $\pi\pi^0$. The kaon pairs from ϕ decay are produced in a pure $J^{PC} = 1^{--}$ quantum state, so that observation of a K^+ in an event signals, or tags, the presence of a K^- and vice versa; highly pure and nearly monochromatic K^\pm beams can thus be obtained and exploited to achieve high precision in the measurement of absolute BRs. KLOE DC constitutes a fiducial volume for K^\pm decays extending for $\sim 1\lambda_\pm$. The momentum resolution for tracks at large polar angle is $\sigma_p/p \leq 0.4\%$. The c.m. momenta reconstructed from identification of 1-prong $K^\pm \rightarrow \mu\nu, \pi\pi^0$ decay vertices in the DC peak around the expected values with a resolution of 1–1.5 MeV, thus allowing clean and efficient K^\pm tagging. Given the K^\pm decay length, the selection of one-prong K^\pm decays in the DC required to tag K^\mp has an efficiency smaller than 50%. In order to keep the statistical uncertainty on the number of $K \rightarrow e\nu$ counts below 1%, a “direct search” for $K \rightarrow e\nu$ and $K \rightarrow \mu\nu$ decays is performed, without tagging. Since the wanted observable is a ratio of BRs for two channels with similar topology and kinematics, one expects to benefit from some cancellation of the uncertainties on tracking, vertexing, and kinematic identification efficiencies. Small deviations in the efficiency due to the different masses of e 's and μ 's will be evaluated using MC. Selection starts by requiring a kaon track decaying in a DC fiducial volume (FV) with laboratory momentum between 70 and 130 MeV, and a secondary track of relatively high momentum (above 180 MeV). The FV is defined as a cylinder parallel to the beam axis with length of 80 cm, and inner and outer radii of 40 and 150 cm, respectively. Quality cuts are applied to ensure good track fits. A powerful kinematic variable used to distinguish $K \rightarrow e\nu$ and $K \rightarrow \mu\nu$ decays from the background is calculated from the track momenta of the kaon and the secondary particle: assuming $m_\nu = 0$, the squared mass of the secondary particle (m_ℓ^2) is evaluated. The selection applied is enough for clean identification of a $K \rightarrow \mu\nu$ sample, while further rejection

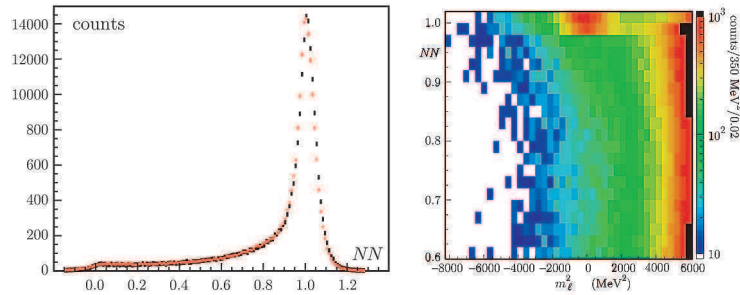


Fig. 1. – (Colour on-line) Left: neural-network output, NN , for electrons of a $K_L \rightarrow \pi e \nu$ sample from data (black) and MC (red). Right: data density in the (NN, m_e^2) -plane: the signal is clearly visible at $m_e^2 \sim 0$ and $NN \sim 1$.

is needed in order to identify $K \rightarrow e \nu$ events: the background, which is dominated by badly reconstructed $K \rightarrow \mu \nu$ events, is ~ 10 times more frequent than the signal in the region around m_e^2 .

Information from the EMC is used to improve background rejection. To this purpose, we extrapolate the secondary track to the EMC surface and associate it to a nearby EMC cluster. For electrons, the associated cluster is close to the EMC surface and the cluster energy E_{cl} is a measurement of the particle momentum p_{ext} , so that E_{cl}/p_{ext} peaks around 1. For muons, clusters tend to be more in depth in the EMC and E_{cl}/p_{ext} tends to be smaller than 1, since only the kinetic energy is visible in the EMC. Electron clusters can also be distinguished from μ (or π) clusters, since electrons shower and deposit their energy mainly in the first plane of EMC, while muons behave like minimum ionizing particles in the first plane and deposit a sizable fraction of their kinetic energy from the third plane onward, when they are slowed down to rest (Braggs peak). Particle identification has been therefore based on the asymmetry of energy deposits between the first and the next-to-first planes, on the spread of energy deposits on each plane, on the position of the plane with the maximum energy, and on the asymmetry of energy deposits between the last and the next-to-last planes. All information is combined with neural network (NN) trained on $K_L \rightarrow \pi l \nu$ data, taking into account variations of the EMC response with momentum and impact angle on the calorimeter. The distribution of the NN output for an independent $K_L \rightarrow \pi e \nu$ sample is shown in the left panel of fig. 1 for data and Monte Carlo (MC). Additional separation has been obtained using time-of-flight information. The number of $K \rightarrow e \nu(\gamma)$ is determined with a binned likelihood fit to the two-dimensional NN vs. m_e^2 distribution. The data distribution of NN as a function of m_e^2 is shown in fig. 1 right. A clear $K \rightarrow e \nu$ signal can be seen at $m_e^2 \sim 0$ and $NN \sim 1$. Distribution shapes for signal and $K \mu 2$ background, other sources being negligible, are taken from MC; the normalization factors for the two components are the only fit parameters. In the fit region, a small fraction of $K \rightarrow e \nu(\gamma)$ events is due to the direct-emission structure-dependent component (DE): the value of this contamination, f_{DE} , is fixed in the fit to the expectation from simulation. This assumption has been evaluated by performing a dedicated measurement of DE, which yielded as a by-product a determination of f_{DE} with a 4% accuracy [24]. This implies a systematic error on $Ke2$ counts of 0.2%, as obtained by repeating the fit with values of f_{DE} varied within its uncertainty. In the fit region, we count $7064 \pm 102 K^+ \rightarrow e^+ \nu(\gamma)$ and $6750 \pm 101 K^- \rightarrow e^- \nu(\gamma)$ events.

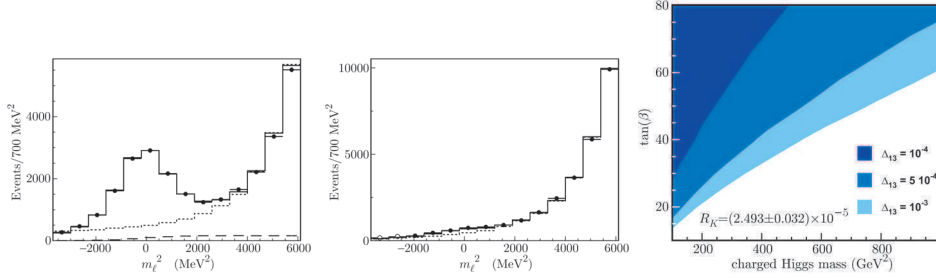


Fig. 2. – Fit projections onto the m_ℓ^2 axis for $NN > 0.98$ (left) and $NN < 0.98$ (center), for data (black dots), MC fit (solid line), and $K\mu 2$ background (dotted line). The contribution from $Ke2$ events with $E_\gamma > 10$ MeV is visible in the left panel (dashed line). Right: excluded regions at 95% CL in the plane M_H - $\tan\beta$ for $\Delta_R^{31} = 10^{-4}, 5 \times 10^{-4}, 10^{-3}$.

Figure 2 shows the sum of fit results for K^+ and K^- projected onto the m_ℓ^2 axis in a signal ($NN > 0.98$) and a background ($NN < 0.98$) enhanced region. To assess the uncertainty on the R_K measurement arising from limited knowledge of the momentum resolution we have examined the agreement between the m_ℓ^2 distributions for data and MC in the $K\mu 2$ region. For the NN distribution, the EMC response at the cell level has been tuned by comparing data and MC samples. In order to evaluate the systematic error associated with these procedures, we studied the result variation with different fit range values, corresponding to a change for the overall $Ke2$ purity from $\sim 75\%$ to $\sim 10\%$. The results are stable within statistical fluctuations. A systematic uncertainty of 0.3% for R_K is derived *à la* PDG [11] by scaling the uncorrelated errors so that the reduced χ^2 value of results is 1.

The number of $K\mu 2$ events in the same data set is extracted from a fit to the m_ℓ^2 distribution. The fraction of background events under the muon peak is estimated from MC to be $< 0.1\%$. We count $2.878 \times 10^8 (2.742 \times 10^8) K_\mu^+ 2 (K_\mu^- 2)$ events. Difference in K^+ and K^- counting is ascribed to K^- nuclear interactions in the material traversed.

The ratio of $Ke2$ to $K\mu 2$ efficiency is evaluated with MC and corrected for data-to-MC ratios using control samples. To check the corrections applied we also measured $R_3 = \text{BR}(Ke3)/\text{BR}(K\mu 3)$, in the same data sample and by using the same methods for the evaluation of the efficiency as for the R_K analysis. We found $R_3 = 1.507(5)$ and $R_3 = 1.510(6)$, for K^+ and K^- , respectively. These are in agreement within a remarkable accuracy with the expectation from world-average [7] form-factor slope measurements, $R_3 = 1.506(3)$.

The final result is $R_K = (2.493 \pm 0.025 \pm 0.019) \times 10^{-5}$ [24]. The 1.1% fractional statistical error has contributions from signal count fluctuation (0.85%) and background subtraction. The 0.8% systematic error has a relevant contribution (0.6%) from the statistics of the control samples used to evaluate corrections to the MC. The result does not depend on K charge: quoting only the uncorrelated errors, $R_K(K^+) = 2.496(37)10^{-5}$ and $R_K(K^-) = 2.490(38)10^{-5}$. The result in agreement with SM prediction of eq. (2). Including the new KLOE result, the world average reaches an accuracy at the % level: $R_K = 2.468(25) \times 10^{-5}$. In the framework of MSSM with LFV couplings, the R_K value can be used to set constraints in the space of relevant parameters (see eq. (3)). The regions excluded at 95% CL in the plane $\tan\beta$ charged Higgs mass are shown in the right panel of fig. 2 for different values of the effective LFV coupling Δ_R^{31} .

5. – Conclusions

The experimental precision in leptonic and semileptonic kaon decays is nicely matched below the percent level by theoretical precision, allowing to perform very precise measurements of SM parameters and to set stringent bounds on physics beyond the SM. KLOE contributed with the most comprehensive set of results from a single experiment, giving a fundamental contribution to the 0.2% world accuracy on the determination of $|V_{us}|f_+(0)$. KLOE result on R_K improves the accuracy with which it is known by a factor of 5 with respect to the present world average and allows severe constraints to be set on new physics contributions in the MSSM with lepton flavor violating couplings.

REFERENCES

- [1] MARCIANO W. J. and SIRLIN A., *Phys. Rev. D*, **35** (1987) 1672.
- [2] HAGIWARA K., MATSUMOTO S. and YAMADA Y., *Phys. Rev. Lett.*, **75** (1995) 3605, [hep-ph/9507419](#).
- [3] KURYLOV A. and RAMSEY-MUSOLF M. J., *Phys. Rev. Lett.*, **88** (2002) 071804, [hep-ph/0109222](#).
- [4] CIRIGLIANO V., JENKINS J. and GONZALEZ-ALONSO M., *Nucl. Phys. B*, **830** (2010) 95, [0908.1754](#).
- [5] BOSSI F., DE LUCIA E., LEE-FRANZINI J., MISCETTI S. and PALUTAN M. (KLOE), *Riv. Nuovo Cimento*, **31** (2008) 531, [0811.1929](#).
- [6] BECK R. *et al.* (KLOE-2), Letter of Intent for the KLOE-2 Roll-in (2007) LNF-07/19(IR).
- [7] ANTONELLI M. *et al.*, FLAVIANet working group on kaon decays (2008) [0801.1817](#).
- [8] ANTONELLI M. *et al.*, *Eur. Phys. J. C*, **69** (2010) 399.
- [9] AMBROSINO F. *et al.* (KLOE), *Phys. Lett. B*, **626** (2005) 15, [hep-ex/0507088](#).
- [10] AMBROSINO F. *et al.* (KLOE), *JHEP*, **04** (2008) 059, [0802.3009](#).
- [11] AMSLER C. *et al.* (PARTICLE DATA GROUP), *Phys. Lett. B*, **667** (2008) 1.
- [12] RAMSEY-MUSOLF M. J., SU S. and TULIN S., *Phys. Rev. D*, **76** (2007) 095017, [0705.0028](#).
- [13] DAVIER M., HOCKER A. and ZHANG Z., *Rev. Mod. Phys.*, **78** (2006) 1043, [hep-ph/0507078](#).
- [14] MARCIANO W. J., *Phys. Rev. Lett.*, **93** (2004) 231803, [hep-ph/0402299](#).
- [15] AMBROSINO F. *et al.* (KLOE), *Phys. Lett. B*, **632** (2006) 76.
- [16] HARDY J. C. and TOWNER I. S., *Phys. Rev. C*, **79** (2009) 055502.
- [17] MARCIANO W. J., *PoS, KAON* (2008) 003.
- [18] AMBROSINO F. *et al.* (KLOE), *Phys. Lett. B*, **632** (2006) 43, [hep-ex/0508027](#).
- [19] BOCCHETTA S. *et al.* (KLOE), *PoS, KAON09* (2009) 006.
- [20] AOKI S. *et al.*, *Astron. Astrophys.*, **105** (1982) 359.
- [21] DREUCCI M. *et al.* (KLOE), *PoS, EPS-HEP09* (2009) 198.
- [22] CIRIGLIANO V. and ROSELL I., *Phys. Rev. Lett.*, **99** (2007) 231801, [0707.3439](#).
- [23] MASIERO A., PARADISI P. and PETRONZIO R., *Phys. Rev. D*, **74** (2006) 011701, [hep-ph/0511289](#).
- [24] AMBROSINO F. *et al.* (KLOE), *Eur. Phys. J. C*, **64** (2009) 627, [0907.3594](#).

Recent charmonium results from CLEO-c

C. M. TARBERT for the CLEO COLLABORATION

Department of Physics, Indiana University - Bloomington, Indiana 47405, USA

(ricevuto il 14 Settembre 2010; pubblicato online il 12 Gennaio 2011)

Summary. — In this paper I present three of the latest results in charmonium from the CLEO-c experiment.

PACS 13.20.Fc – Decays of charmed mesons.

PACS 13.40.Em – Electric and magnetic moments.

1. – Introduction

The CLEO Collaboration was formed in 1975 initially with the goal of studying e^+e^- collisions between $\sqrt{s} = 8$ and 16 GeV at the newly proposed Cornell Electron Storage Ring (CESR). Over the last 35 years, CLEO have operated a series of experiments at CESR using bottomonium, B -decays, charmonium and D -decays as laboratories for QCD studies. The latest, and final, incarnation of the CLEO detector system was dubbed CLEO-c, with the suffix indicating its intended purpose; detailed studies of charm physics. Large data sets were acquired both above and below open charm threshold and here, I will present three of the latest results obtained in charmonium. The goals of these analyses are varied and give an indication of the scope of physics accessible in this region of the charmonium spectrum. The first result is the outcome of a search for higher-order multipole transitions in charmonium radiative transitions [1]. These transitions provide access to one of the fundamental properties of the charm quark: its anomalous magnetic moment. The second result is a measure of the relative rate of hadronic and radiative decays of the $\psi(2S)$, a ratio which is sensitive to the strong coupling constant [2]. Finally, I will present the latest precision measurements of hadronic χ_{cJ} branching fractions to $p\bar{p}\pi^0$, $p\bar{p}\eta$ and $p\bar{p}\omega$ [3] which have applications to studies of nucleon-nucleon interactions as well as $p\bar{p}$ -annihilation experiments.

2. – CLEO-c experiment and data sets

CLEO-c [4] is a hermetic and symmetric detector covering 93% of the 4π sr of solid angle. It features a 1 T superconducting solenoid which houses drift chambers for tracking and particle identification and a ring imaging Cerenkov (RICH) system to further

differentiate between charged particle species. Also housed within the solenoid volume is an electromagnetic calorimeter composed of 7784 CsI(Tl) crystals. The photon energy resolution is 2.2% at 1 GeV and 5% at 100 MeV and the momentum resolution achieved using the drift chambers is typically 0.6% at 1 GeV/ c .

The data sets taken with the CLEO-c configuration include 600 pb^{-1} at $\sqrt{s} = 4.170 \text{ GeV}/c^2$ and 818 pb^{-1} at $\sqrt{s} = 3.770 \text{ GeV}/c^2$. At centre-of-mass energies above the threshold for $D\bar{D}$ production, these data are designed for open charm studies. The results presented here, however, utilise a 54 pb^{-1} data set taken at $\sqrt{s} = 3.686 \text{ GeV}/c^2$ equivalent to the production of 27×10^6 $\psi(2S)$ mesons. Since it is below $D\bar{D}$ -production threshold, the $\psi(2S)$ cannot decay to open charm as favoured according to the Okubo-Zweig-Iizukawere (OZI) rule. Instead, the $\psi(2S)$ frequently transitions to a lower mass charmonium state with a branching fraction of 59% for $\psi(2S) \rightarrow J/\psi X$ and around 9% for each of the radiative transitions $\psi(2S) \rightarrow \gamma\chi_{cJ}$ where $J = 0, 1$ and 2 . As a result, this data set provides not only access to the $\psi(2S)$ but to the entire charmonium spectrum below $D\bar{D}$ threshold.

3. – Higher-order multipole transitions in charmonium radiative transitions

The radiative transitions

$$(1) \quad \psi' \rightarrow \gamma' \chi_{cJ}, \quad \chi_{cJ} \rightarrow \gamma J/\psi,$$

where $J = 0, 1, 2$ and $\psi' \equiv \psi(2S)$, are dominated by processes where $E1$ photons are emitted. However, angular momentum and parity conservation do not rule out the possibility of higher-order multipole transitions. When the decay proceeds through the χ_{c0} , only an $E1$ transition is allowed. However, when the decay involves the χ_{c1} both $E1$ and $M2$ transitions are allowed and in the χ_{c2} case, $E1$, $M2$ and $E3$ transitions are permitted although the single quark radiation hypothesis predicts that the $E3$ amplitude should be zero in the absence of $\psi(2S)$ S - D -mixing and χ_{cJ} P - F -mixing. One can picture electric transitions in the $c\bar{c}$ bound state as arising due to interactions between the charge of one quark and the electric field of the other. Similarly, magnetic transitions originate from the magnetic moment of one quark interacting with the magnetic field of the other. The presence of higher-order magnetic multipole radiative transitions can therefore act as a probe of the c -quark magnetic moment. The first attempt to measure $M2$ amplitudes in charmonium transitions was made shortly after the discovery of the J/ψ . That measurement and subsequent results are in some disagreement with the theoretical predictions [5], and it is the aim of this analysis to apply the large statistics CLEO-c data set to the problem.

If the $\psi(1S, 2S)$ are pure S states and the χ_{cJ} 's are pure P states, then one can assume the following non-relativistic interaction Hamiltonian for photon emission from a $+2/3$ charged quark:

$$(2) \quad H = -\frac{e_c}{2m_c} (\mathbf{A}^* \cdot \mathbf{p} + \mathbf{p} \cdot \mathbf{A}^*) - \mu\sigma \cdot \mathbf{H}^*,$$

where $\mu \equiv (e_c/2m_c)(1+\kappa_c)$ and m_c , e_c and κ_c are the mass, electric charge and anomalous magnetic moment of the c -quark. The electric and magnetic fields of the emitted photon are represented by \mathbf{A}^* and \mathbf{H}^* , respectively. Expanding (2) in powers of E_γ/m_c , the

normalised magnetic quadrupole amplitudes can be expressed (to first order) as

$$(3) \quad \begin{aligned} a_2^{J=1} &\equiv \frac{M2}{\sqrt{E1^2 + M2^2}} = -\frac{E_\gamma}{4m_c} (1 + \kappa_c), \\ a_2^{J=2} &\equiv \frac{M2}{\sqrt{E1^2 + M2^2 + E3^2}} = -\frac{3}{\sqrt{5}} \frac{E_\gamma}{4m_c} (1 + \kappa_c), \\ b_2^{J=1} &\equiv \frac{M2}{\sqrt{E1^2 + M2^2}} = -\frac{E_{\gamma'}}{4m_c} (1 + \kappa_c), \\ b_2^{J=2} &\equiv \frac{M2}{\sqrt{E1^2 + M2^2 + E3^2}} = -\frac{3}{\sqrt{5}} \frac{E_{\gamma'}}{4m_c} (1 + \kappa_c). \end{aligned}$$

The letter b is used to denote amplitudes before the χ_{cJ} , *i.e.* $\psi' \rightarrow \gamma' \chi_{cJ}$ and a denotes amplitudes after the χ_{cJ} , *i.e.* $\chi_{cJ} \rightarrow \gamma J/\psi$. The subscript indicates the multipole order and the superscript gives the angular momentum of the χ_{cJ} . Using (3) and choosing values for κ_c and m_c , one can obtain predictions for the magnetic quadrupole amplitudes. It is also important to note that the ratios of these amplitudes are independent of κ_c and m_c to first order in E_γ/m_c .

Events are fully reconstructed in the CLEO-c apparatus in the decay mode $\psi' \rightarrow \gamma' \chi_{cJ}$; $\chi_{cJ} \rightarrow \gamma J/\psi$; $J/\psi \rightarrow l^+ l^-$, where l is an electron or muon. To extract $a_2^{J=1}$, $b_2^{J=1}$ and $a_2^{J=2}$, $b_2^{J=2}$ from the data, the joint angular distribution of the two radiated photons, W , is first constructed in the helicity formalism:

$$(4) \quad \begin{aligned} W(\cos \theta', \phi', \cos \theta_{\gamma\gamma'}, \cos \theta, \phi) \\ \propto \sum \rho^{(\mu' - \nu', \mu' - \bar{\nu}')}(\theta', \phi') B_{|\nu'|} B_{|\bar{\nu}'|} d_{-\nu'\nu'}^{J_x}(\theta_{\gamma\gamma'}) \\ \times d_{-\bar{\nu}'\bar{\nu}}^{J_x}(\theta_{\gamma\gamma'}) A_{|\nu|} A_{|\bar{\nu}|} \rho^{*(\nu - \mu, \nu - \bar{\mu})}(\theta, \phi), \end{aligned}$$

where μ' , ν' , μ and ν are the helicities of the γ' , χ_{cJ} , γ and J/ψ , respectively. The angles θ' and ϕ' are defined in the ψ' rest frame and are sensitive to the polarisation of the ψ' , while θ and ϕ are defined in the J/ψ frame and are sensitive to the polarisation of the J/ψ . The final angle needed to completely define the decay, $\theta_{\gamma\gamma'}$, gives the relative orientation of the ψ' - and J/ψ -frames. The helicity amplitudes A and B are extracted from the data via a five-dimensional unbinned extended maximum likelihood fit and are related to the normalised magnetic dipole amplitudes, a_2^J , b_2^J via Clebsch-Gordon coefficients.

Initially, two-parameter fits to the χ_{c1} and χ_{c2} data were performed to extract $a_2^{J_x=1}$, $b_2^{J_x=1}$ and $a_2^{J_x=2}$, $b_2^{J_x=2}$, respectively. The results from these fits are shown in fig. 1(A) where the data are overlaid with projections of the fitted PDF. The projections were generated by weighting MC samples containing 4.5×10^6 phase space events with W . From inspection of fig. 1(A), it is clear that the data is better described by the fitted PDF containing non-zero $M2$ amplitudes and in fact the pure $E1$ amplitude is inconsistent with the data at the 11σ and 6σ level for the χ_{c1} and χ_{c2} cases, respectively. These fits were repeated, fixing the ratio of $a_2^{J_x=1}/b_2^{J_x=1}$ and $a_2^{J_x=2}/b_2^{J_x=2}$; the results from these one-parameter fits were consistent with the initial two-parameter fits. In the χ_{c2} data, there is also potentially an electric octupole component to the decay. An iteration of fits was performed introducing an $E3$ amplitude and allowing it to float in the fit. Again, the fits were repeated, fixing the ratios of the $a_3^{J_x=2}/b_3^{J_x=2}$. In all cases, there is at least 6σ evidence for non-zero $M2$ amplitudes.

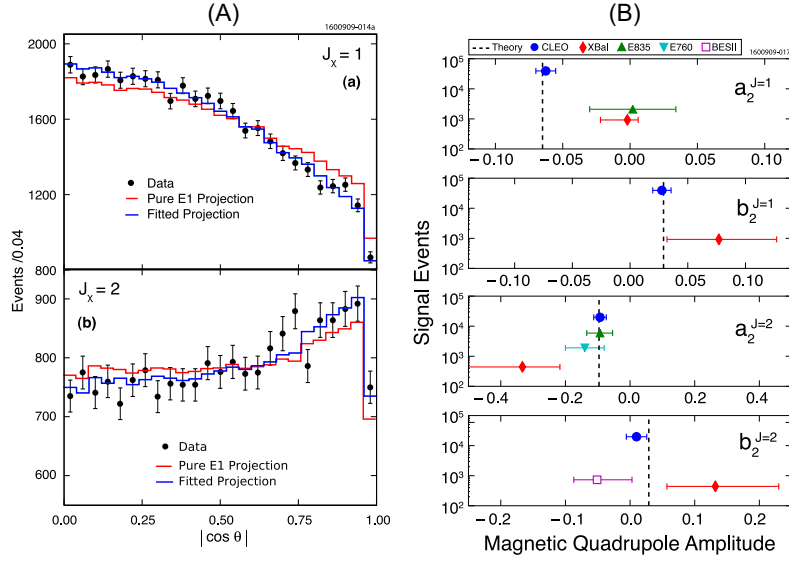


Fig. 1. – Results of the unbinned maximum likelihood fit to extract the normalised magnetic quadrupole amplitudes. (A) Points are data. Red line: projection of W using only a pure $E1$ amplitude for the χ_{c1} data (a) and the χ_{c2} (b). Blue line: projection of W using the fitted non-zero $M2$ amplitudes. (B) Results from this analysis are solid circles, Crystal Ball results are diamonds, the E760 and E835 results [5] are triangles. The line is the theoretical value calculated using (3) and $\kappa_c = 0$, $m_c = 1.5 \text{ GeV}/c^2$.

Figure 1(B) shows a comparison with previous experimental results and highlights the greatly increased statistics available to the current measurement. A comparison with a theoretical calculation performed using (3) and assuming $\kappa_c = 0$ and $m_c = 1.5 \text{ GeV}/c^2$ is also presented and shows the current result to be in excellent agreement with theory. Furthermore, ratios of the normalised $M2$ amplitudes, which are independent of κ_c and m_c , were also found to be in consistent with the values predicted by eq. (3).

4. – Inclusive ψ' decays

The OZI-favoured decay channels to open charm are not available to the $\psi(2S)$ and instead, it must decay via $c\bar{c}$ -annihilation. The next lowest-order decay processes are annihilation to three gluons ($c\bar{c} \rightarrow ggg$), to two gluons and a photon ($c\bar{c} \rightarrow \gamma gg$) or to a virtual photon ($c\bar{c} \rightarrow \gamma^* \rightarrow q\bar{q}$). Given that $\Gamma(\psi(2S) \rightarrow \gamma gg) \propto \alpha_s^2 \alpha_{em}$ and $\Gamma(\psi(2S) \rightarrow ggg) \propto \alpha_s^3$ a rough expectation for the ratio $R_\gamma(\psi(2S))$ can be obtained:

$$(5) \quad R_\gamma(\psi(2S)) = \frac{\Gamma(\psi(2S) \rightarrow \gamma gg)}{\Gamma(\psi(2S) \rightarrow ggg)} \propto q_c^2 \frac{\alpha_{em}}{\alpha_s}.$$

There are no previous measurements of $R_\gamma(\psi(2S))$, however, a new measurement of $R_\gamma(J/\psi)$ was recently reported by the CLEO Collaboration [6]. Prior to that, a survey of R_γ in bottomonium was made [7] and these results are summarised in table I. Examining table I, one would naively expect to see a similar trend in charmonium, that is, $R_\gamma(\psi(2S)) \sim R_\gamma(J/\psi)$.

TABLE I. – Summary of latest R_γ measurements [2, 6, 7]. Errors are statistical then systematic.

$R_\gamma(J/\psi)$	$(0.137 \pm 0.001 \pm 0.016)$
$R_\gamma(\psi(2S))$	$(0.097 \pm 0.002 \pm 0.026)$
$R_\gamma(\Upsilon(1S))$	$(0.027 \pm 0.001 \pm 0.003)$
$R_\gamma(\Upsilon(2S))$	$(0.032 \pm 0.001 \pm 0.005)$
$R_\gamma(\Upsilon(3S))$	$(0.027 \pm 0.001 \pm 0.005)$

The ratio R_γ can be expressed as $R_\gamma = N_{\gamma gg}/(N_{ggg}\epsilon_{\gamma gg})$, where $N_{\gamma gg}$ is the number of direct photon decays observed in the data, N_{ggg} , the number of three gluon decays, and $\epsilon_{\gamma gg}$ is the direct photon finding efficiency. The denominator of this expression was previously measured by CLEO [8]. The experimental approach to obtain $R_\gamma(\psi(2S))$ is then to measure the inclusive photon spectrum from $\psi(2S) \rightarrow \gamma X$, and subtract off everything that does not arise due to $\psi(2S) \rightarrow \gamma gg$. An analysis of Monte Carlo samples (fig. 2(A)) gives an indication of the relative strength of backgrounds competing with the $\psi(2S) \rightarrow \gamma gg$ signal to contribute to the observed photon spectrum. The background is dominated by the two photon decays of π^0 and η mesons as well as radiative decays of the J/ψ , which are produced copiously via the hadronic transitions $\psi(2S) \rightarrow J/\psi X$. The J/ψ direct photon decay spectrum in this data set has been previously measured [6] and can be subtracted off directly. Two different techniques are then used to account for the $(\pi^0, \eta) \rightarrow \gamma\gamma$ background.

In the first method, an exponential function is fitted to the observed photon spectrum in a region where $\pi^0 \rightarrow \gamma\gamma$ processes dominate; $0.27 < z_\gamma < 0.32$. The distribution is then extrapolated to higher photon energies and subtracted off the observed spectrum. An alternative background subtraction technique exploits the isospin relationship between the π^0 , π^+ and π^- and the resulting expected similarities in kinematics. The four-momenta of charged pions found in the data are used to generate an estimated background spectrum by treating them as neutral pions, and forcing them to decay to two back-to-back photons in the pion rest frame. After applying the photon-finding efficiency extracted from Monte Carlo simulations, the resulting “pseudophoton” energy spectrum is normalised according to isospin constraints and subtracted from the observed photon spectrum. This pseudophoton approach has been used in previous analyses and is described in more detail in ref. [6]. The photon spectrum after each of these subtractions has been applied is shown in fig. 2(B). Below $z_\gamma \sim 0.4$, the distribution is dominated by soft photons from radiative transitions to lower mass $c\bar{c}$ states; the peak around $z_\gamma \sim 0.34$ is from transitions to the η_c . Two values of $N_{\gamma gg}$ are initially obtained by integrating the exponential-subtracted and pseudophoton-subtracted distributions above $z_\gamma \sim 0.4$ and extrapolating to $z_\gamma \rightarrow 0$. Since the background elimination techniques give rise to the possibility of over- or under-subtraction, a cross check is performed exploiting the prominent $\psi(2S) \rightarrow \gamma\eta_c$ line. First, a distribution is obtained by averaging the exponential- and pseudophoton-subtracted spectra. A fit is performed in the interval $0.32 < z_\gamma < 0.38$ to obtain the number of $\psi(2S) \rightarrow \gamma\eta_c$ events which can then be used to normalise the distribution using the known $\psi(2S) \rightarrow \gamma\eta_c$ branching fraction. By integrating and normalising the averaged distribution, a third value for $R_\gamma(\psi(2S))$ is obtained. A weighted averaged of all three values of R_γ is made and this is included in table I. As fig. 2(A) demonstrates, the signal-to-noise ratio in the direct photon spectrum is small. As a result, fluctuations in the estimated background have a large effect on the extracted value

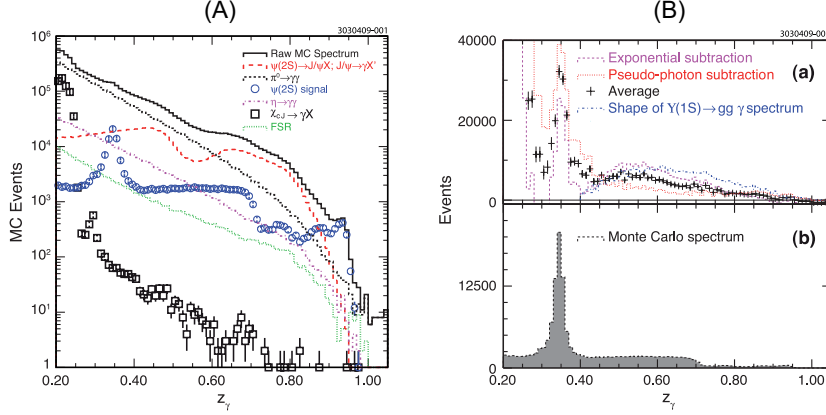


Fig. 2. – Figures from inclusive $\psi(2S)$ radiative decays analysis. $z_\gamma = E_\gamma/E_{\text{beam}}$. (A) Relative contribution of backgrounds to the inclusive $\psi(2S)$ direct photon decay spectrum from analysis of Monte Carlo samples. (B) Inclusive $\psi(2S)$ decay photon spectrum in data after background subtraction (a). $\psi(2S) \rightarrow \gamma gg$ direct photon spectrum from analysis of Monte Carlo samples (b).

of R_γ . Investigations of the sensitivity of R_γ to the background scale have led to the assignment of a systematic error due to uncertainties in the background level of 27% and this is by far the dominating systematic.

Since $\Gamma(\psi(3770) \rightarrow \gamma gg)$ is immeasurably small, this completes the set of R_γ for the ψ $J^{PC} = 1^{--}$ states. Although the difference between $R_\gamma(J/\psi)$ and $R_\gamma(\psi(2S))$ is considerably larger than the corresponding differences in the Υ results, the large systematic error on $R_\gamma(\psi(2S))$ means the difference is only equivalent to $\sim 1\sigma$ deviation. However, it is possible that this large systematic is masking another example of unexpected $\psi(2S)$ to J/ψ partial widths ratios, *e.g.*, the “ $\rho\pi$ puzzle” [9].

5. – Exclusive χ_{cJ} decays

The recent theoretical work of Barnes *et al.* [10, 11] emphasises the importance of studying processes such as $\Psi \rightarrow p\bar{p}m$ where Ψ is any $c\bar{c}$ state and m is a light meson. Their work allows measured $\Psi \rightarrow p\bar{p}m$ partial widths to be used to estimate the production cross sections $\sigma(p\bar{p} \rightarrow \Psi m)$, circumventing the calculation of some of the complicated underlying QCD processes. These theoretical studies are particularly important for the upcoming PANDA experiment which will use associated charmonium production in $p\bar{p}$ annihilation ($p\bar{p} \rightarrow \Psi m$) as a tool in its search for exotic hybrid mesons in the charm sector. Furthermore, the techniques developed in refs. [10] were extended in ref. [11] to allow for the prediction of $\Psi \rightarrow p\bar{p}m$ partial widths. In their meson emission model, the authors assume the sequential decay $\Psi \rightarrow p\bar{p} \rightarrow p\bar{p}m$ and they estimate $\Gamma(\Psi \rightarrow p\bar{p}m)$ using the measured $\Psi \rightarrow p\bar{p}$ widths and well-known $p\bar{p}m$ coupling constants. If this sequential decay mechanism is in fact the dominant means by which $\Psi \rightarrow p\bar{p}m$ decays proceed, then the branching fractions to $p\bar{p}m$ final states would provide a means of extracting other meson-nucleon coupling constants [11]. The first measurements of $\mathcal{B}(\chi_{cJ} \rightarrow p\bar{p}\pi^0)$ and $\mathcal{B}(\chi_{cJ} \rightarrow p\bar{p}\eta)$ were reported by CLEO in 2007 [12]. Here, we exploit a factor of 10 increase in statistics to improve on those measurements. Furthermore, we report the first measurement of $\mathcal{B}(\chi_{cJ} \rightarrow p\bar{p}\omega)$.

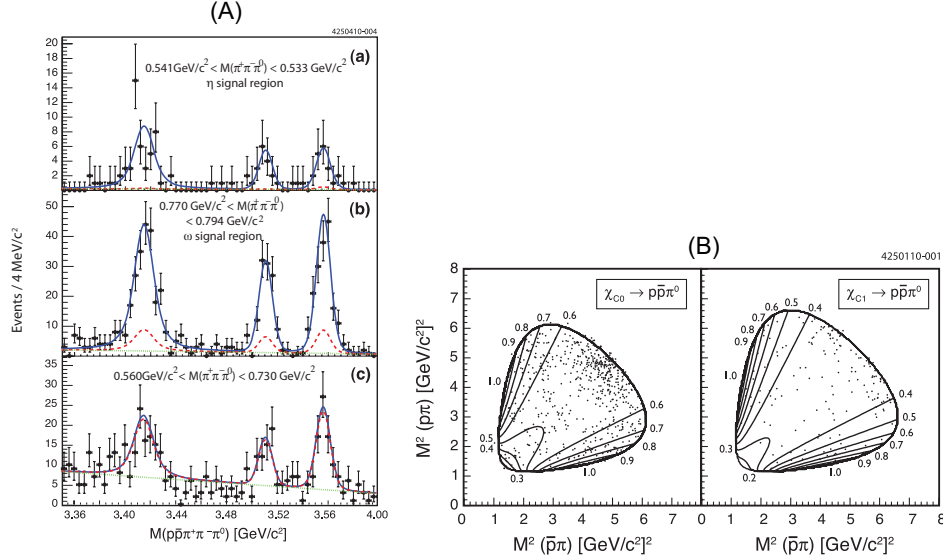


Fig. 3. – Figures from analysis of exclusive χ_{cJ} decays. (A) Projections of best fit to $M(p\bar{p}\pi^+\pi^-\pi^0)$, $M(\pi^+\pi^-\pi^0)$ for three regions of $M(\pi^+\pi^-\pi^0)$. Markers are data. Solid line: total fitted PDF. Dashed line: non-resonant background component of fitted PDF. Dotted line: linear background component of fit. (B) Dalitz plot for $\chi_{cJ} \rightarrow p\bar{p}\pi^0$. Points are data, contours are from the meson emission model of ref. [11].

In this analysis, two final states are fully reconstructed in the CLEO-c apparatus: $\psi(2S) \rightarrow \gamma\chi_{cJ}$; $\chi_{cJ} \rightarrow p\bar{p}\gamma\gamma$ and $\psi(2S) \rightarrow \gamma\chi_{cJ}$; $\chi_{cJ} \rightarrow p\bar{p}\pi^+\pi^-\pi^0$. As well as giving access to the $\chi_{cJ} \rightarrow p\bar{p}\omega$ channel, this allows the $\chi_{cJ} \rightarrow p\bar{p}\eta$ channel to be reconstructed in two separate decay modes. The desired branching fractions are calculated according to

$$(6) \quad \mathcal{B}(\chi_{cJ} \rightarrow p\bar{p}m) = \frac{N_m}{\epsilon_m N_{\psi(2S)} \mathcal{B}(\psi(2S) \rightarrow \gamma\chi_{cJ}) \mathcal{B}(m \rightarrow Y)}.$$

$N_{\psi(2S)}$ is the number of $\psi(2S)$ present in the data and ϵ_m is the signal efficiency evaluated via analysis of MC samples. The branching fractions $\mathcal{B}(\psi(2S) \rightarrow \gamma\chi_{cJ})$ are those measured by CLEO [13] and values for $\mathcal{B}(m \rightarrow Y)$, where Y represents either $\gamma\gamma$ or $\pi^+\pi^-\pi^0$, are taken from the 2008 Particle Data Group report. The signal yield, N_m , is extracted from the data using slightly different techniques for the $p\bar{p}\gamma\gamma$ and $p\bar{p}\pi^+\pi^-\pi^0$ final states. In the first case, the strength is extracted via a one-dimensional unbinned extended maximum likelihood fit to the candidate χ_{cJ} mass spectrum. There is a large non-resonant background in the $p\bar{p}\pi^+\pi^-\pi^0$ channel, making it impossible to reliably extract the signal strengths from fits to $M(p\bar{p}\pi^+\pi^-\pi^0)$ alone. Instead, a two-dimensional unbinned extended maximum likelihood fit is performed in $M(p\bar{p}\pi^+\pi^-\pi^0)$ and $M(\pi^+\pi^-\pi^0)$ and the $p\bar{p}\eta[\pi^+\pi^-\pi^0]$ and $p\bar{p}\omega$ yields are extracted simultaneously. Fitting in both variables provides sensitivity to the non-resonant shape over a wide range of $M(\pi^+\pi^-\pi^0)$ and allows the contribution in the η and ω signal regions to be pinned down.

The results of the fit to the $p\bar{p}\pi^+\pi^-\pi^0$ final state are shown in fig. 3(A) and the extracted branching fractions for all channels are listed in table II. The meson emission model predictions for the two branching fractions $\mathcal{B}(\chi_{c0} \rightarrow p\bar{p}\pi^0)_{\text{theory}} = 2.5 \times 10^{-4}$ and

TABLE II. – Final $\chi_{cJ} \rightarrow p\bar{p}m$ branching fractions. Uncertainties are statistical then systematic, then a separate systematic error due to the uncertainty in the $\psi(2S) \rightarrow \gamma\chi_{cJ}$ branching fractions.

($\times 10^{-4}$)	χ_{c0}	χ_{c1}	χ_{c2}
$p\bar{p}\pi^0$	$(7.76 \pm 0.37 \pm 0.51 \pm 0.39)$	$(1.75 \pm 0.16 \pm 0.13 \pm 0.11)$	$(4.83 \pm 0.25 \pm 0.35 \pm 0.31)$
$p\bar{p}\eta$	$(3.73 \pm 0.38 \pm 0.28 \pm 0.19)$	$(1.56 \pm 0.22 \pm 0.14 \pm 0.10)$	$(1.76 \pm 0.23 \pm 0.14 \pm 0.11)$
$p\bar{p}\omega$	$(5.57 \pm 0.48 \pm 0.50 \pm 0.28)$	$(2.28 \pm 0.28 \pm 0.20 \pm 0.14)$	$(3.68 \pm 0.35 \pm 0.31 \pm 0.24)$

$\mathcal{B}(\chi_{c1} \rightarrow p\bar{p}\pi^0)_{\text{theory}} = 0.2 \times 10^{-4}$ [11] are well below our observed branching fractions, by factors of about 3 and 10, respectively. This suggests that meson emission, as described by this model, is not the dominant decay mechanism. This can be further demonstrated by comparing the theoretical Dalitz plot event densities calculated in ref. [11] with our data; this comparison is shown in fig. 3(B). The meson emission model predicts strength in regions of low $p\pi^0$ and $\bar{p}\pi^0$ invariant mass, whereas the data show a clear enhancement at low $p\bar{p}$ invariant mass.

* * *

The author wishes to thank the CLEO Collaboration and in particular the Indiana group for helpful discussions in the preparation of this talk.

REFERENCES

- [1] ARTUSO M. *et al.*, *Phys. Rev. D*, **80** (2009) 112003.
- [2] LIBBY J. *et al.*, *Phys. Rev. D*, **80** (2009) 112003.
- [3] ONYISI P. *et al.*, LEPP Report No. CLNS 10/2064 (2010).
- [4] ARTUSO M. *et al.*, *Nucl. Instrum. Methods A*, **554** (2005) 147; PETERSON D. *et al.*, *Nucl. Instrum. Methods A*, **478** (2002) 142; BRIERE R. A. *et al.* (CESR-C AND CLEO-C TASKFORCES, CLEO-C COLLABORATION, CORNELL UNIVERSITY), LEPP Report No. CLNS 01/1742 (2001) unpublished.
- [5] OREGLIA, M *et al.* (CRYSTAL BALL COLLABORATION), *Phys. Rev. D*, **79** (1982) 252259; ARMSTRONG T. *et al.* (E760 COLLABORATION), *Phys. Rev. D*, **48** (1993) 3037; ABILIKIM M. *et al.* (BES COLLABORATION), *Phys. Rev. D*, **70** (2004) 092004.
- [6] BESSON D. *et al.*, *Phys. Rev. D*, **78** (2008) 032012.
- [7] BESSON D. *et al.*, *Phys. Rev. D*, **74** (2006) 012003.
- [8] BESSON D. *et al.*, *Phys. Rev. D*, **78** (2008) 1011102.
- [9] GU Y. *et al.*, *Phys. Rev. D*, **63** (2001) 114019.
- [10] LUNDBORD A. *et al.*, *Phys. Rev. D*, **73** (2006) 096003; BARNES T. *et al.*, *Phys. Rev. D*, **75** (2007) 054018; **77** (2008) 056001.
- [11] BARNES T. *et al.*, *Phys. Rev. D*, **81** (2010) 034025.
- [12] ATHAR S. B. *et al.*, *Phys. Rev. D*, **75** (2007) 032002.
- [13] ATHAR S. B. *et al.*, *Phys. Rev. D*, **70** (2004) 112002.

SESSION V - ELECTROWEAK AND TOP PHYSICS

<i>Andreas Wildauer</i>	Start-up and first physics results with the ATLAS detector at the LHC
<i>Pierluigi Catastini</i>	Electroweak Physics at the Tevatron
<i>Alex Melnitchouk</i>	W mass and width measurements at the Tevatron
<i>Daniel Wicke</i>	Single and double top quark production at the Tevatron
<i>Gabriele Compostella</i>	Top quark properties at the Tevatron

Start-up and first physics results with the ATLAS detector at the LHC

A. WILDAUER on behalf of the ATLAS COLLABORATION

IFIC - Apartado de Correos 22085, 46071 Valencia, Spain

(ricevuto il 14 Settembre 2010; pubblicato online l'11 Gennaio 2011)

Summary. — An overview of the first data taking with the ATLAS detector at the Large Hadron Collider (LHC) is given. Data were collected in December 2009 during approximately ten days of running at a centre-of-mass energy of 900 GeV (and shortly at 2.36 TeV). An impressive amount of studies have been carried out by the ATLAS Collaboration on these data. A small selection of results from detector performance and combined performance groups are presented as well as results from the first physics analysis of ATLAS on charged-particle multiplicities in 900 GeV collisions.

PACS 13.85.-t – Hadron-induced high- and super-high-energy interactions (energy > 10 GeV).

1. – Introduction

An excerpt of detector performance and first physics results of the ATLAS Collaboration using the 2009 data taking of the LHC [1] at 900 GeV centre-of-mass energy is presented. The ATLAS detector [2] at the LHC has been designed to study a wide range of physics topics at LHC energies. It covers almost the whole solid angle around the collision point with layers of tracking detectors, calorimeters and muon chambers.

The ATLAS inner detector has full coverage in ϕ and covers the pseudorapidity range⁽¹⁾ $|\eta| < 2.5$. It consists of a silicon pixel detector (Pixel), a silicon microstrip detector (SCT) and a transition radiation tracker (TRT). These detectors cover a sensitive radial distance from the interaction point of 50.5–150 mm, 299–560 mm and 563–1066 mm, respectively, and are immersed in a 2 T axial magnetic field. The inner-detector barrel (end-cap) parts consist of 3 (2×3) pixel layers, 4 (2×9) double-layers of single-sided silicon microstrips with a 40 mrad stereo angle, and 73 (2×160) layers of TRT straws. These detectors have position resolutions of typically 10, 17 and 130 μm for the R - ϕ coordinate and, in case of the Pixel and SCT, 115 and 580 μm for the second measured

⁽¹⁾ Pseudorapidity is defined as $\eta = -\ln \tan(\theta/2)$.

coordinate. A track from a particle traversing the barrel detector would typically have 11 silicon hits (3 pixel clusters and 8 strip clusters), and more than 30 straw hits.

High-granularity liquid-argon (LAr) electromagnetic sampling calorimeters, with excellent performance in terms of energy and position resolution, cover the pseudorapidity range of up to $|\eta| = 4.9$. The hadronic calorimetry in the range $|\eta| < 1.7$ is provided by a scintillator-tile calorimeter, which is separated into a large barrel and two smaller extended barrel cylinders, one on either side of the central barrel.

The calorimeter is surrounded by the muon spectrometer. The air-core toroid system, with a long barrel and two inserted end-cap magnets, generates strong bending power in a large volume within a light and open structure. Multiple-scattering effects are thereby minimised, and excellent muon momentum resolution is achieved with three layers of high-precision tracking chambers. The muon instrumentation includes, as a key component, trigger chambers with timing resolution of the order of 1.5-4 ns. The muon spectrometer defines the overall dimensions of the ATLAS detector.

2. – Data taking and trigger

ATLAS recorded approximately 538000 collisions under LHC stable beam conditions (which means that it is safe for ATLAS to turn on the full inner detector). The integrated luminosity recorded by ATLAS during stable beams corresponds to $\approx 9 \mu\text{b}^{-1}$ with a systematic uncertainty of about 30%. The maximum peak luminosity as measured in ATLAS was $L \approx 7 \times 10^{26} \text{ cm}^{-2} \text{ s}^{-1}$. The operational fraction of all ATLAS detector and trigger systems was close to 100% at all times.

The ATLAS detector has a three-level trigger system: Level 1 (L1), Level 2 (L2) and Event Filter (EF). The main physics trigger during the 2009 data taking relied on the L1 signals from the Beam Pickup Timing devices (BPTX) and the Minimum Bias Trigger Scintillators (MBTS). The BPTX are composed of beam pick-ups attached to the beam pipe at $z = \pm 175 \text{ m}$ from the centre of the ATLAS detector. The MBTS are mounted at each end of the detector in front of the liquid-argon end-cap calorimeter cryostat at $z = \pm 3.56 \text{ m}$.

3. – Detector and combined performance plots

ATLAS has produced an impressive amount of results of detector and combined performance studies on the 2009 data at 900 GeV centre-of-mass energy. This section can only show a small selection of these results trying to span all detectors from the inner detector to the muon spectrometer.

The Pixel detector has an analogue read-out and can therefore measure the energy loss of traversing particles. Figure 1(a) shows the energy loss *versus* the charge times the momentum of the traversing particles. The bands for protons, kaons and pions can clearly be seen. A cross-check has been done by reconstructing the decay of particles such as $\Lambda \rightarrow p\pi^-$ as shown in fig. 3. When only plotting the energy loss for the decay product of the Λ (and $\bar{\Lambda}$) decay only the bands for protons and pions remain (see fig. 1(b)).

The TRT has the capability to separate electrons and pions by measuring the photon radiation of the traversing particle. The intensity of this transition radiation is proportional to the Lorentz factor $\gamma = \frac{E}{m_0 c^2}$ of the traversing particle. Figure 2(a) shows the probability to produce the so-called high-threshold hits which are due to transition radiation in the TRT for data and Monte Carlo. Pions in the momentum range 1–10 GeV radiate far fewer photons than electrons in the same momentum range due to the large

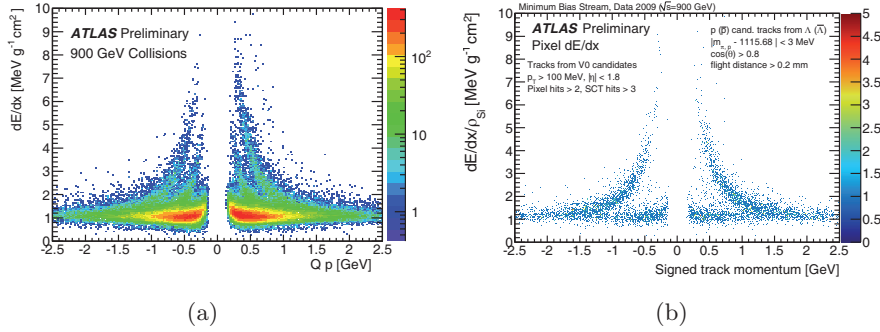


Fig. 1. – (a) Energy loss in the pixel detector for all reconstructed tracks. The bands for pions, kaons and protons are clearly visible. (b) A pre-selection of tracks using only the proton of $\Lambda \rightarrow p\pi^-$ (and \bar{p} of $\bar{\Lambda} \rightarrow \bar{p}\pi^+$) removes the kaon band.

mass difference between the two particles. A cross-check of this can be done by using identified electrons from photon conversions ($\gamma \rightarrow e^+e^-$). Figure 2(b) shows the fraction of high-threshold hits for all reconstructed tracks in data and Monte Carlo. The shaded area towards higher fractions of high-threshold hits is entirely due to electrons from photon conversions.

The reconstruction of well-known particle decays such as $K_S^0 \rightarrow \pi^+\pi^-$, $\Lambda \rightarrow p\pi^-$ or $\bar{\Lambda} \rightarrow \bar{p}\pi^+$ is a powerful tool to understand and validate the performance of the detector. Figure 3 shows the reconstructed invariant mass spectra of the K_S^0 and the Λ . The mean values of the reconstructed particle mass for the K_S^0 , Λ and $\bar{\Lambda}$ (the latter is not shown) agree very well with the world average [3]. The widths of the distributions are in very good agreement between data and Monte Carlo. This underlines the good understanding of the detector (*e.g.*, the material in the inner detector) at this early stage of data taking.

The electromagnetic calorimeter measures the energy of electrons and photons. Its response to single isolated tracks is a good measure for the understanding of the calorimeter and also of the material in the inner detector. Figure 4 shows the energy deposited in the calorimeter over the momentum of a track as measured in the inner detector in the barrel

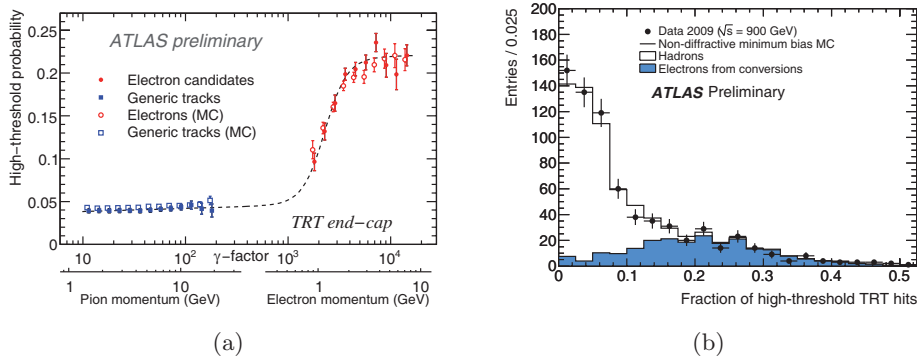


Fig. 2. – (a) The probability of a high-threshold hit in the TRT as a function of the Lorentz factor $\gamma = \frac{E}{m_0 c^2}$. (b) Fraction of high-threshold hits in the TRT for all reconstructed tracks in data and Monte Carlo.

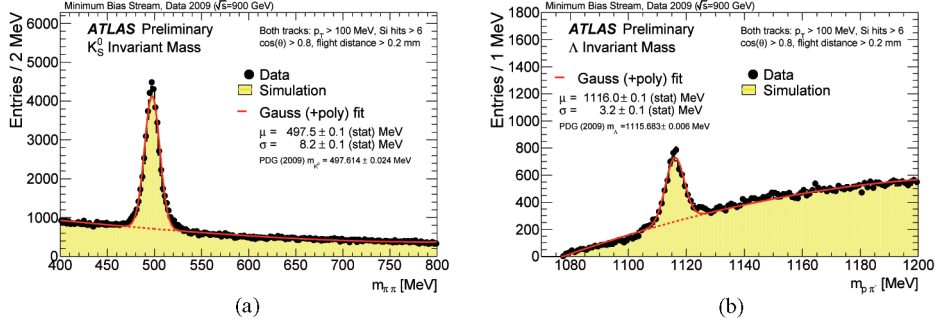


Fig. 3. – Reconstructed invariant mass spectra of (a) $K_S^0 \rightarrow \pi^+\pi^-$ and (b) $\Lambda \rightarrow p\pi^-$.

region ($|\eta| < 0.8$) for isolated hadrons for data and Monte Carlo. The transverse momentum of all reconstructed tracks was required to be within the range 0.5 and 10 GeV. An isolation requirement of no other tracks within a cone in η and ϕ of 0.4 was made. The peak at zero is due to particles that stopped in the inner detector (*e.g.*, due to hadronic interactions) and hence did not deposit any energy in the calorimeter. The agreement between simulation and data is remarkable and also reflects a good understanding of the material in the inner detector in the simulation.

The muon spectrometer will play an important role in triggering on interesting physics channels at higher centre-of-mass energies. However, already at $\sqrt{s} = 900$ GeV, where the cross sections for prompt muon production and decays such as $J/\Psi \rightarrow \mu^+\mu^-$ are very low around 50 muon candidates were reconstructed using the combined performance of the inner detector and the muon spectrometer. Figure 5(a) shows the pseudorapidity and fig. 5(b) the transverse momentum of these muon candidates. Reconstructed muon candidates are very forward (*i.e.* large $|\eta|$) and have rather low transverse momenta around several GeV (compared to what is expected at higher centre-of-mass energies).

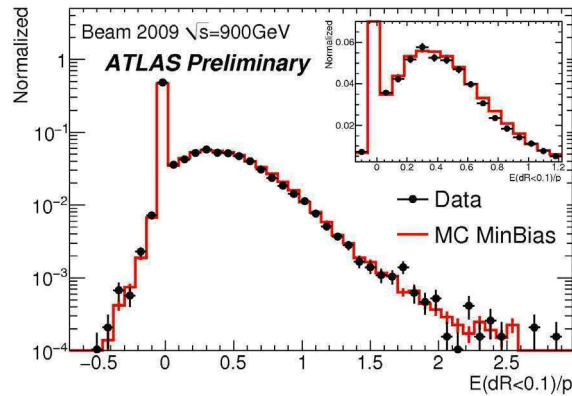


Fig. 4. – The energy deposited in the calorimeter over the momentum, as measured in the inner detector, of an isolated track.

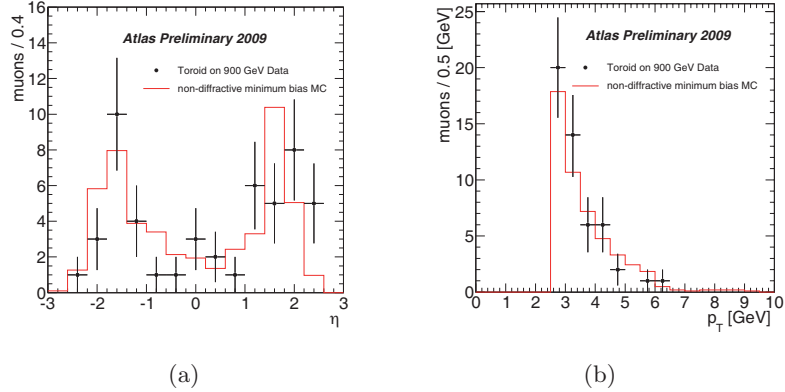


Fig. 5. – Muon candidates reconstructed in the inner detector and muon spectrometer as a function of (a) pseudorapidity, and (b) transverse momentum.

4. – Charged-particle multiplicities at $\sqrt{s} = 900$ GeV

The study of charged-particle multiplicities at a centre-of-mass energy of 900 GeV is described in the first physics paper released by ATLAS [4]. The measurement of charged-particle multiplicities in proton-proton reactions constrains phenomenological models of soft Quantum Chromodynamics (QCD) and therefore is an important ingredient for future studies of high transverse momentum phenomena at the LHC.

The charged-particle multiplicities were measured at 900 GeV within the kinematic range of $|\eta| < 2.5$, $p_T > 500$ MeV and the requirement of one charged-particle within this range. The data were presented as fully corrected inclusive-inelastic distributions at the particle level:

$$\frac{1}{N_{\text{ev}}} \cdot \frac{dN_{\text{ch}}}{d\eta}, \quad \frac{1}{N_{\text{ev}}} \cdot \frac{1}{2\pi p_T} \cdot \frac{d^2N_{\text{ch}}}{d\eta dp_T}, \quad \frac{1}{N_{\text{ev}}} \cdot \frac{dN_{\text{ev}}}{dn_{\text{ch}}} \quad \text{and} \quad \langle p_T \rangle \text{ vs. } n_{\text{ch}},$$

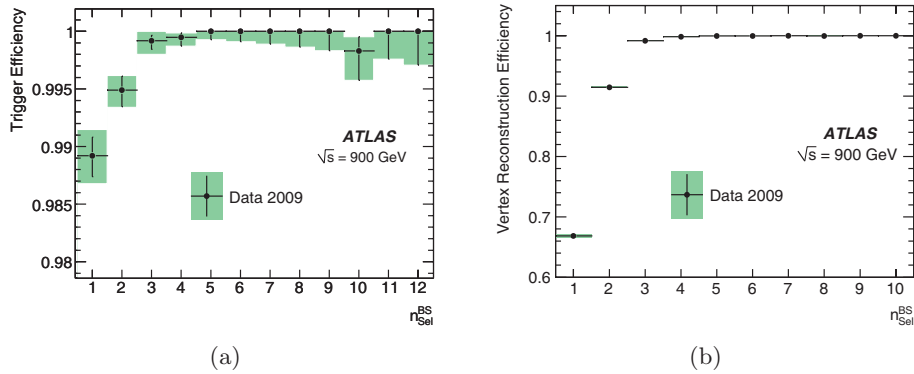


Fig. 6. – (a) Trigger and (b) primary vertex reconstruction efficiency as derived from data versus the number of reconstructed tracks ($n_{\text{Sel}}^{\text{BS}}$). The bands include statistical and systematic uncertainties.

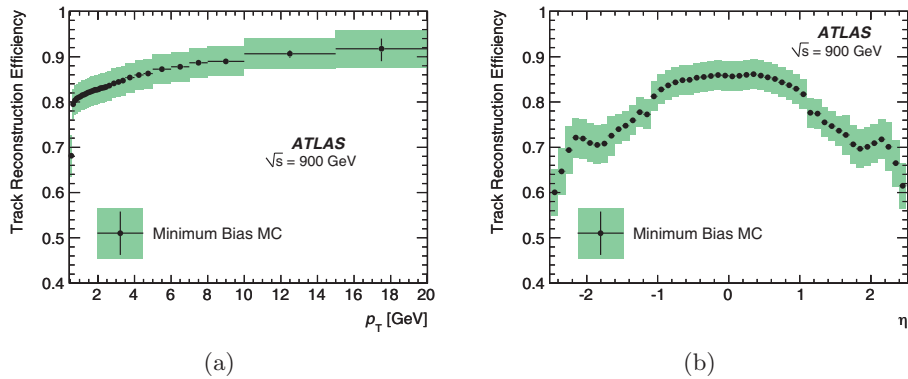


Fig. 7. – The track-reconstruction efficiency as derived from Monte Carlo is shown *vs.* pseudorapidity (a) and transverse momentum (b). The bands include statistical and systematic uncertainties.

where N_{ev} is the number of events with at least one charged particle inside the selected kinematic range, N_{ch} is the total number of charged particles, n_{ch} is the number of charged particles in an event and $\langle p_T \rangle$ is the average p_T for a given number of charged particles. A primary charged particle was defined as a particle with a mean lifetime of $\tau < 0.3 \times 10^{-10}$ s which is either directly produced in the pp collision or stems from a subsequent decay of a particle with a shorter lifetime.

The trigger used for this analysis was a combination of the BPTX and the MBTS as described in sect. 2. The MBTS trigger was configured to require one hit above threshold from either side of the detector (so-called: single-arm trigger). The efficiency of this trigger was derived from data and was obtained by comparison with an independent prescaled L1 BPTX trigger which was filtered to obtain inelastic interactions by loose inner detector requirements at L2 and EF. The primary vertex reconstruction efficiency was also derived from data and was measured with respect to the L1 MBTS trigger. It was found to only depend on the number of reconstructed tracks per event and, in case of only one reconstructed track also on η of the track. Figure 6 shows trigger and primary vertex reconstruction efficiency as a function of the number of reconstructed tracks per event. The efficiencies are close to 100% except for events with very few reconstructed tracks. The background contributions from cosmic-rays and beam-induced background were measured to be of the order of 10^{-4} and 10^{-6} , respectively. The contribution from secondary tracks which have been reconstructed as primary tracks was estimated to be $(2.20 \pm 0.05(\text{stat.}) \pm 0.11(\text{syst.}))\%$.

The track-reconstruction efficiency was derived from Monte Carlo. The understanding of and the agreement between Monte Carlo and data concerning track-reconstruction in the inner detector had therefore to be studied in great detail. It was found that the global uncertainty on the amount of material in the inner detector was less than 10%. The track-reconstruction efficiency *versus* η and p_T as derived from Monte Carlo is shown in fig. 7.

All distributions were corrected for trigger, primary vertex and track-reconstruction efficiency. The final corrected distributions of primary charged particles are shown in fig. 8, where they are compared to predictions of models tuned to a wide range of measurements. The charged-particle pseudorapidity density is shown in fig. 8(a). It is measured to be approximately flat in the range $|\eta| < 1.5$. The charged-particle multiplicity

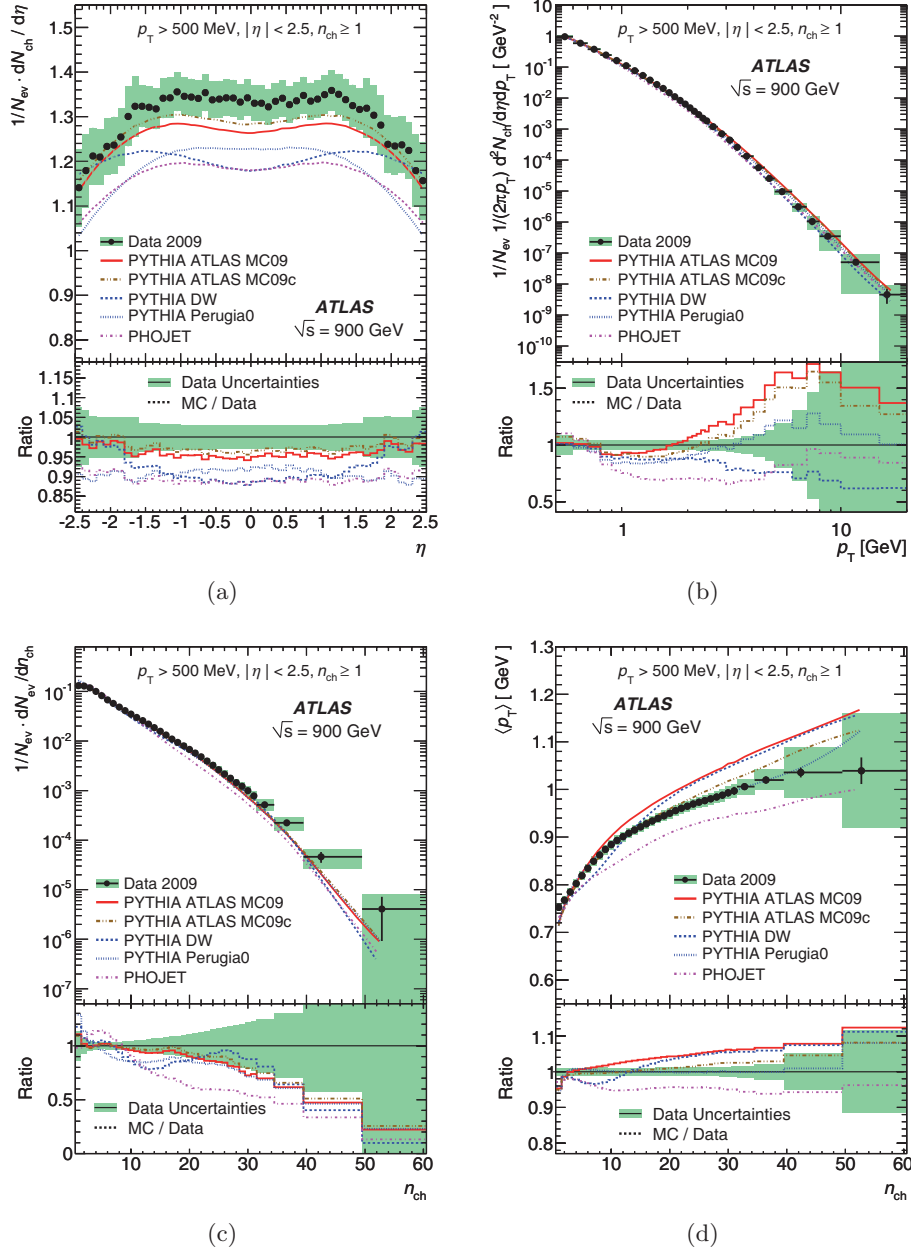


Fig. 8. – Inclusive-inelastic distributions of primary charged particles at a centre-of-mass energy of $\sqrt{s} = 900$ GeV, in the kinematic range $p_T > 500$ MeV, $|\eta| < 2.5$ and the requirement of one charged particle within this range.

per event and unit of pseudorapidity at $\eta = 0$ is measured to be $1.333 \pm 0.003(\text{stat.}) \pm 0.040(\text{syst.})$, which is 5–15% higher than the Monte Carlo model predictions. The particle density is found to drop at higher values of $|\eta|$. The N_{ch} distribution in bins of p_{T} is shown in fig. 8(b) and is constructed by weighting each entry by $1/p_{\text{T}}$. The multiplicity distribution as a function of n_{ch} is shown in fig. 8(c) and finally fig. 8(d) shows the average p_{T} as a function of n_{ch} . The latter is found to increase with increasing n_{ch} and a change of slope is observed around $n_{\text{ch}} = 10$. This behaviour was already observed by the CDF experiment in pp collisions at 1.96 TeV [5].

5. – Conclusion

First performance and physics results from the ATLAS detector at the LHC are presented. An impressive amount of detector and combined performance results have been produced and only a small excerpt could be shown here. These studies show that the ATLAS detector is performing extremely well. The many years of preparation from test-beam, cosmic-ray, and Monte Carlo studies have paid off, ensuring such a successful start to data taking. The first physics measurements of inclusive-inelastic primary charged-particle multiplicities in 900 GeV proton-proton collisions have been presented. The charged-particle multiplicity per event and unit of pseudorapidity at $\eta = 0$ is measured to be $1.333 \pm 0.003(\text{stat.}) \pm 0.040(\text{syst.})$, which is 5–15% higher than the Monte Carlo model predictions.

REFERENCES

- [1] EVANS L. and BRYANT P. (Editors), *JINST*, **3** (2008) S08001.
- [2] AAD G. *et al.* (ATLAS COLLABORATION), *JINST*, **3** (2008) S08003.
- [3] AMSLER C. *et al.*, *Phys. Lett. B*, **667** (2008) 1.
- [4] AAD G. *et al.* (ATLAS COLLABORATION), *Phys. Lett. B*, **688** (2010) 1.
- [5] ABE F. *et al.* (CDF COLLABORATION), *Phys. Rev. D*, **41** (1990) 2330.

Electroweak Physics at the Tevatron

P. CATASTINI on behalf of the CDF and D0 COLLABORATIONS

Fermilab - Batavia, IL, USA

(ricevuto il 14 Settembre 2010; pubblicato online l'11 Gennaio 2011)

Summary. — We discuss recent results in the electroweak sector at the Tevatron. We will focus on latest results in the measurement of diboson production cross sections and limits on anomalous triple gauge coupling. At first, we will consider purely leptonic decays. Then, we will describe the recent observations of diboson processes with jets in the final state.

PACS 14.70.Fm – W bosons.

PACS 14.80.Bn – Standard-model Higgs bosons.

1. – Introduction

The study of diboson production represents a relevant portion of the current Electroweak Physics program at the Tevatron. Dibosons are of great interest because they provide unique opportunities to test the Standard Model at the TeV scale and they are a relevant probe to new physics through deviations of Triple Gauge Couplings (TGCs) from Standard Model (SM) predictions. Moreover, each combination of associated production of W and Z boson decaying in any final state has a counterpart search channel for the Higgs boson at the Tevatron. Worth mentioning: $WW + WZ \rightarrow l\nu + jj$ that shares the same topology of $WH \rightarrow l\nu + b\bar{b}$, the golden process for low mass Higgs searches; $WW \rightarrow l\nu + l\nu$ that is the dominant background for $H \rightarrow WW$, the golden process for high mass Higgs searches.

As a consequence, establishing diboson production, at first in their leptonic decays and more recently with jets in the final state, represented an important milestone for the development and the assessment of techniques used in Higgs boson searches at the Tevatron. In this paper we examine diboson production in 1.96 TeV $p\bar{p}$ collision using the CDF and D0 detectors, compare this production to Standard Model predictions, and set limits on the strength of some anomalous couplings. Signals of the WW , WZ , ZZ are searched through their leptonic and semi-leptonic final states.

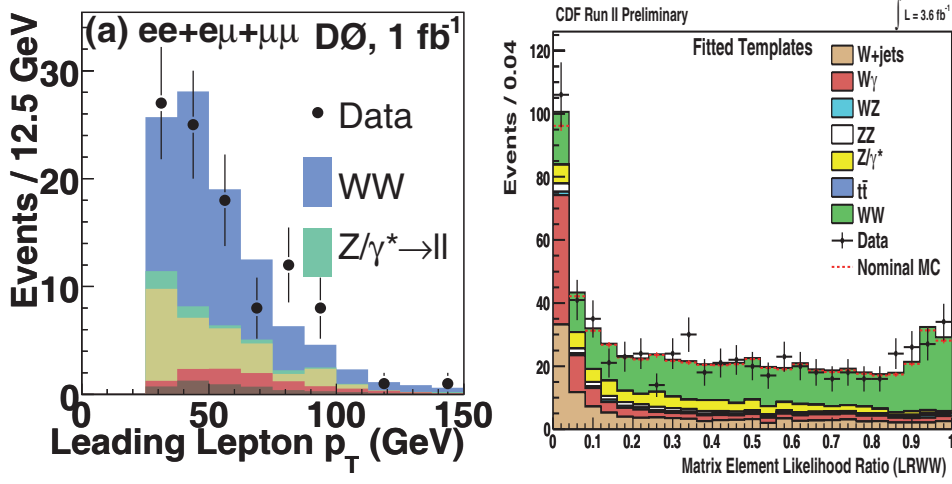


Fig. 1. – (Left) Leading lepton P_T distribution in $WW \rightarrow l^+l^-\nu\bar{\nu}$ candidate events at D0. (Right) Likelihood ratio used to extract the $WW \rightarrow l^+l^-\nu\bar{\nu}$ signal at CDF.

2. – $WW \rightarrow l\nu + l\nu$

The process $WW \rightarrow l\nu + l\nu$ is interesting for several reasons. Among them, we might mention the measurement of WW cross section to test the SM prediction and the search for anomalous trilinear gauge couplings. In addition, it represents the main background of the process $H \rightarrow WW$, the golden process for high mass Higgs boson searches at the Tevatron.

D0, using a data sample of 1 fb^{-1} , studied the process $WW \rightarrow l^+l^-\nu\bar{\nu}$ and measured the WW cross section to be $\sigma(p\bar{p} \rightarrow WW) = 11.5 \pm 2.1(\text{stat} + \text{syst}) \pm 0.7(\text{lum})\text{ pb}$, in agreement with the SM expectation of $12.0 \pm 0.7\text{ pb}$. In addition, D0 imposed also limits on TGC [1].

CDF measured the WW production cross section in the two charged lepton (e or μ) and two neutrino final state using an integrated luminosity of 3.6 fb^{-1} [2]. The WW signal is separated from backgrounds using matrix element based likelihood ratios. The WW cross section is extracted using a binned maximum likelihood method which best fits LR_{WW} signal and background shapes to data (see fig. 1, right). The measured WW cross section is $12.1 \pm 0.9(\text{stat})_{-1.4}^{+1.6}(\text{syst})\text{ pb}$. It is in good agreement with the Standard Model prediction and it represents the most precise measurement up to date. An updated version of this analysis sets limits on TGC [3].

3. – ZZ

The SM prediction for the total ZZ production cross section in $p\bar{p}$ collisions at $\sqrt{s} = 1.9\text{ TeV}$ is $\sigma(ZZ) = 1.4 \pm 0.1\text{ pb}$. Therefore, ZZ has the smallest SM diboson production cross section. The requirement of leptonic Z boson decays provides a clear signature with extremely low background; on the other hand, it reduces the ZZ observable cross section, making its measurement rather challenging.

Using 1.7 fb^{-1} of data, D0 observed, for the first time at a hadron collider, $ZZ \rightarrow$

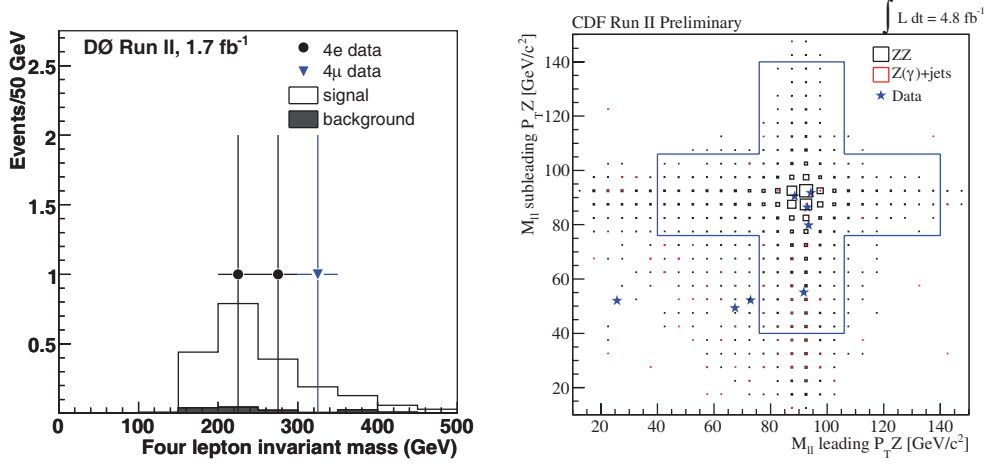


Fig. 2. – (Left) Four-lepton invariant mass distribution at D0. (Right) M_{jj} of the leading P_T Z candidate *vs.* the subleading one at CDF.

$l^+l^-l'^+l'^-$ ($l, l' = e$ or μ) production with a significance of 5.3 standard deviations, fig. 2 (left). D0 also combined this channel with $ZZ \rightarrow l^+l^-\nu\bar{\nu}$, yielding a significance of 5.7 standard deviations and measured $\sigma(ZZ) = 1.60 \pm 0.63(\text{stat})^{+0.16}(\text{syst})$ pb [4].

Recently, CDF re-observed $ZZ \rightarrow l^+l^-l'^+l'^-$ with a significance of 5.7 standard deviations, using 4.8 fb^{-1} of data, fig. 2 (right). CDF measured $\sigma(ZZ) = 1.56^{+0.80}(\text{stat}) \pm 0.25(\text{syst})$ pb [5]. D0 and CDF measurements are in agreement with the SM prediction.

4. – Combined limits on anomalous trilinear gauge couplings

D0 combined different diboson production and decay channels to set limits on $WW\gamma$ and WWZ trilinear gauge couplings [6]. Four channels were considered: $WW + WZ \rightarrow l\nu + jj$, $WW \rightarrow l^+l^-\nu\bar{\nu}$, $WZ \rightarrow l\nu + l^+l^-$ and $W\gamma \rightarrow l\nu\gamma$.

The corresponding results, shown in fig. 3, set the most stringent limits to date on W magnetic dipole μ_W and quadrupole q_W .

5. – $VV \rightarrow \cancel{E}_T + jj$

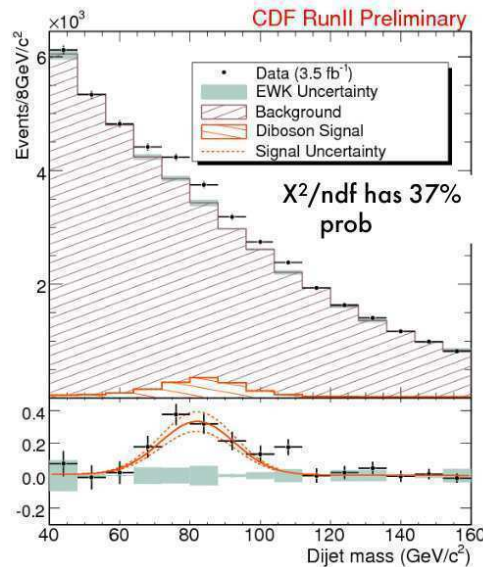
The VV ($VV = WW, WZ, ZZ$) production and decay into hadronic final states are topologically similar to the VH production and decay which is the most promising Higgs discovery channel at low Higgs mass. Also, study of the diboson production is sensitive to extra gauge couplings not present in the Standard Model.

CDF observed diboson production with jets in the final states for the first time at a hadron collider using a sample of events with large \cancel{E}_T ($> 60 \text{ GeV}$) and two jets with E_T above 25 GeV [7]. Due to limited energy resolution it is impossible to distinguish between WW , WZ and ZZ events so what CDF measured was a sum of these processes. No requirement on the number of leptons in the event was applied, therefore the analysis was also sensitive to lepton decays of the gauge bosons. The multijet QCD contribution, which is large in this channel, is heavily suppressed through novel algorithms related to \cancel{E}_T significance. Diboson signal was extracted from the background using the invariant

Results respecting $SU(2)_L \otimes U(1)_Y$ symmetry			
Parameter	Minimum	68% C.L.	95% C.L.
$\Delta\kappa_\gamma$	0.07	[-0.13, 0.23]	[-0.29, 0.38]
Δg_1^Z	0.05	[-0.01, 0.11]	[-0.07, 0.16]
λ	0.00	[-0.04, 0.05]	[-0.08, 0.08]
μ_W	2.02	[1.93, 2.10]	[1.86, 2.16]
q_W	-1.00	[-1.09, -0.91]	[-1.16, -0.84]
Results for equal-couplings			
Parameter	Minimum	68% C.L.	95% C.L.
$\Delta\kappa$	0.03	[-0.04, 0.11]	[-0.11, 0.18]
λ	0.00	[-0.05, 0.05]	[-0.08, 0.08]
μ_W	2.02	[1.94, 2.09]	[1.88, 2.15]
q_W	-1.02	[-1.09, -0.94]	[-1.16, -0.87]

Fig. 3. – Combined D0 limits on TGC.

mass distribution of the two selected jets (fig. 4). The extraction of the signal did not use the theoretical calculation of the V +jets integral cross section and its invariant mass shape was cross checked with γ +jets events from the data, hence considerably reducing the systematic uncertainty on the shape of this main background. The final dijet mass fit was an unbinned extended maximum likelihood with jet energy scale, and the slope and the normalization of the multijet background treated as nuisance parameters and allowed to float in the fit within their predetermined uncertainties. The EWK background

Fig. 4. – $VV \rightarrow \cancel{E}_T + \text{jets}$ search fit result at CDF.

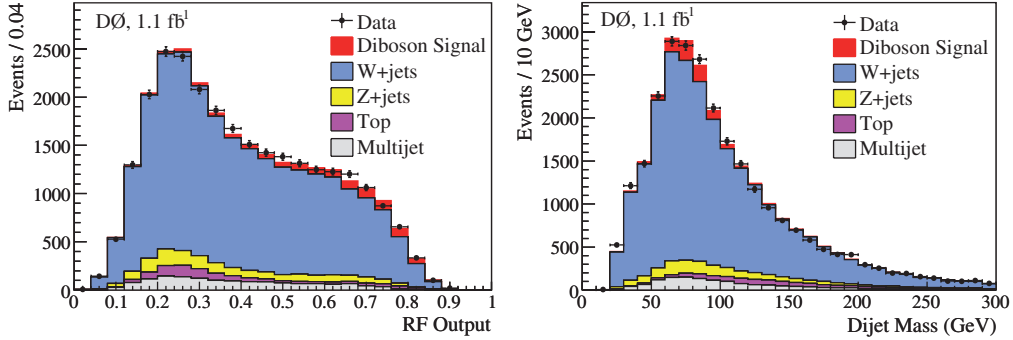


Fig. 5. – $WV \rightarrow l \cancel{E}_T + jj$: (left) Random Forest discriminant fit at D0. (right) dijet mass fit at D0.

and diboson signal normalization are also freely floating in the fit with no constraints. Using a sample of 3.5 fb^{-1} of data, CDF observed $1516 \pm 239(\text{stat}) \pm 144(\text{syst})$ diboson events with a significance of 5.3σ . The corresponding cross section was measured to be $\sigma(p\bar{p} \rightarrow VV + X) = 18.0 \pm 2.8(\text{stat}) \pm 2.4(\text{syst}) \pm 1.1(\text{lum}) \text{ pb}$, in good agreement with the Standard Model predictions.

6. – $WV \rightarrow l \cancel{E}_T + jj$

D0 and CDF utilize similar selections to reconstruct $WV \rightarrow l \cancel{E}_T + jj$ with $V = W, Z$. At first we look for an energetic lepton, electron or muon; we then require large \cancel{E}_T and at least two additional jets in the event. Moreover, both CDF and D0 further select events with higher transverse mass of the lepton- \cancel{E}_T system. The main background for the process $WV \rightarrow l \cancel{E}_T + jj$ is $W + jets$ with much less, but not negligible, contributions from $t\bar{t}$, single t , $Z + jets$ and multijet QCD background.

D0 reported the first evidence of $WW + WZ$ production in lepton+jets final states with a statistical significance of 4.4σ using 1.1 fb^{-1} of data [8]. Diboson signal was separated from backgrounds using a multivariate classifier to combine information from several kinematic variables. A Random Forest (RF) classifier was built using thirteen kinematic variables characterized by separation between signal and at least one of the backgrounds. The signal cross section is determined by a fit to the RF distribution by varying the diboson and the dominant background W +jet templates. Other background contributions are normalized to the SM predictions. D0 measured $\sigma(WW + WZ) = 20.2 \pm 2.5(\text{stat}) \pm 3.6(\text{syst}) \pm 1.2(\text{lum}) \text{ pb}$ from the fit to the RF distribution, fig. 5 (left). A consistent result was found by performing a fit to the dijet invariant mass distribution as a cross check, fig. 5 (right).

CDF observed $WW/WZ \rightarrow l + \nu jj$ production and decay [9]. Two different approaches were used: the first looks for a bump in the dijet mass distribution (M_{jj}), while the second uses Matrix Element computation (ME) to exploit additional kinematic information. In 3.9 fb^{-1} , the M_{jj} method result had a significance of 4.6σ , while the ME approach resulted in the first $WW/WZ \rightarrow l\nu jj$ observation, with a significance of 5.4σ .

Both CDF analyses have been recently updated using additional data. The M_{jj} method now uses a data sample corresponding to approximately 4.3 fb^{-1} of integrated luminosity to reconstruct WW/WZ events [10]. The diboson signal is extracted from

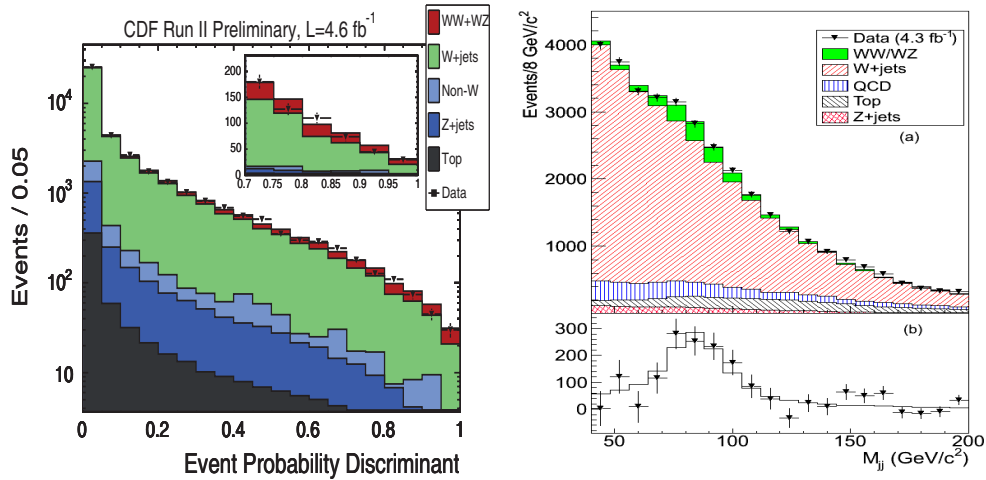


Fig. 6. – $WW \rightarrow l \cancel{E}_T + jj$: (left) EPD discriminant fit at CDF, (right) dijet mass fit at CDF.

the background using a χ^2 fit of the invariant mass distribution of the two leading jet separately for the electron and muon samples. This simple method allows to search for a signal peak over a smooth background. The fit (fig. 6 right) estimates $1582 \pm 275(\text{stat}) \pm 107(\text{syst})$ $WW + WZ \rightarrow l\nu jj$ events, corresponding to a statistical significance of 5.2σ (5.1σ expected) and measured $\sigma(WW + WZ) = 18.1 \pm 3.3(\text{stat}) \pm 2.5(\text{syst})$.

The ME approach uses 4.6 fb^{-1} and takes advantage of a multivariate technique to exploit all the information in the event [11]. Event probability densities are calculated under the signal and background hypotheses using a set of measured variables of each event (the 4-vectors of the lepton and the two jets). The probability is constructed by integrating over the parton-level differential cross-section, which includes the matrix element for the process, the parton distribution functions, and the detector resolutions. These probabilities are used to construct a discriminant variable for each event, referred to as the Event Probability Discriminant, or EPD. To quantify the $WW + WZ$ content in the data, a binned maximum likelihood fit to the data was performed (fig. 6 left) by fitting a linear combination of signal and background shapes of the event probability discriminant. CDF, using the ME method, measured $\sigma(WW + WZ) = 16.5^{+3.3}_{-3.0}(\text{stat} + \text{syst})$ pb, with a significance of 5.4σ . The results from the two approaches at CDF are in agreement with each other and with the Standard Model prediction.

7. – Conclusions

The Electroweak Physics program at the Tevatron is producing exciting results in the diboson sector. Both CDF and D0 have well-established final states with leptons and jets. These processes represent important tests of the Standard Model by measuring the production cross sections and setting limits on TGC. Moreover, dibosons represent an important milestone for the development of techniques used in low-mass and high-mass Higgs boson searches.

REFERENCES

- [1] ABAZOV V. M. *et al.*, *Phys. Rev. Lett.*, **103** (2009) 191801.
- [2] AALTONEN T. *et al.*, arXiv:/0912.4500v1.
- [3] <http://www-cdf.fnal.gov/physics/ewk/2009/wwtgc/index.html>.
- [4] ABAZOV V. M. *et al.*, *Phys. Rev. Lett.*, **101** (2008) 171803.
- [5] http://www-cdf.fnal.gov/physics/ewk/2009/ZZ1111/ZZWeb/cdf9910_ZZ_4leptons_public.pdf.
- [6] ABAZOV V. M. *et al.*, arXiv:/0907.4952.
- [7] AALTONEN T. *et al.*, *Phys. Rev. Lett.*, **103** (2009) 091803.
- [8] ABAZOV V. M. *et al.*, *Phys. Rev. Lett.*, **102** (2009) 161801.
- [9] AALTONEN T. *et al.*, *Phys. Rev. Lett.*, **104** (2010) 101801.
- [10] http://www-cdf.fnal.gov/physics/ewk/2010/WW_WZ/index.html.
- [11] http://www-cdf.fnal.gov/physics/new/hdg//Results_files/results/wwwz_oct09/.

W mass and width measurements at the Tevatron

A. MELNITCHOUK for the CDF and D0 COLLABORATIONS

University of Mississippi - Mississippi, 38677, USA

(ricevuto il 14 Settembre 2010; pubblicato online l'11 Gennaio 2011)

Summary. — Most recent results of W boson mass and width measurements performed by CDF and D0 are reported at the center-of-mass energy of 1.96 TeV. Integrated luminosity ranges from 0.2 fb^{-1} to 1.0 fb^{-1} depending on the analysis.

PACS 14.70.Fm – W bosons.

PACS 13.38.Be – Decays of W bosons.

1. – Introduction

Measurement of the W boson mass (M_W) provides us with a uniquely powerful key to uncovering the origin of the electroweak symmetry breaking and learning about new physics. A precision measurement of M_W is one of the highest priorities for the Tevatron experiments. M_W measurement combined with precise measurement of the top quark mass (M_{top}) constrains the mass of the Higgs boson.

On the other hand, the width of the W boson (Γ_W) is expected to be insensitive to new physics. Therefore its precise measurement is very important for improving the experimental knowledge of the Standard Model. Currently CDF [1] and D0 [2] provide most precise direct measurements of both M_W [3, 4] and Γ_W [5, 6]. For these measurements CDF uses both electron and muon decay channels of the W , while D0 uses only electron channel.

2. – Identification of electrons and muons

Electrons are identified as an electromagnetic (EM) cluster reconstructed with a simple cone algorithm. To reduce the background of jets faking electrons, electron candidates are required to have a large fraction of their energy deposited in the EM section of the calorimeter and pass energy isolation and shower shape requirements. Electron candidates are classified as *tight* if a track is matched spatially to EM cluster and if the track transverse momentum is close to the transverse energy of the EM cluster. In CDF electrons are reconstructed both in the central calorimeter and plug calorimeter ($|\eta| < 2.8$) while electrons in D0 are reconstructed in the central and endcap calorimeters ($|\eta| < 1.05$).

and $1.5 < |\eta| < 3.2$). Here $\eta = -\ln \tan(\theta/2)$, and θ is the polar angle with respect to the proton direction. Both CDF and D0 require *tight* electrons in the central calorimeter ($|\eta| < 1.05$) for $W \rightarrow e\nu$ candidates. Electron energies are measured with the calorimeter, while electron direction is measured with tracking detectors, using tracks that are matched to electron cluster in the calorimeter.

Muons are identified by a track in the muon system matched to a track in the central tracking system. Measurements include the muons reconstructed in the central muon extension sub-detector which extends the coverage from $|\eta| < 0.6$ to $|\eta| < 1$.

3. – W mass

M_W is measured using three transverse kinematic variables: the transverse mass $m_T = \sqrt{2p_T^{e,\mu} p_T^\nu (1 - \cos \Delta\phi)}$, the lepton ($p_T^{e,\mu}$) and neutrino (p_T^ν) transverse momentum distributions, where $\Delta\phi$ is the opening angle between the electron(muon) and neutrino momenta in the plane transverse to the beam. Neutrino transverse momentum (p_T^ν) is inferred from the imbalance of transverse energy. We also call it missing E_T (MET).

A sophisticated parametrized fast Monte Carlo simulation is used for modeling these variables as a function of M_W . Fast simulation includes models of electron, recoil system, and backgrounds. Electron efficiencies, resolution and energy scale parameterizations are tuned to $Z \rightarrow ee$ data. Recoil system represents energy deposited in the calorimeter from all sources except the electron(s). Recoil system consists of three major components: hard recoil (particles that collectively balance the p_T of the W or Z boson), underlying event, and additional interactions. Contribution from the third component depends on the instantaneous luminosity. Hard recoil is modeled using full detector simulation, while the other two components are described by real data events. Full recoil model is tuned to $Z \rightarrow ee$ data, using imbalance between Z boson momentum measured with electrons and with recoil system. Sources of backgrounds to $W \rightarrow e\nu$ events include $W \rightarrow \tau\nu \rightarrow e\nu\nu$, QCD, and $Z \rightarrow ee$ processes.

M_W is extracted from a binned maximum-likelihood fit between the data and simulation. Γ_W is measured with m_T variable using the same analysis framework as M_W . Figure 1 shows a comparison between data and fast simulation. It also shows final M_W results from D0 and CDF along with other M_W measurements and combinations. D0 result agrees with the world average and the individual measurements and is more precise than any other M_W measurement from a single measurement. Figure 2 shows comparison between data and fast simulation for CDF M_W measurement.

Dominant uncertainties in M_W measurements come from lepton energy scale measurements. At first-order fractional error on the lepton energy scale translates to fractional error on the W mass [8].

D0 determines electron energy scale using high- p_T electrons from $Z \rightarrow ee$ decays. Precision of such calibration is limited mostly by the size of the $Z \rightarrow ee$ sample.

CDF relies on tracking detector for both electron and muon energy scale calibration. First tracking detector is calibrated using $J/\psi \rightarrow \mu\mu$ events. J/ψ invariant mass is measured as a function of muon momentum. Figure 3 shows the correction needed to make measured J/ψ mass to be at its PDG value (overall offset) and independent of muon momentum (slope). This correction was implemented in the simulation by adjusting the energy-loss model. Then tracker calibration is transported to the calorimeter using $W \rightarrow e\nu$ electrons near the peak of the E/p distribution, shown also in fig. 3. Tables I and II show uncertainties for M_W measurements by D0 and CDF, respectively.

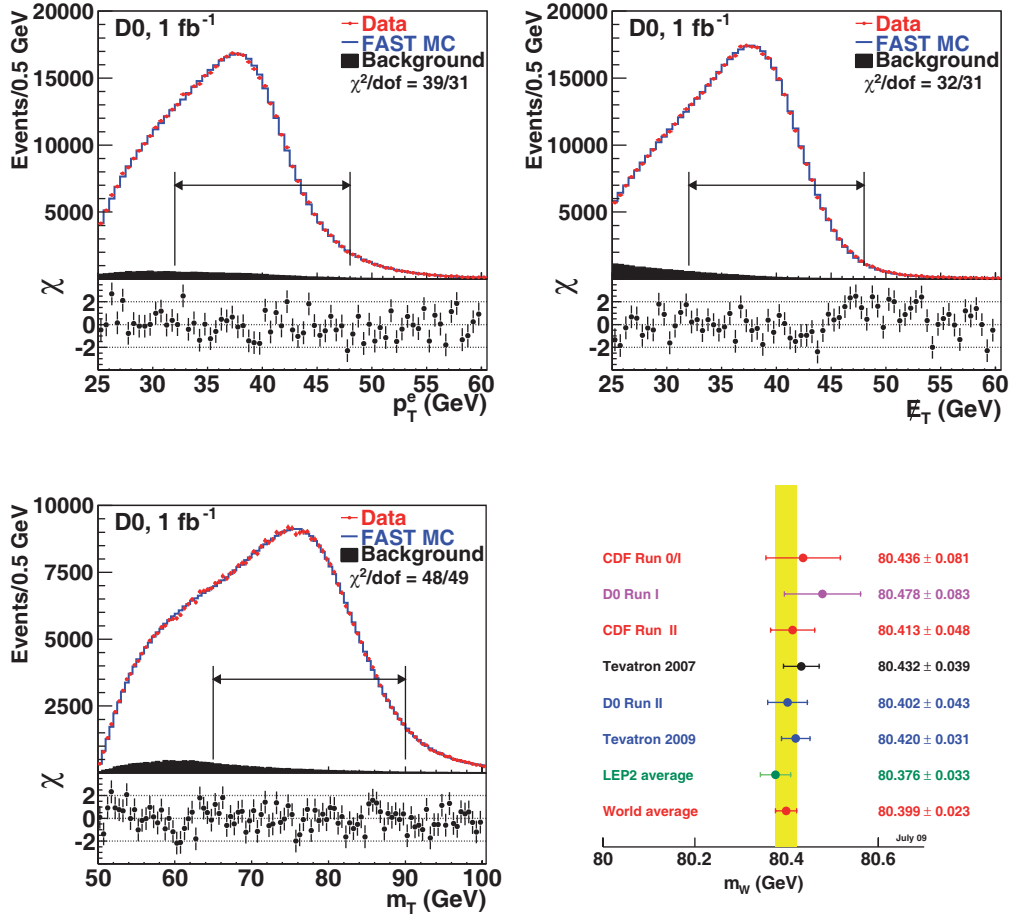


Fig. 1. – Top left, top right, and bottom left show electron p_T , m_T , and MET distributions in $W \rightarrow e\nu$ data and fast simulation (FASTMC). Added background is shown as well. Signed χ distributions are shown in the bottom part of each plot. Signed χ is defined as $\chi_i = [N_i - (\text{FASTMC}_i)]/\sigma_i$ for each point in the distribution, N_i is the data yield in bin i and σ_i is the statistical uncertainty in bin i . Bottom right: summary of the measurements of the W boson mass and their average. The result from the Tevatron corresponds to the values which include corrections to the same W boson width and PDFs. The LEP II results are from [7]. An estimate of the world average of the Tevatron and LEP results is made assuming no correlations between the Tevatron and LEP uncertainties.

4. – W width

Although M_W and Γ_W measurements are performed with the same method and both rely on m_T distribution, they are mostly sensitive to different features of the latter. M_W is mostly sensitive to the position of the Jacobian peak. Γ_W is mostly sensitive to the tail of the m_T distribution. At first order Γ_W is proportional to the fraction of events in the tail. Fit for Γ_W is performed in the high m_T tail region (90–200 GeV for both CDF and D0). This region is sensitive to the Breit-Wigner lineshape and less sensitive to the detector resolution.

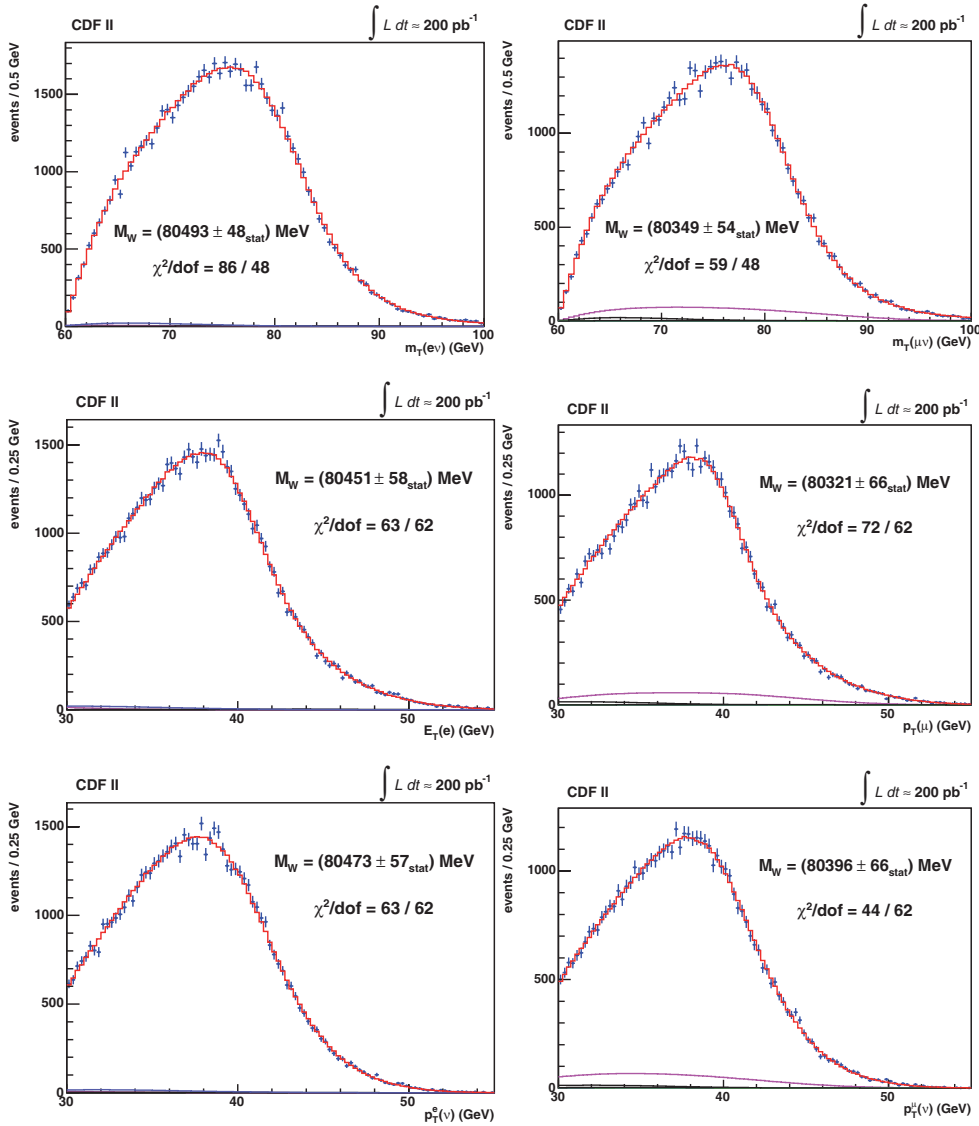


Fig. 2. – (Colour on-line) Distributions of M_W observables in CDF measurement. Blue—data. Red—fast simulation. Fit results and statistical errors are indicated. Left column: electron channel. Right column: muon channel. Top row: m_T . Middle row: charged lepton p_T . Bottom row: neutrino p_T .

Figure 4 shows m_T distributions from CDF and D0 as well as final results compared with other measurements and combinations. D0 result is $\Gamma_W = 2.028 \pm 0.039(\text{stat}) \pm 0.061(\text{syst}) = 2.028 \pm 0.072 \text{ GeV}$. CDF result is $\Gamma_W = 2.032 \pm 0.045(\text{stat}) \pm 0.057(\text{syst}) = 2.032 \pm 0.073 \text{ GeV}$. Combined Tevatron average is $\Gamma_W = 2.046 \pm 0.049 \text{ GeV}$ [9]. Tables III and IV give the detailed breakdown of uncertainties for Γ_W measurements at D0 and CDF.

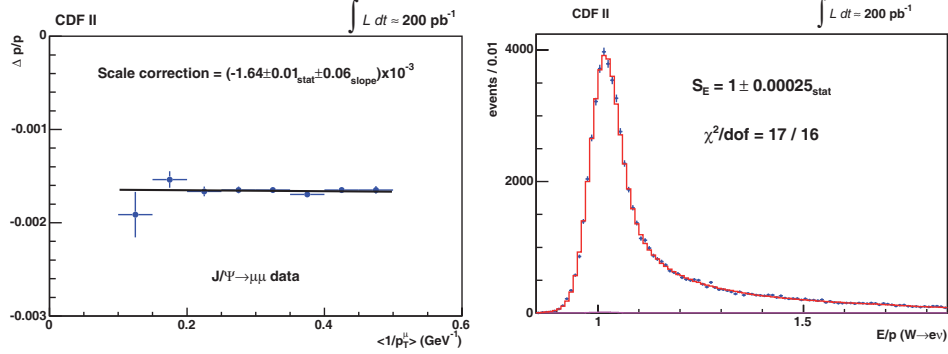


Fig. 3. – Left: fractional muon momentum correction as a function of inverse momentum. Right: ratio of electron energy measured in the calorimeter to electron momentum measured by the tracking system in $W \rightarrow e\nu$ events.

TABLE I. – Uncertainties of $D0 M_W$ measurement (MeV).

Source	m_T	p_T^e	\cancel{E}_T
Experimental			
Electron energy calibration	34	34	34
Electron resolution model	2	2	3
Electron energy offset	4	6	7
Electron energy loss model	4	4	4
Recoil model	6	12	20
Electron efficiencies	5	6	5
Backgrounds	2	5	4
Experimental subtotal	35	37	41
Production model			
PDF	10	11	11
QED	7	7	9
Boson p_T	2	5	2
Production model subtotal	12	14	14
Statistical	23	27	23
Total	37	40	43

TABLE II. – *Uncertainties of CDF M_W measurement (MeV).*

Source	m_T	p_T^e	\cancel{E}_T
	e, μ, common	e, μ, common	e, μ, common
Lepton scale	30,17,17	30,17,17	30,17,17
Lepton resolution	9,3,0	9,3,0	9,5,0
Recoil scale	9,9,9	17,17,17	15,15,15
Recoil resolution	7,7,7	3,3,3	30,30,30
$U_{ }$ efficiency	3,1,0	5,6,0	16,30,0
Lepton removal	8,5,5	0,0,0	16,10,10
Backgrounds	8,9,0	9,19,0	7,11,0
$p_T(W)$	3,3,3	9,9,9	5,5,5
PDF	11,11,11	20,20,20	13,13,13
QED	11,12,11	13,13,13	9,10,9
Total systematic	39,27,26	45,40,35	54,46,42
Statistical	48,54,0	56,68,0	57,66,0
Total	62,60,26	73,77,35	79,80,42

TABLE III. – *Uncertainties of D0 Γ_W measurement (MeV).*

Source	$\Delta\Gamma_W$ (MeV)
Electron energy scale	33
Electron resolution model	10
Recoil model	41
Electron efficiencies	19
Backgrounds	6
PDF	20
Electroweak radiative corrections	7
Boson p_T	1
M_W	5
Total systematic	61
Statistical	39
Total	72

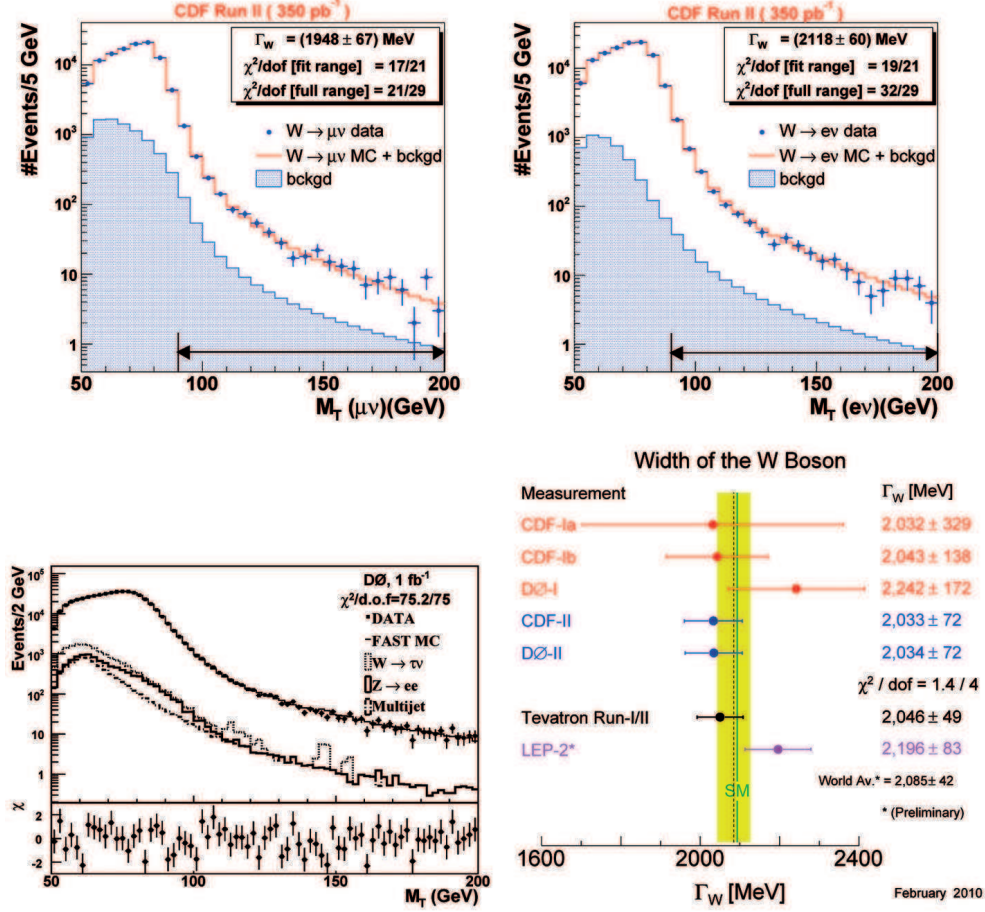


Fig. 4. – Top left, top right, and bottom left: M_T distributions for data and fast MC simulation with background added. Two top plots: CDF. Bottom left plot from D0 shows also signed χ values for each bin (bottom part of the plot). Signed χ is defined in the caption of fig. 1. D0 used fitted Γ_W value for the fast MC prediction rather than the PDG value. The distribution of the fast MC simulation with background added is normalized to the number of data events in the region $50 < M_T < 100 \text{ GeV}$ (D0) and $50 < M_T < 90 \text{ GeV}$ (CDF).

TABLE IV. – *Uncertainties of CDF Γ_W measurement (MeV).*

Source	e	μ	common
Lepton scale	21	17	12
Lepton resolution	31	26	0
Simulation	13	0	0
Recoil	54	49	0
Lepton ID	10	7	0

TABLE IV. – *Continued.*

Source	e	μ	common
Backgrounds	32	33	0
$p_T(W)$	7	7	7
PDF	20	20	20
QED	10	6	6
M_W	9	9	9
Total systematic	79	71	27
Statistical	60	67	0
Total	99	98	27

REFERENCES

- [1] ACOSTA D. *et al.* (CDF COLLABORATION), *Phys. Rev. D*, **71** (2005) 032001.
- [2] ABAZOV V. M. *et al.* (D0 COLLABORATION), *Nucl. Instrum. Methods Phys. Res. A*, **565** (2006) 463.
- [3] ABAZOV V. M. *et al.* (D0 COLLABORATION), *Phys. Rev. Lett.*, **103** (2009) 141801.
- [4] AALTONEN T. *et al.* (CDF COLLABORATION), *Phys. Rev. Lett.*, **99** (2007) 151801; *Phys. Rev. D*, **77** (2008) 112001.
- [5] ABAZOV V. M. *et al.* (D0 COLLABORATION), *Phys. Rev. Lett.*, **103** (2009) 231802.
- [6] AALTONEN T. *et al.* (CDF COLLABORATION), *Phys. Rev. Lett.*, **100** (2008) 071801.
- [7] THE LEP ELECTROWEAK WORKING GROUP, CERN-PH-EP/2008-20, arXiv:0811.4682 (hep-ex).
- [8] KOTWAL ASHUTOSH V. and STARK JAN, *Annu. Rev. Nucl. Part. Sci.*, **58** (2008) 147.
- [9] TEVATRON ELECTROWEAK WORKING GROUP, FERMILAB-TM-2460-E.

Single and double top quark production at the Tevatron

D. WICKE(*) for the CDF and D0 COLLABORATIONS

Johannes Gutenberg Universität Mainz - Staudingerweg 7, 55099 Mainz, Germany

(ricevuto il 14 Settembre 2010; pubblicato online il 10 Gennaio 2011)

Summary. — The CDF and D0 experiments have measured single and double top quark production in $p\bar{p}$ collisions at the Tevatron at a centre-of-mass energy of 1.96 TeV. The applied methods are used to constrain properties of the top quark and to search for new physics. Several methods of signal-to-background separation and of the estimation of the background contributions are discussed. Experimental results using an integrated luminosity up to 5.3fb^{-1} are presented.

PACS 14.65.Ha – Top quarks.

PACS 14.70.Pw – Other gauge bosons.

1. – Introduction

Since the top quark was discovered by CDF and D0 at the Tevatron in 1995 [1,2] the number of top events available for experimental studies has been increased by more than an order of magnitude. Tevatron delivered a luminosity of more than 7fb^{-1} and up to 5.3fb^{-1} have been used for top quark analyses in CDF and D0.

In the Standard Model (SM) top quarks can be produced through the strong or through the weak interaction. The strong interaction creates top quarks in pairs. The process is expected to be dominated by quark anti-quark annihilation with a contribution of only 15% from the gluon fusion processes. The cross-section for this process is around 7 pb. In the weak interaction top quarks can be produced singly. At the Tevatron the two mechanisms known as s -channel and the t -channel contribute to single top production with the ratio 1 : 2 to a total of about 3.5 pb.

Immediately after production top quarks decay to a W boson and a b quark with a branching fraction of nearly 100%. The decay channels of top quark pairs are thus fully specified through the W boson decay modes. For the top pair production dileptonic decays including electrons and muons allow for the highest purity, but suffer from the low branching fraction of about 5%. The semileptonic decays are considered as the golden channel due to a sizable branching fraction combined with the possibility to reach a

(*) Now at Bergische Universität, Gaußstr. 20, 42097 Wuppertal, Germany.

reasonable signal-to-background ratio. The all-hadronic decay channel has the largest cross-section, but due to the absence of leptons it suffers from a huge background due to multijet production. Channels including τ leptons are kept separately due to the difficulties in their identification. For single top production the events are categorised by production and decay channel. So far only leptonic decays were studied.

In the following first some new results on the top quark pair production cross-section are described, followed by a selection of related and derived results. Then the observation of single top production and some related results are discussed. A discussion of measurements of the top quark mass and further top quark properties can be found in [3].

2. – Top pair production cross-section

The total cross-section of top pair production has been computed in perturbation theory using various approximations [4-8]. For a top quark pole mass of 172.5 GeV Moch and Uwer [7] find $\sigma_{t\bar{t}} = 7.46_{-0.67}^{+0.48}$ pb, based on the CTEQ6.6 [9] PDF. Experimentally it is important to measure this value in various decay channels. In addition some measurements are done requiring identified b jets while others avoid b jet identification and rely on topological selections. Most analyses use sideband data to evaluate the normalisation of the important background contributions. In the lepton plus jets channel the precision is already dominated by systematic uncertainties. In this channel production of W -bosons with additional jets yields the dominating background. Due to the difficulties in computing absolute cross-sections for this process at high accuracy it is important to take the corresponding background estimate from data.

A sizable contribution of the systematic uncertainties of these measurements also stems from the luminosity determination. To overcome this limitation CDF has measured the ratio of top quark pair production to the Z boson production cross-sections [10, 11]. In 4.6 and 4.3 fb⁻¹ of data CDF finds $\sigma_{Z \rightarrow \ell\ell}/\sigma_{t\bar{t}} = 35.7$ and $\sigma_{Z \rightarrow \ell\ell}/\sigma_{t\bar{t}} = 33.0$ for the analysis using b jet identification and the topological analysis, respectively. In the analysis using identified b jets, the background is normalised from data without identification requirement. In the topological analysis this normalisation is obtained from fits to the topological likelihood discriminant. The cross-section ratios are converted to top quark pair production cross-sections using the theoretical prediction for Z boson production. The theoretical uncertainty induced by this step is much smaller than the luminosity uncertainties and thus yield results with an uncertainty comparable to the uncertainty on the prediction for top quark pair production:

$$(1) \quad \begin{aligned} \sigma_{t\bar{t}} &= 7.14 \pm 0.35_{(\text{stat})} \pm 0.58_{(\text{syst})} \pm 0.14_{(\text{theory})} \text{ pb} \quad \text{using } b \text{ jet identification,} \\ \sigma_{t\bar{t}} &= 7.63 \pm 0.37_{(\text{stat})} \pm 0.35_{(\text{syst})} \pm 0.15_{(\text{theory})} \text{ pb} \quad \text{using topological selection.} \end{aligned}$$

D0 has recently published an analysis of the full hadronic channel. The analysis requires 6 jets two of which need to be identified as b jets. In this channel the background is dominated by multijet production from gluons and quarks other than the top quark. It is modeled from data with 4 and 5 jets by adding jets taken from 6-jet events. Only jets with lowest (and second lowest) p_T in the event are taken from 6-jet event. They must remain the lowest (or second lowest) jet in the newly constructed event. This method of event constructed has been validated by adding one jet to 4-jet events and compare them to normal 5-jet events.

The final cross-section is obtained by fitting a likelihood discriminant as observed in data to the prediction for top quark pairs from simulation and the background model

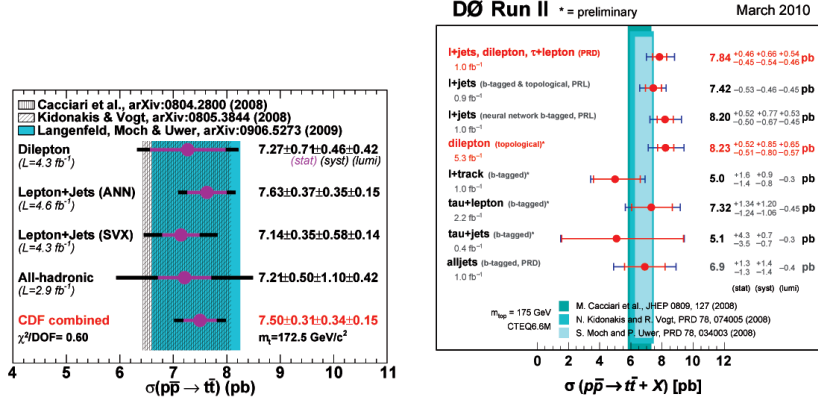


Fig. 1. – Top quark cross-section measured in various channels by CDF (left) and D0 (right).

described above. In 1.0 fb^{-1} D0 finds [12]

$$(2) \quad \sigma_{t\bar{t}} = 6.9 \pm 1.3(\text{stat}) \pm 1.4(\text{syst}) \pm 0.4(\text{lumi}) \text{ pb}.$$

Figure 1 summarises the cross-sections for top quark pair production as measured by CDF and D0 in various channels including the D0 dilepton result that was updated to 5.3 fb^{-1} since the conference [13]. All measurements agree well with the theory predictions shown as vertical bands.

2.1. Top quark mass from cross-section. – The theoretical predictions and (through the selection efficiency) also the experimental results depend on the assumed top quark mass. This can be used to determine the top quark mass in the well-defined pole mass scheme. Comparing the experimental results from three channels (ℓ +jet, the dilepton and the τ +other lepton) to the prediction from Moch and Uwer [7] D0 obtains

$$(3) \quad m_t^{\text{pole}} = 169.1^{+5.9}_{-5.2} \text{ GeV}.$$

This results has larger experimental uncertainties but is consistent with direct mass determinations for which the mass scheme, however, is not well defined.

2.2. Search for resonant top quark pair production. – In the SM no resonant top quark production is expected. However, unknown heavy resonances decaying to top pairs may add a resonant part to the SM production mechanism. Such resonant production occurs in several models of new physics: *e.g.*, for massive Z -like bosons in extended gauge theories [14], for Kaluza-Klein states of the gluon or Z boson [15, 16], for axigluons [17], in Topcolor [18, 19]. D0 investigated the invariant mass distribution of top pairs in up to 3.6 fb^{-1} of ℓ +jets events [20–22]. Signal simulation is created for various resonance masses between 350 and 1000 GeV. The width of the resonances was chosen to be 1.2% of their mass, which is much smaller than the detector resolution. The top pair invariant mass, $M_{t\bar{t}}$, is reconstructed directly from the reconstructed physics objects. A constrained kinematic fit is not applied. Instead the momentum of the neutrino is reconstructed from the transverse missing energy, \cancel{E}_T , which is identified with the transverse momentum of

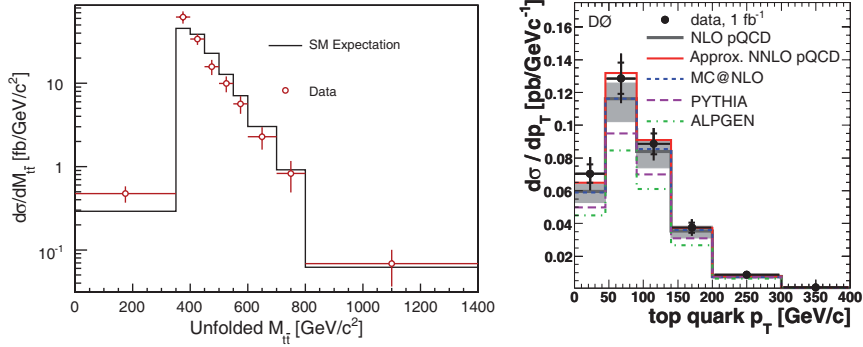


Fig. 2. – Differential cross-section of top quark pair production. Left as a function of the invariant top quark pair mass measured by CDF [24] and right as a function of the top quark transverse momentum by D0 [25].

the neutrino. The z -component is obtained by solving $M_W^2 = (p_\ell + p_\nu)^2$, where p_ℓ and p_ν are the four-momenta of the lepton and the neutrino, respectively.

As the data agrees with the SM expectations, limits on the possible contribution of resonant production $\sigma_X \mathcal{B}(X \rightarrow t\bar{t})$ are set. The benchmark model of Topcolor assisted Technicolor can be excluded for Z' masses of $M_{Z'} < 820 \text{ GeV}$. A CDF study of 2.8 fb^{-1} in the all hadronic channel excludes $M_{Z'} < 805 \text{ GeV}$ in this model [23].

2.3. Unfolded differential cross-sections. – Besides the total cross-section in different channels, differential cross-sections can be used to validate our understanding of top quark pair production.

CDF has recently published a measurement of the unfolded differential cross-section with respect to the invariant top quark pair mass, $d\sigma_{t\bar{t}}/dM_{t\bar{t}}$ [24]. Lepton plus four or more jet events are selected with at least one identified b jet using 2.7 fb^{-1} of CDF data. The invariant mass $M_{t\bar{t}}$ is computed from the four leading jets, the lepton and the missing transverse energy. The neutrino z momentum is set to zero. The expected background is subtracted from the observed distribution, then distortions are unfolded using the singular value decomposition of the response matrix obtained from simulations. The final result is shown in fig. 2 (left). The consistency with the SM expectation is tested using Anderson-Darling statistics. The observed result has a probability of 0.28 to occur if the SM is correct, showing good agreement with the SM.

D0 has determined the unfolded differential cross-section with respect to the top quark transverse momentum, $d\sigma_{t\bar{t}}/dp_T^t$ using 1.0 fb^{-1} [25]. In lepton plus jet events including at least one identified b -jet the top quark transverse momentum is reconstructed using a kinematic fit. The fit utilises the measured momenta of the four leading jets, the charged lepton and the missing transverse energy to determine the momenta of the top quark decay products (four quarks, a charged lepton and a neutrino). Constraints on the W -boson mass and on the equality of the top and anti-top quark masses are applied. The expected background contributions are subtracted from the measured distribution. Then regularised unfolding is used to determine the final $d\sigma_{t\bar{t}}/dp_T^t$ shown in fig. 2 (right) [25]. The result is compared to prediction of perturbative QCD (in approximately NNLO) and various event generators. Perturbative QCD and MC@NLO show the best agreement, but Pythia and Alpgen reproduce the observed shape at high p_T .

3. – Single top quark production

The cross-section for single top quark production is only half that of top quark pair production. The same backgrounds as in top quark pair analyses contribute and top quark pair production itself becomes a background. Moreover, in single top quark events have a signature containing fewer jets than for top quark pairs. The signature selection requires an isolated lepton, missing transverse energy and two to four jets, at least one of which must be identified as b -jet. After this selection the signal-to-background ratio is at best 1:10. Multivariate techniques are required to further separate single top quark events from the backgrounds.

Both experiments employ multiple such methods, including boosted decision trees, various neural network methods, matrix element and likelihood techniques. The different multivariate methods are sensitive to different single top quark events. Thus a combination of the different analyses improves the significance of the result. The 5σ observations that were reported in 2009 at this conference have been published [26, 27] and combined cross-section [28] of

$$(4) \quad \sigma_t = 2.76^{+0.58}_{-0.47} \text{ pb}$$

is in good agreement with the SM expectations [29, 30].

In addition to the results obtained in the channels involving electrons or muons (marked as “Lepton+jets”), fig. 3 contains two more recent results. One by CDF [31] with 2.1 fb^{-1} omits the explicit requirement for an isolated electron or muon. This picks up events failing the lepton requirements and events with taus in the final state. No explicit tau reconstruction was done here. The second additional analysis done by D0 [32] uses boosted decision trees to explicitly reconstruct hadronic tau decays. This reconstruction is trained individually for three tau decay modes that are classified as $\tau \rightarrow \pi^\pm + \nu_\tau$, $\tau \rightarrow \rho^\pm + \nu_\tau$ and $\tau \rightarrow 3\pi^\pm + \nu_\tau (+\pi^0)$. Signal efficiencies between 59% and 76% are achieved at a background rejection rate of 98%. In 4.8 fb^{-1} D0 determines the single top cross-section in the τ +jets channel as $\sigma_t = 3.4^{+2.0}_{-1.8} \text{ pb}$.

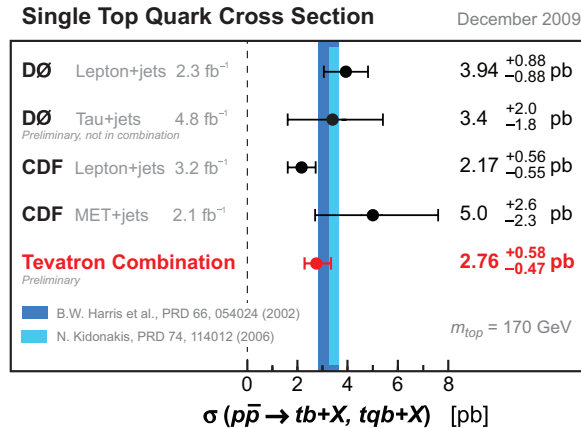


Fig. 3. – Single top quark cross-section measured by CDF and D0.

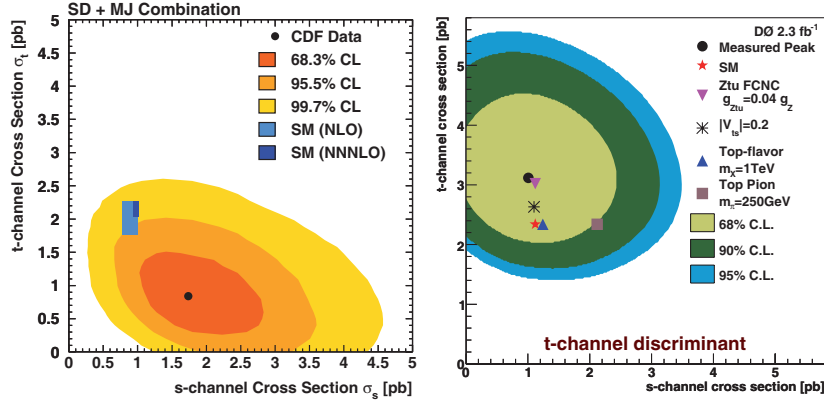


Fig. 4. – Simultaneous fit of s - and t -channel contribution to the CDF (left) and D0 (right) data [34, 35]. Results are compared to the SM expectations and some selected alternative models [36].

3.1. Determination of V_{tb} . – The single top quark production in the SM is directly proportional to the CKM-matrix element $|V_{tb}|^2$. Thus the results presented above can be easily interpreted as a measurement of $|V_{tb}|$. For the combined result CDF and D0 obtain $|V_{tb}| = 0.88 \pm 0.07$. Constraining the value to the allowed range between 0 and 1 yields a lower limit of $|V_{tb}| > 0.77$ at 95% confidence level [28]. This limit is valid independent of the number of generations, it however assumes $|V_{tb}|^2 \gg |V_{td}|^2 + |V_{ts}|^2$. This assumption is supported by measurements in top quark pairs, see *e.g.* [33].

3.2. Separation of s - and t -channel. – As explained in the introduction, single top quark production at the Tevatron actually consists of two separate processes, the s - and the t -channel. The results presented so far consider the sum of the two channels. CDF and D0 have also determined the two contributions separately [34, 35]. The two-dimensional results are shown in fig. 4. The CDF results show a deviation to the SM expectation of a little more than two standard deviations, while D0 result agrees very well with the SM. Figure 4 (right) shows the D0 results for a discriminant that was optimised to determine the t -channel cross-section. For this individual channel D0 finds in 2.3 fb^{-1}

$$(5) \quad \sigma_t^{t\text{-channel}} = 3.14_{+0.80}^{+0.94} \text{ pb}$$

with a significance of 4.8 standard deviation.

3.3. Polarisation of the top quark. – In the presence of non-SM contributions to the top quark production [36], the polarisation of the top quarks may be modified with respect to the SM expectations. CDF considered a contribution of a production through right-handed couplings, keeping the SM left-handed decay. Such a process could be implemented through a heavy right-handed W' -boson. CDF trained their likelihood discriminant separately for the the right-handed exotic and left-handed SM case. With this the corresponding two cross-sections σ_R and σ_L are measured and combined to a polarisation $\mathcal{P} = (\sigma_R - \sigma_L)/(\sigma_R + \sigma_L)$. In 3.2 fb^{-1} CDF obtains $\mathcal{P} = -1.0_{-0}^{+1.5}$ [37] in agreement with the pure SM production.

4. – Conclusions

The increasing Tevatron luminosity allows to measure the top quark cross-section and properties with improved precision. The integrated top quark pair production cross-section is measured in various decay channels and used to obtain the top quark pole mass. Measurements of the differential cross-section as a function of p_T or $M_{t\bar{t}}$ complement the verification of our understanding of top quark pair production and are used to search for deviations from the SM. Since the observation of single top quark production at the previous La Thuile conference, new selection channels have been added to the studies and s - and t -channel contributions have been measured separately. In addition polarisation studies have been studied in these events.

This paper only describes a small fraction of all measurements. The Tevatron experiments measure the full spectrum of top quark properties to check the production, the decay and inherent properties of the top quark against the SM expectation. So far no evidence for new physics has been found.

REFERENCES

- [1] ABE F. *et al.* (CDF COLLABORATION), *Phys. Rev. Lett.*, **74** (1995) 2626.
- [2] ABACHI S. *et al.* (DØ COLLABORATION), *Phys. Rev. Lett.*, **74** (1995) 2632.
- [3] COMPOSTELLA G., these proceedings.
- [4] KIDONAKIS N. and VOGT R., *Phys. Rev. D*, **68** (2003) 114014.
- [5] CACCIARI M. *et al.*, *JHEP*, **09** (2008) 127.
- [6] MOCH S. and UWER P., *Phys. Rev. D*, **78** (2008) 034003.
- [7] MOCH S. and UWER P., *Nucl. Phys. Proc. Suppl.*, **183** (2008) 75.
- [8] KIDONAKIS N. and VOGT R., *Phys. Rev. D*, **78** (2008) 074005.
- [9] PUMPLIN J. *et al.*, *JHEP*, **07** (2002) 012.
- [10] CDF COLLABORATION, *Measurement of the ratio of the top pair cross section with the z boson cross section*, CDF Note 9616 (Nov. 2008).
- [11] CDF COLLABORATION, *Measurement of the $t\bar{t}$ Cross Section in the Lepton Plus Jets Channel Using Neural Networks in 2.8 fb⁻¹ of CDF data. Including: Ratio of $t\bar{t}$ to Z Cross Sections*, CDF Note 9474 (Dec. 2008).
- [12] ABAZOV V. M. *et al.* (D0 COLLABORATION), *Phys. Rev. D*, **82** (2010) 032002, [ArXiv:0911.4286 \[hep-ex\]](#).
- [13] ABAZOV V. M. *et al.* (D0 COLLABORATION), *Measurement of the $t\bar{t}$ production cross section in dilepton final states at D0 using 5.3 fb⁻¹ of data*, D0 Note 6038 Conf (2010).
- [14] LEIKE A., *Phys. Rep.*, **317** (1999) 143.
- [15] LILLIE B., RANDALL L. and WANG L.-T., *JHEP*, **09** (2007) 074.
- [16] RIZZO T. G., *Phys. Rev. D*, **61** (2000) 055005.
- [17] SEHGAL L. M. and WANNINGER M., *Phys. Lett. B*, **200** (1988) 211.
- [18] HILL C. T. and PARKE S. J., *Phys. Rev. D*, **49** (1994) 4454.
- [19] HARRIS R. M., HILL C. T. and PARKE S. J., *Cross section for topcolor Z'(t) decaying to $t\bar{t}$* , [ArXiv:hep-ph/9911288](#) (1999).
- [20] ABAZOV V. M. *et al.* (D0 COLLABORATION), *Phys. Lett. B*, **668** (2008) 98.
- [21] ABAZOV V. M. *et al.* (D0 COLLABORATION), *Search for $t\bar{t}$ resonances in the lepton+jets final state in $p\bar{p}$ collisions at $\sqrt{s} = 1.96$ TeV*, D0 Note 5600 conf (2008).
- [22] ABAZOV V. M. *et al.* (D0 COLLABORATION), *Search for $t\bar{t}$ resonances in the lepton+jets final state in $p\bar{p}$ collisions at $\sqrt{s} = 1.96$ TeV*, D0 Note 5882 conf (2009).
- [23] CDF COLLABORATION, *Search for resonant $t\bar{t}$ production in $p\bar{p}$ collision at $\sqrt{s} = 1.96$ TeV*, CDF Note 9844 (July 2009).
- [24] AALTONEN T. *et al.* (CDF COLLABORATION), *Phys. Rev. Lett.*, **102** (2009) 222003.

- [25] ABAZOV V. M. *et al.* (D0 COLLABORATION), *Phys. Lett. B*, **693** (2010) 515, [ArXiv:1001.1900](#).
- [26] ABAZOV V. M. *et al.* (D0 COLLABORATION), *Phys. Rev. Lett.*, **103** (2009) 092001.
- [27] AALTONEN T. *et al.* (CDF COLLABORATION), *Phys. Rev. Lett.*, **103** (2009) 092002.
- [28] CDF and D0 COLLABORATION, TEVATRON ELECTROWEAK WORKING GROUP, *Combination of CDF and D0 Measurements of the Single Top Production Cross Section*, [ArXiv:0908.2171](#) (2009).
- [29] HARRIS B. W., LAENEN E., PHAF L., SULLIVAN Z. and WEINZIERL S., *Phys. Rev. D*, **66** (2002) 054024.
- [30] KIDONAKIS N., *Phys. Rev. D*, **74** (2006) 114012.
- [31] AALTONEN T. *et al.* (THE CDF COLLABORATION), *Search for single top quark production in $p\bar{p}$ collisions at $\sqrt{s} = 1.96$ TeV in the missing transverse energy plus jets topology*, [ArXiv:1001.4577](#) (2010).
- [32] ABAZOV V. M. *et al.* (D0 COLLABORATION), *Search for single top quarks in the tau+jets channel using 4.8fb^{-1} of $p\bar{p}$ collision data*, [ArXiv:0912.1066](#) (2009).
- [33] ABAZOV V. M. *et al.* (D0 COLLABORATION), *Phys. Rev. Lett.*, **100** (2008) 192003.
- [34] ABAZOV V. M. *et al.* (D0 COLLABORATION), *Phys. Lett. B*, **682** (2010) 363.
- [35] AALTONEN T. *et al.* (CDF COLLABORATION), *Observation of single top quark production and measurement of $|V_{tb}|$ with CDF*, [ArXiv:1004.1181](#) (2010).
- [36] TAIT T. M. P. and YUAN C. P., *Phys. Rev. D*, **63** (2001) 014018.
- [37] CDF COLLABORATION, *Measurement of single top polarization with 3.2fb^{-1}* , CDF Note 9920 (Sep. 2009).

Top quark properties at the Tevatron

G. COMPOSTELLA(*) on behalf of the CDF and DØ COLLABORATIONS

INFN and Università di Padova - via Marzolo 8, 35131 Padova, Italy

(ricevuto il 14 Settembre 2010; pubblicato online l'11 Gennaio 2011)

Summary. — Precise determination of the top quark properties allows for stringent tests of the Standard Model. In this paper we report the latest results from the CDF and DØ Collaborations on a data sample of $p\bar{p}$ collisions at 1.96 TeV collected at the Fermilab Tevatron up to an integrated luminosity of 4.8 fb^{-1} .

PACS 14.65.Ha – Top quarks.

1. – Introduction

In the Standard Model of Particle Physics, the top quark is the “up-type” quark of the third generation, weak isospin partner of the bottom quark, with charge $Q = +2/3$.

After the top quark discovery in 1995 at the Tevatron by both the CDF and DØ Collaborations [1, 2], many measurements have been performed to map its properties. Being the most massive fundamental particle known up to date, it is the dominant contributor to radiative corrections for many Standard Model processes. The top quark has also very large coupling to the not yet observed Higgs boson and may be related to the electroweak symmetry breaking mechanism, and thus sensitive to new physics, which could be constrained by measuring its production and decay properties. Thanks to the increasing quantity of data delivered by the Tevatron, amounting to more than 5 fb^{-1} to date, precision measurements on top quark physics can be performed, allowing to improve the understanding of the observed particle and its role within the Standard Model.

This paper reports the most recent results of measurements of top quark properties performed by both the CDF and DØ Collaborations, in particular in the areas of top intrinsic properties and decay, providing a short summary of a few of them.

In $p\bar{p}$ collisions at $\sqrt{s} = 1.96 \text{ TeV}$ top quarks are mainly produced in pairs through quark-antiquark annihilation (85%) or gluon fusion (15%). Since within the Standard Model the top quark decays almost exclusively to a W boson and a b quark, the top

(*) E-mail: compostella@pd.infn.it

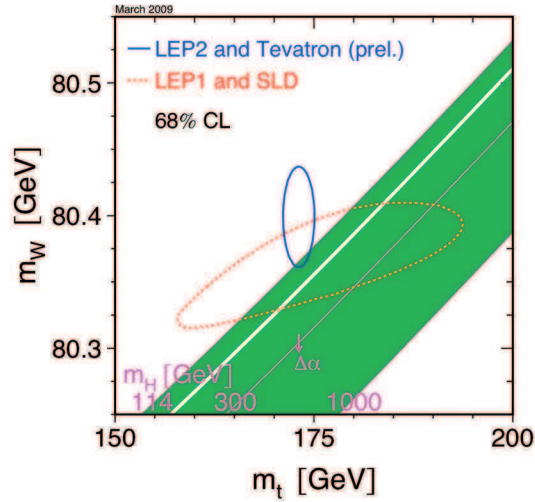


Fig. 1. – (Colour on-line) W boson mass *vs.* top quark mass plane. The green band is consistent with the Standard Model for a Higgs mass in the range $114 \text{ GeV} < m_H < 1 \text{ TeV}$.

pair production signatures can be classified with respect to the decay modes of the W boson. In 6% of all the $t\bar{t}$ decays, when both W 's decay into electrons or muons, we have the so-called dilepton channel; in 38% of the decays, when only one W decays into electrons or muons, the lepton plus jets channel. In the remaining 56% of the cases, when no electron or muon from the W decay are present in the event, we have the so-called all-hadronic channel.

The presence of a b -quark in its decay can also be exploited to identify the top quark: b -quarks give rise to jets containing long-lived b -hadrons, and those jets can be identified by looking for the presence of tracks in the detector compatible with a secondary decay vertex distinct from the primary interaction point. Such jets are called b -tagged, and the requirement of at least one b -tagged jet in the event is a powerful tool to increase the signal-to-background ratio in data.

2. – Top quark mass

The top quark mass m_{top} is a fundamental parameter of the Standard Model, and its precise knowledge is necessary to calculate physics observables involving top quark quantum loops to high precision. Additionally, the determination of m_{top} can also give valuable indirect information on the Higgs boson mass m_H . The dominant radiative corrections to the W boson mass m_W come from loops containing top and bottom quarks, which are proportional to m_{top}^2 , and from loops containing Higgs bosons, which are proportional to $\log(m_H)$. Thus for each value of m_H , a unique line in the m_{top} and m_W parameter space is defined within the Standard Model. By measuring precisely the W boson and top quark masses, we can limit the range of values for m_H allowed by the Standard Model, as shown in fig. 1.

The measurement of the top quark mass relies on the precise reconstruction of the energy of its decay products. This is a major experimental challenge: while electrons and muons energies can be calibrated using well-known $Z \rightarrow ee$ and $Z \rightarrow \mu\mu$ decays, dealing

with quarks energies is more complicated. Since quarks manifest themselves as jets in the detector, the energy measurement of the calorimeter in the jet cone must be calibrated to the energy of the particles coming from the hadronization of the original quark in the same cone. Calorimeter response is calibrated by balancing the transverse momentum in events with a photon and a jet, and propagating this calibration to the parton level using Monte Carlo derived corrections. Variations in calorimeter response and gain are determined using dijet events, in order to determine the relative jet energy scale and have a uniform response in the calorimeter at all momenta. This allows to determine the jet energy calibration with a systematically limited precision of about 2–3%.

The jet energy scale is one of the dominant contributions to the systematic error in top quark mass measurements, with a relative effect of 3–6%. In order to reduce this uncertainty, we can use the hadronic decays of W bosons coming from the top decay to calibrate *in situ* the jet energy scale by constraining the invariant mass of the non- b -tagged jets in the event to be equal to the W mass. This procedure provides an additional overall calibration factor for jet energies which is only statistically limited by the number of hadronic W decays in the sample, and allows the overall jet energy systematic on the top quark mass to scale directly with the luminosity.

Top mass measurements are currently performed following two basic classes of algorithms, that will be briefly described. In the template method a set of observables sensitive to m_{top} are reconstructed and used as estimators of the top quark mass. Their distributions for a range of top quark masses are derived from Monte Carlo simulations and the shape of these distributions determine the so-called templates. The behaviours of the chosen observables in data are compared to template expectations for different values of m_{top} and fractions of top signal in the sample, performing a likelihood maximization. Since the shape of a template depends both on the top quark mass and on the jet energy scale, which are free parameters in the likelihood, this technique can provide a determination of both of them. The CDF Collaboration has recently used this method to measure the top quark mass in a data sample of dilepton and lepton plus jets events corresponding to an integrated luminosity of 4.8 fb^{-1} . Due to the presence of neutrinos in the final state, the kinematics of dilepton events is underconstrained, so that estimators of m_{top} must be calculated integrating over some unknown quantities. This analysis uses the neutrino weighting algorithm: the unknown pseudorapidities of the two neutrinos are integrated over, and different solutions for a given top quark mass are weighted by the agreement with the missing transverse energy in the detector. The most probable value of the top quark mass is used as estimator for the true value of m_{top} . On the contrary, in lepton plus jets channel, the kinematic of the event is overconstrained. By using a kinematic fitter it is possible to select the single best assignment of jets to quarks in the hypothesis of a top pair decay, and determine the top quark mass in the selected configuration. The results of the first and second best assignment are used as estimators of the true value of the top quark mass. By combining the two template based measurements into the same likelihood, the result $m_{\text{top}} = 171.9 \pm 1.1 \text{ (stat + JES)} \pm 0.9 \text{ (syst)} \text{ GeV}/c^2$ is obtained [3].

Another algorithm used for the top quark mass measurement is the so-called Matrix Element method, which tries to extract the most possible information from every event by constructing a per-event likelihood as a function of the top quark mass. The likelihood uses leading-order theoretical predictions for the production and decay of the $t\bar{t}$ pairs, considering the matrix element of the process. In order to turn parton level predictions coming from the matrix element calculation into indications on the observed physics, it is necessary to take into account transfer functions: those functions depend on the jet

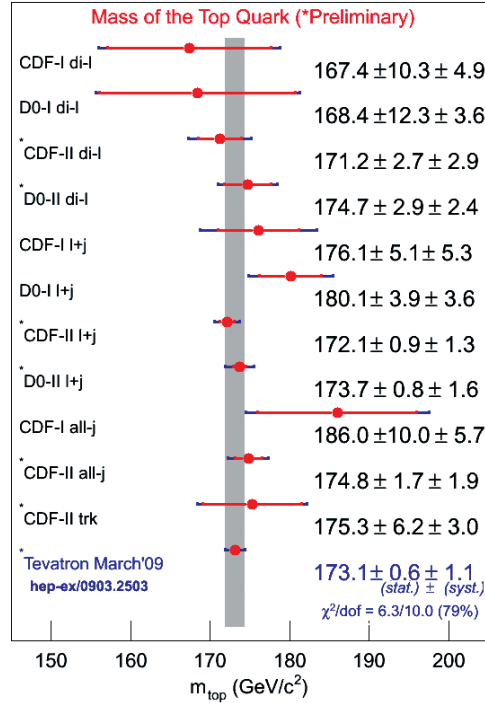


Fig. 2. – Summary of top quark mass measurements from the two Tevatron experiments CDF and DØ in the different channels, compared with the world-average determination. The summary is updated to March 2009.

energy scale and map the probability to observe a particular kinematics in the detector given an event configuration at the parton level. This way every observed event can be weighted according to its probability to come from a $t\bar{t}$ decay as a function of the top quark mass and the jet energy scale, which can be constrained through a likelihood maximization. The DØ Collaboration has performed a top quark mass measurement in the lepton plus jets channel using the matrix element technique with an integrated luminosity of 3.6 fb^{-1} , obtaining the result $m_{\text{top}} = 173.7 \pm 0.8$ (stat) ± 0.8 (JES) ± 1.4 (syst) GeV/c^2 [4].

The CDF Collaboration has recently approved a new measurement of the top quark mass in the lepton plus jets channel in 4.8 fb^{-1} of data where the matrix element method was combined with an additional per event discriminant based on the output of a neural network trained to discriminate between top events and W +jets and QCD backgrounds [5]. Thanks to this improvement, this analysis measures the top quark mass with an unprecedented precision, with a result of $m_{\text{top}} = 172.8 \pm 0.7$ (stat) ± 0.6 (JES) ± 0.8 (syst) GeV/c^2 . It is interesting to note that total relative error on this measurement is even lower than the error on the world average for m_{top} , shown in fig. 2 along with the summary of the different measurements performed by the Tevatron experiments in the various top pair decay channels [6].

Another interesting measurement related to the top quark mass has been performed

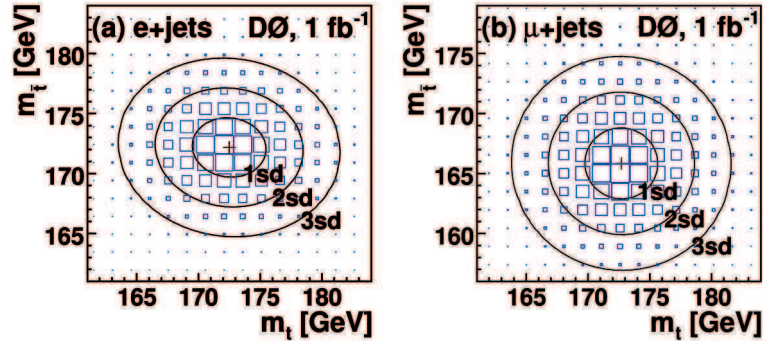


Fig. 3. – (Colour on-line) Direct measurement of the top antitop mass difference performed by the DØ Collaboration in 1 fb^{-1} of data in the lepton plus jets channel. The lines show fitted contours of equal probability for the two-dimensional likelihoods as a function of m_t and $m_{\bar{t}}$ for electron (left) and muon (right) plus jets events. The blue boxes have areas proportional to the value of the likelihood evaluated at the bin center.

by the DØ Collaboration in [7]. Using the matrix element method and a sample of 1 fb^{-1} of electron plus jets and muon plus jets events, and using the charge of the lepton to tag the presence of a top or antitop in the event, the first direct measurement of the mass difference between a quark and its antiquark partner has been carried out. This measurement is a direct test of the CPT theorem, fundamental to any local Lorentz-invariant quantum field theory, that requires that the mass of a particle and that of its antiparticle be identical. The result of the measurement for the two different samples is shown in fig. 3. The measured mass difference is $3.8 \pm 3.7 \text{ GeV}/c^2$, consistent with the equality of top and antitop masses.

3. – Top quark decay width

Using a template based method very similar to those employed to measure the top quark mass, the CDF Collaboration has performed a measurement of the top quark decay width in the lepton plus jets channel using 4.3 fb^{-1} of data [8]. In the Standard Model the theoretical top quark lifetime is very short, of the order of $5 \cdot 10^{-25} \text{ s}$, making the top quark decay before top-flavored hadrons or $t\bar{t}$ -quarkonium bound states can form. The predicted top quark decay width is 1.5 GeV which is out of reach of current experiments. Deviations of the top quark decay width from the Standard Model predicted value could indicate the presence of additional top decay modes and would result in a change of the reconstructed top mass lineshape. Using Monte Carlo simulations for different input top quark widths ranging from 0.1 GeV to 30 GeV with a fixed input top quark mass $m_{\text{top}} = 172.5 \text{ GeV}/c^2$, templates for the distributions of the invariant top quark mass and dijet mass of W boson in the lepton plus jets topology are reconstructed, forming a two-dimensional template for each sample. By comparing the shapes of these two observables with that of the events in the data, the top quark width can be extracted using a maximum likelihood fit. A Feldman-Cousins construction is used to build 95% confidence intervals and an upper limit is set on the top quark width of $\Gamma_{\text{top}} < 7.5 \text{ GeV}$ at 95% confidence level.

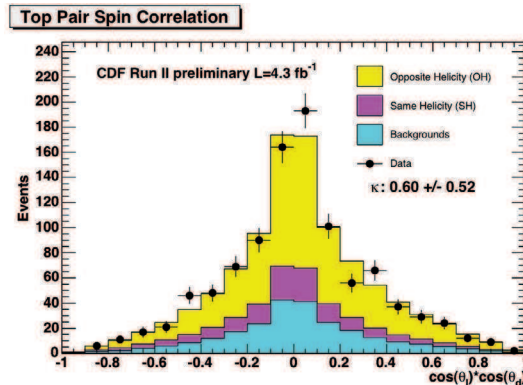


Fig. 4. – CDF measurement of the top antitop spin correlation factor in the lepton plus jets channel. The plot shows the distribution of $\cos(\theta_l) \cdot \cos(\theta_d)$, where θ_l and θ_d are the helicity angles of the lepton and the down-type quark from the top decay, for $t\bar{t}$ signal samples with same and opposite helicity and backgrounds.

4. – Top antitop spin correlations

The fact that due to its short lifetime, top quark decays weakly before any hadronization processes take effect, enables the top spin information to be transmitted to the top quark decay products. Standard Model top pair production produces a characteristic spin correlation which can be modified by new production mechanisms such as Z' bosons or Kaluza-Klein gluons. The spin correlation coefficient k can be defined as $k = (N^S - N^O)/(N^S + N^O)$, where N^S and N^O are the number of $t\bar{t}$ pairs with parallel and antiparallel spin, respectively.

CDF has performed a measurement of the top antitop spin correlations in the lepton plus jets channel with 4.3fb^{-1} of data in the helicity basis [9]. The analysis uses the helicity angles of the lepton, the down quark, and the bottom quark which come from the hadronically decaying top. The helicity angle, defined as the angle between the decay product momentum (in the top rest frame) and the top quark momentum (in the top quark pair rest frame) carries information about the spin of the parent top quark. The top and top pair rest frames are determined using a kinematic fitter with constrained top quark mass. Monte Carlo samples for $t\bar{t}$ signal and for the various backgrounds are used to derive templates for the helicity angles of the top pair decay products in the two cases of t and \bar{t} having either the same or opposite helicity. Finally a fit of the data to the sum of opposite helicity, same helicity and background templates is performed and the correlation factor is measured to be $k = 0.60 \pm 0.50$ (stat) ± 0.16 (syst) to be compared with a Standard Model expected value of $k_{\text{SM}}^H = 0.40$ in the helicity basis. The result of the fit is shown in fig. 4.

The DØ Collaboration has also performed a measurement of the top antitop spin correlations in the dilepton decay topology using 4.2fb^{-1} of data in the beam axis basis [10]. The analysis considers the angles between the direction of flight of each of the two leptons in the rest frame of their parent top quark and the reference direction of the beam axis. Selected dilepton events are reconstructed using the neutrino weighting algorithm to integrate over the unknown neutrinos pseudorapidities and calculate a weight distribution for each event as a function of the lepton angles defined above.

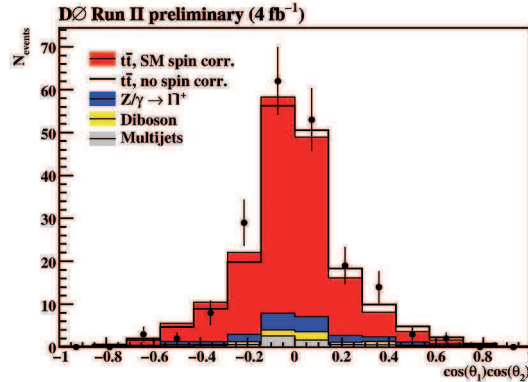


Fig. 5. – DØ measurement of the top antitop spin correlation factor in the dilepton channel. The plot shows the distribution of $\cos(\theta_1) \cdot \cos(\theta_2)$, where θ_1 and θ_2 are the angles of the leptons with the beam axis in the parent top rest frame for $t\bar{t}$ signal with and without spin correlations and backgrounds.

The data distributions for the angles are compared with Monte Carlo derived templates for $t\bar{t}$ signal built with different correlation hypotheses and with templates for the backgrounds to obtain the best fit value for the spin correlation factor, that is measured to be $k = -0.17^{+0.65}_{-0.53}$ (stat + syst), to be compared with a Standard Model expected value of $k_{SM}^{BA} = 0.78$ in the beam axis basis. The result of the fit is shown in fig. 5.

5. – Top quark charge

In the Standard Model the top quark is expected to have charge $2/3$; due to its fast decay, a direct measurement of the charge is impossible, and only the total charge of the top decay products can be measured. Assuming that top quarks decay to a W boson and a b quark, exotic models have been proposed in the literature as part of a fourth generation of quarks and leptons [11], where the top decays to a W^- and a b quark, hence having a charge of $4/3$, rather than to a W^+ and a b quark as predicted by the Standard Model. The CDF Collaboration has recently performed a measurement in the lepton plus jets channel in 2.7 fb^{-1} . The charge of the two W 's and two b -quarks is determined for each data event, using a kinematic fitter to select the best jet to parton assignment compatible with the top quark decay. The charge of one of the two W 's is obtained by identifying the charge of the lepton in the event while the charge of the b -tagged jets is obtained considering the charge of soft leptons in the event compatible with the semileptonic decay of a b quark. Based on the total number of reconstructed top charges in agreement with the Standard Model hypothesis or with the exotic hypothesis, limits can be set on the validity of the two models. With this method, CDF observes 29 events consistent with the Standard Model and 16 events consistent with a $4/3$ charge top quark. This results in a 95% confidence level exclusion of the $4/3$ charge hypothesis [12].

The DØ Collaboration has performed a similar measurement in the past on 0.37 fb^{-1} , using the JetCharge algorithm to determine the charge of the b -quarks in the event. With a similar technique, DØ excluded the $4/3$ charge hypothesis with a 92% confidence level [13].

6. – Forward-backward asymmetry

The measurement of the $t\bar{t}$ charge asymmetry is equivalent in the Tevatron system to quantifying the forward-backward asymmetry on the top production. Several beyond the Standard Model physics predict a detectable forward-backward asymmetry, and in addition QCD at next-to-leading order predicts a non-zero asymmetry in $q\bar{q} \rightarrow t\bar{t}$. While at the LHC the top quark production is dominated by gluon fusion, at the Tevatron top pairs are mostly produced by $q\bar{q}$ annihilation, making it the best place to study these effects. Both the CDF and DØ Collaborations have performed similar measurements to determine the forward-backward asymmetry in top pair production. Events in the lepton plus jets channel are fully reconstructed using a kinematic fitter, which fits the final states jets and leptons to the $t\bar{t}$ decay hypothesis, allowing to reconstruct the rapidities of the top and antitop. The asymmetry is defined as $A_{fb} = (N^f - N^b)/(N^f + N^b)$ where N^f and N^b are the number of events in which the signed rapidity of the top is larger and smaller than that of the antitop, respectively.

Once detector effects, bias and dilution from backgrounds, acceptance and reconstruction are taken into account, a measurement of A_{fb} can be performed that can be directly compared with theoretical values. In 3.2fb^{-1} of data CDF measures $A_{fb} = 0.19 \pm 0.07$ (stat) ± 0.02 (syst) and in 1.0fb^{-1} of data DØ measures $A_{fb} = 0.12 \pm 0.08$ (stat) ± 0.01 (syst) to be compared with the theoretical value from next-to-leading order QCD calculations of $A_{fb}^{\text{th}} = 0.05 \pm 0.015$.

7. – W boson helicity in top quark decays

In the Standard Model the top quark decays almost exclusively to a W boson and b quark through the $V-A$ charged weak current interaction. As a consequence, the top quark is expected to decay around 70% of the times to longitudinal and the rest to left-handed polarized W bosons. A different structure of the Wtb vertex or the presence of any new particle could alter the fractions of W bosons produced in each polarization state, therefore a measurement of this fraction allows to perform a test of the $V-A$ nature of the Wtb vertex. The polarization of the W boson can be described using the angle θ^* between the momenta of the down-type fermion and the top quark in the W boson rest frame for each top. The DØ Collaboration has measured the longitudinal and right-handed fractions of the W boson helicity combining the lepton plus jets and dilepton $t\bar{t}$ decay channels using 2.7fb^{-1} of data [14]. Lepton plus jets events are reconstructed using a kinematic fitter that allows to reconstruct the four vectors of the two top quarks and their decay products, and then calculate $\cos\theta^*$. For hadronic W boson decays, since it is impossible to know which of the jets from the W boson arose from a down-type quark, a jet is chosen at random to calculate the variable $|\cos\theta^*|$, that does not discriminate between left- and right-handed W bosons but adds information for determining the fraction of longitudinal W bosons. In the dilepton channel, since there is a four-fold ambiguity in the reconstruction of the event, $\cos\theta^*$ is determined for each of the four possible combinations and the average value is taken for the considered jet. These distributions in $\cos\theta^*$ are compared with Monte Carlo derived templates for different W boson helicity models, corrected for background and reconstruction effects, using a binned maximum likelihood method. Finally a fit is made simultaneously to the three sets of templates measuring the fraction of longitudinal W bosons $f_0 = 0.49 \pm 0.11$ (stat) ± 0.09 (syst) and the fraction of right-handed W bosons $f_+ = 0.11 \pm 0.06$ (stat) ± 0.05 (syst).

The CDF Collaboration has performed a similar measurement in the lepton plus jets channel using 2.7 fb^{-1} of data [15]. This analysis is based on a matrix element method adapted to include the dependence on the W boson helicity fractions. The likelihood function is calculated for each event from the leading-order matrix element expression for $t\bar{t}$ signal and for the dominant background (W plus jets) as a function of longitudinal and right-handed W bosons fractions, and a total joint likelihood is then formed by taking the product of the per event likelihood. By maximizing the joint likelihood of the sample of selected lepton plus jets events CDF measures $f_0 = 0.88 \pm 0.11$ (stat) ± 0.06 (syst) and $f_+ = -0.15 \pm 0.07$ (stat) ± 0.06 (syst).

* * *

I would like to thank the members of the CDF and DØ Collaborations for all their hard work and dedication, and in particular the authors of the mentioned analyses. I also would like to thank the organizers of the XXIV Rencontres de Physique de la Vallée d'Aoste in La Thuile.

REFERENCES

- [1] ABE F. *et al.* (THE CDF COLLABORATION), *Phys. Rev. Lett.*, **74** (1995) 2626.
- [2] ABACHI S. *et al.* (THE DØ COLLABORATION), *Phys. Rev. Lett.*, **74** (1995) 2632.
- [3] THE CDF COLLABORATION, CDF Conference Note 10033 (2010).
- [4] THE DØ COLLABORATION, DØ Conference Note T78 (2009).
- [5] THE CDF COLLABORATION, CDF Conference Note 10077 (2010).
- [6] TEVATRON ELECTROWEAK WORKING GROUP for the CDF and DØ COLLABORATIONS, arXiv:0903.2503 [hep-ex].
- [7] ABAZOV V. M. *et al.* (THE DØ COLLABORATION), *Phys. Rev. Lett.*, **103** (2009) 132001.
- [8] THE CDF COLLABORATION, CDF Conference Note 10035 (2010).
- [9] THE CDF COLLABORATION, CDF Conference Note 10048 (2010).
- [10] THE DØ COLLABORATION, DØ Conference Note T84 (2009).
- [11] CHANG D. *et al.*, *Phys. Rev. D*, **59** (1999) 091503.
- [12] THE CDF COLLABORATION, CDF Conference Note 9939 (2010).
- [13] ABAZOV V. M. *et al.* (THE DØ COLLABORATION), *Phys. Rev. Lett.*, **98** (2007) 041801.
- [14] THE DØ COLLABORATION, DØ Conference Note T69 (2008).
- [15] THE CDF COLLABORATION, CDF Conference Note 10004 (2009).

SESSION VI - HIGGS SEARCHES, HOT TOPICS

Song-Ming Wang

Searches for low mass Higgs boson at the Tevatron

Alvaro De Rújula

To be or not to be: Higgs impostors at the LHC

Searches for low mass Higgs boson at the Tevatron

SONG-MING WANG for the CDF and DØ COLLABORATIONS

Institute of Physics, Academia Sinica - Taipei, Taiwan

(ricevuto il 14 Settembre 2010; pubblicato online il 12 Gennaio 2011)

Summary. — This paper summarized the latest results on the search for the standard model Higgs boson in the low mass regions by the CDF and DØ Collaborations, which were presented at the Les Rencontres de Physique de la Vallée d'Aoste conference 2010. The results are based on data samples collected up to 5.4 fb^{-1} .

PACS 14.80.Bn – Standard-model Higgs bosons.

1. – Introduction

The last particle predicted by the standard model (SM), which has not yet been observed in experiments, is the Higgs boson. In the SM, the electroweak gauge symmetry is broken through the Higgs mechanism, which postulates the existence of a Higgs field that permeates the entire universe. The SM particles acquire their masses by interacting with the Higgs fields through the exchange of a particle, the Higgs boson. Although the Higgs boson mass is not predicted by the theory, however it can be constrained due to its predicted couplings to the other particles. Global fits to precision electroweak data favors a light Higgs with mass below $157 \text{ GeV}/c^2$ [1]. Direct Higgs searches performed at LEP set a lower limit of $114 \text{ GeV}/c^2$ [2]. If this limit is included into the previous calculation, the upper limit increases to $186 \text{ GeV}/c^2$.

At the Tevatron the Higgs boson can be produced in $p\bar{p}$ interactions through several processes [3]. The production cross section for Higgs mass between $100\text{--}200 \text{ GeV}/c^2$ varies between $\sim 1 \text{ pb}$ to $\sim 0.01 \text{ pb}$, depending on their production mechanisms. The gluon fusion ($gg \rightarrow H$) is the dominant production process followed by the associated productions ($q\bar{q}' \rightarrow WH/ZH$) and the vector boson fusion process ($qq \rightarrow qqH$). In the low Higgs mass region ($m_H < 135 \text{ GeV}/c^2$), the dominant decay channel is $H \rightarrow b\bar{b}$ ($BR \sim 73\%$ at $m_H = 115 \text{ GeV}/c^2$), followed by the $H \rightarrow \tau\bar{\tau}$ channel whose branching fraction is ~ 10 times smaller than $H \rightarrow b\bar{b}$. For the Higgs boson mass above $135 \text{ GeV}/c^2$ the decay channel $H \rightarrow W^+W^-$ becomes the dominant decay channel. Although the gluon fusion process has the largest production rate, however it is difficult to search for low mass Higgs boson in this production channel with Higgs decays in $H \rightarrow b\bar{b}$ due to huge QCD multi-jet background. The production and decay modes that have the best discovery sensitivities for a single search channel at low Higgs mass are the associated

productions ($q\bar{q}' \rightarrow WH/ZH$) with the decays $H \rightarrow b\bar{b}$ and $W \rightarrow l\nu$ or $Z \rightarrow l^+l^-/\nu\bar{\nu}$ ($l = e$ or μ).

As the predicted Higgs signal is several orders of magnitude smaller than other SM backgrounds, both Tevatron experiments, CDF and DØ, have devised search strategies to optimize the Higgs detection performances. The Higgs acceptance is increased by extending the region of lepton identification in the detector, and the b jet tagging efficiency is improved by developing advanced tagging algorithms. Both experiments also employ multivariate discriminant tools such as artificial neural network (NN), Boosted Decision Tree (BDT) and Matrix Element (ME) probabilities to further discriminate the Higgs signal from the background. To achieve the best search sensitivity, both experiments analysed as much data samples as possible (up to $\sim 5.4\text{fb}^{-1}$ of data sample were analysed when the results were presented at the conference), and the results from all search channels are combined.

2. – Low mass Higgs boson searches

The following sections describe the searches for low mass Higgs boson in various production and decay final states performed by the CDF and DØ experiments.

2.1. Searches for the Higgs boson in the $WH \rightarrow l\nu b\bar{b}$ channel. – CDF and DØ have searched for the SM Higgs boson in the channel where the Higgs boson is assumed to be produced in association with a W boson [4]. The search is focused on the signal events in which the W boson decays leptonically ($W \rightarrow e\nu$ or $W \rightarrow \mu\nu$) and the Higgs boson decays into $b\bar{b}$. Thus the final state signature consists of a high- p_T lepton (e or μ), a pair of b jets and large missing transverse energy (\cancel{E}_T) from the escaping neutrino. To select the Higgs events, each candidate event should have an isolated lepton, two or more jets and large \cancel{E}_T . At least one of the jets in the selected events is required to be tagged as a b jet candidate. The main sources of background are from productions of $W + bb/cc, t\bar{t}$, single top, di-boson, QCD multi-jet production that fakes a W production signature, and misidentification of non- b jets as b jets (mis-tag) in W boson production with light-flavor jets. To improve the search sensitivity, DØ used a NN based b jet tagging algorithm. This algorithm enables the experiment to have good efficiency in tagging the b jets of the Higgs signal and maintain an overall low mis-tag rate. CDF uses NN to correct the measured jet energy and improves the di- b jet invariant mass (m_{bb}) resolution.

After the event selection, CDF uses a Matrix Element approach to extract the possible signal from the background. This technique uses leading order Matrix Element to compute event probability densities for the signal and backgrounds, thus creating a discriminant for each event. The discriminant distributions are shown in fig. 1. DØ trains a NN algorithm to separate the signal from background. No evidence for a Higgs signal is seen in both searches and upper limits at 95% confidence level (CL) are set on its production cross section times branching ratio. For Higgs mass of $115\text{GeV}/c^2$, CDF sets an observed (expected) limit of 3.3 (3.8) times the SM predicted cross section, and DØ sets an observed (expected) limit of 5.1 (6.9) times the SM prediction.

2.2. Searches for the Higgs boson in the $ZH \rightarrow l^+l^-b\bar{b}$ channel. – At the Tevatron the Higgs boson can also be produced in association with a Z boson. CDF and DØ have searched for the Higgs boson in this production channel and in the decay modes of $Z \rightarrow l^+l^-$ ($l = e, \mu$) and $H \rightarrow b\bar{b}$. The searches are performed on data samples of 4fb^{-1} [5]. The events are first selected by requiring a pair of opposite charged electrons

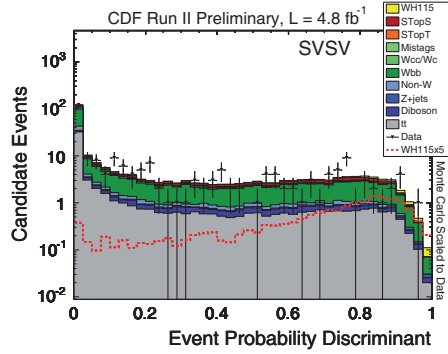


Fig. 1. – Event probability density distributions for the Matrix Element WH analysis by CDF.

or muons whose invariant mass is consistent with the Z boson. The selected events are to have at least two jets and at least one jet tagged as a b jet. The dominant backgrounds are the production of Z plus heavy-flavor jets (b or c jets), Z plus light-flavor jets with light-flavor jets mis-identified as b jets, $t\bar{t}$, ZZ , ZW , and events with fake leptons.

Some of the advantages in performing the search in this $ZH \rightarrow l^+l^-b\bar{b}$ channel are that all the physics objects in the final state can be detected if they fall within the instrumented region, and the two charged leptons are constrained to the Z mass. Thus CDF and DØ make use of the kinematic constraints to correct the measured jets' energies and improve the di-jet mass m_{bb} resolution. This improvement is illustrated in fig. 2.

To maximize the search sensitivity, both experiments perform the analysis in several sub-channels (*i.e.* loose and tight lepton identification and single and double b -tagged jets categories). To further enhance the possible Higgs signal over the backgrounds, CDF trains a two-dimensional NN to distinguish ZH signal from Z +jets and $t\bar{t}$, which are the two most dominant backgrounds. DØ uses the BDT algorithm to improve the separation. The discriminant distributions from the BDT are shown in fig. 3. The observed events in the data are consistent with the expected background events. Thus there is no evidence of a Higgs signal in the data. The observed (expected) upper limit

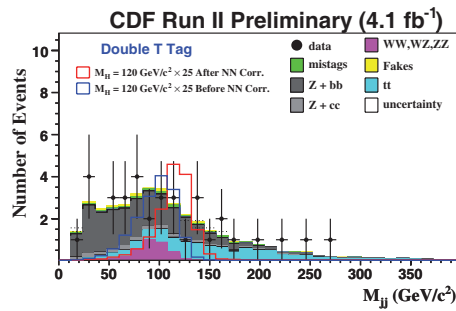


Fig. 2. – (Colour on-line) m_{jj} mass distribution from a $ZH \rightarrow l^+l^-b\bar{b}$ analysis. The blue histogram is the reconstructed $m_{b\bar{b}}$ mass distribution of a ZH simulated sample, with $m_H = 120 \text{ GeV}/c^2$, before correcting the jets' energy. The red histogram is after applying the correction.

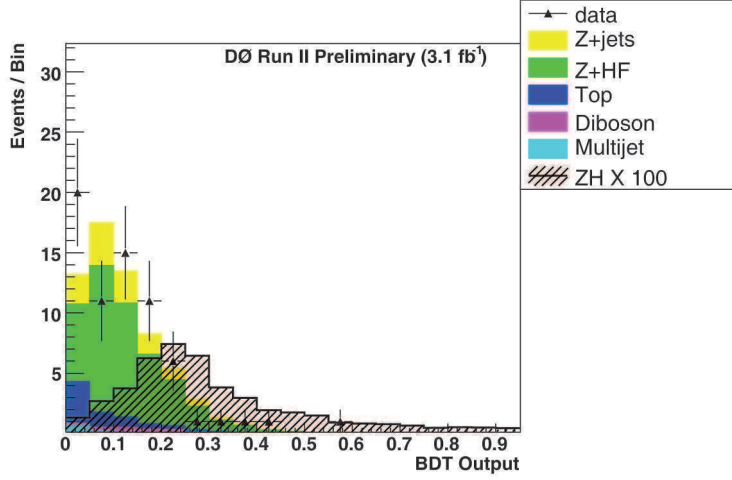


Fig. 3. – Discriminant distributions for the Boosted Decision Tree $ZH \rightarrow l^+l^-b\bar{b}$ analysis by DØ.

at 95% CL on $\sigma(p\bar{p} \rightarrow ZH) \times BR(H \rightarrow b\bar{b})$ for $m_H = 115 \text{ GeV}/c^2$ is 5.9 (6.8) times the SM prediction for CDF and 8.0 (9.1) times the SM prediction for DØ.

2.3. Searches for the Higgs boson in the $\cancel{E}_T + b\bar{b}$ channel. – CDF and DØ also consider a search for associated Higgs production using a final state signature of $\cancel{E}_T + b\bar{b}$, which is mostly sensitive to the signal of $ZH \rightarrow \nu\bar{\nu}b\bar{b}$. The search also has some sensitivity to $WH \rightarrow \nu b\bar{b}$ where the charged lepton is not identified, or an electron that does not pass the electron identification selection is classified as a jet, or a tau lepton that decays hadronically and reconstructed as a jet. For both production channels the Higgs decay considered is $H \rightarrow b\bar{b}$. The analyses are performed on data samples of 3.6 fb^{-1} for CDF and 5.2 fb^{-1} for DØ [6]. The main sources of background are from the production of W or Z bosons with jets, single top quark, $t\bar{t}$, and di-boson. In these processes, the \cancel{E}_T is mostly the result of neutrinos escaping detection. QCD multi-jet production is another source of background. In this case the \cancel{E}_T is due to the mis-measurement of the energy of one or more jets. To reduce the QCD multi-jet background, both experiments look at the correlation between a track based missing transverse momentum \cancel{P}_T , which is defined as the opposite of the vector sum of the measured charged particles transverse momentum, and the calorimeter based \cancel{E}_T . For collision events with real large missing transverse energy, there will be a strong correlation between the calorimeter based \cancel{E}_T and the track based \cancel{P}_T . Whereas for events with no real missing transverse energy, there will be no/weak correlation between \cancel{E}_T and \cancel{P}_T .

In this analysis both experiments also apply multivariate algorithms to first separate the QCD multi-jet background from the signal, and then a second training is performed to separate the non-QCD multi-jet background from the signal. The discriminant distributions from the second training for the double b -tagged category from DØ are shown in fig. 4. No evidence of Higgs signal is seen by both experiments in this final state signature search. The observed (expected) upper limit at 95% CL on the signal production cross section times branching ratio at $m_H = 115 \text{ GeV}/c^2$ is 6.1 (4.2) times the SM prediction for CDF, and 3.7 (4.6) times the SM prediction for DØ.

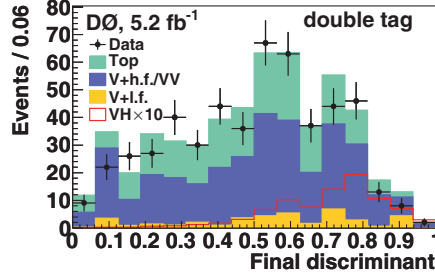


Fig. 4. – Discriminant distributions for the Higgs search in the $E_T + b\bar{b}$ final state by D0.

2.4. Searches for the Higgs boson in the all-hadronic channel. – CDF has performed a search for low mass Higgs bosons from WH/ZH production in the decay modes $W \rightarrow qq'$ or $Z \rightarrow q\bar{q}$ and $H \rightarrow b\bar{b}$, and from vector boson fusion ($qq \rightarrow qqH$) where the Higgs boson decays into $b\bar{b}$ [7]. The final state signature consists of four jets with at least two b jets. The signal events, which are selected from a data sample of 4 fb^{-1} , are required to have at least four jets with two jets tagged as b jets in the event. The dominant background is from QCD multi-jet production with heavy-flavor jets in the final state. In order to distinguish between signal and background events, CDF uses a NN algorithm. The distributions of the NN output for the expected background contributions and for the data, for one of the double b tagged category of the associated production search, are shown in fig. 5. There is no evidence of the Higgs signal in the most signallike region of the NN output distributions for all the sub-channels considered in this analysis. The observed (expected) upper limit at 95% CL on the Higgs production cross section times branching ratio is 10.4 (19.9) times the SM prediction for Higgs mass of $120 \text{ GeV}/c^2$.

2.5. Searches for the Higgs boson in the τ plus jets final states. – The search for low mass Higgs boson with tau leptons in the final states has been explored by the D0 experiment. In the first analysis, which uses a data sample of $\sim 4 \text{ fb}^{-1}$, the Higgs signal is searched in the final state signature that consists of a tau lepton, large E_T and a pair of b jets [8]. The signal contributions come from the WH and ZH associated productions where the W decays into a tau lepton and a neutrino, and the Z boson decays into a

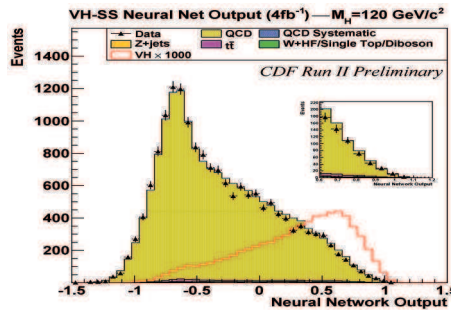


Fig. 5. – Output distributions of the neural network trained for the Higgs search in the all hadronic final state by CDF.

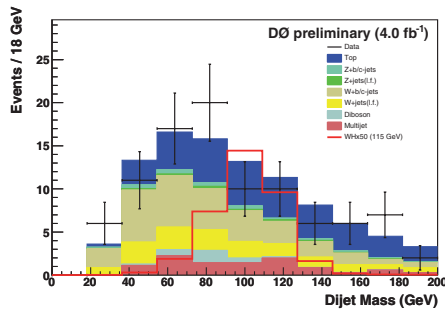


Fig. 6. – Reconstructed di-jet mass distribution for Higgs search in $\tau + \cancel{E}_T + b\bar{b}$ final state by DØ.

pair of tau leptons but with one tau lepton not identified in the detector. The Higgs boson is considered to decay into a pair of b quarks. The signal events are selected with one identified hadronic tau candidate, large \cancel{E}_T and at least two jets with at least one jet tagged as a b jet. The dominant background contributions come from $t\bar{t}$ and $W + b\bar{b}$ productions. The reconstructed di-jet invariant mass distributions of the selected data events, expected background and predicted Higgs signal, are shown in fig. 6. No evidence of the Higgs signal is observed in the data. An observed (expected) upper limit of 14.1 (22.4) times the SM prediction on the Higgs production cross section times branching ratio is being set for the mass of $m_H = 115 \text{ GeV}/c^2$ at 95% CL.

In the second Higgs search analysis, DØ looks at the final state that contains two tau leptons and two jets [9]. The signal production and decay channels that contribute to this final state include WH/ZH associated productions with $W/Z \rightarrow qq$ and $H \rightarrow \tau\bar{\tau}$ or $Z \rightarrow \tau\bar{\tau}$ and $H \rightarrow q\bar{q}$, vector boson fusion ($qq \rightarrow qqH$) with $H \rightarrow \tau\bar{\tau}$, and gluon fusion $gg \rightarrow H + \text{jets}$, where the additional jets are originated from QCD initial state radiation and with $H \rightarrow \tau\bar{\tau}$. The signal events consist of two tau candidates and at least two jets. One of the tau candidates is required to decay hadronically, and the other tau candidate decays into a muon lepton and neutrinos. Similarly no evidence of the Higgs signal is seen in this analysis. The observed (expected) upper limit at 95% CL on the Higgs production cross section times branching ratio is 27.0 (15.9) times the SM prediction for Higgs mass of $115 \text{ GeV}/c^2$.

2'6. Searches for the Higgs boson in the inclusive di-photon final state. – In the SM, low mass Higgs boson can decay into a pair of photons with a predicted branching ratio of $\sim 0.2\%$. Although its branching ratio is many times smaller than $BR(H \rightarrow b\bar{b})$ and $BR(H \rightarrow \tau\bar{\tau})$, however the energy resolution of a measured photon is much better than the measurement of a b jet. Additionally the photon's energy is well contained within the detector, whereas for the tau lepton, some of its energy is not measured due to the escaping neutrino. Therefore one may discover the Higgs boson by searching for a mass peak in the di-photon mass spectrum.

CDF and DØ have searched for the Higgs boson in the di-photon final state using data samples of 5.4 fb^{-1} and 4.2 fb^{-1} , respectively [10]. The signal productions that are considered in the search include the gluon fusion, the WH/ZH associated productions, and the vector boson fusion. The main sources of background are QCD di-photon production, $\gamma + \text{jet}$ and di-jet productions where the jet fakes as a photon, and Drell-Yan

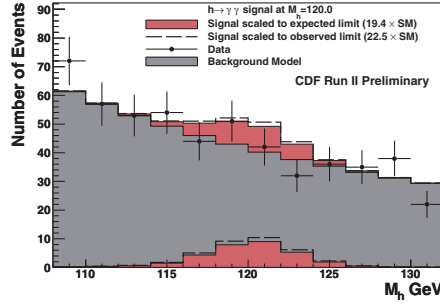


Fig. 7. – Reconstructed di-photon mass distribution for Higgs search in $H \rightarrow \gamma\gamma$ decay channel by CDF.

($Z/\gamma^* \rightarrow e^+e^-$) production where the electron is mis-identified as a photon. To search for the Higgs signal, CDF ($D\emptyset$) looks for a mass peak in a mass window of $\pm 12 \text{ GeV}/c^2$ ($\pm 15 \text{ GeV}/c^2$) around the assume Higgs mass. The di-photon invariant mass distribution in the mass window for an assume Higgs mass of $120 \text{ GeV}/c^2$, from CDF, is shown in fig. 7. Both experiments do not observe evidence of a Higgs signal in the di-photon mass distribution. CDF sets an observed (expected) limit of 22.5 (19.4) times the SM prediction for Higgs mass of $120 \text{ GeV}/c^2$, and $D\emptyset$ sets an observed (expected) limit of 13.1 (17.3) times the SM prediction. The limits are given at 95% CL.

3. – Combined results from all searches

In the earlier sections the results on various searches for the SM Higgs boson in the low mass region by the CDF and $D\emptyset$ experiments were presented. Although some channels' sensitivities are similar or are different from others, however each channel is exploring different production and decay modes. The combination of these results will further improve the sensitivity of the Higgs search. The combined results from each experiment and the Tevatron combined results (combining CDF and $D\emptyset$'s results) are given in table I [11-13]. The Tevatron combined results are also presented in fig. 8. The limits presented in table I and fig. 8 are the ratios of the upper limit at 95% CL on the production cross section times branching ratio to the SM prediction. The combined limit in the low mass region also receives contributions from the high mass searches.

TABLE I. – CDF, $D\emptyset$ and Tevatron combined upper limit on SM Higgs boson production in the low mass region. The limits are expressed as ratios to the SM prediction.

Mass (GeV/c^2)		100	105	110	115	120	125	130	135	140	145	150
CDF	Exp	2.01	2.09	2.14	2.38	2.72	2.84	2.92	2.66	2.51	2.21	1.92
	Obs	2.58	2.62	2.88	3.12	3.37	3.93	3.80	3.80	3.53	2.66	2.26
$D\emptyset$	Exp	2.35	2.40	2.85	2.80	3.25	3.31	3.30	3.35	2.95	2.71	2.46
	Obs	3.53	3.40	3.47	4.05	4.03	4.19	4.53	5.58	4.33	3.86	3.20
Tev	Exp	1.52	1.58	1.73	1.78	2.1	2.2	2.2	2.1	1.91	1.75	1.49
	Obs	2.11	2.35	2.28	2.70	2.7	3.1	3.1	3.4	3.03	2.17	1.80

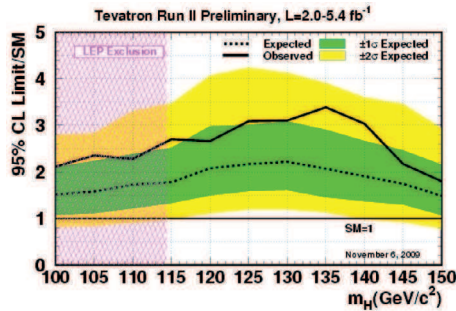


Fig. 8. – Tevatron combined upper limit on SM Higgs boson production in the low mass region.

4. – Projection

Over the past few years both Tevatron experiments have improved their sensitivity to the search for the SM Higgs boson by increasing the data size used in the searches and by improving the analysis techniques. By analyzing more data, each experiment gains better understanding of its detector's performance and is then able to discover new ways to improve the Higgs search sensitivity. Some of the improvement techniques are mentioned in earlier sections. The results presented earlier are based on data samples up to $\sim 5.4 \text{ fb}^{-1}$. The Tevatron is expected to deliver a total integrated luminosity between $10\text{--}12 \text{ fb}^{-1}$ by the end of 2011. By doubling the existing data samples, both experiments will be able to make more improvements to the Higgs search. The plot in fig. 9 shows the predicted probability of observing a three-sigma evidence of the Higgs signal by the Tevatron, as a function of the Higgs mass, for an integrated luminosity of 5 fb^{-1} and 10 fb^{-1} collected by each experiment [11]. The plot also shows the sensitivities when using the current analysis techniques and when adding in new improvements. The probabilities are calculated by scaling the CDF's expected performance at 5 fb^{-1} and 10 fb^{-1} , to twice the integrated luminosity so as to estimate the performance when both CDF's and DØ's results are combined. The plot shows that if the Higgs boson exists within the low mass region, there is a $\sim 35\%$ chance of observing a three-sigma evidence of the Higgs signal with an integrated luminosity of 10 fb^{-1} collected by both experiments.

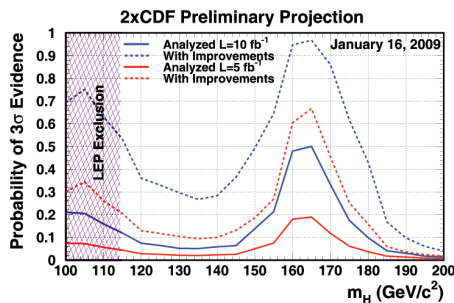


Fig. 9. – Predicted probability of observing a three-sigma evidence of the Higgs signal by the Tevatron.

5. – Conclusions

The CDF and DØ Collaborations have searched for the SM Higgs boson in various production and decay channels with data samples up to 5.4 fb^{-1} . No Higgs signal has been observed so far. By combining all the results from both experiments, the observed (expected) 95% CL upper limit on the production cross section times branching fraction for a Higgs mass of $115 \text{ GeV}/c^2$ is 2.70 (1.78) times the SM prediction. Both CDF and DØ are working on further improving search techniques. With an integrated luminosity of $\sim 10 \text{ fb}^{-1}$ from each experiment, there is a $\sim 35\%$ chance of observing a three-sigma evidence of the Higgs signal in the low mass region, if it exists there.

* * *

I would like to thank our colleagues in the CDF and DØ Collaborations for their outstanding work, and the Fermilab accelerator division for providing excellent colliding beams to each CDF and DØ experiment.

REFERENCES

- [1] LEP ELECTROWEAK WORKING GROUP, status of August 2009, <http://lepewwg.web.cern.ch/LEPEWWG/>.
- [2] ABBIENDI G. *et al.* (THE ALEPH COLLABORATION, THE DELPHI COLLABORATION, THE L3 COLLABORATION and THE OPAL COLLABORATION, THE LEP WORKING GROUP for HIGGS BOSON SEARCHES), *Phys. Lett. B*, **565** (2003) 61.
- [3] CARENA M. *et al.*, Report of the Tevatron Higgs Working Group, in arXiv:hep-ph/0010338.
- [4] CDF COLLABORATION, *Search for Standard Model Higgs Boson Production in Association with a W Boson Using Matrix Element Techniques with 4.8 fb^{-1} of CDF data*, CDF Note 9483 (2010); DØ COLLABORATION, *Search for WH associated production using neural network with 5.0 fb^{-1} of Tevatron data*, DØ Note 5972-CONF (2009).
- [5] CDF COLLABORATION, *A Search for the Standard Model Higgs Boson in the Process $ZH \rightarrow l^+l^-b\bar{b}$ Using 4.1 fb^{-1} of CDF II Data*, CDF Note 9889 (2009); DØ COLLABORATION, *Search for $ZH \rightarrow e^+e^-b\bar{b}$ and $ZH \rightarrow \mu^+\mu^-b\bar{b}$ Production in 4.2 fb^{-1} of data with the DØ Detector in $p\bar{p}$ Collisions at $\sqrt{s} = 1.96 \text{ TeV}$* , DØ Note 5876-CONF (2009).
- [6] CDF COLLABORATION, *Search for the Standard Model Higgs Boson in the E_T plus jets sample*, CDF Note 9642 (2009); ABAZOV V. M. *et al.* (DØ COLLABORATION), *Phys. Rev. Lett.*, **104** (2010) 071801.
- [7] CDF COLLABORATION, *A Search for the Higgs Boson in the All Hadronic Channel with Data Sample of 4 fb^{-1}* , CDF Note 10010 (2009).
- [8] DØ COLLABORATION, *Search for the standard model Higgs boson in the $WH \rightarrow \tau\nu b\bar{b}$ channel in 4.0 fb^{-1} of $p\bar{p}$ collisions at $\sqrt{s} = 1.96 \text{ TeV}$* , DØ Note 5977-CONF (2009).
- [9] DØ COLLABORATION, *Search for the SM Higgs boson in the $\tau^+\tau^-q\bar{q}$ final state*, DØ Note 5845-CONF (2009).
- [10] CDF COLLABORATION, *Search for a SM Higgs Boson with the Diphoton Final State at CDF*, CDF Note 10065 (2010); DØ COLLABORATION, *Search for the Standard Model Higgs Boson in $\gamma\gamma$ final states at DØ with $L = 4.2 \text{ fb}^{-1}$ data*, DØ Note 5858-CONF (2009).
- [11] CDF COLLABORATION, *Combined Upper Limit on Standard Model Higgs Boson Production*, CDF Note 9999 (2009).
- [12] DØ COLLABORATION, *Combined Upper Limit on Standard Model Higgs Boson Production from the DØ experiment in $2.1\text{--}5.4 \text{ fb}^{-1}$ of Data*, DØ Note 6008-CONF (2009).
- [13] THE TEVATRON NEW PHENOMENA and HIGGS WORKING GROUP for the CDF and DØ COLLABORATIONS, *Combined CDF and DØ Upper Limits on Standard Model Higgs-Boson Production with $2.1\text{--}5.4 \text{ fb}^{-1}$ of Data*, arXiv:0911.3930v1 (2009).

To be or not to be: Higgs impostors at the LHC

A. DE RÚJULA

*Instituto de Física Teórica, Universidad Autónoma & CIEMAT - Madrid, Spain
CERN - Geneva, Switzerland
Boston University - Boston, MA, USA*

(ricevuto il 14 Settembre 2010; pubblicato online l'11 Gennaio 2011)

Summary. — Consider the day when an invariant mass peak, roughly compatible with “the Higgs”, begins to emerge, say at the LHC, . . . and may you see that day. There will be a difference between discovery and scrutiny. The latter would involve an effort to ascertain what it is, or is not, that has been found. It turns out that the two concepts are linked: Scrutiny will naturally result in deeper knowledge—is *this* what you were all looking for?—but may also speed up discovery.

PACS 14.80.Bn – Standard-model Higgs bosons.

1. – Introduction

Let the single missing scalar of the Standard Model (SM) be called “the Higgs”, to stick to a debatable misdeed. Because the idea is so venerable, one may have grown insensitive to how special a Higgs boson would be. Its quantum numbers must be those of the vacuum, which its field permeates. The boson itself would be the vibrational quantum *of* the vacuum, not a mere quantum *in* the vacuum, or in some other substance. The couplings of the Higgs to quarks and leptons are proportional to their masses. So are its couplings to W^\pm and Z , a fact that, within the SM, is in a sense verified. A significantly precise direct measurement of the Higgs couplings to fermions is not an easy task. Even for the heaviest of them, the top quark, the required integrated luminosity is large, as illustrated by the ATLAS Collaboration on the left of fig. 1.

In the past, given a newly discovered particle, one had to figure out its J^{PC} quantum numbers (or its disrespect of the super-indexed ones) to have it appear in the Particle Data Book. Publication in the New York Times was not considered that urgent, nor was it immediate for bad news. Times have changed. Yet, two groups [1,2] have thoroughly studied the determination of the quantum numbers and coupling characteristics of a putative signal at the LHC, that could be the elementary scalar of the SM, or an impostor thereof, both dubbed H here. The “golden channel” for this exercise is $H \rightarrow (ZZ \text{ or } ZZ^*) \rightarrow \ell_1^+ \ell_1^- \ell_2^+ \ell_2^-$, where $\ell_{1,2}^\pm$ is an e or a μ , and Z^* denotes that, for $M_H < 2M_Z$, one of the Z s is “off-shell”. For a review of previous work on the subject, see *e.g.* [3].

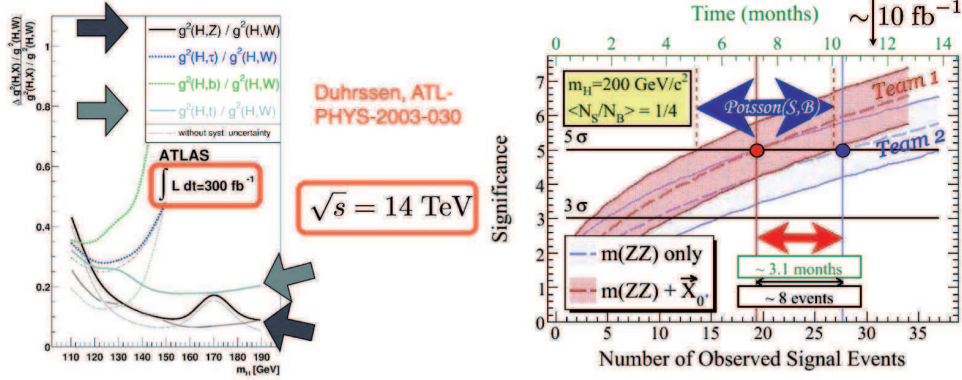


Fig. 1. – Left: fractional precision on the measurable ratios of branching ratios for SM H decays into W , Z , t and τ pairs as functions of M_H . Right: an example of discovery and scrutiny plot of a SM scalar with $M_H = 200$ GeV, not specially chosen for effect.

To be realistic (?) let me consider two competing teams. They are working at a pp collider of energy $\sqrt{s} = 10$ TeV, luminosity $10^{33} \text{ cm}^{-2} \text{ s}^{-1}$ and Snowmass factor of 3 (on average, things work well 1/3 of the time). The SM is correct, $M_H = 200$ GeV and the estimates of signals and backgrounds are reliable. As the number of events increases, Team 2 would then gather evidence for an M_{ZZ} peak at the rate shown on the right of fig. 1. Team 1 is additionally checking that, indeed, the object has $J^{PC} = 0^{++}$. T1 reaches “discovery” (5σ significance) some three months before T2. The horizontal error bars, dominated by fluctuations in the expected background, tell us that the two teams are *only* 1σ apart (iff from two different experiments!). But that means the probability of T1 (from experiment A) being 3 months ahead of T2 (from experiment $B \neq A$) is $\sim 66\%$ ($\sim 100\%$ for $B = A$). The odds for winning with dice, if your competitor lets you win for 4 out of the 6 faces are also 66%. If the stakes are this high, would you not play? It is interesting to compare the H -identity-determining integrated luminosities in figs. 1, more so since event numbers on its right refer to the chain $H \rightarrow ZZ \rightarrow e^+e^- \mu^+\mu^-$ and are approximately quadrupled when all 4ℓ channels are considered.

Standard signal and background cross sections times branching ratios were used in fig. 1. In discussing H impostors we accept that they should not be distinguished from a SM H on these grounds, which, for all impostors, are hugely model dependent.

2. – Methodology

The technique to be used to measure J^{PC} for a putative H signal has some pedigree. Its quantum-mechanical version (called nowadays the “matrix element” method) capitalizes on the entanglement of the two Z polarizations and dates back at least to the first (correct) measurements of the correlated γ polarizations in parapositronium (0^{-+}) decay [4]. The technique is even older, as it actually consists in comparing theory and observations. The art is in exploiting *a maximum of the information* from both sides.

The event-by-event information on the channel at hand is very large, some of it is illustrated in fig. 2, for the decay chain $H \rightarrow ZZ \rightarrow e^+e^- \mu^+\mu^-$, with H brought to rest. The angular variables $\vec{\Omega}$ describe Z -pair production relative to the annihilating gg or $q\bar{q}$ pair. The variables $\vec{\omega}$ are the Z -pair decay angles. For fixed $\vec{\Omega}$, $\vec{\omega}$, and M^* (the mass of

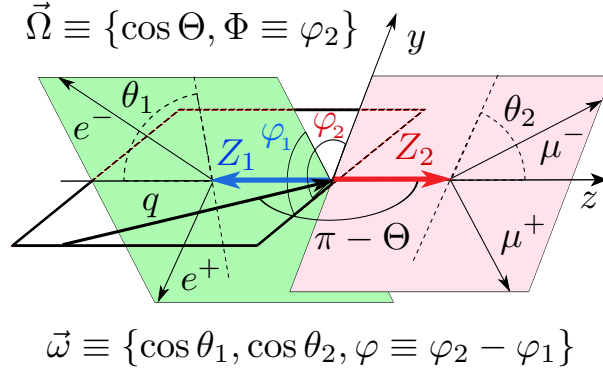


Fig. 2. – The angles of ZZ pair-production and leptonic decay.

a lepton pair if its parent Z is off-shell) that is all there is: none less than six beautifully entangled variables ($M[4\ell]$ is also measured event by event, M_H is traditionally extracted from a fit to the $M[4\ell]$ distribution).

Real detectors have limited coverage in angles and momenta, they “mis-shape” the theoretical distributions in the quantities just described. An example for a realistic detector and an unrealistic flat expectation is illustrated on the right of fig. 3. For an

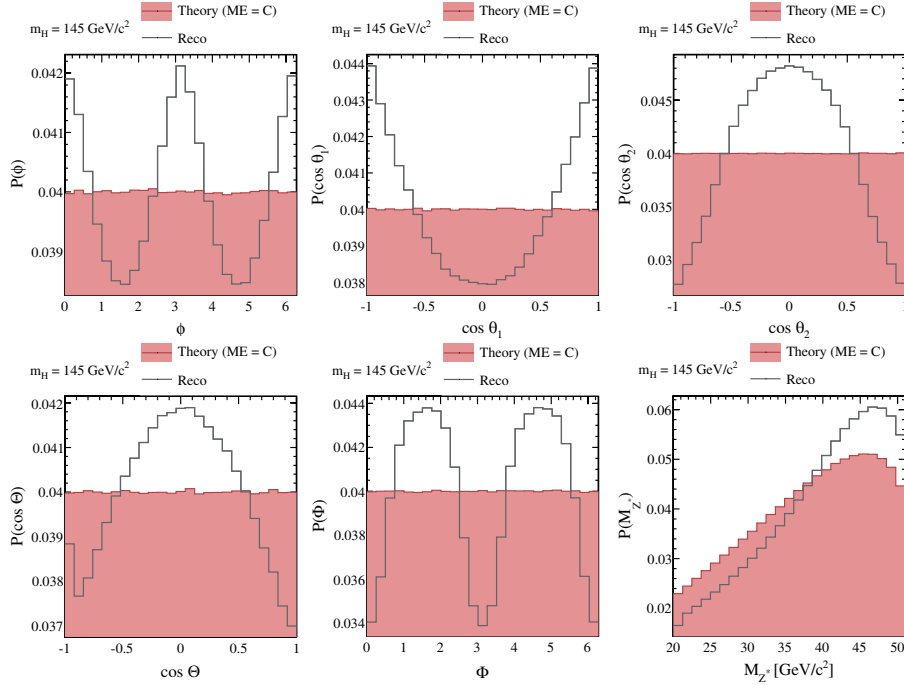


Fig. 3. – Detector-shaping effects at $M_H = 145$ GeV, for all relevant angles and M^* . The trigger and energy thresholds, resolutions and angular coverage are those of a “typical” detector.

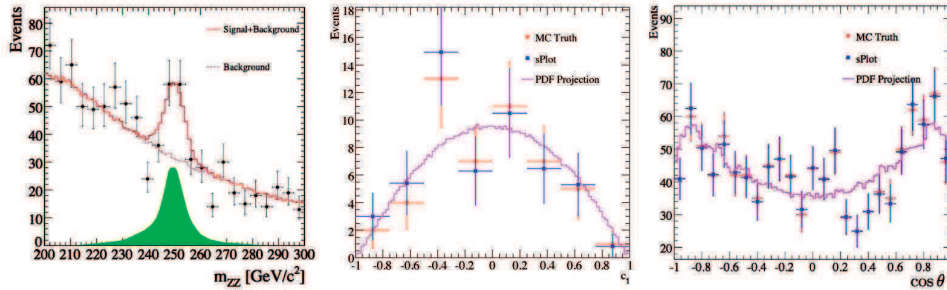


Fig. 4. – Left: a signal on an $M(ZZ)$ distribution. Middle: sPlot of the $\cos\theta$ distribution of the “signal” events, compared with the Monte Carlo truth and the (detector-shaped) expected distribution, for $J^{PC} = 0^{++}$. Right: same as middle, for the “background” events.

H with $J = 0$, the distribution in $\vec{\Omega}$ is flat, so that its inclusion (in this case) would seem like an overkill. Not so! detector-shaping effects and the correlations between the angular variables conspire to make the use of the full machinery a necessity [2].

There is a wonderful “s-weighing” method for (much of) the exercise of ascertaining the LHC’s potential to select the preferred hypothesis for an observed H candidate. Consider an $M[4\ell]$ distribution with an H peak at 250 GeV, constructed with the standard expectations for signal and background, as in fig. 4. Performing a maximum-likelihood fit to this distribution one can ascertain the probability of events in each $M[4\ell]$ bin to be signal or background. Next one can astutely (and even statistically optimally) reweigh the events into “signal” and “background” categories, to study their distributions in other variables [5], such as $\cos\theta = \cos\theta_1$ or $\cos\theta_2$ in fig. 4. In this pseudo-experiment one knows the “Monte Carlo truth”, compared in the figure with the impressive s-outcomes and the detector-shaped expectation. We use the full (correlated) distributions in all mentioned variables, but M_H , to confront “data” with different hypotheses.

The astute reader has noticed that I have not mentioned the η and p_T distributions of the ZZ or ZZ^* pair (be it an H signal or the irreducible background). Event by event, one can undo the corresponding boost but, to ascertain the detector-shaping effects, as in fig. 3, for all the various SM or impostor H objects, one has to use a specific event generator. We have done it [2], but we chose to “pessimize” our results in this respect, *not* exploiting the (η, p_T) distributions as part of the theoretical expectations (which for impostors would be quite model dependent). One reason is that the relevant parton distribution functions (PDFs) will be better known by the time a Higgs hunt becomes realistic. Another is that one can use the s-weigh technique to extract and separately plot the (η, p_T) distribution for signal and background. The production of a SM H —but not that of most conceivable impostors—is dominated by an extremely theory-laden process: gluon fusion via a top loop. As a first step it is preferable *to see* whether or not the (η, p_T) distribution of the s-sieved signal events is that expected for gg fusion, as opposed to $q\bar{q}$ annihilation⁽¹⁾. The answer would be fascinating.

⁽¹⁾ The only impact of the difference between the two processes is on the detector-shaping effects. But these are not large enough for the ensuing differences to affect our results.

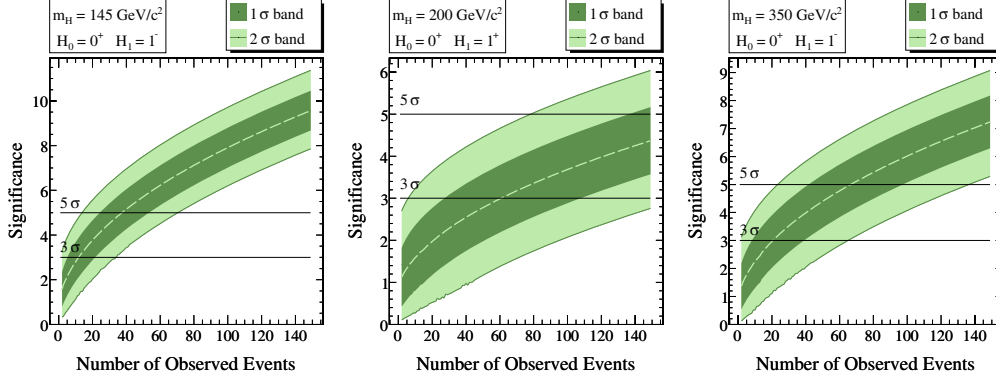


Fig. 5. – Expected confidence levels, as functions of the number of events, to reject the wrong hypothesis (H_0 , the SM in this case) in favour of the right one (H_1). Left and right: H_1 is 1^- , for $M_H = 145$ and 350 GeV. Middle: H_1 is 1^+ , $M_H = 200$ GeV.

3. – Theory

The most general Lorentz-invariant couplings of $J = 0, 1$ particles to the polarization vectors ϵ_1^μ and ϵ_2^α of two Z s of four-momenta p_1 and p_2 are given by the expressions:

$$\begin{aligned} -i L_{\mu\alpha} &= X_0 g_{\mu\alpha} + (P_0 + i Q_0) \epsilon_{\mu\alpha\sigma\tau} p_1^\sigma p_2^\tau / M_Z^2 - (Y_0 + i Z_0) (p_1 + p_2)_\alpha (p_1 + p_2)_\mu / M_Z^2, \\ -i L^{\rho\mu\alpha} &= X_1 (g^{\rho\mu} p_1^\alpha + g^{\rho\alpha} p_2^\mu) + (P_1 + i Q_1) \epsilon^{\rho\mu\alpha\sigma} (p_1 - p_2)_\sigma. \end{aligned}$$

The vertex for $J = 2$ is cumbersome. The quantities $X_i, P_i \dots$ can be taken to be real, but for small absorptive effects. The expressions can be used to derive the distribution functions $\text{pdf}(J^{PC}; M^*, \cos \Theta, \Phi, \cos \theta_1, \cos \theta_2, \varphi)$ allowing one to determine the spin of an H and the properties of the HZZ coupling. To give some $J = 0$ examples: in the SM only $X_0 = g M_Z / \cos \theta_W$ is nonvanishing. For $J = 0^-$ only $Q_0 \neq 0$. If X_0 and Q_0 (or P_0) $\neq 0$, the HZZ vertex violates P (or CP). For a “composite scalar” $X_0, Y_0 \neq 0$.

4. – Some results

While Team 1 members are trying to establish the significance of the discovery of an object of specified properties (as in fig. 1, right), they may, with a few extra lines of code, be extracting much more information from the same data set, by asking leading questions, NLQs,>NNLQs. . . , whose answers are decreasingly statistically significant.

The quintessential LQ is which of two hypotheses describes the data best, assuming that one of them is right. If the hypotheses are “simple” (contain no parameters to be fit) the Neyman-Pearson lemma guarantees that the test is *universally most powerful*. Three examples are given in fig. 5. On its left and right it is seen that it is “easy” (it takes a few tens of events) to rule out the SM, if the observed resonance is an $M_H = 145$ or 350 GeV vector. On its middle, we see that, if the object is an axial vector, it would be much harder. This it is not due to the differing J^P , but to the choice $M_H = 200$ GeV. For masses close to the $H \rightarrow ZZ$ threshold, the level arm provided by the lepton three-momenta is short, and the differences between pdfs is diminished. In fact, as an answer to a NLQ, we have shown that it is “easy” to tell any $J = 0$ from

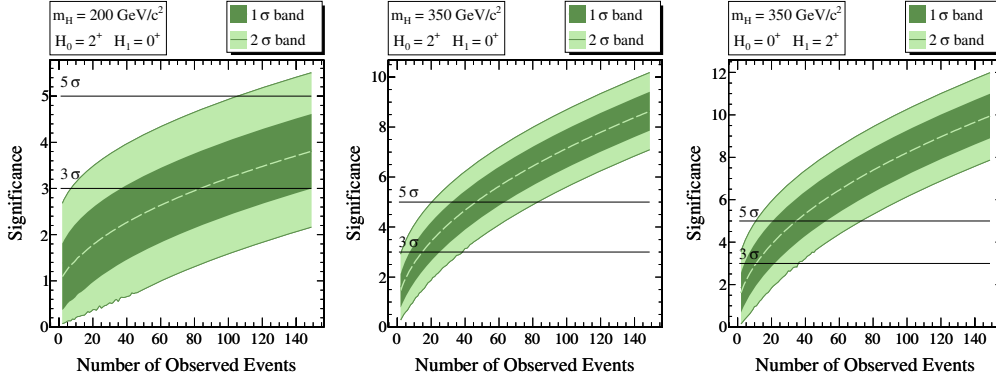


Fig. 6. – The same as fig. 5, with the hypotheses $J^P = 2^+$ and 0^+ , once interchanged.

any $J = 1$ object, no matter how general their HZZ couplings are [2]. In fig. 6 we see that it is easy, if the SM is right, to exclude $J = 2^+$ at $M_H = 350$ GeV, but not at 200. We also see that the interchange of right and wrong hypotheses leads to very similar expectations.

On the right of fig. 7 is the answer to a NNLQ. We have assumed that a composite $J^{PC} = 0^{++}$ Higgs has been found and parametrized its ZZ coupling by an angle $\xi_{XY} = \arctan(Y_0/X_0)$. The measured value of ξ_{XY} is seen to be the input one, but for 50 events the uncertainties on what the input was, to be read horizontally, are large. For this case of a specific J^{PC} , but a complicated coupling, the various terms in the pdf are not distinguishable on grounds of their properties under P and CP . They do strongly interfere for specific values of ξ_{XY} , and the results of fig. 7 are not easy to obtain, requiring a full Feldman-Cousins belt construction [2].

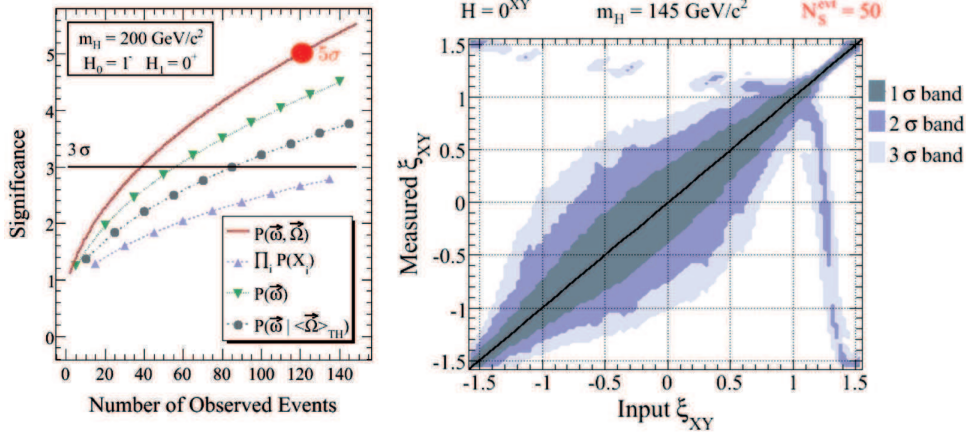


Fig. 7. – Left: various choices of pdfs, employing different sub-optimal choices of likelihood functions, are compared with a pdf containing all angular variables and their correlations. Right: true and measured values of the mixing angle describing a composite scalar, for $M_H = 145$ GeV.

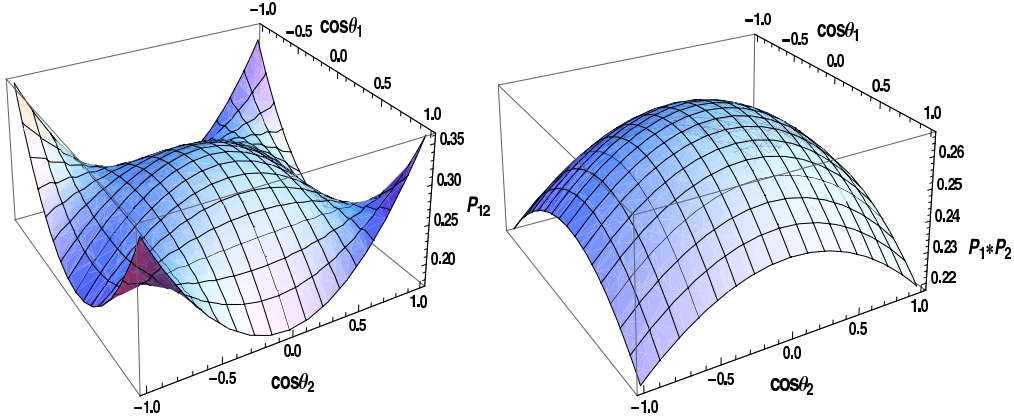


Fig. 8. – The pdfs of the SM at $M_H = 200$ GeV, integrated in all variables but $\cos \theta_1$ and $\cos \theta_2$. Left: the correct $P(\cos \theta_1, \cos \theta_2)$. Right: the “approximation” $P(\cos \theta_1) \times P(\cos \theta_2)$.

Given a small data set constituting an initial discovery, one might settle for a stripped-down analysis. The cost of such a sub-optimal choice is shown on the left of fig. 7 for $M_H = 200$ GeV, illustrating the discrimination between the 0^+ and 1^- hypotheses for likelihood definitions that exploit different sets of variables. N -dimensional pdfs in the variables $\{a_1, \dots, a_N\}$ are denoted $P(a_1, \dots, a_N)$, while $\prod_i P(X_i)$ is constructed from one-dimensional pdfs for all variables, ignoring (erroneously) their correlations. $P(\vec{\omega} | \langle \vec{\Omega} \rangle_{\text{TH}})$ are pdfs including the variables $\vec{\omega}$ and their correlations, but with the hypothesis 1^- represented by a pdf in which the variables $\vec{\Omega}$ have been integrated out. The likelihood $P(\vec{\omega} | \langle \vec{\Omega} \rangle_{\text{TH}})$ performs badly even relative to $P(\vec{\omega})$, which uses fewer angular variables. The two differ only in that the first construction implicitly assumes a uniform 4π coverage of the observed leptons (an assumption customary in the literature) as if the muon p_T and η analysis requirements did not depend on the $\vec{\Omega}$ angular variables.

Treating the correlated angular variables as uncorrelated, as in the $\prod_i P(X_i)$ example of fig. 7, not only degrades the discrimination significance but would lead to absurdly time-dependent conclusions. Assume, for example, the SM with $m_H = 200$ GeV. Let the data be fit to either a fully correlated pdf or an uncorrelated one. The projections of the corresponding theoretical pdfs, involving only the variables $\cos \theta_1$ and $\cos \theta_2$, are illustrated in fig. 8. On the left (right) of the figure we see $P[\cos \theta_1, \cos \theta_2]$ ($P[\cos \theta_1] \times P[\cos \theta_2]$). With limited statistics—insufficient to distinguish between the correlated and uncorrelated distributions—the correct conclusion will be reached: the data are compatible with the SM. But, as the statistics are increased, the data will significantly deviate from the $P[\cos \theta_1] \times P[\cos \theta_2]$ distribution, and a false rejection of the SM hypothesis would become increasingly supported.

The difference between $P[\cos \theta_1, \cos \theta_2]$ and $P[\cos \theta_1] \times P[\cos \theta_2]$ is *precisely* what an unbelieving Einstein called *spooky action at a distance*. But, mercifully for physicists, the Lord is subtle *and* perverse.

5. – Conclusions

I have alleged, by way of example, that for a fixed detector performance and integrated luminosity (and no extra Swiss Francs) it pays to have *ab initio* an analysis combining discovery and scrutiny. This is arguably true for many physics items other than $H \rightarrow 4\ell$. They readily come to mind.

REFERENCES

- [1] GAO Y., GRITSAN A. V., GUO Z., MELNIKOV K., SCHULZE M. and TRAN N. V., arXiv:1001.3396.
- [2] DE RÚJULA A., LYKKEN J., PIERINI M., ROGAN C. and SPIROPULU M., arXiv:1001.5300.
- [3] DJOUADI A., *Phys. Rep. A*, **457** (2008) 1 [arXiv:hep-ph/0503172].
- [4] WU C. S. and SHAKNOV I., *Phys. Rev. A*, **77** (1950) 136.
- [5] PIVK M. and LE DIBERDER F. R., *Nucl. Instrum. Methods A.*, **555** (2005) 356.

SESSION VII - SEARCHING FOR NEW PHYSICS

<i>Martin Schmaltz</i>	New Physics with earliest LHC data
<i>Giancarlo Piredda</i>	First results from the MEG experiment
<i>Bostjan Golob</i>	Super KEKB/Belle II Project
<i>Chris Quigg</i>	Looking into particle production at the Large Hadron Collider
<i>Paolo Spagnolo</i>	Search for neutral Higgs bosons decaying into four taus at LEP2
<i>Mihail V. Chizhov</i>	Anomalously interacting extra neutral bosons

New Physics with earliest LHC data

C. W. BAUER⁽¹⁾⁽²⁾, Z. LIGETI⁽¹⁾⁽²⁾, M. SCHMALTZ⁽¹⁾⁽²⁾⁽³⁾, J. THALER⁽¹⁾⁽²⁾
and D. G. E. WALKER⁽¹⁾⁽²⁾⁽⁴⁾

⁽¹⁾ *Theoretical Physics Group, Lawrence Berkeley National Laboratory
Berkeley, CA 94720, USA*

⁽²⁾ *Berkeley Center for Theoretical Physics, University of California
Berkeley, CA 94720, USA*

⁽³⁾ *Physics Department, Boston University - Boston, MA 02215, USA*

⁽⁴⁾ *Center for the Fundamental Laws of Nature, Jefferson Physical Laboratory
Harvard University - Cambridge, MA 02138, USA*

(ricevuto il 14 Settembre 2010; pubblicato online il 12 Gennaio 2011)

Summary. — We investigate which new physics models could be discovered in the first year of the LHC. Such a “Supermodel” is a new physics scenario for which the LHC sensitivity with only 10 pb^{-1} useful luminosity is greater than that of the Tevatron with 10 fb^{-1} . The simplest supermodels involve s -channel resonances in the quark-antiquark and especially in the quark-quark channels. We concentrate on easily visible final states with small standard model backgrounds, and suggest simple searches, besides those for Z' states, which could discover new physics in early LHC data.

PACS 12.90.+b – Miscellaneous theoretical ideas and models.

1. – Introduction

In this paper, we explore the new physics discovery potential of the first LHC run. A more detailed description of this work can be found in [1]. The latest LHC schedule calls for collisions at 7 TeV throughout much of 2010 and 2011, with the hope of delivering about 100 pb^{-1} integrated luminosity in 2010 and 1 fb^{-1} by the end of 2011 [2, 3]. Given the inherent uncertainties in this schedule, we take a look at the new physics capabilities of a 10 pb^{-1} low-luminosity data set. We allow ourselves to contemplate new physics which is not motivated by model building goals such as unification, weak scale dark matter, or solving the hierarchy problem.

We find that there is a set of interesting new physics scenarios that could give a clean, observable signal in early LHC data, while not being detected with 10 fb^{-1} of Tevatron data (the projected integrated luminosity at the end of 2010). These models are also consistent with previous experiments such as LEP II, precision electroweak constraints, and flavor physics. Moreover, some of these scenarios have similar signatures to “well-motivated” new physics models that require higher luminosity for discovery.

To set the stage, recall that the production cross sections for new hypothetical particles can be quite large. For example, QCD pair production of 500 GeV colored particles have cross sections in the pb range, such that tens of such particles could be produced in early LHC. Of course, in order for the new particles to be observable, they must have sufficiently large branching fractions to final states with distinctive signatures and controllable standard model backgrounds. Also, the new particles should not be ruled out by current or future Tevatron searches, implying that the cross section times integrated luminosity at the LHC should be larger than the corresponding quantity at the Tevatron.

Thus, the four criteria for a new physics scenario to be discovered in early LHC with low luminosity are:

- 1) Large enough LHC cross section for at least 10 signal events with 10 pb^{-1} of data.
- 2) Small enough cross section to evade detection by 2010 at the Tevatron with 10 fb^{-1} .
- 3) Large branching fraction to an “easy” final state with essentially no backgrounds.
- 4) Consistency with other existing bounds.

We call a new physics scenario satisfying these conditions a *supermodel*.

The classic example for a candidate supermodel is a TeV-scale Z' boson [4]. Assuming the Z' mass exceeds the Tevatron reach, but is light enough and has large enough couplings so that it can be produced copiously at the LHC, it can be discovered through its decay to electron and muon pairs. Such leptonic final states are “easy” to reconstruct with a peak in the invariant mass distribution, which reduces the already low standard model backgrounds.

However, a typical leptonically decaying Z' is not a supermodel. First, since the Z' is produced via the quark-antiquark initial state, the Tevatron is quite competitive with the LHC. Second, the leptonic branching fraction is severely bounded by LEP II data, which restricts the couplings of the Z' to leptons. It is therefore nontrivial to find supermodels that are as discoverable as a standard Z' but consistent with known bounds on new physics.

2. – Production modes

In this section, we discuss which production modes have the potential to be supermodels, deferring detailed model building to sect. 3. Since the expected integrated luminosity at the Tevatron ($\sim 10 \text{ fb}^{-1}$) is orders of magnitude larger than our 10 pb^{-1} benchmark luminosity for early LHC analysis, and since $p\bar{p}$ parton luminosities are not so different from pp parton luminosities, one must consider sufficiently heavy new particles to evade the Tevatron reach. We will find that the most promising perturbative scenarios accessible with 10 pb^{-1} of LHC data are $q\bar{q}$ and $q\bar{q}$ resonances.

In fig. 1 we plot the LHC parton luminosities, defined as

$$(1) \quad \mathcal{F}_{ij}(\hat{s}, s) = \int_{\hat{s}/s}^1 dx_i \frac{\hat{s}}{x_i s} f_i(x_i) f_j[\hat{s}/(x_i s)],$$

and the ratios of parton luminosities at the LHC and Tevatron. Here \sqrt{s} is the center-of-mass energy of the collider, $\sqrt{\hat{s}}$ is the invariant mass of the two interacting partons, and $f_i(x_i)$ are parton distribution functions [5] at momentum fraction x_i and scale $\sqrt{\hat{s}}$.

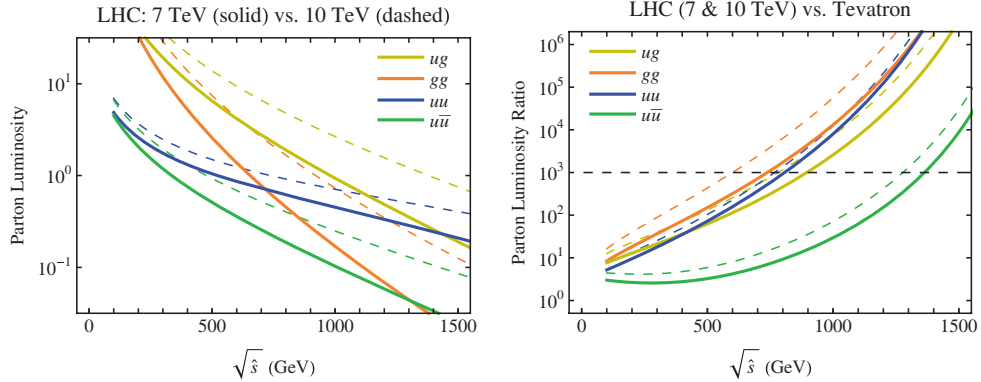


Fig. 1. – Left panel: LHC parton luminosities as defined in eqs. (1), as functions of the partonic invariant mass. The solid (dashed) curves are for the 7 TeV (10 TeV) LHC. The up quark has been chosen as a representative quark, and each curve includes the contribution from the CP conjugate initial partons. Right panel: ratios of the parton luminosities for 7 TeV (solid) and 10 TeV (dashed) LHC compared to the 1.96 TeV Tevatron, as functions of the partonic invariant mass. When this ratio is above the 10^3 horizontal dashed line, the LHC with 10 pb^{-1} will have greater sensitivity than the Tevatron with 10 fb^{-1} .

Figure 1 shows that the gg parton luminosity only dominates for small invariant mass, where the initial LHC data set cannot compete with the Tevatron. At large invariant masses the LHC parton luminosities become sufficiently enhanced compared to the Tevatron. Thus supermodels will always involve high invariant masses in order to beat the Tevatron. We will emphasize this point in the next subsection by showing why QCD pair production is not a supermodel, and then go on to consider supermodels constructed from s -channel resonances.

2.1. QCD pair production? – A simple process initiated by gluons is QCD pair production of new colored particles. For not too heavy states, it can have a cross section above a pb, yielding $\mathcal{O}(10)$ events with 10 pb^{-1} of LHC data. However, such processes are generically not supermodels. For concreteness, we study the production of a color-triplet quark Q . Assuming decays to a highly visible final state and perfect reconstruction efficiencies one can use standard QCD to calculate the largest value of m_Q for which the Tevatron would observe 10 $Q\bar{Q}$ pair production events with 10 fb^{-1} of data. In this idealized example, the hypothetical Tevatron bound is $m_Q > 500 \text{ GeV}$. The same exercise can be repeated for the LHC as a function of the center-of-mass energy and integrated luminosity, and the result is shown in fig. 2.

To reach the Tevatron sensitivity for QCD pair production at a 7 TeV LHC, the required luminosity is about 50 pb^{-1} . While this is likely within the reach of an early LHC run, the LHC will not easily surpass Tevatron bounds in this channel, and it is unlikely that a 5σ LHC discovery is possible without the Tevatron already having seen some events. The situation is improved if there is a large multiplicity of near-degenerate new colored states or if the new states are color octets (like gluinos in supersymmetry). Then the total cross sections are larger by a multiplicity factor and the LHC reach can surpass that of the Tevatron by going to higher masses.

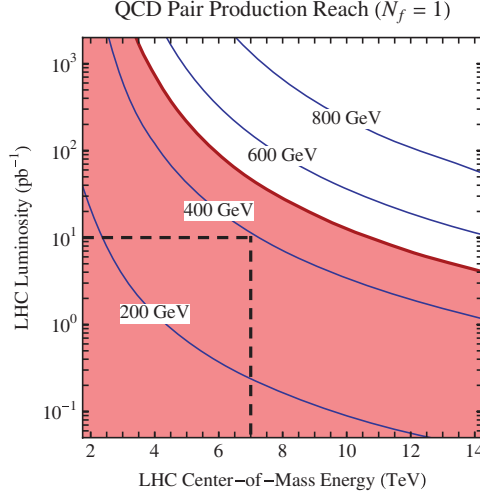


Fig. 2. – LHC reach for pair production of a single flavor of heavy quark as a function of energy and luminosity. Each contour corresponds to the production of 10 events at the LHC for the indicated quark mass. The shaded region corresponds to the would-be Tevatron bound (see text). The intersection of the straight dashed lines corresponds to the maximum quark mass (~ 400 GeV) probed by the 7 TeV LHC with 10 pb^{-1} of data.

2.2. Resonance production. – While pair production of new colored particles is not a supermodel, production of an s -channel resonance has the potential to be a supermodel, as long as the resonance has renormalizable couplings to the partonic initial states. Recall that parametrically the production cross section for a single resonance is enhanced over pair production by a phase space factor of $16\pi^2$.

In the narrow width approximation, we parametrize single resonance production by

$$(2) \quad \sigma(p_i p_j \rightarrow X) = [g_{\text{eff}}^2]_{ij} \delta(\hat{s} - m_X^2),$$

where $p_{i,j}$ denote the two partons which participate in the hard scattering, m_X is the mass of the resonance, and $[g_{\text{eff}}^2]_{ij}$ encodes all information about the production of resonance X from the two partons, including couplings, polarization, and color factors. Using the parton luminosities defined in eq. (1), the hadronic cross section is

$$(3) \quad \sigma(pp \rightarrow X) = \frac{1}{m_X^2} \sum_{ij} [g_{\text{eff}}^2]_{ij} \mathcal{F}_{ij}(m_X^2, s).$$

For the resonances considered in this paper, one production channel dominates, allowing us to drop the ij label from g_{eff}^2 . For reasonably narrow resonances with dimension-four couplings, g_{eff}^2 can be order 1, which is the case for the $q\bar{q}$ and qq initial states. However, for the gg or gq initial states $SU(3)$ gauge invariance forbids renormalizable couplings to a single resonance. Thus the effective coupling of such a resonance either includes a loop factor, or it is suppressed by a high scale. Either way this suppresses cross sections for gg and gq resonances, and we will not consider them further.

In fig. 3, we show our estimate of the generic early LHC reach in m_X , as a function of the energy and luminosity, for the two promising resonance channels $q\bar{q}$ and qq using

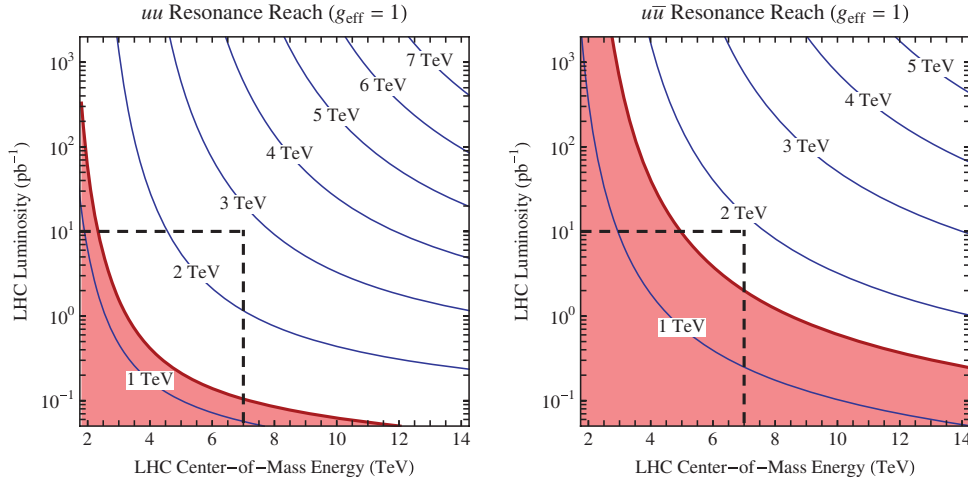


Fig. 3. – (Colour on-line) LHC reach for single resonance production as a function of energy and luminosity. As in fig. 2, the contours show the production of 10 events for a given resonance mass, the red regions show the Tevatron sensitivity with 10 fb^{-1} , and the intersection of the dashed lines shows the maximum resonance mass which can be probed by the 7 TeV LHC with 10 pb^{-1} data. One sees that the early LHC can exceed the Tevatron sensitivity for $q\bar{q}$ and especially for $q\bar{q}$ resonances.

the effective coupling $g_{\text{eff}}^2 \sim 1$. As in fig. 2, we assume 100% branching fraction of X to highly visible final states and assume perfect detector efficiency, though we will relax these assumptions below.

In the $u\bar{u}$ and especially in the uu channels the first LHC run even with modest energy and luminosity will supersede the Tevatron. Thus, $q\bar{q}$ and $q\bar{q}$ resonances are good starting points for constructing supermodels, examples will appear in sect. 3.

2.3. Production of $q\bar{q}$ and $q\bar{q}$ resonances. – The plots in fig. 3 give a rough idea of the LHC discovery potential for s -channel resonances. They are valid for a particular value of the effective coupling, g_{eff}^2 , and assume that the X resonance is observed with 100% efficiency. For $q\bar{q}$ and $q\bar{q}$ resonances, we are interested in the dependence of the reach on g_{eff}^2 and on branching fractions/efficiencies. Here, we introduce a new kind of plot which is convenient for reading off cross sections at the LHC and comparing them to the Tevatron for variable couplings and detection efficiencies. In fig. 4, we plot in the LHC energy *vs.* resonance mass plane the contours of constant production cross section and contours of constant ratio of LHC *vs.* Tevatron cross section.

The solid curves in fig. 4 show contours of constant LHC cross sections for $g_{\text{eff}}^2 = 1$. From these, one can read off how many events are produced for a given LHC luminosity as a function of the resonance mass and the LHC energy. For example, assuming 100% visible decay rate and detection efficiency, the region to the right of the curve labeled “ 10^0 pb ” will yield at least 10 events with 10 pb^{-1} of LHC data. The dashed curves in fig. 4 show contours of constant ratio of LHC *vs.* Tevatron cross sections. From these, one can read off the advantage of the LHC compared to the Tevatron for a given model.

Thus the region in which the LHC has better sensitivity than the Tevatron and yields at least a certain number of events is a “wedge” bounded by a solid and a dashed curve.

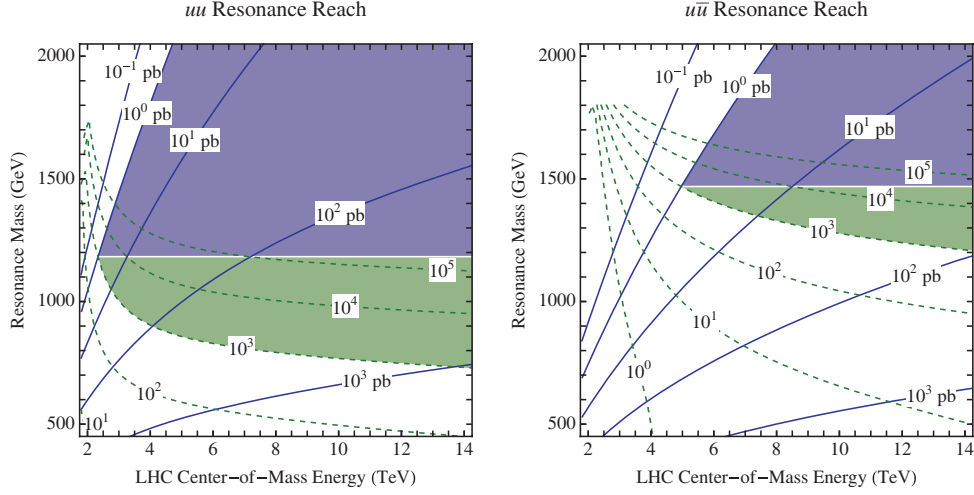


Fig. 4. – (Colour on-line) The LHC reach for uu and $u\bar{u}$ resonances in the LHC energy *vs.* resonance mass plane. The solid lines are contours of constant LHC production cross sections for $g_{\text{eff}}^2 = 1$, and the dashed green lines are contours of constant LHC to Tevatron cross section ratios. The blue shaded regions show where the discovery reach of a 10 pb^{-1} LHC run is beyond that of the 10 fb^{-1} Tevatron. The green regions show where the LHC sensitivity is greater than that of the Tevatron, but the Tevatron can also see at least 10 events.

For example, the wedge to the right of the intersection of the “ 10^0 pb ” and the “ 10^3 ” curves gives the region for which at least 10 events are produced with 10 pb^{-1} of LHC data and the number of events at the LHC is greater than that at the Tevatron. Everywhere in the shaded wedge in fig. 4 the LHC sensitivity is better than that of the Tevatron. However, in the lower region, the sensitivity of the Tevatron is still sufficient to rule out the new physics. Thus only the upper region is the true LHC discovery region.

Using these plots, one can also estimate the minimum value of m_X and $g_{\text{eff}}^2 \mathcal{B} \text{Eff}_{\text{LHC}}$ for a scenario to be a supermodel. Take a $q\bar{q}$ resonance as an example. A 7 TeV and 10 pb^{-1} early LHC run supersedes the Tevatron sensitivity for a $m_X > 1.4 \text{ TeV}$ (the value of the “ 10^3 ” dashed curve at 7 TeV). We can then read off that $g_{\text{eff}}^2 \mathcal{B} \text{Eff}_{\text{LHC}} > 0.1$ is required to observe at least 10 events.

3. – Example supermodels

Considering production cross sections alone, $q\bar{q}$ and qq resonances emerged as the best starting points for constructing supermodels. In this section, we consider some concrete supermodel examples to demonstrate what kind of final states can be obtained from the decay of these resonances. Since we are interested in final states that involve the cleanest signatures and least background contamination, we concentrate on decay chains yielding at least two charged leptons or two other stable charged particles in the final state.

3.1. The case against a standard Z' . – For a $q\bar{q}$ resonance to be supermodel, it must have a large branching fraction to visible final states. In particular, since a $q\bar{q}$ resonance can have zero electric charge, it is natural for such a resonance to decay to pairs of oppositely charged leptons, in particular e^+e^- and $\mu^+\mu^-$. However, the same resonance

also induces a low energy effective four-lepton vertex, and such operators are severely constrained by LEP II. As recently emphasized in ref. [6], once the LEP II bound is imposed, the branching fraction of the $q\bar{q}$ resonance to $\ell^+\ell^-$ has to be too small to realize a supermodel. There are ways to evade this conclusion. Since the LEP II bound only applies for the electron coupling, one could imagine coupling the Z' only to muons. However, such flavor non-universal couplings typically require significant fine-tuning to avoid constraints from flavor changing neutral currents.

3'2. Decays to quasi-stable particles. – While the decay of a Z' to standard model charged leptons does not give a viable supermodel example of topology A, one could imagine a $q\bar{q}$ resonance that instead decayed with a large branching fraction to new quasi-stable charged particles. Since ATLAS and CMS trigger on penetrating charged particles as if they were muons [7], such scenarios are as visible in the early LHC data as a Z' decaying to muons. Alternatively, one could consider a Z' that decayed to quasi-stable colored particles that then form R -hadron-like bound states with QCD partons. Such R -hadron final states could potentially be visible in early LHC data, though charge flipping interactions [7] complicate both triggering and momentum reconstruction.

3'3. Fun with diquarks. – From fig. 4, one sees that qq resonances can yield an impressive early LHC reach. Such resonances are known as diquarks, and they have spin zero or one, carry baryon number $2/3$, and electric charge $4/3$, $1/3$ or $-2/3$. They may transform as a $\mathbf{6}$ or $\mathbf{\bar{3}}$ of color. Their couplings are necessarily non-trivial in flavor space because the initial quarks carry flavor. Flavor changing neutral currents impose constraints on couplings of new states with masses of order TeV and large couplings to first generation quarks. We chose diquarks with the same flavor quantum numbers as the quarks which produce them, allowing the couplings of the diquark to quarks to be flavor invariant.

To be concrete, we consider a spin-zero and color-six diquark D , with couplings to the $SU(2)$ singlet up-type quarks only and symmetric in flavor indices. The production operator can be written as $\mathcal{O}_D = \frac{\kappa_D}{2} D u^c u^c$, where u^c are the up-type singlet quarks and D is the diquark. Then the partonic cross section is

$$(4) \quad \sigma(uu \rightarrow D) = \frac{\pi}{6} \kappa_D^2 \delta(\hat{s} - m_D^2).$$

If \mathcal{O}_D were the only coupling of the diquark, then any produced diquark would simply decay back to the initial state with a partial width given by $\Gamma = \kappa_D^2 m_D / (16\pi)$. To be a supermodel, the diquark has to have a large branching fraction to a visible final state. By color conservation, diquark decays must yield at least two jets in the final state, so the most Z' -like decay possible for a diquark yields two oppositely charged leptons in addition to two jets in the final state.

For example, we can introduce a vector-like fermion L and L^c , with the quantum numbers $L = (6, 1, 7/3)$ under $SU(3)_C \times SU(2)_L \times U(1)_Y$. Given its quantum numbers, L/L^c would be called a “leptodiquark”. The diquark can decay via the operator $\bar{\kappa}_D D L^c e^c$ with a decay width of $\Gamma = \bar{\kappa}_D^2 m_D / (16\pi)$. Thus, as long as $\bar{\kappa}_D > \kappa_D$, the diquark preferentially decays to the leptodiquark and a lepton. The L^c will finally decay via its two couplings given above leading to the full decay chain:

$$(5) \quad uu \rightarrow D \rightarrow \ell^- L \rightarrow \ell^- \ell^+ 2j.$$

While this diquark-leptodiquark system may strike the reader as baroque, the identical decay topology appears in the case of a W'_R gauge boson [8,9], where the diquark plays the role of the W'_R and the leptodiquark plays the role of a right-handed neutrino. However, discovering a left-right symmetric model through this channel typically requires 1 fb^{-1} of LHC data, whereas the diquark-leptodiquark example motivates a search for the $2j+\ell^+\ell^-$ final state in early LHC data.

3'4. Resurrecting pair production. – In subject. 2'1, we argued that QCD pair production of new colored resonances was not a supermodel. However, one could still get pair production of new particles via decay of a supermodel resonance.

For example, using either a $q\bar{q}$ or a qq resonance, one can produce vector-like up-type quarks U and U^c with quantum numbers $U = (3, 1, 2/3)$. They can be produced via the Z' through $Z' \rightarrow \bar{U}U$ or via the diquark through $D \rightarrow U^c U^c$. If these new colored particles were exactly stable, they would form R -hadron-like bound states as mentioned above. However, the heavy U/U^c quarks could also decay via small CKM-like mixings with the standard model quarks, leading to $U \rightarrow Z+u/c/t$ and $U \rightarrow W+d/s/b$. However, such decays are not ideal for making a supermodel, since the W (Z) boson only has 22% (7%) branching fraction to electrons and muons.

Another option to force leptons to appear in the final state is to have a resonance decay to pairs of colored particles that also carry lepton number such as leptoquarks.

Finally, a neutral $q\bar{q}$ resonance can dominantly decay to two secondary resonances that carry no standard model charges. These secondary resonances have a huge range of possible final states. Such scenarios will be supermodels as long as the secondary resonances have an $\mathcal{O}(1)$ branching fraction to highly visible final states.

* * *

This work was supported in part by the Director, Office of Science, Office of High Energy Physics of the U.S. Department of Energy under contract DE-AC02-05CH11231. MS is supported by DE-FG02-01ER-40676. JT acknowledges support from the Miller Institute for Basic Research in Science. DW was supported by a University of California Presidential Fellowship. MS and JT thank the Aspen Center for Physics for their hospitality while this work was in preparation.

REFERENCES

- [1] BAUER C. W., LIGETI Z., SCHMALTZ M., THALER J. and WALKER D. G. E., arXiv:0909.5213 [hep-ph].
- [2] MYERS S., *LHC Machine Status Report*, in *101st LHCC Meeting, Geneva, Switzerland, 5–6 May 2010*, <http://indico.cern.ch/conferenceDisplay.py?confId=92525>.
- [3] *LHC Performance Workshop, Chamonix, France, 25–29 January 2010*, <http://indico.cern.ch/conferenceOtherViews.py?view=standard&confId=67839>.
- [4] See the review *Z'-boson searches*, in AMSLER C. *et al.* (PARTICLE DATA GROUP), *Phys. Lett. B*, **667** (2008) 1.
- [5] LAI H. L. *et al.* (CTEQ COLLABORATION), *Eur. Phys. J. C*, **12** (2000) 375 [hep-ph/9903282]; and <http://www.phys.psu.edu/~cteq/>.
- [6] SALVIONI E., VILLADORO G. and ZWIRNER F., *JHEP*, **0911** (2009) 068 [arXiv:0909.1320]; SALVIONI E., STRUMIA A., VILLADORO G. and ZWIRNER F., arXiv:0911.1450.
- [7] FAIRBAIRN M., KRAAN A. C., MILSTEAD D. A., SJOSTRAND T., SKANDS P. and SLOAN T., *Phys. Rep.*, **438** (2007) 1 [hep-ph/0611040].
- [8] AAD G. *et al.* (THE ATLAS COLLABORATION), arXiv:0901.0512.
- [9] BAYATIAN G. L. *et al.* (CMS COLLABORATION), *J. Phys. G*, **34** (2007) 995.

First results from the MEG experiment

G. PIREDDA on behalf of the MEG COLLABORATION

INFN, Sezione di Roma Sapienza - Rome, Italy

(ricevuto il 14 Settembre 2010; pubblicato online il 13 Gennaio 2011)

Summary. — The MEG experiment, searching for the rare decay $\mu^+ \rightarrow e^+\gamma$, started the data taking at PSI in 2008. Based on data from the initial three months of operation an upper limit on the branching ratio $\text{BR}(\mu \rightarrow e\gamma) < 2.8 \cdot 10^{-11}$ at 90% confidence level is reported. This corresponds to the measurement of positrons and photons from $\sim 10^{14}$ stopped μ^+ -decays by a superconducting positron spectrometer and a 900 litre liquid-xenon photon detector.

PACS 13.35.-r – Decays of leptons.

PACS 13.35.Bv – Decays of muons.

1. – Introduction

The MEG experiment [1] aims at the search for the lepton flavor violating decay $\mu \rightarrow e\gamma$ with a sensitivity of 10^{-13} in the branching ratio, improving the current limit [2] by two orders of magnitude.

The long quest (see fig. 1) for the $\mu \rightarrow e\gamma$ started many decades ago, in the forties of the 20th century. It is interesting to note that the search for the nowadays exotic decay marks different periods of the long process of building the Standard Model (SM) of the elementary particles. In fact in the pioneer search of the $\mu \rightarrow e\gamma$ in the cosmic radiation, the goal was just to determine the nature of the recently ascertained μ meson particle. Later on in the 60-ies pions at rest produced by the new accelerators were used and the lack of a signal at 10^{-3} level was a clear indication of the existence of (at least) two neutrino species. Finally dedicated muon beams become available allowing better sensitivities able to set stringent constraints on new physics models. Let us notice that despite the $\nu_\mu \rightarrow \nu_e$ oscillation has been established, yet the 10^{-54} SM branching ratio prediction is experimentally out of reach. In extensions of SM, lepton flavor violation rates may become much larger [3, 4] and experimentally accessible. Hence improving existing experimental bounds, is of great relevance to search for new physics, especially on the very sensitive $\mu \rightarrow e\gamma$ channel.

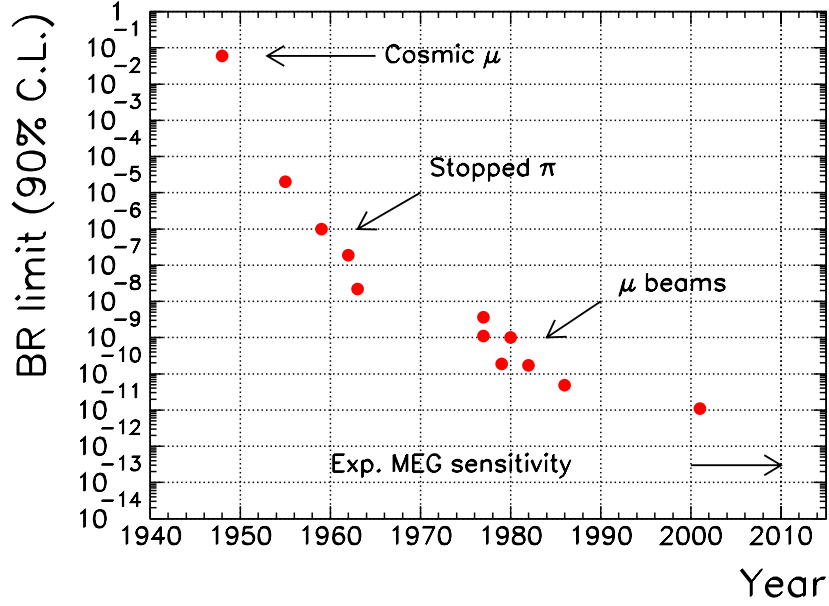


Fig. 1. – The $\mu \rightarrow e\gamma$ upper limit as a function of the year. The MEG expected sensitivity is also shown.

2. – Signal signature and the backgrounds

The $\mu \rightarrow e\gamma$ signal has a simple topology if the muon decays at rest, and appears as two-body final state of a positron and a γ -ray, emitted back-to-back with an energy of 52.8 MeV each, corresponding to half of the muon mass. The signal detection is, in principle, rather easy. One needs in fact to have a very intense continuous muon beam and to measure the positron and photon energies (E_e, E_γ), the relative angle $\theta_{e\gamma}$ and the time difference $t_{e\gamma}$. However to achieve the mentioned sensitivity, the following very high resolutions are needed: $\delta E_e/E_e = 0.35\%$, $\delta E_\gamma/E_\gamma = 1.8\%$, $\delta t_{e\gamma} = 65$ ps, $\delta\theta_{e\gamma} = 10$ mrad. These are very ambitious goals that can be achieved only with optimized detectors and very careful calibrations.

The backgrounds come from the radiative muon decay (RMD) $\mu \rightarrow e\nu\nu\gamma$ and the accidental coincidences between a positron from the normal Michel decay ($\mu \rightarrow e\nu\bar{\nu}$) and a high energy photon from RMD decay, positron annihilation in flight or bremsstrahlung. The accidental events dominate and it can be shown that the expected contribution is $N_{acc} = R_\mu^2(\Delta\theta_{e\gamma})^2(\Delta E_\gamma)^2\Delta t_{e\gamma}\Delta E_e$, where R_μ is the muon beam rate and the other terms are the resolutions on the measured observable already mentioned.

3. – The detector

The MEG experiment (fig. 2) is located at the Paul Scherrer Institut (PSI) in Switzerland and operates at the 590 MeV proton cyclotron. Three key elements enable the excellent sensitivity of the experiment: i) a high rate continuous muon (positive to avoid formation of muonic atoms and muon capture) beam, ii) an innovative liquid-xenon (LXe) scintillation γ -ray detector [5], and iii) a specially designed positron spectrometer [6] with a gradient magnetic field (0.4–1.2 T) and a scintillation timing-counter array

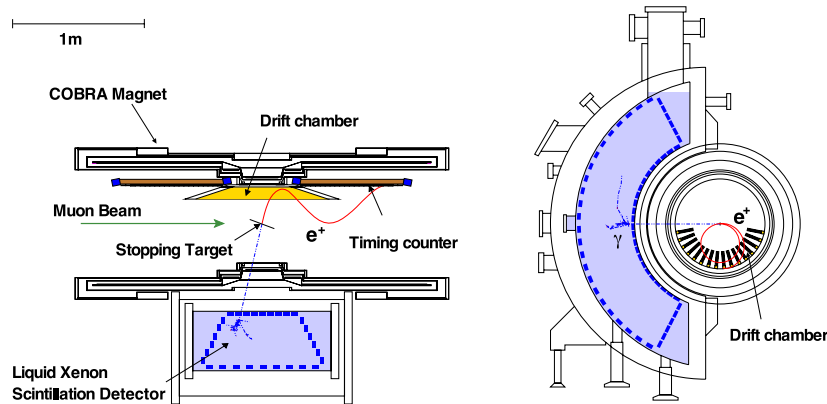


Fig. 2. – Top (left) and front (right) view of the MEG detector.

for fast timing and triggering [7].

Surface muons of $28 \text{ MeV}/c$ from the $\pi E5$ channel at PSI are stopped in a $18 \text{ mg}/\text{cm}^2$ thin polyethylene target. The transport system, which includes a Wien filter and a superconducting transport solenoid, is able to separate to 7.5σ the eight time more abundant positron contamination to provide a pure muon beam. Positrons from the muons decaying in the target are detected by a system of drift chambers (DCH) immersed in a superconducting gradient field magnet. The magnet, ranging from 1.27 T at the center to 0.49 T at either end, has been designed in such a way that the trajectory of positron from the target with the same momentum is independent of the emission angle, optimizing the DCH acceptance and sweeping away low momentum particles more efficiently, compared to a uniform field.

The drift chambers are sixteen radial modules placed on a half circumference around the target. A module has two staggered layers of anode wire planes each of nine cells. The two layers are separated and enclosed by $12.5 \mu\text{m}$ thick cathode foils with a Vernier pattern structure used for the precise z -coordinate determination. A (50:50) helium-ethane gas mixture is used allowing a low mass structure of only $2.0 \cdot 10^{-3} X_0$ along the positron trajectory.

The positron time is measured by the Timing Counters (TC). Each of the two sectors (up and downstream the target) of the TC is made of $15 \cdot 4 \times 4 \times 80 \text{ cm}^3$ BC404 plastic scintillating bars with approximately square cross-section, placed parallel to the z -axis (μ -beam direction), along a circumference with a radius of about 30 cm from the target. Each bar is read-out at either end by a fine-mesh photomultiplier tube able to stand the spectrometer magnetic field.

The total energy of the photon as well as the time and the position are measured in a 9001 LXe calorimeter whose scintillation light is detected by 846 photomultiplier tubes internally mounted on all surfaces. The use of liquid xenon ensures fast response, large light yield and short radiation length.

3.1. Trigger and data acquisition. – All the signals coming from the detector are processed by two waveform digitizers in parallel. A 2 GHz custom digitizer (DRS [8]) is used for offline analysis and its resolution is mandatory to search for possible pile-up effects. A 100 MHz FADC-based digitizer is used for trigger purposes. It receives the

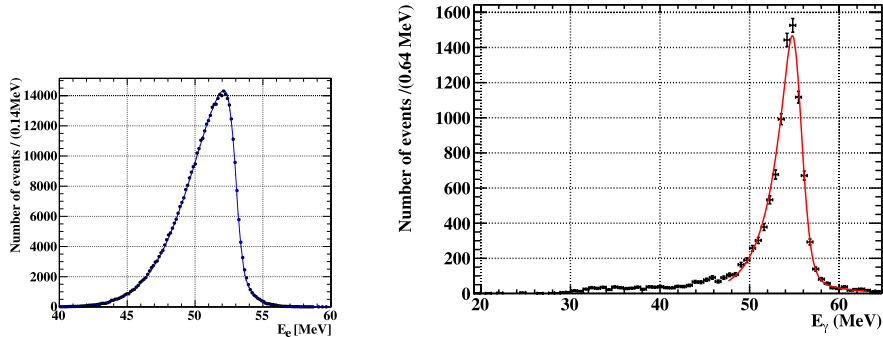


Fig. 3. – Measured Michel positron energy (left) and measured energy for 54.9 MeV photons (right). The solid lines are the respective fit functions.

signals from the LXe detector and the TC and selects on-line events with a photon energy around 52.8 MeV, a time coincident positron hit on the TC and a rough collinearity of the two particles. This reduces the flux from the initial $3 \cdot 10^7 \mu$ decays per second to an acquisition rate of ~ 7 Hz.

3.2. Calibration. – The performances of the detector and their stability as a function of the time have been monitored with extreme care. Standard checks have been done for the LXe temperature and pressure and the DCH gas composition and pressure. More sophisticated measurements have been routinely performed for the LXe energy calibration and the TC-LXe time synchronization. The outmost important methods for calibrating rely on the exploitation of a Cockcroft-Walton 1 MeV auxiliary accelerator. Photons of 17.67 MeV from ${}^7\text{Li}(p, \gamma){}^8\text{Be}$ allow the calibration of the LXe energy scale (in the low energy region) while two simultaneous photons from the reaction $\text{B}(p, \gamma)\text{C}$ detected in the LXe and TC determine the time offsets of the TC bars.

Letting a beam of negative pions impinge on a hydrogen target we took data from the charge exchange process $\pi^- p \rightarrow \pi^0 n$ (CEX). The 54.9 MeV photons from the π^0 decay (fig. 3) were used for the absolute energy calibration of the LXe calorimeter and to extract its energy resolution which is about 5.5% FWHM.

Positron energy scale and resolution were found by fitting the edge of the Michel spectrum on data (fig. 3). We parameterize the resolution function with a core Gaussian component (60%) with a sigma of 374 keV and two tails with sigma 1.06 MeV and 2.00 MeV contributing 33% and 7%, respectively. This performance is far from the goal and is due to the instability of the DCH in the course of the run. This problem has been solved during the 2009 shutdown.

Intrinsic time resolution of TC bars were extracted by comparing times measured in two adjacent bars by the same positron passing through. We find a value better than 60 ps. The $t_{e\gamma}$ time resolution has been studied and monitored by taking RMD events at reduced beam intensity by relaxing the trigger requirement to include acollinear positron and photons. Moreover we are able to see the RMD $t_{e\gamma}$ peak also during normal physics run (see fig. 4) and to estimate a time resolution for the signal of (148 ± 17) ps.

The angular resolutions, $\sigma_\theta = 18$ mrad and $\sigma_\phi = 10$ mrad, were found by fitting separately two segments of the same track and propagating them to the point of closest approach to the beam axis.

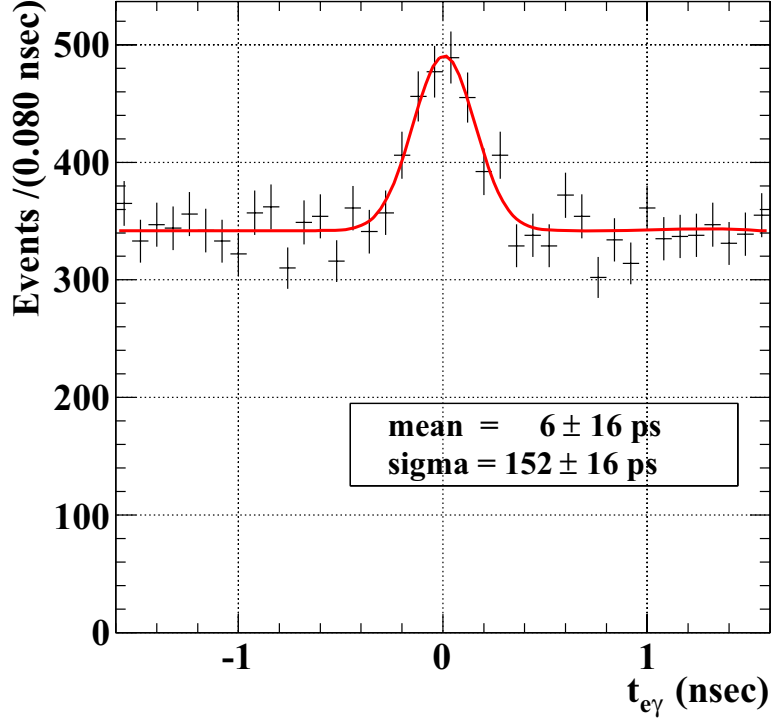


Fig. 4. $-t_{e\gamma}$ distribution for RMD events taken during normal data taking with the selection $40 \text{ MeV} < E_\gamma < 45 \text{ MeV}$.

4. – Data analysis and result

Thanks to the excellent performance of the PSI cyclotron, we collected data corresponding to about $9.5 \cdot 10^{13}$ muons stopped on target in a period of 10 weeks which represents about the 10% of the total foreseen statistics. We adopt a blind analysis technique. Events with E_γ close to 52.8 MeV and $t_{e\gamma}$ close to 0 were removed from the main stream until the full analysis was finalized to avoid any biases. The analysis algorithms were calibrated and validated in a large data sample in a kinematical region where no signal is expected (the sidebands) out of the blind box. The upper limit on the number of the signal events is determined by a maximum likelihood fit in the analysis region defined by $46 \text{ MeV} < E_\gamma < 60 \text{ MeV}$, $50 \text{ MeV} < E_e < 56 \text{ MeV}$, $|t_{e\gamma}| < 1 \text{ ns}$, $\theta_{e\gamma}, \phi_{e\gamma} < 100 \text{ mrad}$.

An extended likelihood function L is constructed as

$$(1) \quad \mathcal{L}(N_s, N_{\text{RMD}}, N_b) = \frac{N^{\text{Nobs}} e^{-N}}{N_{\text{obs}}!} \prod_{i=1}^{N_{\text{obs}}} \frac{1}{N} [N_{\text{sig}} S + N_{\text{RMD}} R + N_b B],$$

where N_s , N_{RMD} , N_b are the number of the signal, RMD and accidental background events with their respective PDFs S, R and B. N_{obs} is the number ($= 1189$) found in the analysis window and $N = N_s + N_{\text{RMD}} + N_b$. Each PDF is the product of the specific PDF associated to each variable and determined as follows. The probability density functions for the signal, the RMD and the accidental background were taken from data whenever

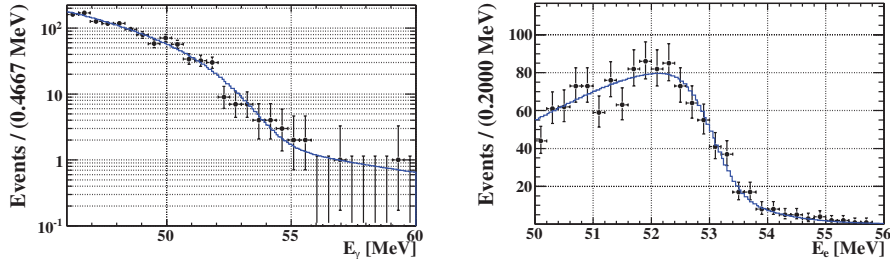


Fig. 5. – E_γ (left) and E_e (right) distributions for all the events in the analysis window. The line is the likelihood function fit.

possible or from Monte Carlo computations using experimental inputs. In particular for the signal E_γ was taken from MC, E_e and $\theta_{e\gamma}$ from data and $t_{e\gamma}$ from the RMD sample. For the RMD component the energies and the angle were extracted from a MC simulation based on the Kuno-Okada [9] model while $t_{e\gamma}$ was taken from data as for the signal. Finally for the accidental background E_γ and $\theta_{e\gamma}$, were extracted from a fit to a $t_{e\gamma}$ sideband, E_e from data and for $t_{e\gamma}$ a flat distribution was taken. The distributions of photon and positron energies in the analysis window are shown in fig. 5, together with the projections of the fitted likelihood function.

The 90% confidence levels (c.l.) on N_{sig} and N_{RMD} are determined by the Feldman-Cousins method [10]. A contour of 90% c.l. on the $(N_{\text{sig}}, N_{\text{RMD}})$ plane is built by a toy Monte Carlo simulation. We obtain an upper limit on $N_{\text{sig}} < 14.7$ including the systematic error.

The largest contribution comes from the uncertainty of the selection of photon pile-up events ($\Delta N_{\text{sig}} = 1.2$), the response function of the positron energy ($\Delta N_{\text{sig}} = 1.1$), the photon energy scale ($\Delta N_{\text{sig}} = 0.4$) and the positron angular resolution ($\Delta N_{\text{sig}} = 0.4$).

The upper limit on $\text{BR}(\mu \rightarrow e\gamma)$ is computed by normalizing the u.l. on N_{sig} to the number of Michel decay positrons counted simultaneously with the signal and using the same analysis cut and taking into account the small differences in efficiencies and acceptances. In this way, the result is independent of the instantaneous beam rate and is almost insensitive to the positron acceptance and efficiency associated with the DCH and TC.

The final result turns out to be $\text{BR}(\mu \rightarrow e\gamma) < 2.8 \cdot 10^{-11}$ at 90% c.l. [11]. This result can be compared with the estimated sensitivity of the experiment with the available data sample. This is defined as the mean of the distribution of the upper limit computed by toy Monte Carlo simulations and assuming no signal and the same number of accidental background and RMD events as in the data. The mean of the distribution is $1.3 \cdot 10^{-11}$, which is comparable with the present best limit established by MEGA [2], while the probability to obtain an upper limit greater than $2.8 \cdot 10^{-11}$ is 5%.

5. – Conclusions and perspectives

After a start-up engineering run in 2007 we had the first MEG physics run at the end of 2008, which suffered from detector instabilities. Data from the first three months of operation of the MEG experiment give a result which is competitive with the previous limit. During 2009 shutdown the problem with the drift chamber instability was

solved and the detector operated for all the 2009 run without degradation. Additional physics data were taken in November and December 2009 with many improvements regarding efficiency, electronics and resolutions. We are confident, therefore, in obtaining a sensitivity that should allow us to improve the present experimental limit.

* * *

I am grateful to the many MEG colleagues who helped me in the preparation of the talk and of these proceedings. A special thank to the Conference Organizers that invited me to present MEG and to enjoy the beautiful slopes of La Thuile.

REFERENCES

- [1] BALDINI A. *et al.* (MEG COLLABORATION), Research Proposal to PSI R-99-05 (1999).
- [2] BROOKS M. L. *et al.* (MEGA COLLABORATION), *Phys. Rev. Lett.*, **83** (1999) 1521.
- [3] BARBIERI R. *et al.*, *Nucl. Phys. B*, **445** (1995) 225.
- [4] CALIBBI L. *et al.*, *Phys. Rev. D*, **74** (2006) 116002.
- [5] SAWADA R., *Nucl. Instrum. Methods A*, **623** (2010) 258.
- [6] HILDEBRANDT M., *Nucl. Instrum. Methods A*, **623** (2010) 111.
- [7] DUSSONI S. *et al.*, *Nucl. Instrum. Methods A*, **617** (2010) 387.
- [8] RITT S., *Nucl. Instrum. Methods A*, **518** (2004) 470.
- [9] KUNO Y. and OKADA Y., *Rev. Mod. Phys.*, **73** (2001) 151.
- [10] FELDMAN G. J. and COUSINS R. D., *Phys. Rev. D*, **57** (1998) 3873.
- [11] ADAM J. *et al.* (MEG COLLABORATION), *Nucl. Phys. B*, **834** (2010) 1.

Super KEKB/Belle II Project

B. GOLOB(*)

*Faculty of Mathematics and Physics, University of Ljubljana and Jozef Stefan Institute
Ljubljana, Slovenia*

(ricevuto il 14 Settembre 2010; pubblicato online il 12 Gennaio 2011)

Summary. — We present the status of the KEKB accelerator and the Belle detector upgrade, along with several examples of physics measurements to be performed with Belle II at Super KEKB.

PACS 07.05.Fb – Design of experiments.

PACS 14.40.Nd – Bottom mesons.

1. – Introduction

The B factories—the Belle detector taking data at the KEKB collider in KEK [1, 2] and the BaBar detector [3] at the PEP II in SLAC—have in more than a decade of data taking outreached the initial expectations on the physics results. They proved the validity of the Cabibbo-Kobayashi-Maskawa model of the quark mixing and CP violation (CPV). Perhaps even more importantly, they pointed out few hints of discrepancies between the Standard Model (SM) predictions and the results of the measurements. Facing the finalization of the data-taking operations the question thus arises about the future experiments in the field of heavy flavour physics, to experimentally verify the current hints of possible new particles and processes often addressed as the New Physics (NP). Part of the answer are the planned Super B factories in Japan and Italy, that could perform highly sensitive searches for NP, complementary to the long expected ones at the Large Hadron Collider. The so-called precision frontier represented by the two machines requires the achieved luminosities of the B factories to be raised by $\mathcal{O}(10^2)$. In the present paper we summarize the plan and the status of the Belle detector upgrade (Belle II) at the upgraded KEKB (Super KEKB) e^+e^- collider.

In the following section we first briefly discuss the necessary upgrade of the KEKB accelerator. In subsects. 3.1 to 3.3 we summarize the upgrade of the vital parts of the Belle detector—the vertexing, the particle identification system and the electromagnetic

(*) Representing the Belle II Collaboration.

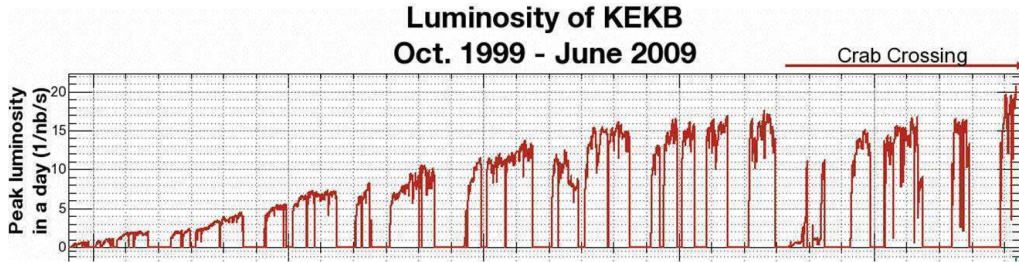


Fig. 1. – Daily peak luminosity of the KEKB collider.

calorimeter, respectively. The upgrade is illustrated with examples of planned measurements that will greatly benefit from the improved collider and detector performance. Finally we draw short conclusions in sect. 4.

2. – From KEKB to Super KEKB

The KEKB accelerator is an asymmetric e^+e^- collider operating at and near the center-of-mass energy of 10.58 GeV, corresponding to the mass of the $\Upsilon(4S)$ resonance. The asymmetry of the beams results in a Lorentz boost factor of $\beta\gamma = 0.425$ which enables the time-dependent measurements in the system of B mesons. The history of the KEKB luminosity is presented in fig. 1. The highest luminosity ever reached in the accelerator ($2.1 \times 10^{34} \text{ cm}^{-2} \text{ s}^{-1}$) is a result of the crab cavities installed in 2007 [4]. The continuous injection scheme and a very stable operation made it possible to collect data corresponding to the integrated luminosity of more than 1 ab^{-1} .

The luminosity of the collider is governed by several factors. The crucial ones for the upgrade of the KEKB are⁽¹⁾ the beam currents (I_{\pm}), the vertical beta function at the interaction point ($\beta_{y\pm}^*$) and the beam-beam parameter $\xi_{y\pm}$. To start from the latter, the beam-beam parameter, $\xi_{y\pm} = \sqrt{\beta_{y\pm}^*/\epsilon_y}$, will remain almost unchanged at Super KEKB, $\xi_{y\pm} \sim 0.1$. The beta function, however, will be extremely reduced: $\beta_{y\pm}^* = 5.9 \text{ mm}/5.9 \text{ mm} \rightarrow 0.27 \text{ mm}/0.41 \text{ mm}$ ⁽²⁾. The emittance will be reduced accordingly to match the current $\xi_{y\pm}$. Both beam currents will be also increased by roughly a factor of two. In terms of the e^+e^- bunches the foreseen upgrade corresponds to the reduction of the current size in direction perpendicular to the beam direction from $\sigma_x \sim 100 \mu\text{m}$, $\sigma_y \sim 2 \mu\text{m}$ to $\sigma_x \sim 10 \mu\text{m}$, $\sigma_y \sim 60 \text{ nm}$. To achieve the desired goal the main tasks during the upgrade will be the installation of longer bending radius in the LER, more arc cells in the HER, re-design of the interaction region with the new final focusing quadrupoles closer to the interaction point, new beam pipe and a new damping ring (see fig. 2). The outstanding problems are a rather small dynamic aperture, larger Touschek background and consequently a shorter lifetime of the beams, directly affecting the luminosity. To cope with these the upgrade includes an increased crossing angle of the two beams (from 22 mrad to 83 mrad) and a slightly smaller asymmetry of the beams (from 3.6 GeV/8 GeV to 4 GeV/7 GeV).

⁽¹⁾ The subscripts \pm denote the high energy electron and the low energy positron beam, HER and LER, respectively.

⁽²⁾ Due to the so-called hourglass effect this requires also a reduction of the $\beta_{x\pm}^*$.

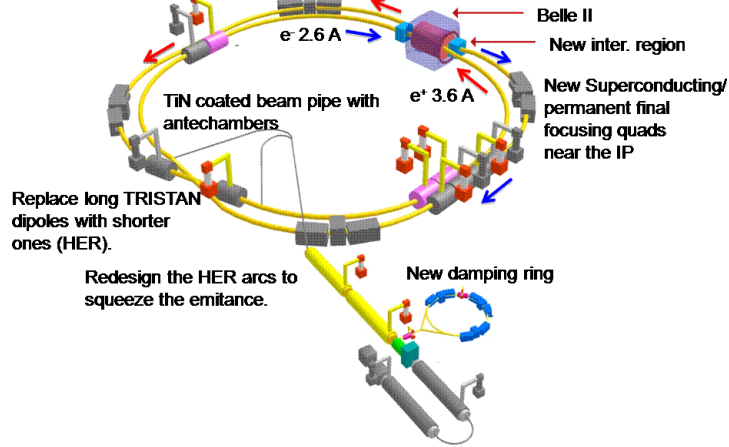


Fig. 2. – The main parts of the KEKB upgrade.

The luminosity of the Super KEKB will reach $\mathcal{L} = 8 \times 10^{34} \text{ cm}^{-2} \text{ s}^{-1}$. Assuming the startup of the machine in 2014, and a rather conservative increase of the starting luminosity to the design value, already in two years of data-taking the available data sample will correspond to 5 ab^{-1} . Integrated luminosity of 50 ab^{-1} is expected in 2020. To illustrate the precision that could be achieved with such a large sample of B meson decays we use the measurement of the lepton forward-backward asymmetry A_{FB} in $B \rightarrow K^* \ell^+ \ell^-$ decays. This observable (or even more so, the zero crossing-point of the $A_{FB}(q^2)$, with $q^2 \equiv m^2(\ell\ell)$) is not very sensitive to the theoretical uncertainties arising from the unknown form factors [5]. In fig. 3 the current Belle measurement [6] is compared to the expected sensitivity at Belle II with $\int \mathcal{L} dt = 5 \text{ ab}^{-1}$. It can be seen that such a measurement will make possible a distinction among various models, for example the SM and the Supergravity models with the reversed sign of the C_7 Wilson coefficient⁽³⁾.

3. – From Belle to Belle II

A rough overview of the Belle detector upgrade is sketched in fig. 4. In the environment of the beams with luminosity of $\mathcal{O}(10^{35}) \text{ cm}^{-2} \text{ s}^{-1}$ the detector will have to cope with an increased background (10–20 times compared to the present), which will be the cause of an increased occupancy and radiation damage. The first level trigger rate is expected to increase from the current 0.5 kHz to around 20 kHz. For several detector components we nevertheless foresee an improved performance and a better overall hermiticity of the detector after the upgrade. The task of vertexing will rely on two layers of DEPFET pixel detectors (PXD) and four layers of double-sided silicon detectors (SSVD). The main tracking device, the Central Drift Chamber (CDC), will have a smaller cell size and an improved read-out system. The particle identification will be performed

⁽³⁾ Note that this specific measurement can also be performed with a high precision at the LHCb. In the following we give examples of measurements that are completely complementary to NP searches at the LHC.

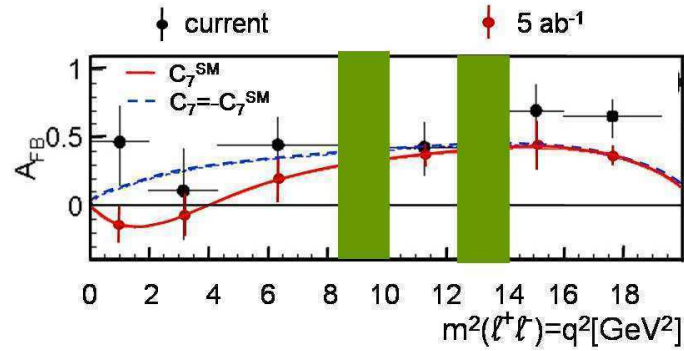


Fig. 3. – The measurement of the lepton forward-backward asymmetry in $B \rightarrow K^* \ell^+ \ell^-$ with 600 fb^{-1} [6] and 5 ab^{-1} data. Shaded regions correspond to the charmonium veto q^2 intervals.

mainly by the Time-of-Propagation counter (TOP) in the barrel and the Rich detector with aerogel radiator (ARICH) in the forward part. For the electromagnetic calorimeter (ECL) the electronics enabling a wave form sampling will be introduced, and some of the current CsI crystals doped with Tl are going to be replaced by the pure CsI. The detector of muons and K_L 's (KLM) will be upgraded with scintillator strips in the endcaps.

3'1. Vertexing. – A schematic view of the future semiconductor detector of Belle II is shown in fig. 5 (left) and is composed of two layers of pixel detectors [7] followed by four layers of double-sided silicon strip detectors. The improvement compared to the current

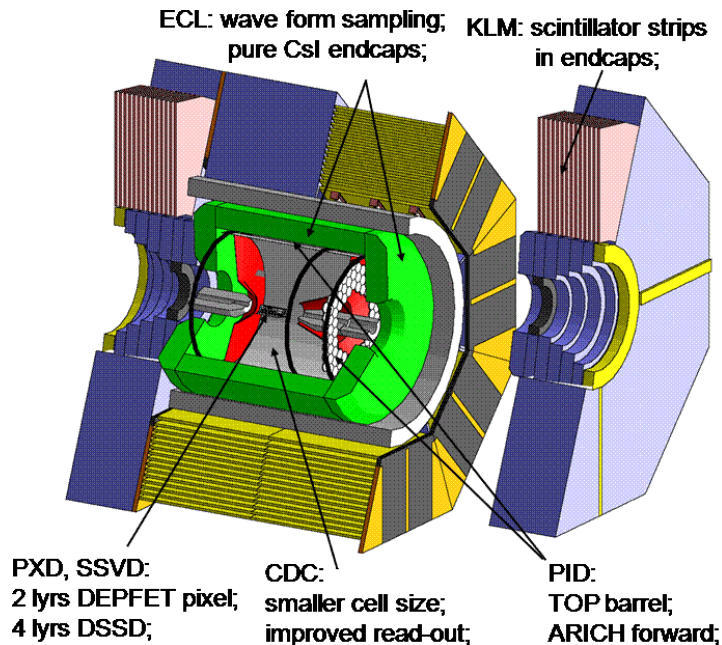


Fig. 4. – The main ingredients of the Belle detector upgrade.

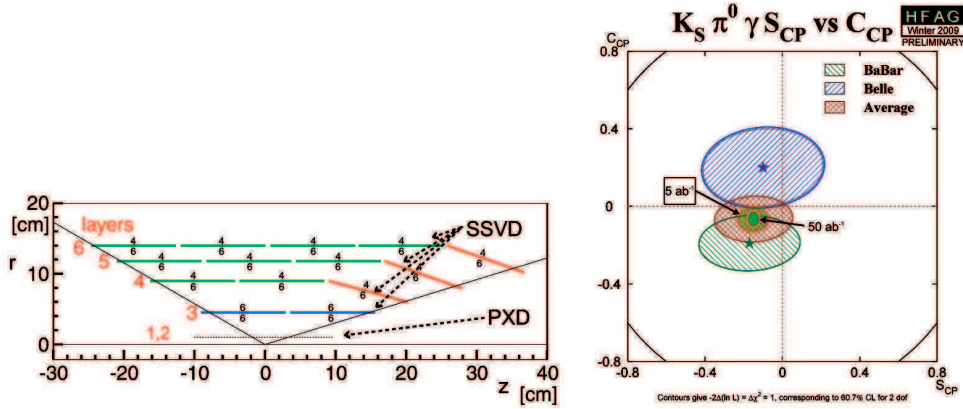


Fig. 5. – Left: A schematic view of the upgraded semiconductor detector. Right: Comparison of the current [10] and expected precision on direct and indirect CPV in $B^0 \rightarrow K_S \pi^0 \gamma$.

detector is twofold: a better spatial resolution of the vertex determination (for around 25% in the case of $B \rightarrow J/\psi K_S$ vertex), and an improved reconstruction efficiency of $K_S \rightarrow \pi^+ \pi^-$ decays with pion signals in the detector, due to the increased radii of the layers. The latter is important for the time-dependent measurements of various decay modes with K_S 's in the final state (increase of around 30%). Since the dependence on the radius of the layers is opposite for the two mentioned improvements a careful optimization of the design was performed.

To illustrate the expected performance, a search for possible right-handed currents in $B^0 \rightarrow K_S \pi^0 \gamma$ is used as a benchmark mode. In these decays only the K_S direction is used together with the interaction point constraint to determine the B meson decay vertex [8]. While the indirect CPV is heavily suppressed in the SM due to the helicity structure of the Hamiltonian, it can be largely increased in some NP models [9]. Figure 5 (right) shows a comparison of the current values of the direct and indirect CPV parameters in this mode [10] with the approximate expected precision including the statistical and systematic uncertainties. While in the Left-Right Symmetric Models S_{CP} can be as high as 0.5, the sensitivity with 50 ab^{-1} of data is smaller than the SM predictions.

3.2. Particle identification. – Particle identification at Belle II will rely on the TOP [11] counter in the barrel part, and ARICH detector in the forward [12]. The TOP detector will consist of a single quartz bar with mirrors on one side and microchannel plate photomultipliers on the other. For high momentum ($3 \text{ GeV}/c$) kaons we expect around 10% better identification efficiency (90–95%) in the barrel at a similar misidentification probability as for the current detector (5% misident. probability).

The particle identification is of course crucial in several measurements, for example the measurements related to the so-called direct CPV puzzle, which arises from the observed difference between the direct CPV asymmetry in $B^0 \rightarrow K^+ \pi^-$ and $B^+ \rightarrow K^+ \pi^0$ decays [13]. While in the explicit calculations of the asymmetries $A_{K\pi}$ several model uncertainties are present, a model-independent sum rule was proposed [14] to test the consistency of the SM. It relates the asymmetries and the branching fractions of several decay modes: $A_{K^+ \pi^-} + A_{K^0 \pi^+} [\mathcal{B}_{K^0 \pi^+} / \mathcal{B}_{K^+ \pi^-}] [\tau_{B^0} / \tau_{B^+}] = A_{K^0 \pi^0} [2\mathcal{B}_{K^0 \pi^0} / \mathcal{B}_{K^+ \pi^-}] + A_{K^+ \pi^0} [2\mathcal{B}_{K^+ \pi^0} / \mathcal{B}_{K^+ \pi^-}] [\tau_{B^0} / \tau_{B^+}]$. Figure 6 (left) shows the

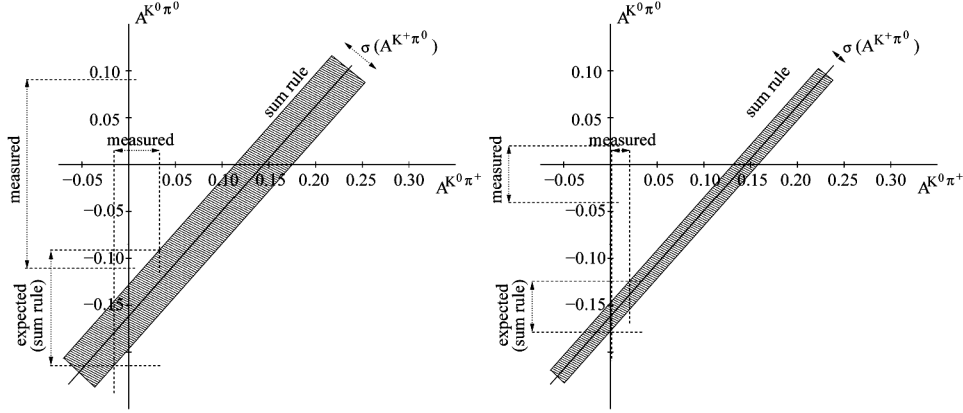


Fig. 6. – Left: direct measurements of $A_{K^0\pi^0}$ and $A_{K^0\pi^+}$ [10] compared to the sum rule [14] prediction. The width of the band is determined by the experimental uncertainties on other quantities entering the sum rule. Right: the same comparison assuming uncertainties expected with 50 ab^{-1} of data.

current status of the measurements using the world average values of the measured observables [10], where $A_{K^0\pi^0}$ is expressed as a function of the $A_{K^0\pi^+}$ using the sum rule. The predictions of the sum rule are in agreement with the direct measurements. With 50 ab^{-1} , and assuming the same central values, a discrepancy between the measurements and the sum rule prediction would be significant (fig. 6 (right)).

3.3. Electromagnetic calorimeter. – In the electromagnetic calorimeter (ECL) upgrade the replacement of the current electronics is foreseen. The new one will enable amplitude-time measurements for the signals in the ECL and will thus help to suppress the background from clusters caused mainly by the off-time beam background (we expect the reduction of this background by a factor of 7). Beside this a partial replacement of the Tl doped CsI crystals with the pure CsI is being under the consideration. Due to the increased rate of backgrounds at Belle II the expected photon detection efficiency of the ECL is around 5–10% lower, while keeping the background at the current level.

The importance of the ECL performance can be best illustrated by the measurement of the $\mathcal{B}(B^+ \rightarrow \tau^+\nu)$ [15]. The method consists of full or partial reconstruction of the tagging B meson, identification of hadrons or charged leptons from the τ decay, and examination of the distribution of the remaining measured energy in the event. For the signal, where the undetected particles are neutrinos, this distribution of energy measured in the ECL peaks at zero. The leptonic B meson decays are interesting since, for example, in the Type II Two Higgs Doublet Models, the SM branching fraction receives a contribution from the charged Higgs boson exchange, expressed as a multiplicative factor: $\mathcal{B}(B^+ \rightarrow \tau^+\nu) = \mathcal{B}^{\text{SM}}[1 - (m_B^2/m_{H^\pm}^2)\tan^2\beta]^2$. With an increased statistical power of the data, and assuming the existing ECL performance, one obtains the five standard deviations discovery region for the charged Higgs boson as shown in fig. 7 [16]. It can be seen that a large area of the $(m_{H^\pm}, \tan\beta)$ -plane (compared to the current exclusion regions) can be covered by this search, especially at larger values of the mass

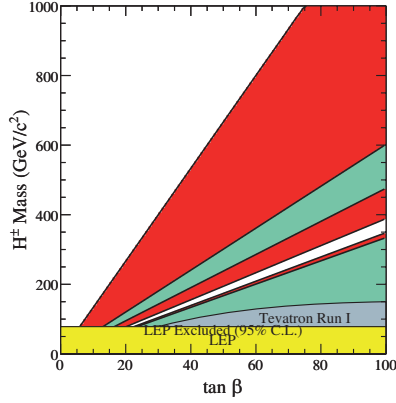


Fig. 7. – (Colour on-line) Five standard deviations discovery region (red, dark shaded) for the charged Higgs boson in the $(m_{H^\pm}, \tan \beta)$ -plane, from the measurement of $\mathcal{B}(B^+ \rightarrow \tau^+ \nu)$ with 50 ab^{-1} [16]. Other shaded regions show the current 95% CL exclusion region.

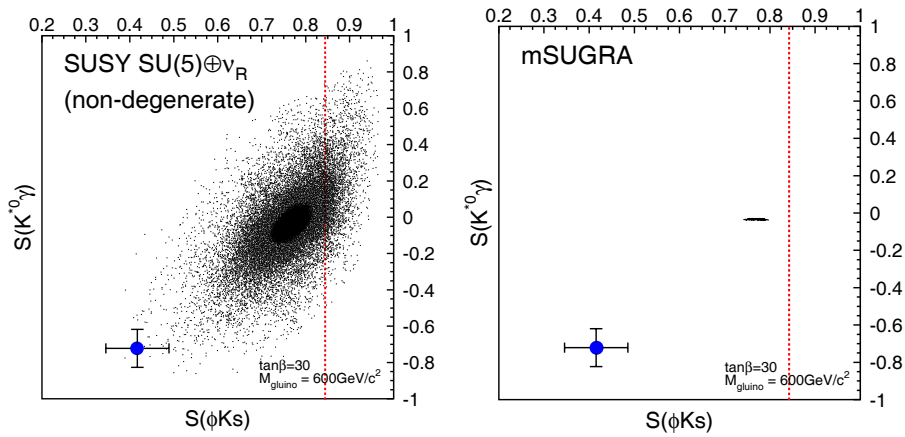


Fig. 8. – Comparison of the correlation between the indirect CPV parameter in $B^0 \rightarrow K^{*0}(\rightarrow K_S \pi^0)\gamma$ and $B^0 \rightarrow \phi K_S$ decays [16] for two models: the minimal supergravity model (mSUGRA) and supersymmetric grand-unification theory with right-handed neutrinos (SUSY $SU(5)$). The points with error bars denote the expected sensitivity at Belle II with 5 ab^{-1} of data.

and $\tan \beta$ ⁽⁴⁾. Such a measurement is to some extent complementary to the measurements of the $b \rightarrow s\gamma$ transition branching fraction which constrain the mass of the charged Higgs boson almost independently of the $\tan \beta$ value.

⁽⁴⁾ In the estimation of the expected sensitivity we also assumed an improvement in the $|V_{ub}|$ and f_B values precision to $\pm 3\%$ each.

4. – Conclusions

In summary, we presented a short overview of the KEKB accelerator and Belle detector upgrade. While technologically most challenging, the preparation of the Super B factory at KEK is well on the way. The key features of the upgrade are illustrated by several measurements that will be possible at Belle II and will represent a highly sensitive search for NP effects, complementary to searches at the LHC. A comprehensive program of physics measurements can be found in [16].

The value of the Super B factory lies not only in a highly sensitive search of NP in individual processes, but to a large extent in the possibility of performing measurements of various observables which through their correlations can help identifying the nature of NP. As an example, fig. 8 [16] shows correlations between the indirect CPV in $B^0 \rightarrow K^{*0}(\rightarrow K_S\pi^0)\gamma$ (see subsect. 3.1) and in the $B^0 \rightarrow \phi K_S$ with the underlying penguin quark process $b \rightarrow s\bar{s}s$ (a naive SM prediction is $S_{\phi K_S} = S_{J/\psi K_S} = \sin 2\phi_1$). In the minimal super gravity model (mSUGRA) and supersymmetric grand-unification theory with right-handed neutrinos (SUSY $SU(5)$) the correlations between the two observables exhibit a different pattern, while the mass spectra of the particles predicted in the two models are similar. If hints of new particles consistent with these predictions arise from the LHC, at Belle II one can distinguish the two models with already $\int \mathcal{L}dt = 5 \text{ ab}^{-1}$ of data.

The preparation of the Belle II detector at Super KEKB is proceeding according to the plan, with the aim of starting the data taking in 2014.

REFERENCES

- [1] ABASHIAN A. *et al.* (BELLE COLLABORATION), *Nucl. Instrum. Methods A*, **479** (2002) 117.
- [2] KUROKAWA S. *et al.*, *Nucl. Instrum. Methods A*, **499** (2003) 1, and other papers in that volume.
- [3] AUBERT B. *et al.* (BABAR COLLABORATION), *Nucl. Instrum. Methods A*, **479** (2002) 1.
- [4] FUNAKOSHI Y., *ICFA Beam Dyn. Newslett.*, **40** (2006) 27.
- [5] See for example BURDMAN G., *Phys. Rev. D*, **52** (1995) 6400; HOVHANNISYAN A., HOU W.-S. and MAHAJAN N., *Phys. Rev. D*, **77** (2008) 014016.
- [6] WEI J.-T. *et al.* (BELLE COLLABORATION), *Phys. Rev. Lett.*, **103** (2009) 171801.
- [7] See for example KEMMER J. and LUTZ G., *Nucl. Instrum. Methods A*, **253** (1987) 356; PERIC I., *Nucl. Instrum. Methods A*, **579** (2007) 685.
- [8] USHIRODA Y. *et al.* (BELLE COLLABORATION), *Phys. Rev. D*, **74** (2006) 111104.
- [9] See for example ATWOOD D. *et al.*, *Phys. Rev. D*, **71** (2005) 076003; GRINSTEIN B. *et al.*, *Phys. Rev. D*, **71** (2005) 011504.
- [10] BARBERIO E. *et al.* (HEAVY FLAVOR AVERAGING GROUP), arXiv:0808.1297, and updates at <http://www.slac.stanford.edu/xorg/hfag/>.
- [11] INAMI K., *Nucl. Instrum. Methods A*, **595** (2008) 96.
- [12] HASHIMOTO S. *et al.*, KEK-REPORT 2004-4.
- [13] LIN S.-W. *et al.* (BELLE COLLABORATION), *Nature*, **452** (2008) 332.
- [14] GRONAU M., *Phys. Lett. B*, **627** (2005) 82; ATWOOD D. and SONI A., *Phys. Rev. D*, **58** (1998) 036005.
- [15] ADACHI I. *et al.* (BELLE COLLABORATION), arXiv:0809.3834.
- [16] AKEROYD A. G. *et al.*, arXiv:1002.5012.

Looking into particle production at the Large Hadron Collider

C. QUIGG(*)

Fermi National Accelerator Laboratory - Batavia, Illinois 60510, USA

(ricevuto il 14 Settembre 2010; pubblicato online il 12 Gennaio 2011)

Summary. — Lightly triggered events may yield surprises about the nature of “soft” particle production at LHC energies. I suggest that event displays in coordinates matched to the dynamics of particle production (rapidity and transverse momentum) may help sharpen intuition, identify interesting classes of events, and test expectations about the underlying event that accompanies hard-scattering phenomena.

PACS 13.85.Hd – Inelastic scattering: many-particle final states.

1. – Introduction

1.1. *Early running at the LHC.* – At this 2010 La Thuile meeting, we have heard accounts of the first analyses of proton-proton collisions in CERN’s Large Hadron Collider, at energies of 450 GeV and 1.18 TeV per beam⁽¹⁾. On 30 March 2010, the LHC experiments observed first collisions at 3.5 TeV per beam, commencing a program that aims to deliver 1 fb^{-1} of integrated luminosity by the end of 2011. With each step in energy beyond the Tevatron Collider’s $\sqrt{s} = 1.96 \text{ TeV}$, the LHC experiments will open new worlds.

During early low-luminosity running, the experiments will record significant numbers of lightly triggered events. Later in the run, more selective triggers will dominate the data taking. What is true of the search for the agent of electroweak symmetry breaking and other new phenomena to be sought in hard-scattering events is also true for the minimum-bias events that will dominate the early samples:

We do not know what the new wave of exploration will reveal.

(*) E-mail: quigg@fnal.gov

⁽¹⁾ See the talks by Fabiola Gianotti, Andrey Golutvin, Paolo Meridiani, Francesco Prino, and Andreas Wildauer, and the first publications from ALICE [1], ATLAS [2], and CMS [3].

The staged commissioning of the Large Hadron Collider offers the chance to map the gross features of particle production over a wide energy range. I would identify three goals: i) Validate assumptions that underlie searches for new phenomena in hard-scattering events. ii) Develop intuition for LHC experimenters (many of whom had never—or not since the $S\bar{p}pS$ collider experiments—seen two protons hit until 23 November 2009) and for interested theorists. iii) Make the most of the opportunity for exploration and discovery. This talk supplements my recent note [4] on this subject, where additional references may be found.

1.2. Ken Wilson’s ancient program. – To orient ourselves, it is useful to look back to the early studies of multiple production in the 1970s. Exploration of the terrain opened up by the Fermilab bubble chambers and the CERN Intersecting Storage Rings was catalyzed, in part, by Ken Wilson’s celebrated paper, “Some Experiments in Multiple Production” [5]. Wilson’s “experiments” amounted to a catalogue of informative plots to address incisive questions.

- 1) *Topological cross sections:* Do multiplicity distributions exhibit a two-component structure, suggestive of diffractive plus multiperipheral production mechanisms?
- 2) *Feynman scaling:* Is the single-particle density $\rho_1(k_z/E, k_\perp, E)$ independent of the beam energy E , when plotted in terms of Feynman’s scaling variable $x_F \equiv k_z/E$?
- 3) *Factorization:* Is the single-particle density $\rho_1(k_z/E, k_\perp, E)$ in the backward (proton) hemisphere independent of the projectile (the same for πp and pp scattering)?
- 4) *dx/x spectrum:* Does the single-particle density exhibit a flat plateau in the central region when plotted in terms of the rapidity, $y \equiv \frac{1}{2} \ln[(k_0 + k_z)/(k_0 - k_z)]$?
- 5) *Correlation length experiment:* Does the two-particle correlation function $C(y_1, y_2) \equiv \rho_2(y_1, y_2) - \rho_1(y_1)\rho_1(y_2)$ display short-range order, $\propto \exp[-|y_1 - y_2|/L]$?
- 6) *Factorization test (#3) with central trigger* (to eliminate diffraction).
- 7) *Double Pomeron exchange:* Do some events display low central multiplicity with large rapidity gaps on both ends?

The experimental studies responded affirmatively to questions 1)–6). The CDF Collaboration has recently reported the production of isolated charmonium states in the central region, characteristic of the reaction $PP \rightarrow \chi_{c0}$ [6], as anticipated in question 7).

2. – Particle production at the LHC

2.1. New phenomena ahead? – This does not mean, however, that “soft” particle production should be regarded as settled knowledge. It has not yet been exhaustively studied at the Tevatron (see [7, 8] for recent important progress), and so we cannot be sure that what was inferred from experiments up to $\sqrt{s} = 63$ GeV accounts for all the important features at Tevatron energies. At the highest energies, well into the ($\propto \ln^2 s$) growth of the pp total cross section, long-range correlations might show themselves in new ways. The high density of partons carrying $p_z = 5$ to 10 GeV may give rise to hot spots in the spacetime evolution of the collision aftermath, and thus to thermalization or other phenomena not easy to anticipate from the QCD Lagrangian. We might

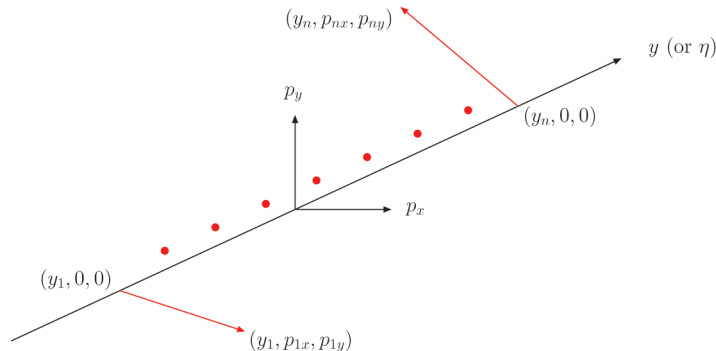


Fig. 1. – Schematic event display in (y, \vec{p}_\perp) space.

anticipate a growing rate of multiple-parton interactions [9], perhaps involving correlations among partons. For example, the quark-diquark component of the proton might manifest itself in elementary collisions involving diquarks. The $\ln s$ expansion of the rapidity plateau softens kinematical constraints in the central region, and the sensitivity to high-multiplicity events (or otherwise rare occurrences) of modern experiments vastly exceeds what could be seen with bubble-chamber statistics. The CMS Collaboration reports [3] that the standard PYTHIA tunes underestimate the growth with energy of the central density of charged particles, $dN_{\text{ch}}/d\eta|_{\eta=0}$, from $\sqrt{s} = 900$ GeV to 2.36 TeV. At $\sqrt{s} = 900$ GeV, the ATLAS experiment observes [2] that $dN_{\text{ch}}/d\eta|_{\eta=0}$ lies some (5–15)% above the predictions of the Monte Carlo models. For all these reasons, I suspect that a few percent of minimum-bias events collected at $\sqrt{s} \gtrsim 1$ TeV might display unusual event structures⁽²⁾. We should look! But how?

2.2. Learning to see. – I believe that *looking at events* can be an important part of the answer. Blind analysis [11] has won a secure place in our practice of particle physics, as a talisman against experimenter’s bias, but it is not apposite when we are seeking to get the lay of the land. It would be a big mistake to suppose that we know all the important questions, even before we arrive in the new world! Bjorken suggested long ago [12] a three-dimensional representation of multiparticle events that could engage our human powers of visualization and pattern recognition, in the hope of identifying important new questions. For particle production in soft collisions, it is not spatial coordinates that are most apt, but a representation in terms of (pseudo)rapidity and (two-dimensional) transverse momentum. To begin, draw a (pseudo)rapidity axis as an oblique line. Represent each track i in the event by a vector drawn from $(y_i, 0, 0)$ to (y_i, p_{ix}, p_{iy}) , as in the example shown in fig. 1 (all scales linear). The (y, p_\perp) representation is none other than a curled-up vector representation of the LEGO[®] plot for individual tracks, with thresholds for display set as low as possible.

As a start, I encourage the LHC collaborations to produce (y, \vec{p}_\perp) displays of minimum-bias events acquired during early running. Samples as small as a few hundred events would already build intuition, but I would go further.

⁽²⁾ Many of the questions posed in the FELIX physics document [10] are apt for the detectors now taking data at the LHC.

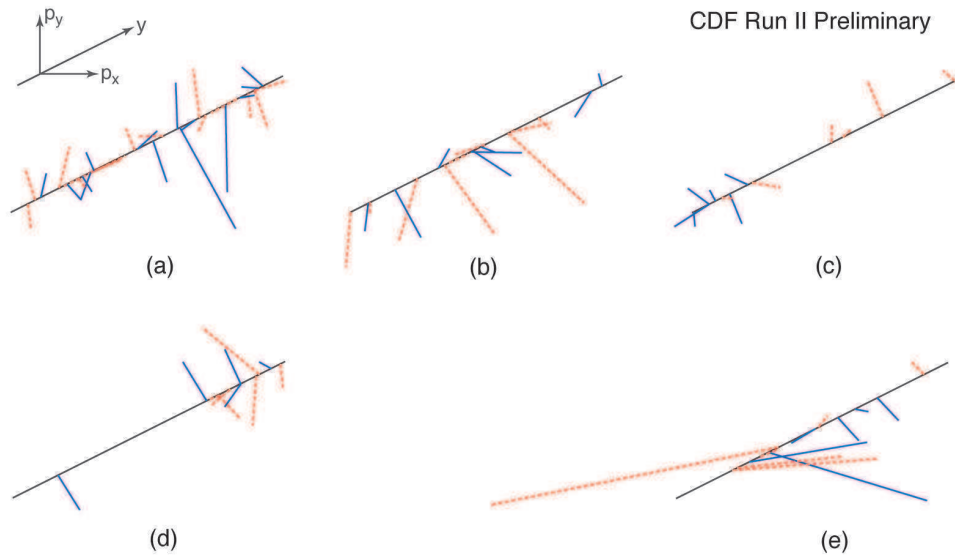


Fig. 2. – (Colour on-line) Example (y, \vec{p}_\perp) event displays from Run 2 of the CDF Experiment at Fermilab. These are chosen from a sample of “zero-bias” events with at least 10 tracks in the central region and one good primary vertex. Each rapidity axis spans $-1 \leq y \leq 1$; the length of the transverse-momentum axes is 1 GeV. Dashed red and solid blue lines label positively and negatively charged tracks, respectively. (a) Local compensation of \vec{p}_\perp and electric charge. (b) Local \vec{p}_\perp imbalance. (c) Local charge imbalance. (d) Rapidity gap. (e) Hot spot.

I suggest that the collaborations make available live streams of (y, \vec{p}_\perp) representations, along with the online displays of events that show the structure in terms of detector elements in ordinary space. It is useful to color the tracks to label their charges, and to identify species where possible.

More is to be learned from the river of events than from a few specimens!

Changes in event structure as a function of beam energy, or the onset of new features, might raise important questions.

Thanks to work of Niccolò Moggi [13] and William Wester, I can show in fig. 2 a few example (y, \vec{p}_\perp) displays of events recorded by the CDF Collaboration in Run 2 at the Tevatron, in $\bar{p}p$ collisions at $\sqrt{s} = 1.96$ TeV. The events shown there are chosen from a “zero-bias” sample after selections to ensure a single primary vertex within 30 cm (1σ) of the nominal crossing point and require (for visual interest) at least 10 well-matched tracks in the rapidity interval $-1 \leq y \leq 1$. (By selecting higher-than-average-multiplicity events, we are excluding candidates for $\gamma\gamma$ and double-Pomeron events that would be restricted to low central multiplicities.) Event (a) exhibits the average behavior familiar at lower energies, whereby transverse momentum and additive quantum numbers such as electric charge are compensated locally in rapidity. Each of the remaining events deviates from the typical expectations, inviting further study of large numbers of events to ascertain whether they fit neatly into fluctuations about the mean or suggest new event classes. Transverse momentum is unbalanced in event (b); positive and negative charges are separated in event (c); a rapidity gap of slightly more than one unit appears in event (d); and a good deal of the action in event (e) seems concentrated in a “hot spot” in rapidity.

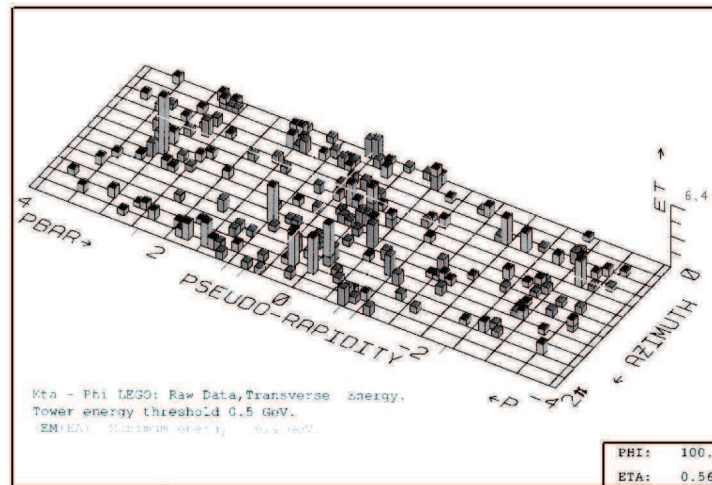


Fig. 3. – An unusual event captured in the CDF Run 1 detector.

By scanning many events, it should be possible to (quickly) develop intuition about what is “normal,” both for lightly triggered events and for events that satisfy a hard trigger. It will also be valuable to compare streams of real events with streams of simulated events. It is certain that something is missing from the Monte Carlo programs. We need to learn what the omissions are, and how important they are to our understanding. Attentive scanning could well yield the suggestion of unanticipated phenomena—at the level of a few percent, one in a thousand, even one in 10 000. Modern computer tools make it straightforward to construct (y, p_{\perp}) displays that can be zoomed, panned, and rotated in three dimensions. The ability to manipulate events and regard them from changing perspectives can engage our human powers of perception more fully.

2.3. New Physics in the Weeds. – The strong interactions are extraordinarily rich. Even as we learn to extend the reach of perturbative QCD beyond reactions involving a few partons in the final state, we should be attentive to the whole range of strong-interaction phenomena. The rest of the story includes common processes with large cross sections such as “soft” particle production, elastic scattering, and diffraction. It may well be that interesting, *unusual* occurrences happen outside the framework of perturbative QCD—happen in some collective, or intrinsically nonperturbative, way. A powerful technique to isolate hard-scattering reactions is to impose stringent cuts in the data selection, or to clarify the essential structure of events by setting display thresholds high. When scanning event displays for hints of new phenomena, however, it may be advantageous to set the display thresholds *as low as possible*.

An interesting example—an *atypical* event observed in $\bar{p}p$ interactions at $\sqrt{s} = 1.8$ TeV by CDF’s Run 1 detector, is shown in fig. 3⁽³⁾. This event was accepted by a $\sum E_{\perp}$ trigger, without any topological requirement. The LEGO[®] plot shows many bursts of energy: More than a hundred active towers pass the display threshold of

⁽³⁾ See Figure 3(c) of [14] for a similarly isotropic event recorded in the UA1 Detector in $\bar{p}p$ collisions at $\sqrt{s} = 630$ GeV, in which $\sum E_{\perp} = 209$ GeV for $|y| < 1.5$.

0.5 GeV. The total transverse energy in the event is 321 GeV, but it is not concentrated in a few sprays, it is everywhere. The central tracking chamber records about sixty charged particles.

I am assured that this “hedgehog” event is authentic; it is not merely coherent noise in the counters. The colleague who selected this specimen estimated similar events to be about as common in the online event stream as Z^0 production and decay into lepton pairs: about one in ten thousand triggers. I include this outlier as a reminder that when we think about the strong interactions outside the realm of a single hard scattering, we should think not only about the large diffractive and “multiperipheral” cross sections, but also about less common phenomena.

3. – Opportunities for exploration and discovery

The minimum-bias and lightly triggered data recorded during early LHC running will be valuable for developing intuition and for validating the assumptions that underlie searches for new physics in hard-scattering events. However, these data sets, to be gathered over steps in beam energy, also represent an important opportunity for exploration and discovery. One promising track will be to emulate the early studies of multiple production, which emphasized observables constructed from individual particles: topological cross sections (multiplicity distributions, including forward-backward asymmetries of multiplicity distributions), inclusive and semi-inclusive two-particle correlation functions, and charge-transfer studies. Some measurements that would be especially informative for refining Monte Carlo event generators are suggested in [15]. For some classes of events, analyses of bulk properties, such as studies of elliptic flow and determinations of thermodynamic parameters may prove powerful. We will need all the established methods—plus novel techniques—to learn to see what the LHC data have to show.

It is not too late to characterize particle production more completely in the Tevatron experiments. The existing samples of lightly triggered events can be mined further, with an eye to establishing in detail the mechanisms at play in particle production and identifying suggestive classes of unusual events. It is worth considering a brief, dedicated, Tevatron run at $\sqrt{s} = 900$ GeV, to match the samples collected in the LHC’s pilot run at the end of 2009. The similarities and differences between pp and $\bar{p}p$ collisions may be revealing.

I advocate looking at individual events, not just distributions. Beyond honing intuition, the first effect of *looking at events*, displayed in appropriate coordinates, may be to validate in broad terms the prevailing picture of particle production. We should also be able to test the completeness of the Monte Carlo frameworks that have become so indispensable to the search for new (hard-scattering) phenomena. I think it likely that we will encounter suggestions of new event classes, to be pursued in focused studies that go beyond visual inspection. New trends may emerge with increasing beam energy, or at the extremes of high and low multiplicity. The comparison of events with and without a hard trigger should be revealing. The goal of the visual approach is to discover as completely as we can the richness of phenomena that our theories will have to explain, and to orient us for detailed exploration of the new worlds.

* * *

I thank N. MOGGI and W. WESTER for the example event displays from CDF Run 2, and the CDF QCD convenors, C. MESROPIAN and S. PRANKO, for permission to include them in this presentation. D. JOVANOVIĆ provided the hedgehog event in fig. 3, and

J. ROHLF called my attention to the earlier UA1 observations. I thank J. BJORKEN for many stimulating conversations. I am grateful to the organizers of these Rencontres de Physique de la Vallée d'Aoste for their kind invitation to take part. Fermilab is operated by Fermi Research Alliance, LLC under Contract No. DE-AC02-07CH11359 with the United States Department of Energy.

REFERENCES

- [1] ALICE COLLABORATION, *Eur. Phys. J. C*, **65** (2010) 111 [arXiv:0911.5430].
- [2] ATLAS COLLABORATION, *Phys. Lett. B*, **688** (2010) 21.
- [3] CMS COLLABORATION, *JHEP*, **02** (2010) 041 [arXiv:1002.0621].
- [4] QUIGG C., *Learning to See at the Large Hadron Collider*, arXiv:1001.2025 (2010).
- [5] WILSON K. G., *Some Experiments in Multiple Production*, Cornell Report CLNS-131 (1970).
- [6] AALTONEN T. *et al.* (CDF COLLABORATION), *Phys. Rev. Lett.*, **102** (2009) 242001 [arXiv:0902.1271].
- [7] AALTONEN T. *et al.* (CDF COLLABORATION), *Phys. Rev. D*, **79** (2009) 112005, arXiv:0904.1098.
- [8] AALTONEN T. *et al.* (CDF COLLABORATION), *Studying the Underlying Event in Drell-Yan and High Transverse Momentum Jet Production at the Tevatron*, arXiv:1003.4220.
- [9] BERNHARD R. *et al.*, *Proceedings of the First International Workshop on Multiple Partonic Interactions at the LHC (MPI08)*, DESY-PROC-2009-06, arXiv:1003.4220.
- [10] AGEEV A. *et al.*, *J. Phys. G*, **28** (2002) R117.
- [11] KLEIN J. R. and ROODMAN A., *Annu. Rev. Nucl. Part. Sci.*, **55** (2005) 141.
- [12] BJORKEN J. D., *Multiple Processes at High Energy*, SLAC-PUB-0974 (1971).
- [13] MOGGI N., *Nuovo Cimento C*, **32** (2009) 113.
- [14] ALBAJAR C. *et al.* (UA1 COLLABORATION), *Z. Phys. C*, **36** (1987) 33.
- [15] SKANDS P., *Min-Bias Models – the Modeling of SD, DD, and ND*, Talk given at *Minimum-Bias and Underlying-Event Working Group Meeting at CERN, March 1–2 2010*, <http://indico.cern.ch/conferenceDisplay.py?confId=83609>.

Search for neutral Higgs bosons decaying into four taus at LEP2

P. SPAGNOLO

*INFN, Sezione di Pisa - Pisa, Italy
CERN - Geneva, Switzerland*

(ricevuto il 14 Settembre 2010; pubblicato online il 14 Gennaio 2011)

Summary. — A search for the production and non-standard decay of a Higgs boson, h , into four taus through intermediate pseudoscalars, a , is conducted on 683 pb^{-1} of data collected by the ALEPH experiment at centre-of-mass energies from 183 to 209 GeV. No excess of events above background is observed, and exclusion limits are placed on the combined production cross section times branching ratio, $\xi^2 = \frac{\sigma(e^+e^- \rightarrow Zh)}{\sigma_{\text{SM}}(e^+e^- \rightarrow Zh)} \times B(h \rightarrow aa) \times B(a \rightarrow \tau^+\tau^-)^2$. For $m_h < 107 \text{ GeV}/c^2$ and $4 < m_a < 10 \text{ GeV}/c^2$, $\xi^2 > 1$ is excluded at the 95% confidence level.

PACS 14.80.Ec – Other neutral Higgs bosons.

1. – Introduction

Searches conducted at LEP2 have excluded the standard model (SM) Higgs boson decaying into $b\bar{b}$ or $\tau^+\tau^-$ for masses below $114.4 \text{ GeV}/c^2$ [1]. The LEP experiments observed a $\sim 2.5\sigma$ excess in the $b\bar{b}$ final state for a Higgs boson mass around $100 \text{ GeV}/c^2$, which is consistent with SM-like production and a reduced branching ratio into $b\bar{b}$ [2]. This excess, the mild tension with electroweak precision tests [3], and the fine-tuning needed in the minimal supersymmetric standard model (MSSM) have prompted the consideration of models with exotic Higgs boson decays, such as those of the next-to-minimal supersymmetric standard model (NMSSM) [4,5] as well as more general frameworks [6,7]. In these models, new decay channels can dominate over $h \rightarrow b\bar{b}$ and render the Higgs boson “invisible” for conventional searches. In particular, a Higgs boson decaying into two light pseudoscalars is well motivated by these models and results in a four-body final state as the pseudoscalars decay into light fermions. A search for $h \rightarrow 2a \rightarrow 4\tau$ with ALEPH data, extending the mass range to $m_h \approx 110 \text{ GeV}/c^2$, is presented in this paper. The pseudoscalar a may arise from a two-higgs doublet model, as in the MSSM, or it can include a component from an additional singlet field as in the NMSSM. These possibilities differ in their details and relations between model parameters. The present search is performed in a model-independent manner and simply adopts the two main characteristics of the pseudoscalar: the coupling to a Higgs boson resulting in $h \rightarrow aa$

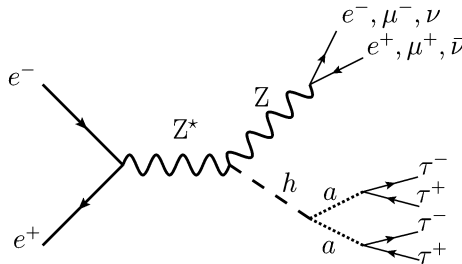


Fig. 1. – Higgs boson production and decay modes considered in this analysis.

decay and the coupling to SM fermions proportional to their Yukawa couplings. The present analysis concentrates on the region $2m_\tau < m_a < 2m_b$, where the $a \rightarrow \tau^+\tau^-$ decay mode is expected to be substantial. The Higgs boson production mode considered here is the higgsstrahlung process, shown in fig. 1 with $Z \rightarrow e^+e^-, \mu^+\mu^-, \nu\bar{\nu}$.

A detailed description of the ALEPH detector can be found in ref. [8]. The detector’s performance is described in ref. [9]. The average centre-of-mass energies at which the machine operated and the corresponding integrated luminosities used in this analysis are presented in table I.

2. – Signal and background generation

Both signal and background were generated for all centre-of-mass energies shown in table I using the GEANT3-based simulation of ALEPH [10]. Backgrounds were generated with a variety of generators listed in table II.

3. – Event selection

For the mass range considered, the Higgs boson is produced approximately at rest, and thus the decay $h \rightarrow 2a \rightarrow 4\tau$ results in a pair of taus recoiling against another pair of taus. The JADE algorithm [20,21] was employed to cluster into jets all energy-flow objects except for those identified as energetic, isolated photons, energy deposits in the LICAL and SICAL, and the two hardest, oppositely-charged leptons in the case of the $Z \rightarrow \ell^+\ell^-$ channels. Given that each jet is expected to arise from the on-shell decay $a \rightarrow \tau^+\tau^-$, an effective way to target the signal topology is to use the JADE algorithm with y_{cut} chosen to merge proto-jets up to a mass of $m_{\text{jet}} = 15 \text{ GeV}/c^2$. Because the taus from the same a decay are highly collimated, the identification of jets containing the decay products of two taus was based only on the track multiplicity of the jets, denoted n_i^{track} , with the index i ordered in decreasing jet energy. Because the tau predominantly decays either to one charged particle (“one-prong” decay) or three charged particles (“three-prong” decay), each jet is expected to contain two, four, or six tracks. To maximize the tracking efficiency, the jets were required to be well contained in the tracking volume.

TABLE I. – *Integrated luminosities collected at the different average centre-of-mass energies.*

$E_{\text{CM}}(\text{GeV})$	182.65	188.63	191.58	195.52	199.52	201.62	204.86	206.53
$\int \mathcal{L} dt(\text{pb}^{-1})$	56.8	174.2	28.9	79.9	86.3	41.9	81.4	133.2

TABLE II. – Details on SM background processes and their categorisation. Fragmentation, hadronisation and final state radiation were simulated with PYTHIA 6.1 [11]. PHOTOS [12] was used to model final state radiation, and TAUOLA [13] was used for tau decays. More details can be found in ref. [14].

Category	Process	Software
2f	$e^+e^- \rightarrow Z/\gamma^* \rightarrow q\bar{q}(\gamma)$	KK 4.14 [15]
	Bhabha and $e^+e^- \rightarrow Z/\gamma^* \rightarrow e^+e^-(\gamma)$	BHWIDE 1.01 [16]
	$e^+e^- \rightarrow Z/\gamma^* \rightarrow \mu^+\mu^-(\gamma)$	KK 4.14 [15]
	$e^+e^- \rightarrow Z/\gamma^* \rightarrow \tau^+\tau^-(\gamma)$	KK 4.14 [15]
	$e^+e^- \rightarrow Z \rightarrow \nu\bar{\nu}(\gamma)$	PYTHIA 6.1 [11]
4f	$e^+e^- \rightarrow Z/\gamma^* \rightarrow W^+W^-$	KORALW 1.51 [17]
	$e^+e^- \rightarrow ZZ$	PYTHIA 6.1 [11]
	$e^+e^- \rightarrow Ze^+e^-$	PYTHIA 6.1 [11]
	$e^+e^- \rightarrow Z\nu\bar{\nu}$	PYTHIA 6.1 [11]
	$e^+e^- \rightarrow W^\pm e^\mp \nu$	PYTHIA 6.1 [11]
$\gamma\gamma$	$\gamma\gamma \rightarrow \ell^+\ell^-$	PHOT02 [18, 19]
	$\gamma\gamma \rightarrow q\bar{q}$	PHOT02 [18, 19]
$n\gamma$	$e^+e^- \rightarrow n\gamma$	PYTHIA 6.1 [11]

The $Z \rightarrow \ell^+\ell^-$ decay is often accompanied by additional photons from final state radiation, which can carry substantial momentum. The photon was considered part of the candidate Z system when the invariant mass of the $\ell^+\ell^-\gamma$ system was closer to the Z mass than the invariant mass of the lepton pair alone. This algorithm resulted in an increase of $\sim 20\%$ in the signal efficiency after the Z mass window cut, $80 < m_Z < 102 \text{ GeV}/c^2$. For each of the channels below, a loose selection and final selection are presented. The loose selection isolates the broad characteristics of the signal events and allows for comparison of the data and simulated backgrounds.

3.1. $Z \rightarrow \ell^+\ell^-$. – The loose selection consisted of the following requirements. An e^+e^- or $\mu^+\mu^-$ pair and the presence of two jets (or 3 jets with $n_3^{\text{track}} \leq 2$) were required for consistency with the final state of the signal. The three-jet events are kept to recover signal efficiency for events with converted photon arising from final state radiation. Proper containment of the jet in the tracking volume was ensured by requiring $|\cos\theta_{j_1}| < 0.9$ and $|\cos\theta_{j_2}| < 0.9$, where θ_{j_i} is the angle of the i -th jet with respect to the beam axis. Additional lepton isolation was imposed by requiring that a cone of 10° around each lepton contained less than 5% of the visible energy of the event and $\cos\theta_{j_1}^{\text{min}} < 0.95$, where $\theta_{j_1}^{\text{min}}$ is the minimum angle between each pairing of a jet and lepton.

The final selection consisted of the following requirements and maintained an acceptable signal efficiency while rejecting most backgrounds. A mass window for the candidate Z between $80\text{--}102 \text{ GeV}/c^2$ was effective at removing two-fermion backgrounds. Due to the neutrinos from tau decays the signal was separated from fully hadronic final states by requiring a missing energy $E_{\text{mis}} > 20 \text{ GeV}$. The expected jet configuration of the signal was enforced by requiring $\cos\theta_{j_1j_2} < 0$, where $\theta_{j_1j_2}$ is the angle between the two jets. Finally, the remaining backgrounds were suppressed by requiring $n_{1,2}^{\text{track}} = 2$ or 4, the

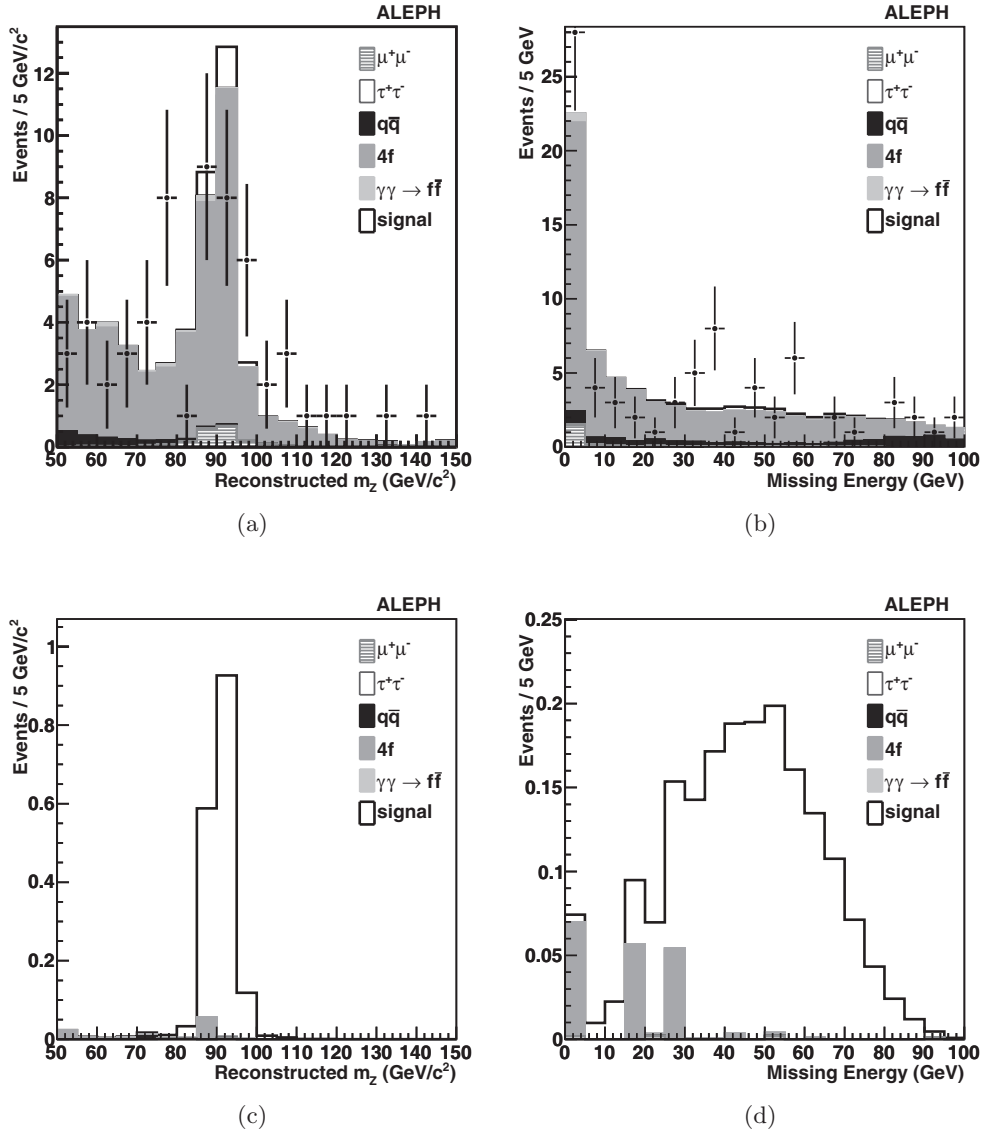


Fig. 2. – Distributions for the $Z \rightarrow \mu^+\mu^-$ channel after the loose selection for (a) the reconstructed Z invariant mass and (b) missing energy, where signal corresponds to $m_h = 100 \text{ GeV}/c^2$, $m_a = 4 \text{ GeV}/c^2$ with $\xi^2 = 1$. The same distributions are shown in (c) and (d) after the final selection, excluding any requirements on the variable shown.

dominant track multiplicities expected in the signal. Figures 2 show the distribution of the reconstructed Z mass and missing energy for the $Z \rightarrow \mu^+\mu^-$ channel. The numbers of events passing loose and final selection in data and simulated background are shown in table III.

TABLE III. – Number of events passing loose and final selections in each channel, in data, simulated background, and simulated signal ($m_h = 100$, $m_a = 4 \text{ GeV}/c^2$). The numbers of events passing the final selection are categorised by track multiplicity.

Channel	Selection ($n_1^{\text{track}}, n_2^{\text{track}}$)	Data	Total background	Background category				Signal
				2f	4f	$\gamma\gamma$	$n\gamma$	
$Z \rightarrow e^+e^-$	Loose	299	332	183	137	12.31	0.65	2.27
	(2,2)	0	0.034	0.034	0.000	0.000	0.000	0.689
	(2,4)+(4,2)	0	0.055	0.014	0.005	0.037	0.000	0.610
	(4,4)	0	0.031	0.019	0.013	0.000	0.000	0.126
$Z \rightarrow \mu^+\mu^-$	Loose	83	74.50	12.79	60.64	1.07	0.00	2.37
	(2,2)	0	0.058	0.005	0.053	0.000	0.000	0.800
	(2,4)+(4,2)	0	0.005	0.000	0.005	0.000	0.000	0.676
	(2,2)	0	0.006	0.000	0.006	0.000	0.000	0.127
$Z \rightarrow \nu\bar{\nu}$	Loose	206	200	135	47.97	13.50	3.74	12.63
	(2,2)	0	1.312	0.663	0.408	0.240	0.000	5.097
	(2,4)+(4,2)	0	1.948	0.528	0.575	0.845	0.000	4.741
	(4,4)	2	2.569	0.461	0.820	1.288	0.000	1.089

3.2. $Z \rightarrow \nu\bar{\nu}$. – All objects found in the event were clustered into jets as described above. The loose selection consisted of the following requirements. Missing energy greater than 30 GeV and missing mass, m_{mis} , greater than $20 \text{ GeV}/c^2$ were used to reject dijet and other two-fermion backgrounds. In order to further reject the $\gamma\gamma$ background, events were required to have $E_{\text{vis}} > 0.05 E_{\text{cm}}$ and $|\cos \theta_{\text{me}}| < 0.9$, where E_{vis} is the visible energy and θ_{me} is the angle between the missing momentum vector and the beam axis. Events were required to have two well-contained jets with $|\cos \theta_j| < 0.85$, dijet invariant mass $m_{j_1 j_2} > 10 \text{ GeV}/c^2$, dijet angular separation $\cos \theta_{j_1 j_2} < 0$, and the highest energy jet was required to have $E_{j_1} > 25 \text{ GeV}$ and $n_1^{\text{track}} = 2$ or 4 .

The final selection consisted of the following requirements. First, the requirement $E_{j_1} + E_{j_2} + E_{\text{mis}} > E_{\text{cm}} - 5 \text{ GeV}$ was used to reject events with energy deposits in the forward regions of the detector. Consistency with $Z \rightarrow \nu\bar{\nu}$ was ensured by requiring $E_{\text{mis}} > 60 \text{ GeV}$ and $m_{\text{mis}} > 90 \text{ GeV}/c^2$. Finally, the second jet was also required to have $n_2^{\text{track}} = 2$ or 4 . The numbers of events passing loose and final selection in data and simulated background are shown in table III.

3.3. Signal efficiency. – The $h \rightarrow 2a \rightarrow 4\tau$ signal efficiency is shown in fig. 3 as a function of the Higgs boson mass with $m_a = 4\text{--}10 \text{ GeV}/c^2$ for the three Z decay channels considered.

4. – Systematic uncertainties

Uncertainties and inaccuracies in the Monte Carlo simulation lead to systematic effects in the analysis. The impact of uncertainties in jet energy and direction, missing energy, and lepton identification and isolation were estimated. For the $Z \rightarrow \ell^+\ell^-$ channels, the total relative systematic uncertainties from lepton identification and isolation were found to be 0.6%, 2.6% and 7.5% for the signal, ZZ, and Zee backgrounds, respectively. The systematic uncertainties for WW, $W\nu$, $q\bar{q}$, and other backgrounds were all smaller than

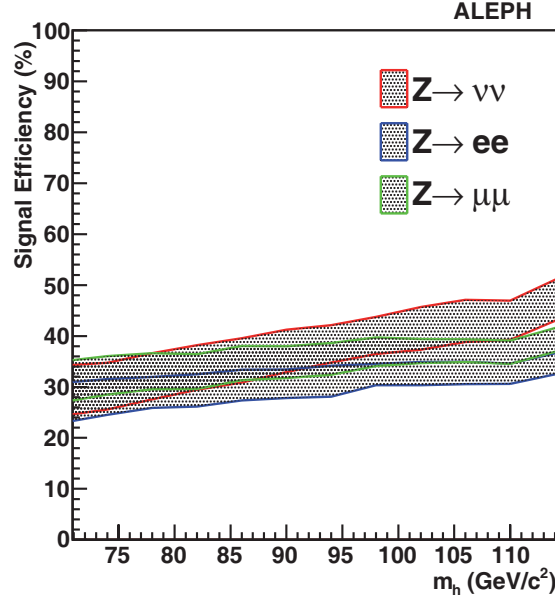


Fig. 3. – Signal efficiency as a function of the Higgs boson mass for the three channels considered in this work, $Z \rightarrow e^+e^-$, $\mu^+\mu^-$, and $\nu\bar{\nu}$. The upper (lower) portion of the efficiency band corresponds to $m_a = 4$ (10) GeV/c^2 .

30%. Based on these estimates and the background composition, a 10% uncertainty is estimated for the background in the $Z \rightarrow \ell^+\ell^-$ channels. The agreement between the background estimate and the observed number of events in data with the loose selection is within the systematic and statistical uncertainty for all three channels. Given the low numbers of selected events, the final measurements are statistically limited.

5. – Results

No excess of events above the background was observed. Limits on the cross section times branching ratio with respect to the SM higgsstrahlung production cross section, $\xi^2 = \frac{\sigma(e^+e^- \rightarrow Zh)}{\sigma_{\text{SM}}(e^+e^- \rightarrow Zh)} \times B(h \rightarrow aa) \times B(a \rightarrow \tau^+\tau^-)^2$ were determined. Figure 4a shows the 95% confidence level upper-limit on ξ^2 as a function of m_h for $m_a = 10 \text{ GeV}/c^2$. Figure 4b shows 95% confidence level contours of ξ^2 in the (m_h, m_a) -plane. Because the selection has no m_h or m_a dependence, the resulting upper limits are fully correlated. The observed number of events is consistent with a downward fluctuation of the background, which leads to stronger than expected limits on ξ^2 .

6. – Conclusions

A search for a Higgs boson produced via higgsstrahlung at LEP2 energies has been performed, where $h \rightarrow 2a \rightarrow 4\tau$ and $Z \rightarrow e^+e^-$, $\mu^+\mu^-$, $\nu\bar{\nu}$. No evidence for an excess of events above background was observed, and a limit on the combined production cross section times branching ratio, $\xi^2 = \frac{\sigma(e^+e^- \rightarrow Zh)}{\sigma_{\text{SM}}(e^+e^- \rightarrow Zh)} \times B(h \rightarrow aa) \times B(a \rightarrow \tau^+\tau^-)^2$ is

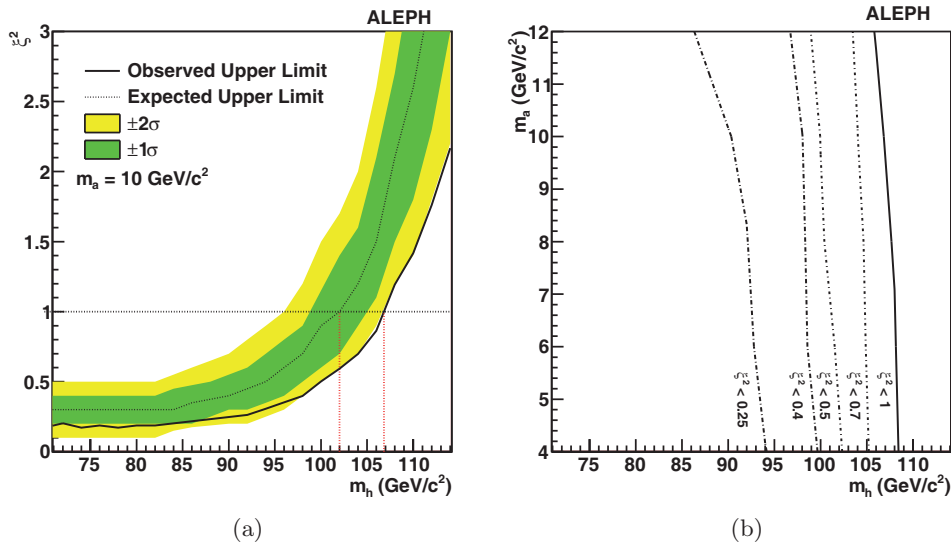


Fig. 4. – (a) Observed and expected 95% confidence level limit on ξ^2 as a function of the Higgs boson mass for $m_a = 10$ GeV/c². (b) Contours of observed 95% confidence level limit on ξ^2 in the (m_h, m_a) -plane.

presented. For $m_h < 107$ GeV/c² and $4 < m_a < 10$ GeV/c², $\xi^2 > 1$ is excluded at the 95% confidence level. This analysis covers a region of parameter space previously left unexplored, and further constrains models with non-standard Higgs decays, such as the NMSSM.

* * *

I wish to thank J. BEACHAM, K. STUART CRANMER and I. YAVIN for the impressive work, N. WEINER and R. BARBIERI for the encouragement and motivation, and all the ALEPH Collaboration for the support.

REFERENCES

- [1] The LEP Working Group for Higgs Boson Searches, ALEPH, DELPHI, L3, and OPAL COLLABORATIONS, *Phys. Lett. B*, **565** (2003) 61, [[hep-ex/0306033](#)].
- [2] The LEP Working Group for Higgs Boson Searches, ALEPH, DELPHI, L3, and OPAL COLLABORATIONS, *Eur. Phys. J. C*, **47** (2006) 547, [[hep-ex/0602042](#)].
- [3] BARBIERI R. and STRUMIA A., *Phys. Lett. B*, **462** (1999) 144, [[hep-ph/9905281](#)].
- [4] DERMISEK R. and GUNION J. F., *Phys. Rev. Lett.*, **95** (2005) 041801, [[hep-ph/0502105](#)].
- [5] DERMISEK R. and GUNION J. F., *Phys. Rev. D*, **76** (2007) 095006, [[arXiv:0705.4387](#)].
- [6] CHANG S., FOX P. J. and WEINER N., *JHEP*, **08** (2006) 068, [[hep-ph/0511250](#)].
- [7] CHANG S., DERMISEK R., GUNION J. F. and WEINER N., *Annu. Rev. Nucl. Part. Sci.*, **58** (2008) 75, [[arXiv:0801.4554](#)].
- [8] THE ALEPH COLLABORATION, *Nucl. Instrum. Methods A*, **294** (1990) 121.
- [9] THE ALEPH COLLABORATION, *Nucl. Instrum. Methods A*, **360** (1995) 481.
- [10] BRUN R. *et al.*, CERN Internal Report No. CERN DD/EE/84-1 (1987).
- [11] SJÖSTRAND T. *et al.*, *Comput. Phys. Commun.*, **135** (2001) 238, [[hep-ph/0010017](#)].
- [12] BARBERIO E. and WAS Z., *Comput. Phys. Commun.*, **79** (1994) 291.

- [13] JADACH S., WAS Z., DECKER R. and KUHN J. H., *Comput. Phys. Commun.*, **76** (1993) 361.
- [14] THE ALEPH COLLABORATION, *Eur. Phys. J. C*, **38** (2004) 147.
- [15] JADACH S., WARD B. F. L. and WAS Z., *Comput. Phys. Commun.*, **130** (2000) 260, [[hep-ph/9912214](#)].
- [16] JADACH S., PLACZEK W. and WARD B. F. L., *Phys. Lett. B*, **390** (1997) 298, [[hep-ph/9608412](#)].
- [17] JADACH S., PLACZEK W., SKRZYPEK M., WARD B. F. L. and WAS Z., *Comput. Phys. Commun.*, **140** (2001) 475, [[hep-ph/0104049](#)].
- [18] VERMASEREN J. A. M., *Proceedings of the IV International Workshop on Gamma Gamma Interactions*, edited by COCHARD G. and KESSLER P. (1980).
- [19] THE ALEPH COLLABORATION, *Phys. Lett. B*, **313** (1993) 509.
- [20] THE JADE COLLABORATION, *Z. Phys. C*, **33** (1987) 339.
- [21] THE JADE COLLABORATION, *Phys. Lett. B*, **213** (1988) 235.

Anomalously interacting extra neutral bosons

M. V. CHIZHOV⁽¹⁾⁽²⁾, V. A. BEDNYAKOV⁽²⁾ and J. A. BUDAGOV^{(2)(*)}

⁽¹⁾ *CSRT, Faculty of Physics, Sofia University - 1164 Sofia, Bulgaria*

⁽²⁾ *DLNP, Joint Institute for Nuclear Research - 141980, Dubna, Russia*

(ricevuto il 14 Settembre 2010; pubblicato online il 12 Gennaio 2011)

Summary. — We study phenomenological consequences of the Standard Model extension by the new spin-1 chiral fields with the internal quantum numbers of the electroweak Higgs doublets. There are at least three different classes of theories, all motivated by the hierarchy problem, which predict new vector weak-doublets with masses not far from the electroweak scale. We discuss resonance production of these neutral chiral Z^* bosons at hadron colliders. The bosons can be observed as a Breit-Wigner resonance peak in the invariant dilepton mass distributions in the same way as the well-known extra gauge Z' bosons. This includes them into a list of very interesting objects for early searches with the first LHC data. Moreover, the Z^* bosons have unique signatures in transverse momentum, angular and pseudorapidity distributions of the final leptons, which allow to distinguish them from the other heavy neutral resonances.

PACS 12.60.Cn – Extensions of electroweak gauge sector.

PACS 13.85.Fb – Inelastic scattering: two-particle final states.

PACS 14.70.Pw – Other gauge bosons.

1. – Introduction

The method of the covariant derivatives leads to the unique minimal form of the gauge bosons couplings to the fermions. Although the gauge symmetry allows anomalous interactions in the initial Lagrangian, all known fundamental spin-1 bosons, photon, W^\pm , Z and gluons, possess only renormalizable minimal interactions with the known fermions. The anomalous interactions are considered as effective ones. They are generated on the level of the quantum loop corrections. Usually they are proportional to the additional square of a small coupling constant and can be neglected in the first-order approximation.

A different picture is realized at the low energy QCD domain, where gluon and quark degrees of freedom are substituted by physical hadronic states. The latter can be described by an effective field theory. For example, spin-1 boson states, associated with

(*) In memory of Alexei Norairovich Sissakian.

the vector fields, interact with baryons in all possible ways. So, due to strong dynamics, the vector ρ meson has both, comparable by the magnitude, minimal and anomalous couplings with $\bar{\psi}\gamma^\mu\psi$ and $\partial_\nu(\bar{\psi}\sigma^{\mu\nu}\psi)$ currents, respectively [1]. Both currents have the same quantum numbers $J^{PC} = 1^{--}$ and since the parity and charge conjugation are conserved in QCD they define the quantum numbers of the meson.

The axial-vector meson a_1 has different quantum numbers 1^{++} , which allow it also to have both a minimal interaction with $\bar{\psi}\gamma^\mu\gamma^5\psi$ current and an anomalous interaction with $\partial^\mu(\bar{\psi}\gamma^5\psi)$ current. But the most interesting is another axial-vector meson b_1 with the quantum numbers 1^{+-} . Due to the latter the meson has only anomalous interaction with the tensor current $\partial_\nu(\bar{\psi}\sigma^{\mu\nu}\gamma^5\psi)$. In fact, this QCD feature can be applied to the electroweak physics as well. We will see how it plays a key role below.

Let us assume that the electroweak gauge sector of the Standard Model (SM) is extended by a doublet of new spin-1 *chiral* bosons \mathbf{W}_μ^* with the internal quantum numbers of the SM Higgs boson. They can originate, for example, from the extensions of the SM such as Gauge-Higgs unification, larger gauge groups [2] or technicolor models. However, due to the lack of fully realistic models, the collider expectations for signals from these chiral bosons have not yet been studied in details. Nevertheless, it is possible to point out several model-independent and unique signatures, which allow to identify the production of such bosons at the hadron colliders [3].

Since the tensor current mixes the left-handed and the right-handed fermions, which in the SM are assigned to the different representations, the gauge doublet should have only anomalous interactions:

$$(1) \quad \mathcal{L}^* = \frac{g}{M} \left(\partial_\mu W_\nu^{*-} \quad \partial_\mu \bar{W}_\nu^{*0} \right) \cdot \bar{D}_R \sigma^{\mu\nu} \begin{pmatrix} U_L \\ D_L \end{pmatrix} + \frac{g}{M} \begin{pmatrix} \bar{U}_L & \bar{D}_L \end{pmatrix} \sigma^{\mu\nu} D_R \cdot \begin{pmatrix} \partial_\mu W_\nu^{*+} \\ \partial_\mu W_\nu^{*0} \end{pmatrix},$$

where M is the boson mass, g is the coupling constant of the $SU(2)_W$ weak gauge group, and U and D generically denote up-type and down-type leptons and quarks⁽¹⁾. The bosons, coupled to the tensor quark currents, are some types of *excited* states as far as the only orbital angular momentum with $L = 1$ contributes to the total angular momentum, while the total spin of the system is zero. This property manifests itself in their derivative couplings to fermions and in the different chiral structure of the interactions in contrast to the minimal gauge interactions.

For simplicity in (1) we have introduced only interactions with the down-type right-handed singlets, D_R . The coupling constant is chosen in such a way that in the Born approximation all partial fermionic decay widths of the well-known hypothetical W' boson with the SM-like interactions

$$(2) \quad \mathcal{L}'_{CC} = \frac{g}{\sqrt{2}} W_\mu'^- \cdot \bar{D}_L \gamma^\mu U_L + \frac{g}{\sqrt{2}} \bar{U}_L \gamma^\mu D_L \cdot W_\mu'^+$$

and the charged $W^{*\pm}$ boson with the same mass are identical.

In the same way as in many of the SM extensions several Higgs doublets are introduced the realistic model could include several gauge doublets. Using the charge-conjugated

⁽¹⁾ Here we assume also universality of lepton and quark couplings with different flavors.

doublet

$$(3) \quad \mathbf{W}_\mu^{*c} = \begin{pmatrix} \overline{W}_\mu^{*0} \\ -W_\mu^{*-} \end{pmatrix}$$

(or new ones with the hypercharges opposite to the \mathbf{W}_μ^* doublet) it is possible to construct more complicated models including up-type right-handed singlets, U_R , as well.

2. – The model

The minimal set of the chiral heavy bosons in the proposed extension of the SM consists of the four spin-1 particles: the two charged $W^{*\pm}$ states and the two neutral CP -even $Z^* = (W^{*0} + \overline{W}^{*0})/\sqrt{2}$ and CP -odd $\tilde{Z}^* = (W^{*0} - \overline{W}^{*0})/\sqrt{2}i$ combinations. The corresponding Lagrangian for the neutral states reads

$$(4) \quad \mathcal{L}_{\text{NC}}^* = \frac{g}{\sqrt{2}M} \left(\bar{D}\sigma^{\mu\nu}D \cdot \partial_\mu Z_\nu^* + i\bar{D}\sigma^{\mu\nu}\gamma^5 D \cdot \partial_\mu \tilde{Z}_\nu^* \right).$$

In the present paper we will discuss only the resonance production of the neutral heavy bosons and their subsequent decay into a pair of the light charged leptons. This process is the “golden channel” for early discovery at the hadron colliders. However, in this case it is impossible to discriminate the multiplicative quantum numbers of the neutral bosons, namely P and C , due to their identical signatures. Therefore, in the following calculations we will consider only one of them, for instance, Z^* boson.

In order to compare the experimentally accessible distributions between the tensor couplings and the vector ones, we introduce topologically analogous but minimal gauge interactions of the Z' boson

$$(5) \quad \mathcal{L}'_{\text{NC}} = \frac{g}{2} \bar{D}\gamma^\mu D \cdot Z'_\mu.$$

In the Born approximation eqs. (4) and (5) lead to the same cross-sections for the hadro-production and decay of both neutral heavy bosons, $Z^*(\tilde{Z}^*)$ and Z' , when they have the same mass. As we have assumed, the lepton and the quark couplings are characterized by the same coupling constant, g , of the $SU(2)_W$ weak gauge group. So, the leptonic branching ratio is $\mathcal{B}(Z^*/Z' \rightarrow \ell^+\ell^-) = 1/12 \approx 8\%$ and the total fermionic decay width

$$(6) \quad \Gamma = \frac{g^2}{4\pi} M \approx 0.034 M$$

is around 3% of the mass of the resonance.

All calculations we carried out in the framework of the CompHEP package [4]. To this end a new model has been implemented, which includes additional new bosons and their corresponding interactions.

3. – Numerical simulations for neutral bosons

Up to now, the excess in the Drell-Yan process with high-energy invariant mass of the lepton pairs remains the clearest indication of a new heavy boson production at the

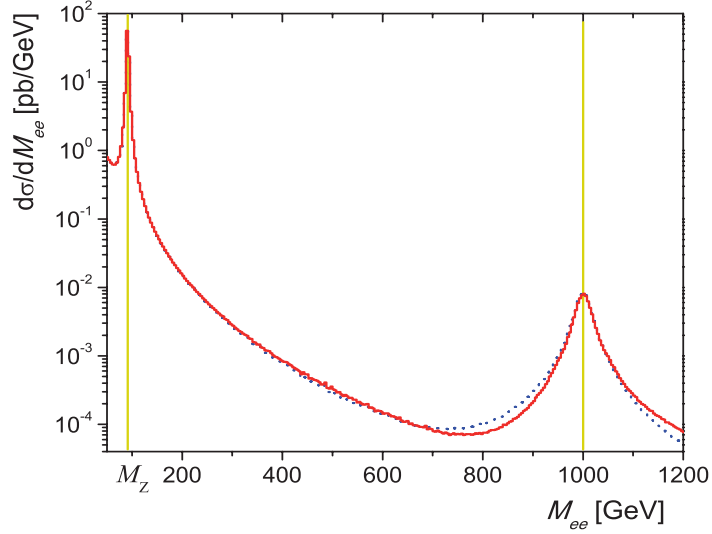


Fig. 1. – The invariant dilepton mass distributions for the Z' boson (dotted) and the chiral excited Z^* boson (solid) with the Drell-Yan SM background (from the photon and the Z boson) at the LHC for $\sqrt{s} = 10$ TeV.

hadron colliders on the early stage. Therefore, we will concentrate on the production and decay of the neutral bosons, where the full kinematics is experimentally reconstructible. In the following we will use the CompHEP package [4] for the numeric calculations of various distributions for the inclusive processes $pp \rightarrow \gamma/Z/Z^*/Z' \rightarrow \ell^+\ell^-$ with a CTEQ6L choice for the proton parton distribution set. For both final leptons we impose angular cuts relevant to the LHC detectors on the pseudorapidity range $|\eta_\ell| < 2.5$ and the transverse momentum cuts $p_T > 20$ GeV.

Since the current direct constraints from the D0 and CDF Collaborations place a lower bound on the mass of new heavy neutral resonances decaying into light lepton pairs about 1 TeV, we set $M \geq 1$ TeV. For the high dilepton masses the cross sections of the new boson productions with $M = 1$ TeV at the peaks are about two orders of magnitude higher than the corresponding Drell-Yan background (fig. 1). Therefore, the peak should be clearly visible.

For an estimation of the statistical significance of expected signal we can use the simplest “number counting” approach, which is based on the expected rate of events for the signal, s , and background processes, b . The significance can be calculated by the formula

$$(7) \quad S_{cL} = \sqrt{2 \left((s+b) \ln \left(1 + \frac{s}{b} \right) - s \right)}$$

according to the method presented in Appendix A of ref. [5], which follows directly from the Poisson distribution.

We will focus on the LHC reach with an integrated luminosity of up to 100 pb^{-1} of data at $\sqrt{s} = 10$ TeV. As far as the center-of-mass energy for the 2010–2011 runs is 7 TeV , at which the cross-sections are roughly two times lower, 200 pb^{-1} of data will be equivalent to the first scenario. In order to estimate the discovery potential and the

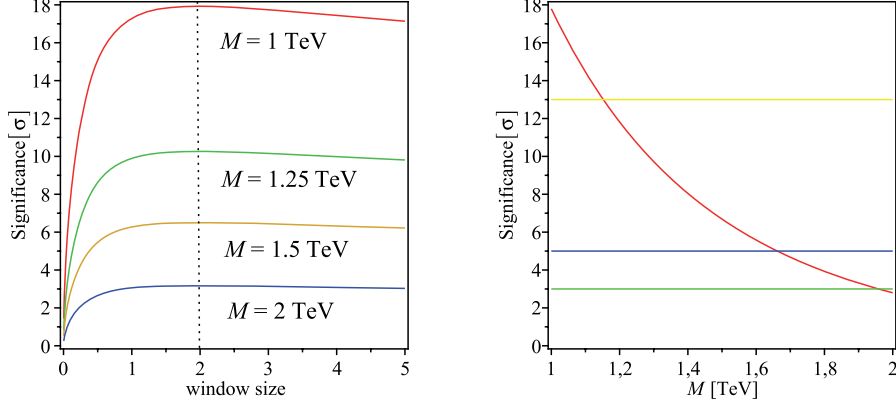


Fig. 2. – Left: the signal significance as a function of the window size is given for the different masses. Right: the Z^* boson discovery potential at $\sqrt{s} = 10$ TeV for 100 pb^{-1} .

exclusion limit for the first LHC data, we need to generate several samples for different resonance masses. In the “number counting” approach, we simply count the expected number of events within some window under the resonance including the background. The optimal window size $[M - 2\Gamma, M + 2\Gamma]$ can be guessed from the left panel of fig. 2.

For different Z^* masses the statistical significance of the expected signal can be evaluated using window size $\pm 2\Gamma$ around the resonance positions (the right panel of fig. 2). The lowest horizontal line in this plot corresponds to 3σ level and shows the evidence for discovery, which can be obtained for the resonance masses up to 2 TeV. The middle horizontal line shows the discovery potential at 5σ level for the masses of the chiral bosons up to 1.65 TeV.

The peaks in the invariant mass distributions originate from the Breit-Wigner propagator form, which is the same both for Z' and Z^* bosons in the leading Born approximation. Therefore, in order to discriminate them we need to investigate additional

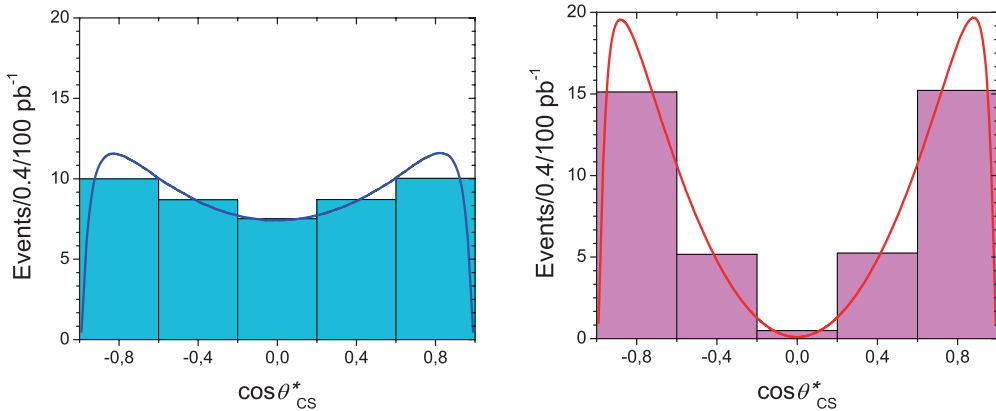


Fig. 3. – The differential distributions of the gauge Z' boson (left) and the chiral excited Z^* boson (right) as functions of $\cos \theta_{CS}^*$ for $M = 1$ TeV.

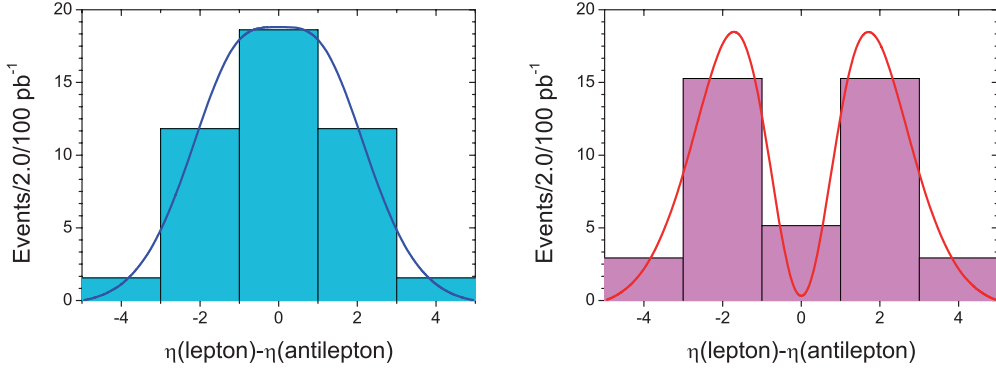


Fig. 4. – The differential distributions for the gauge Z' boson (left) and the chiral excited Z^* boson (right) as functions of the difference of the lepton pseudorapidities for $M = 1$ TeV.

distributions selecting only “on-peak” events with the invariant dilepton masses in the chosen range $[M - 2\Gamma, M + 2\Gamma]$. According to paper [6] a crucial difference between the chiral bosons and other resonances should come from the analysis of the angular distribution of the final-state leptons with respect to the boost direction of the heavy boson in the rest frame of the latter (the Collins-Soper frame [7]) (fig. 3).

Indeed, the angular distribution for the Z^* bosons will lead to the large negative value of the centre-edge asymmetry A_{CE} [8],

$$(8) \quad \sigma A_{CE} = \int_{-\frac{1}{2}}^{+\frac{1}{2}} \frac{d\sigma}{d \cos \theta_{CS}^*} d \cos \theta_{CS}^* - \left[\int_{+\frac{1}{2}}^{+1} \frac{d\sigma}{d \cos \theta_{CS}^*} d \cos \theta_{CS}^* + \int_{-1}^{-\frac{1}{2}} \frac{d\sigma}{d \cos \theta_{CS}^*} d \cos \theta_{CS}^* \right],$$

while the distributions of other known resonances (even with different spins) possess positive or near to zero asymmetries. The corresponding calculations show that for resonance masses up to 1.15 TeV it is possible to disentangle between the most interesting cases of Z^* and Z' resonances (horizontal upper line in the right-hand plot of fig. 2). Another “unexpected” consequence of the new angular distribution is shown in fig. 4. Combining these distributions should allow to differentiate these bosons for higher resonance masses.

To estimate the exclusion limit for given statistics we will apply simple considerations. For example, if looking for an excess in the invariant dilepton mass distribution with chosen window above 1 TeV, we do not find any event (which is in agreement with the SM), then it is still allowed for 3 signal events to fluctuate down to 0 with a probability of 5%. It means that the resonances up to masses 1.65 TeV, which should give more than 3 events, will be excluded at 95% confidence level.

4. – Remarks on the charged bosons case

The cleanest method for discovery of the charged heavy bosons at the hadron colliders is the detection of their subsequent leptonic decays into isolated high transverse-momentum leptons without a prominent associated jet activity. In this case they can be

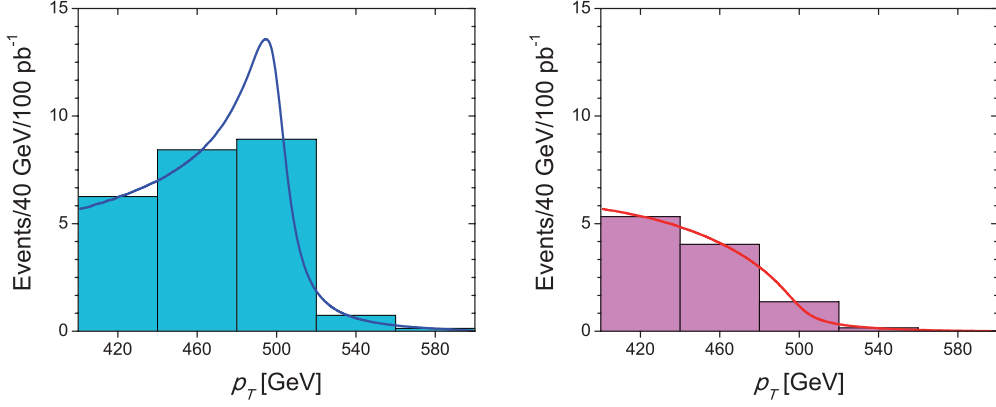


Fig. 5. – The differential distributions for the Z' boson (left) and the chiral excited Z^* boson (right) as functions of the lepton transverse momentum p_T for $M = 1$ TeV.

observed through the Jacobian peak in the transverse momentum distribution. It has become proverbial (see, for example, the textbook [9]) that the Jacobian peak is characteristic of all two-body decays. However, it is not the case for the decay of the new chiral bosons [10].

It has been found in [11] that tensor interactions lead to a new angular distribution of the outgoing fermions

$$(9) \quad \frac{d\sigma(q\bar{q} \rightarrow Z^*/W^* \rightarrow f\bar{f})}{d\cos\theta} \propto \cos^2\theta,$$

in comparison with the well-known vector interaction result

$$(10) \quad \frac{d\sigma(q\bar{q} \rightarrow Z'/W' \rightarrow f\bar{f})}{d\cos\theta} \propto 1 + \cos^2\theta.$$

It was realized later [10] that this property ensures a distinctive signature for the detection of the new interactions at the hadron colliders. At first sight, the small difference between the distributions (9) and (10) seems unimportant. However, the absence of the constant term in the first case results in new experimental signatures.

The angular distribution for vector interactions (10) includes a nonzero constant term, which leads to the kinematical singularity in p_T distribution of the final fermion

$$(11) \quad \frac{1}{\cos\theta} \propto \frac{1}{\sqrt{(M/2)^2 - p_T^2}}$$

in the narrow width approximation $\Gamma \ll M$

$$(12) \quad \frac{1}{(s - M^2)^2 + M^2\Gamma^2} \approx \frac{\pi}{M\Gamma} \delta(s - M^2).$$

This singularity is transformed into a well-known Jacobian peak due to a finite width of the resonance. In contrast to this, the pole in the decay distribution of the Z^*/W^* bosons

is canceled out and the fermion p_T distribution even reaches zero at the kinematical endpoint $p_T = M/2$ (fig. 5).

The Z^*/W^* boson decay distribution has a broad smooth hump with the maximum below the kinematical endpoint, instead of a sharp Jacobian peak. Therefore, in contrast to the usual procedure of the direct and precise determination of the resonance mass the new distribution does not allow to do it. Moreover, a relatively small decay width of the chiral bosons leads to a wide distribution, that obscures their identification as resonances at hadron colliders.

5. – Conclusions

In conclusion we would like to stress that the new type of spin-1 chiral bosons can exist. They are well motivated from the hierarchy problem point of view and are predicted by at least three different classes of theories that represent different approaches for explaining the relative lightness of the Higgs doublets. The decay distributions of the chiral bosons differ drastically from the distributions of the known gauge bosons. Therefore, the discovery of such type of distributions will point out to an existence of a compositeness, of a new symmetry and, even, of extra dimensions.

* * *

The authors thank the organizers, G. BELLETTINI, G. CHIARELLI, M. GRECO and G. ISIDORI for the invitation and highly appreciate the possibility to present the results of their work at Les Rencontres de Physique de la Vallée d'Aoste.

REFERENCES

- [1] BALL P. and BRAUN V. M., *Phys. Rev. D*, **54** (1996) 2182; BECIREVIC D. *et al.*, *JHEP*, **05** (2003) 007; BRAUN V. M. *et al.*, *Phys. Rev. D*, **68** (2003) 054501; CHIZHOV M. V., *JETP Lett.*, **80** (2004) 73.
- [2] CHIZHOV M. V. and DVALI G.I.A., arXiv:0908.0924 [hep-ph].
- [3] CHIZHOV M. V., BEDNYAKOV V. A. and BUDAGOV J. A., *Phys. Atom. Nucl.*, **71** (2008) 2096, arXiv:0801.4235 [hep-ph].
- [4] BOOS E. *et al.* (COMPHEP COLLABORATION), *Nucl. Instrum. Methods A*, **534** (2004) 250, hep-ph/0403113; PUKHOV A. *et al.*, INP MSU report 98-41/542, hep-ph/9908288; Home page: <http://comphep.sinp.msu.ru>.
- [5] BAYATIAN G. L. *et al.* (CMS COLLABORATION), *J. Phys. G*, **34** (2007) 995.
- [6] CHIZHOV M. V., arXiv:0807.5087 [hep-ph].
- [7] COLLINS J. C. and SOPER D. E., *Phys. Rev. D*, **16** (1977) 2219.
- [8] GOUNARIS G., LAYSSAC J., MOULTAKA G. and RENARD F. M., *Int. J. Mod. Phys. A*, **8** (1993) 3285.
- [9] BARGER V. D. and PHILLIPS R. J. N., *Collider Physics* (Addison-Wesley Publishing Company) 1987.
- [10] CHIZHOV M. V., hep-ph/0609141.
- [11] CHIZHOV M. V., hep-ph/0008187.

SESSION VIII - PHYSICS AND SOCIETY

Rajan Gupta

The Global Energy Observatory: A one-stop site for information on global energy systems

The Global Energy Observatory: A one-stop site for information on global energy systems

R. GUPTA

Theoretical Division, Los Alamos National Laboratory - Los Alamos, New Mexico, USA

(ricevuto il 14 Settembre 2010; pubblicato online il 12 Gennaio 2011)

Summary. — This paper reviews the energy-development-environment-climate challenge that the world faces and makes a case for why we need to act with urgency and collectively to address it. It introduces an open web-based tool called the Global Energy Observatory (GEO) that is being developed as a moderated wiki to serve as a one-stop site for information on energy systems. GEO's purpose is to help experts and the public understand the dynamics of change in the highly complex network of energy systems and to help accelerate the transition to carbon-neutral and sustainable systems.

PACS 88.05.-b – Energy analysis.

PACS 88.05.Bc – Energy efficiency; definitions and standards.

PACS 88.05.Np – Environmental aspects.

PACS 88.05.Jk – Policy issues; resource assessment.

1. – The Energy-Development-Environment-Climate (EDEC) challenge

The second half of the twentieth century was phenomenally successful in raising the living standards of over two billion people to unprecedented levels. The scientific and technological innovations, advances in all branches of arts and sciences, and maturation of institutions (social, economic, political) that facilitated this rapid transition are too numerous to recount. The issue I will focus on is energy: a key enabler of this development. During the 20th century the ability to harness the chemical energy stored in fossil fuels (oil, natural gas and coal) and convert it to electric energy and transportation fuels was exploited at gigaton scale. Today the world has over \$40 trillion invested in fossil-fuel based energy infrastructure that continues to provide electric power and transportation at relatively low cost. In spite of the environmental consequences, this growth is hard to argue against since, by the year 2000, about 2.2 billion people (the entire population of the world in 1950) became empowered to live the modern dream: they and their children have the opportunities and support systems to realize their full potential. The energy-development-environment-climate (EDEC) challenge for the 21st century can be summarized by the following three questions:

- Is the fossil-fuel driven path to development and maintaining the standard of living enjoyed by 2.2 billion people sustainable in terms of availability of resources and the impacts of the use of fossil fuels on the environment and the climate?
- Can this standard of life be made available to the current world population of about 6.8 billion and by 2060 to the anticipated 10–11 billion people?
- If the historic fossil-fuel driven growth is not sustainable and reducing CO₂ emissions becomes a global imperative, then what are the carbon-neutral and cost-effective alternatives, R&D and investments needed, and window of time available?

I will attempt to address these questions broadly and, with apologies to many, not delve into details and many important issues. Let me start by first briefly addressing the phenomena of peak oil. I give four reasons for why discussions centered around “peaking” are not compelling motivators for change:

- It is amply demonstrated that any non-renewable reservoir (mine, field, region) exhibits a peak in the rate of extraction. Viewed from this perspective “peaking” is a feature of extraction valid for all non-renewable finite resources of any size.
- The timing, shape and magnitude of this peak depends on many factors such as the technology available, the cost of extraction and delivery, the demand, regulatory environment, and social and political pressures. It is the reduction of this multitude of factors into a phenomenological model that leads to predictions such as Hubbert’s curve for peak oil. These projections are *real and very important* but can be changed if there is social and political will. For example, Saudi Arabian government has the reserves, control, and financial resources to double its oil production. Whether or not it chooses to make the investments to do so depends on the above factors.
- Fossil fuels are fungible but not equivalent in value, the pollution they cause, and emissions. Ordered by their overall value today they are oil, heavy oil, natural gas, tar sands, coal, shale, peat, clathrates, etc. The global sum of their known resources could guarantee the world a few hundred years energy supply. Thus, scientifically, the question one can ask is how much oil would be produced from all possible resources if there was a guaranteed floor price of say \$60 per barrel. The problem we are grappling with is how to include into the calculation all the direct and indirect costs including impacts on the environment and the climate.
- The geographic distribution of fossil fuels is very uneven with three regions (North America, Persian Gulf, and Russia) holding about 70% of the reserves. Thus, for many, it is a problem of distribution and not scarcity. Wind and solar resources too are uneven and not located close to demand centers. This uneven distribution raises the more serious and immediate concerns of economic and national security.

Given these facts many people feel there is no energy crunch—to them it is simply a matter of opening new areas to harvest plentiful resources especially in North America, Russia and the Persian Gulf and letting prosperity drive innovation so that technological solutions emerge in time before these resources run out. The EDEC challenge then is: can such accelerated exploitation of resources be extended to all resources needed to maintain affluent lifestyles including natural (fossil fuels, ores, important trace minerals), water, environmental, and biosphere resources and sustained for at least the next 50 years?

The second knotty issue whose discussion I will also short-change is that of the scale and timing of the impacts of anthropogenic emissions of greenhouse gases (GHGs)—the climate change challenge. Said differently, even if there was unlimited supply of fossil fuels, do/will we have the time and resources to arrest and mitigate the impacts of pollution and climate change. Again, I briefly summarize my understanding of the subject and provide the basic arguments for why I am convinced that we have to start addressing and implementing climate change mitigation and adaptation strategies *now*.

- A number of gases such as CO₂, CH₄, O₃, N₂O, are emitted when fossil fuels are extracted and combusted and these contribute to the greenhouse effect. While their quantities, lifetimes in the atmosphere and magnitude of effect differ by orders of magnitude, they all provide a positive radiative forcing that heats the Earth.
- CO₂ is of most serious concern because i) the scale of emissions is enormous, currently about 30 gigatons per year; ii) it is the highest oxidized form of carbon and nature processes CO₂ slowly, mainly through photosynthesis, mineralization and absorption by water in oceans. These processes cycle only about 16 gigatons per year. iii) The remainder, about 14 gigatons of CO₂ per year, gives rise to increase in concentration in the atmosphere by about 1.8–2.0 ppm per year since 2000 (the Keeling curve). Thus nature is able to recycle only about half the current emissions. iv) At this accumulation rate deep oceanic water is the primary remaining reservoir but its time scale to cycle CO₂ is thousands of years. Thus, to first approximation, half of all CO₂ emissions will continue to accumulate, and this fraction may increase due to non-linear feedbacks. v) There are no easy or cost-effective technologies available to remove CO₂ from the atmosphere at this scale. Carbon Capture and Sequestration (CCS) from point sources such as power plants is still a field in its infancy and CCS will add significant cost. Thus, any CCS mitigation strategy, if feasible at gigatons scale, will have to be developed over many decades. vi) There are other contributors, both positive and negative, to radiative forcing including aerosols and black carbon. Their emission rate can be changed dramatically over a ten-year period through regulations mandating scrubbers since relatively cost-effective technologies are available and have been demonstrated at scale by many developed countries. There is concern that their combined impact may be to mask the full radiative forcing of CO₂, in which case the predicted warming could be much worse once the desired-for regulations restricting their emissions are enforced globally. For these reasons climate change mitigation strategies focus on CO₂.
- Our current understanding is that every 100 ppm increase in atmospheric concentration of CO₂ will lead to 0.8–1.0°C rise in temperature; and a further 2°C rise in average surface temperature could be disastrous for many parts of the (highly populated) world. It is this part of the argument that has attracted the largest debate because untangling the various radiative forcings and converting radiative forcing into consequences (temperature rise, changes in weather and biosphere) has been hard and with large uncertainties due to the complexities of the various factors and their interactions and feedbacks. I am convinced by the growing body of scientific evidence of the connection between use of fossil fuels, increase in GHGs and temperature rise. I, therefore, advocate action to reduce emissions of GHGs.
- Many of these natural phenomena have multiple feedback loops that we do not fully understand, and worse we have almost no knowledge of when non-linearities

in them will start to grow significantly. Thus, we have little or no knowledge of the onset of runaway solutions, *i.e.* points in time (or CO₂ concentration), when we will not have the technical or the financial resources to put into place mitigation and adaptation strategies even if social and political will to take action could be generated globally. This very high impact possibility calls for *urgency in action*.

With this current understanding of the EDEC challenge, and the need to share development (rather than condemn 50% of world population to poverty), the question is: what should our strategy be to simultaneously address development, environmental stewardship and mitigation/adaptation to climate change? Before discussing options it is useful to discuss the scale of change required to appreciate the magnitude of the challenge.

2. – What constitutes a part of the solution?

History demonstrates clearly that while people will transition rapidly to non-polluting forms of energy given a chance, in need they will also use any and all fuels available. The problem with fossil fuels is that they are amazing! They are unsurpassed in terms of their energy density (both gravimetric and volumetric), portability, safety and ease of use, and power density (rate of heat delivery). While many innovative and entrepreneurial people will continue to invent novel ways to exploit alternate resources and develop niche markets, in the long run they have to address the comparative issues of scale, density, intermittency and life-cycle cost. The question is not if a given technology will sell and be profitable, but whether it is sustainable and can cost-effectively scale up to global needs. The two scales that, to my mind, constitute a part of the “solution” are:

- *1 terawatt for electric power:* To provide 21st century opportunities to 10 billion people will require about 7–10 terawatts of electric generation capacity; the range reflecting uncertainty in how much more energy efficient industrial processes, gadgets and lifestyles become. This is 2.5-3.5 times the current capacity. To meet this demand and reach my criteria of a “solution”, *i.e.* 1 TW, nuclear power (current fleet of 438 reactors with 372 Gigawatts capacity) would have to grow by a factor of 2.7! Hydroelectric installed capacity is about 800 GW globally and unlikely to even double as the most productive sites have already been exploited. Today, only fossil fuel based generation, with about 2 terawatts installed capacity, qualifies. Geothermal heat pumps for home airconditioning are cost-effective, as is utility scale wind where the intermittency and transmission issues have been addressed.
- *10 million barrels a day (Mbd) for liquid fuels:* The second leading source of liquid fuels after oil are biomass derivatives (ethanol, biodiesel and green diesel) at about 1.5 Mbd. They contribute about 2% of the 85 Mbd used globally. Even if we are able to improve liquid fuel efficiency in the transport sector by a factor of three globally, the demand will not decrease significantly if 10 billion people use some form of personal liquid fuel driven transport. Thus, 85 Mbd is a reasonable target for meeting global demand and a 10 Mbd wedge a part of the “solution” if transportation continues to be driven by internal combustion engines albeit far more efficient. If fully electric cars become the norm, then the total demand for oil could reduce very significantly to about 20 Mbd, but the above projections for electric power generation capacity may need to be doubled to 14–20 terawatts.

3. – Evolutionary transformation of the current energy systems

The existing infrastructure is too large to change overnight, nevertheless it is in the midst of very significant transformation in both the developing and the developed world. In the developed world the first generation power plants (those installed before 1970) will mostly be replaced by 2020. The developing world is installing its capacity for the first time. Some specific examples of the ongoing changes are:

- *Fuel substitution:* In almost all countries thermal generation based on fuel oil is being rapidly replaced by natural gas and combined cycle gas turbines (CCGT). Examples include Mexico, Persian Gulf countries, Egypt and Israel. The main challenges are replacing coal for base load power generation and oil for transport.
- *Fuel mix:* The Asian Tigers (Japan, South Korea, Taiwan) are evolving to a roughly 40-30-30 mix, *i.e.* 40% nuclear, 30% fossil (coal and natural gas), and 30% renewables. Coal and nuclear plants provide base load. Gas turbines and hydro (conventional reservoir based, run-of-river, and pumped storage) are used to address peak demand and integrate intermittent resources such as wind and solar into the grid.
- *Efficiency:* There is growing emphasis on improving the efficiency of all coal and gas plants by transitioning to Cogen (ultra) super-critical coal and CCGT gas plants. Similarly, fuel efficiency of cars is improving and by 2020 significant penetration of the market by fully electric vehicles is considered realistic. Home appliances are increasingly more energy efficient but each home now has more gadgets.
- *Pollution control:* In this aspect the record is mixed. The developed world is installing low NO_x burners and desulphurizing units on both new and retrofit power plants, while in the developing world there is lack of consensus on their necessity, so regulations are inadequate and adoption is on case by case basis driven by cost.

These changes are all clearly in the right direction of increasing energy efficiency and decreasing carbon intensity, but their combined impact has been overshadowed by the growth in demand, consequently global emissions of CO₂ are still increasing at about 3% annually. This growth reflects the first priority of a large part of the world—to continue to address the development challenge and the needs of 4.6 billion under-served people. To simultaneously mitigate climate change will need a paradigm shift. Whether this shift is brought about by technological innovations alone or whether it also requires a change in our expectations, living standards and use of energy is a much debated question.

4. – Seven scientific grand challenges that can provide a paradigm shift

A radical change from the above market-driven incremental evolution of energy systems, *i.e.* the business-as-usual scenario, to meet climate change mitigation goals requires one or more of the following innovations to take place if technology is to provide “solutions”. In the US, competitive edge *versus* coal for any renewable power generation occurs when tariff is below \$0.10 (\$0.05) per kilowatt hour if CO₂ is (not) priced.

- *Carbon Capture and Sequestration (CCS):* For continued development based on fossil fuels, CCS is a must. Today, the cost of CO₂ separation from even point sources such as power plants is high, and enough sequestration sites with adequate capacity have not been adequately characterized nor long-term risks fully quantified.

- *Solar at \$1 per firm Watt:* Solar (both PV and thermal) technology is evolving fast, however, without any subsidies the cost of installed PV today is \$5–7 per peak Watt (or \$20–30 per realizable Watt or \$0.25–0.3 per kwh) and \$5 per Watt for thermal with 8 hours of heat storage. Furthermore, integration of large scale solar (and wind) into the grid requires overcoming the intermittency of generation issue.
- *Storage and transmission:* Wind and solar, the two cleanest resources, are intermittent and cannot provide guaranteed supply as they depend on the sun shining and the wind blowing. Two cost-effective backup systems are pumped storage hydroelectric and gas turbines, but these cannot be counted on to provide firm capacity for days as is often the case, otherwise there is no real replacement of fossil-fuel fired capacity by renewables. Current battery technology has provided a good backup solution for essential home needs, but battery packs are inadequate for say home air-conditioners. It is unlikely that conventional batteries with significantly higher charge density can be realized (they are close to explosive limits already), so one needs new concepts for energy storage. One option is storage in chemical bonds, *i.e.* mimicking photosynthesis, as discussed in the next item. To use geographical distribution of solar and wind resource to balance demand and supply over continental distances requires transporting electric energy long-distance in very large quantities. Rough estimates indicate US needing a hundred times larger long-distance transmission grid—something that is impractical using “copper” wire technology. An attractive option is superconducting technology if it can be made cost-effective and easy to deploy and maintain at the required scales.
- *H₂ and liquid fuels from photochemical or thermal splitting of water:* The cleanest chemical storage medium that can be scaled up, and comes close to fossil fuels in gravimetric energy density is hydrogen, especially if it is converted to hydrocarbons for easier storage and use. The challenge is to produce hydrogen without using fossil fuels as feed-stock. Options are photochemical splitting of water using cells with cheap, efficient and corrosion resistant electrodes (mimicking photosynthesis) or thermal splitting using high temperature gas cooled nuclear reactors.
- *Closed nuclear fuel cycle:* To deploy nuclear power at Terawatt scale, and in many more countries than the present 29, will require higher guarantees of safety at every stage of the fuel cycle and the nuclear complex, security of nuclear materials, and waste management. A closed nuclear fuel cycle is one option, but it carries the concern that any country with this technology is, *de facto*, a nuclear weapon state albeit virtual. Furthermore, cost-effective fuel processing, and an international framework for issues such as assured supply and take-back need to be worked out.
- *Tailored biomass:* The hope is biomass cultivation will not displace food (take over agricultural land) but use large tracts of marginal lands, and without further stressing water resources or significantly increasing the use of fertilizers and pesticides. Thus, biomass for fuel needs to be pest resistant, low water- and fertilizer-consuming, and easily degradable. This is a challenge for the bio-chemical industry.
- *Fusion:* The principles of fusion are known, however, in spite of very significant progress over the last 50 years, creating and maintaining extreme conditions of temperature and radiation in test and eventually commercial reactors remains a challenge for our colleagues in plasma physics, chemistry and material sciences.

A huge effort is being made globally to achieve these scientific/technological breakthroughs. The drivers are obvious—there is an enormous pot of gold at the end of this rainbow and fame for addressing the challenge of the 21st century. My belief is that there will not be *one* solution but, as history shows, a combination of *all* depending on cost and relative measure of “cleanliness” based on a life-cycle analysis. Also, many options will be profitable in niche markets (representing billions of dollars) but will not grow to the terawatt scale. My bet is that solutions to the EDEC challenge this time around, that provide ever more freedom, choice and productive lifestyles to 10–11 billion people, will not be simply technological. Society will need to redefine its priorities, needs, and measures of well-being and happiness.

Given the enormous complexity and magnitude of the EDEC challenge, what extra contribution can a high energy physicist make to help facilitate the transition? My answer has been to create a web-based tool called the Global Energy Observatory to help the public understand the development needs of countries, existing networks of energy systems and their emissions, and the dynamics of change in them, so that there is better analysis, planning, policy and execution.

5. – The Global Energy Observatory (<http://globalenergyobservatory.org>)

GEO is a web-based collaborative tool (a moderated Wiki with built in real-time analysis tools) that aims to provide a one-stop site for detailed unit-by-unit information on 29 different types of infrastructures that constitute a very large fraction of global energy systems. The relational database (MySQL) is organized into four categories:

- *Power plants:* Coal, gas, geothermal, hydro, nuclear, oil, solar PV, solar thermal, waste and wind electric generation plants.
- *Fuels and resources:* Oil and gas fields; coal and uranium mines; crude oil refineries; solar and wind potential; biomass and water resources; CO₂ sequestration.
- *Energy transmission infrastructure:* Oil and gas pipelines; coal, LNG, oil ports; rail and road and shipping links; electric power grid.
- *Consumers:* This database (under construction) will quantify demand and track consumption/demand by the industrial, commercial and residential sectors.

All infrastructure and consumption data are geospatially and time referenced. The goal is to integrate them with real-time analysis tools to understand global energy networks, emissions and the impacts on the environment, and the dynamics of change in them.

GEO is a framework for collecting data by i) harvesting open “official” databases and ii) facilitating the public to volunteer information. Data for a given infrastructure unit is entered/accessed as a web-editable page. Large structured databases are input directly using scripts. Some of the challenges of traditional wikis we are addressing are:

- Open “official” databases exist in many different formats (HTML, excel, pdf) and are often highly fragmented. GEO brings them together in one integrated system and in a structured format for archiving, databrowsing and multi-level analyses.
- Facilitate multi-level and multi-sector analysis by a comprehensive collection of data and linking associated infrastructures in the database.

- “Official” data are not complete, and updates lag by 2-5 years. To facilitate completion, the GEO framework accepts edits and volunteered information from users.
- “Official” data compilations miss the opportunity to capture a large body of high-quality data. For example, published and unpublished data collected and analyzed by academic departments, journalists, advocacy and environmental groups. Our aim is to provide these organizations with an easy to use and download compilation which, in turn, serves as sufficient motivation for them to partner in building GEO and validating the framework and databases further.
- GEO includes a framework for continuous moderation and validation of data that is analogous to peer reviewed referee system followed by scientific journals.
- We have found that both kinds of data, “official” and volunteered by the users, requires validation and verification but at different levels. We are therefore building algorithms that will run in the background to flag possible inconsistencies.

We are currently focusing on building analysis tools and collecting and analyzing data. I look forward to many of you exercising the system and providing us feedback.

6. – Things we can do today to address the EDEC challenge

In addition to educating ourselves and helping others adopt the many energy saving and less carbon intensive technologies, there are two areas that need far more public engagement and action:

- A dramatic shift from dependence on private cars to public transport, and all countries facilitating this by planning and timely implementation of efficient public transport systems. Public transport is especially important to implement in the developing world while it urbanizes to prevent unwieldy congested cities. In addition, there need to be global agreements on very aggressive fuel efficiency standards, for example, a car and small truck fleet average of 25 km per liter by 2030.
- *Population stabilization:* There remains a lack of convincing analyses that the Earth can sustain 10–11 billion people and provide all with 21st century opportunities. We must, therefore, confront the social, political and religious sensitivities and start serious discussion on whether population stabilization through education and voluntary adoption of birth control methods should be a global goal. Also, to implement current efforts in the developing world there is need for a global fund to provide all people of reproductive age free, uninterrupted and easy access to high-quality methods. Such a global fund will require about \$10 billion per year.

In my view overcoming the EDEC challenge will require assuming collective responsibility and making it a global priority. This has not yet happened. Until technological solutions emerge, countries and individuals will have to rethink the balance between profit, competitive edge and cooperation and what each of these means and what responsibility each requires. To summarize, the question we face today is age old—how many people will share the opportunities and the wealth of this planet and be its stewards? Will the answer in the 21st century be the 20th century one, about 30%, or the Utopian one, 100% of the global population?

Further reading: The online wikipedia is a good and easy to access starting point for information on fossil-fuels, Hubbert's curve and "peaking", Keeling curve, climate change, greenhouse gases, radiative forcings, energy density of fuels, solar and wind technology, energy storage and transmission technology, CCS, biomass and biofuels, nuclear fuel cycle, and fusion. Population data are available at <http://prb.org/>. A good databrowser for viewing 2009 BP statistical data is <http://mazamascience.com/>.

* * *

This work has been supported by the New Mexico Consortium and Regional Climate Initiative at Los Alamos. I would like to thank G. ISIDORI and M. GRECO for inviting me to share my understanding of this highly complex and urgent issue.

SESSION IX - PERSPECTIVES

Michael S. Zisman The muon collider

Martin L. Perl The possible detection of dark energy on earth using atom interferometry

The muon collider

M. S. ZISMAN(*)

Lawrence Berkeley National Laboratory - Berkeley, CA 94720, USA

(ricevuto il 14 Settembre 2010; pubblicato online il 12 Gennaio 2011)

Summary. — We describe the scientific motivation for a new type of accelerator, the muon collider. This accelerator would permit an energy-frontier scientific program and yet would fit on the site of an existing laboratory. Such a device is quite challenging, and requires a substantial R&D program. After describing the ingredients of the facility, the ongoing R&D activities of the Muon Accelerator Program are discussed. A possible U.S. scenario that could lead to a muon collider at Fermilab is briefly mentioned.

PACS 29.20.db – Storage rings and colliders.

Introduction

A muon-based collider would represent a powerful addition to the experimentalist's arsenal. In the U.S., design and performance evaluations for such a facility have been ongoing for more than 10 years. Until this year, this work was carried out as a coordinated program of two organizations, the U.S. Neutrino Factory and Muon Collider Collaboration (NFMCC) [1] and Fermilab's Muon Collider Task Force (MCTF) [2]. R&D program coordination has been managed by a coordinating committee comprising the management of the two groups.

At the behest of the U.S. Department of Energy (DOE) Office of High Energy Physics, these two groups are now being merged into a single entity, the Muon Accelerator Program (MAP). MAP will operate under the oversight of the Fermilab director. A MAP proposal has been submitted to DOE and a review is anticipated during 2010.

Motivation

Muon beam accelerators can address several of the outstanding accelerator-related particle physics questions. At the energy frontier, the fact that the muon, like the

(*) Work supported by U.S. Dept. of Energy, Office of Science, under contract no. DE-AC02-05CH11231.

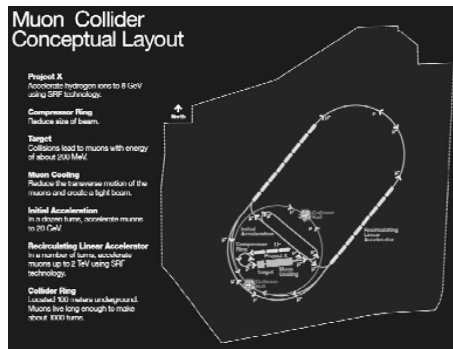


Fig. 1. – Schematic layout of muon collider on the Fermilab site.

electron, is a point particle means that the full beam energy of a muon collider is available for particle production. Because of its heavier mass compared with the electron, the muon couples strongly to the Higgs sector. Moreover, the muon emits almost no synchrotron radiation, which makes possible a circular collider that uses the expensive RF equipment efficiently and can fit on the site of an existing laboratory. Figure 1 illustrates how such an accelerator complex would fit on the Fermilab site.

A muon accelerator could also explore the neutrino sector. The high-energy neutrino beam (above the τ threshold) derived from the decay of stored muons in a ring (a “neutrino factory”) has well-understood properties, with minimal hadronic uncertainties in the spectrum and flux. Oscillations from electron to muon neutrinos give rise to easily detectable “wrong-sign” muons, that is, muons whose sign is opposite to that of the stored muon beam. This channel can be observed with low background, giving the neutrino factory unmatched sensitivity for studies of charge-conjugation–parity (CP) violation, the mass hierarchy, and unitarity in the neutrino sector.

Challenges

While there are clear advantages to making use of muon beams, there are equally clear challenges. Because muons are created as a tertiary beam ($p \rightarrow \pi \rightarrow \mu$), the production rate is low, necessitating a multi-MW proton source and a target that can withstand it. The production process also results in a beam with very large transverse phase space and energy spread, necessitating a mechanism for emittance cooling and, even so, a large acceptance downstream acceleration system.

The short muon lifetime ($2.2 \mu\text{s}$ at rest) is also challenging from an accelerator perspective. All beam manipulations must be very rapid, requiring high-gradient RF cavities that operate in a magnetic field (for the cooling channel), use of the presently untested ionization cooling technique, and a fast acceleration system.

Finally, the decaying muons produce an intense beam of decay electrons in the mid-plane of the collider ring or neutrino factory decay ring. These electrons produce a substantial heat load for the superconducting magnets and potentially create backgrounds in the collider detectors.

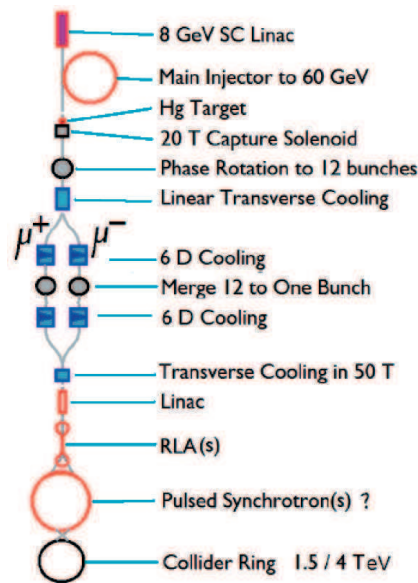


Fig. 2. – Schematic layout for muon collider.

Muon collider systems

The layout of a muon collider is illustrated schematically in fig. 2. The following systems are included:

- a 4-MW proton driver that produces the primary beam for the production target,
- a target, capture, and decay region where the pions are created, captured, and decay into muons; the MERIT experiment [3] addressed this part of the facility,
- a bunching and phase rotation section where the muons are rotated in longitudinal phase space to reduce their energy spread,
- a cooling section to reduce the transverse and longitudinal emittance of the muon beam; the MICE experiment [4] addresses the transverse cooling part of the facility,
- an acceleration section, where the muon beam energy is increased in stages from about 130 MeV to about 1 TeV,
- a collider ring where the beam is stored for ~ 500 turns.

Much of the front end of a muon collider—up to and including the transverse cooling section—is identical to what is needed for a neutrino factory. The early portion of the acceleration system is likewise identical. Because of this, the R&D program for a muon collider is largely in common with that for a neutrino factory.

Typical parameters for two muon collider scenarios are summarized in table I. The required proton driver power is about 4 MW, based on nominal transmission values. As the design is refined, this requirement will undoubtedly evolve, and could well increase.

TABLE I. – *Typical parameters of 1.5 and 3 TeV c.m. muon colliders.*

\sqrt{s} (TeV)	1.5	3
Av. luminosity/IP ($10^{34} \text{cm}^{-2} \text{s}^{-1}$)	0.77	3.4
Max. bending field (T)	10	14
Av. bending field in arcs (T)	6	8.4
Circumference (km)	3.1	4.5
No. of IPs	2	2
Repetition rate (Hz)	15	12
Beam-beam parameter/IP	0.087	0.087
β^* (cm)	1	0.5
Bunch length (cm)	1	0.5
No. bunches/beam	1	1
No. muons/bunch (10^{11})	20	20
Norm. trans. emit. (μm)	25	25
Beam size at IP (μm)	6	3
Energy spread (%)	0.1	0.1
Norm. long. emit. (m)	0.07	0.07
Total RF voltage (MV) at 805 MHz	77	886
μ^+ in collision/8 GeV proton	0.008	0.007
8 GeV proton beam power (MW)	4.8	4.3

Collider subsystems

Proton beam energy

Our simulations are based on pion production estimates for 8 GeV protons from the MARS15 code [5]. Recently, it has been shown [6] that the steep fall-off in pion production at low proton energy predicted by the code is inconsistent with experimental data from HARP [7]. The MARS15 code is presently being updated to account for the new data. While 8 GeV still appears to be a reasonable choice, lower proton energies, say 5 GeV, are likely to be acceptable.

Proton bunch length

The proton bunch length has a significant influence on the production rate. An rms bunch length of 1 ns is preferred, but bunch lengths of 2–3 ns are considered acceptable. This parameter presents a challenge for the proton driver, as achieving such short bunches is difficult at the proton energies and intensities required for a muon collider.

Proton repetition rate

The maximum proton beam repetition rate is limited by disruption of the Hg-jet target. This was studied by the MERIT experiment [3]. As shown in fig. 3, the target disruption length seen in MERIT was about 22 cm. If the jet velocity is 15 m/s, it takes about 15 ms to recover from the disruption. The nominal repetition rate adopted for a muon collider (see table I) is about 15 Hz, and that for a neutrino factory is 50 Hz. Both are compatible with the limit inferred from the MERIT data.

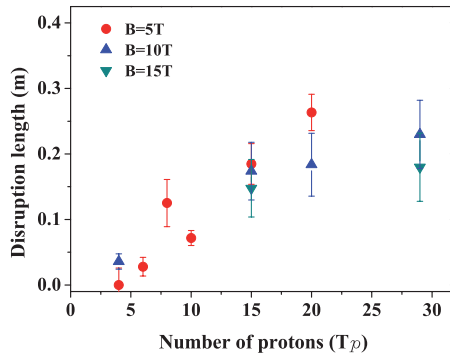


Fig. 3. – Hg target disruption length seen in the MERIT experiment.

The minimum repetition rate is limited by space-charge tune shift in the compressor ring of the proton driver. It may be possible to work around this limit to some degree by accelerating and compressing several bunches and then combining them at the target. The lower the beam energy, the more severe this limitation becomes.

Target, capture, and decay

The target, capture, and decay channel makes use of a free Hg jet contained within a tapered solenoid field, as shown in fig. 4. At the target, the solenoidal field is 20 T, falling to 1.75 T at the end of the decay channel. The channel captures low energy pions, with kinetic energies between 100 and 300 MeV.

Bunching and phase rotation

Beam from the target requires “conditioning” before it can be used in the downstream systems. The conditioning involves a rotation in longitudinal phase space (*i.e.*, trading bunch length for energy spread) and bunching the beam into 201-MHz bunches, as illustrated in the left-hand side of fig. 5. These tasks are accomplished [8] with an RF system similar to that of the cooling channel (discussed below), but having many frequencies (see right-hand side of fig. 5).

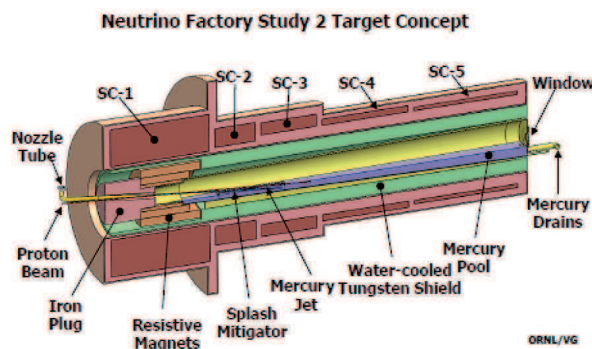


Fig. 4. – Diagram of target area showing initial portion of field taper.

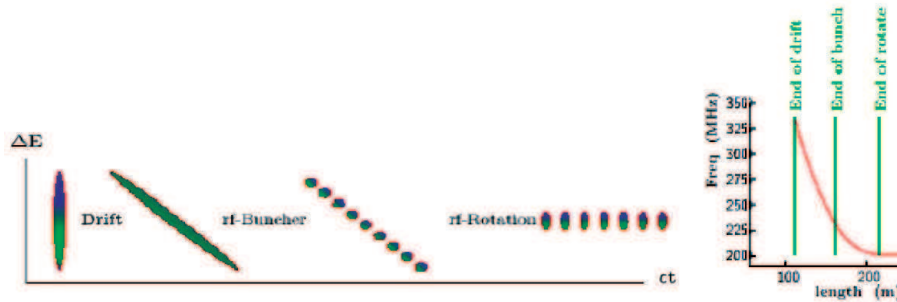


Fig. 5. – (Left) schematic of phase rotation and bunching process; (right) frequencies of RF cavities along the channel.

For a muon collider, only a few bunches are preferred, whereas a neutrino factory can accommodate more bunches. The phase rotation and bunching scheme for the collider is presently being optimized to reduce the number of bunches produced. Ultimately, the muon collider needs only a single bunch of each sign, so an additional bunch-merging operation is envisioned in the cooling channel, as indicated in fig. 2.

Ionization cooling section

This section is one of the most critical in the collider. Transverse cooling is a straightforward process, analogous to synchrotron radiation damping. In ionization cooling, the energy loss mechanism is ionization energy loss (dE/dx) in a low- Z material, which reduces p_x , p_y , and p_z . Restoration of p_z is done with RF cavities. A number of cooling channel implementations have been investigated during the past 10 years. The current baseline design is the so-called Study 2a [9] channel, illustrated in fig. 6. This channel is able to transmit muons of both signs, interleaved at opposite phases of the RF cavities. The actual implementation of such a channel is complicated, due to the proximity of RF cavities, strong solenoids, and absorbers.

For a muon collider, we must also reduce the longitudinal phase space by means of emittance exchange. The process requires creating a dispersive section where there is a correlation between a muon's energy and its position. It is then possible to arrange

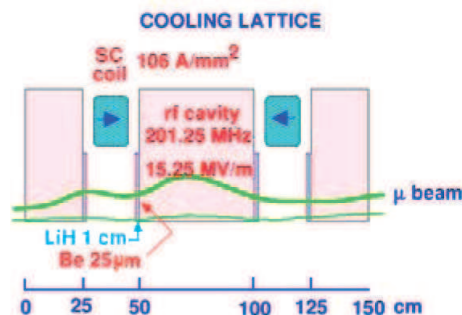


Fig. 6. – Layout of Study 2a transverse cooling channel.

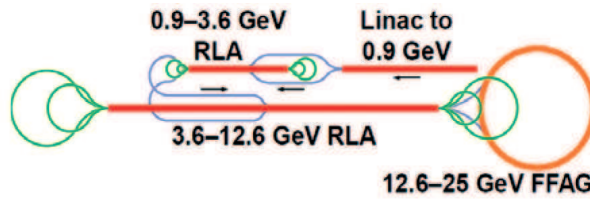


Fig. 7. – Low-energy acceleration system suitable for neutrino factory or muon collider.

for an absorber that provides more energy loss for higher energy particles than for lower energy ones, which reduces the beam energy spread.

Final cooling to an emittance of $25 \mu\text{m-rad}$ is accomplished in a linear cooling channel using very strong solenoids. Present simulations assume 50 T solenoids, which is, to say the least, on the high end of what is practical. There is no “hard edge” for this parameter, however. Lower field solenoids would work, but at the expense of the maximum luminosity of the collider.

Acceleration section

The low energy acceleration section includes a linac followed by a pair of dog-bone-shaped recirculating linear accelerators (RLAs), as illustrated in fig. 7. This system has been studied extensively [10] as part of the neutrino factory design and is capable of accommodating 30 mm-rad transverse and 150 mm longitudinal emittance, and of transmitting both muon signs.

At higher energies, a different scheme is employed. The baseline design makes use of a pair of rapid cycling synchrotrons [11], the first from 25–400 GeV, and the second from 400–750 GeV. To achieve the fast cycling rate in the lower energy RCS, the magnets must be fabricated from grain-oriented silicon steel. For the higher energy RCS, superconducting magnets are needed, but these cannot cycle rapidly. A hybrid ring has been designed (see fig. 8) with fixed-field superconducting magnets interleaved with silicon steel magnets that ramp from +1.8 T to –1.8 T in order to maintain an orbit with acceptable excursions.

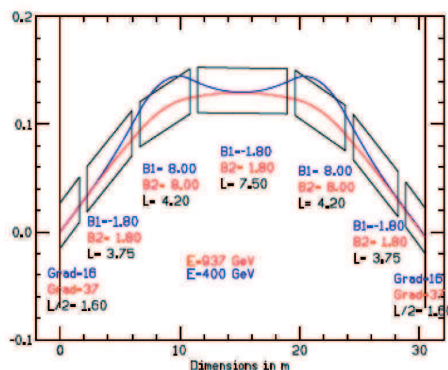


Fig. 8. – Magnet layout and beam orbits for hybrid RCS.

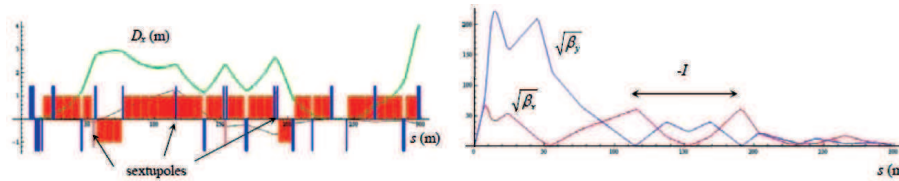


Fig. 9. – (Left) magnet layout and dispersion function for collider interaction region; (right) interaction region beta functions.

Collider ring

A lattice design for a 1.5 TeV collider is under development [12]. At the present time, the bare lattice has a dynamic aperture of 4.7σ and a momentum acceptance of 1.2%. The interaction region layout and optics are shown in fig. 9.

A key design activity is to understand the machine-detector interface. This understanding is needed to determine the ultimate physics capability of the facility and to assess and mitigate the expected backgrounds. A successful collider requires that the detector and its shielding be tightly integrated into the machine design. Help with this task from the experimental particle physics community is sorely needed.

R&D program

As mentioned earlier, a combined R&D program, MAP, has now been put in place to deliver a Design Feasibility Study (DFS) for a muon collider, technology development to support the DFS (including participation in MICE and planning for a future 6D cooling experiment), and the U.S. portion of the neutrino factory Reference Design Report being prepared under the auspices of the International Design Study for a Neutrino Factory (IDS-NF) [13]. A parallel physics and detector study for a muon collider is also being launched.

The muon collider R&D effort includes simulations, technology development, and system tests. Simulation work focuses on design and performance optimizations. Technology development includes RF cavities, magnets, and absorbers; the main focus presently is the development of high-gradient RF cavities that operate in a magnetic field. System tests are major efforts to demonstrate proof-of-principle, typically undertaken by international collaborations; both MERIT (already completed) and MICE fall in this category.

Conclusion

We have described the main features of a muon collider and indicated the scope of the supporting R&D program. A concept for the possible evolution of a muon beam accelerator complex at Fermilab is being discussed. The system would make use of the hoped-for Project X proton driver feeding the existing Recycler and Main Injector, along with a new high-power target facility, to create intense muon beams. These would be used for cooling R&D that would ultimately lead to either a muon collider, a neutrino factory, or possibly both, on the Fermilab site.

R&D toward a muon collider is making steady progress. The MERIT experiment has been completed and MICE is well under way, with all components in production. The

muon collider design is also progressing well, with a promising lattice and all of the main subsystems simulated at least partially. Finalizing the system matching details and end-to-end simulations remain to be done. Development of muon based accelerator facilities offers great scientific promise and is a worthy—and challenging—goal to pursue.

REFERENCES

- [1] See http://www.cap.bnl.gov/mumu/mu_home_page.html.
- [2] See <http://apc.fnal.gov/MUONRD/>.
- [3] KIRK H. G. *et al.*, in *Proc. EPAC 2008*, p. 2886.
- [4] ZISMAN M. S., in *Proc. 2007 Particle Accelerator Conference, Albuquerque, New Mexico, June 25–29, 2007*, p. 2996.
- [5] See <http://www-ap.fnal.gov/MARS/>.
- [6] STRAIT J., talk at *11th International Workshop on Neutrino Factories, Superbeams and Beta Beams–NuFact09, Chicago, July 20–25, 2009*, see http://nufact09.iit.edu/wg3/wg3_strait-marsvsharp.ppt.
- [7] APOLLONIO M. *et al.* (HARP COLLABORATION), *Phys. Rev. C*, **80** (2009) 035208 [arXiv:hepex/0902.2105].
- [8] NEUFFER D., *Exploration of the “High-Frequency” Buncher Concept*, NFMCC note MUC-269, <http://nfmcc-docdb.fnal.gov/cgi-bin/RetrieveFile?docid=269&version=1&filename=muc0269.pdf>.
- [9] BERG J. S. *et al.*, *Phys. Rev. ST-AB*, **9** (2006) 011001.
- [10] BOGACZ S. A., in *Proc. 11th International Workshop on Neutrino Factories, Superbeams and Beta Beams–NuFact09, Chicago, July 20–25, 2009, AIP Conf. Proc.* **1222**, p. 363.
- [11] SUMMERS D. *et al.*, *Muon Acceleration to 750 GeV in the Tevatron Tunnel for a 1.5 TeV $\mu^+ \mu^-$ Collider*, in *Proc. 2007 Particle Accelerator Conference, Albuquerque, New Mexico, June 25–29, 2007*, p. 3178.
- [12] SNOPOK P. *et al.*, in *Proc. 2007 Particle Accelerator Conf., Albuquerque, June 25–29, 2007*, p. 3483; ALEXAHIN Y., see <http://www.cap.bnl.gov/mumu/conf/collider-091201/talks/YAlexahin2-091201.ppt>.
- [13] See <https://www.ids-nf.org/wiki/FrontPage>.

The possible detection of dark energy on earth using atom interferometry

M. L. PERL(*)

*SLAC National Accelerator Laboratory
2575 Sand Hill Road, Menlo Park, California, 94025, USA*

(ricevuto il 14 Settembre 2010; pubblicato online il 13 Gennaio 2011)

Summary. — This paper describes the concept and the beginning of an experimental investigation of whether it is possible to directly detect dark energy density on earth using atom interferometry. The concept is to null out the gravitational force using a double interferometer. This research provides a non-astronomical path for research on dark energy. The application of this method to other hypothetical weak forces and fields is also discussed. In the final section I discuss the advantages of carrying out a dark energy density search in a satellite in earth orbit where an even more sensitive search can be achieved.

PACS 95.36.+x – Dark energy.

1. – Table of contents

- 1) History of concept of using atom interferometry to investigate dark energy.
- 2) Conventional beliefs about the nature of dark energy.
- 3) Comparison of dark energy density with energy density of a weak electric field.
- 4) The terrestrial gravitational force field and a possible dark energy force.
- 5) Preliminary considerations on how well we can null out g .
- 6) Our assumptions about the properties of dark energy that make the experiment feasible.
- 7) Brief description of experimental search method.
- 8) Nature of sought signal.

(*) E-mail: martin@slac.stanford.edu

- 9) Other very weak forces and fields.
- 10) This experimental search method using an earth orbit satellite.

2. – Origin of paper

This paper is a summary of the talk I presented at the Les Rencontres de Physique de la Valle d'Aoste, Results and Perspectives in Particle Physics, March 6, 2010.

3. – History of concept of using atom interferometry to investigate dark energy

The majority of astronomers and physicists accept the reality of dark energy but also believe it can only be studied indirectly through observation of the structure and motions of galaxies. Astronomical investigation of dark energy are limited by their nature to:

- Measurement of the dark energy density, ρ_{DE} .
- Search for gross variations of ρ_{DE} in the visible universe.
- Elucidation of the change in ρ_{DE} in the past.
- There is no known way to investigate the intrinsic nature of dark energy using observational astronomy.

Several years ago [1] I began to search for non-astronomical ways to investigate the nature of dark energy and realized that there was a possibility, albeit experimentally speculative, to use atom interferometry [2]. Atom interferometry is a research technology whose practice is about three decades old [3].

I was then joined in this research area by Holger Mueller of the Physics Department, University of California at Berkeley and we continue to work together [2]. This present paper recapitulates that paper [2] in sects. **1-9** and discusses three important new aspects of this research in sects. **10-12**.

- The character of our signal is noiselike because of the motion of the earth through space, sect. **10**.
- The research method is applicable to searches for hypothetical very weak forces and fields, sect. **11**.
- There are substantial advantages to eventually carrying out these searches in a satellite in an earth orbit, sect. **12**.

We use MKS units rather than astronomical units to emphasize practical laboratory experimental designs and considerations. Recall

- Critical energy density = $\rho_{\text{crit}} = 9 \times 10^{-10} \text{ J/m}^3$.
- Dark energy density = $\rho_{DE} = 0.70 \times \rho_{\text{crit}} = 6.3 \times 10^{-10} \text{ J/m}^3$.
- $\hbar = 1.054 \times 10^{-34} \text{ Js}$.
- $G = 6.67 \times 10^{-11} \text{ m}^3 \text{ kg}^{-1} \text{ s}^{-2}$.

4. – Conventional beliefs about the nature and investigation of dark energy

Present conventional beliefs about dark energy density are that it is uniformly distributed in space and that its magnitude is given by $6.3 \times 10^{-10} \text{ J/m}^3$. The usual assumption is that every cubic meter of space contains the same dark energy density so that as the visible universe expands there is more total dark energy. I find it disquieting that most physicists and astronomers are content to live with this violation of the conservation of energy, it leads to my doubts that the community has basic understanding of dark energy and has encouraged me to go in this new research direction.

$\rho_{DE} = 6.3 \times 10^{-10} \text{ J/m}^3$ initially strikes one as a very small energy density but as shown in the next section we experiment with smaller electric field energy densities in the laboratory.

5. – Comparison of dark energy density with the energy density of a weak electric field

Consider a weak electric field $E = 1 \text{ volt/m}$. Using

$$(1) \quad \rho_{\text{electric field}} = \epsilon_0 E^2 / 2,$$

$$(2) \quad \rho_{\text{electric field}} = 4.4 \times 10^{-12} \text{ J/m}^3.$$

Hence the energy density of this electric field is 100 times smaller than the dark energy density, $\rho_{DE} = 6.3 \times 10^{-10} \text{ J/m}^3$, yet this weak electric field is easily detected and measured. Thus we work with fields whose energy densities are much less than ρ_{DE} . This realization first started me thinking about the possibility of direct detection of dark energy.

Of course, it is easy to sense and measure tiny electromagnetic fields; on the other hand there are obviously severe experimental problems in detecting dark energy density.

- Unlike an electric field in the laboratory, we cannot turn dark energy on and off.
- We do not know if there is a zero dark energy field to use as an experimental reference. In the fixed value, cosmological constant, explanation of dark energy, ρ_{DE} has the same value in all space.
- Even if the dark energy density should have a gradient, what force does it exert on a material object?

6. – The terrestrial gravitational force field and a possible dark energy force

In atom interferometry the phase change of atoms depends upon the integral of the potential difference between two separate trajectories of the atom in space. Of course at present we know nothing about whether or not dark energy exerts such a force. Indeed investigating this question is one of the purposes of our proposed experiment. In analogy we designate this force as g_{DE} in units of force per unit mass.

Comments on g and g_{DE} .

- 1) The gravitational force per unit mass on earth is $g = 9.8 \text{ m/s}^2$.

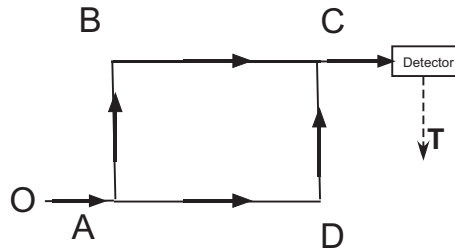


Fig. 1. – Diagram of an atom interferometer using the Mach-Zehnder concept.

- 2) Atom interferometry studies have reached a sensitivity of much better than $10^{-9}g$ in measurements of the gravitational acceleration [4] and found no anomaly. Even though a definite analysis for this has not been performed, it is probably safe to say that there is no evidence for g_{DE} at this level.
- 3) Therefore $g_{DE} \leq 10^{-8} \text{ m/s}^2$ using our assumptions about the properties of dark energy.

7. – Preliminary considerations on how well we can null out g

Based on preliminary considerations we believe we can null out g to a precision perhaps as small as 10^{-17} . This sets the smallest g_{DE} that we can investigate at 10^{-16} m/s^2 .

8. – Assumptions about the properties of dark energy that make the experiment feasible

We assume:

- A dark energy force, F_{DE} , exists other than the gravitational force equivalent of ρ_{DE} .
- F_{DE} is sufficiently local and ρ_{DE} is sufficiently non-uniform so that F_{DE} varies over a length of the order of centimeters to meters.
- F_{DE} acts on atoms leading to a potential energy V_{DE} .
- The ratio g_{DE}/g is large enough for g_{DE} to be detected in this experiment by nulling signals from g .

9. – Brief description of our experimental method

The search for F_{DE} requires the nulling of all the known forces that can change the atomic phase. The effects of electric and magnetic forces are nulled by shielding and by using atoms such as cesium in quantum states which are not sensitive to the linear Zeeman and Stark effects. The gravitational force is nulled by using two identical atom interferometers as described next.

Figure 1 is a schematic diagram of an atom interferometer using the Mach-Zehnder concept, the solid lines represent atom beams. An atom beam from source O is split at A so that each atom quantum mechanically follows the two paths ABC and ADC. At D

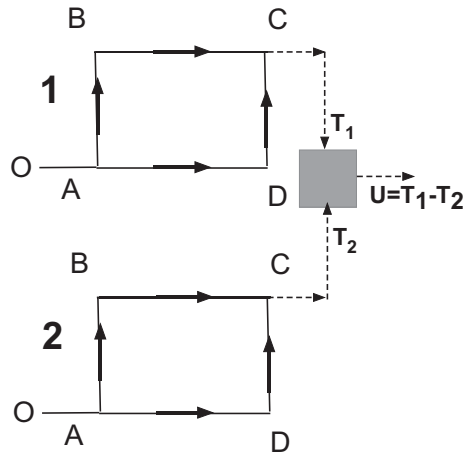


Fig. 2. – Diagram of the double atom interferometer.

the two states arrive with relative phases, ϕ_{ABC} and ϕ_{ADC} . The interference produces a signal T proportional to the phase difference $\phi_{ABC} - \phi_{ADC}$. T depends upon the potentials acting on the atoms in the space ABCD. The plane of the interferometer may be vertical or horizontal with respect to the earth's surface, our present preference is the vertical orientation.

Figure 2 shows the double apparatus schematically, two identical atom interferometers are used with the solid lines representing atom beams and the dashed lines representing signal flow. The apparatus is in the vertical orientation. Interferometers 1 and 2 produce signals T_1 and T_2 , each signal being dependent on the potentials acting on the atoms in the spaces ABCD. Considering just the earth's gravitational force \vec{g} , T is proportional to the change in gravitational potential between the upper path ABC and the lower path ADC, and thus proportional to the gravitational acceleration g .

$U = T_1 - T_2$ is given by the difference between the accelerations of free fall at the locations of the first and second interferometers. If we assume \vec{g} to be nearly constant at the earth's surface, $U = 0$ for contributions from \vec{g} , except for small corrections. Thus signals from the gravitational force are nulled by this interferometer design.

One realization of this design is a pair of fountain interferometers as described by Chung and his coworkers [4]. Even in a single interferometer, suppression of the signal due to g to the $10^{-10}g$ level has already been demonstrated by subtracting a Newtonian model of tidal variations caused by the Moon, the Sun, and the planets. Using the pair of interferometers described above, we expect to be able to cancel the effects of gravity by a factor of 10^{-17} .

10. – Nature of sought signal

Figure 3 is a schematic illustration of how inhomogeneous dark energy density could produce a non-zero signal U with a value dependent upon the degree of inhomogeneity, the force exerted by dark energy on atoms, and the configuration of the double interferometer.

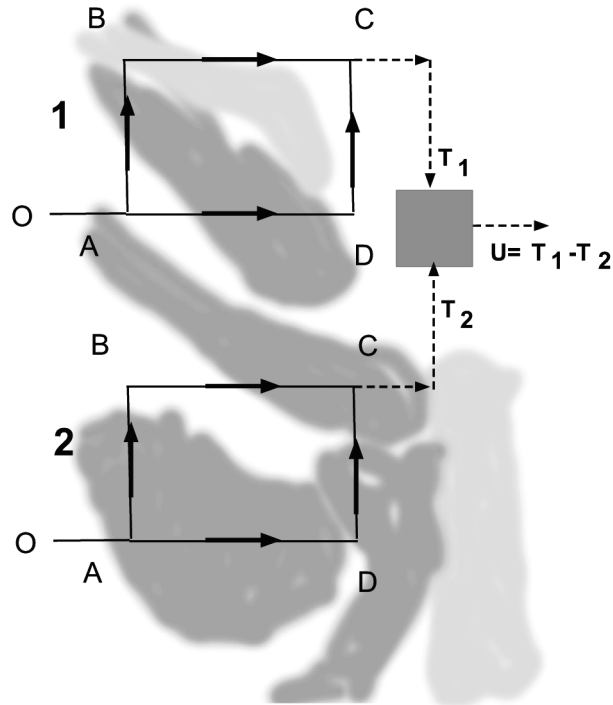


Fig. 3. – Illustration of how inhomogeneous dark energy density could produce a non-zero signal. The gray shapes represent the assumed inhomogeneity of the distribution of dark energy density.

In this experiment the interferometers are fixed to the earth. The earth is spinning and moving in the Galaxy and the Galaxy is moving in the CMB frame with a velocity about 400 km/s. Using present atom interferometer readout methods, U will be sampled at time intervals of the order of seconds to minutes. In this search dark energy density is assumed to be inhomogeneous, but of course we know nothing about what the velocity of the dark energy density might be. In any case, the dark energy clumps are not tied to the earth. Therefore the sought signal will average over many samplings of different dark energy densities and will *appear to be a noise signal*. This noise signal appearance has three consequences:

- If a noiselike signal is found from output of the double interferometer, we must show that it is not instrumental noise.
- If a noiselike signal is found, we do not know how to show that it is related to dark energy.
- As noted in the next section the absence of a non-instrumental noiselike signal puts an upper bound on some other kinds of hypothetical forces and fields that might pervade the universe.

11. – Other very weak forces and fields

My colleagues Holger Mueller and Ronald Adler have emphasized that this atom interferometry search is a general exploration of the possible existence of very weak forces, forces much weaker than gravity. Of course the criteria of inhomogeneity and an effect on matter must be met.

Incidentally, to the best of my understanding, this research method is irrelevant to the grand old problem of understanding the cosmological significance of total zero-point vacuum energy.

12. – This experimental search method using an earth orbit satellite

Stern *et al.* [5] and Ertmer and Rasael [6] have emphasized the substantially increased precision obtained by carrying out atom interferometry experiments in the microgravity environment of an earth orbit satellite. There is a second advantage using an earth orbit satellite for atom interferometry searches for dark energy and other very weak forces. The nulling of g is much easier.

* * *

I am deeply indebted to H. MUELLER and R. ADLER for their patience in educating me in subjects ranging from the design of a magnetic optical trap to the proper application of general relativity to dark energy. I am grateful to my friends in the SLAC National Accelerator Laboratory for lunch table discussions and insightful criticisms of this speculative research. I thank my partner in life, J. BEATTIE, for her willingness to accept my preoccupation with this research. This research is presently supported by Stanford University funds and by the author. The SLAC National Accelerator Laboratory is providing laboratory space and its continuing stimulating atmosphere.

REFERENCES

- [1] PERL M. L., *Int. J. Mod. Phys. A*, **24** (2009) 3426.
- [2] PERL M. L. and MUELLER H., arXiv:1001.4061.
- [3] There is a large literature on atom interferometer but no textbooks or monographs completely devoted to the subject. For practical introductions to laser cooling and atom interferometry I recommend: WIEMAN C., FLOWERS G. and GILBERT S., *Am. J. Phys.*, **63** (1995) 317; MELISH A. S. and WILSON A. C., *Am. J. Phys.*, **70** (2002) 965; FOOT C. J., *Cont. Phys.*, **36** (1991) 369; CARNAL O. and MLYNEK J., *Phys. Rev. Lett.*, **66** (1991) 2689; PETERS A. *et al.*, *Philos. Trans. R. Soc. London, Ser. A*, **355** (1997) 2223; DE ANGELIS M., *Meas. Sci. Technol.*, **20** (2009) 022001; CRONIN A. D. *et al.*, *Rev. Mod. Phys.*, **81** (2009) 1051.
- [4] CHUNG K.-Y., CHIOU S.-w., CHU S. and MUELLER H., *Phys. Rev. D*, **80** (2009) 016002.
- [5] STERN G. *et al.*, *Eur. Phys. J. D*, **53** (2009) 353.
- [6] ERTMER W. and RASAEEL E. M., *Nucl. Phys. B (Proc. Suppl.)*, **166** (2007) 307.

PARTICIPANTS

APOLLINARI Giorgio	Fermilab	USA
ARNOWITT Richard	Texas A&M University	USA
BARAK Liron	Weizmann Insitute	Israel
BASCHIERA Bruno	Aosta	Italy
BEAUCERON Stephanie	VUB Brussels	Belgium
BELLETTINI Giorgio	Università di Pisa/INFN	Italy
BENITEZ Jose	SLAC	USA
BERNAGOZZI Andrea	Oss. Astronomico della Valle d'Aosta	Italy
BERNARD Denis	LLR	France
BERTOLINI Enzo	Oss. Astronomico della Valle d'Aosta	Italy
BERTOLUCCI Sergio	CERN	Switzerland
BILLER Steven	Oxford University	UK
BILOKON Halina	INFN-LNF	Italy
BOUTOUIL Sara	Univesity Mohamed I-Oujda	Morocco
CATASTINI Pierluigi	Fermilab	USA
CHIARELLI Giorgio	INFN-Pisa	Italy
CHIZHOV Mihail	JINR/Sofia University	Bulgaria
CIOCCI Maria Agnese	Università di Siena/INFN	Italy
CIRELLI Marco	CERN/IPhT CEA/Saclay	Switzerland
COMPOSTELLA Gabriele	INFN-CNAF	Italy
COSTANTINI Flavio	INFN-Pisa	Italy
CURATOLO Maria	INFN-LNF	Italy
DAR Arnon	Technion	Israel
DE MIN Alberto	INFN-MIB	Italy
DE RUJULA Alvaro	CERN	Switzerland
DEL DUCA Vittorio	INFN-LNF	Italy
DENISOV Dmitri	Fermilab	USA
DOKUCHAEV Viacheslav	INR-Moscow	Russia
DOLGOV Alexander	Università di Ferrara	Italy
DUEHRSEN Michael	CERN	Switzerland
ELAMRI Mohamed	Univesity Mohamed I-Oujda	Morocco
ESPOSITO Bellisario	INFN-LNF	Italy
FERRONI Fernando	Università di Roma/INFN	Italy
GASTALDI Ugo	INFN-LNL	Italy
GERVINO Gianpiero	INFN-Torino	Italy
GIANOTTI Fabiola	CERN	Switzerland
GIUNTI Carlo	INFN-Torino	Italy
GOLOB Bostjan	University of Ljubljana	Slovenia
GOLUTVIN Andrei	CERN	Switzerland
GRECO Mario	INFN-Roma Tre	Italy
GREINER Daniel	University of Tübingen	Germany
GUPTA Rajan	Los Alamos National Lab	USA

IBARRA Alejandro	Technical University of Munich	Germany
IMPERIAL Albino	Aosta	Italy
INGUGLIA Gianluca	KVI-Groningen University	The Netherlands
IODICE Mauro	INFN-Roma Tre	Italy
ISIDORI Gino	INFN-LNF	Italy
ITOH Ryosuke	KEK	Japan
JACEWICZ Marek	Uppsala University	Sweden
KERZEL Ulrich	University of Cambridge	USA
KIM Young-kee	Fermilab	USA
KNÖDLSIEDER Jürgen	CESR-Toulouse	France
KONIGSBERG Jacobo	University of Florida	USA
KRAML Sabine	LPSC-Grenoble	France
LAMONT Michael	CERN	Switzerland
LATRONICO Luca	INFN-Pisa	Italy
LEONE Sandra	INFN-Pisa	Italy
MAKI Tuula	CERN	Switzerland
MARINOVA Evelina M.	INFN-Perugia	Italy
MARIOTTI Mosè	INFN-Padova	Italy
MARIŞ Ioana C.	LPNHE-Paris	France
MASIERO Antonio	INFN-Padova	Italy
MATEEV Matey	University of Sofia	Bulgaria
MELNITCHOUK Alex	University of Mississippi	USA
MERIDIANI Paolo	CERN	Switzerland
MIHARA Satoshi	KEK	Japan
NAKADAIRA Takeshi	KEK	Japan
NIERSTE Ulrich	Karlsruhe Institute of Technology	Germany
NISHIMURA Kurtis	University of Hawaii at Manoa	USA
NOVIKOV Victor	ITEP-Moscow	RUSSIA
PALESTINI Sandro	CERN	Switzerland
PALEY Jonathan	Argonne National Lab	USA
PANICO Beatrice	INFN-Roma 2	Italy
PAOLETTI Riccardo	Università di Siena/INFN	Italy
PENNACCHIO Elisabetta	IPN-Lyon	France
PERL Martin	SLAC	USA
PETERS Krisztian	University of Manchester	UK
PICOT CLEMENTE Nicolas	CPPM-Marseille	France
PIREDDA Giancarlo	INFN-Roma 1	Italy
PRINO Francesco	INFN-Torino	Italy
PUNZI Giovanni	INFN-Pisa	Italy
QUIGG Chris	Fermilab	USA
RAIMONDI Pantaleo	INFN-LNF	Italy
ROLLI Simona	Tufts University	USA
ROZEN Yoram	Technion	Israel
SCHMALTZ Martin	Boston University	USA
SCIASCIA Barbara	INFN-LNF	Italy

SICILIANO Melinda	Università di Torino	Italy
SPAGNOLO Paolo	INFN-Pisa	Italy
SPARVOLI Roberta	INFN-Roma 2	Italy
STEFANINI Arnaldo	Università di Pisa/INFN	Italy
STEWART Iain	MIT	USA
STROM Derek	University of Illinois at Chicago	USA
SUVOROV Yury	INFN-LNGS/Kurchatov	Italy
TACKMANN Frank	MIT	USA
TAKAHASHI Maiko	University of Manchester	UK
TARBERT Claire	Indiana University	USA
TENCHINI Roberto	INFN-Pisa	Italy
TRUC Fabio	Aosta	Italy
VENEZIANO Gabriele	Collège de France/CERN	France
VERDIER Patrice	IPN-Lyon	France
WANG Song-ming	Academia Sinica-Taiwan	Taiwan
WICKE Daniel	Universität Mainz	Germany
WILDAUER Andreas	IFIC-Valencia	Spain
YI Kai	University of Iowa	USA
ZISMAN Michael	LBNL	USA
ZUO Jiayu	IHEP-Beijing	China

FRASCATI PHYSICS SERIES VOLUMES

Volume I

Heavy Quarks at Fixed Target
Eds.: S. Bianco and F.L. Fabbri
Frascati, May 31–June 2, 1993
ISBN 88-86409-00-1

Volume II – Special Issue

*Les Rencontres de Physique de la Vallée d'Aoste –
Results and Perspectives in Particle Physics*
Ed.: M. Greco
La Thuile, Aosta Valley, March 5–11, 1995
ISBN 88-86409-03-6

Volume III

Heavy Quarks at Fixed Target
Ed.: B. Cox
University of Virginia, Charlottesville
October 7–10, 1994, 11
ISBN 88-86409-04-4

Volume IV

Workshop on Physics and Detectors for DAΦNE
Eds.: R. Baldini, F. Bossi, G. Capon, G. Pancheri
Frascati, April 4–7, 1995
ISBN 88-86409-05-2

Volume V – Special Issue

*Les Rencontres de Physique de la Vallée d'Aoste –
Results and Perspectives in Particle Physics*
Ed.: M. Greco
La Thuile, Aosta Valley, March 3–9, 1996
ISBN 88-86409-07-9

Volume VI

Calorimetry in High Energy Physics
Eds.: A. Antonelli, S. Bianco, A. Calcaterra, F.L. Fabbri
Frascati, June 8–14, 1996
ISBN 88-86409-10-9

Volume VII

Heavy Quarks at Fixed Target
Ed.: L. Köpke
Rhinefels Castle, St. Goar, October 3–6, 1996
ISBN 88-86409-11-7

Volume VIII

ADONE a milestone on the particle way

Ed.: V. Valente 1997

ISBN 88-86409-12-5

Volume IX – Special Issue

*Les Rencontres de Physique de la Vallée d'Aoste –
Results and Perspectives in Particle Physics*

Ed.: M. Greco

La Thuile, Aosta Valley, March 2–8, 1997

ISBN 88-86409-13-3

Volume X

Advanced ICFA Beam Dynamics

Workshop on Beam Dynamics Issue for e^+e^- Factories

Eds.: L. Palumbo, G. Vignola

Frascati, October 20–25, 1997

ISBN 88-86409-14-1

Volume XI

*Proceedings of the XVIII International Conference on
Physics in Collision*

Eds.: S. Bianco, A. Calcaterra, P. De Simone, F. L. Fabbri

Frascati, June 17–19, 1998

ISBN 88-86409-15-X

Volume XII – Special Issue

*Les Rencontres de Physique de la Vallée d'Aoste –
Results and Perspectives in Particle Physics*

Ed.: M. Greco

La Thuile, Aosta Valley, March 1–7, 1998

ISBN 88-86409-16-8

Volume XIII

Bruno Touschek and the Birth of e^+e^-

Ed.: G. Isidori

Frascati, 16 November, 1998

ISBN 88-86409-17-6

Volume XIV – Special Issue

*Les Rencontres de Physique de la Vallée d'Aoste –
Results and Perspectives in Particle Physics*

Ed.: M. Greco

La Thuile, Aosta Valley, February 28–March 6, 1999

ISBN 88-86409-18-4

Volume XV

Workshop on Hadron Spectroscopy

Eds.: T. Bressani, A. Feliciello, A. Filippi

Frascati, March 8-2 1999

ISBN 88-86409-19-2

Volume XVI

Physics and Detectors for DAΦNE

Eds.: S. Bianco, F. Bossi, G. Capon, F.L. Fabbri,

P. Gianotti, G. Isidori, F. Murtas

Frascati, November 16-19, 1999

ISBN 88-86409-21-4

Volume XVII – Special Issue

*Les Rencontres de Physique de la Vallée d'Aoste –
Results and Perspectives in Particle Physics*

Ed.: M. Greco

La Thuile, Aosta Valley, February 27-March 4, 2000

ISBN 88-86409-23-0

Volume XVIII

LNf Spring School

Ed.: G. Panzeri

Frascati, 15-20 May, 2000

ISBN 88-86409-24-9

Volume XIX

XX Physics in Collision

Ed.: G. Barreira

Lisbon June 29-July 1st. 2000

ISBN 88-86409-25-7

Volume XX

Heavy Quarks at Fixed Target

Eds.: I. Bediaga, J. Miranda, A. Reis

Rio de Janeiro, Brasil, October 9-12, 2000

ISBN 88-86409-26-5

Volume XXI

*IX International Conference on Calorimetry in
High Energy Physics*

Eds.: B. Aubert, J. Colas, P. Nédélec, L. Poggioli

Anncy Le Vieux Cedex, France, October 9-14, 2000

ISBN 88-86409-27-3

Volume XXII – Special Issue

*Les Rencontres de Physique de la Vallée d'Aoste –
Results and Perspectives in Particle Physics*

Ed.: M. Greco

La Thuile, Aosta Valley, March 4–10, 2001

ISBN 88–86409–28–1

Volume XXIII

XXI Physics in Collision

Ed.: Soo-Bong Kim

Seoul, Korea, June 28–30, 2001

ISBN 88–86409–30–3

Volume XXIV

*International School of Space Science – 2001 Course on:
Astroparticle and Gamma-ray Physics in Space*

Eds.: A. Morselli, P. Picozza

L'Aquila, Italy, August 30–September 7, 2000

ISBN 88–86409–31–1

Volume XXV

*TRDs for the 3rd Millennium Workshop on
Advanced Transition Radiation Detectors for
Accelerator and Space Applications*

Eds. N. Giglietto, P. Spinelli

Bari, Italy, September 20–23, 2001

ISBN 88–86409–32–X

Volume XXVI

KAON 2001 International Conference on CP Violation

Eds.: F. Costantini, G. Isidori, M. Sozzi

Pisa Italy, June 12th–17th, 2001

ISBN 88–86409–33–8

Volume XXVII – Special Issue

*Les Rencontres de Physique de la Vallée d'Aoste –
Results and Perspectives in Particle Physics*

Ed.: M. Greco

La Thuile, Aosta Valley, March 3–9, 2002

ISBN 88–86409–34–6

Volume XXVIII

Heavy Quarks at Leptons 2002

Eds.: G. Cataldi, F. Grancagnolo, R. Perrino, S. Spagnolo

Vietri sul mare (Italy), May 27th–June 1st, 2002

ISBN 88–86409–35–4

Volume XXIX

*Workshop on Radiation Dosimetry: Basic Technologies,
Medical Applications, Environmental Applications*

Ed.: A. Zanini

Rome, Italy, February 56, 2002

ISBN 88-86409-36-2

Volume XXIX – Suppl.

*Workshop on Radiation Dosimetry: Basic Technologies,
Medical Applications, Environmental Applications*

Ed.: A. Zanini

Rome, Italy, February 56, 2002

ISBN 88-86409-36-2

Volume XXX – Special Issue

*Les Rencontres de Physique de la Vallée d'Aoste –
Results and Perspectives in Particle Physics*

Ed.: M. Greco

La Thuile, Aosta Valley, March 9–15, 2003

ISBN 88-86409-39-9

Volume XXXI

*Frontier Science 2002 – Charm, Beauty and CP,
First International Workshop on Frontier Science*

Eds.: L. Benussi, R. de Sangro, F.L. Fabbri, P. Valente

Frascati, October 6–11, 2002

ISBN 88-86409-37-0

Volume XXXII

19th International Conference on x-ray and Inner-Shell Processes

Eds.: A. Bianconi, A. Marcelli, N.L. Saini

Università di Roma La Sapienza June 24–28, 2002

ISBN 88-86409-39-07

Volume XXXIII

Bruno Touschek Memorial Lectures

Ed.: M. Greco, G. Pancheri

Frascati, May 11, 1987

ISBN 88-86409-40-0

Volume XXXIV – Special Issue

*Les Rencontres de Physique de la Vallée d'Aoste –
Results and Perspectives in Particle Physics*

Ed.: M. Greco

La Thuile, Aosta Valley, February 29 – March 6, 2004

ISBN 88-86409-42-7

Volume XXXV

Heavy Quarks And Leptons 2004

Ed.: A. López

San Juan, Puerto Rico, 1–5 June 2004

ISBN 88–86409–43–5

Volume XXXVI

DAΦNE 2004: Physics At Meson Factories

Eds.: F. Anulli, M. Bertani, G. Capon, C. Curceanu–Petrascu,

F.L. Fabbri, S. Miscetti

Frascati, June 7–11, 2004

ISBN 88–86409–53–2

Volume XXXVII

Frontier Science 2004, Physics and Astrophysics in Space

Eds.: A. Morselli, P. Picozza, M. Ricci

Frascati, 14–19 June, 2004

ISBN 88–86409–52–4

Volume XXXVIII

II Workshop Italiano sulla Fisica di ATLAS e CMS

Eds.: Gianpaolo Carlino and Pierluigi Paolucci

Napoli, October 13 – 15, 2004

ISBN 88–86409–44–3

Volume XXXIX – Special Issue

Les Rencontres de Physique de la Vallée d’Aoste –

Results and Perspectives in Particle Physics

Ed.: M. Greco

La Thuile, Aosta Valley, February 27 – March 5, 2005

ISBN 88–86409–45–1

Volume XL

Frontier Science 2005 – New Frontiers in Subnuclear Physics

Eds.: A. Pullia, M. Paganoni

Milano, September 12 - 17, 2005

ISBN 88–86409–46–X

Volume XLI

Discoveries in Flavour Physics at e^+e^- Colliders

Eds.: L. Benussi, S. Bianco, C. Bloise, R. de Sangro, C. Gatti,

G. Isidori, M. Martini, F. Mescia, S. Miscetti

Frascati, February 28th - March 3rd, 2006

ISBN 88–86409–51–6

Volume XLII – Special Issue

*Les Rencontres de Physique de la Vallée d'Aoste –
Results and Perspectives in Particle Physics*

Ed.: M. Greco

La Thuile, Aosta Valley, March 5 - March 11, 2006

ISBN 88-86409-47-8

Volume XLIII – Special Issue

*Neutral Kaon Interferometry at A Phi-Factory: from Quantum Mechanics
to Quantum Gravity*

Ed.: A. Di Domenico

Frascati, March 24th 2006

ISBN 978 88-86409-50-8

Volume XLIV – Special Issue

*Les Rencontres de Physique de la Vallée d'Aoste –
Results and Perspectives in Particle Physics*

Ed.: M. Greco

La Thuile, Aosta Valley, February 28th - March 5th, 2007

ISBN 978 88-86409-49-4

Volume XLV Frontier Science – Science with the New Generation

High Energy Gamma-ray Experiments

Eds.: A. Lionetto, A. Morselli

Villa Mondragone, Monteporzio, Italy, June 18 -20, 2007

ISBN 978 88-86409-54-0

Volume XLVI

XII International Conference on Hadron Spectroscopy

Eds.: L. Benussi, M. Bertani, S. Bianco, C. Bloise, R. de Sangro, P. de Simone,
P. di Nezza, P. Giannotti, S. Giovanella, M.P. Lombardo, S. Pacetti

Laboratori Nazionali di Frascati, October 7-13, 2007

ISBN 978-88-86409-55-1

Volume XLVII – Special Issue

*Les Rencontres de Physique de la Vallée d'Aoste –
Results and Perspectives in Particle Physics*

Ed.: M. Greco

La Thuile, Aosta Valley, February 24th - March 1st, 2008

ISBN 978-88-86409-56-8

Volume XLVIII

*The XIV LNF Spring School “Bruno Touschek” in Nuclear,
Subnuclear and Astroparticle Physics*

Young Researchers Workshop “Physics Challenges in the LHC Era”

Ed.: E. Nardi

Laboratori Nazionali di Frascati, Frascati, May 11th - May 14th, 2009

ISBN 978-88-86409-57-5

Volume XLIX

Workshop on Monte Carlo’s, Physics and Simulations at the LHC

Ed. P. Nason

Laboratori Nazionali di Frascati, Frascati, February 27-28, 2006

ISBN 978-88-86409-58-2

Volume L – Special Issue

*Les Rencontres de Physique de la Vallée d’Aoste –
Results and Perspectives in Particle Physics*

Ed.: M. Greco

La Thuile, Aosta Valley, March 1st - 7th, 2009

ISBN 978-88-7438-053-4

Volume LI

Second Young Researchers Workshop

“Physics Challenges in the LHC Era” 2010

Ed. E. Nardi

Laboratori Nazionali di Frascati, Frascati, May 10-13, 2010

ISBN 978-88-86409-60-5

FRASCATI PHYSICS SERIES VOLUMES – Italian Collection

Collana: Scienza Aperta Vol. I (2006) - Comunicare Fisica 2005

Atti 1° Convegno “Comunicare Fisica e altre Scienze”,

Frascati, 24-27 Ottobre, 2005

Eds: Franco L. Fabbri, Piero Patteri

ISBN 88-86-409-48-6

Finito di stampare
nel mese di Gennaio 2011
Compositori Ind. Grafiche - Bologna

